The Dissertation Committee for Amr Mohamed Morsy Mohamed Certifies that this is the approved version of the following dissertation:

EVALUATION OF SOIL-REINFORCEMENT COMPOSITE INTERACTION IN GEOSYNTHETIC-REINFORCED SOIL STRUCTURES

Committee:

Jorge G. Zornberg, Supervisor

Robert B. Gilbert

Chadi S. El-Mohtar

Todd A. Helwig

Maša Prodanović

EVALUATION OF SOIL-REINFORCEMENT COMPOSITE INTERACTION IN GEOSYNTHETIC-REINFORCED SOIL STRUCTURES

by

Amr Mohamed Morsy Mohamed

Dissertation

Presented to the Faculty of the Graduate School of

The University of Texas at Austin

in Partial Fulfillment

of the Requirements

for the Degree of

Doctor of Philosophy

The University of Texas at Austin

December 2017

Dedication

This dissertation is lovingly dedicated to my family.

Acknowledgements

First and foremost, I praise God for His endless bounties and guidance through my life endeavors. He blessed me with more than I can ever comprehend.

I would like to express my heartfelt gratitude to Professor Jorge G. Zornberg, my Ph.D. dissertation adviser. He guided me to efficiently achieving the research objectives of this study. Professor Zornberg introduced me to the soil-reinforcement world through various enlightening research projects. He provided me the opportunity to meet and work with the gurus of this field. It was under his tutelage that I developed my academic vision and factors. I could not have been any prouder of my academic profile for which I owe him my eternal gratitude.

Very special appreciation goes out to the geotechnical engineering program faculty at the University of Texas at Austin, who contributed significantly to establishing my scientific and academic profiles; namely, Professor Kenneth H. Stokoe II, Professor Jorge G. Zornberg, Professor Robert B. Gilbert, Professor Ellen M. Rathje, Professor Chadi S. El-Mohtar, and Professor Brady R. Cox. Special appreciation also goes to the geotechnical engineering program faculty at Cairo University, especially Professor Manal A. Salem who was the first to introduce me to geotechnical engineering during my Bachelor's degree and Master's degree studies.

I would like to thank the research team members of the NCHRP 24-41 project whom I was honored to be among; namely, Professor Jorge G. Zornberg, Dr. Barry R. Christopher, Professor Dov Leshchinsky, Professor Jie Han, and Professor Burak F. Tanyu.

Their outstanding collaboration and performance boosted my research potentiality to a whole new level.

Special gratitude is due my Ph.D. dissertation committee members for their contribution in reviewing my Ph.D. dissertation; namely, Professor Jorge G. Zornberg, Professor Robert B. Gilbert, Professor Chadi S. El-Mohtar, Professor Todd A. Helwig, and Professor Maša Prodanović.

Sincere thanks and appreciation are due my research team comrades in the Geoenvironmental and Geosynthetics Laboratory for our fruitful debates and exchanges of knowledge and skills; in particular, Hossein Roodi, Subramanian Sankaranarayanan, Calvin Blake, and Sevket Imamoglu. I would also like to thank Federico Castro and Joe Friedrichsen for their technical assistance along the way. In addition, I would like to thank all the graduate students whom I met and interacted with during my stay in the graduate school that enriched my experience in a stimulating environment.

I would not have contemplated this path if not for my family: my father Mohamed Morsy, my mother Hoda Thakeb, and my brother Karim M. Morsy. They crafted the path that led to where I am today. They instilled within me the love of creativity, science, and language along with ethics; all of which plays a role in this dissertation.

This research was funded by the National Co-operative Highway Research Program (NCHRP). NCHRP is administered by the Transportation Research Board (TRB) and sponsored by the state departments of transportation of the American Association of State Highway and Transportation Officials (AASHTO), in co-operation with the Federal

Highway Administration (FHWA). Additional support was received from the Geosynthetic Institute (GSI) in the form of GSI fellowship.

Amr M. Morsy

5 September 2017

EVALUATION OF SOIL-REINFORCEMENT COMPOSITE INTERACTION IN GEOSYNTHETIC-REINFORCED SOIL STRUCTURES

Amr Mohamed Morsy Mohamed, Ph.D.

The University of Texas at Austin, 2017

Supervisor: Jorge G. Zornberg

Soil reinforcement has become a well-established technology, providing alternatives to an increasingly large number of critical geotechnical structures. While significant advances have been made to characterize the soil-reinforcement interaction of individual reinforcement layers, field evidence has been collected that suggests unaccounted benefits in structures where the vertical spacing between reinforcements is comparatively small. The nature of the complex interactions that may develop between contiguous reinforcement layers, possibly leading to a "composite" behavior of the reinforced soil mass, requires full characterization. The degree of interaction between adjacent reinforcement layers is expected to impact, perhaps significantly, the mechanical response of the reinforced soil mass. The added benefits from interaction among reinforcement layers would be particularly relevant for critical structures, such as reinforced soil bridge abutments and piers, reinforced soil pile platforms, and reinforced soil foundations. Accordingly, this study aims at assessing the effect of geosynthetic

reinforcements on the behavior of the surrounding soil, contiguous reinforcements, and the geosynthetic-reinforced soil mass at large.

The findings of this study on the behavior of soil-reinforcement interaction is expected to lead to practical implications such as the selection of the reinforcement vertical spacing in geosynthetic-reinforced soil (GRS) structures. The specific objectives of this research are to (1) evaluate mechanisms involved in soil-reinforcement interaction, (2) identify and characterize the shear zone of influence surrounding a reinforcement layer under tension, (3) evaluate the interaction that develops between a reinforcement and its neighboring reinforcement layers, and (4) understand and quantify the potential benefits of closely-spaced reinforcements in GRS structures.

Significant information was initially gained by reevaluating data collected from other research studies in order to assess soil-reinforcement interaction with focus on the impact of reinforcement vertical spacing on GRS structures. Specifically, a detailed evaluation of data sources was conducted, including actual experimental and field monitoring data. The data sources reevaluated in this dissertation include (1) evaluation of the performance of large-scale experimental GRS structures, (2) analysis of soil arching in GRS structures, (3) evaluation of the performance of GRS structures using geotechnical centrifuge, and (4) assessment of the performance of the Founders/Meadows GRS bridge abutments.

A state-of-the-art device was developed as part of this research to comprehensively assess the soil-reinforcement composite interaction under both working stress and failure conditions. The new equipment was able to assess the mechanical behavior of a

geosynthetic-reinforced soil mass considering varying reinforcement vertical spacings. In addition, it allowed investigating the interface shear stress transfer mechanisms. The device provided suitable measurements of the strains developed in both actively tensioned and the adjacent reinforcement layers. It allowed direct visualization of the kinematic response of soil particles adjacent to the geosynthetic reinforcement layers, which facilitated evaluation of the soil displacement field via digital image analysis. Evaluation of the soil displacement field allowed quantification of the extent of the zone of shear influence around a tensioned reinforcement layer. Finally, the device allowed monitoring of dilatancy within the reinforced soil mass, providing additional insight into the effect of reinforcement vertical spacing on the reinforced soil mass.

A comprehensive testing program was conducted using the newly developed experimental device. The testing program was tailored to evaluate the following aspects: (1) test repeatability; (2) effect of reinforced soil confinement on the soil-reinforcement composite interaction behavior; (3) effect of reinforcement vertical spacing on the soil-reinforcement composite interaction behavior; (4) effect of reinforcement properties on the soil-reinforcement composite interaction behavior; (5) effect of boundary type on the soil-reinforcement composite interaction behavior; and (6) effect of backfill properties on the soil-reinforcement composite interaction behavior. Analysis of the experimental results revealed that the existence of the zone of shear influence and its extent can be directly related to the interaction between contiguous reinforcement layers. In particular, for the uniform gravel evaluated in this study, the zone of shear measured from the soil-reinforcement interface ranged from 0.10 to 0.30 m for the normal stress range involved in

this study. It was concluded that reducing the vertical spacing between reinforcement layers in a GRS mass increases the strain compatibility between the reinforcement layers and the soil mass in between.

Table of Contents

List of Tables

List of Figures

Chapter 1: Introduction

1.1. MOTIVATION

Soil reinforcement has become a well-established technology, providing grade separation in an increasingly large number of critical geotechnical structures such as bridge abutments. While significant advances have been made to characterize the soil-reinforcement interaction of individual reinforcement layers, field evidence has been collected that suggests unaccounted benefits in structures where the vertical spacing between reinforcements is comparatively small. The nature of the complex interactions that may develop between contiguous reinforcement layers, possibly leading to a "composite" behavior of the reinforced soil mass, requires full characterization. The degree of interaction between adjacent reinforcement layers is expected to impact, perhaps significantly, the mechanical response of the reinforced soil mass. The added benefits from interaction among reinforcement layers would be particularly relevant for critical structures such as geosynthetic-reinforced soil (GRS) bridge abutments and piers, reinforced soil pile platforms, and reinforced soil foundations.

This research aims to develop an experimental approach that captures the complex interactions that take place in GRS structures: (1) the interaction between reinforcement layers and soil; and (2) the interlayer interaction between neighboring reinforcement layers. These complex interactions are referred to in this study as soil-reinforcement composite interaction. Specifically, this research assesses and characterizes the shear band at soil-reinforcement interface (zone of influence of soil-reinforcement interaction) (Figure 1.1). In addition, it evaluates the effect of reinforcement spacing on the soil-reinforcement

interaction in order to identify the reinforcement spacing below which the reinforcements and the soil behave as a composite (Figure 1.2). Figure 1.2 shows a continuum for the effect of reinforcement vertical spacing on the behavior of GRS mass with two threshold values $S_{v,cr,u}$ and $S_{v,cr,l}$ for the upper and lower vertical spacings through which the GRS behavior may change, respectively. Overall, the specific objectives of this research are to (1) evaluate mechanisms involved in soil-reinforcement interaction, (2) identify and characterize the shear zone of influence surrounding a reinforcement layer under tension, (3) evaluate the interaction that develops between a reinforcement and its neighboring reinforcement layers, and (4) understand and quantify the potential benefits of closely-spaced reinforcements in GRS structures. This study shall help refining the current design procedures to account for the effect of reinforcement spacing in GRS structures.

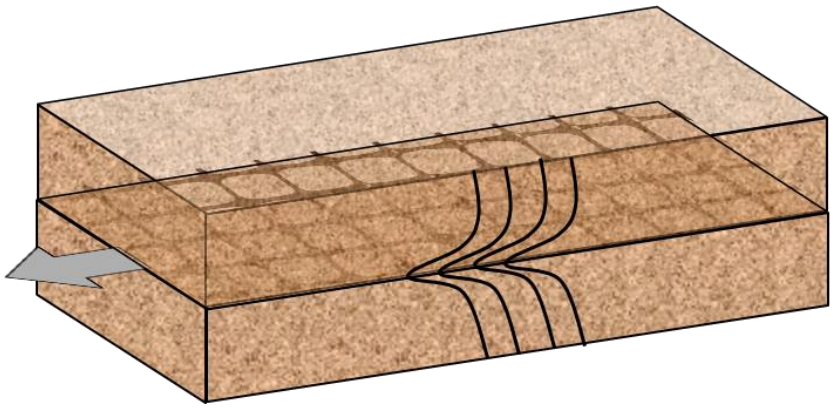

Figure 1.1. Soil-reinforcement interface shear band (zone of shear influence).

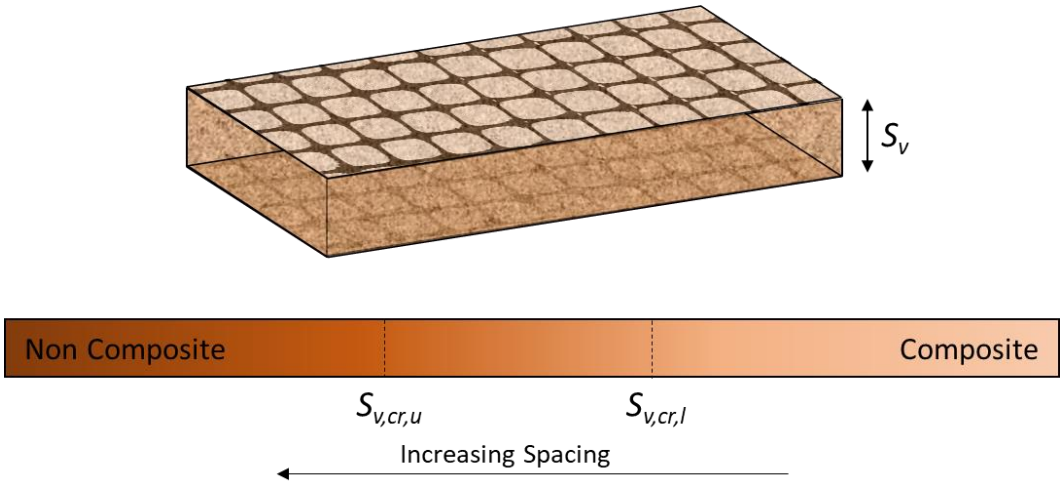

Figure 1.2. Boundaries of soil-reinforcement composite interaction.

1.2. OVERVIEW OF THE RESEARCH APPROACH

The research is divided into two main components: (1) reevaluation of data on GRS structures from the technical literature; and (2) implementation of an experimental study designed to identify and quantify the benefits of closely-spaced reinforcement. This research is conducted within the context of a larger, multi-university project. Specifically, this research is complemented by a field implementation component, led by George Mason University, with focus on monitoring a GRS-IBS (Geosynthetic-Reinforced Soil—Integrated Bridge System) structure and a numerical modeling component, led by The University of Kansas, which aims at extending the available hard data into a wide range of additional configurations and material properties. Collectively, the multi-university research is expected to refine the design methods for GRS structures by accounting for the benefits resulting from a soil-reinforcement interaction zone of influence. Overall, this

multi-university research aims at refining design guidelines and specifications for GRS structures.

1.3. OUTLINE OF THE DISSERTATION

This section includes an outline for the dissertation, which starts with an introduction presented in Chapter 1 (Introduction). The state of the practice on the use of GRS technology in bridge abutments is subsequently presented in Chapter 2 (Geosynthetic-Reinforced Soil Bridge Abutments Worldwide: State-Of-The-Practice). The research conducted in the dissertation is grouped in two main sections: Section I (Reevaluation of available data from the literature), which includes Chapters 3 through 6; and Section II (Evaluation of Soil-Reinforcement Composite Interaction and Shear Band Characterization), which includes Chapters 7 through 9. The dissertation then concludes with Chapter 10 (Conclusions and Recommendations for Future Studies). The two main sections of the research conducted in this dissertation are briefly introduced next.

1.3.1. Section I: Reevaluation of data from the literature

A significant source of information was acquired by reviewing the technical literature, particularly by having access to the source data. This capitalized the understanding of the composite behavior of GRS structures. Specifically, a detailed evaluation of actual data sources was conducted, including actual experimental and field monitoring data. Interpretation of the source data was important and useful to support the findings of the other components of this research. Each chapter in this section is a self-contained study. The various sources of this information are as follows:

- **Chapter 3 (Evaluation of the performance of large-scale experimental geosynthetic-reinforced soil structures):** A number of research studies have been conducted to define the service limit states of deformations and stresses of GRS bridge abutments and piers. Adequate prediction of the service state of these structures is crucial for their serviceability assessment. This study collects published data from both full-scale and experimental structures. It also assesses the practical models that have been recently developed by FHWA.
- **Chapter 4 (Soil arching in geosynthetic-reinforced soil structures):** The interaction between soil backfill and geosynthetic reinforcement may be affected by phenomena that are related to the reinforcement vertical spacing. The phenomena developing in a reinforced soil mass may be related to soil arching, as described by Terzaghi's classic trap-door theory. Soil arching develops during soil deformation and can take different arching shapes. Previous studies have been conducted on GRS to study the impact of closely-spaced reinforcement. The study presented in Chapter 4 reevaluates the data from research led by Professor Leshchinsky at the University of Delaware to assess the composite nature of GRS mass. This reseach included experimental, field, and numerical components.
- **Chapter 5 (Evaluation of the performance of geosynthetic-reinforced soil centrifuge models):** Several research studies have been conducted to evaluate the type of behavior expected from GRS structures. The study

presented in Chapter 5 investigates the composite behavior of GRS structures for a wide range of reinforcement spacings. This study consolidates data from research studies tested used centrifuge tests on GRS models prepared at various reinforcement vertical spacing.

- **Chapter 6 (Assessment of the Founder Meadows geosynthetic-reinforced soil bridge abutments performance):** The Founders/Meadows Bridge was the first in the United States to use GRS bridge-supporting abutments on a major US highway. The structure is located in Castle Rock, 20 miles south of downtown Denver, Colorado, USA along Founders/Meadows Parkway crossing US Interstate Highway 25 (I-25). The study presented in Chapter 6 evaluates the field monitoring data of the Founder/Meadows bridge abutments during construction and around four service years. The study provides insightful conclusions into the behavior of the structure, which can also be generalized to similar structures.

1.3.2. Section II: Experimental evaluation of the effect of soil thickness on the soil-geosynthetic interaction

The main objectives of the experimental component of this research are to: (1) design a novel experimental equipment that features the soil-reinforcement interaction experimental aspects that should be considered to properly characterize the interaction between soil and multiple reinforcement layers, and (2) implement a testing program that aims at assessing the soil-reinforcement interaction in order to identify and quantify the benefits of closely-spaced reinforcement. The chapters of this section are as follows:

- **Chapter 7 (Experimental material identification):** This chapter presents the properties of the materials used in the testing program of Section II of this dissertation. Specifically, this chapter discusses the properties of the fill materials, reinforcements, and soil-reinforcement interface.
- **Chapter 8 (Development of soil-geosynthetic composite interaction experimental approach):** This chapter includes a description of the state-of-the-art testing equipment developed to comprehensively assess soil-reinforcement interaction under both working stress and failure conditions. The new equipment was able to assess the mechanical behavior of a GRS mass considering variable reinforcement spacing. In addition, it allowed investigation of the interface shear stress transfer mechanisms as well as direct visualization of the kinematic response of soil particles adjacent to reinforcement layers.
- **Chapter 9 (Parametric evaluation of soil-geosynthetic composite interaction):** A comprehensive testing program was conducted using the experimental approach and equipment detailed in Chapter 8. The testing program was tailored to evaluate the following aspects: (1) test repeatability; (2) effect of reinforced soil normal stress; (3) effect of reinforcement vertical spacing; (4) effect of reinforcement properties; (5) effect of boundary type; and (6) effect of backfill properties.

Chapter 2: Geosynthetic-Reinforced Soil Bridge Abutments Worldwide: State-Of-The-Practice

2.1. INTRODUCTION

Soil reinforcement is an intuitive technology which was employed by the human in the early ages where straw, sticks, and branches were used to reinforce soil piles. For instance, branches were used to reinforce levees in China for a thousand years. Also, the French people who settled in Canada used sticks to reinforce dikes in the 17th and 18th centuries (Elias et al. 2001). Over the past few decades, soil reinforcement has gained significant attention in the civil engineering field. Soil reinforcement has provided many structural alternatives which showed good performance and high efficacy. In the 1960s, the French architect Henri Vidal developed the modern form of soil reinforcement, which is termed as Mechanically Stabilized Earth (MSE). Subsequently, The Reinforced Earth Company (RECo) was founded since the invention of Reinforced Earth® in 1957, in which steel strips reinforcement was employed. This led to construction of thousands of MSE walls around the world. The first MSE wall in the United States was built in 1971 on State Route 39 near Los Angeles and it used the Reinforced Earth® technology (Elias et al. 2001). Meanwhile, the use of geosynthetic reinforcement emerged in soil reinforced retaining structures. The first geosynthetic-reinforced wall employed geotextile reinforcement was constructed in France in 1971.

Several research studies have been conducted to understand the expected response type of geosynthetic-reinforced soil walls. Recently, the use of these structures has evolved to support bridges. This technology has shown very promising performance in supporting bridge loads and in providing the necessary flexibility to alleviate the bumps at the ends of

bridges. Also, adoption of this alternative has provided a better construction environment, where it facilitated construction. Herold (2006) reported that approximately 60-80% of the concrete work is reduced upon employing reinforced soil abutments instead of conventional reinforced concrete abutments. Geosynthetic-reinforced soil (GRS) bridge abutments are favored for being cost-effective alternatives compared to the traditional abutment types. Herold (2005, 2006) stated that GRS abutments cost approximately 20 to 30% less than alternative reinforced concrete abutments. Adams et al. (2011) reported that the bridges constructed using GRS abutments cost 25 to 60% less than the traditional methods. Furthermore, the usage of GRS abutments minimizes the construction time when compared to the other abutment alternatives. Adams et al. (2011) reported that the construction time can be reduced to weeks rather than months, thus reducing traffic disruptions and shutdowns. Herold (2005, 2006) noted that the simplicity of dismantling of the overall system allows recycling of both the geosynthetics and soil for applications that require a temporary abutment construction. Thus, it results in a high environmental performance of the overall construction.

Many studies have been conducted to provide a design methodology to GRS abutments (e.g. Allen and Bathurst 2003; Herold 2005, 2006; Wu et al. 2007; Berg et al. 2009; Adams et al. 2011, 2012; RTRI 2012; AASHTO 2014; Lenart 2014). However, a full understanding of the loading transfer mechanism has not been reached yet. Consequently, a very few bridges were constructed using this technology around the world. This article synthesizes information on the structures identified worldwide to date. This information is specifically about the various structures' components gathered from several

published and unpublished sources. The article also reports a few case histories from different states-of-the-practice. Finally, the article provides some insights into the major components of GRS abutments and the alternatives that have been adopted in practice.

2.2. GEOGRAPHIC DISTRIBUTION OF LOAD-CARRYING GRS BRIDGE ABUTMENTS

A few GRS bridge abutments were built around the world, which might be due to the lack of confidence and current understanding to the behavior expected from these structures. Figure 2.1 shows the distributions of the bridges supported by GRS abutments by country on the world map. Note that the number of bridges in each country may not represent the total number of bridges that have been constructed. Instead, it represents the number of bridges identified by the writers though an extensive search in published and unpublished sources. In North America, the United States comes at the top of the world's list with 174 identified bridges. Many experimental GRS abutments were constructed in the United States of America as parts of several research studies to understand their behavior. However, this article does not consider the experimental structures and focuses only on real bridges. In addition, four bridges were identified in each of Puerto Rico, Canada, and Panama. One bridge was also identified in Jamaica. In South America, five bridges were identified in Brazil, three bridges in Peru, and one bridge in each of Bolivia and Chile. In Europe, 13 bridges were identified in the Netherlands, seven bridges in Germany, and one bridge in each of Denmark, Italy, Slovenia, France and the United Kingdom. While full-scale experimental abutments were identified in Austria and Latvia, no bridges were identified to have used GRS technology in these countries. Other experimental abutments were also identified in Germany, Italy, Turkey, and France. In

Asia, Tatsuoka et al. (1997) reported that 17 bridges were constructed in Japan until April 1997. The design of GRS reinforced abutments in Japan were then modified such that the bridge superstructure rests on the facing rather than the reinforced soil mass; 34 bridges were identified to have been adopted this design. However, these structures were not considered in this article since the bridge load does not transfer directly to the reinforced soil mass. In addition, five bridges were identified in the United Arab Emirates and one bridge in each of China, Hong Kong, and Iran. Finally in Oceania, one structure was identified in Australia. The following subsections describe many of the identified structures in regards of the descriptive information gathered for every structure and information on their performance.

Figure 2.1. Global geographic spread of bridges supported by GRS abutments by country.

2.3. CASE HISTORIES

2.3.1. Founders/Meadows Bridge in the United States of America

Founders/Meadows Bridge, shown in Figure 2.2, was the first bridge in the United States constructed on a major highway and to have its superstructure supported directly by GRS abutments. The bridge was constructed in Castle Rock, Colorado, USA in 1999 (Abu-Hejleh et al. 2002). The abutments were extended to support not only the bridge superstructure but also the approaching roadway structures. The bridge replaced an old two-span bridge where the abutments and the superstructure were replaced while the middle pier was reemployed in the new bridge. The superstructure of the new bridge spanned 34.5 m and consisted of 20 precast prestressed concrete girders. The heights of the GRS abutments were 4.5 and 5.9 m measured from the base of the reinforced soil to the bearing seats. Figure 2.3 shows a schematic diagram for a section in the GRS abutments. The bridge load was conveyed to the reinforced soil mass through reinforced concrete bearing seats that rested directly on the reinforced soil mass. The bearing seats consisted of U-shaped concrete walls on shallow strip footings. The footings were 3.81-m wide and placed at a setback distance of 1.55 m measured from the outside surface of the facing. The abutments were constructed directly on the native bedrock with a minimum of 0.45-m embedment depth in front of the abutment.

Three different reinforcement types were employed: (1) uniaxial geogrid reinforcement with a tensile strength of 157.3 kN/m, which was used to reinforce the backfill material beneath the bridge footings; (2) uniaxial geogrid reinforcement with a tensile strength of 64.2 kN/m; and (3) uniaxial geogrid with a tensile strength of 39.3 kN/m.

The latter two reinforcement types were used to reinforce the backfill material behind the bearing seats and beneath the roadway approach structures as shown in Figure 2.2. The reinforcement layers were placed at a vertical spacing of 0.4 m. The backfill material used was angular crushed stone that was classified as SW-SM according to the Unified Soil Classification System (USCS). The backfill was characterized by a maximum grain size of 18 mm, a friction angle of 40 degrees, and cohesion of 70 kPa. A drainage system was used which included (1) a drainage blanket with pipe drains, which was installed at the bottom of the reinforced soil mass, and (2) a geomembrane with a collector pipe, which was installed underneath the approaching roadway structures. An expanded polystyrene layers 75-mm thick were used behind the bearing seats to mitigate the lateral earth pressure exerted on their back. The facing system included segmental blocks that were mechanically attached to the reinforcement layers. The facing blocks were backed with 0.3-m thick zone of crushed stone.

Figure 2.2. View of the Founders/Meadows Bridge.

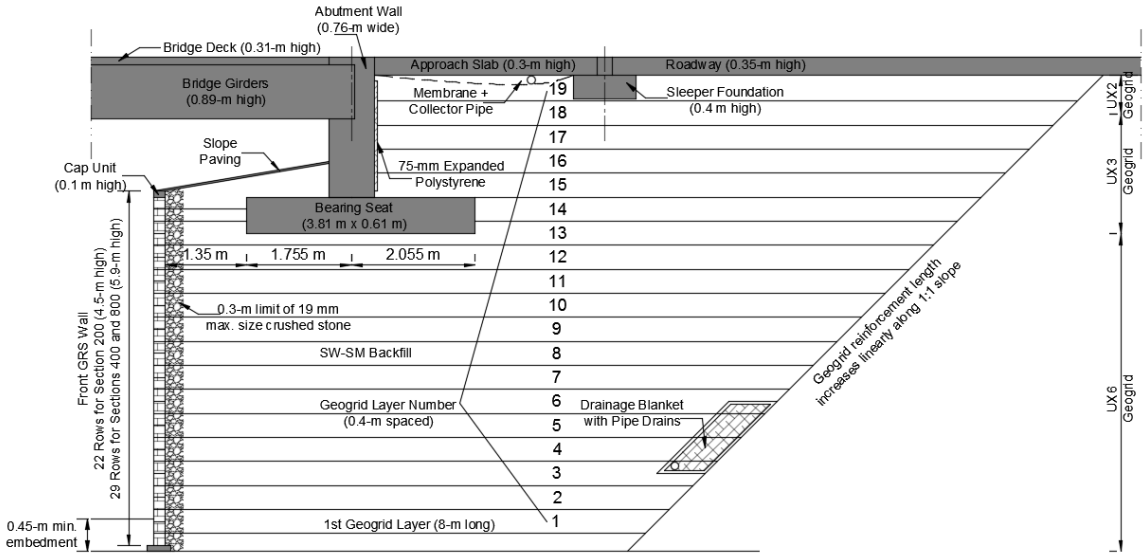

Figure 2.3. Founders/Meadows Bridge abutment cross-section (redrawn after Abu-Hejleh et al. 2002).

2.3.2. Maringa Railway Line Bridges in Brazil

A trench was excavated to downgrade the railroad tracks of a railway line passing through approximately three kilometers in Maringa City in Paraná, Brazil. This project involved the use of GRS retaining structures on the sides of the excavated trench as shown in Figure 2.4 (Da Silva et al. 2012; Brugger et al. 2012). Four bridges were constructed across the railway line which involved using GRS abutments. The bridge abutments were designed in accordance with Ehrlich and Mitchell (1994). All the bridges had single-span superstructures which were 19-m long crossing three-track railway line. The height of the abutments ranged between 8.0 to 9.0 m and were constructed directly on the local soil. Bearing seats were used to rest the superstructures on the GRS abutments. The width of

the bearing seats ranged from 1.8 to 2.0 m placed at a setback distance that ranged from 0.5 to 1.5 m measured from the outside surface of the facing.

Da Silva et al. (2012) and Brugger et al. (2012) reported that the backfill material used in the abutments was local Vemelhas clay from north Paraná, Brazil. The backfill was characterized with a friction angle of 27 degrees and cohesion of 8 kPa. The backfill was compacted at its optimum moisture content. The facing system utilized included segmental hollow blocks. The facing blocks were hollow and filled with gravel. The facing blocks were frictionally connected to the reinforcement layers. The blocks were filled with gravel to enhance the friction connection with the reinforcement layers. In addition, the reinforcement layers were folded at 1.0 m to provide a double-layer connection. Polyvinyl alcohol geogrid reinforcement was utilized with a tensile strength of 110 and 200 kN/m for the upper-half layers and lower-half layers, respectively, as shown in Figure 2.5. The reinforcement vertical spacing was 0.4 m for the upper-half layers and 0.6 m for the lower-half layers.

Figure 2.4. A bridge over Maringa Railway Line (Brugger et al. 2012).

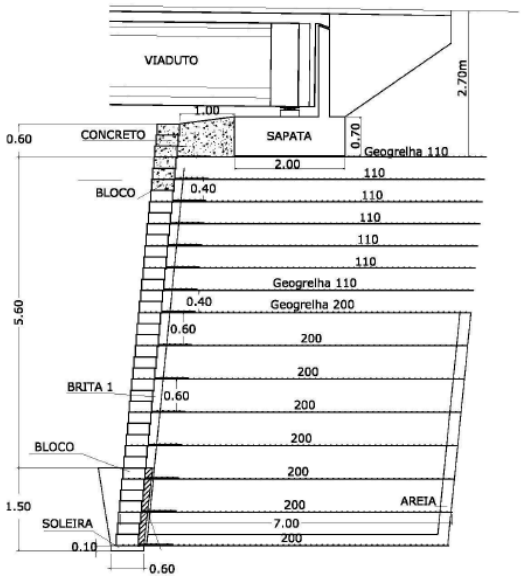

Figure 2.5. Maringa Railway Line Bridges abutment cross-section (Da Silva et al. 2012).

2.3.3. Ilsenburg Bridge in Germany

Ilsenburg Bridge, shown in Figure 2.6, was constructed in Ilsenburg, Saxony-Anhalt, Germany in 2000. This bridge is deemed the first permanent bridge supported by GRS abutments in Germany. The bridge was constructed over the River Ilse as a part of K1355 district road rehabilitation (Herold 2002). The superstructure spanned 22 m and rested on GRS abutments 2.7-m high. The superstructure conveyed the bridge load to the abutments through 1.5-m wide bearing seats placed at a setback distance of 1.6 m as shown in Figure 2.7.

The backfill material used was recycled, crushed, concrete fill that had a friction angle of 35 degrees and zero cohesion. The backfill was compacted to 100% of its Proctor density, which was checked on site for every layer. The reinforcement used was polyvinyl alcohol geogrid layers with tensile strength of 140 kN/m. The reinforcement layers were

placed at a vertical spacing of 0.35 m. The facing consisted of galvanized gabion baskets filled with rip-rap stones and stiffened by diagonal metal rods. The reinforcement layers were mechanically attached to the facing by wrapping their ends around the gabion baskets for 1.0 m (Herold 2002).

The horizontal deformation of the abutments was monitored by a vertical inclinometer in each abutment. The maximum horizontal deformation recorded three months after the bridge was inaugurated to traffic was around 0.08 mm, whereas the deformation recorded five years after construction was 0.2 mm. It was observed that the maximum lateral deformation occurred near the top surface of the abutment. However, as the deformation progressed, the maximum deformation became more uniform over the upper segment of the abutment. The vertical deformation was monitored by six settlement gauges placed for each abutment in the superstructure, bearing seat, and abutment wings. The settlement recorded for the top surface of the abutments five years after construction ranged between 3.0 to 4.5 mm. In addition, the soil pressure was monitored under static and rolling (dynamic) load testing. The rolling tests were implemented by running a four-axle HGV (heavy goods vehicle) of 40-t weight at speeds of 20, 40, and 60 km/h. The rolling tests were conducted for two years after construction, for which an earth pressure sensor was placed under the superstructure at the elevation of the uppermost reinforcement layer. This enabled the measurement of any tensile stresses that might arise beneath the superstructure in its static condition or during rolling tests (Herold 2002).

Figure 2.6. Ilsenburg Bridge (Herold 2006).

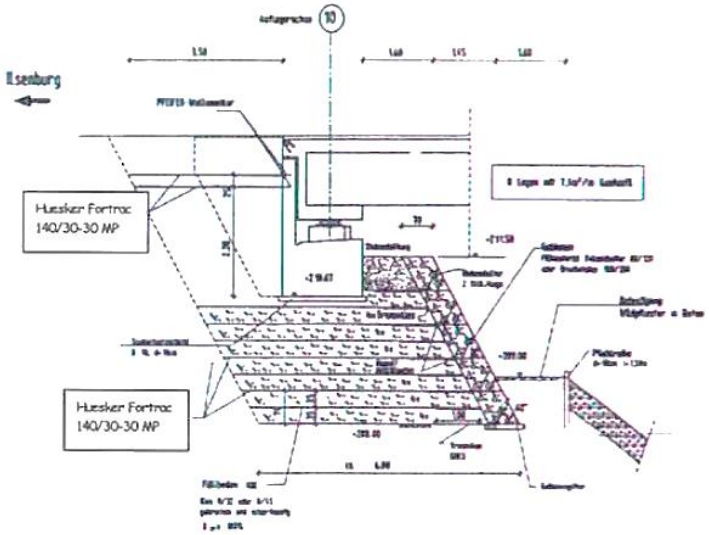

Figure 2.7. Cross-section of Ilsenburg Bridge abutment (Herold 2002).

2.3.4. Venlo Bridges in the Netherlands

Two bridges were constructed in tandem, as shown in Figure 2.8, in 2011 near Venlo, the Netherlands to provide a direct connection, A74, between the Dutch A73 and the German BAB61. The superstructures of the bridges spanned approximately 31 m and were supported directly by GRS abutments. The heights of the abutments were 10 m for one bridge and 7.4 m for the other. Polyvinyl Alcohol reinforcement geogrid layers were employed at a vertical spacing of 0.5 m. The reinforcement tensile strength was 400 kN/m for the top four layers and 200 kN/m for the reist of the layers. The backfill material used was compacted crushed recycled material. The abutments were preloaded with 100 kPa surcharge for two months after their construction. The preloading aimed at mobilizing the initial deformation of the abutments before the placing the bearing seat and the bridge superstructure. The facing system used resembled the gabion facing to provide protection and aesthetic appearance (van Duijnen et al. 2012).

Two sections were instrumented in each abutment (van Duijnen et al. 2012). The instrumentation included 26 markers where 8 markers for each section of the 10-m high abutment and 5 markers for each section of the 7.4-m high abutment as shown in Figure 2.9. Monitoring started after construction and before preloading. The vertical deformation measured at the top of the abutments was approximately 11 mm for the 10-m high abutment and 6 mm for the 7.4-m high abutment; whereas, the vertical deformation measured at the base of the abutments was approximately 8 mm for the 10-m high abutment and 6 mm for the 7.4-m high abutment. The vertical deformation measured at the base of the abutments was in the same order of the deformation measured at the top of the abutments, which implied that the settlement is mainly due to subsoil compression (Van Duijnen et al. 2012;

Detert and Thomson 2013). The deformation maintained almost constant during the 2-month application of the preload. After the preload removal and decks installation, the vertical deformation at the top of the abutments increased to approximately 26 mm for the 10-m high abutment and 23 mm for the 7.4-m abutment. However, the bridge deck weight was almost the same as the preload applied. The vertical deformation at the base of the abutments after the placement of the decks was approximately 22 mm for both abutments. This does not, however, agree with the experimental observations reported by Gourc et al. (1995), Gotteland et al. (1997), Alexiew (2007, 2008), Alexiew and Detert (2008), and Detert and Thomson (2013) in which the load-reload cycles of reinforced-soil mass does not increase its deformation. The maximum horizontal deformation measured after preloading was approximately 13 mm for the 10-m high abutment and occurred approximately 2.5 m below the bearing seat; whereas, the maximum deformation was 8 mm for the 7.4-m high abutment and occurred approximately 1.5 m below. On the other hand, the maximum deformation after the decks placement was approximately 20 mm for the 10-m high abutment and occurred at approximately 1 m below the bearing seat; whereas, the maximum deformation was 9 mm for the 7.4-m high abutment and occurred approximately 2 m below the bearing seat.

Figure 2.8. Venlo Bridges (van Duijnen et al. 2012).

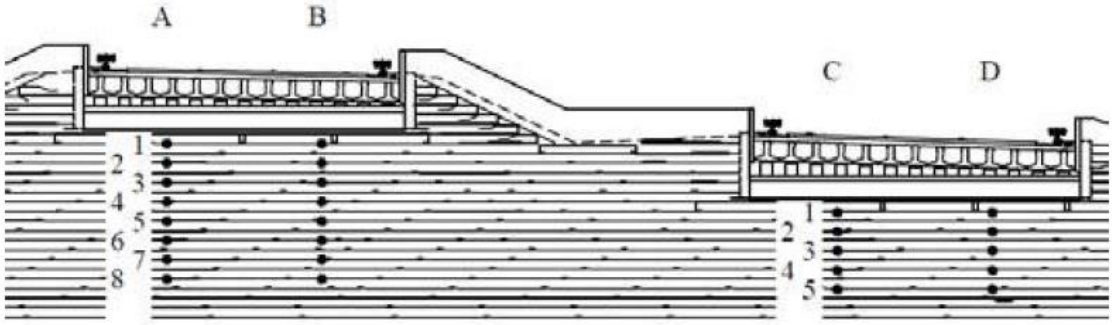

Figure 2.9. Instrumented sections for the abutments of Venlo Bridges (van Duijnen et al. 2012).

2.3.5. Nagoya Bridge in Japan

A railway bridge was constructed at Nagoya station of the Tokaido Shinkansen (the Japanese Bullet Train) in Nagoya City, Japan. The bridge superstructure was supported by

GRS abutments 6-m high as shown in Figure 2.10. The reinforcement used in the abutments involved geogrid layers made of vinylon covered with vinyl chloride; the tensile strength of the reinforcement was 60 kN/m. The vertical spacing between the reinforcement layers was 0.3 m. The backfill material utilized was high-quality, well-graded gravel compacted to dry density of 2.2 g/cm3. Full Height Rigid facing system was adopted in both abutments to resist the seismic lateral loads exerted by the bridge superstructure during extreme events. The facing walls were backed by gabions, which were wrapped by the reinforcement layers. These gabions mitigate the possible connection failure upon differential settlement between the rigid facing walls and the backfill. Anchor elements were used to support the facing walls to the reinforced soil as shown in Figure 2.10. Drainage system was used to avoid the water accumulation behind the facing walls (Kasugai and Tateyama 1992).

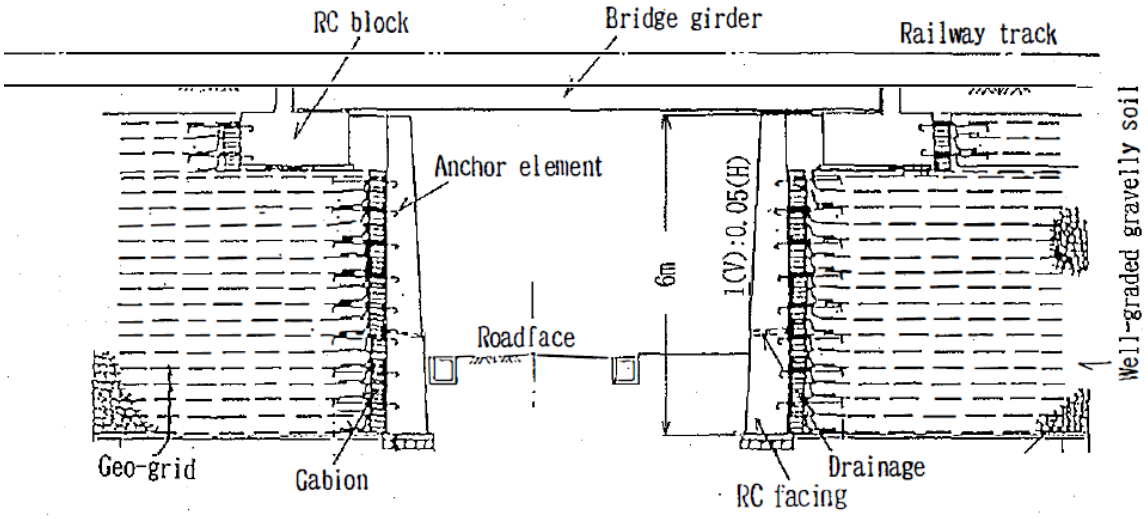

Figure 2.10. Cross-section of Nagoya Bridge (Kasugai and Tateyama 1992).

2.3.6. New South Wales Bridge in Australia

New South Wales Bridge was constructed in 1994 and is considered a major bridge on the Pacific Highway at its intersection over the Tweed River. The bridge is located 104 km south of Brisbane, Australia and is considered the first large scale use of GRS structures in supporting bridges. The bridge consisted of a nine-span superstructure whose ends rest on bearing seats supported directly by GRS abutments. The bearing seats were 2.5-m wide and placed at setback distance of 2.5 m. Polystyrene layers were used behind the bearing seats. The abutments were tiered as shown in Figure 2.11. One of the abutment consisted of three tiers forming 6.5-m total height; whereas, the other abutment consisted of four tiers forming 9.5-m total height. The reinforcement layers were employed at vertical spacing of 0.4 m for lower layers and 0.6 mm for upper layers. (Won et al. 1994).

The reinforcement employed in the abutments involved uniaxial geogrid layers with 80-kN/m tensile strength for upper layers and 110-kN/m tensile strength for lower layers as shown in Figure 2.12. The backfill material used was sand compacted to 95% standard relative density and characterized by a friction angle of 32 degrees. The facing system adopted was masonry segmental blocks, which was chosen over gabion facing for its durability and its pleasant appearance. The blocks were stacked and connected by fiberglass dowels. The strength of the connection between the facing units and the reinforcement layers included the friction and shear strength of the dowels. The blocks were partially voided and were filled with aggregate during construction (Won et al. 1994).

The maximum vertical deformation at the foundation level of the abutment was measured 80 mm and was observed towards the rear side of the abutment (Won et al. 1994). This value maintained the same over about 40 months after the bridge erection (Lo 2004).

Figure 2.11. New South Wales Bridge abutment (Lo 2004).

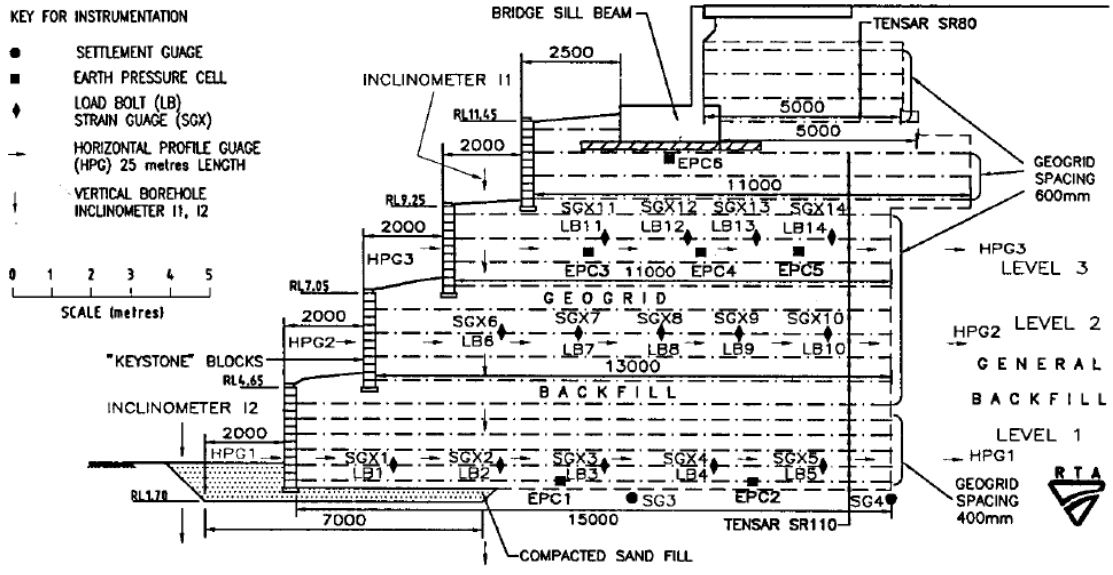

Figure 2.12. New South Wales Bridge abutment cross-section (Won et al. 1994).

2.3.7. San Francisco Bridge

San Francisco Bridge, shown in Figure 2.13, was constructed in 2001 along Route H-10 overpassing a railway line in Mostazal, O'Higgins Region, Chile. The superstructure spanned over 30 m and rested on bearing seats, which rested directly on the reinforced soil mass. The superstructure comprised four precast prestressed concrete girders skewed at an angle of 39.53 degrees. The bridge is oriented approximately east-west. The heights of the east and west abutments were 7.72 and 8.49 m, respectively, measured form the leveling pads (the base of the reinforced soil mass) up to the foundation level of the bearing seats (Morsy and Zornberg 2017).

The foundation soil on which the abutments were constructed had unit weight of 20 kN/m3, friction angle of 32 degrees, and cohesion of 15 kPa. The backfill material used in the abutments was cohesionless material with friction angle of 42 degrees. The reinforcement employed in the abutments was High-Density Polyethylene (HDPE) uniaxial geogrids layers. The vertical spacing in the east abutment was 0.4 m near the top and the bottom of the abutments, and 0.6 m near the mid-height of the abutments; whereas, the spacing in the west abutment was 0.4 m and 0.2 m near the top as shown in Figure 2.14. In addition, the reinforcement spacing in the wing-walls (sloping reinforced mass of the abutments) was 0.6 m through the entire height. Three different reinforcements were used with three different ultimate tensile strengths: (1) 144-kN/m reinforcement near the bottom; (2) 114-kN/m near the mid-height; and (3) 70-kN/m near the top.

Figure 2.13. San Francisco Bridge (courtesy of Alejandro Mendez).

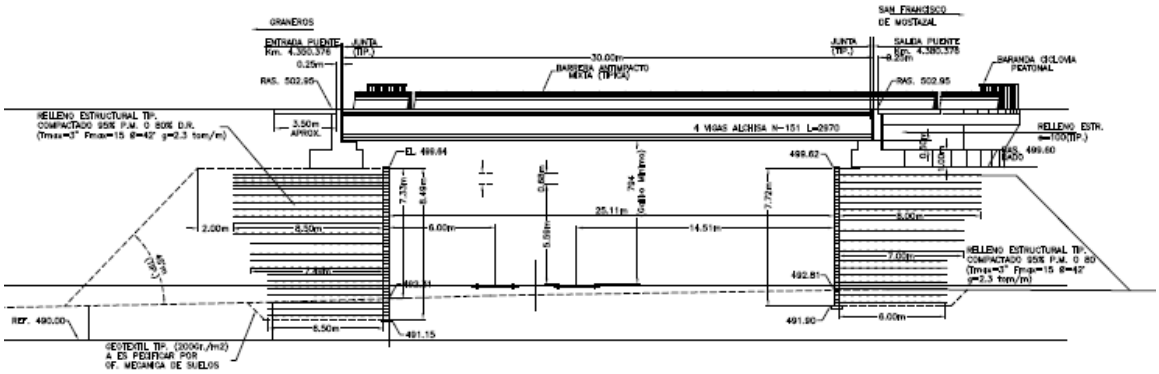

Figure 2.14. San Francisco Bridge layout: (a) plan; (b) sectional elevation (courtesy of Alejandro Mendez).

San Francisco Bridge has been exposed to a major extreme event, the 2010 Maule earthquake in Chile. The 2010 Maule Earthquake in Chile struck central Chile on 17 February 2010 at 03:34:14 AM local time (06:34:14 UTC). The United States Geological

Survey (USGS) estimated the magnitude of the earthquake as Mw 8.8 (moment magnitude scale) with the epicenter located at 35.909 degrees S (latitude), 72.733 degrees W (longitude) and the hypocenter was 35 km deep. Note that the geographical coordinates of the San Francisco are approximately -34.03 degrees S (latitude) and -70.72 degrees W (longitude). The epicenter was located 95 km from Chillán, 105 km from Concepción, 115 km from Talca, and 335 km from Santiago, which are the major Chilean cities. The distance between the bridge and the epicenter was identified to be approximately 300 km. The earthquake was the deemed the fifth strongest earthquake recorded in worldwide history (Elnashai et al. 2010). Lay et al. (2010) simulated the fault rupture in which they showed that the duration of the earthquake exceeded 3 min. However, the significant energy was released within the first the 2 min. It is also concluded that the fault was bilateral, with the rupture propagating away from the epicenter towards the north and south directions. Elnashai et al. (2010) reported that the ground uplift movement reached up to 2 m, whereas the ground settlement reached up to 0.4 m. In addition, the Chilean coast moved towards the west into the ocean. The movement reached up to 6 m at some locations.

The earthquake strongly affected a considerably large area as shown in Figure 2.15. The Figure 2.shows that the intensity reached IX in accordance with Modified Mercalli Intensity Scale at some locations. San Francisco Bridge was located in a region where the intensity had reached VII (denoted by red arrows in Figure 2.15). According to the USGS, the number of aftershocks recorded after the main shock exceeded 130 by 6 March (13 of which had magnitudes greater than Mw 6.0) and 304 of magnitude 5 Mw of more by 26 April 2010 (21 of which had magnitudes greater than Mw 6.0). San Francico Bridge was

oriented in the east-west direction, which is perpendicular to the direction of rupture propagation of the earthquake. Yen et al. (2011) observed ground movement at the San Francisco Bridge area due to weak sensitive clays. In general, San Francisco Bridge abutments performed very well, exhibiting no signs of lateral or vertical movement due to the earthquake. Yen et al. (2011) reported that the bridge suffered some relatively minor damage; however, the damage was not caused by the abutments. It was also reported that the damage was probably due to the large skew angle of the superstructure. They reported similar observations to other skewed bridges investigated in Chile after the same earthquake event. In addition, they suggested that the damage could have also happened due to the bridge tendency to slide downhill as the bridge was located on a downhill roadway grade.

Figure 2.15. Instrumental intensity map for the main shock (after USGS 2012).

Table 2.1. Summary of the characteristics of some of the identified bridges supported by GRS abutments.

No.	*Structure(s)*	*Location*	*Year*	*Maximum Abutment Height*	*Bridge Span*	*Reinforcement Type*	*Reinforcement Strength*	*Reinforcement Spacing*	*Facing Type*	*Bearing Seat Width (m)*	*Setback Distance (m)*	*Reference*
1	New South Wales	Australia	1994	10.0 m		Geogrids	80, 110 kN/m	0.6 m (0.4 m at the bottom)	Segmental blocks	2.5 m	2.5 m	Won et al. (1996)
2	Carretera Uyuni – Condo K, Potosí	Bolivia	2015	5.9 m		Geogrids			Concrete panels			Tensar®
3	BR 101-SC Hwy	Brazil				Geogrids	200 kN/m	0.4 m				Ortiago et al. (2001); Fahel et al. (2000)
4	Maringa Railway Line (4 bridges)	Brazil	2011	7.6 m	19 m	Geogrids	110 kN/m (upper half), 200 kN/m (lower half)	0.4 m (upper half), 0.6 m (lower half)	Segmental blocks	2.0 m	1.5 m	DaSilva & Brugger (2012)
5	Nadahini Creek	Canada	2013	6.9 m	15.3 m	Geotextiles	70 kN/m	0.2 m (lower), 0.275 m (upper), 0.1375 m (bed)	Aluminum sheeting	0.9 m	0.38 m	Wadey & Idrees (2014)
6	Fullerton	Canada				Geogrids			Segmental blocks			Tensar®
7	San Francisco, Mostazal	Chile	2001	8.5 m	30 m	Geogrids	70 kN/m (top), 114 kN/m (middle), 144 kN/m (bottom)	0.4 m (0.2 m near top), 0.6 m (0.4 m near top and bottom)	Segmental blocks	3.0 m	1, 1.5 m	Mendez (2016)
8	Chu Xiangyun Highway	China		6.35 m	16, 30, 16 m	Geogrids	80, 110 kN/m	0.4 m	Segmental blocks	2.5 m		Zhou et al. (2000)
9	Ullerslev	Denmark	1992	8.0 m	15.5 m	Geogrids	110 kN/m	0.5 m	Full-height wall	1.0 m	1.1 m	Kirschner & Hermansen (1994)
10	The Lagoons (5 bridges)	United Arab Emirates	2008	8.4, 13.3 m	33, 45 m	Geogrids	110, 80, 55, 30 kN/m		Steel mesh			Huesker®
11	RN 38 at Saint Saturnin	France	2005	9.5 m		Geotextiles	150 kN/m	0.39 m	Segmental blocks	1.5 m	0.33 m	Nancey et al. (2006)
12	Arnstadt	Germany	1996	4.0 m	26 m							Herold (2005, 2006, 2007)

Table 2.1. Summary of the characteristics of some of the identified bridges supported by GRS abutments (Continued).

No.	*Structure(s)*	*Location*	*Year*	*Maximum Abutment Height*	*Bridge Span*	*Reinforcement Type*	*Reinforcement Strength*	*Reinforcement Spacing*	*Facing Type*	*Bearing Seat Width (m)*	*Setback Distance (m)*	*Reference*
13	Ilsenburg	Germany	2000	4.0 m	22 m	Geogrids	140 kN/m	0.35 m	Gabions	1.5 m	1.6 m	Herold (2002, 2005, 2006, 2007)
14	Magdeburg	Germany	2001	9.0 m	6 m	Geogrids	110 kN/m	0.3 m		2.5 m	0.5 m	Herold (2005, 2006, 2007)
15	Mainzer	Germany	2003									Herold (2005, 2006, 2007)
16	Weimar	Germany	2003			Geogrids		0.25 m	Gabions			Herold (2005)
17	Mandelholz	Germany	2006	3.0 m	15 m			0.5 m	Segmental blocks	1.75 m	0.75 m	Herold (2007, 2008)
18	Lust	Germany	2007	3.3 m		Geogrids		0.25 m	Segmental blocks	2.5 m	1.0 m	Herold (2005, 2006)
19	Tuen Mun	Hong Kong		14.0 m		Geogrids	30 kN//m	0.4 m (middle), 0.35 m (top and bottom)	Full-height wall	3.5 m	0.5 m	Ng and Mak (1988)
20	Tehran, Iran	Iran	2009	7.5 m	114 m	Geogrids	80 kN/m	0.4 m	Gabions	3.5 m	1.85 m	Mirlatifi (2012)
21	State Road NR 28	Italy	2000s	30.4 m		Geogrids	80 kN/m	0.6 m	Vegetation			Rimoldi & Intra (2009)
22	Queens River	Jamaica				Geotextiles	70, 31.5 kN/m	0.3 m	Segmental blocks			Barrett & Ruckman (1996)
23	Nagoya	Japan		6.0 m		Geogrids	60 kN/m	0.3 m	Full-height wall	2.0 m	1.0 m	Kasugai & Tateyama (1992)
24	Seibu Railway (2 bridges)	Japan		4.0, 5.0 m	13.2 m	Geogrids	60 kN/m	0.3 m	Full-height wall	2.5 m	1.0 m	Tatsuoka et al. (1997)
25	Venlo (2 bridges)	Netherlands	2011	7.4, 10.0 m	31 m	Geogrids	200 kN/m (400 kN/m at the top)	0.5 m	Gabions			Duijnen et al. (2012); Deret & Thomson (2013)
26	N242 Road KW-B	Netherlands				Geogrids	110 kN/m	0.5 m	Clay over fly ash and sand	3.5 m	0.6 m	Snijders & Brok (2007)
27	N242 Road KW-O	Netherlands			5.6 m	Geogrids	300 kN/m (150 kN/m at the top)	0.5 m	Clay over fly ash and sand	3.5 m	0.85 m	Snijders & Brok (2007)

Table 2.1. Summary of the characteristics of some of the identified bridges supported by GRS abutments (Continued).

No.	*Structure(s)*	*Location*	*Year*	*Maximum Abutment Height*	*Bridge Span*	*Reinforcement Type*	*Reinforcement Strength*	*Reinforcement Spacing*	*Facing Type*	*Bearing Seat Width (m)*	*Setback Distance (m)*	*Reference*
28	A2, Gleen	Netherlands			27, 34.5 m	Geogrids	150 kN/m	0.5 m				Huesker®
29	N302 Fietsburg Harderwijk	Netherlands		6.0 m		Geogrids	110 kN/m	0.5 m				Huesker®
30	S-27	Peru	2008	10.5 m		Geogrids		0.5 m (0.25 m at the bottom)	Vegetation	2.5 m	2.5 m	Tecnologia de Materilas
31	(2 bridges)	Peru				Geogrids			Segmental blocks			Tecnologia de Materilas
32	PR-2, Yauco	Puerto Rico		10.0 m	13 m	Geotextiles		0.2 m				
33	Barceloneta	Puerto Rico										
34	Utuado	Puerto Rico										
35	Pavlovski potok Stream in Zerovinci	Slovenia				Geogrids	80 kN/m	0.3 m (0.1 m at the top)	Full-height wall	0.85 m	0.45 m	Lenart et al. (2016)
36	Naadestraat, Laarderhoogt, Laren	Netherlands				Geogrids			Segmental Blocks			Pauls et al. (2016)
37	A1, Laarderhoogt, Laren	Netherlands				Geogrids			Full-height wall			Pauls et al. (2016)
38	N417 National Road, Zwaluwerberg, North Holland	Netherlands				Geogrids			Full-height wall			Pauls et al. (2016)
39	Utrecht-Hilversum Railway, Zwaluwerberg, North Holland	Netherlands				Geogrids			Steel mesh			Pauls et al. (2016)
40	A27 Motorway, Zwaluwerberg, North Holland	Netherlands				Geogrids			Segmental blocks			Pauls et al. (2016)

Table 2.1. Summary of the characteristics of some of the identified bridges supported by GRS abutments (Continued).

No.	*Structure(s)*	*Location*	*Year*	*Maximum Abutment Height*	*Bridge Span*	*Reinforcement Type*	*Reinforcement Strength*	*Reinforcement Spacing*	*Facing Type*	*Bearing Seat Width (m)*	*Setback Distance (m)*	*Reference*
41	Boele Staal, Soesterberg, Utrecht	Netherlands		4.5 m		Geogrids			Full-height wall			Pauls et al. (2016)
42	Smit Vest, Boerenverdriet	Netherlands	2016									Wurck
43	River Aire, Kirkstall, Leeds	United Kingdom	2015		30 m	Geogrids	35, 55 kN/m	0.4 m	Segmental blocks			Scotland et al. (2016)

2.4. DESIGN IMPLICATIONS

This section provides some insights into the major components of GRS bridge abutments and the alternatives that have been adopted in the state-of-the-practice. A significant amount of information has been gathered from all the identified structures in technical literature. Table 2.1 shows a summary of the characteristics of some of the identified bridges supported by GRS abutments. Some alternatives were found favored over others based on the environment of the construction site where the bridge is being built. The following subsections emphasize on (1) the bridge geometry in regards of the number of spans, span length, and abutment height, (2) the backfill material in regards of its type, strength, and compaction level, (3) the reinforcement type in regards of geosynthetic type, polymer type, and tensile strength, (4) the reinforcement vertical spacing in regards of its value and variability over the height of the abutment, (5) the facing system in regards of type, rigidity, and attachment to the GRS mass, and (6) the bearing seat in regards of its presence, width, and setback distance.

2.4.1. Bridge geometry

This section focuses on the maximum span length and number of spans a bridge superstructure have been adopted in the state-of-the-practice. In addition, it covers the maximum height for a GRS abutment in real bridges. Figure 2.16 shows the maximum span length identified in each geographic continent. The bridges of the maximum span lengths in North America are (1) CR 55 Bridge overpassing Montana Southern Railway in Montana, USA (span = 42.7 m), and (2) Steve road bridge overpassing Tiffin River in Ohio, USA (span = 42.7 m). In South America, the bridge identified to be of the maximum

span length is San Francisco Bridge in Mostazal, Chile (span = 30 m). The bridge of the maximum span length in Europe was identified to be A2 Bridge in Gleen, Netherlands (span = 34 m). The maximum span identified in Asia was 114 m in Milad Bridge (cable-stayed bridge) in Iran, which is the bridge of the maximum span length among all the identified structures.

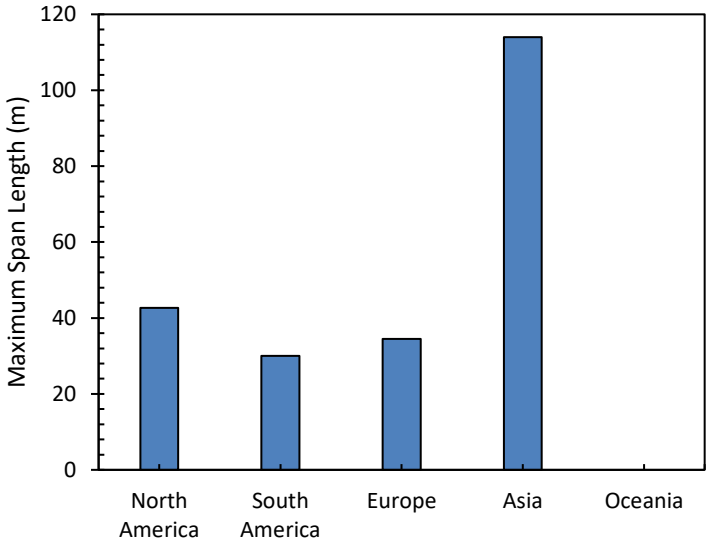

Figure 2.16. Maximum span length by geographic continent.

Herold (2005, 2006) reported that single span bridges with precast superstructure are preferred; however, multi-span bridges with shallow or deep founded piers and soil reinforced soil abutments are also possible. Adams et al. (2011) reported that the geosynthetic-reinforced soil abutments are suitable to support single-span bridges. Figure 2.17 shows the maximum number of spans identified in each geographic continent. The bridge of the maximum number of spans identified in North America is the I-70 Bridge

constructed near Denver in Colorado, USA (three spans). Other bridges were identified in North America that had more than one span, such as (1) Founders/Meadows Bridge in Castle Rock, Colorado, USA (two spans), and (2) Knox County Beach Bridge in Maine, USA (two spans). All the bridges identified in South America were single-span bridges. In Europe, the bridge identified with the maximum number of spans is A2 Bridge in Gleen, Netherlands (two spans, which were 27-m and 34-m long). In Asia, the bridge identified with the maximum number of spans was Chu Xiangyun Highway Bridge in China (three spans, which were 16-m, 30-m, and 16-m long). The maximum number of spans identified was in New Wales Bridge in Australia (nine spans).

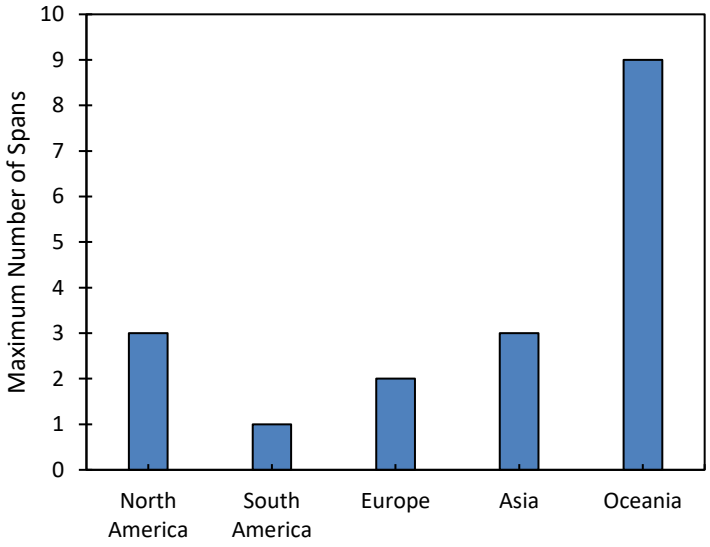

Figure 2.17. Maximum number of spans by geographic continent.

Figure 2.18 shows the maximum abutment height identified in each geographic continent. In North America, the maximum height for abutments identified was 7.5 m in

Black Hawk Bridge in Colorado, USA. Meanwhile in South America, the maximum abutment height was identified was 10.5 m in S-27 Bridge in Yanacocha, Peru. The maximum abutment height among the identified European bridges was 30.4 m in State Road NR 28 Bridge in Imperia, Italy. This abutment is deemed the highest among all the identified abutments. In Asia, the maximum abutment height was 14 m in Tuen Mun Bridge in Hong Kong. New Wales Bridge in Australia rested on abutments of 10-m maximum height.

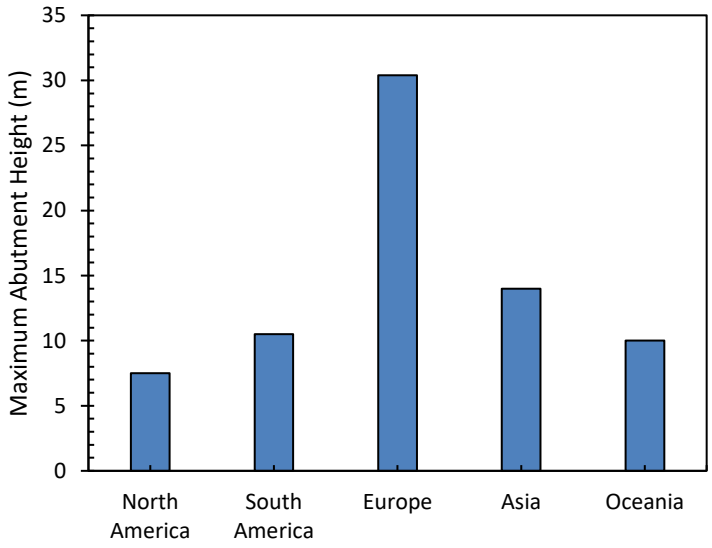

Figure 2.18. Maximum abutment height by geographic continent.

2.4.2. Backfill type

The backfill material used in the GRS structures is deemed a key component. Typically, compacted crushed aggregate or gravel is used to facilitate construction and minimize deformations. Sand backfill material was also employed in many structures, such

as bridges in Brazil, Netherlands, Australia, and Japan. Also, sandy gravel backfill material was used in some project, such as in Milad Bridge in Iran and in Ullerslev Bridge in Denmark. The backfill material of the minimum friction angle was employed in New South Wales Bridge reported in Won et al. (1994), where the material was fine sand with a friction angle of 32 degrees. The backfill material is typically compacted between the reinforcement layers. Based on the compaction relative compaction levels identified for the case studies reported herein, the minimum relative compaction for a backfill was 94% in 250th Street Bridge reported in Vennapusa et al. (2012, 2014).

The use of low quality local soil as a backfill material might be necessary if high quality backfill material is expensive to procure to the construction site. For instance, nearly saturated clay backfill showed good performance as a backfill material in many geosynthetic-reinforced walls constructed in Japan (Tatsuoka et al. 1986, 1987; Tatsuoka and Yamauchi 1987; Yamauchi et al. 1987; Tatsuoka 1993; Ling et al. 1995; Tatsuoka et al. 1997). In addition, the bridges constructed over Maringa Railway line in Brazil utilized clay backfill for the GRS abutments. Ling and Tatsuoka (1994) showed experimentally good performance for saturated clay as a backfill material when reinforced with geotextile composite, which allows consolidation of the clay backfill to take place anisotopically.

2.4.3. Reinforcement type

One of the key items in the reinforced soil mass is the geosynthetic reinforcement layers. The properties of the reinforcement, such as reinforcement type, strength, and material, play a master role in the design. As conceptualized in literature, the reinforcement inclusion in soil improves the properties of the composite mass through (1) increasing

confinement; (2) enhancing strength; or (3) reducing normal strains (Yang 1972; Yang and Singh 1974; Schlosser and Long 1974; Hausmann 1976; Bassett and Last 1978; Ingold 1982; Athanasopoulos 1993, 1994; Gray and Ohashi 1983; Maher and Woods 1990; Elton and Patawaran 2004, 2005).

Some information was gathered on the reinforcement employed in the case studies reported in this article. Figure 2.19 shows the utilization percentage of geogrid and geotextile reinforcement in the various geographic continents. It was found that the geogrid reinforcement is preferred over the geotextile reinforcement in Europe. Out of 15 bridges 11 bridges were supported by geogrid-reinforced abutments and one bridge was supported on knitted geotextile-reinforced abutments. On contrary, the geotextile reinforcement is preferred over the geogrid reinforcement in North America. Most of the structures constructed in the United States of America employed geotextile reinforcement. Two identified structures in the United States of America employed geogrid reinforcement in Colorado and Minnesota; in addition, Fullerton Bridge in Canada employed geogrid reinforcement. In Japan typically geogrid reinforcement is preferred with cohesionless backfill materials since it provides interlock with the aggregate; whereas, a composite of nonwoven and woven geotextiles reinforcement is preferred for nearly saturated cohesive backfill materials (Tatsuoka et al. 1997). Alexiew et al. (2000) reported that the geogrid reinforcement of adequate aperture size are preferred over the other reinforcement types for their high interface and anchorage strengths in the backfill material and high permeability. In addition, geogrids have less susceptible to installation aggression and have higher resistance against chemical and biological degradation.

Figure 2.19. Reinforcement type by geographic continent.

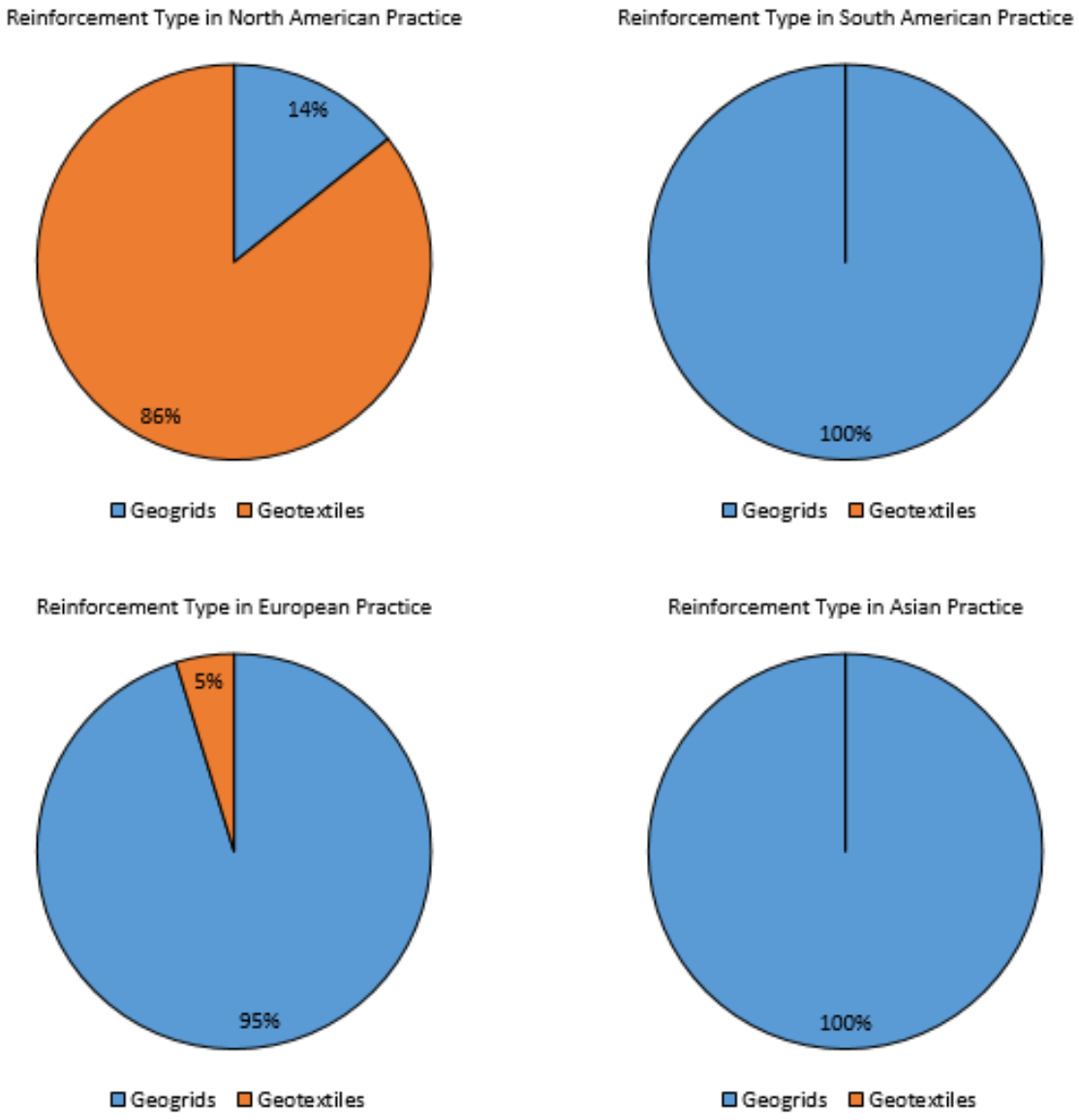

Figure 2.19. Reinforcement type by geographic continent (Continued).

The geosynthetic reinforcement material is composed of plastic polymers, which could be (1) Polyester (usually coated with polyvinyl chloride), (2) Polyethylene, (3)

Polypropylene, or (4) Polyvinyl Alcohol. Reinforcement made of the first three polymers are the most commonly used in soil-reinforcement applications; however, polyvinyl alcohol reinforcement has been used in several bridge abutments around the world. The polymer used in reinforcement manufacturing determines its properties (Alexiew et al. 2000). The selection of the material type depends mainly on the environment of the structure and the expected long-term reinforcement degradation. Alexiew et al. (2000) reported that the polymeric material has to ideally be featured by (1) appropriate tensile strength, (2) low creep tendency, (3) high interface and anchorage strengths in the backfill material, (4) high permeability, (5) low installation aggression susceptibility, (6) high chemical and biological degradation resistance, (7) inexpensive. Alexiew et al. (2000) stated that geogrids made of aramid and polyvinyl alcohol are suitable in soil-reinforcement applications. It was reported these two materials improves the strength, the creep behavior, and the chemical and biological resistance of the geogrids.

Suits and Hsuan (2003) reported that the photo-degradation of geosynthetics depends on several factors: (1) exposure light spectrum range; (2) polymer color; (3) ultraviolet ray stabilizers; and (4) variability of the geosynthetic local climate. Degradation by ultraviolet oxidation and thermal oxidation is more prominent in polypropylene and polyethylene reinforcement (i.e., polyolefins reinforcement). Degradation by hydrolysis is more prominent in polyester reinforcement (AASHTO 2014). The quality of the polyester is represented by the molecular weight of the carboxyl end group; whereas, the quality of the polyethylene and the polypropylene is represented by the anti-oxidation stabilizers (Alexiew et al. 2000). In addition, every reinforcement polymeric material has to its own

response against soil aggressiveness which includes soil pH, gradation, plasticity, organic content, and in-ground temperature (AASHTO 2014).

Adams et al. (2011) reported that reinforcement tensile strength should not be less than 70 kN/m. Figure 2.20 shows the range of ultimate reinforcement tensile strength adopted in the state-of-the-practice in the various geographic continents. The reinforcement of the minimum tensile strength used was in 250th Street in Buchanan County, Iowa, USA (Tult = 21 kN/m). Nevertheless, the reinforcement of the maximum tensile strength used was in Venlo bridges in Netherlands.

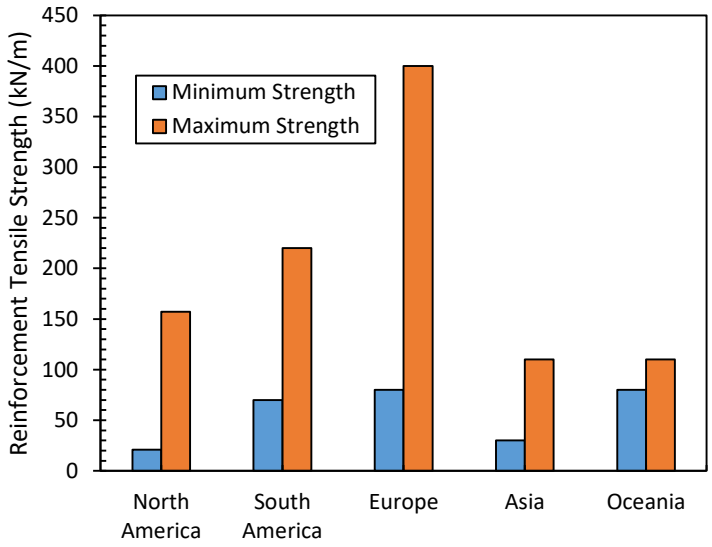

Figure 2.20. Reinforcement ultimate tensile strength range by geographic continent.

2.4.4. Reinforcement vertical spacing

Reinforcement vertical spacing is a key parameter in the design of the GRS structures. As the vertical spacing decreases, the strength of the reinforced-soil mass

increases. Recent studies (e.g. Adams 1997; Adams *et al.* 2007; Ketchart and Wu 2001; Elton and Patawaran 2005; Ziegler *et al.* 2008) have shown that the reinforcement spacing has more effect than the reinforcement tensile strength for closely-spaced reinforced structures. Soil-reinforcement interaction plays an important role on the behavior of the composite nature of the reinforced soil. The shear stress generated at the soil-reinforcement interface propagates to the soil in vicinity. This affects the interaction behavior of the contiguous reinforcement layers. This interaction is related inversely with the vertical spacing between the reinforcement layers. Wu *et al.* (2006) reported that the default design reinforcement spacing for GRS abutments with flexible facing is 0.2 m, while the maximum allowable spacing is 0.4 m. Adams *et al.* (2011) reported that the maximum spacing beyond which the interaction is no longer pronounced is 0.3 m. Figure 2.21 shows the range of reinforcement vertical spacing adopted in the state-of-the-practice in the various geographic continents. This included considered the spacing adopted for secondary reinforcement, if any. According to the structures identified, the vertical spacing ranged from 0.2 m to 0.6 m. The spacing of 0.2 m was adopted by many structures in the United States of America with 0.1 m spacing in the upper layers below the bridge bearing seat. The maximum reinforcement spacing identified was 0.6 m in bridges in South America, Europe, and Oceania.

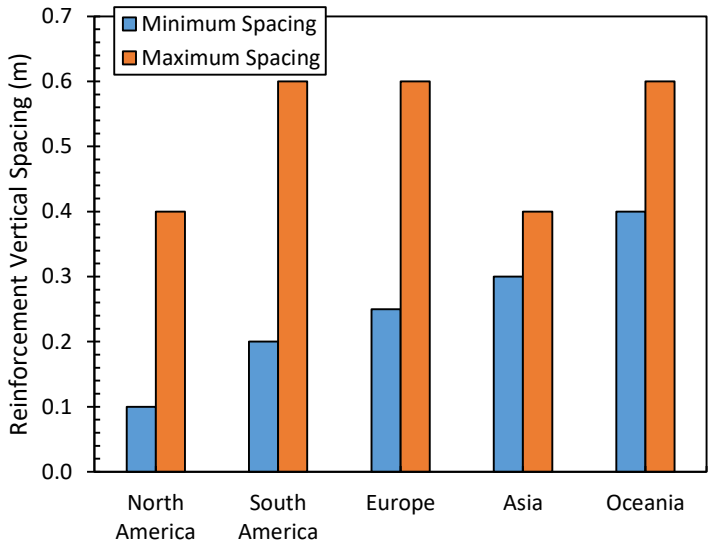

Figure 2.21. Reinforcement vertical spacing range by geographic continent.

The reinforcement pattern may change beneath the bearing seat to account for the stress concentration within the reinforced soil mass. Some structures used double reinforcement layers below the bearing seat; for instance, Mamouth Lakes Bridge reported in Keller and Devin (2003). Nadahini Creek Bridge reported in Wadey and Idrees (2014) used secondary reinforcement in the mid-layers below the bearing area. The same alternative has been adopted recently in many structures in the United States of America (e.g. Adams et al. 2012). Ullerslev Bridge described in Kirschner and Hermansen (1994) used an additional reinforcement layer below the bearing seat level at a reduced spacing. In some structures the vertical spacing was reduced at the bottom of the abutments as in the structures reported in Nadahini Creek Bridge and New Wales Bridge. This increases the reinforcement density at the greater depths where the lateral earth pressure is high. On

the other hand, Maringa Railway Bridges used reduced spacing for the lower layers and denser reinforcement for the upper layers.

2.4.5. Facing system

The facing systems retain the front soil of the reinforced soil mass; the facing systems employed in the GRS abutments varied in the identified structures herein. Generally, the facing systems of reinforced-soil retaining structures include prefabricated modular blocks, segmental precast units, wrapped around reinforcement, steel wire mesh, gabions, and vegetation. Some other rehabilitated structures used old abutments as facing for the new reinforced-soil abutments; for instance, Lake Mamie Bridge reported in Keller and Devin 2003. Figure 2.22 shows the various facing systems adopted in the state-of-the-practice in the various geographic continents. The dominant facing system in North and South Americas is segmental-block systems. These systems can be mechanically or frictionally attached to the reinforcement layers. Various systems were used in the identified European bridges with three major types: (1) segmental-block facing; (2) full-height wall facing; and (3) gabion facing. In Asia, the dominant facing system is the full-height wall systems, which has been extensively used in Japan.

In USA, many of the recent structures adopt the modular block facing system with friction connection to reinforcement layers (e.g., Adams et al. 2012). The reinforcement layers are sandwiched between the modular block rows. Solid modular blocks covered with riprap are more likely used at the bottom of the abutments to prevent erosion and scour; whereas, hollow blocks are more likely used for the upper layers of the abutments to

mitigate the normal pressure on the lower blocks. The upper few rows are connected to each other vertically by means of dowels to secure them from overtopping.

In Canada, Nadahini Creek Bridge reported in Wadey and Idrees (2014) employed 3.175-mm thick corrugated aluminum sheeting to speed up the construction. Deadman anchors were used to maintain the verticality of the sheeting without adding structural support to the reinforced soil mass. This facing system provides a more plumb wall and prevents scour and erosion. However, some difficulties in monitoring the wall verticality and in avoiding reinforcement wrinkles. Sheet-pile facing has also been used in the United States of America in (1) Scott County, Iowa, (2) Kaw Nation, Oklahoma, and (3) I-70 near Denver, Colorado.

In Japan, full height rigid facing is the typical facing system in geosynthetic-reinforced soil abutments (Tatsuoka et al. 1997). This facing comprises cast-in-place lightly-reinforced concrete and backed by wrapped-around geosynthetic-reinforced layers. Gravel-filled bags are used for each reinforcement layer on which the layer is wrapped around. Steel bars are used to secure the concrete wall to the soil; these steel bars have a semi-circular hook embedded in the concrete wall and from the other side mounted to continuous anchorage plates. This facing system was proved excellent performance in resisting seismic lateral loads generated by bridge superstructures and limiting the lateral deformation. This system has been adopted in a structure in Slovenia, which is considered the first bridge to be constructed with full-height rigid facing in Europe (Lenart et al. 2016). In Germany, concrete block (H+P) facing system was employed in some of the identified structures (Herold 2006). This system couples blocks by vertical tubes filled with concrete

while matching with various facing modular composition. The blocks are reinforced such that edge cracking and chipping is avoided. Reinforcement strips are integrated to the facing units in which the reinforcement is procured to the site with its design length rolled.

Figure 2.22. Facing type by geographic continent.

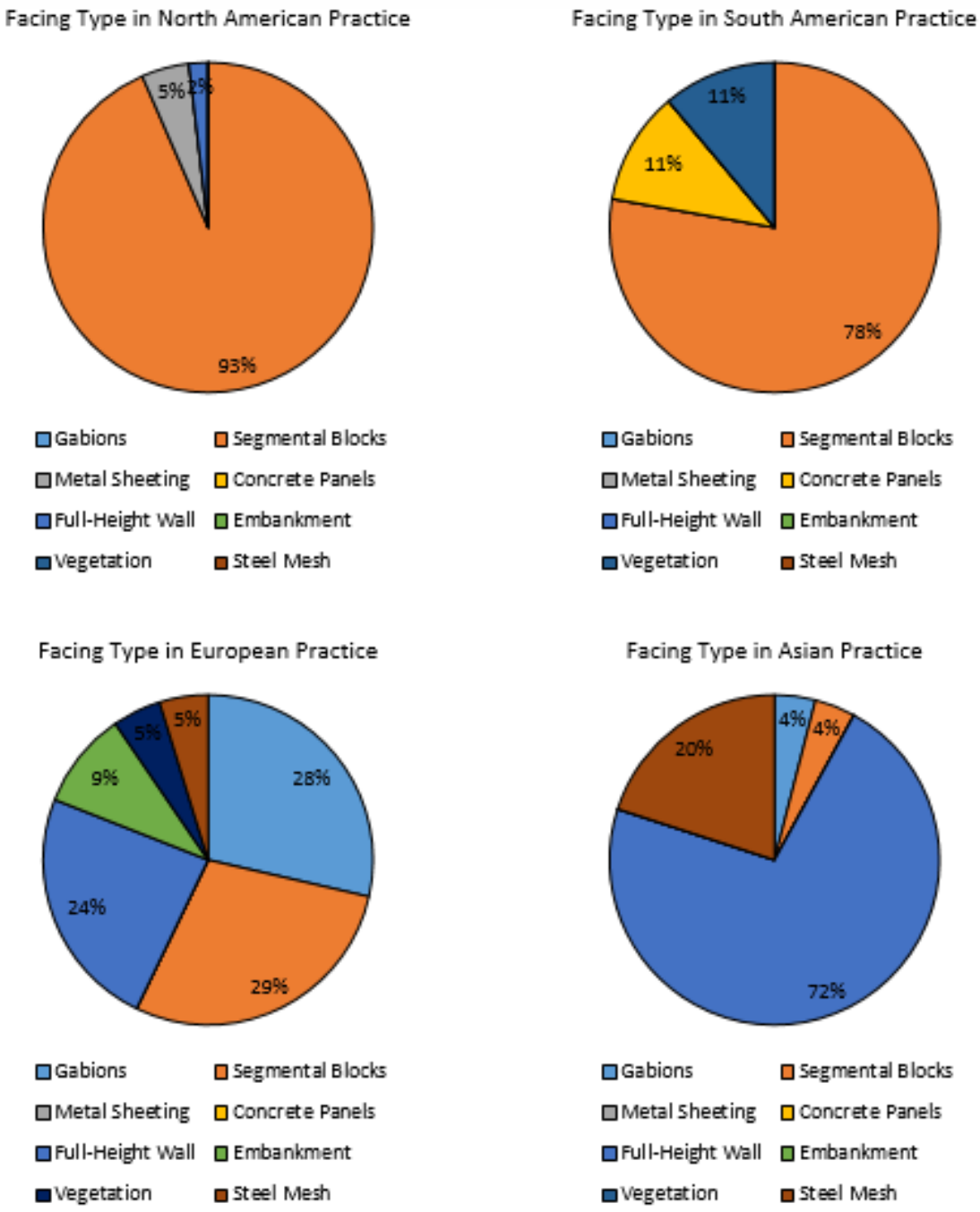

Figure 2.22. Facing type by geographic continent (Continued).

2.4.6. Bearing seat

Bearing seats are placed on the top of the reinforced soil mass and beneath the bridge superstructure. Most of the bridges that have been identified employed bearing seats as an essential component in GRS abutments. In USA, many bridges that have superstructures of adjacent concrete girders are constructed without the use of bearing seats. Instead, foam boards are used behind the facing and on the top of the GRS mass. Concrete blocks are then placed on the top of the foam boards and foam boards are placed on the top of the facing and next to the concrete blocks such that the foam boards of the different levels are touching along the corner. Foam boards are used to mitigate any pressure that might be conveyed from the bridge superstructure to the facing. On the other hand, the bridges that have different types of superstructures (e.g. steel girders) may require a bearing seat (Adams et al. 2012). Figures 23 and 24 show the ranges of the bearing seat width and setback distance, respectively, in the state-of-the-practice in the various geographic continents. In general, the width of the bearing seat ranged from 0.2 to 3.8 m among the structures identified in this study. The setback distance of the bearing seat measured from the front side of the facing and to the outside edge of the bearing seat ranged from 0.2 to 2.5 m. Adams et al. (2012) reported that in USA, the setback distance is usually 0.2 m and can be greater.

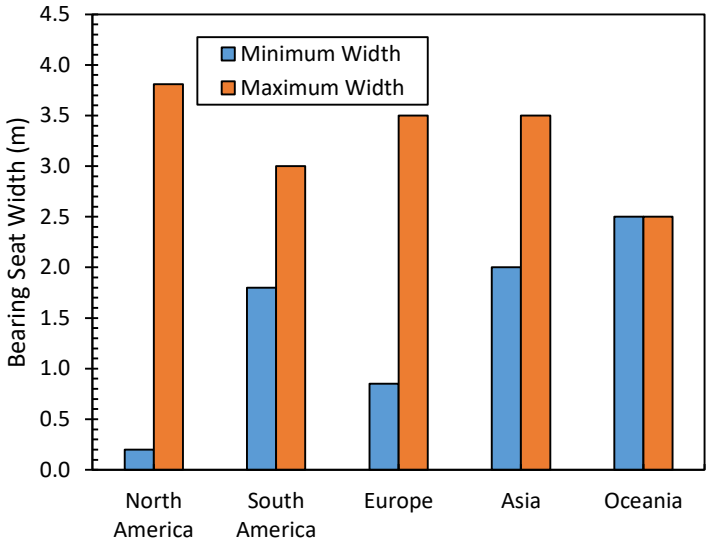

Figure 2.23. Reinforcement bearing seat width range by geographic continent.

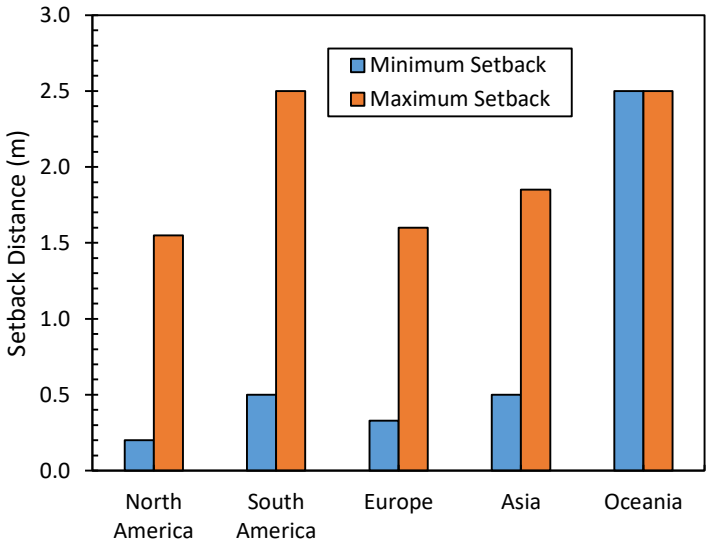

Figure 2.24. Reinforcement setback distance range by geographic continent.

2.5. SUMMARY

Geosynthetic-reinforced soil structures have been recently adopted to support bridges. These structures have shown excellent performance as they provide adequate bearing capacity to support bridge loads and essential flexibility to reduce the possible bumps at the ends of bridges while maintaining minimal deformation. GRS structures are favored for providing a better construction environment. GRS abutments require less construction time compared to other conventional bridge abutment alternatives. For instance, GRS abutments do not require any formwork like concrete abutments, which may also require long curing time. The shorter construction time can reduce traffic disruptions and shutdowns. GRS abutments are deemed cheaper alternatives compared to conventional abutment types as they do not require any special equipment or trained workforce. In addition, the materials required to construct the abutment are cheap and can be recycled and used in other application for temporary bridges.

Many studies have been conducted to provide a design methodology to GRS abutments. A very few bridges were constructed using this technology around the world. This study summarized information about the state-of-the-practice adopted in the various structures' components. The maximum number of spans in the identified bridges was 9 and the maximum span length was 42.7 m. In addition, the maximum abutment height identified was 30.4 m. Regarding the primary materials used, a wide range of backfill types was used in the identified bridges; however, high-quality, open-graded, coarse-aggregate backfills are favored for their high strength, stiffness, and high drainage ability. Various reinforcement types were employed in this study, mainly geogrid and geotextile reinforcements. The reinforcement spacing ranged from 0.1 to 0.6 m in the identified

bridges. Note that, however, these spacings may be adopted at various reinforcement densities (reinforcement pattern) in the same abutment. Various systems were used in the identified European bridges with three major types: (1) segmental-block facing, with mechanical or friction connections; (2) full-height wall facing with mechanical connection; (3) gabion facing with mechanical connection; and (4) metallic sheeting (aluminum sheeting or steel sheet-piles).

2.6. REFERENCES

Abernathy, C. (2013). Geosynthetic-reinforced Soil – Integrated Bridge System (GRS-IBS). Experimental Projects Construction Report. Montana Department of Transportation Research Programs. November 2013.

Abernathy, C. (2014). "Montana DOT Rebuilds an Old Bridge with a New System." Geosynthetics, April 2014, Vol. 32, No. 2.

Abernathy, C. (2015). Geosynthetic-reinforced Soil - Integrated Bridge System (GRS-IBS). Experimental Projects Construction and Site Inspection Report. Montana Department of Transportation Research Programs, June 2015.

Abu-Hejleh, N., Wang, T., and Zornberg, J.G. (2000b). "Performance of geosynthetic-reinforced walls supporting bridge and approaching roadway structures." Geotechnical Special Publication, pp. 218-243.

Abu-Hejleh, N., Zornberg, J.G., Wang, T., and McMullen, M. (2000a). Performance of Geosynthetic-Reinforced Walls Supporting the Founders/Meadows Bridge and Approaching Roadway Structures. Colorado Department of Transportation Report No. CDOT-DTD-R-2000-5.

Abu-Hejleh, N., Zornberg, J.G., Wang, T., and McMullen, M. (2001). Performance of Geosynthetic-Reinforced Walls Supporting the Founders/Meadows Bridge and Approaching Roadway Structures. Colorado Department of Transportation Report No. CDOT-DTD-R-2001-12.

Abu-Hejleh, N., Zornberg, J.G., Wang, T., and Watcharamonthein, J. (2002). "Monitored displacements of unique geosynthetic-reinforced soil bridge abutments." Geosynthetics International, Vol. 1, pp. 71-95.

Adams, M., Ketchart, K., Ruckman, A., DiMillio, A.F., Wu, J.T.H., and Satyanarayana, R. (1999). "Reinforced Soil for Bridge Support Applications on Low-Volume Roads." Transportation Research Board, Washington, D.C.

Adams, M., Nicks, J., Stabile, T., Wu, J., Schlatter, W., and Hartmann, J. (2012). Geosynthetic-reinforced Soil Integrated Bridge System, Interim Implementation Guide. Report No. FHWA-HRT-11-026, Federal Highway Administration, McLean, VA.

Adams, M., Nicks, J., Stabile, T., Wu, J., Schlatter, W., and Hartmann, J. (2011). Geosynthetic-reinforced Soil Integrated Bridge System, Synthesis Report. Report No. FHWA-HRT-11-027, Federal Highway Administration, McLean, VA.

Adams, M., Schlatter, W., and Stabile, T. (2007b). "Geosynthetic-Reinforced Soil Integrated Abutments at the Bowman Road Bridge in Defiance County, Ohio." Geosynthetics in Reinforcement and Hydraulic Applications (GSP 165), Gabr, and Bowders (Eds.). ASCE, Reston, VA, pp. 119-129.

Adams, M.T. (1997). “Performance of a Prestrained Geosynthetic-reinforced Soil Bridge Pier,” Proceedings of the International Symposium on Mechanically Stabilized Backfill, J.T.H. Wu (Ed.), Balkema, Rotterdam, Netherlands.

Adams, M.T., Ketchart, K., and Wu, J.T.H. (2007). “Mini Pier Experiments: Geosynthetic Reinforcement Spacing and Strength as Related to Performance,” Proceedings of Geo- Denver 2007, American Society of Civil Engineers, Denver, CO.

Albert, G.R. (2012). Unpublished monitoring data for the Huston Township, Clearfield 585 County Mount Pleasant Road Bridge.

Alexiew and Detert (2008). “Analytical and Numerical Analyses of a Real Scaled Geogrid Reinforced Bridge Abutment Loading Test.” EuroGeo4 Paper number 257.

Alexiew, D. (2007) “Belastungsversuch an einem 1:1 Modell eines geogitterbewehrten Bruckenwiderlagers.” Proceedings of KGeo 2007, Munich, Germany. (In German).

Alexiew, D. (2008). “Ultimate bearing capacity tests on an experimental geogrid-reinforced vertical bridge abutment without stiffening facing.” New Horizons in Earth Reinforcement, Taylor and Francis Group, London, pp. 507-511.

Alexiew, D., Sobolewski, J., and Pohlmann, H. (2000). “Projects and Optimized Engineering with Geogrids from 'Non-Usual' Polymers.” EuroGeo 2000: Proceedings of the 2nd European Geosynthetics Conference. Volume 1: Mercer Lecture, Keynote Lectures, Geotechnical Applications.

Allen, T. M., Bathurst, R. J., Holtz, R. D., Walters, D., and Lee, W. F. (2003). “A new working stress method for prediction of reinforcement loads in geosynthetic walls.” Canadian Geotechnical Journal, Vol. 40, No. 5, pp. 976-994.

Athanasopoulos, G.A. (1993). “Effect of Particle Size on the Mechanical Behavior of Sand-Geotextile Composite.” Geotextiles and Geomembranes, Vol. 12, pp. 255-273, International Geosynthetics Society, West Palm Beach, FL.

Athanasopoulos, G.A. (1994). “On the Enhanced Normal pressure Approach to the Mechanics of Reinforced Soil.” Geotechnical and Geological Engineering Vol. 12, pp. 122-132, Springer, Netherlands.

Bassett, A.K. and Last, N.C. (1978). “Reinforcing Earth below Footings and Embankments.” Proceedings of the ASCE Spring Convention and Exhibit, Pittsburgh, PA.

Benigni, C., Bosco, G., Cazzuffi, D., Col, R.D., 1996. “Construction, performance of an experimental large-scale wall reinforced with geosynthetics.” In: Ochiai, H., Yasufuku, N., Omine, K. (Eds.), Earth Reinforcement, Vol. 1. A. A. Balkema Publisher, Rotterdam, pp. 315-320.

Berg, R.R., Christopher, B.R., and Samtani, N.C. (2009). Design of Mechanically Stabilized Earth Walls and Reinforced Soil Slopes–Volume II. Report No. FHWA-NHI-10-025. National Highway Institute, Federal Highway Administration, Washington, D.C.

Bloser, S., Shearer, D., Corradini, K., and Scheetz, B. (2012). Geosynthetically Reinforced Soil-Integrated Bridge Systems (GRS-IBS) Specification Development for PennDOT Publication 447. Pennsylvania Department of Transportation Bureau of Planning and Research.

Brugger, P.J., Gomes, R.D.O.M., and Conte, M. (2012). “Rebaixamento da Linha Férrea de Maringá Utilizando Muros em Solo Reforçado.” Proceedings of IGS Brasil CURSOS. (In Portuguese).

Budge, A.S., Dasenbrock, D.D., Mattison, D.J., Bryant, G.K., Grosser, A.T., Adams, M., and Nicks, J. (2014). “Instrumentation and Early Performance of a Large-Grade GRS-IBS Wall.” Geo-Congress 2014 Technical Papers Geo-characterization and Modeling for Sustainability, 4213-4227.

Da Silva, A.E.F., Brugger, P.J., and Engenharia, B. (2012). “Análise do Comportamento de Muro de Contenção Portante em Solo Reforçado a partir de Monitoramento de Campo.” 12th Congresso Brasileiro de Mecanica dos Solos e Engenharia Geotechnica (COBRAMSEG). (In Portuguese).

Detert, O., and Thomson, G. (2013). “Geogrid-Reinforced Bridge Abutments: Report on a Full Scale Test and Executed Projects.” Advances in Geotechnical Infrastructure. Edited by C. F. Leung, S.H. Goh and R.F. Shen. 241-246.

Ehrlich, M., Mitchel, J. K. (1994) Working Stress Design Method For Reinforced Soil Walls, Journal of Geotechnical Engineering, ASCE, Vol. 120, No. 4, pp. 625-647.

Elias, V.E., Christopher, B.R., and Berg, R.R. (2001). Mechanically Stabilized Earth Walls and Reinforced Soil Slopes Design and Construction Guidelines. Technical Report No. FHWA-NHI-00-043, National Highway Institute, Federal Highway Administration, Washington, D.C.

Elton, D.J., and Patawaran, M.A.B. (2004). “Mechanically stabilized earth reinforcement tensile strength from tests of geotextile-reinforced soil.” Transportation Research Record: Journal of the Transportation Research Board, Vol. 1868, pp. 81-88.

Elton, D.J., and Patawaran, M.A.B. (2005). Mechanically stabilized earth (MSE) reinforcement tensile strength from tests of geotextile-reinforced soil. Alabama Highway Research Center, Auburn University, Aurburn, AL.

Fahel, A.R., Palmeira, E.M., and Ortigao, J.A.R. (2000). “Behaviour of Geogrid Reinforced Abutments on Soft Soil in the BR 101-SC Highway, Brazil.” Geotechnical Special Publication, 257-270.

Gotteland, Ph., Gourc, J.P., Villard, P., 1997. “Geosynthetics reinforced structures as bridge abutments: full scale experimentation and comparison with modelisations.” In: Wu, J.T.H. (Ed.), Mechanically Stabilized Backfill. A. A. Balkema Publisher, Rotterdam, pp. 25–34.

Gourc, J.P., Gotteland, P., Haza, E., Perrier, H., and Baraize, E. (1995). “Geotextile reinforced structures as bridge abutments: full-scale experimentation.” Proceedings of Geosynthetics 1995 Conference Proceedings, Nashville, TN, pp. 79-92.

Gray, D.H. and Ohashi, H. (1983). “Mechanics of Fiber Reinforcement in Sand,” Journal of Geotechnical Engineering, Vol. 109, pp. 335–353, American Society of Civil Engineers, Reston, VA.

Hausmann, M.R. (1976). “Strength of Reinforced Earth,” ARRB Proceedings, Vol. 8, ARRB Group, Melbourne, Australia.

Herold, A. (2002). “The first permanent road-bridge abutment in Germany built of geosynthetic-reinforced earth.” Proceedings of the 7th ICG-Delmas, Gourc and Girard (eds).

Herold, A. (2005) “Brückenwiderlager aus KBE-Kunststoffbewehrte Erde, Einsatzgebiete Und Anwendungsgrenzen.” Geotechnik-Kolloquium, Freiberg, Technische Institut für Geotechnik der Universität Bergakademie Freiberg, Heft 2005-2, pp. 195-217. (In German).

Herold, A. (2006) “Brückenwiderlager aus KBE-Kunststoffbewehrte Erde, Einsatzgebiete Und Anwendungsgrenzen.” Sächsisches Textilforschungsinstitut Bautextilien-Symposium, Bautex 2006, Institut für Technische Textilien GmbH, Chemnitz, pp. 1-12. (In German).

Herold, A. (2007) “10 Jahre Verformungsbeobachtungen an KBE-Bauwerken – Ist die Dehnsteifigkeit der Geokunststoffe der Schlüssel zur korrekten Prognose des Verformungsverhaltens von KBE Stützbauwerken?” Geotechnik, Vol. 29, No. 2, pp. 79-86. (In German).

Herold, A. (2008) “Brückenwiderlager aus KBE-Hinweise fur Entwurf und Ausfuhrung.” Kolloquium "Bauen in Boden und Fels" in Ostfildern , Technische Akademie Esslingen e.V., Tagungshandbuch 2008, pp. 533-543. (In German).

Herold, A., Aydoğmuş, T., and Sander, H. (2008). “Large Constructions and Bridge Abutments: Solutions with Geosynthetic-reinforced Earth.” Proceedings of Structures Congress 2008 Crossing Borders, pp. 1-10.

Huesker Synthetic GmbH. The Lagoons – Dubai. Huesker Synthetic GmbH, Gescher.

Ingold, T.S. (1982). Reinforced Earth, Thomas Telford Ltd., London, United Kingdom.

Kasugai, A., and Tateyama, M. (1992). "Application of geosynthetic-reinforced soil for bridge abutments." Earth Reinforcement Practice, Ochiai, Hayashi & Otani (eds), 1992, Balkema, Rotterdam, pp. 363-368.

Keller, G. and Devin, S. (2003). "Geosynthetic-reinforced soil bridge abutments." Transportation Research Record: Journal of the Transportation Research Board, Vol. 1819, pp. 362-368.

Ketchart, K. and Wu, J.T.H. (2001). Performance Test for Geosynthetic-reinforced Soil Including Effects of Preloading. Report No. FHWA-RD-01-018, Federal Highway Administration, Washington, DC.

Kirschner, R., and Hermansen, E. (1994). "Abutments in Reinforced Soil for a Road Bridge." Proceedings of the 5th International Conference on Geotextiles, Geomembranes, and Related Products. Singapore, September, 1994, pp. 259-260.

Lee, K.Z., and Wu, J.T. (2004). "A synthesis of case histories on GRS bridge-supporting structures with flexible facing." Geotextiles and Geomembranes, Vol. 22, No. 4, pp. 181-204.

Lenart, S. (2014). Final report of development of reinforced soil bridge abutments. Report No. P 320/13-710-8, Oddelek za geotehniko in prometnice, Zavod za gradbeništvo Slovenije, 2014 (in Slovenian).

Lenart, S., Kralj, M., Medved, S.P., and Šuler, J. (2016). "Design and construction of the first GRS integrated bridge with FHR facings in Europe." Transportation Geotechnics, Vol. 8, pp. 26-34.

Ling, H.I. and Tatsuoka, F. (1994). “Performance of Anisotropic Geosynthetic-Reinforced Cohesive Soil Mass”, Journal of Geotechnical Engineering, ASCE, Vol. 120, No. 7, pp. 1166-1184.

Ling, H.I., Tatsuoka, F., and Tateyama, M. (1995). “Simulating the Performance of GRS-RW by Finite Element Procedure.” Journal of Geotechnical Engineering, ASCE, Vol. 124, No. 4, pp. 330-340.

Lo, S.R. (2004). Application of Numerical Modelling to the Design of Reinforced Soil Walls for Infrastructure Projects-Some Australian Experiences. In GeoAsia2004: 3rd Asian Regional Conference on Geosynthetics: Now and Future of Geosynthetics in Civil Engineering. June 2004.

Maher, M.H. and Woods, R.D. (1990). “Dynamic Response of Sand Reinforced with Randomly Distributed Fibers,” Journal of Geotechnical Engineering, Vol. 116, pp. 1116–1131, American Society of Civil Engineers, Reston, VA.

Mirlatifi, S., and Fatahi, B. (2012). “Numerical Analysis of Geosynthetic-reinforced Soil Wall as Bridge Abutment.” Proceedings of the 11th Australia - New Zealand (ANZ) Conference on Geomechanics Ground Engineering in a Changing World. Melbourne, Australia. July 2012, pp.1383-1388.

Mirlatifi, S.A.S. (2012). “Analysis, Design, and Construction Stages of Milad Geosynthetic-reinforced Soil Bridge Abutment in Tehran-Iran.” Australian Geomechanics, Vol. 47, No. 3, September 2012, pp. 125-132.

Mohamed, K., Abouzakhm, M., and Elias, M. (2011). “Applications and performance of geosynthetic-reinforced soil abutments on soft subsurface soil conditions.” Transportation Research Board.

Morsy, A.M., and Zornberg, J.G. (2017), “A Tale of Two Bridges: Comparison between the Seismic Performance of Flexible and Rigid Abutments,” In Proceedings of the 3rd African Regional Conference on Geosynthetics (GeoAfrica 2017), International Geosynthetics Society (IGS), October 8-11, 2017 | Marrakech, Morocco, pp. 1000-1007.

Nancey, A., Rossi, D., and Boons, B. (2006). “Survey of a bridge abutment reinforced by geosynthetics, with optic sensors integrated in geotextile strips.” Proceedings of IGC 8th, September 18-22, Yokohama, Japan, pp. 1071-1074.

Nguyen, Q. (2012). GRS Abutments for Bridge Replacement National Wildlife Refuge. A New Era of Partnerships - Investing in America's Treasures, U.S. Department of Transportation, FHWA, EFLHD.

Ortigao, J.A.R., Fahel, A.R., Palmeira, E.M., and Simmonds, A.J. (2001). “Stability and deformation monitoring of geogrid reinforced embankments.” Proceedings of Transportation Research Board Meeting on Geo-Construction Processes, TRB Meeting, pp. 51-62.

Powell, W., Keller, G.R., and Brunette, B. (1999). “Applications for Geosynthetics on Forest Service Low-Volume Roads.” Transportation Research Record, Vol. 1652, pp. 113-120.

Rimoldi, P. and Intra, E. (2009). "Design and Construction of Tall Reinforced Embankments in Static and Seismic Conditions." GIGSA GeoAfrica 2009 Conference, Cape Town, September 2009.

Railway Technical Research Institute (2012). Design Standards for Railway Structures and Commentary Earth Retaining Structure. Edited by Railway Technical Research Institute (RTRI), under supervision of Railway Bureau of Ministry of Land, Infrastructure, Transport and Tourism, (MLIT), Japan.

Schlosser, F. and Long, N.T. (1974). "Recent Results in French Research on Reinforced Earth." Journal of Construction Division, Vol. 100, pp. 223–237, American Society of Civil Engineers, Reston, VA.

Snijders, B., and Brok, C. (2007). "N242 Bridge Abutments on geogrid reinforced soil near the city of Alkmaar in the Netherlands." Proceedings of the 14th European Conference on Soils Mechanics and Geotechnical Engineering (Geotechniek ECSMGE). Madrid, Spain, September 2007, pp. 12-14.

Suits, L.D., and Hsuan, Y.G. (2003). "Assessing the photo-degradation of geosynthetics by outdoor exposure and laboratory weatherometer." Geotextiles and Geomembranes, Vol. 21, No. 2, pp. 111-122.

Tatsuoka, F. (1993). "Roles of Facing Rigidity in Soil Reinforcing." Earth Reinforcement Practice, Keynote Lecture, Ochiai, H.,Hayashi, S. and Otani, J., Editors, Balkema, 1993, Proceedings of the International Symposium on Earth Reinforcement Practice, IS Kyushu 1992, Vol. 2, Kyushu, Fukuoka, Japan, November 1992, pp. 831-870.

Tatsuoka, F., and Yamauchi, H. (1987). “A Reinforcing Method for Steep Clay Slopes Using a Non-Woven Geotextile”, Geotextiles and Geomembranes, Vol. 4, pp. 241-268.

Tatsuoka, F., Tamura, Y., Nakamura, K., Iwasaki, K., and Yamauchi, H. (1987). “Behavior of Steep Slope Clay Embankments Reinforced With a Non-Woven Geotextile Having Various Face Structures.” Proceedings of the Post Vienna Conference on Geotextiles, Singapore, pp. 387-403.

Tatsuoka, F., Tateyama, M., Uchimura, T., and Koseki, J. (1997). Geosynthetic-Reinforced Soil Retaining Walls as Important Permanent Structures 1996-1997 Mercer Lecture. Geosynthetics International, Vol. 4, No. 2, pp. 81-136.

Tatsuoka, F.,Ando,H., Iwasaki, K. and Nakamura, K. (1986). “Performance of Clay Test Embankments Reinforced With a Non-Woven Geotextile”, Proceedings of the Third International Conference on Geotextiles, Vol. 3, Vienna, Austria, April 1986, pp. 355-360.

Tecnologia de Materiales. Muros de Solo Reforçado Como Estribos de Ponte S27 – Yanacocha. Tecnologia de Materiales (TDM), Peru. (In Portuguese).

Tensar North American Green (2001). The Mesa Systems Bridge Commerce in North Vancouver, B.C. Tensar North American Green.

The American Association of State Highway and Transportation Officials (2014). AASHTO LRFD Bridge Design Specifications. Seventh Edition, 2014.

Van Duijnen, P.G., Linthof, T., Brok, C.A.J.M., and Eekelen, S.J.M. (2012). “Measuring deformations of a 10 m high geosynthetic-reinforced earth retaining wall.”

Proceedings of the 5th European Geosynthetics Congress. Valencia, 2012. Proceedings Vol 5. Topic: Soil Improvement and Reinforcement, pp. 157-161.

Vennapusa, P.K., White, D.J., and Keierleber, B. (2014). A Case Study of Geosynthetic-Reinforced Soil in a Low-Volume Bridge Abutment in Iowa. Geo-Congress 2014 Technical Papers Geo-characterization and Modeling for Sustainability. February 2014, pp. 4156-4166.

Vennapusa, P., White, D.J., Klaiber, F.W., Wang, S., and Gieselman, H. (2012). Geosynthetic-reinforced soil for low-volume bridge abutments. Report No. IHRB Project TR-621, Iowa Highway Research Board and Iowa Department of Transportation. 114p.

Wadey, L., and Idrees, M. (2014). Nadahini Creek Geosynthetic-reinforced Soil Integrated Bridge System. In Transportation 2014: Past, Present, Future-2014 Conference and Exhibition of the Transportation Association of Canada//Transport 2014: Du passé vers l'avenir-2014 Congrès et Exposition de'Association des transports du Canada.

Warren, K. A., Schlatter, W., Adams, M., Stabile, T., and LeGrand, D. (2010). "Preliminary Results for a GRS Integrated Bridge System Supporting a Large Single Span Bridge." Proceedings of Earth Retention Conference 3, ASCE, Reston, VA, pp. 612-619.

Warren, K.A., Whelan, M., Adams, M., and Nicks, J. (2013). "Preliminary Evaluation of Thermally Induced Strains and Pressured Developed in GRS Integrated Bridge System." Geosynthetics Conference, Long Beach, CA.

Warren, K. A., Whelan, M. J., Hite, J., and Adams, M. (2014). "Three-Year Evaluation of Thermally Induced Strain and Corresponding Lateral End Pressures for a GRS IBS in Ohio." In Geo-Congress 2014 Technical Papers Geo-characterization and Modeling for Sustainability. February 2014, pp. 4238-4251.

Werner, G., and Resl, S. (1986). "Stability mechanisms in geotextile reinforced earth-structures." In III International Conference on Geotextiles, Vienna, Austria, Vol. 4, pp. 1131-1135.

Won, G.W., Hull, T., De Ambrosis, L. (1996). "Performance of a geosynthetic segmental block wall structure to support bridge abutments." In: Ochiai, H., Yasufuku, N., Omine, K. (Eds.), Earth Reinforcement, Vol. 1. A. A. Balkema Publisher, Rotterdam, pp. 543–548.

Wu, J.T.H. (2006). Design and construction guidelines for geosynthetic-reinforced soil bridge abutments with a flexible facing (No. 556). Transportation Research Board.

Wu, J.T.H., Ketchart, K., and Adams, M. (2001). GRS bridge piers and abutments. Report No. FHWA-RD-00- 038. Federal Highway Administration, US Department of Transportation, Washington, D.C. 136p.

Yamauchi, H. and Tatsuoka, F., Nakamura, K., Tamura, Y. and Iwasaki, K. (1987). "Stability of Steep Slope Clay Embankments ReinforcedWith a Non-WovenGeotextile," Proceedings of the Post Vienna Conference on Geotextiles, Singapore, pp. 370-386.

Yang, Z. (1972). Strength and Deformation Characteristics of Reinforced Sand, PhD. Thesis, University of California at Los Angeles, Los Angeles, CA.

Yang, Z. and Singh, A. (1974). Strength and Deformation Characteristics of Reinforced Sand, International Meeting on Water Resources Engineering, Los Angeles, CA.

Ziegler, M., Heerten, G., and Ruiken. G. (2008). "Progress in the Understanding of Geosynthetic/Soil Composite Material Behaviour in Geosynthetic-reinforced Earth Structures," Presented at The First Pan American Geosynthetics Conference and Exhibition, Cancun, Mexico.

SECTION I: REEVAULATION OF DATA FROM THE LITERATURE

A significant source of information was acquired by reviewing the technical literature, particularly by having access to the source data. This capitalized the understanding of the composite behavior of GRS structures. Specifically, a detailed evaluation of actual data sources was conducted, including actual experimental and field monitoring data. Interpretation of the source data was important and useful to support the findings of the other components of this research. Each chapter in this section is a self-contained study. The various sources of this information are as follows:

- Evaluation of the performance of large-scale experimental geosynthetic-reinforced soil structures.
- Soil arching in geosynthetic-reinforced soil structures.
- Evaluation of the performance of geosynthetic-reinforced soil centrifuge models.
- Assessment of the Founders/Meadows geosynthetic-reinforced soil bridge abutment performance.

Chapter 3: Evaluation of the Performance of Large-Scale Experimental Geosynthetic-Reinforced Soil Structures

3.1. INTRODUCTION

Soil reinforcement technology has become a vital alternative for many structures, such as bridge supports. Soil reinforcement has proven to provide economic, time-efficient structural solutions. Soil-reinforcement technology has been adopted in bridge-supporting structures using (1) metallic reinforcement forming metallically reinforced MSE abutments and (2) geosynthetic reinforcement forming geosynthetically reinforced MSE abutments. Although the US Federal Highway Adminstration (FHWA) has launched many research research programs since the 1980s indicating that reduced stresses develop in the reinforcements towards the face of the wall, AASHTO has conservatively required that the connection stress should be equal the maximum reinforcement tension. Also, US state agencies often rely on manufacturer's design recommendations, which have traditionally placed strong pressure towards using comparatively wider spaced, more economical, higher strength geosynthetic reinforcements. Partly in response to these issues, FHWA has recently developed both empirical and analytical design models for Geosynthetic-Reinforced Soil—Integrated Bridge System (GRS-IBS) structures (Adams et al. 2012 – FHWA-HRT-11-026; Adams et al. 2011 – FHWA-HRT-11-027). FHWA has also calibrated the reliability of these models using results from GRS test piers (Nicks et al. 2013a – FHWA-HRT-13-066), which have been correlated against monitored field results.

The GRS mini-pier tests were performed both with and without facing elements and with a reinforcement spacing of 10 cm (4 in.) at the top of the structure. The program included GRS test piers constructed with various reinforcement vertical spacings,

approximately 10 cm (4 in.), 20 cm (8 in.), 27.5 cm (11 in.), and 37.5 cm (15 in.), as well as with and without facing blocks. The piers were subjected to very large uniform surcharge loading and tested to failure. These tests have been extensively evaluated for vertical and horizontal deformations of the reinforced soil system and some of the results from these experiments have been published (e.g. Nicks et al. 2013a, 2013b). A clear difference was reported in the failure mechanism between GRS piers constructed with large and small reinforcement spacings. This pointed towards a potential effect for the reduction of the reinforcement vertical spacing that can enhance the strain comptatbility between the reinforcement layers and the soil in between leading to, possibly, a compsite behavior.

Although the tests clearly show the difference in load bearing behavior among the constructed structures, as in all laboratory experiments, the results represent conditions unique to those used in the tests. It should be noted, for example, that the surcharge used in the laboratory is uniform and centered over the reinforced pier, while surcharge in a bridge abutment is not necessarily uniform, being often eccentric. Since soil-reinforcement interaction depends on the normal stresses, laboratory observations alone may not be sufficient to predict field performance. That is, the full scope of realistic field conditions needs to be addressed before a design may be considered acceptable by AASHTO LRFD. Accordingly, this study presents an independent reassessment of the published and unpublished monitoring data on the GRS mini-pier tests and instrumented field structures was conducted as part of this study to critically evaluate these boundary effects. In addition, well prediction of the service state of these structures is crucial for their serviceability

assessment. Accordingly, this study collects published data for real and experimental structures. It assess the practical models that were developed recently.

3.2. BACKGROUND

Reinforced soil structures were introduced in 1966 by the French Engineer Henri Vidal who stated: "if we could put in place one layer of grains in contact with one layer of reinforcement, then one layer of grains, and so on, we should not have any need for facing. The facing retains the grain located near the exterior between two layers of reinforcement; it corresponds to a very local problem." While this statement was controversial with the conventional retaining walls, this technology is still accepted to this day. Later, soil-reinforcement has evolved to employ geosynthetic reinforcement. The first geosynthetically reinforced MSE structure in North America, which was a retaining wall, was constructed in 1974 in the United States of America (Berg et al. 2009a). Since then, the use of geosynthetically reinforced MSE walls has become a considerable alternative for retaining structures. They have become even more popular after the introduction of the geogrid reinforcement in 1982, and the segmental facing units in 1985 (Berg et al. 2009a). The technology has been adopted and advancing globally.

FHWA has conducted a long-term research on the MSE technology that started in the 1980s. The first design and construction guidelines were generated and published in Christopher et al. (1990a). The work that has been conducted by that time was summarized in Christopher et al. (1990b). Continued work has resulted in revised design and construction guidelines (Berg et al. 2009a, 2009b). Recently, FHWA has introduced geosynthetic-reinforced soil (GRS) technology as closely-spaced reinforced MSE

structures. FHWA has promoted this technology through its Every Day Counts (EDC) initiative program. A number of publications document the research conducted by FHWA or with the use of FHWA facilities.

Several studies have attempted to study the long-term behavior of GRS structures (e.g. Allen et al. 1992; Wu and Helwany 1996). Wu and Helwany (1996) developed a laboratory performance test (Figure 3.1) to evaluate the creep behavior of geosynthetic reinforcement due to soil-geosynthetic interaction. The geosynthetic reinforcement and the confining soil were loaded for a long period of time and allowed to deform in an interactive manner. Clean sand and kaolin clay were used as backfills for two different tests. The results showed that reinforced soils have higher stiffness and strength unreinforced soils. Yet, some vertical and horizontal deformations have to take place to mobilize the reinforcing effects. In addition, it was also concluded that the time-dependent deformation of the confining soil plays a very important role in the long-term creep potential of a GRS structure. That is, the reinforcement creep deformation is significantly affected by the time-dependent deformation characteristics of soils under confinement. Time-dependent deformation of sands and clays is very different. Sands have tendency to deform at slower rate than the geotextile. On contrary, clays have tendency to deform at a higher rate than the geotextile. Wu and Helwany (1996) concluded that evaluating the soil-geosynthetic composite creep potential could be misleading if it is based on the results of geosynthetic element creep tests only. Ketchart and Wu (1996) reported that the creep deformation with time at a decreasing rate. In sands, vertical and lateral deformation are limited and similar.

In clays, lateral deformation is negligible; however, the vertical deformation is significant. In addition, higher reinforcement strength further reduces the deformation significantly.

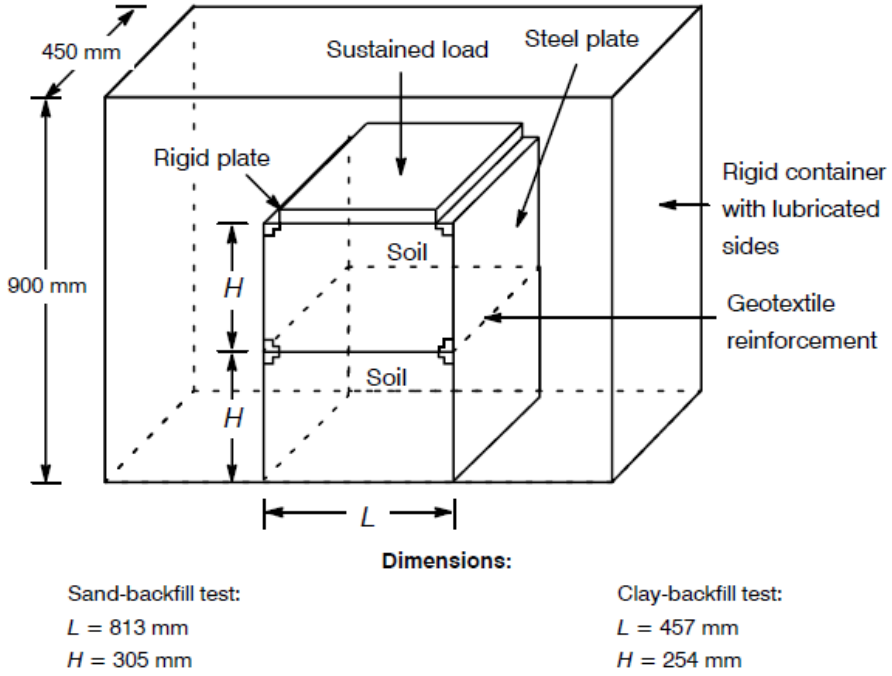

Figure 3.1. Soil-Geosynthetic Performance (SGP) testing apparatus developed by Wu and Helwany (1996).

Christopher et al. (1986) developed a tests for determining the confined stress-strain behavior characteristics of reinforcement, which provided satisfactory results. Also, Ketchart and Wu (FHWA-RD-01-018, 2001) investigated the behavior of GRS masses under various loading conditions. The study aimed at developing a simplified analytical model for predicting deformation characteristics of a generic GRS mass. Specifically, the researchers developed Soil-Geosynthetic Performance (SGP) laboratory test with the

objective of mimicking field placement conditions of GRS structures. This test aimed at capturing the effect of the interaction between the backfill soil and the geosynthetic reinforcement. Ketchart and Wu (2001) conducted a set of SGP tests using various soil types, geosynthetic reinforcements, and loading sequences. The study evaluated the effect of preloading on the GRS behavior. The authors correlated the results of SGP tests to full-scale GRS structures in order to assess the degree of accuracy of the SGP test to predict the reduction in settlement due to preloading. Specifically, two preloaded reinforced soil structures and their corresponding SGP test were examined: (1) FHWA pier (Adams 1997) and the second generation SGP test, and (2) Black Hawk abutments reported by Wu et al. (FHWA-RD-00-038, 2001) and the modified SGP test. The correlations were generated in terms of normalized values of loads and displacements. Ketchart and Wu (2001) concluded that (1) preloading increases soil stiffness, but has no effect on shear strength, while reloading stiffness depends on normal pressure and unloading load level; (2) preloading increases geosynthetic stiffness, very slightly decreases tensile strength, while reloading stiffness reduces with increasing preloading load level; (3) preloading has no effect on shear strength of interface. Reloading stiffness increases with preloading and normal stress applied on the interface; (4) preloading has no effect on the GRS carrying capacity; (5) the creep of geosynthetic reinforcement is negligible when using well-compacted granular fill, and stress relaxation occurs right after construction; and (6) unloading and reloading stress-strain behavior nearly coincides.

Wu et al. (FHWA-RD-038, 2001) describe in detail three projects involving load testing of GRS abutments and piers. The first project is a full-scale bridge pier load test

conducted at the Turner-Fairbank Highway Research Center (TFHRC). This pier is referred to as the Turner-Fairbank pier. The second project involves a full-scale, long-term load test of a bridge abutment and a bridge pier conducted by the Colorado Department of Transportation (CDOT) and the University of Colorado at Denver. These piers and abutment are referred to as the Havana Yard piers and abutment. The third project involves the load test of a production bridge abutment performed by Yenter Companies in Black Hawk, Colorado. This abutment is referred to as the Black Hawk abutment. The abutments evaluated as part of these studies were instrumented to assess behavior under load testing. Wu et al. (2001) provide a comprehensive description to the projects along with testing results and analysis. Recommendations to GRS applications are incorporated in the report.

Ketchart and Wu (2002) developed a Soil-Geosynthetic Interactive Performance (SGIP) testing apparatus (Figure 3.2) to assess the deformation behavior of GRS composites. The test is a modified version of the SGP test developed earlier by Ketchart and Wu (FHWA-RD-01-018, 2001). The test consists of applying a vertical load on a GRS composite under plane strain condition. The applied load is transferred from soil to geosynthetic allowing both to deform in an interactive manner. Lateral and vertical displacements of the GRS mass are measured along with the reinforcement strains. Ketchart and Wu (2002) conducted a set of tests to investigate repeatability, failure mode, and deformation behavior of different GRS composites. The behavior of tested GRS was compared to that of a GRS pier to verify the test applicability. Wu and Adams (2007) investigated the long-term creep behavior of GRS systems and proposed revisions to the current design methods. The authors recommended a cumulative long-term reduction

factor for geosynthetic reinforcement. This reduction factor is a function of the backfill gradation and index properties, reinforcement spacing, and geosynthetic polymer type. The authors presented a procedure to account for soil-geosynthetic interactive creep behavior based on SGIP test.

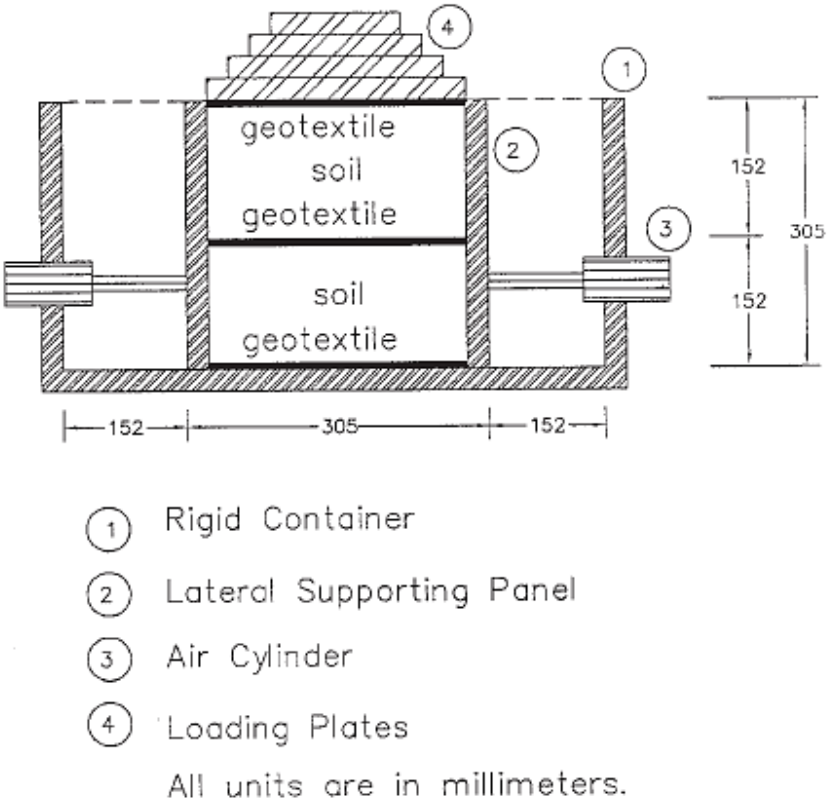

Figure 3.2. Modified Soil-Geosynthetic Interactive Performance (SGIP) testing apparatus developed by Ketchart and Wu (1996).

Wu et al. (NCHRP 556, 2006) developed a design methodology and construction guidelines for GRS bridge abutments with flexible facing (i.e., geotextile-wrapped, timber, and natural rock facing). They depended on the findings reported in the literature along

with findings of full-scale experiments and analytical study performed. Wu et al. (NCHRP 556, 2006) constructed full-scale GRS abutments (Figure 3.3). The tested GRS structures showed good performance and high load-carrying capacity. In addition, the authors compiled a design methodology and construction procedure for GRS abutments with flexible facing. Detailed design examples were also provided. Adams et al. (2007a) conducted five large-scale GRS Mini Pier tests to assess the effect of reinforcement spacing and reinforcement strength on the behavior of GRS masses. The authors reported that the bearing capacity for closely-spaced GRS was significantly improved and that the contribution of the reinforcement spacing was more relevant to the performance of a GRS mass than the reinforcement strength.

Adams et al. (FHWA-HRT-11-026, 2012) provide a design methodology and construction procedure for GRS-IBS structures. This manual aims at providing background knowledge of GRS technology as well as of its fundamental characteristics as an alternative to other construction methods. In addition to providing detailed guidance on the design of GRS-IBS, the manual includes analytical and empirical design methodologies involving both the Allowable Stress Design (ASD) and Load and Resistance Factor Design (LRFD) approaches. Background knowledge in support of the design methodology is summarized by Adams et al. (FHWA-HRT-11-027, 2011), which documents the fundamental characteristics of GRS technology as an alternative construction method. This document supplements the interim implementation manual by Adams et al. (FHWA-HRT-11-026, 2012) and provides a generic design methodology and construction outline of the GRS-IBS. In addition, it includes the results of research conducted to provide the basis for the

design method. Finally, case histories are summarized to document the performance of in-service GRS-IBS and GRS walls.

Nicks et al. (FHWA-HRT-13-066, 2013a) reported the results of a series of experimental GRS performance tests, also identified as mini-pier experiments. The tests were conducted by axially loading a GRS mass while measuring the resulting deformations and, thus, documenting the mini-piers' performance. The mini-piers included alternating layers of compacted granular fill and geosynthetic reinforcement connected frictionally to facing elements. This report documents the testing procedure and provides the axial load-deformation results for the performance tests conducted in this study. In addition, this research aimed at establishing a database of GRS material properties for the purposes of construction of GRS-IBS structures. The results are used to: (1) establish a relationship between reinforcement strength and spacing, (2) quantify the contribution of the frictionally connected facing elements at the service limit and strength limit states, (3) assess the internal stability design method proposed by Adams et al. (2011) for GRS, and (4) provide the basis for a reliability analysis of the soil-geosynthetic capacity equation for LRFD calibration. In addition, Nicks et al. (2013b) determined the material strength properties of particular GRS composites based on GRS mini-pier performance test results. The effects of backfill type and compaction on the GRS composites were also investigated. Nicks et al. (2013b) outlined the performance test methodology along with resulting load-deformation characteristics. Nicks et al. (2013a) concluded that (1) particle angularity of the backfill improves the GRS composite ultimate strength; (2) compaction doesn't affect the GRS ultimate strength but provide much stiffer response; (3) bearing bed (secondary

reinforcement placed at the upper portion of the GRS mass) improves the vertical capacity but not vertical strain; however, it limits its local lateral deformation; (4) frictional CMU facing provides confinement leading to stiffer GRS composite response (increasing ultimate capacity and decreasing vertical strain; and (5) for the same reinforcement strength-to-spacing ratio (Tf/Sv), reinforcement spacing impacts the behavior more than reinforcement strength, unlike largely-spaced GRS (reinforcement spacing greater than 30 cm (12 in.)) where reinforcement spacing is proportional to reinforcement strength.

Wu et al. (FHWA-HRT-10-077, 2013) investigated the composite behavior of a GRS mass by conducting a series of large-scale generic soil geosynthetic composite (GSGC) tests. This involved constructing GRS piers with two fixed sides to mimic a plane-strain condition. Similar test has been conducted by Bathrust and Benjamin (1990), which involved constructing GRS abutment with two fixed sides and unreinforced shored fill behind the GRS mass. Wu et al. (FHWA-HRT-10-077, 2013) designed their tests to assess the behavior of a GRS mass under well-controlled conditions. The experimental results showed that reinforcement spacing influences the GRS behavior more significantly than reinforcement strength. Wu et al. (FHWA-HRT-10-077, 2013) developed analytical model that allowed description to the relative contribution of reinforcement strength and reinforcement spacing. In addition, equations were developed based on the analytical model. These equations were developed to calculate the apparent cohesion of a GRS composite (acquired cohesion due to the reinforcement inclusion), the ultimate load-carrying capacity of a GRS mass, and the required tensile strength of reinforcement for a given reinforcement spacing. The suitability of the developed equations was evaluated by

comparing the predictions against the results of GSGC tests, large-size experiments performed by other researchers, and finite element (FE) simulations. Moreover, an analytical procedure was developed to predict the lateral wall movement and the required tensile strength of reinforcement. In addition, an analytical model for estimating compaction-induced stresses in a GRS mass was proposed. The model predictions were compared against the results of GSGC tests and FE simulations. Wu et al. (FHWA-HRT-10-077, 2013) also investigated the dilatant behavior of GRS composites. They reported that reinforcements tend to suppress dilation of the surrounding soil and reduce its angle of dilation.

3.3. GRS EXPERIMENTAL STRUCTURES DATABASE

Since soil-reinforcement interaction depends on the normal stresses, laboratory observations alone may not be sufficient to predict field performance. Accordingly, an independent reassessment of the published and unpublished monitoring data on the GRS mini-pier tests and some instrumented field structures was conducted to critically evaluate the feasibility of these tests. In addition, well prediction of the service state of these structures is crucial for their serviceability assessment. Accordingly, this study collected a massive amount of published data for particularly experimental structures. This section presents the database established in favor of this evaluation.

3.3.1. GSGC tests by Wu et al. (FHWA-HRT-10-077, 2013)

Wu et al. (FHWA-HRT-10-077, 2013) conducted five experiments large-scale GRS columns. The GRS is fixed from two sides by stiffened transparent walls to simulate a plane-strain condition as shown in Figure 3.3. The GRS mass was 1.94-m high and 1.2 x

1.4 m in plan. The backfill material used was well-gravel classified as A-1-a in accordance to AASHTO and GW-GM in accordance to USCS. The friction angle and the cohesion of the soil were 50 degrees and 70 kPa, respectively, obtained from large-scale triaxial testing. The maximum dry density and optimum moisture content of the backfill were 24.1 kN/m3 and 5.2%, respectively. The backfill had approximately 15% fine content. The soil was reinforced by a medium-strength woven geotextile layers employed at 0.2-m (0.7-ft) vertical spacing. The reinforcement was Geotex® 4×4 polypropylene woven geotextile manufactured by Propex®. The reinforcement spacing varied from 0.2 to 0.4 m. The ultimate tensile strength of the reinforcement was 70 kN/m. The testing program involved using double layer reinforcement so as two different reinforcement types could be used: (1) a single reinforcement layer; and (2) a double reinforcement layer (two glued layers), which showed approximately twice the tensile stiffness and strength of the single layer in uniaxial tension tests. Facing hollow concrete blocks were used for the deformable sides of the GRS mass. The configurations of the five conducted tests are summarized in Table 3.1.

Table 3.1. Test configurations (Wu et al. 2013).

Test Designation	***Geosynthetic Reinforcement***	***Normal pressure (kPa)***	***Wide-Width Strength of Reinforcement (kN/m)***	***Reinforcement Spacing (m)***
GSGC1	None	34	None	None
GSGC2	Geotex® 4x4	34	70	0.2
GSGC3	Double-Sheet Geotex® 4x4	34	140	0.4
GSGC4	Geotex® 4x4	34	70	0.4
GSGC5	Geotex® 4x4	0 (unconfined)	70	0.2

(a)

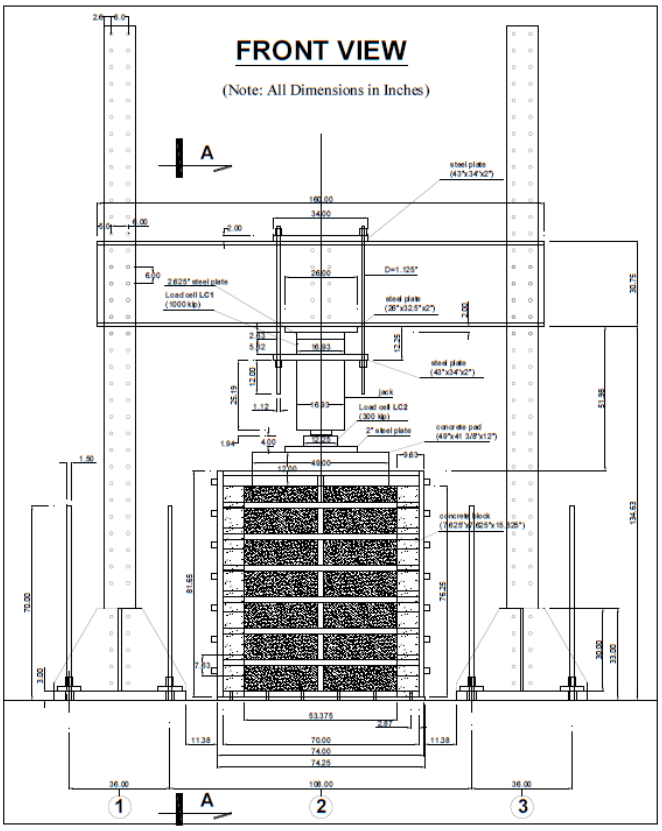

(b)

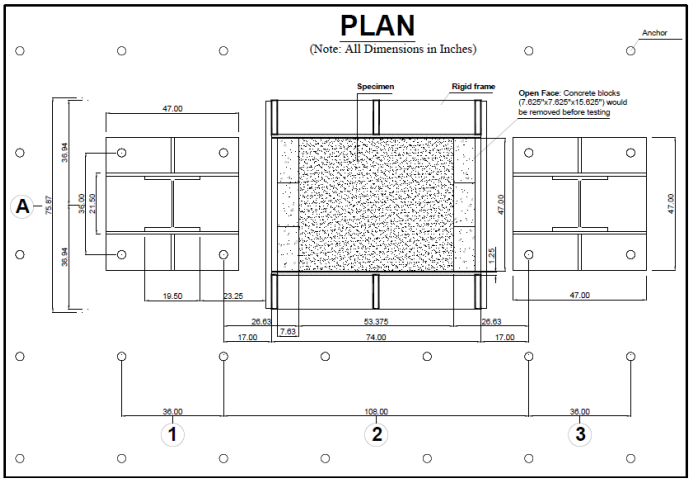

Figure 3.3. GSGC test setup: (a) front view; (b) plan view (Wu et al. 2013 – FHWA-HRT-10-077).

3.3.2. Cylindrical column tests by Elton and Patawaran (2004, 2005)

Elton and Patawaran (2004, 2005) tested GRS cylindrical columns (Figure 3.4) 0.76 m in diameter and 1.52-m high. The backfill material used was poorly graded sand classified as SP in accordance to USCS. The maximum dry density and the optimum moisture content were 18 kN/m3 and 9.3%, respectively. The friction angle and the cohesion of the soil were 40 degrees and 29 kPa, respectively, obtained from direct shear testing. The reinforcement used was polypropylene nonwoven geotextile layers placed at vertical spacing of 0.15 m. Different reinforcement types were used with different mass per unit area. The reinforcement tensile strength varied from 9 to 25 kN/m (51 to 142 lb/in.). Note that the tensile strength of the used reinforcement was different in machine and cross-machine directions.

Figure 3.4. Cylindrical GRS column (Elton and Patawaran 2005).

3.3.3. NCHRP experimental abutments by Wu et al. (NCHRP 556, 2006)

Wu et al. (NCHRP 556, 2006) tested two full-scale experimental GRS bridge abutments 4.65-m high, as shown in Figure 3.5, to assess the behavior of GRS abutments subject to various vertical load levels. These abutments were constructed back-to-back over a rigid floor (reinforced concrete mat). The backfill was a non-plastic silty sand with fines content of 8.5% classified as SP-SM in accordance to USCS. The maximum dry density and the optimum moisture content of the soil were 18.3 kN/m3 and 11.5%, respectively. The backfill material was compacted in the abutments at relative density of 99% and 1.7% wet of optimum moisture content. With the information. The shear strength parameters were obtained by large-scale triaxial and large-scale direct shear tests on samples prepared at the same relative density and moisture as the backfill placed in constructed abutments. The friction angle and the cohesion obtained from the large-scale triaxial tests were 37.3 degrees and 20 kPa, respectively; whereas, the friction angle and the cohesion obtained from the large-scale direct shear tests were 36.5 degrees and 0 kPa, respectively. Polypropylene woven geotextile reinforcement was used in both abutments, which included Amoco 2044 for one abutment and Mirafi 500x for the other abutment. The tensile strength for Amoco 2044 and Mirafi 500x geotextiles were 70 and 21 kN/m, respectively, in their cross-machine direction. The reinforcement was employed at a vertical spacing of 0.2 m for both abutments. Additional reinforcement layers were added near the top of the abutments to form bearing beds as shown in Figure 3.5. The facing used for the abutments involved concrete cinder blocks with a split-face.

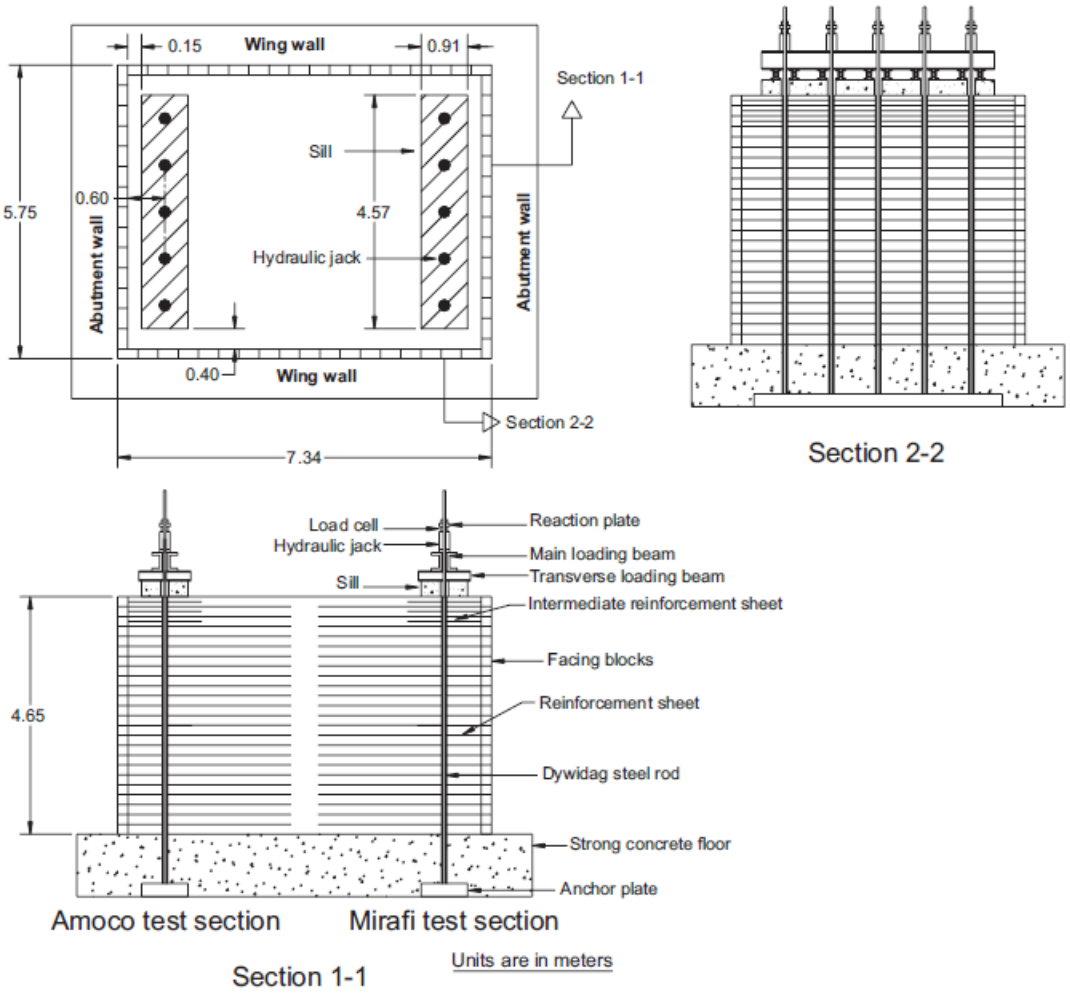

Figure 3.5. Configuration of the NCHRP full-scale test abutments (Wu et al. 2006 – NCHRP 556).

3.3.4. FHWA pier test by Adams (1997)

Adams (1997) conducted a vertical loading test on a full-scale GRS. The pier was 5.4-m high and its base dimensions were 3.6 x 4.8 m. The facing of the pier was battered as shown in Figure 3.6. The backfill material used in the construction of the pier was

compacted road base. The reinforcement employed involved polypropylene woven geotextile with tensile strength of 70 kN/m. The reinforcement layers were placed at a vertical spacing of 0.2 m. The facing used was dry stacked modular blocks (split face cinder blocks). The pier was constructed on reinforced soil foundation, formed on 1.2-m thick compacted backfill and reinforced with three biaxial geogrid layers placed at a vertical spacing of 0.3 m.

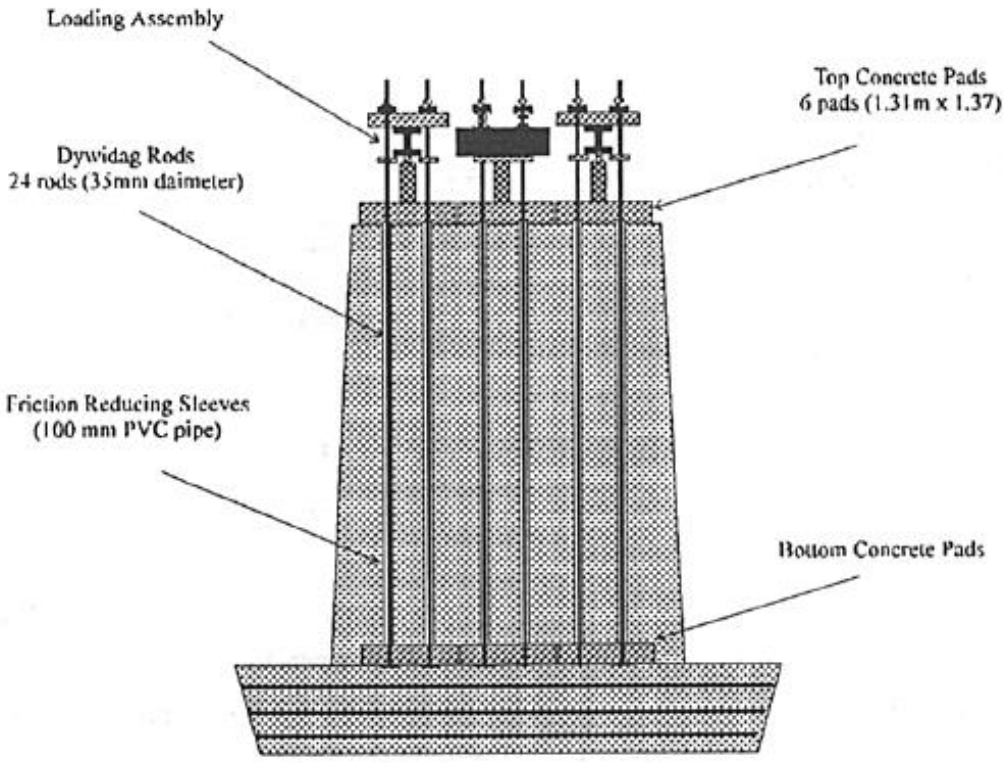

Figure 3.6. Schematic of the FHWA pier (Adams 1997).

3.3.5. Vegas MP mini-pier test by Adams et al. (2002)

Adams et al. (2002) tested a GRS mini-pier, which involved a GRS mass of 1.12 x 1.12 m cross-sectional area (excluding the facing) and 2.4 m in height as shown in Figure 3.7. The backfill material used was gravel classified as GP-GM in accordance to USCS. The facing used was Segemental Retaining Wall (SRW) blocks, which were solid dry cast concrete with split-face. The reinforcement used was polypropylene woven geotextiles with tensile strength of 35 kN/m. The reinforcement was placed at a vertical spacing of 0.15 m with additional two reinforcement courses at the top of the pier (creating a beading bed).

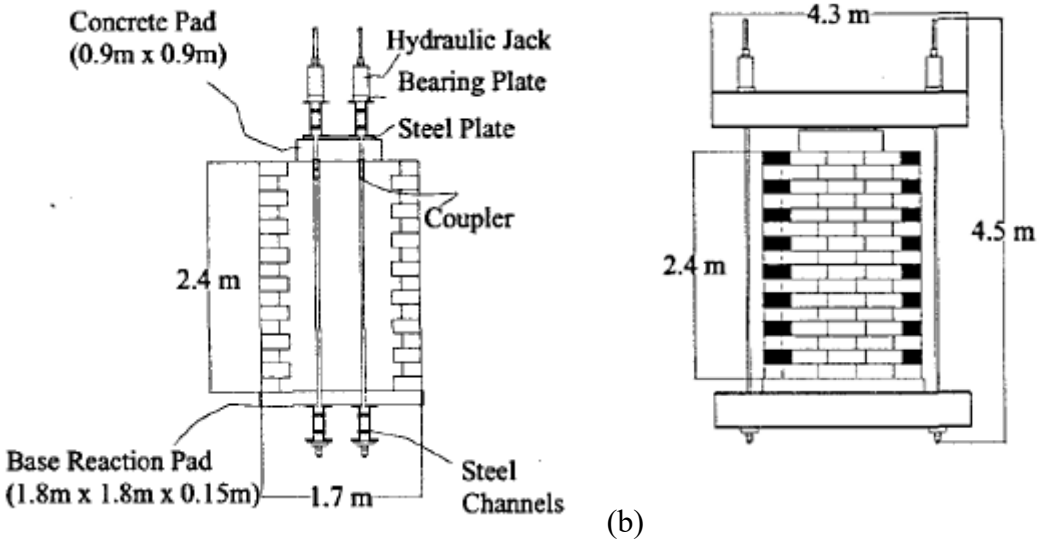

Figure 3.7. Schematic of the Vegas mini-pier: (a) side view; (b) front view (Adams 2002).

3.3.6. Mini-pier tests by Mitchell (2002)

Mitchell (2002) conducted four GRS mini-pier performance tests (Figure 3.8). The backfill material used was well-graded gravelly sand with fines content of 11.5%. The maximum dry density and the optimum moisture content of the soil were 23.1 kN/m3 and 8.75%, respectively. The shear strength properties of the soil was obtained by direct shear testing. The friction angle and cohesion measured were 36 degrees and 30.5 kPa, respectively. The reinforcement used was woven geotextile with tensile strength of 30.7 kN/m. The facing used was concrete blocks known as split face Keystone.

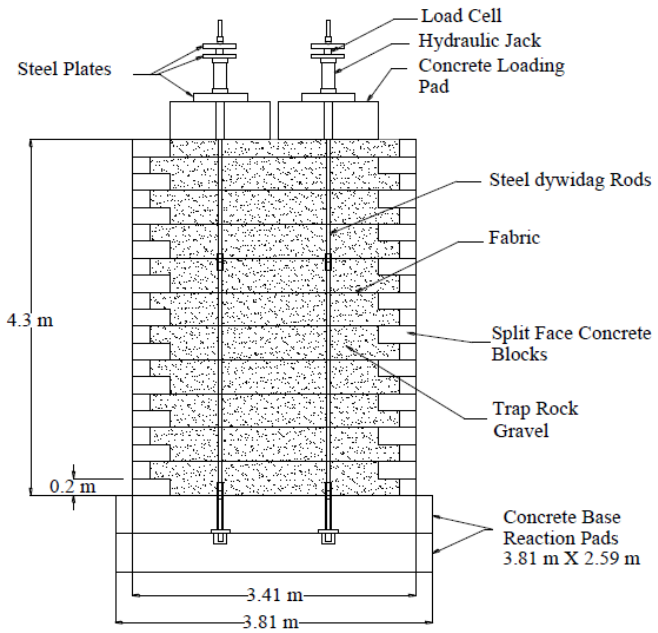

Figure 3.8. Schematic of GRS mini-piers (Mitchell 2002).

3.3.7. MP mini-pier tests by Adams et al. (2007a)

Adams et al. (2007a) conducted four performance tests on the mini piers with the dimensions shown in Figure 3.9. The experiment simulates a large-scale unconfined triaxial test. The testing configurations are summarized in Table 3.2. The facing used involved Concrete Masonry Units (CMUs), which was removed before the load tests to negate its effect on the GRS behavior. The reinforcement used was polypropylene woven geotextile layers with different tensile strength. MP A, MP B, and MP D were constructed with a strong geotextile reinforcement placed at different vertical spacing; whereas, MP C was constructed with a weak geotextile placed at 0.2-m spacing. The backfill material used was well graded crushed base rock classified as GW-GM in accordance to USCS with a fines content of approximately 10%. The maximum dry density and the optimum moisture content of the backfill were 24 kN/m3 and 6%, respectively. The placement density of the backfill material in the various tests is summarized Table 3.2.

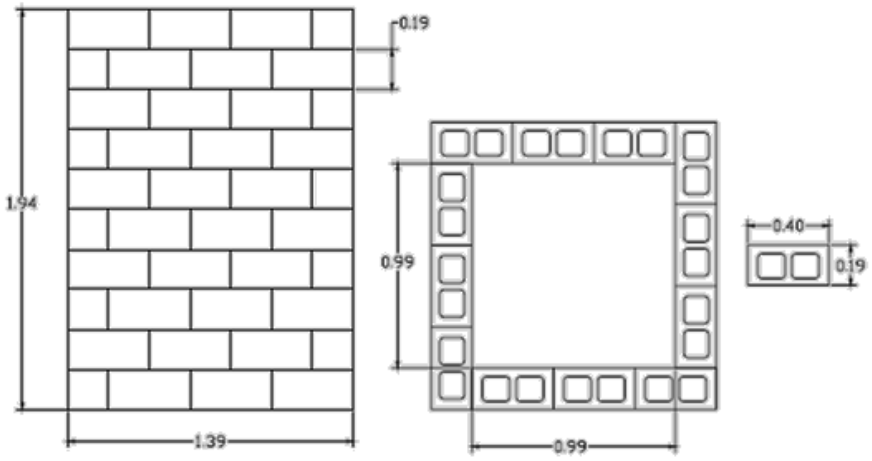

Figure 3.9. Schematic for the mini-piers (Adams et al. 2007a).

Table 3.2. Summary of the testing configurations (Adams et al. 2007a).

Experiment	*Fill Average Density (kN/m^3)*	*Geotextile Reinforcement Schedule*		
		Polypropylene Type	*Strength (kN/m)*	*Spacing (m)*
MP NR	22.4	None	None	None
MP A	23.0	A2044	70	0.4-0.6
MP B	22.7	A2044	70	0.4
MP C	Not Available	A2000	21	0.2
MP D	22.8	A2044	70	0.2

3.3.8. DC and TF mini-pier tests by Nicks et al. (FHWA-HRT-13-066, 2013a)

Nicks et al. (FHWA-HRT-13-066, 2013a) conducted 19 mini-pier performance tests denoted as DC (5 tests) and TF (14 tests) piers. A schematic of the mini-pier test is shown in Figure 3.10. The tests conducted with facing and without facing in which after construction facing units were removed. The facing used was split-faced concrete masonry units (CMUs). Several backfill and reinforcement materials were adopted in the testing program as summarized in Table 3.3.

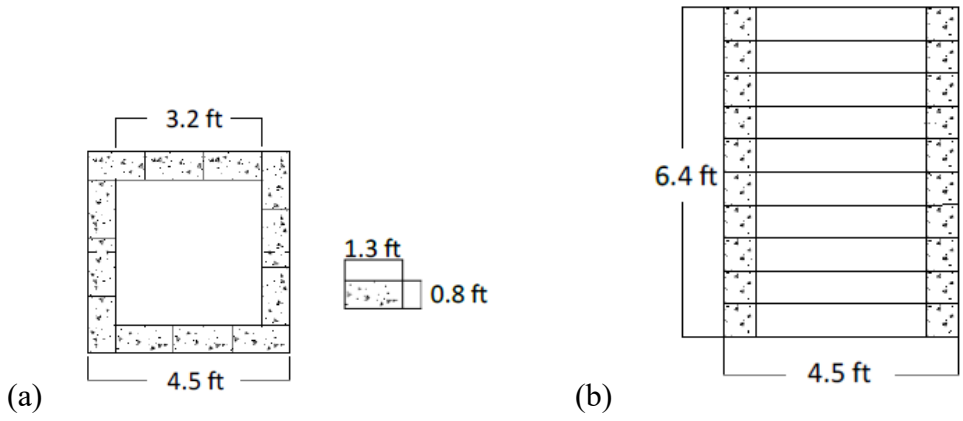

Figure 3.10. Schematic for the Defiance County (DC) mini-pier: (a) plan view; (b) elevation view (Nicks et al. 2013 – FHWA-HRT-13-066).

Table 3.3. Summary of the testing configurations (Nicks et al. 2013a – FHWA-HRT-13-066).

Test No.	Backfill				Reinforcement			Facing
	Type	φ (deg)	c (psf)	d_{max} (in.)	T_f (lb/ft)	S_v (in.)	T_f/S_v (lb/ft^2)	
DC-1	8	54	0	0.5	4,800	7.625**	7,600	CMU
DC-2	8P*	46	0	0.75	4,800	7.625**	7,600	CMU
DC-3	57	52	0	1	4,800	7.625**	7,600	CMU
DC-4	9	49	0	0.375	4,800	7.625**	7,600	CMU
DC-5	8***	54	0	0.5	4,800	7.625**	7,600	CMU
TF-1++	8	55	0	0.5	2,400	7.625	3,800	CMU
TF-2	21A	53	115	1	2,400	7.625	3,800	CMU
TF-3	21A	53	115	1	2,400	7.625	3,800	no CMU
TF-4+	21A	53	115	1	4,800	7.625	7,600	no CMU
TF-5++	21A	53	115	1	4,800	7.625	7,600	no CMU
TF-6++	21A	53	115	1	4,800	7.625	7,600	CMU
TF-7	21A	53	115	1	4,800	7.625	7,600	no CMU
TF-8	21A	53	115	1	4,800	7.625**	7,600	no CMU
TF-9	21A	53	115	1	4,800	15.25	3,800	CMU
TF-10	21A	53	115	1	4,800	15.25	3,800	no CMU
TF-11	21A	53	115	1	1,400	313/16	4,400	no CMU
TF-12	21A	53	115	1	1,400	3.1825	4,400	CMU
TF-13	21A	53	115	1	3,600	11.25	3,800	no CMU
TF-14	21A	53	115	1	3,600	11.25	3,800	CMU

*Rounded pea-gravel angularity.
**Two courses of bearing bed reinforcement placed at the top of the pier.
***Uncompacted sample.
+Technical difficulties required termination during testing.
++Technical difficulties resulted in unloading/reloading of the composite.

3.3.9. Large-scale triaxial tests by Ruiken and Ziegler (2009)

Ruiken and Ziegler (2009) conducted 8 large-scale triaxial tests (4 reinforced and 4 unreinforced) on samples 0.5 m in diameter and 1.1-m high as shown in Figure 3.11. The backfill material they used was crushed base course material compacted at a relative density of either 95% or 100%. The reinforcement employed in the samples involved biaxial polypropylene geogrids with tensile strength of 12 kN/m at 2% axial strain and 24 kN/m at 5% strain. The samples were confined laterally by vacuum; the confinement levels adopted were 10, 30, 50, 70 kN/m². Three geogrid layers were placed at a vertical reinforcement spacing of approximately 0.3 m.

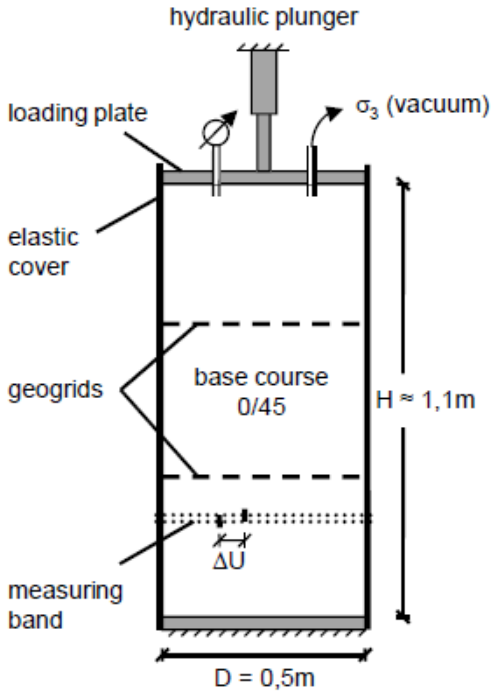

Figure 3.11. Schematic for the large-scale triaxial test (Ruiken and Ziegler 2009).

A summary of the consolidated GRS experimental structures database is presented in Table 3.4. While the information presented in the table does not exclusively include all the compiled data, it includes the essential information about the materials employed in each of the collected experimental structure to complete the summary given earlier. In addition, more information are presented in the analysis section as needed.

Table 3.4. GRS experimental structures database.

Number	*Test Name*	*Facing Type*	S_v *(m)*	T_f *(kN/m)*	d_{max} *(m)*	*c (kPa)*	*Φ (deg)*	*Φ method*	*Geometry*	*Reference*
1	GSGC 1	Concrete Blocks/Plexiglas	N/A	N/A	0.033	70	50	TX	Fixed Wall	Pham (2008); Wu et al. (2013)
2	GSGC 2	Concrete Blocks/Plexiglas	0.2	70	0.033	70	50	TX	Fixed Wall	Pham (2008); Wu et al. (2013)
3	GSGC 3	Concrete Blocks/Plexiglas	0.4	140	0.033	70	50	TX	Fixed Wall	Pham (2008); Wu et al. (2013)
4	GSGC 4	Concrete Blocks/Plexiglas	0.4	70	0.033	70	50	TX	Fixed Wall	Pham (2008); Wu et al. (2013)
5	GSGC 5	Concrete Blocks/Plexiglas	0.2	70	0.033	70	50	TX	Fixed Wall	Pham (2008); Wu et al. (2013)
6	Elton and Patawaran 1	None	0.15	9	0.0127	29	40	DS	Cylindrical Column	Elton and Patawaran (2004, 2005)
7	Elton and Patawaran 2	None	0.3	9	0.0127	29	40	DS	Cylindrical Column	Elton and Patawaran (2004, 2005)
8	Elton and Patawaran 3	None	0.15	14	0.0127	29	40	DS	Cylindrical Column	Elton and Patawaran (2004, 2005)
9	Elton and Patawaran 4	None	0.15	15	0.0127	29	40	DS	Cylindrical Column	Elton and Patawaran (2004, 2005)
10	Elton and Patawaran 5	None	0.15	19	0.0127	29	40	DS	Cylindrical Column	Elton and Patawaran (2004, 2005)
11	Elton and Patawaran 6	None	0.15	20	0.0127	29	40	DS	Cylindrical Column	Elton and Patawaran (2004, 2005)
12	Elton and Patawaran 7	None	0.15	25	0.0127	29	40	DS	Cylindrical Column	Elton and Patawaran (2004, 2005)
13	NCHRP 1	CMU	0.2	21	0.0254	0.0 20	36.5 37.3	LSDS LSTX	Abutment	Wu et al. (2006)
14	NCHRP 2	CMU	0.2	70	0.0254	0.0 20	36.5 37.3	LSDS LSTX	Abutment	Wu et al. (2006)
15	Defiance 1	CMU	0.2	35	0.0127	0	50.7	LSDS	Square Column	Adams et al. (2007b)
16	Defiance 2	CMU	0.2	70	0.0127	0	50.7	LSDS	Square Column	Adams et al. (2007b)
17	Vegas MP	SRW	0.15	35	0.0254	70	50	TX	Square Column	Adams et al. (2002)

Table 3.4. GRS experimental structures database (Continued).

Number	*Test Name*	*Facing Type*	*S_v (m)*	*T_f (kN/m)*	*d_{max} (m)*	*c (kPa)*	*Φ (deg)*	*Φ method*	*Geometry*	*Reference*
18	MP NR	None	N/A	N/A	0.0254	0	53.5	LSDS	Square Column	Adams et al. (2007a)
19	MP A	None	0.6	70	0.0254	0	53.5	LSDS	Square Column	Adams et al. (2007a)
20	MP B	None	0.4	70	0.0254	0	53.5	LSDS	Square Column	Adams et al. (2007a)
21	MP C	None	0.2	21	0.0254	0	53.5	LSDS	Square Column	Adams et al. (2007a)
22	MP D	None	0.2	70	0.0254	0	53.5	LSDS	Square Column	Adams et al. (2007a)
23	DC-1 (VS-1)	CMU	0.2	70	0.0127	0	54	LSDS	Square Column	Nicks et al. (2013a)
24	DC-2 (VS-2)	CMU	0.2	70	0.01905	0	46	LSDS	Square Column	Nicks et al. (2013a)
25	DC-3 (VS-3)	CMU	0.2	70	0.0254	0	52	LSDS	Square Column	Nicks et al. (2013a)
26	DC-4 (VS-4)	CMU	0.2	70	0.009525	0	49	LSDS	Square Column	Nicks et al. (2013a)
27	DC-5 (VS-5)	CMU	0.2	70	0.0127	0	54	LSDS	Square Column	Nicks et al. (2013a)
28	TF-1	CMU	0.2	35	0.0127	0	55	LSDS	Square Column	Nicks et al. (2013a)
29	TF-2	CMU	0.2	35	0.0254	5.5	53	LSDS	Square Column	Nicks et al. (2013a)
30	TF-3	None	0.2	35	0.0254	5.5	53	LSDS	Square Column	Nicks et al. (2013a)
31	TF-4	None	0.2	70	0.0254	5.5	53	LSDS	Square Column	Nicks et al. (2013a)
32	TF-5	None	0.2	70	0.0254	5.5	53	LSDS	Square Column	Nicks et al. (2013a)
33	TF-6	CMU	0.2	70	0.0254	5.5	53	LSDS	Square Column	Nicks et al. (2013a); Iwamoto (2014)
34	TF-7	None	0.2	70	0.0254	5.5	53	LSDS	Square Column	Nicks et al. (2013a); Iwamoto (2014)
35	TF-8	None	0.2	70	0.0254	5.5	53	LSDS	Square Column	Nicks et al. (2013a)
36	TF-9	CMU	0.4	70	0.0254	5.5	53	LSDS	Square Column	Nicks et al. (2013a); Iwamoto (2014)
37	TF-10	None	0.4	70	0.0254	5.5	53	LSDS	Square Column	Nicks et al. (2013a); Iwamoto (2014)

Table 3.4. GRS experimental structures database (Continued).

Number	*Test Name*	*Facing Type*	*S_v (m)*	*T_f (kN/m)*	*d_{max} (m)*	*c (kPa)*	*Φ (deg)*	*Φ method*	*Geometry*	*Reference*
38	TF-11	None	0.1	20	0.0254	5.5	53	LSDS	Square Column	Nicks et al. (2013a); Iwamoto (2014)
39	TF-12	CMU	0.1	20	0.0254	5.5	53	LSDS	Square Column	Nicks et al. (2013a); Iwamoto (2014)
40	TF-13	None	0.3	56	0.0254	5.5	53	LSDS	Square Column	Nicks et al. (2013a); Iwamoto (2014)
41	TF-14	CMU	0.3	56	0.0254	5.5	53	LSDS	Square Column	Nicks et al. (2013a); Iwamoto (2014)
42	Mitchell 1	CMU	0.6	30.6	0.0254	30.5	36	LSDS	Square Column	Mitchell (2002)
43	Mitchell 2	CMU	0.4	30.6	0.0254	30.5	36	LSDS	Square Column	Mitchell (2002)
44	Mitchell 3	CMU	0.2	30.6	0.0254	30.5	36	LSDS	Square Column	Mitchell (2002)
45	Mitchell 4	CMU	0.8	30.6	0.0254	30.5	36	LSDS	Square Column	Mitchell (2002)
46	FHWA Pier	Cinder Block	0.2	70	N/A	N/A	N/A	N/A	Square Column	Adams (1997)
47	Ruiken and Ziegler 1	Elastic Cover	0.3	24	0.0508	0	46.5	TX	Cylindrical Column	Ruiken and Ziegler (2009)
48	Ruiken and Ziegler 2	Elastic Cover	0.3	24	0.0508	0	46.5	TX	Cylindrical Column	Ruiken and Ziegler (2009)
49	Ruiken and Ziegler 3	Elastic Cover	0.3	24	0.0508	0	46.5	TX	Cylindrical Column	Ruiken and Ziegler (2009)
50	Ruiken and Ziegler 4	Elastic Cover	0.3	24	0.0508	0	46.5	TX	Cylindrical Column	Ruiken and Ziegler (2009)
51	Ruiken and Ziegler 5	Elastic Cover	0.3	24	0.0508	0	46.5	TX	Cylindrical Column	Ruiken and Ziegler (2009)
52	Ruiken and Ziegler 6	Elastic Cover	0.3	24	0.0508	0	46.5	TX	Cylindrical Column	Ruiken and Ziegler (2009)
53	Ruiken and Ziegler 7	Elastic Cover	0.3	24	0.0508	0	46.5	TX	Cylindrical Column	Ruiken and Ziegler (2009)

3.4. ANALYSIS

The consolidated database was looked at extensively to account for the differences in the nature of each experimental structure. A thorough reassessment of the monitoring data was conducted to critically evaluate the effects of the several parameters of the GRS structures. In addition, the analysis assessed the practical models that were proposed by Adams et al. (FHWA-HRT-11-027, 2011) for the design of GRS-IBS. This includes the global bearing capacity prediction methods, vertical and horizontal deformation prediction methods, and the lateral earth pressure prediction method.

3.4.1. Bearing capacity

The global bearing capacity of a GRS structure (q_{ult}) was evaluated using an analytical formula proposed by Wu et al. (FHWA-HRT-10-077, 2013a) shown in Equation 3.1. This formula is adopted by Adams et al. (FHWA-HRT-11-027, 2011) and reported to be applicable to GRS structures with vertical surcharge (e.g., GRS bridge abutments). However, Adams et al. (FHWA-HRT-11-027, 2011) reported that the analytical formula applies to GRS structures that employs backfill material characteristics that conform to the criteria in Adams et al. (FHWA-HRT-11-026, 2012).

$$\boldsymbol{q_{ult} = \left[\sigma_c + 0.7^{\left(\frac{S_v}{6d_{max}}\right)}\frac{T_f}{S_v}\right]K_{pr} + 2c\sqrt{K_{pr}}}$$

Equation 3.1

Where

σ_c: the lateral normal pressure.

S_v: the reinforcement vertical spacing.

d_{max}: the maximum grain size of the backfill material.

T_f: the reinforcement ultimate tensile strength.

K_{pr}: the coefficient of passive earth pressure.

This equation was used with all the GRS experimental structures identified in this study (Table 3.4) and were known to have been brought to failure (i.e., structures that did not reach failure were excluded from the comparison). Figure 3.12 shows a comparison between the ultimate bearing capacity values predicted using Equation 3.1 and the measured vertical stress capacity values retrieved from the experimental data. Note that the structures involved in this comparison had different boundary conditions. The structures involved included square columns, cylindrical columns, fixed-wall columns, and experimental abutments. It should be also noted that no correction factors were applied to account for the structure geometrical type. Adams et al. (FHWA-HRT-11-027, 2011) reported that the ultimate capacity used in design should be modified to neglect lateral normal pressure due to its significantly small value and backfill cohesion to account for long-term conditions. However, the comparison was conducted by using the original equation (i.e., by incorporating the normal pressure and backfill cohesion) since some of the experimental structures were exposed to a considerably high normal pressure. Also, the tests were conducted in a short-term condition in which the strength parameters of the backfill material could be reasonably assumed short-term parameters.

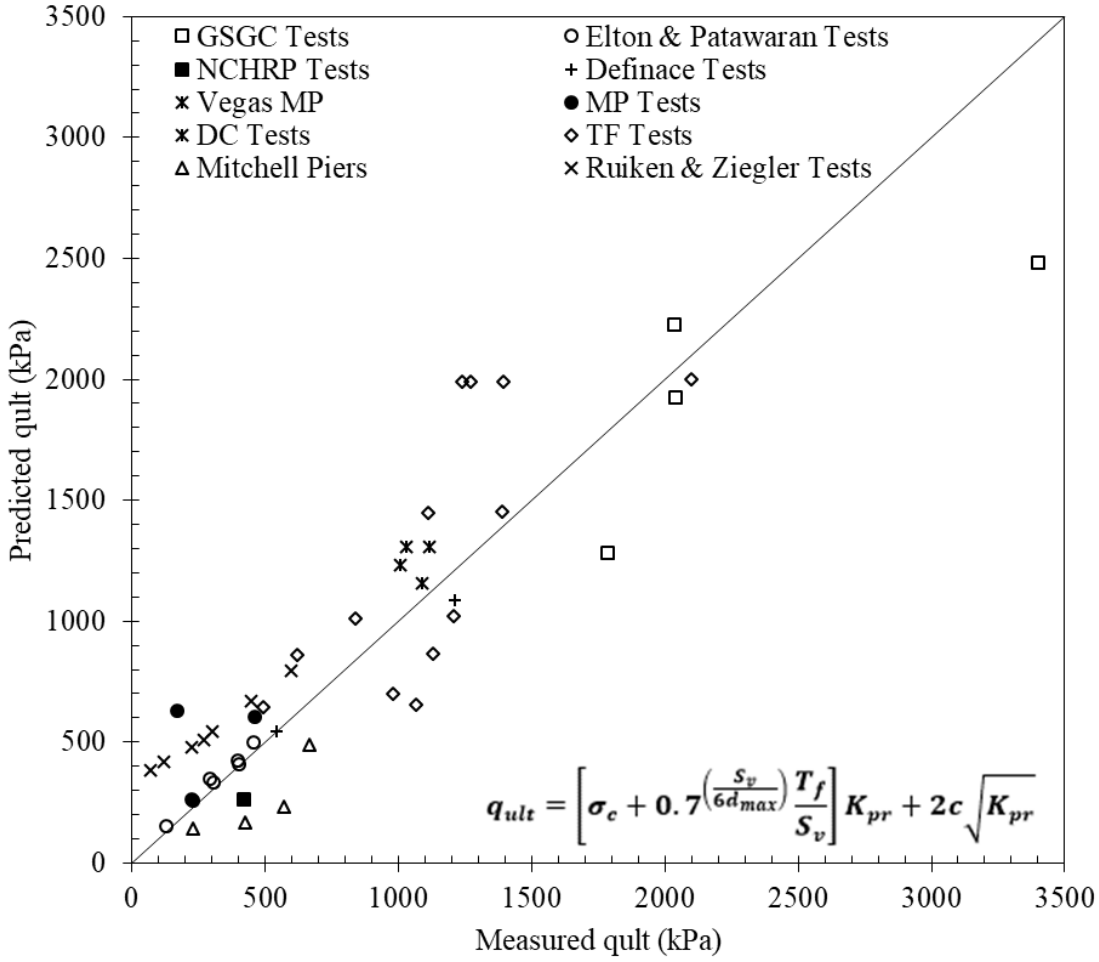

Figure 3.12. Measured vs. predicted (using Wu method) GRS bearing strength.

3.4.2. Vertical stress-strain behavior

The database was extended to include the vertical stress-strain behavior of the GRS experimental structures. Figure 3.13 shows a master presentation of all the data that was compiled for structures that have a wide range of parameters. It can be noticed that the

ultimate capacity for the majority of the structures was significantly high. While this observation enhances the fact that the strength of GRS structures is high enough to support bridge loads, the ultimate capacity is not the most vital information to look at. Instead, the structural behavior under service stress levels up to approximately 200 kPa is more decisive. Whereupon, side-by-side comparisons were made between the behavior of the various structures in the ultimate and service stress levels. A set of figures were prepared and presented in this section to study the effect of the various GRS structural parameters on the behavior of GRS structures in general, in ultimate and service stress conditions.

Note that the comparisons were conducted in terms of vertical stress-strain behavior, where the vertical strain is determined globally (i.e., percentage of settlement to total structure height). The reason for this choice is to evaluate the empirical method proposed by Adams et al. (FHWA-HRT-11-027, 2011) for estimating the ultimate bearing capacity of GRS structures based on representative performance tests, which were conducted by Nicks et al. (FHWA-HRT-13-066, 2013). That is, some structures involved in a single comparison might have different height. However, attention was paid when comparisons were analyzed.

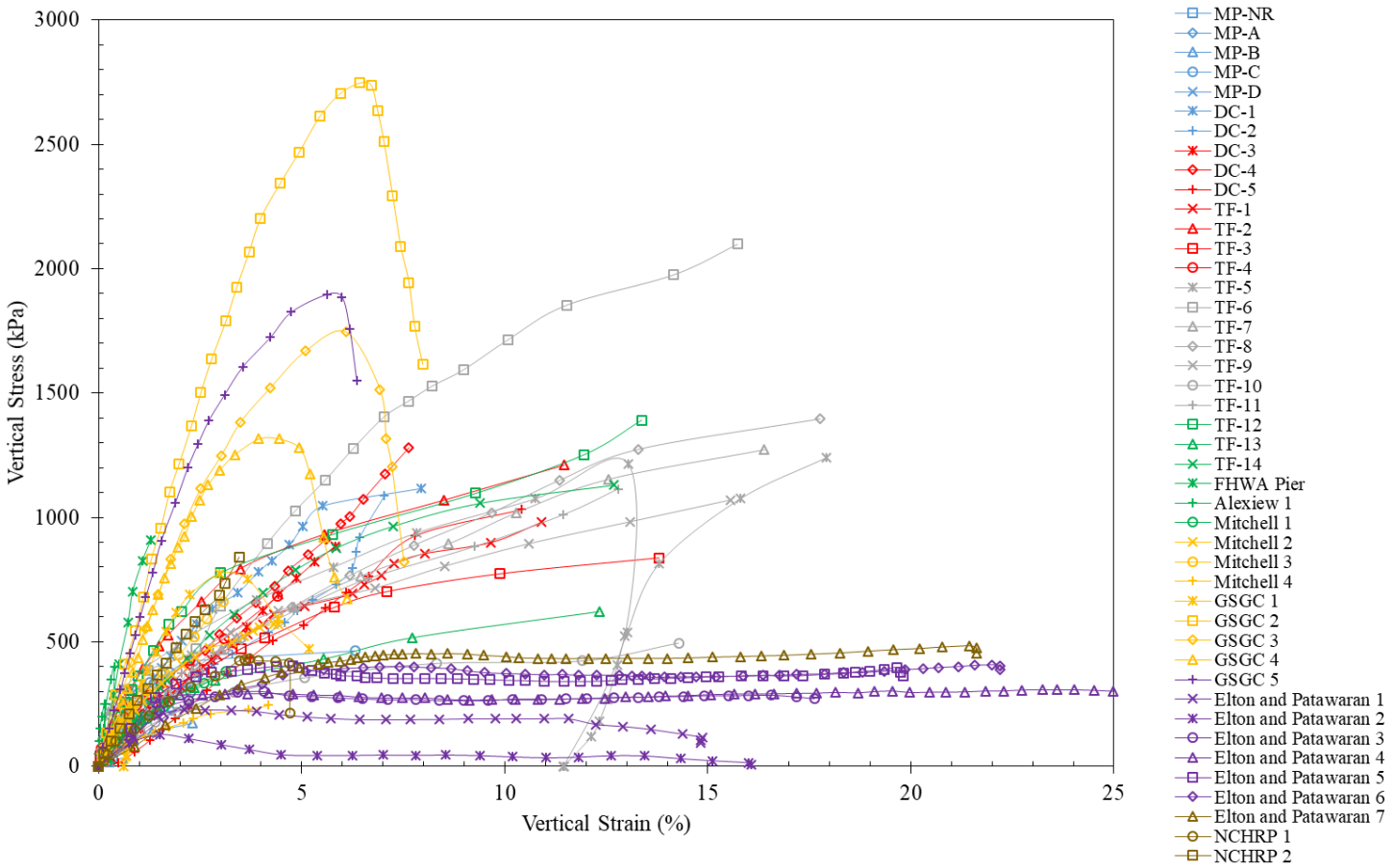

Figure 3.13. Vertical stress-strain behavior for the GRS experimental structures database.

Figure 3.14 comprises data from structures that have reinforcements of the same tensile strength of 70 kN/m and placed at the same vertical spacing of 0.2 m. All three tests did not involve bearing bed reinforcement. GSGC-2 was tested in plane strain condition, NCHRP-2 was an abutment test, and TF-6 and FHWA Pier were square column tests. The backfill material used in GSGC-2 had 50-degree friction angle, 70-kPa cohesion, and 0.033-m maximum grain size (strength parameters obtained from triaxial testing). The backfill materials used in the various structures had different characteristics as shown in summary table in Figure 3.14. Note that the normal pressure might be set to zero; however, some confinement due to facing is possible. For instance, Nicks et al. (FHWA-HRT-13-066, 2013) has estimated that confinement effect of the CMU facing used in the TF tests approximately 0.97 kPa. Figure 3.14a shows a comparison between the behaviors exhibited by the various structures upon loading them vertically. Figure 3.14b shows a close-up of the behavior in the service stress range. Similarity was observed in the behavior of TF-6 and NCHRP 2 and in the behavior of FHWA pier and GSGC 5. However, the characteristics of TF-6 differs than those of NCHRP 2 mainly in the geometry and the higher friction angle of the backfill material. While stiffer backfill material should result in a stiffer behavior, the height of NCHRP 2 was greater than that of TF-6. That is, for the same vertical strain, NCHRP 2 exhibited a bigger settlement than TF-6. An important conclusion can be drawn from this observation. The empirical design based on the data from a representative performance test (design envelopes) proposed by Adams et al. (FHWA-HRT-11-027, 2011) may not be very satisfactory to empirically design GRS abutments since it uses global vertical strain, which is a very rough average value.

Test Name	$q_{ult,measured}$ *(kPa)*	*Facing Type*	$\sigma_{confining}$ *(kPa)*	*H (m)*	S_v *(m)*	T_f *(kN/m)*	T_f/S_v *(kN/m/m)*	d_{max} *(m)*	*c (kPa)*	*φ (deg)*	*c,φ Method*	*Geometry*	*Reference*
GSGC 5	2034	CMU/ Plexiglas	0.0	2.00	0.20	70	350	0.033	70	50	TX	Fixed Wall Column	Pham (2008); Wu et al. (2013)
NCHRP 2	Didn't reach failure	CMU	0.0	4.65	0.20	70	350	0.025	0.0 20	36.5 37.3	LSDS LSTX	Abutment	Wu et al. (2006)
TF-6	2098	CMU	0.97	1.94	0.20	70	350	0.025	5.5	53	LSDS	Square Column	Nicks et al. (2013a); Iwamoto (2014)
FHWA Pier	Didn't reach failure	Cinder Block	0.0	5.40	0.20	70	350	N/A	N/A	N/A	N/A	Square Column	Adams (1997)

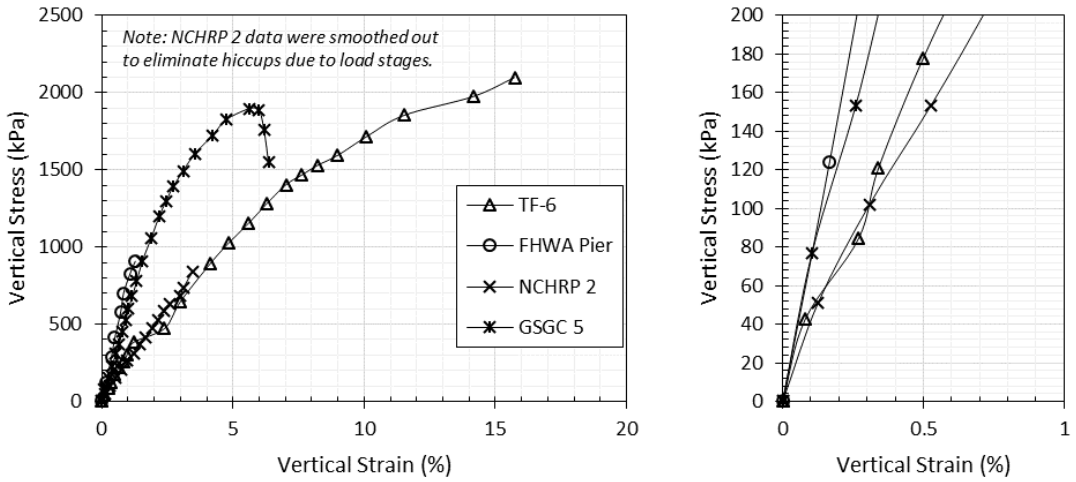

(a) (b)

Figure 3.14. Stress-strain behavior for similar tests: (a) Available stress range; (b) Service stress range.

Figure 3.15 comprises data from structures that have the same characteristics. These tests were conducted by Nicks et al. (FHWA-HRT-13-066, 2013a) to assess the repeatability of the GRS mini-pier performance tests they conducted. The summary table in Figure 3.15 shows the characteristics of the various structures included in this comparison. Geotextile reinforcement layers with 70-kN/m tensile strength were employed in all piers and were spaced at 0.2 m. Nicks et al. (FHWA-HRT-13-066, 2013a) noted that TF-4 test was terminated before reaching failure due to technical difficulties that has caused uneven loading of the pier. In addition, they noted that TF-5 was initially loaded then was unloaded-reloaded up to failure. All test piers did not include bearing bed. Also, the facing units were removed and the reinforcement tails were trimmed from all piers prior loading. The stress-strain behavior of the three tests may look similar when looked at the entire stress-strain range. However, over the service stress range, the discrepancy between the test results was significantly high as shown in Figure 3.15b. The global vertical strain ranged from approximately 0.6% to 1.1% (excluding the reloading of TF-5).

Test Name	$q_{ult,measured}$ *(kPa)*	*Facing Type*	$\sigma_{confining}$ *(kPa)*	*H (m)*	S_v *(m)*	T_f *(kN/m)*	T_f/S_v *(kN/m/m)*	d_{max} *(m)*	*c (kPa)*	*φ (deg)*	*c,φ Method*	*Geometry*	*Reference*
TF-4	Didn't reach failure	None	0.0	1.94	0.20	70	350	0.025	5.5	53	LSDS	Square Column	Nicks et al. (2013a)
TF-5	1241	None	0.0	1.94	0.20	70	350	0.025	5.5	53	LSDS	Square Column	Nicks et al. (2013a)
TF-7	1271	None	0.0	1.94	0.20	70	350	0.025	5.5	53	LSDS	Square Column	Nicks et al. (2013a); Iwamoto (2014)

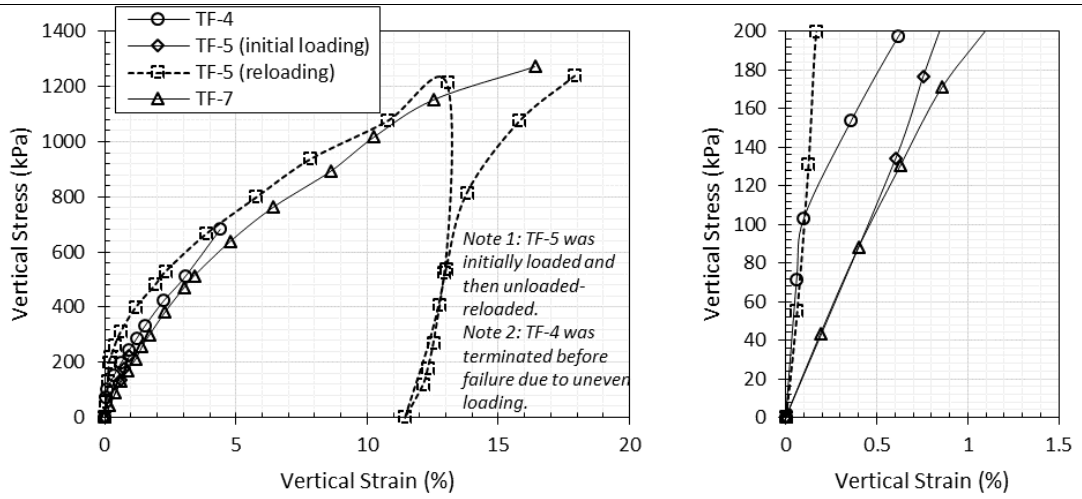

(a) (b)

Figure 3.15. Stress-strain behavior for identical tests: (a) Available stress range; (b) Service stress range.

Figure 3.16 shows the vertical stress-strain behavior of two tests that have similar characteristics. However, the structural geometry was different; GSGC 4 is a column with two fixed walls; whereas, TF-9 is a square column free to deform from all four directions. Also, a relatively high normal pressure was imposed on GSGC 4, whereas TF-9 was only confined by the effect of its facing. A summary of the characteristics of the two structures is shown in the table in Figure 3.16. The characteristics of the backfill materials employed were somewhat different in the two structures, yet both materials conforms to the backfill

properties recommended by Adams et al. (FHWA-HRT-11-026, 2012). Both structures were reinforced with geotextile layers of 70-kN/m tensile strength spaced at 0.2 m; no bearing bed reinforcement was involved. A significantly higher strength and stiffness were observed for GSGC 4 compared to TF-9. This can be attributed to the difference in the confinement imposed on the GRS mass. Another possible reason is the effect of wall fixation in GSGC 4.

Test Name	$q_{ult,measured}$ *(kPa)*	*Facing Type*	$\sigma_{confining}$ *(kPa)*	*H (m)*	S_v *(m)*	T_f *(kN/m)*	T_f/S_v *(kN/m/m)*	d_{max} *(m)*	*c (kPa)*	*φ (deg)*	*c,φ Method*	*Geometry*	*Reference*
GSGC 4	1785	CMU/ Plexiglas	34	2.00	0.40	70	175	0.033	70	50	TX	Fixed Wall Column	Pham (2008); Wu et al. (2013)
TF-9	1068	CMU	0.97	1.94	0.40	70	175	0.025	5.5	53	LSDS	Square Column	Nicks et al. (2013a); Iwamoto (2014)

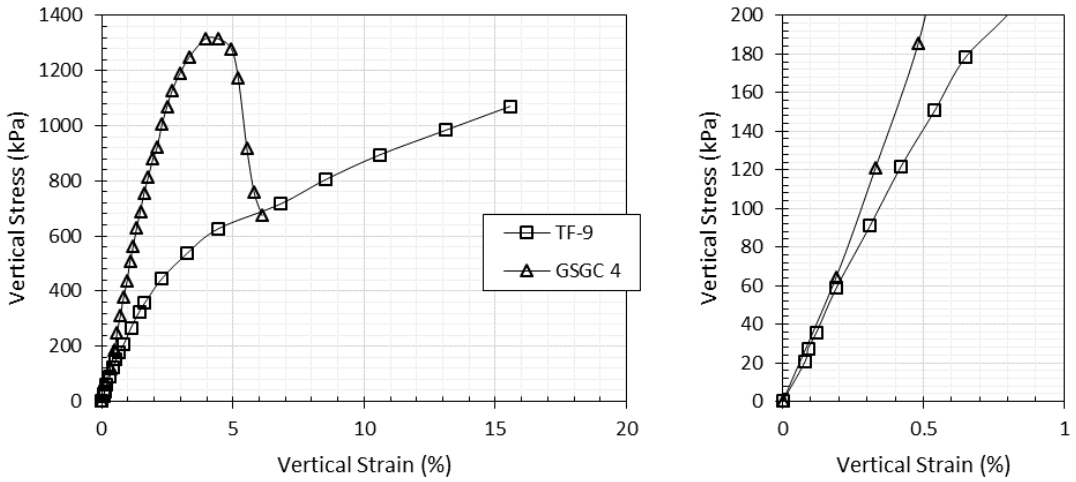

(a) (b)

Figure 3.16. Stress-strain behavior for similar tests: (a) Available stress range; (b) Service stress range.

Figure 3.17 shows the vertical stress-strain behavior for six experimental structures. The summary table in Figure 3.17 shows the characteristics of the various structures. The structures had similar characteristics except that the backfill materials had different friction angles and maximum grain sizes. The friction angle of the various backfill ranged from 36.5 to 54 degrees determined by large-scale direct shear testing and the maximum grain size ranged from 0.01 to 0.025 m. All structures employed geotextile reinforcement layers of 70-kN/m tensile strength placed at a vertical spacing of 0.2 m. Also, note that NCHRP 2 is an abutment and did not include bearing bed reinforcement, whereas all the other structures are piers and included bearing bed reinforcement. While DC-1 and DC-5 have identical characteristics, Nicks et al. (FHWA-HRT-13-066, 2013a) reported that DC-5 was constructed with uncompacted backfill unlike DC-1. In addition, technical difficulties were reported during loading of DC-5. Also, the backfill of DC-2 was round pea gravel.

The only testing parameter changing from one test to another is the friction angle of the backfill material used, which is a result of the different grain size of these cohesionless materials. Figure 3.17a shows unreasonable rank in the ultimate bearing capacity of the structures (excluding DC-3 and DC-4 tests, which were not loaded to failure). In addition, Figure 3.17b also does not show a reasonable rank in the stiffness of the reinforced soil. Typically, structures constructed with a higher friction angle backfill would be expected to exhibit a higher bearing capacity and loading stiffness than structures constructed with a lower friction angle backfill. Nicks et al. (FHWA-HRT-13-066, 2013) attributed this observation to the difference in gradation of the backfill materials used. DC-4 was prepared with a more graded soil, which provided a better performance than that of

DC-3 despite the lower friction angle of the backfill of DC-4. While NCHRP 2 had the weakest backfill among all the structures in comparison, and it did not include bearing bed reinforcement unlike all the other tests in comparison, it showed the stiffest behavior as shown in Figure 3.17b. This can be explained by the difference in structure height. The height of NCHRP 2 is approximately 2.4 times that of the DC structures.

Test Name	$q_{ult,measured}$ *(kPa)*	*Facing Type*	$\sigma_{confining}$ *(kPa)*	*H (m)*	S_v *(m)*	T_f *(kN/m)*	T_f/S_v *(kN/m/m)*	d_{max} *(m)*	*c (kPa)*	*φ (deg)*	*c,φ Method*	*Geometry*	*Reference*
NCHRP 2	Didn't reach failure	CMU	0.0	4.65	0.20	70	350	0.025	0.0 20	36.5 37.3	LSDS LSTX	Abutment	Wu et al. (2006)
DC-1	1116	CMU	0.97	1.94	0.20	70	350	0.013	0.0	54	LSDS	Square Column	Nicks et al. (2013a)
DC-2	1087	CMU	0.97	1.94	0.20	70	350	0.019	0.0	46	LSDS	Square Column	Nicks et al. (2013a)
DC-3	Didn't reach failure	CMU	0.97	1.94	0.20	70	350	0.025	0.0	52	LSDS	Square Column	Nicks et al. (2013a)
DC-4	Didn't reach failure	CMU	0.97	1.94	0.20	70	350	0.010	0.0	49	LSDS	Square Column	Nicks et al. (2013a)
DC-5	1031	CMU	0.97	1.94	0.20	70	350	0.013	0.0	54	LSDS	Square Column	Nicks et al. (2013a)

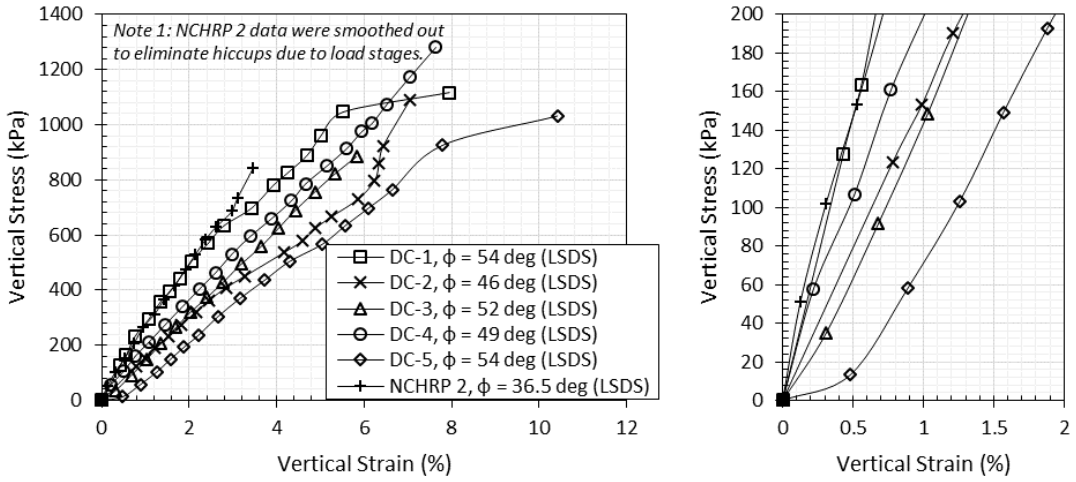

(a) (b)

Figure 3.17. Effect of backfill friction angle on the stress-strain behavior: (a) Available stress range; (b) Service stress range.

Figure 3.18 presents the vertical stress-strain behavior of three GRS experimental structures. This includes a square column (TF-1) and the two abutments (NCHRP 1 and NCHRP 2). The characteristics of these structures are summarized in the table in Figure 3.18. The structures were constructed with geotextile reinforcement of different tensile strength values. The reinforcement was placed at a vertical spacing of 0.2 m and did not involve bearing bed. Figure 3.18a shows that the stiffness of the reinforced soil mass in NCHRP 2 was the highest, which employed the strongest reinforcement, followed by that of the reinforced soil in TF-1, whereas that of NCHRP 1 exhibited the least stiffness, which had the weakest reinforcement. However, over the service stress range TF-1 and NCHRP 1 showed very similar behavior. This similarity is deemed misleading, since TF-1 had not only stronger reinforcement but also stronger backfill material than NCHRP 1. However, since the height of NCHRP 1 is greater than that of TF-1, similar vertical strains reflects more settlement. This observation strengthen the conclusion made earlier that the empirical design based on the data from representative performance tests proposed by Adams et al. (FHWA-HRT-11-027, 2011) may not be very satisfactory in design as they use global vertical strain, which is a very rough average value and because of the difference in the boundary conditions between the test piers and real bridge abutments.

Test Name	$q_{ult,measured}$ *(kPa)*	*Facing Type*	$\sigma_{confining}$ *(kPa)*	*H (m)*	S_v *(m)*	T_f *(kN/m)*	T_f/S_v *(kN/m/m)*	d_{max} *(m)*	*c (kPa)*	*φ (deg)*	*c,φ Method*	*Geometry*	*Reference*
NCHRP 1	Didn't reach failure	CMU	0.0	4.65	0.20	21	105	0.025	0.0 20	36.5 37.3	LSDS LSTX	Abutment	Wu et al. (2006)
NCHRP 2	Didn't reach failure	CMU	0.0	4.65	0.20	70	350	0.025	0.0 20	36.5 37.3	LSDS LSTX	Abutment	Wu et al. (2006)
TF-1	981	CMU	0.97	1.94	0.20	35	175	0.013	0.0	55	LSDS	Square Column	Nicks et al. (2013)

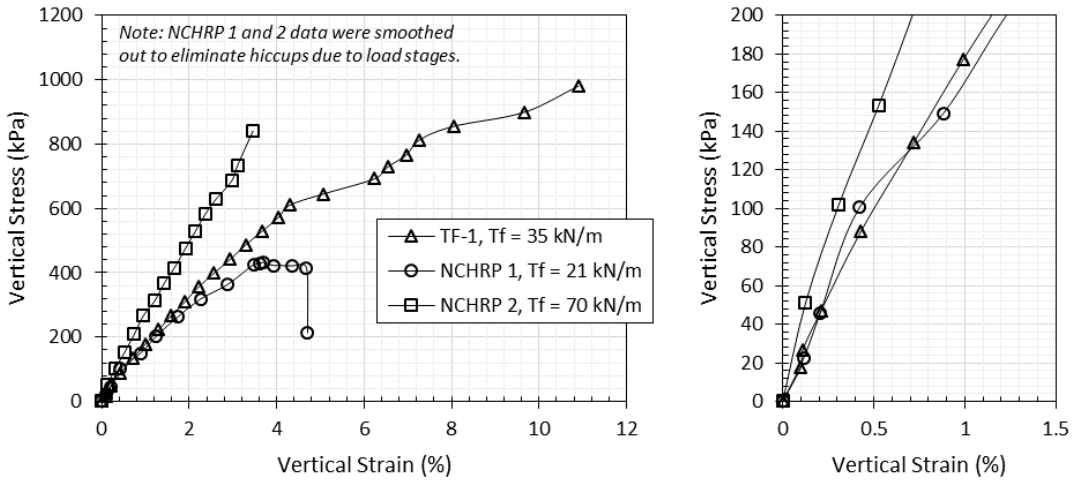

(a) (b)

Figure 3.18. Effect of reinforcement tensile strength on the stress-strain behavior: (a) Available stress range; (b) Service stress range.

Figure 3.19 shows the performance of three vertical loading tests on GRS experimental structures. The table in Figure 3.19 comprises a summary of the characteristics of the three structures. The reinforcement employed in all tests was geotextile layers of 70-kN/m tensile strength. The reinforcement vertical spacing varied amongst the structures. No bearing bed reinforcement nor facing were included. Note that MP-D was not loaded to failure. As shown in Figure 3.19a and 3.19b the highest stiffness was exhibited by the structure in which the reinforcement spacing was the smallest (MP-

D). However, MP-A showed higher stiffness than MP-B, yet the reinforcement spacing in MP-A was larger than that in MP-B. Adams et al. (2007) explained this unexpected rank that the compaction of the backfill material in MP-A was better than that in MP-B. They referred to the measured average backfill density, which was 23.0 kN/m3 for MP-A and 22.7 kN/m3 for MP-B. This difference, however, is not significant to cause this big difference in the performance of GRS structures.

Test Name	$q_{ult,measured}$ *(kPa)*	*Facing Type*	$\sigma_{confining}$ *(kPa)*	*H (m)*	S_v *(m)*	T_f *(kN/m)*	T_f/S_v *(kN/m/m)*	d_{max} *(m)*	*c (kPa)*	*φ (deg)*	*c,φ Method*	*Geometry*	*Reference*
MP-A	225	None	0.0	1.94	0.60	70	116.7	0.025	0.0	53.5	LSDS	Square Column	Adams et al. (2007a)
MP-B	170	None	0.0	1.94	0.40	70	175	0.025	0.0	53.5	LSDS	Square Column	Adams et al. (2007a)
MP-D	Didn't reach failure	None	0.97	1.94	0.20	70	350	0.025	0.0	53.5	LSDS	Square Column	Adams et al. (2007a)

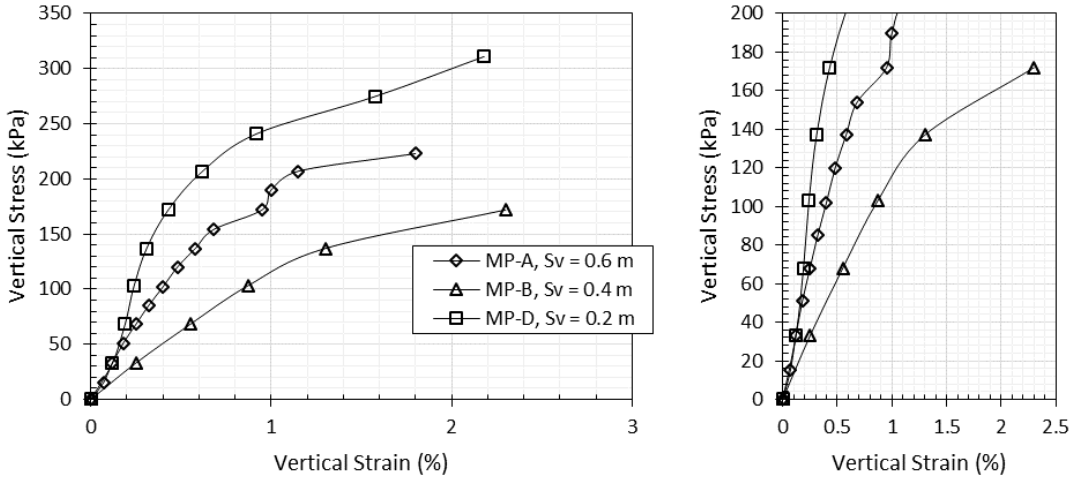

(a) (b)

Figure 3.19. Effect of reinforcement vertical spacing on the stress-strain behavior: (a) Available stress range; (b) Service stress range.

Figure 3.20 shows the behavior of loading tests conducted on two GRS experimental structures. The table in Figure 3.20 summarizes the characteristics of the two structures. Both structures were constructed using the same reinforcement, which was geotextile layers of 70-kN/m tensile strength. The reinforcement vertical spacing was different between the two structures. GSGC 2 showed higher bearing strength and stiffness than GSGC 4 as shown in Figures 3.20a and 3.20b, respectively, which is due to the difference in the reinforcement spacing.

Test Name	$q_{ult,measured}$ *(kPa)*	*Facing Type*	$\sigma_{confining}$ *(kPa)*	*H (m)*	S_v *(m)*	T_f *(kN/m)*	T_f/S_v *(kN/m/m)*	D_{max} *(m)*	*c (kPa)*	*φ (deg)*	*c,φ Method*	*Geometry*	*Reference*
GSGC 2	3400	CMU/Plexiglas	34	2.00	0.20	70	350	0.033	70	50	TX	Fixed Wall Column	Pham (2008); Wu et al. (2013)
GSGC 4	3400	CMU/Plexiglas	34	2.00	0.40	70	350	0.033	70	50	TX	Fixed Wall Column	Pham (2008); Wu et al. (2013)

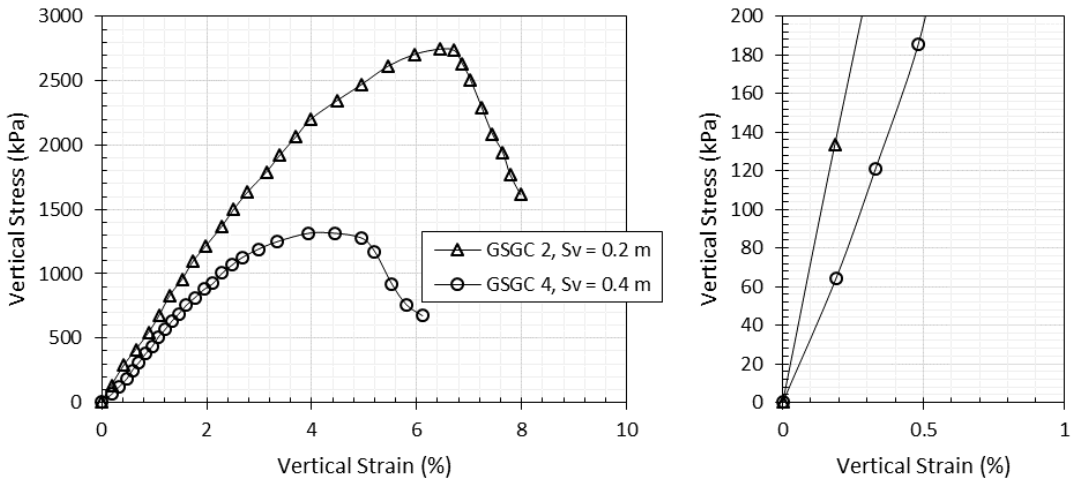

(a) (b)

Figure 3.20. Effect of reinforcement vertical spacing on the stress-strain behavior: (a) Available stress range; (b) Service stress range.

3.4.3. Lateral earth pressure

Wu (2001) studied the lateral earth pressure on the facing of GRS structures. It was reported that the lateral earth pressure on the facing is quite small compared to the lateral pressure predicted from Rankine earth pressure theory. In addition, it was reported earth pressure near the reinforcement levels approaches zero; however, some pressure may build up upon reinforcement straining. Wu (2001) proposed a method to estimate the lateral earth pressure exerted on the facing of GRS structures. The proposed distribution involves bin pressure diagram shown in Figure 3.21a, which depends on the reinforcement spacing, the shear strength parameters of the backfill material, and the facing rigidity. It was indicated that the main function of the facing is to prevent soil sloughing for GRS structures reinforced at small spacing (less than 0.3 m).

Wu and Ooi (FHWA-HRT-14-094, 2015) conducted a comparison between some measured lateral earth pressure values and two prediction methods: (1) Wu (2001) method, whose distribution is shown in Figure 3.21a; and (2) Soong and Koerner (1997) method, whose distribution is shown in Figure 3.21b. The comparison was not very robust though since it included few measured values, most of which were negative values retrieved from Mitchell (2002). Whereupon, more reliable data was sought and compiled to strengthen the assessment of the prediction models. In addition, lateral pressure using Rankine theory was assessed; however, the effect of the superstructure loading was ignored (i.e., prediction was conducted based on backfill self-weight only). Note that the models by Wu (2001) and Soong and Koerner (1997) also do not basically involve the effect of additional superstructure loading.

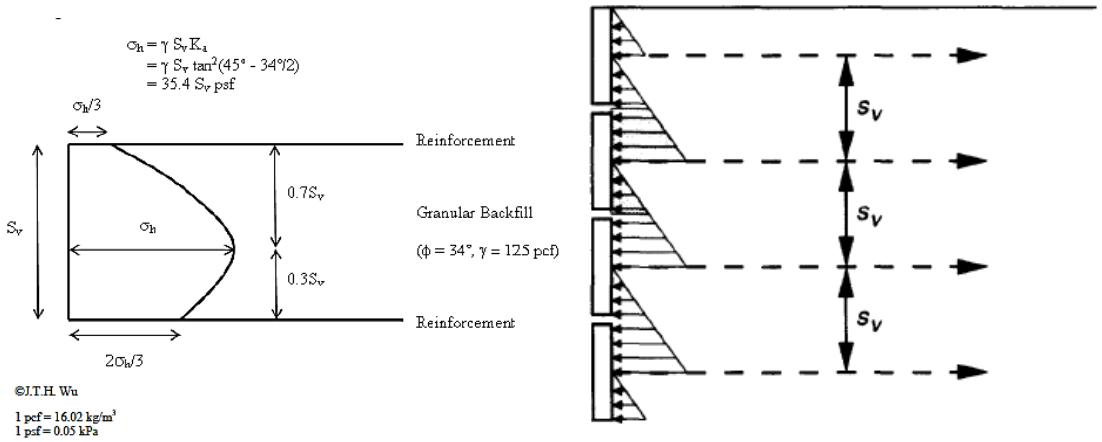

(a) (b)

Figure 3.21. Idealized lateral earth pressure distribution: (a) Wu (2001); (b) Soong and Koerner (1997).

Figure 3.22 shows a comparison between the measured lateral earth pressure values and the predicted values. A good agreement between the measured values and the predicted values using Rankine Theory. Note that, however, the effect of additional superstructure loading was not accounted for. On the other hand, the other two prediction models significantly underestimated the lateral earth pressure. Rankine theory has always shown a good prediction in GRS structures in which no additional loading is imposed. However, adding the lateral earth pressure due to additional vertical pressure predicted by Boussinesq elastic solution results in a significant overestimation to the lateral earth pressure. Overall, a continuum in the reduction in lateral earth pressure may need to be defined to consider the effect of reinforcement spacing reduction.

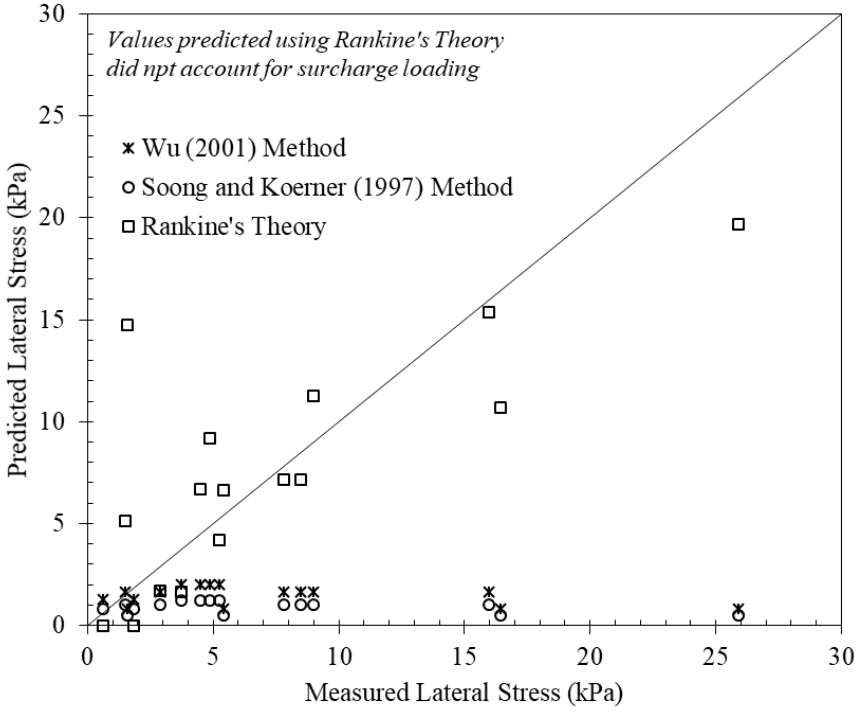

Figure 3.22. Measured vs. predicted lateral earth pressure on GRS facing.

3.4.4. Lateral strain

Adams et al. (FHWA-HRT-11-026, 2012) proposed a method for predicting the maximum lateral displacement in GRS abutments. This method has been referred to as "Adams method" in Xiao et al. (FHWA-HRT-15-080, 2016) and Khosrojerdi et al. (2016). This method assumes that there no volume change in GRS abutments. That is, the vertical strain is compensated by equivalent lateral strain preserving the same volume of GRS mass. This is deemed a conservative approach (Adams et al. 2012 – FHWA-HRT-11-026). It was reported that the composite behavior of GRS mass ideally results in monolithic defamation of the reinforcement and soil. Adams et al. (FHWA-HRT-11-026, 2012) proposed that the

maximum lateral displacement and strain can be estimated using Equations 3.2 and 3.3, respectively.

$$\boldsymbol{D_L = 2\ x\ B\ x\ \frac{D_V}{H}}$$

Equation 3.2

$$\boldsymbol{\varepsilon_L = 2\varepsilon_V}$$

Equation 3.3

Where

D_L: The maximum lateral displacement.

B: The width of the load along the top of the wall including the setback.

D_V: The vertical settlement of the load.

H: The height of the structure.

ε_L: The maximum lateral strain.

ε_V: The vertical strain.

This method is derived based on a simplified geometry of deformation diagram. That is, assuming that the vertical deformation under the load is uniform and that the lateral deformation takes the shape of a triangular prism. Regardless the location of the maximum ordinate, the equation would still give a rough estimate of the magnitude of the maximum lateral displacement (the peak of the triangle). Whereupon, in order to properly assess the performance of this method initially proposed by Adams et al. (FHWA-HRT-11-026, 2012), a modification had to be done to account for the fact that abutments are allowed to deform from only one side; whereas, square piers deform from four sides and fixed-wall

piers deform from two side as shown in Figure 3.23. This modification allows using this method with structures of different geometry configurations. Equations 3.4 and 3.5 modify the maximum lateral displacement and strain, respectively.

$$D_L = 2\ x\ B\ x\ \frac{D_V}{H}\ x\ \frac{1}{n}$$

Equation 3.4

$$\varepsilon_L = \frac{2\varepsilon_V}{n}$$

Equation 3.5

Where

n: The number of deformable sides of the structure (n = 4 for square piers; n = 2 for fixed-wall piers; and n = 1 for abutments).

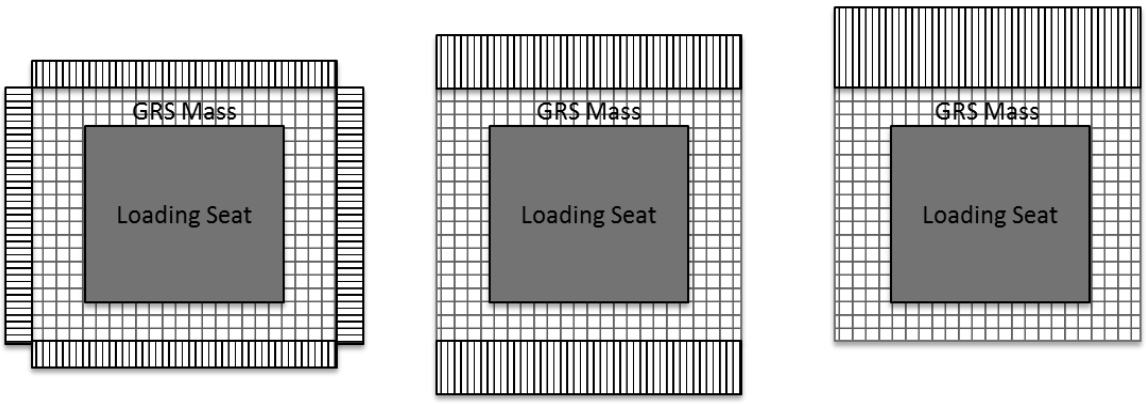

(a) (b) (c)

Figure 3.23. Typical deformation diagrams in plan: (a) square pier; (b) fixed-wall pier; (c) abutment.

Figure 3.24a shows the comparison between the measured and predicted values of the maximum lateral strain (regardless its location). The method seems to overestimate the deformation of the fixed-wall piers and underestimate the deformation of the abutments. It should be noted that GSGC 1 is an unreinforced fixed-wall pier. However, its performance conformed well to the predicted values. That is, the method is deemed a rough estimate that applied to any flexible wall/abutment where triangular lateral deformation is likely.

Adams et al. (FHWA-HRT-11-026, 2012) reported that the maximum lateral strain should be limited to 1.0%. Accordingly, Figure 3.24b was constructed to show a close-up on the comparison in Figure 3.24a up to lateral strain of 2%. A considerable scatter was observed in the prediction of the maximum lateral strain using this method.

(a)

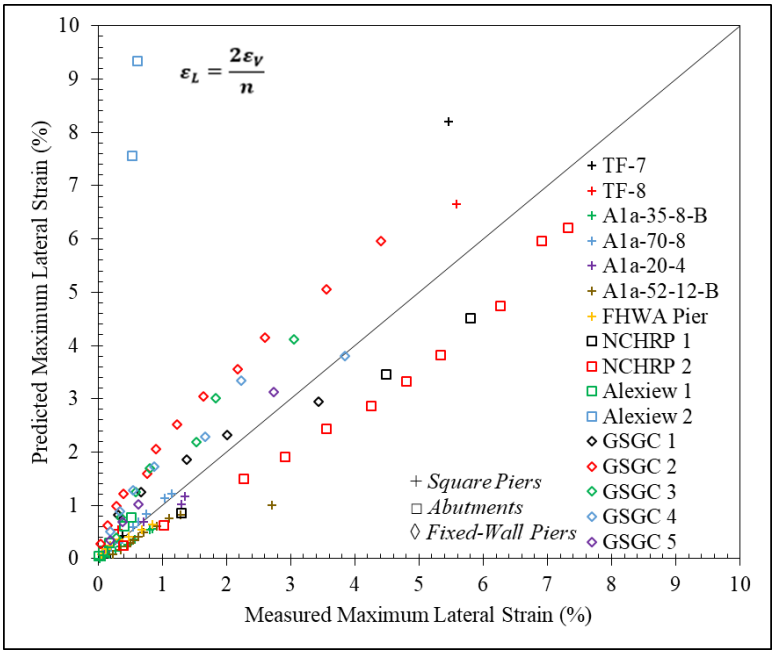

(b)

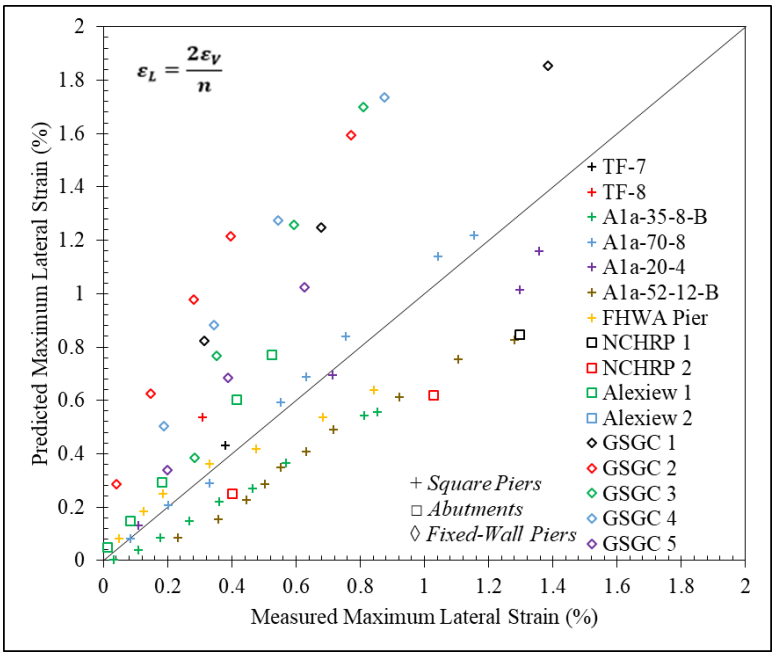

Figure 3.24. Measured vs. predicted maximum lateral strain of GRS facing: (a) Available strain range; (b) Service strain range.

3.5. DISCUSSION

The data collected pointed towards the effect of reinforcement spacing in reducing the lateral deformation and settlement, and increasing the bearing capacity of the reinforced soil mass. However, these conclusions are limited to the configurations tested by Nicks et al. (2013). This study led to the following findings:

This chapter aimed at evaluating the design models used in the FHWA GRS-IBS design guidelines (Adams et al. 2011, 2012). It should be noted that the experimental data reported in the reviewed research studies points towards the effect of reinforcement vertical spacing in reducing the lateral deformation and settlement, and increasing the bearing capacity of the reinforced soil mass. This study led to the following findings:

- The empirical design proposed by FHWA using the vertical stress-strain envelopes from a representative GRS Performance Test (Mini-Pier) was reevaluated at working stress levels (vertical stresses below 200 kPa). While the proposed envelopes were found to provide a very good repeatability on the full range of vertical stress-strain relationship, reassessment of the data was found not to be repeatable at working stress levels. In addition, the comparison conducted on the behavior of GRS structures of comparable materials and different boundary conditions revealed differences in performance (structural vertical and lateral deformation). A relevant outcome of the reassessment is that the difference in the boundary conditions between test piers and actual abutments may need to be taken into consideration to predict the behavior of GRS structures.

- The FHWA design guidelines do not account for the possible failure that can take place at the facing connection because the expected lateral earth pressures are small when the reinforcement layers are placed at comparatively close vertical spacings. However, reassessment of the collected data revealed that the reduction of lateral earth pressure due to the decrease in the reinforcement spacing could still be considered, although as a function in the reinforcement spacing and the type of backfill material used in the GRS structure.
- The FHWA design guidelines ruled out reinforcement pullout as a possible mode of failure. However, the decrease in the reinforcement spacing below a specific limit may decrease the mobilization of pullout resistance at the soil-reinforcement interfaces causing pullout failure in reinforcement groups similar to the group failure in piles (refer to Chapter 4 of this dissertation).
- It was reported that densifying reinforcement near the top of the GRS mass (i.e., bearing bed) can reduce the lateral deformation below the load.
- The GRS piers of closely-spaced reinforcement layers exhibited less lateral deformation and reinforcement strain than GRS piers of largely-spaced reinforcement layers of the same T_f/S_v ratio. However, no information was mentioned about the reinforcement tensile stiffness or the soil-reinforcement interaction, which are believed to explain the behavior of the GRS mass.

3.6. REFERENCES

Adams, M.T. (1997). "Performance of a Prestrained Geosynthetic-Reinforced Soil Bridge Pier." International Symposium on Mechanically Stabilized Backfill, Wu, J.T.H. (ed), Denver, USA, Balkema, pp. 35-53.

Adams, M.T., Ketchart, K., and Wu, J.T. (2007a). "Mini pier experiments–geosynthetic reinforcement spacing and strength as related to performance." Proceedings of Geo-Denver.

Adams, M.T., Lillis, C.P., Wu, J.T.H., and Ketchart, K. (2002). "Vegas GRS Mini Pier Experiment and the Postulate of Zero Volume Change." Proceedings of Geosynthetics 7th ICG, Delmas, Gourc and Girad (eds.), pp. 389-394.

Adams, M.T., Nicks, J.E., Stabile, T., Wu, J.T.H., Schlatter, W., and Hartmann, J. (2012). Geosynthetic Reinforced Soil Integrated Bridge System Interim Implementation Guide. Report No. FHWA-HRT-11-026, Federal Highway Administration, McLean, VA.

Adams, M.T., Nicks, J.E., Stabile, T., Wu, J.T.H., Schlatter, W., and Hartmann, J. (2011). Geosynthetic Reinforced Soil Integrated Bridge System, Synthesis Report. Report No. FHWA-HRT-11-027, Federal Highway Administration, McLean, VA.

Adams, M.T., Schlatter, W., and Stabile, T. (2007b). "Geosynthetic Reinforced Soil Integrated Abutments at the Bowman Road Bridge in Defiance County, Ohio." Proceedings of Geo-Denver, 2007, pp. 01-11.

Allen, T.M., Christopher, B.R., and Holtz, R.D. (1992). "Performance of a 12.6 m High Geotextile Wall in Seattle, Washington." International Symposium on

Geosynthetic-Reinforced Soil Retaining Walls, Balkema Publishers, Netherlands, pp. 81-100.

Bathurst, R.J. and Benjamin, D.J. (1990). “Failure of a Geogrid-Reinforced Soil Wall.” Transportation Research Record, Vol. 1288, pp. 109-116.

Berg, R.R., Christopher, B.R., and Samtani, N.C. (2009a). Design of Mechanically Stabilized Earth Walls and Reinforced Soil Slopes–Volume I. Report No. FHWA-NHI-10-024, Federal Highway Administration. National Highway Institute.

Berg, R.R., Christopher, B.R., and Samtani, N.C. (2009b). Design of Mechanically Stabilized Earth Walls and Reinforced Soil Slopes–Volume II. Report No. FHWA-NHI-10-025, Federal Highway Administration. National Highway Institute.

Christopher, B.R., Gill, S.A., Giroud, J.P., Juran, I., Mitchell, J.K., Schlosser, F., and Dunnicliff, J. (1990a). Reinforced soil structures Volume I. Design and construction guidelines. Report No. FHWA-RD-89-043. Federal Highway Administration.

Christopher, B.R., Gill, S.A., Giroud, J.P., Juran, I., Mitchell, J.K., Schlosser, F., and Dunnicliff, J. (1990b). Reinforced soil structures Volume II. Summary of Research and Systems Information. Report No. FHWA-RD-89-044. Federal Highway Administration.

Christopher, B.R., Holtz, R.D. and Bell, W.D. (1986). "New Tests for Determining the In-Soil Stress-Strain Properties of Geotextiles." Proceedings of the Third International Conference on Geotextiles, Vol. 3, Vienna, Austria, April 1986, pp. 683-686.

Elton, D., and Patawaran, M.A. (2004). "Mechanically Stabilized Earth Reinforcement Tensile Strength from Tests of Geotextile-Reinforced Soil." Transportation Research Record: Journal of the Transportation Research Board, Vol. 1868, pp. 81-88.

Elton, D., and Patawaran, M.A. (2005). Mechanically Stabilized Earth (MSE) Reinforcement Tensile Strength from Tests of Geotextile-Reinforced Soil. A report to the Alabama Highway Research Center, June 2005, 77p.

Iwamoto, M.K., Ooi, P.S.K., Adams, M.T., and Nicks, J.E. (2013). "Composite Properties from Instrumented Load Tests on Soil Columns Reinforced with Geotextiles." Transportation Research Broad, TRB 2014 Annual Meeting.

Ketchart, K. and Wu, J.T.H. (1996). Long-Term Performance Tests of Soil-Geosynthetic Composites. Report No. CDOT-CTI-96-1, Colorado Department of Transportation, Denver, CO.

Ketchart, K. and Wu, J.T.H. (2002). "A Modified Soil-Geosynthetic Interactive Performance Test for Evaluating Deformation Behavior of GRS Structures." ASTM International, Vol. 25, No. 4, pp. 405-413.

Ketchart, K., and Wu, J.T.H. (2001). Performance Test for Geosynthetic-Reinforced Soil Including Effects of Preloading. Report No. FHWA-RD-01-118, Federal Highway Administration, McLean, VA.

Nicks, J.E., Adams, M.T., Ooi, P.S.K., and Stabile, T. (2013a). Geosynthetic Reinforced Soil Performance Testing—Axial Load Deformation Relationships. Report No. FHWA-HRT-13-066, Federal Highway Administration, McLean, VA.

Nicks, J.E., Adams, M.T., and Stabile, T. (2013b). "Performance Testing for Geosynthetic Reinforced Soil Composites." Proceedings of the 5th International Young Geotechnical Engineers' Conference.

Pham, T.Q. (2009). Investigating Composite Behavior of Geosynthetic-Reinforced Soil (GRS) Mass. Ph.D. thesis, University of Colorado Denver, Colorado, USA.

Ruiken, A. and Ziegler, M. (2009). "Large Scale Laboratory Element Testing of Geogrid Reinforced Soil." Proceedings of GIGSA GeoAfrica 2009 Conference, Cape Town, September.

Soong, T-Y. and Koerner, R.M. (1997). "On the Required Connection Strength of Geosynthetically Reinforced Walls." Geotextiles and Geomembranes, Vol. 15, pp. 377-393.

Wu, J.T.H. (2001). Revising the AASHTO Guidelines for Design and Construction of GRS Walls. Report No. CDOT-DTD-R-2001-16, Colorado Department of Transportation, 148 p.

Wu, J., Pham, T.Q., and Adams, M. (2013). Composite Behavior of Geosynthetic-Reinforced Soil (GRS) Mass. Report No. FHWA-HRT-10-077, Federal Highway Administration, McLean, VA.

Wu, J.T.H. and Helwany, S.M.B. (1996). "A Performance Test for Assessment of Long-Term Creep Behavior of Soil-Geosynthetic Composites." Geosynthetic International, Vol. 3, No. 1, pp. 107-124.

Wu, J.T.H., Ketchart, K., and Adams, M.T. (2001). GRS Bridge Piers and Abutments. Report No. FHWA-RD-00-038, Federal Highway Administration, McLean, VA.

Wu, J.T.H., Lee, K.Z.Z., Helwany, S.B., and Ketchart, K. (2006). Design and Construction Guidelines for Geosynthetic-Reinforced Soil Bridge Abutments with a Flexible Facing. Report No. 556, National Cooperative Highway Research Program, Washington, DC.

Chapter 4: Soil Arching in Geosynthetic-Reinforced Soil Structures

4.1. INTRODUCTION

The interaction between soil backfill and geosynthetic reinforcement may be affected by phenomena that are related to the reinforcement vertical spacing. Such phenomena developing in a reinforced soil mass may be related to soil arching, as described by Terzaghi's classic trap-door theory (Terzaghi 1936). Soil arching develops during soil deformation and can take different arching shapes (e.g. Chen et al. 2008, Costa et al. 2009, Iglesias et al. 2013, Rui et al. 2016). This phenomenon may also take place in reinforced soil, especially in cases involving closely-spaced reinforcement. Such phenomenon is expected to depend on the soil density, grain size distribution, overburden pressure, and interface characteristics. Previous studies have been conducted on GRS to study the impact of closely-spaced reinforcement. Specifically, an experimental testing program was conducted by Leshchinsky et al. (1994) on GRS unit cells to study the impact of reinforcement vertical spacing with focus on the soil arching phenomenon. Specifically, a pullout testing device was developed to evaluate the displacement and strain fields within a reinforced soil unit cell. The testing program included pullout of single reinforcement layers and of two reinforcement layers connected to a rigid facing panel. This study presents a reevaluation of the experimental results obtained by Leshchinsky et al. (1994) and their integration to assess the performance of field monitoring and numerical results, which were also conducted to evaluate the effect of geosynthetic reinforcement vertical spacing. The field research component involves the evaluation of two GRS walls, and was complemented with numerical simulations conducted to extrapolate the findings of the

field study with focus on the effect of reinforcement spacing. The integrated experimental, field, and numerical results aim at assessing the interaction of the various wall components that may affect wall performance with varying reinforcement vertical spacing.

4.2. EXPERIMENTAL AND ASSOCIATED NUMERICAL COMPONENTS

Leshchinsky et al. (1994) conducted an experimental study to evaluate the effect of vertical reinforcement spacing on the failure mechanism in geosynthetic-reinforced structures. The motivation of their study was to assess failure mechanisms based on limit state analysis, which involve development of a failure slip surface extending from the toe to the crest of the structure. The reinforcement must extend beyond the slip surface to tie back the unstable zone to the stable zone. Limit equilibrium analysis does not account for the interaction occurring in soil and reinforcement layers considering spacing. For instance, the interaction among reinforcement layers may increase with decreasing vertical reinforcement spacing. In this case, the interaction between largely-spaced reinforcement layers would be comparatively minor, making the limit state a practical design approach. However, for closely-spaced reinforcement, the assumption may no longer be valid as the interaction (or load shedding) would increase with decreasing reinforcement spacing.

Two testing series were performed: (1) pullout of single reinforcement layer embedded in a confined soil mass, which assessed the performance of a reinforcement layer in a soil mass in conventional testing conditions; and (2) pullout of two reinforcement layers embedded in a confined soil mass, which assessed the effect of interaction between reinforcement layers. Two devices were used to evaluate the behavior of single and double reinforcement layers embedded in soil mass, respectively. Figure 4.1a shows a schematic

view of the device where a single reinforcement layer was employed. The device involved a steel frame that accommodates samples that were 60 cm long, 19 cm wide, and 30 cm high. The reinforcement layers were of the same width as the box. A normal normal pressure was applied to the top surface of the reinforced soil mass using a pressurized air bag. The second device was similar to the first one except that it was twice as high (i.e., 60 cm high), as shown in Figure 4.1b. The side walls of both devices were made of transparent Plexiglas to enable photogrammetric measurement of soil movements as the pullout load increases. This allowed evaluation of the interaction between the reinforcements and the soil mass. The transparent walls also allowed evaluation of the kinematics of the shear band that developed upon generation of shear stresses at the soil-reinforcement interface. The second device allowed placement of two reinforcement layers, enabling assessment of the interaction between two contiguous reinforcement layers. The vertical spacing of the reinforcement layers was 20 cm. A horizontal force was applied to a panel connected to the reinforcement layers. Accordingly, the test was conducted by imposing lateral displacements to a facing unit located between two reinforcement layers (rather than by increasing the overburden pressure on the reinforced soil mass). The test results suggest that the vertical reinforcement spacing influences the stiffness of the reinforced soil mass composite. For closely-spaced reinforcement of typical stiffness and strength, the failure surface was not likely to develop within the reinforced soil mass. Instead, the failure surface developed behind the reinforced soil zone. Closely-spaced reinforcement allowed formation of composite material that behaved as monolithic mass.

The backfill material used in the testing program was Ottawa sand, which classifies as poorly graded sand (SP according to the Unified Soil Classification System). The average and maximum particle sizes were 0.26 and 0.90 mm, respectively. The backfill was compacted dry to a relative density of 70%, which corresponds to an average unit weight of 16.8 kN/m3. The backfill was placed in six lifts by pluviation and was densified by slight tapping on the walls of the box. Triaxial tests conducted on specimens prepared at a 70% target relative density resulted in peak and residual friction angles of 38 and 34 degrees, respectively. The reinforcement used in this study was polypropylene biaxial geogrid with a tensile strength of 45.2 kN/m in the testing direction.

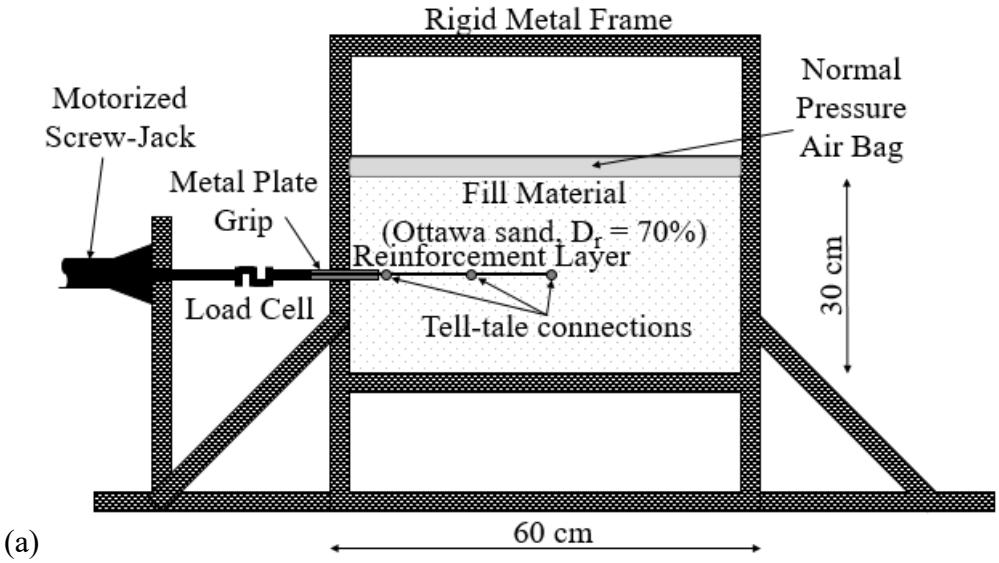

(a)

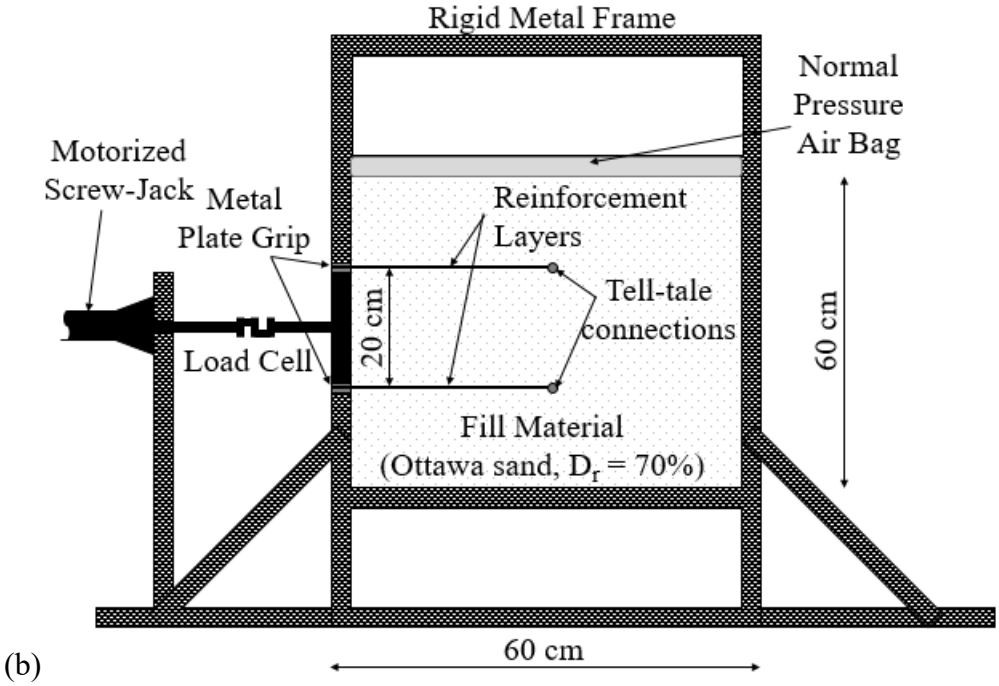

(b)

Figure 4.1. Pullout equipment: (a) Single-reinforcement test; and (b) Double-reinforcement test (redrawn after Leshchinsky et al. 1994).

Overall, the pullout process was observed to progressively propagate from the front end of the reinforcement to its rear end. Accordingly, the portions of the reinforcement closer to the line of load application reached pullout resistance capacity prior to the further portions. Accordingly, the soil-reinforcement interface strength in the front zones reached residual condition before the rear zones, which may still mobilize strength pre-peak, reach peak, and ultimately post-peak shear strength.

The results of single-reinforcement tests showed that the shear stresses generated at soil-reinforcement interface influenced a soil region ranging in thickness from 2.5 to 5 cm on each side of the reinforcement. This zone can be referred to as shear band and is schematically shown in Figure 4.2a. This pattern was found to be independent of the confinement. Note that since measurements are those observed on the latex membrane assumed to deform in unison with the adjacent soil. It was concluded that, for the geogrid and sand used in the study, the zone of influence of a single deforming geogrid is about 3 cm on each side. This implies that two deforming geogrids (i.e., two geogrid subjected to tension load) interact with each other (i.e., behave as a composite soil-geogrid material) if the vertical spacing is at most 6 cm. Note that this is valid for the type of backfill employed in the study, for which D_{50} = 0.26 mm, ϕ_{peak} = 38° and $\phi_{residual}$ = 34°. Backfill with particles larger than the sand used in these tests are expected to have larger effects. The tests conducted in this study were not intended to simulate pullout performance but rather to identify mechanisms and a response that could be deemed as composite material behavior.

The results of the double-reinforcement tests showed that the pullout resistance was essentially the same as that obtained using a single-reinforcement of the same length and

confinement configuration. That is, the soil between the reinforcement layers was found to stiffen, resulting in the soil/reinforcement unit to behave as a monolithic block. This block involves two outer interfaces on which shear stresses develop against the adjacent soil, while no shear displacements (and associated shear stresses) could be identified on the two inner interfaces adjacent to the stiffened soil block. This resulted in a pullout resistance in the double-reinforcement tests equivalent to that in the single-reinforcement tests. However, this response was found to apply only at comparatively high normal pressures, which is when the soil between the reinforcements is stiff enough to behave as a monolithic block. On the other hand, at low normal pressure the pullout resistance in the double-reinforcement tests was higher than that in the single-reinforcement layer tests. This is probably due to the generation of shear stresses at the inner interface between the reinforcement layers and the soil between the reinforcement layers. In addition, the tensile stiffness in the double-reinforcement test was higher than that in the single-reinforcement test. The observed deformation field is schematically represented in Figure 4.2b.

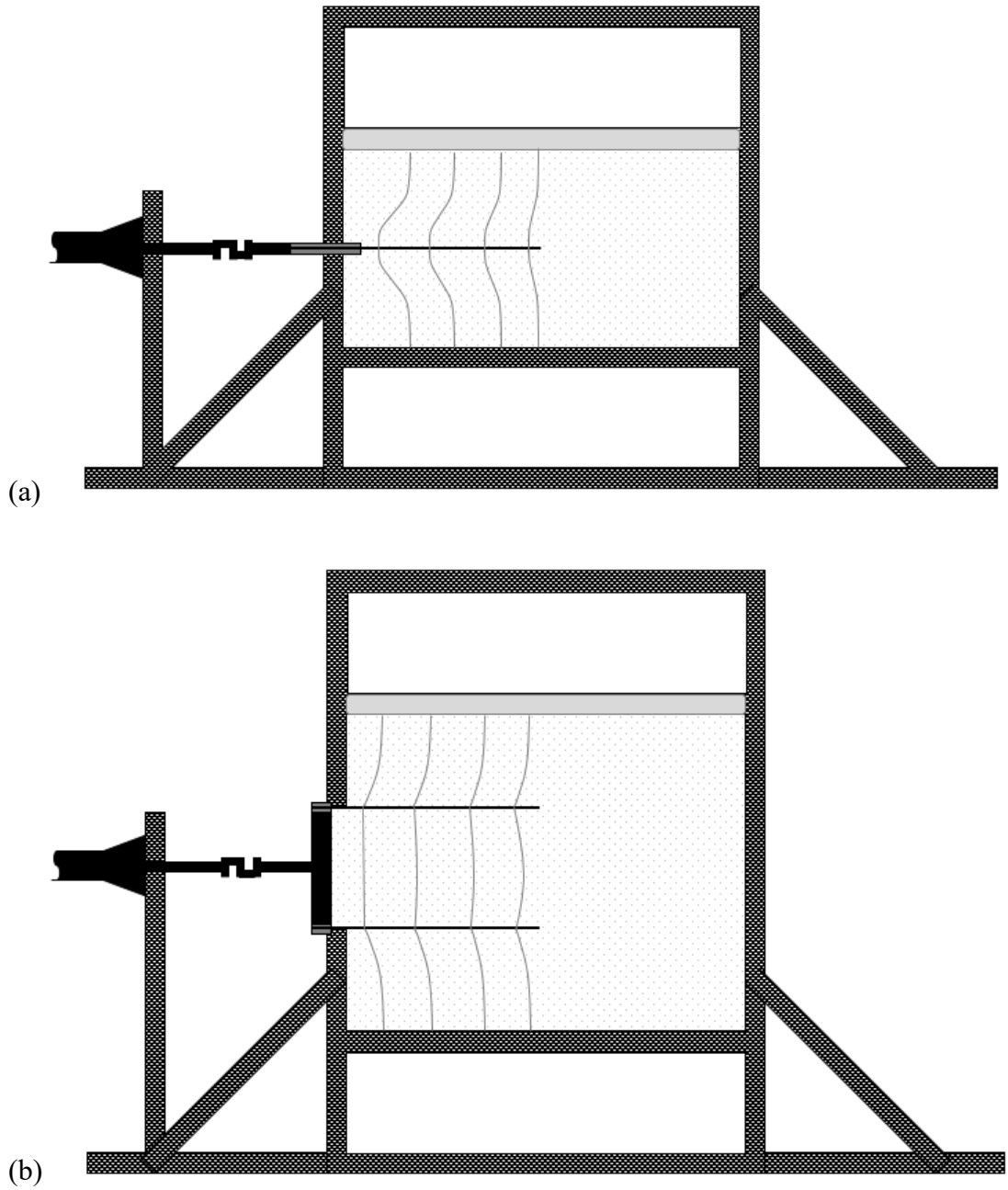

Figure 4.2. Schematic representation of shear band: (a) single-reinforcement test; and (b) double-reinforcement test (redrawn after Leshchinsky et al. 1994).

Figure 4.3a shows the expected failure mechanism, consistent with current design methodologies, when the active state is reached. However, the active state mechanism depicted in Figure 4.3a was not observed in the double-reinforcement tests. In addition, the load measured in the load cell after completion of the expected pullout test is compressive, consistent with those predicted by active earth pressure theory. Instead, they were zero. Accordingly, it appears that some 'silo' or arching effects developed, which resisted the lateral pressures that were expected to act in the block between the two geogrids. Figure 4.3b shows the actual failure mechanism observed in the double-reinforcement tests. As shown in Figure 4.3b, deformation in the soil mass followed the facing movement. For the spacing and geogrid stiffness used in this experimental program, only an external failure occurred (i.e., in a soil mass outside that bounded by the two layers). The soil between the two geogrids moved 'rigidly' with the geogrids, without developing an active slip surface.

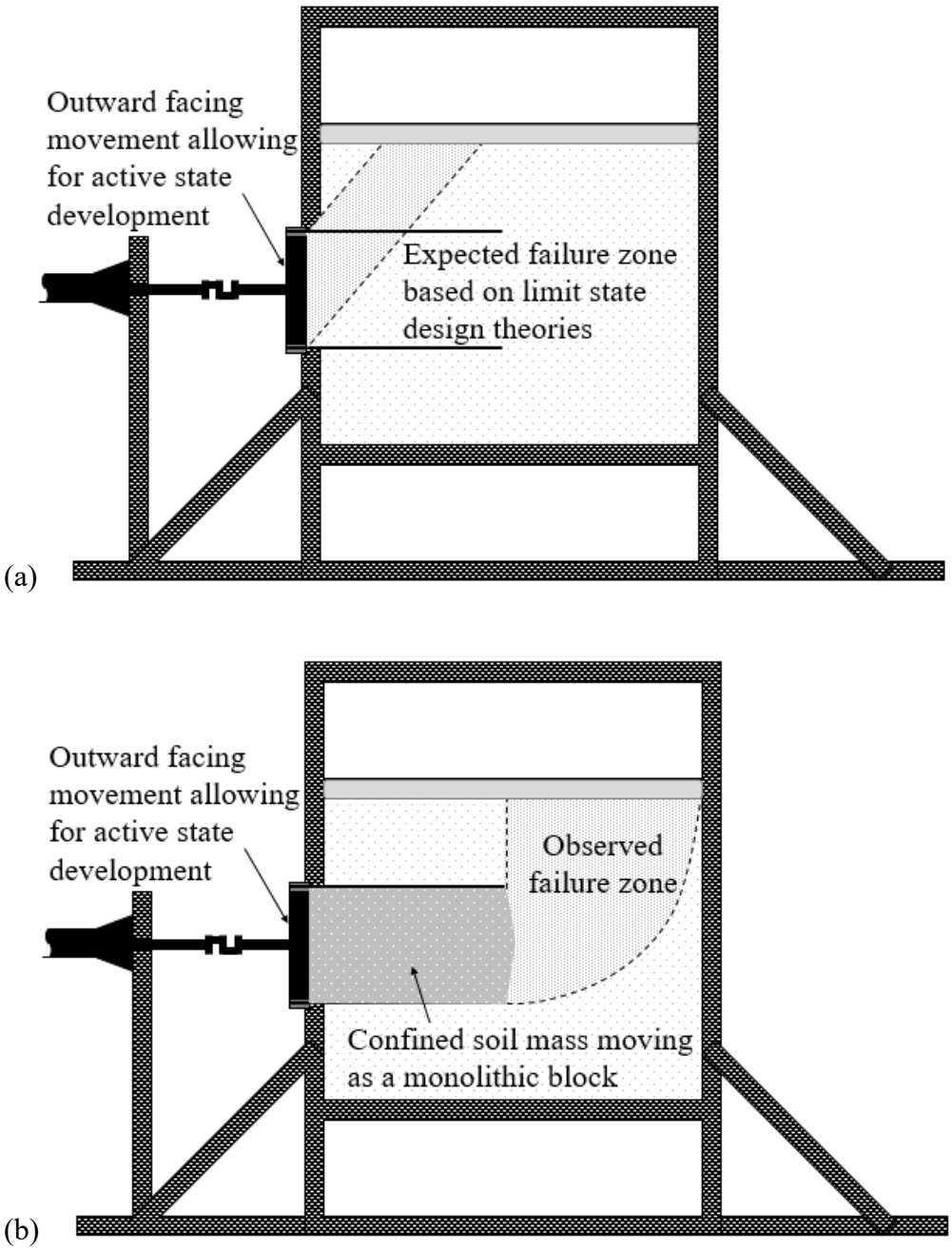

Figure 4.3. Failure mechanism: (a) postulated failure mechanism in active-state design; and (b) observed failure (redrawn after Leshchinsky et al. 1994).

A numerical evaluation was conducted to study the effects of vertical reinforcement spacing (Leshchinsky and Vulova 2001). Extensive parametric studies were conducted using a finite difference software, which employs a finite difference approach. The numerical model adopted "moving reference" algorithm where every new soil layer and block row are placed on top of a preceding layer that is allowed to deform during construction. This allowed the wall facing to undergo lateral outward deformation cumulatively as construction progresses. Simulated construction continued until a prevailing mode of failure occurred.

The results indicated that the effect of closely-spaced reinforcement increases with increasing backfill shear strength. This trend was found to be more pronounced if the foundation soil is stiff (i.e., competent foundation). For reinforcement spacing values below 200 mm, the reinforced soil mass was found to behave as a coherent mass and did not develop internal plastic zones. On the other hand, comparatively large spacing (beyond 600 mm) were found to lead to connection failure. Reinforcement spacing was found to play a major role in wall behavior and, inconsistent with current design approaches, it significantly affected the prevailing mode of failure. Overall, the numerical results indicated that interaction of all wall components (i.e., facing, foundation, retained soil, reinforced soil, and reinforcement properties) may affect wall performance. Also, the numerical results implied that, for high quality backfill, "close spacing" corresponds to values below 400 mm; although this value was found to be highly dependent on multiple factors. Also, the parametric studies indicated that, for closely spaced reinforcement, commonly used methods for external stability analysis (e.g., direct sliding, toppling, deep-

seated failure, and compound) are adequate for design. However, current design guidelines may not be accurate for the case of predicting reinforcement strength requirements.

4.3. FIELD STUDY

Based on the findings of the experimental component of this research, a field evaluation was conducted, which involved two GRS retaining walls constructed in Stockbridge, Georgia. Construction started in November 1994 and was completed in August 1995. The walls utilized segmental concrete blocks; the walls are referred to herein as WALL 1 and WALL 2. The walls were 6.84 m-high (36 block rows) and were reinforced at vertical spacing values of 0.4 and 0.8 m (i.e., every two and four block courses), respectively. The walls were subjected to a surcharge corresponding to a 0.76-m thick soil layer. The geosynthetic reinforcement used in the walls involved uniaxial geogrids with an ultimate tensile strength of 70 and 114 kN/m for WALL 1 and WALL 2, respectively. The reinforced backfill material, which was the same as the retained soil, was a concrete sand characterized by an average grain size, D_{50}, of 0.79 mm. The reinforcement length to wall height ratio, L/H, was approximately 0.3, which is significantly lower than the minimum ratio of 0.7 established by the American Association of State Highway and Transportation Officials (AASHTO) requirements and of 0.6 established by the National Concrete Masonry Association (NCMA) requirements. However, an L/H ratio of 0.3 had already been adopted by Tatsuoka (1994) while using rigid facing. Short reinforcement was deemed acceptable, particularly considering that planar reinforcements (i.e. geosynthetic sheets) are used. This reinforcement enhances the stability of the structures due to its large contact area with backfill, unlike strip reinforcements that should be longer in order to

transfer similar loads in a smaller contact area (Tatsuoka 1994). The comparatively large contact area results in a comparatively large pullout resistance as long as the tensile capacity is comparatively high. The short reinforcement length adopted in these walls was defined based on external stability calculations assuming factors of safety of 1.5 for sliding and overturning. It should be noted that AASHTO requires a factor of safety of 2.0 for overturning. The foundation soil was competent, so bearing capacity was not a governing design issue. The premise was that the proximity of layers in the walls under investigation was deemed close for the particle size and the friction angle of the well-graded, angular sand in the walls. Consistent with the results of the previous experimental component of this study, a consistent performance of the full-scale walls would be expected to show no development of internal failure surfaces.

Figure 4.4 shows the instrumented cross-sections of the constructed walls. Both walls were boosted with eight survey targets on the facing units (rows 1, 4, 8, 12, 16, 20, 24, and 28). Four reinforcement layers were instrumented by 15 displacement sensors attached to the layers along their length using tell-tales. Layers instrumented in WALL 1 were layers 2, 4, 8, and 12; whereas, those instrumented in WALL 2 were layers 1, 2, 4, and 6. Note that the instrumented layers in both walls are placed at the same elevation. In addition, two lateral earth pressure cells were installed at the back of facing block 5 in both walls.

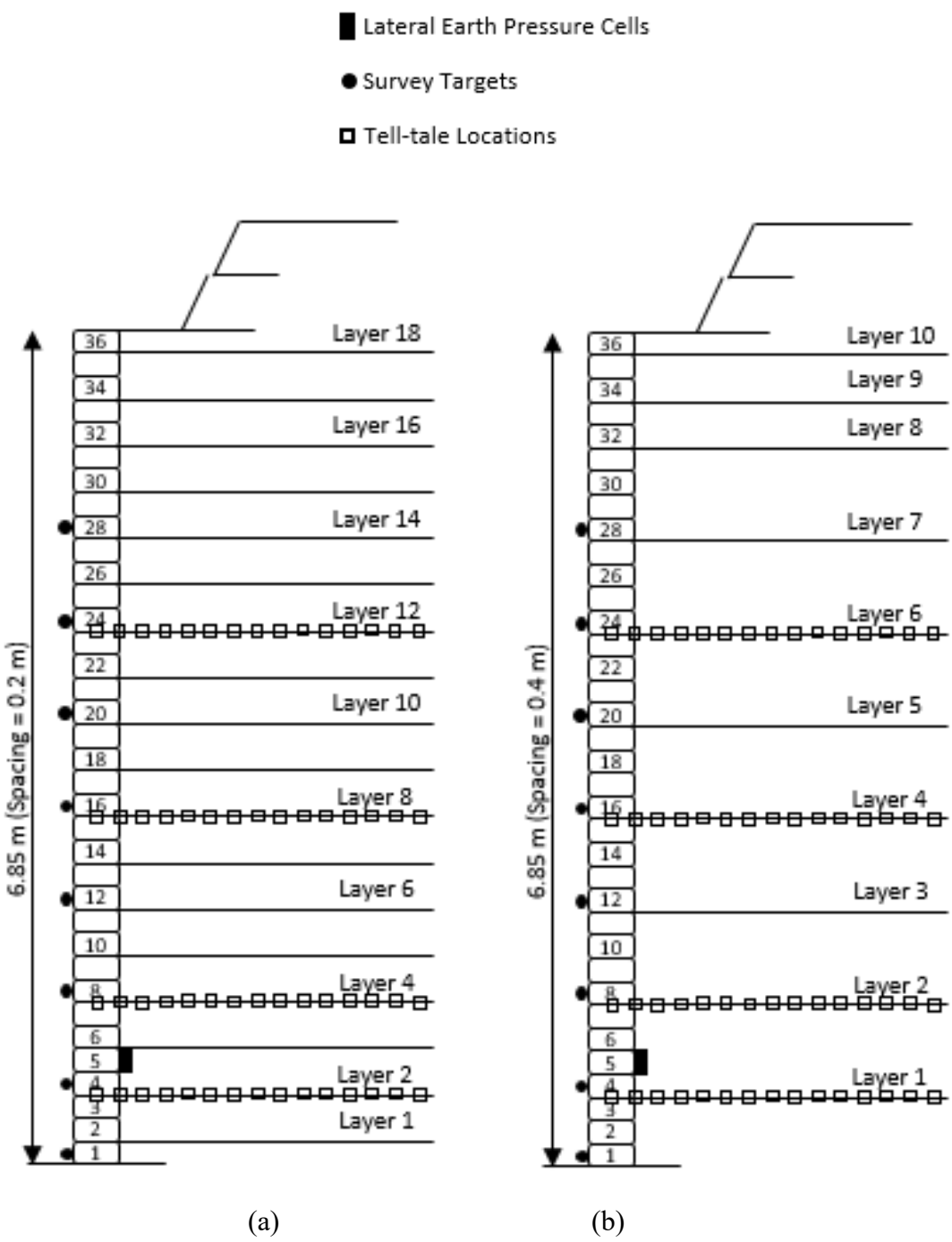

Figure 4.4. Instrumented cross-sections of the GRS walls: (a) WALL 1; and (b) WALL 2.

The outward facing displacement profiles, as measured in the field for WALL 1 and WALL 2, are presented in Figures 4.5a through 4.5d for various construction stages. The maximum displacement for both walls was observed at one third of the wall height. The outward displacements for WALL 1 were found to be slightly smaller than those for WALL 2. The measured displacement in both walls were comparatively small (less than 1.5 cm at the facing's mid-height). Note that the difference in in outward displacement at a given elevation increased as the construction advanced (i.e., as the vertical stress increased). No significant difference in the outward displacement was observed on both walls near the top where the reinforcement spacing was the same.

Figure 4.6 shows the reinforcement straining at various levels for WALL 1 and WALL 2. Figures 4.6a and 4.6b show the reinforcement displacements at various construction stages for layers 8 and 12, respectively. On the other hand, Figures 4.7a and 4.7b show the reinforcement tensile strains at various construction stages for layers 4 and 6, respectively,. That is, the elevations where strains were measured in WALL 1 correspond to the same elevations where some of the reinforcements were also measured in WALL 2. The measured strain values fluctuate somewhat between tension and compression. However, as shown in Figures 4.6 and 4.7, overall reinforcement strains were below 0.4%. It should be noted that reinforcement strains increased from 0.1% to less than 0.4% after adding the surcharge. The largest value of tensile strain was observed at reinforcement layers close to one third of the wall height. Note that the reinforcement displacements (and strains) measured in WALL 2 were higher than those measured in WALL 1 in layers at corresponding elevations.

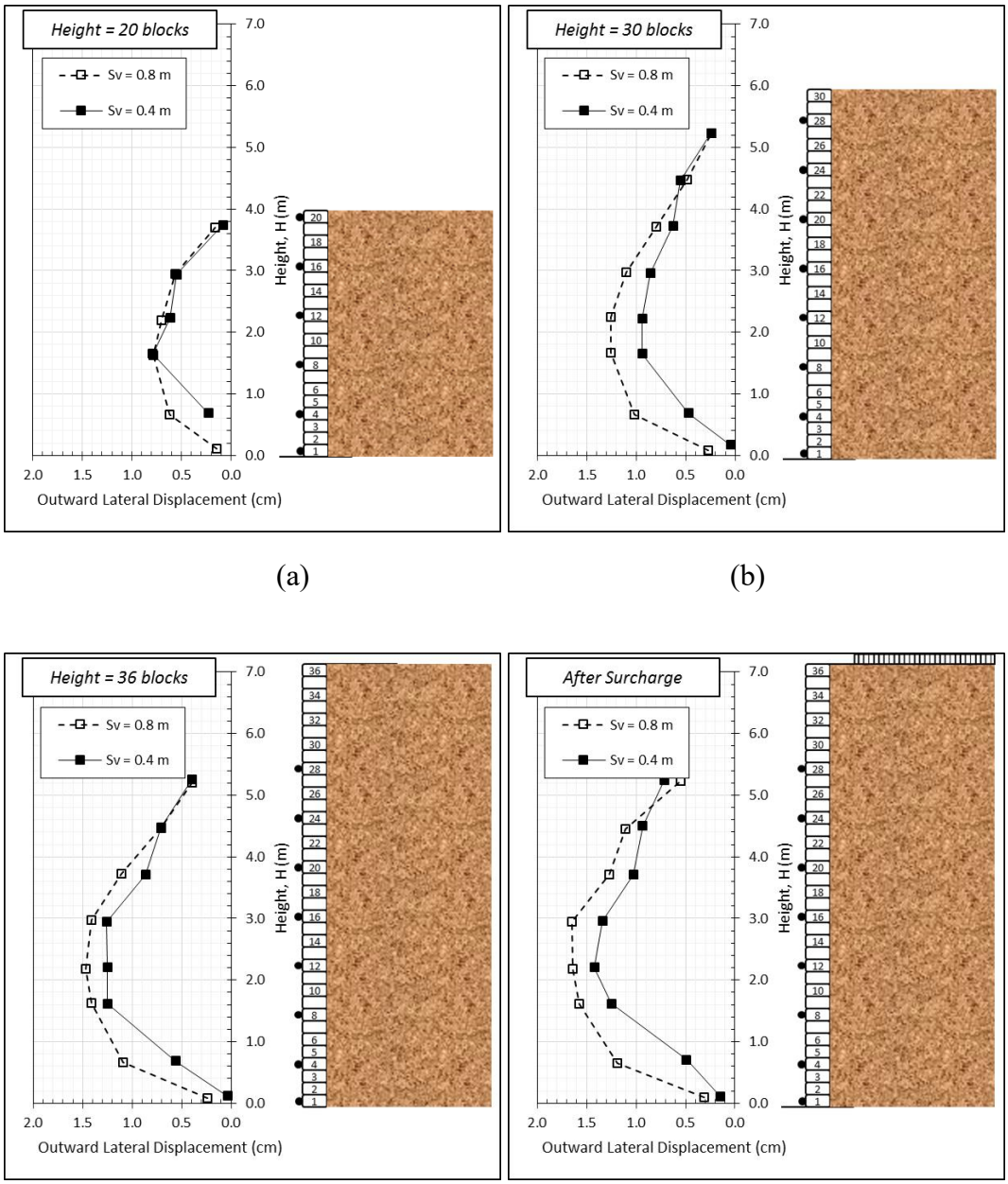

Figure 4.5. Outward lateral displacement profile at various construction stages: (a) At height, H = 20 blocks; (b) At height, H = 30 blocks; (c) At height, H = 36 blocks; and (d) After surcharge (after Morsy et al. 2017a).

(a)

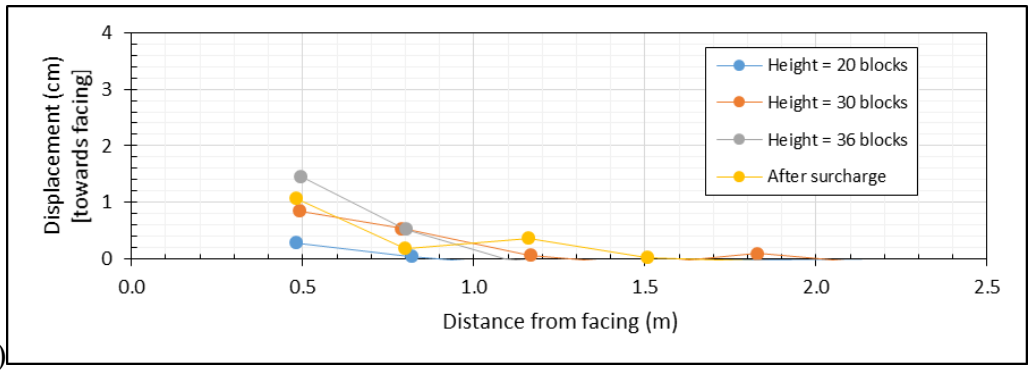

(b)

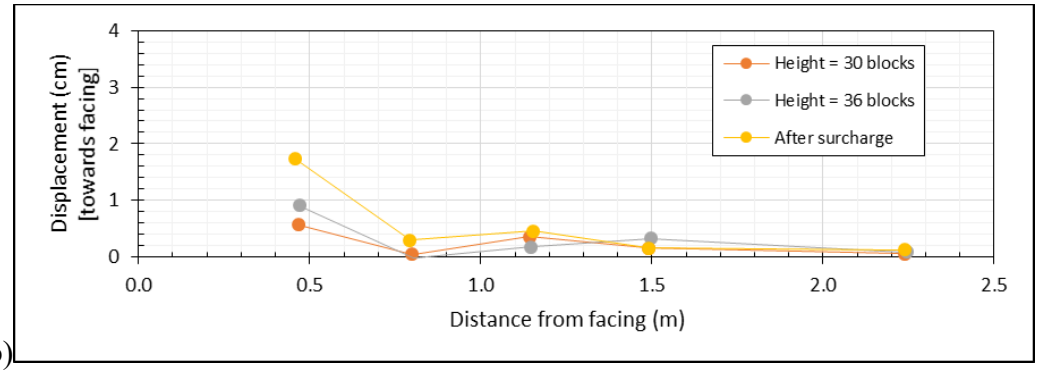

Figure 4.6. Reinforcement displacement profiles: (a) Layer 8 in WALL 1; and (b) Layer 12 in WALL 1.

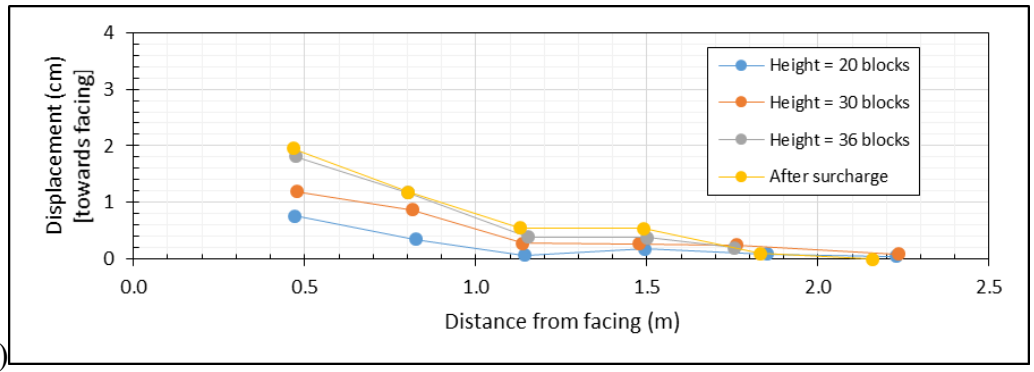

(a)

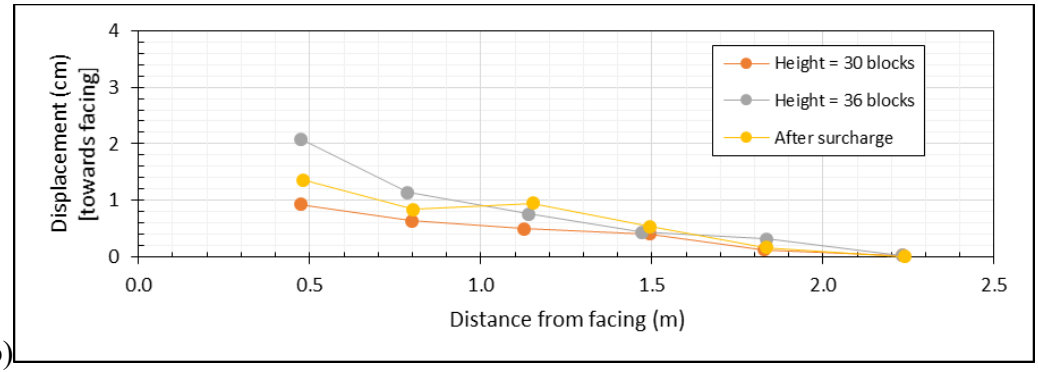

(b)

Figure 4.7. Reinforcement displacement profiles: (a) Layer 4 in WALL 2; and (b) Layer 6 in WALL 2.

Lateral pressure transducers showed comparatively small stresses acting against the block facing. When the height of the wall was reduced after completion of the field tests, no collapse occurred as the facing units were removed. It was concluded that the soil confined between the geogrids (in both walls) acted as a monolithic block, which is consistent with the experimental findings of the experimental component of the study. This is in spite of differences in backfill materials and reinforcement vertical spacing.

4.4. CONCLUSIONS

An experimental data reevaluation was conducted, which indicated that the interaction of reinforcement layers in a geosynthetic-reinforced structure may be significant and could render a composite material behavior. For the conditions evaluated in this experimental component, which used a sand backfill, a mobilization of a single geosynthetic reinforcement indicted that a spacing of 6 cm would render such behavior, although mobilization of a double geosynthetic reinforcement system indicated that 20 cm may also be adequate to render composite behavior. Results of the double geosynthetic reinforcement system indicated that the soil mass between reinforcements was mobilized as a monolithic system. In a recent discussion with Professor Dov Leshchinsky, he pointed out that soil arching can be significant if a slight cohesion is added to the backfill.

Subsequent study conducted by Leshchinsky and Vulova (2002) showed that the failure plane is likely to take place behind the reinforced soil zone instead of inside the reinforced soil zone when the reinforcement spacing is reduced. This conclusion strengthened the observation made by the experimental study by Leshchinsky et al. (1994). These conclusions pointed towards a composite mass acting as one big block. Leshchinsky and Vulova (2002) suggested that reinforcement vertical spacing of 0.4 m is a reasonable value below which a GRS mass can behave as a composite.

A field evaluation, involving monitoring of two geosynthetic-reinforced walls with different vertical reinforcement spacing, was also conducted. The results showed that wall displacements, reinforcement strains, and lateral pressure on facing were comparatively small. This observation implied that the soil confined between reinforcement acted as a monolithic block, which is consistent with the observations gathered in the experimental

program. Field results indicated that the composite behavior occurred but was limited to reinforcement spacings below 0.6 m for the geogrids used in this research component.

Leshchinsky et al. (1994) reported that this composite behavior is more likely to happen at high confinement levels where the stiffened zone around the reinforcement is bigger. This points towards the dependency of the "close" spacing effect on the level of confinement of the GRS mass. The field study showed that the effect of reinforcement spacing is not pronounced until confinement is added.

Overall, results of the experimental and field components of this investigation, jointly point towards the beneficial impact of closely-spaced reinforcement on the performance of reinforced soil structures and, particularly, on the impact of closely-spaced reinforcement on the stresses acting against the wall facing components. While a value was not established for the reinforcement vertical spacing below which a composite behavior should be expected, the following practical recommendations can be drawn: (1) composite behavior is not expected for reinforcement vertical spacing values beyond 0.6 m, although this value is expected to correspond to a minimum value of geosynthetic reinforcement stiffness; (2) the length of geosynthetic reinforcement is expected to be governed by external stability considerations (e.g. direct sliding, overturning/eccentricity); and (3) the impact of closely-spaced reinforcement on decreasing the stresses acting against the wall facing components is significant.

4.5. REFERENCES

Boulanger, R.W., Bray, J.D., Chew, S.H., Seed, R.B., Mitchell, J.K., & Duncan, J.M. (1991). SSCOMPPC: Finite element analysis program for evaluation of soil-

structure interaction and compaction efforts. Report No. UCB/GT/91-02, Univ of California, Berkeley.

Bray, J.D. (1995). Personal Communications, Univ of California, Berkeley.

Broms, B.B., (1978). "Design of fabric reinforced retaining structures." Proc. of the Symposium on Earth Reinforcement, ASCE, Pittsburgh, PA, April 27, 1978, 282-304.

Chen, Y.M., Cao, W.P., & Chen, R.P. (2008). "An experimental investigation of soil arching within basal reinforced and unreinforced piled embankments." J. G&G, 26(2):164–74.

Costa, Y.D., Zornberg, J.G., Bueno, B.S., & Costa, C.L. (2009). "Failure Mechanisms in Sand over a Deep Active Trapdoor." JGGE, ASCE, 135(11):1741-1753.

Duncan, J.M. & Chang, C-Y. (1970). "Nonlinear analysis of stress and strain in soils." J. of the Soil Mechanics & Foundations Division, ASCE, 96(SM5):1629-1653.

Iglesias G.R., Einstein H.H., & Whitman R.V. (2013). "Investigation of soil arching with centrifuge tests." JGGE, 140(2):248–56.

Leshchinsky, D., (1997). Design procedure for geosynthetic reinforced steep slopes. Technical Report REMR-GT-23, Jan. 1997, WES, Vicksburg, MS.

Leshchinsky, D., Kaliakin, V., Bose, P., & Collin, J. (1994). "Failure Mechanism in Geogrid-Reinforced Segmental walls: Experimental Implications." Soils & Foundations, Journal of the Japanese Society of Soil Mechanics & Foundation Engineering, 34(4):33-41.

Leshchinsky, D. & Vulova, C. (2001). "Numerical investigation of the effects of geosynthetic spacing on failure mechanisms in MSE block walls." Geosynthetics Int., 8(4):343-365

Ling, H.I., Cardany, C.P., Sun, L-X., & Hashimoto, H. (2000). "Finite Element Study of a Geosynthetic-Reinforced Soil Retaining Wall with Concrete-Block Facing." Geosynthetics Int., 7(2):137-162.

Morsy, A.M., Leshchinsky, D., and Zornberg, J.G. (2017a), "Effect of Reinforcement Spacing on the Behavior of Geosynthetic-Reinforced Soil," In Proceedings of Geotechnical Frontiers 2017, American Society of Civil Engineers (ASCE), March 12-15, 2017 | Orlando, Florida, USA, pp. 112-125.

Rui, R., van Tol, F., Xia, X. L., van Eekelen, S., Hu, G., & Xia, Y. Y. (2016). "Evolution of soil arching; 2D DEM simulations." Journal of Computers & Geotechnics, 73, 199-209.

Seed, R.B. & Duncan, J.M. (1984). A finite element analysis program for evaluating soil-structure interaction & compaction efforts. Report No. UCB/GT/84-02, Univ of California, Berkeley.

Tatsuoka, F., Tateyama, M., Murata, O. & Tamura, Y. (1994). "Closure on 'Geosynthetic-Reinforced Soil Retaining Walls with Short Reinforcement and a Rigid Facing.'" Recent Case Histories of Permanent GRS Retaining Walls, Balkema, Proc. of Seiken Sym. 11, Tokyo, Japan, 323-344.

Terzaghi K. (1936). “Stress distribution in dry and in saturated sand above a yielding trap-door.” Proc. of 1st int. conference on soil mechanics & foundation engineering. Cambridge, MA.

Terzaghi, K. & Peck, R.B. (1967). Soil mechanics in engineering practice. 2nd edition, John Wiley & Sons, Inc.

Chapter 5: Effect of Reinforcement Spacing on the Behavior of Geosynthetic-Reinforced Soil Centrifuge Models

5.1. ABSTRACT

The adoption of geosynthetic-reinforced soil (GRS) systems for soil retention projects has been steadily increasing over the past few decades. Specifically, the use of GRS in slopes, walls, and bridge abutments has resulted in economic, time-efficient solutions that provide excellent long-term performance. While extensive research has been conducted to evaluate the behavior of GRS structures, the technical literature has not fully addressed the effect of the reinforcement vertical spacing on the behavior of GRS structures. Consequently, the effect of the reinforcement spacing may have been overlooked in current design procedures for GRS structures. This study presents the results of centrifuge tests on GRS models prepared at varying reinforcement vertical spacing in order to assess its impact on the structure stability. The experimental results are presented within the context of centrifuge test results from previous GRS centrifuge studies. The evaluation involved rigorous consolidation and reassessment of available information on the behavior of GRS centrifuge models with emphasis on testing programs where vertical reinforcement spacing was varied. Finally, the study discusses the observed trends of the effects of reinforcement spacing and reinforcement tensile strength on the behavior of GRS structures under both working stress and ultimate state conditions. The results indicate that the effect of reinforcement vertical spacing on the behavior of GRS structures is not strictly proportional to the effect of reinforcement mechanical properties (e.g. stiffness, ultimate tensile strength), but it may outweigh the relevance of the mechanical properties for particularly small values of vertical spacing.

5.2. INTRODUCTION

A significant volume of data has been generated over the years with the objective of assessing the performance of GRS structures using centrifuge modeling. An advantage of centrifuge modeling is that the stress state of reduced-scale models corresponds to that of prototypes because of the increased gravitational field. Accordingly, centrifuge tests are useful to validate experimentally a number of design aspects. This includes the effect of reinforcement vertical spacing, which is of key relevance to the GRS behavior. A number of centrifuge research projects have been conducted to evaluate the performance of GRS structures (Jaber 1989; Zornberg et al. 1997, 1998a, 1998b; Zornberg and Arriaga 2003; Woodruff 2003; Kniss et al. 2007; Yang et al. 2008, 2011; Lee et al. 2010a, 2010b; Costa et al. 2016). The centrifuge testing programs in these studies were conceived to address specific aspects in GRS design. Collectively, however, they represent a vast source of experimental data that can be mined to assess additional aspects of GRS behavior and provide significant insight into the composite behavior of GRS structures. This study involved implementation of a testing program that aimed at evaluating the effect of the reinforcement spacing and surcharge loading on the behavior of GRS structures. This was rigorously conducted thorough consolidating and reassessing the information generated using the entire portfolio of centrifuge data on GRS structures with an emphasis on data in which vertical reinforcement spacing are varied.

5.3. BACKGROUND

Full-scale field studies are deemed time consuming and are costly, which makes them infeasible to generate a good database from which solid conclusions can be drawn.

Hence, many research studies have developed small-scale laboratory methods. For instance, the behavior of GRS structures subjected to vertical load has been studied in small-scale models at normal gravity, i.e. 1 g (e.g. Lee et al. 1973, Palmeira and Lanz 1994; Gomes et al. 1994; Vafaeian and Abbaszadeh 2006). However, these reduced-scale models were not subjected to the same stress levels that can mimic real structures. Subsequently, geotechnical centrifuge modeling technique has emerged allowing accurate analysis of the performance of soil structures subjected to representative stress levels (Schofield 1980).

Geotechnical centrifuge modelling has proven a time-saving and efficient way to simulate many of the geotechnical problems. This has significantly facilitated understanding of the mechanical behavior through observation of realistic results. Geotechnical centrifuge creates an environment in which the inertial acceleration is higher than the gravitational acceleration. This replicates as-real environment for the test models, which in turn replicates soil behavior in terms of stresses, strength, and stiffness. That is, centrifuge modelling enables implementation of parametric studies on small-scale structures, but with generating as-real behavior of prototype structures. Several published research studies were identified in the technical literature in which the reinforcement vertical spacing was varied. Table 5.1 presents a summary of the studies that were identified in technical literature. Other references have also been identified that are of relevance such as Santamrina (1984), Goodings (1990), Porbaha and Goodings (1994), and Arriaga (2003). Note that quite limited research has been conducted on vertically loaded GRS structures, for which GRS bridge abutments are still short of replacing traditional abutments in major projects.

Vertical reinforcement spacing is deemed to play a crucial role in the behavior of GRS structures. It was reported that reducing the reinforcement spacing improves significantly the behavior of GRS structures: (1) improves the bearing strength of the GRS mass (Vafaeian and Abbaszadeh 2006; Sommers and Viswanadham 2009); (2) curbs significantly the deformation (Sommers and Viswanadham 2009; Lin et al. 2013; Iacorossi et al. 2013; Malinowska 2015); and (3) enhances the overall stability (Woodruff 2003; Iacorossi et al. 2013). Sommers and Viswanadham (2009) observed that the vertical deformation depended greatly on the reinforcement distribution. They reported that the reinforcement vertical spacing significantly affects the vertical loading capacity of the GRS mass. In addition, they concluded that placement of closely-spaced reinforcement layers in the upper half of the reinforced soil mass can enhance the performance of loaded GRS structures.

Palmeira and Lanz (1994) and Gomes et al. (1994) tested 1-g models reinforced with various reinforcement patterns, which included hybrid vertical spacings and reinforcement lengths. It was concluded that reinforcement arrangement has a significant effect on external and internal deformation of the reinforced soil mass (Palmeira and Lanz 1994; Viswanadham and Mahajan 2007). Specifically, they concluded that short secondary reinforcement layers with largely spaced primary reinforcement facilitates the construction but has a limited benefit on curbing deformation (Palmeira and Lanz 1994). Zornberg and Arriaga (2003) and Viswanadham and Mahajan (2007) reported that maximum peak strain in reinforcement layers occurs at mid-height of GRS structures, which contradicts with the

conventional triangular distribution of reinforcement tension. Zornberg and Arriaga (2003) added that the maximum peak strain occurs below the structure's crest.

Table 5.1. Centrifuge modelling studies for geosynthetic-reinforced soil structures at various reinforcement spacing.

Structure Type	Structure Height (mm)	Backfill Type	Reinforcement Type	Facing Type	Various Spacing	Spacing Range (mm)	Added Surcharge	Year	Reference
GRS slopes	229	Sand	Geotextile	Wrapped around	No	20	No	2016	Costa et al. (2016)
GRS walls	320	Sand	Geogrid	Gabions	Yes	20-40	No	2015	Malinowska (2015)
GRS walls	320	Sand	Geogrid	Gabions	Yes	20-40	No	2013	Lin et al. (2013)
GRS walls	145	Sand	Geogrid	Modular blocks	Yes	22-66	No	2013	Iacorossi et al. (2013)
GRS slopes	270	Sand	Geotextile	Wrapped around	Yes	30-40	Yes	2009	Sommers & Viswanadham (2009)
GRS slopes	270	Sand	Geotextile	Wrapped around	Yes	30-40	No	2007	Viswanadham & Mahajan (2007)
GRS slopes	229	Sand	Geotextile	Wrapped around	Yes	19.05-25.4	No	2004	Costa (2004)
GRS walls	228	Sand	Geotextile	Wrapped around	Yes	10-50	No	2003	Woodruff (2003)
GRS slopes	228	Sand	Geotextile	Wrapped around	Yes	12.7-25.4	No	2003	Zornberg & Arriaga (2003)
GRS walls	240	Sand/Gravel-Sand	Geotextile	Wrapped around	Yes	20-60	No	2002	Zhang et al. (2002)
GRS slopes	228	Sand	Geotextile	Wrapped around	Yes	12.7-38.1	No	1998	Zornberg et al. (1998a)
GRS walls	152	Clay	Geotextile	Wrapped around	Yes	12.7-25.3	No	1996	Porbaha & Goodings (1996)
GRS slopes	228	Sand	Geotextile	Wrapped around	Yes	12.7-38.1	No	1994	Zornberg (1994)
GRS walls	240-440	Sand	Geotextile	Wrapped around	Yes	50-100	Yes	1994	Gomes et al. (1994)

5.4. CONCEPT OF CENTRIFUGE MODELLING

Many research studies have been conducted to study the scaling of the centrifuge models to real structures. Principally, virtually increasing the gravitational force in centrifuge models can result in a proportional increase in stresses. This can be done by spinning the structural model in a centrifuge to create large centrifugal acceleration, which acts as an increased virtual gravitational acceleration for the model. The model has to be placed in the centrifuge such that its initial gravity direction aligns with the centrifugal acceleration during its flight in the centrifuge. The increased stresses in centrifuge models are representative to those in real structures. Bucky (1935) concluded that substituting the gravitational force by centrifugal force that is N times higher than the gravitational force produces a model environment that replicates the real environment. This simulated environment has the same stress and strain conditions as that of the real structure.

5.4.1. Scaling in centrifuge modelling

Table 5.2 shows the scaling relations for various physical quantities as reported by Ko (1988b). The table was modified to include the dimensions of each quantity, which help identifying the scaling relation for any other physical or engineering quantity. The fundamental dimensions M, L, and T are modeled by scaling factors of 1/N3, 1/N, and 1/N, respectively. The scaling factors for reinforcement tensile strength and stiffness have been investigated extensively in literature (e.g., Springman et al. 1992; Porbaha and Goodings 1996; Zornberg et al. 1997; Viswanadham and König 2004; Mahajan 2007). It was reported that scaling factor of 1/N for both parameters (Springman et al. 1992; Zornberg et al. 1997; Viswanadham and König 2004). This factor also conforms to the scaling factors reported

by Ko (1988a) for the stresses and strains. Table 5.3 summarizes the scaling relations of the various parameters of reinforced soil structures. Lee (2010) conducted a study on the effect of the geogrid aperture size and observed no influence on the performance of the walls. It was also concluded that the performance of GRS-shoring systems is sensitive to the backfill relative density.

Table 5.2. Centrifuge scaling relations (after Ko 1988b)

Quantity	**Prototype**	**Model**
Length [L]	N	1
Area [L^2]	N^2	1
Volume [L^3]	N^3	1
Velocity [LT^{-1}]	1	1
Acceleration [LT^{-2}]	1	N
Mass [M]	N^3	1
Force [MLT^{-2}]	N^2	1
Energy [ML^2T^{-2}]	N^3	1
Stress [$ML^{-1}T^{-2}$]	1	1
Strain [-]	1	1
Mass Density [ML^{-3}]	1	1
Energy Density [$ML^{-1}T^{-2}$]	1	1
Time (Dynamic) [T]	N	1
Time (Diffusion) [L^2]	N^2	1
Time (Creep) [-]	1	1
Frequency [T^{-1}]	1	N

Table 5.3. Centrifuge scaling relations of reinforced soil structures (after Zornberg et al. 1998a)

Quantity	**Prototype**	**Model**
Soil parameters		
Friction angle, Φ [-]	1	1
Cohesion, c [$ML^{-1}T^{-2}$]	1	1
Stress-strain behavior [$ML^{-1}T^{-2}$]	1	1
Reinforcement parameters		
Tensile strength, T_{ult} [MT^{-2}]	N	1
Tensile modulus, J [MT^{-2}]	N	1
Interface parameters		
Interface shear strength, tanδ [-]	1	1
Interface stress-strain behavior [$ML^{-1}T^{-2}$]	1	1

5.4.2. Limitations of centrifuge modelling

Geotechnical centrifuge modeling has some limitations, which may result in sources of error. Zornberg et al. (1997) categorized the mains limitation into four sources: (1) the variability of the acceleration field within the centrifuge model; (2) the discrepancy between stress paths of the prototype and the model, (3) the boundary effects of the model, and (4) scale effects of the model. The acceleration field within the centrifuge model is directly proportional to the radius of the arm. However, the variation in g-level within the model is proportional to the size of the model compared to the arm of the centrifuge. That is, this effect fades in relatively large arm centrifuges. The stress paths in the model are not identical to those in a prototype structure is subjected during construction. For instance,

compaction loading exerted in the field during construction cannot be replicated in the model since the model is constructed at acceleration 1g before being brought to a prototype scale in the centrifuge. The boundary effects result from the sidewalls of the container in which the model is placed. These effects can be mitigated by employing a low interface frictional material to line the internal surfaces of the container to ascertain a plane strain testing condition. Scale effects are a concern in centrifuge modeling caused by the relative size of backfill particles between model and prototype. These effects are eliminated by using backfill and reinforcement materials that can still behave as a continuum. In addition, Ovesen (1975) showed that the width of a contact zone must be larger than about 15 particle diameters.

5.5. EXPERIMENTAL PROGRAM

A testing program was implemented by Woodruff (2003) that included five centrifuge test models. The main scope of the program is to study the effect of reinforcement vertical spacing on the behavior of GRS structures. These test models were constructed at various reinforcement spacing ranging from 10 to 50 mm. The models were constructed in a metal box with transparent sides to allow real-time, in-flight imaging during the test. The models were built directly on the metal surface of the box and were 229-mm high on a 30-mm thick foundation. The models employed the same reinforcement type with a reinforcement-length-to-model-height ratio (L/H) of 0.25. Reinforcement layers were wrapped around at the front and were free at their rear ends. A generic schematic diagrams for the model sectional elevation and plan are shown in Figures 5.1a

and 5.1b, respectively. Table 5.4 summarizes the testing configurations including reinforcement length, model height, reinforcement strength, and reinforcement spacing.

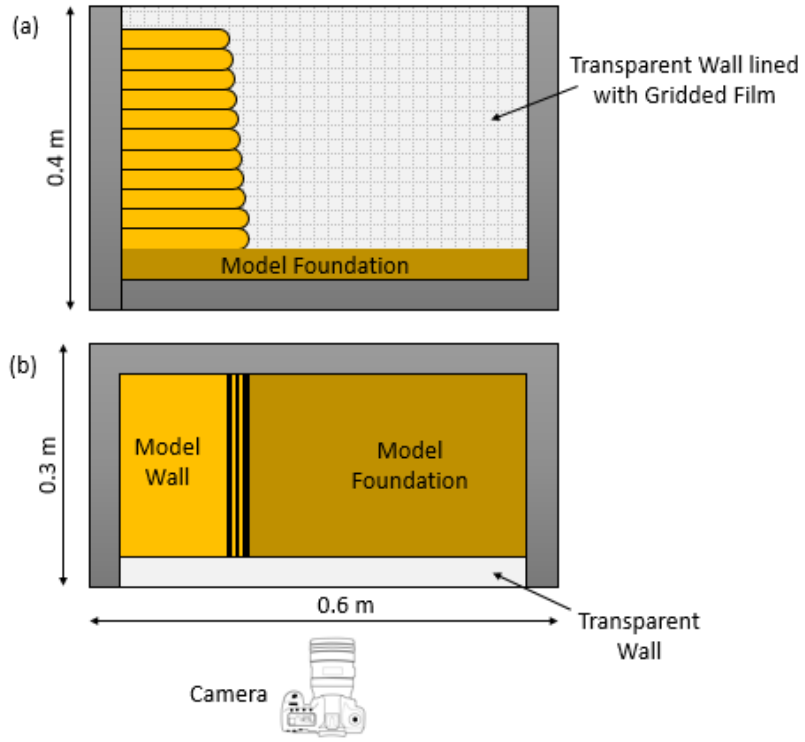

Figure 5.1. Schematic diagram for the centrifuge models: (a) Sectional Elevation; (b) Plan.

Table 5.4. Testing configurations (after Woodruff 2003).

Model Number	*Reinforcement Length, L*	*Model Height, H (mm)*	*Reinforcement Strength (kN/m)*	*Backfill Material*	*Reinforcement Spacing (mm)*	*Shoring Interface*	*Surcharge Loading*
7a	0.25 H	229	1.12	Backfill A	10	Vertical	None
5c	0.25 H	229	1.12	Backfill A	20	Vertical	None
7b	0.25 H	229	1.12	Backfill A	30	Vertical	None
7c	0.25 H	229	1.12	Backfill A	40	Vertical	None
7d	0.25 H	229	1.12	Backfill A	50	Vertical	None

5.6. TESTING MATERIALS

The engineering properties of the model backfill materials and the model reinforcement material are discussed in this section.

5.6.1. Backfill materials

The backfill material used in the model structures was Monterey No. 30 sand. This soil is uniformly graded clean sand classified as SP (poorly graded) according to the Unified Soil Classification System (USCS). This sand has rounded to sub-rounded particles and consists predominantly of quartz with a trace of feldspars and other minerals. The grain size of this Monterey No. 30 sand ranges from 0.2 to 2.0 mm with a mean grain size of 0.7 mm; the grain size distribution is presented in Figure 5.2. The coefficients of uniformity and curvature are 1.9 and 1.3, respectively. The backfill has a specific gravity of 2.65 and its maximum and minimum dry unit weight of 14.76 and 16.70 kN/m^3, respectively. That is, the maximum and minimum void ratios are 0.76 and 0.56, respectively. The shear strength of the backfill used in this study was evaluated by a set of triaxial tests. The peak

friction angle for Monterey No. 30 sand at relative density of 70% is estimated to be 36.7 degrees.

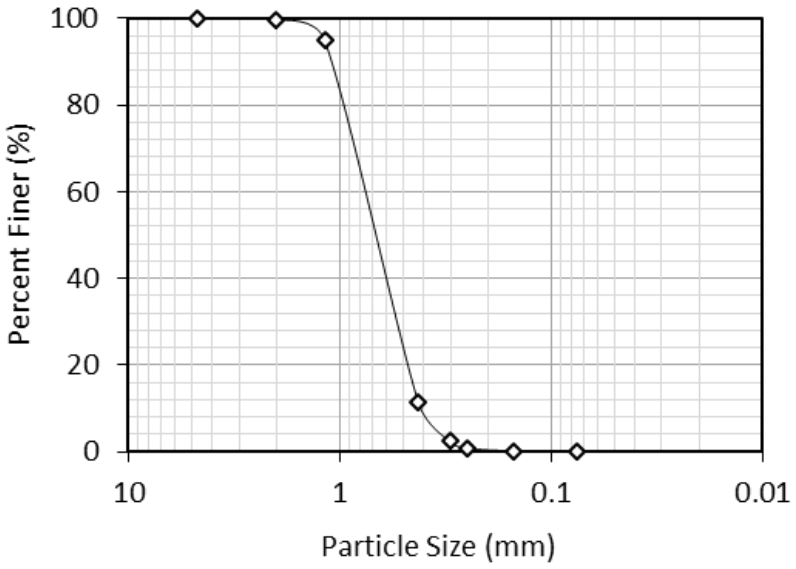

Figure 5.2. Grain size distribution of Monterey No. 30 sand (after Woodruff 2003).

5.6.2. Reinforcement material

One reinforcement type was employed in the conducted centrifuge tests that was made of woven fabric to model geotextile reinforcement. Similar reinforcement types were used in past centrifuge studies (e.g., Guler and Goodings 1992; Zornberg 1998a; Zornberg and Arriaga 2003). The reinforcement used was Pellon True-grid geotextile, which made of 100% polyester with mass per unit area of 24.5 g/m^2. The reinforcement was used in the cross-machine direction in which the tensile strength was 1.12 kN/m.

5.7. TESTING PROCEDURE

The testing procedure adopted in this study is described in the following sections. This includes preparation procedures and monitoring techniques.

5.7.1. Model preparation

All structural models were constructed using the same procedure to enhance testing consistency. The construction procedure follows the procedure adopted by Zornberg et al. (1997). The model foundation was constructed by pluviation at a controlled discharge rate from a constant height. The backfill placement method was calibrated to achieve 70% target relative density. The model reinforcement layers were cut to size with additional side tabs at the face of the wall. These side tabs were folded around the sides of the wall at the face to maintain backfill particles from falling.

Wooden blocks of the same thickness as the vertical reinforcement spacing were used to prop the structure during construction. Every reinforcement layer was rolled against the corresponding wooden block and the side tabs were folded inwards. A 50-mm trench was excavated at every layer parallel to the facing to overlap the wrapped-around reinforcement layers. The trenches were excavated by vacuuming through a small tube. The reinforcement is then wrapped around in the trench. The trenches were then backfilled using the same pluviation technique. Dyed sand particles were placed against the transparent wall every 30 mm along the reinforcement direction. The block propping system was removed after the completion of model construction. All test models were constructed with a facing batter of 11V:1H.

5.7.2. Behavior monitoring

Test models were set to fly under a gradually increasing g-level up to failure or 50 g, whichever happens earlier. Digital imaging involved recording frequent frames, which were then investigated in a sequential order to determine the acceleration level at failure and to examine the deformation patterns and the mode of failure. The movements of the top and face of the walls were measured digitally. This involved taking images corresponding to g-levels and tracking particular points on the wall. That is, the procedure involved identifying the trajectories of specific sand grains at various g-levels. The locations of these grains were then plotted to identify the progression of deformations occurred for every structural model. These images were then analyzed to identify the progressive deformation of the models. In addition, all models were forensically investigated after every test. This involved visual inspection of the models after the tests were terminated. Each model was dissected and its reinforcement layers were examined to verify the failure mode, if any.

5.8. RESULTS AND ANALYSIS

To study the failure mechanisms of the GRS systems, the g-level was raised gradually until failure happens; that is, the scaling of the model changes over time. However, the purpose was to visualize the failure in GRS-shoring systems and to comparatively assess the effect of changing the reinforcement spacing on the behavior of GRS structures and their overall stability. The failure types observed in the tested models can be categorized into two categories: (1) reinforcement pullout failure, in which the reinforcement layers are pulled away; and (2) global overturning failure, in which the GRS

mass slides along the shoring interface. To the study the effect of reinforcement vertical spacing, five models have the same testing parameters but different reinforcement spacing were compared. The reinforcement spacing in these models ranges from 10 to 50 mm as shown in Table 5.5. The table also summarizes the failure type, g-level at failure, g-level at pull-away, and average crest settlement near failure identified for every model.

Table 5.5. Comparison of models behavior (after Woodruff 2003).

Model Number	***Reinforcement Spacing (mm)***	***Failure Type***	***g-Level at Failure***	***g-Level at Pull-away***	***Average Crest Settlement Moment before Failure (mm)***
7a	10	Pullout	38	31	12.6
5c	20	Overturning	32	13	12.6
7b	30	Overturning	2.4	1	4.2
7c	40	Overturning	1	1	0.0
7d	50	Overturning	1	1	0.0

The profiles of the progressive deformation of Models 7a, 5c, 7b, 7c, and 7d are shown in Figures 5.3a through 5.3e, respectively. It was observed that Models 7c and 7d failed instantaneously after the propping system was dismantled (i.e., at 1g); this failure occurred due to global overturning. Models 7a and 7b failed after increasing the g-level. However, only the top reinforcement layer in Model 7a was pulled out at g-level of 38g due to the small L/H ratio (L/H = 0.25). The rest of the structure maintained stability up to g-level of 80g. Model 7b exhibited considerable deformation up on dismantling the propping system (i.e., at 1g); in addition, a trench developed at the shoring interface. This model failed at g-level of 2.5g where the top layer was pulled out. As the g-level increased,

more layers were pulled out progressively. Figure 5.3 shows the progressive facing deformation up to failure of all test models.

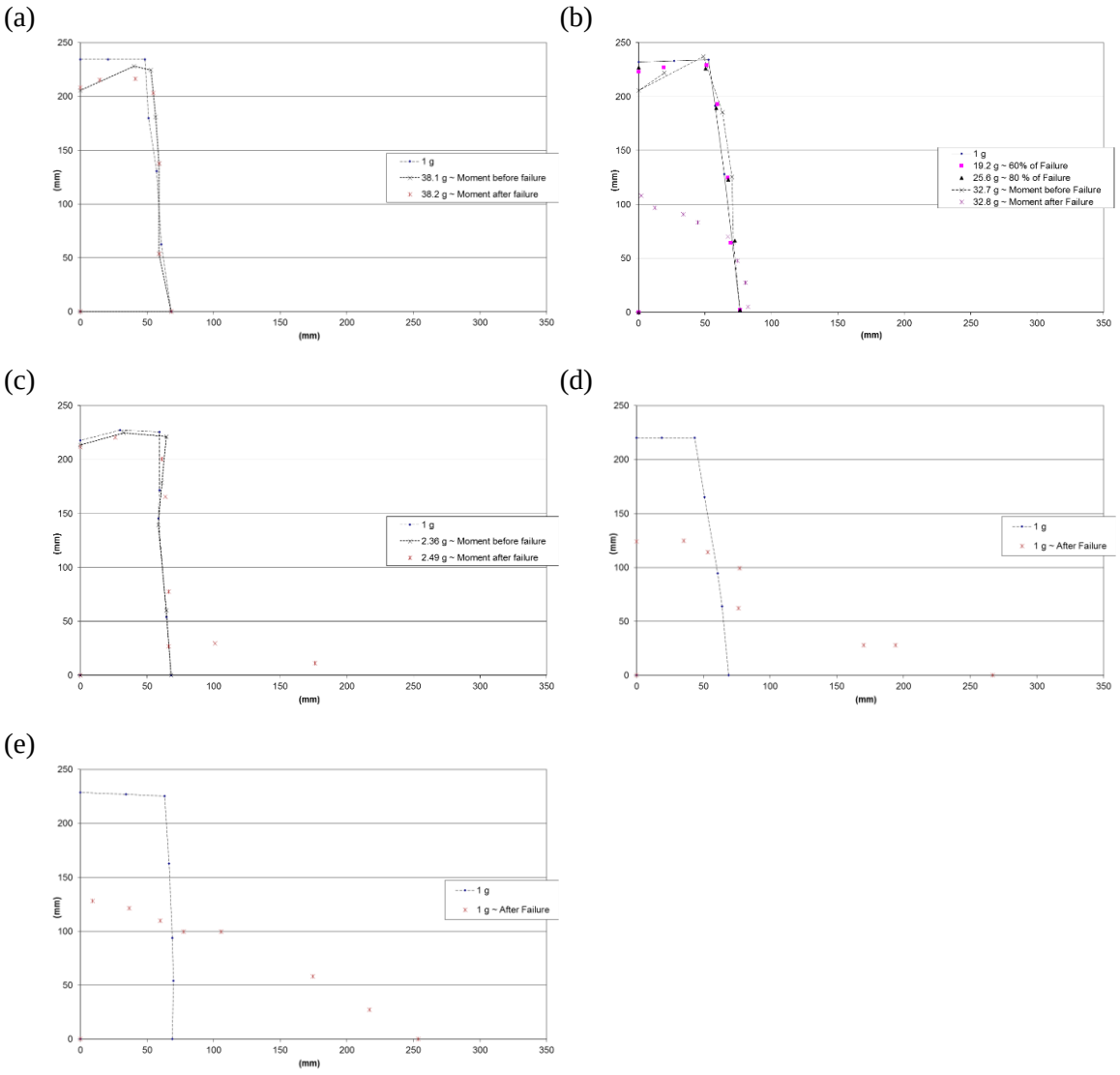

Figure 5.3. Progressive facing deformation up to failure of Models (a) 7a; (b) 5c; (c) 7b; (d) 7c; (e) 7d (after Woodruff 2003).

Figure 5.4 shows the average crest settlement of the GRS models during centrifuge testing as g-level increased. It was concluded that decreasing the reinforcement spacing enhanced the structural stability despite the small L/H ratio. Similar observations were reported by Zornberg et al. (1998a), Zhang et al. (2002), and Iacorossi et al. (2013). It was also observed that failure occurred catastrophically for Models 7c and 7d; whereas, the failure was progressive for Models 7a, 5c, and 7b. The vertical displacement at g-levels up to 25g was very similar for Models 7a and 5c. To reproduce reasonable scaled prototypes of the models, a comparison was conducted between the vertical displacements exhibited by the models at g-level of 10g. In this case, the reinforcement spacings in the prototypes are 0.1 m, 0.2 m, 0.3 m, 0.4 m, and 0.5 m for Models 7a, 5c, 7b, 7c, and 7d, respectively. It was observed Models 7a and 5c exhibited the same vertical displacement as shown in Figure 5.4. On the other hand, Models 7b, 7c, and 7d failed without reaching the 10-g g-level.

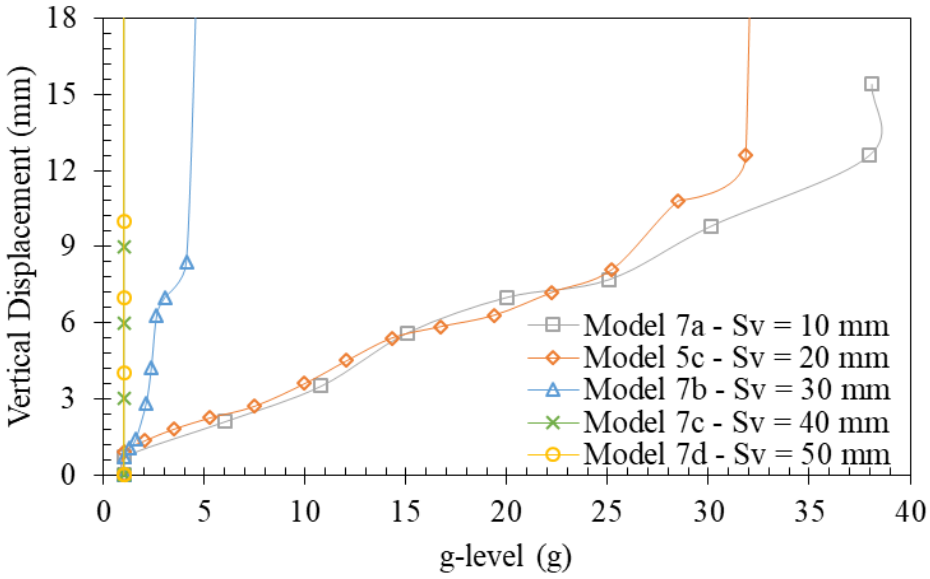

Figure 5.4. Vertical displacement on top of GRS models during centrifuge testing.

5.9. ASSESSMENT OF REINFORCEMENT SPACING EFFECT

To investigate the effect of reinforcement spacing and tensile strength on the behavior of GRS structures. Many studies proved the fact that increasing the reinforcement density (number of layers of the same reinforcement type) should result in enhance the overall performance and structural stability of GRS structures. Figure 5.5 shows the g-level at failure for many centrifuge tests data retrieved from centrifuge models portfolio generated as a part of this study (Table 5.6). The figure shows the effect of decreasing the reinforcement spacing while maintaining the same reinforcement tensile strength in GRS models (i.e., increasing the T_f/S_v ratio).

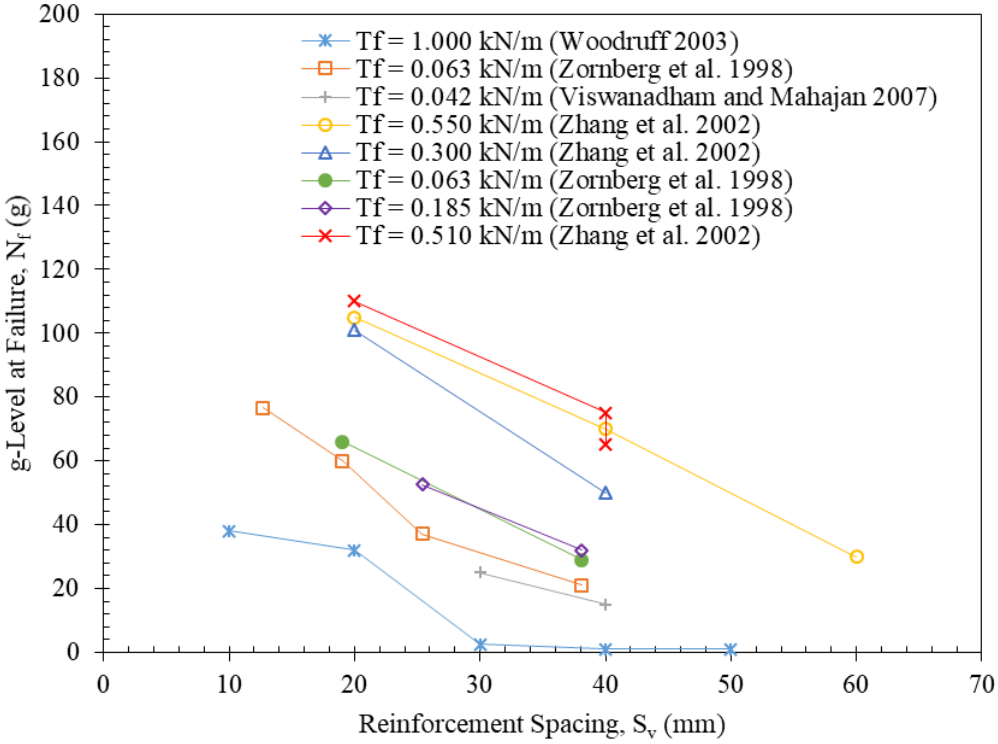

Figure 5.5. Effect of reinforcement vertical spacing on the g-level at failure.

Table 5.6. Summary of the models used in the assessment of the effect of reinforcement spacing.

#	Reference	ID	Type	Facing Type	Reinforcement Type	H (mm)	L/H	S_v (mm)	T_f (kN/m)	T_f/S_v (kN/m/m)	J (kN/m)	J/S_v (kN/m/m)	Backfill Type	φ (deg)	D_{50} (mm)	γ (kN/m³)	D_r (%)
1	Zornberg et al. (1998a)	B18	Slope	Wrapped Around	Geotextile	228	0.89	12.7	0.063	4.96	0.38	29.92	Sand	35.00	0.400	15.64	55
2	Zornberg et al. (1998a)	B12	Slope	Wrapped Around	Geotextile	228	0.89	19.05	0.063	3.31	0.38	19.95	Sand	35.00	0.400	15.64	55
3	Zornberg et al. (1998a)	B9	Slope	Wrapped Around	Geotextile	228	0.89	25.4	0.063	2.48	0.38	14.96	Sand	35.00	0.400	15.64	55
4	Zornberg et al. (1998a)	B6	Slope	Wrapped Around	Geotextile	228	0.89	38.1	0.063	1.65	0.38	9.97	Sand	35.00	0.400	15.64	55
5	Zornberg et al. (1998a)	D12	Slope	Wrapped Around	Geotextile	228	0.89	19.05	0.063	3.31	0.38	19.95	Sand	37.50	0.400	16.21	75
6	Zornberg et al. (1998a)	D6	Slope	Wrapped Around	Geotextile	228	0.89	38.1	0.063	1.65	0.38	9.97	Sand	37.50	0.400	16.21	75
7	Zornberg et al. (1998a)	S9	Slope	Wrapped Around	Geotextile	228	0.89	25.4	0.185	7.28	0.75	29.53	Sand	35.00	0.400	15.64	55
8	Zornberg et al. (1998a)	S6	Slope	Wrapped Around	Geotextile	228	0.89	38.1	0.185	4.86	0.75	19.69	Sand	35.00	0.400	15.64	55
9	Costa et al. (2016)	F1	Slope	Wrapped Around	Geotextile	229	0.87	20	0.033	1.65	0.30	15.00	Sand	36.40	0.700		70
10	Costa et al. (2016)	F2	Slope	Wrapped Around	Geotextile	229	0.87	20	0.033	1.65	0.30	15.00	Sand	36.40	0.700		70
11	Costa et al. (2016)	F3	Slope	Wrapped Around	Geotextile	229	0.87	20	0.033	1.65	0.30	15.00	Sand	36.40	0.700		70
12	Costa et al. (2016)	F4	Slope	Wrapped Around	Geotextile	229	0.87	20	0.033	1.65	0.30	15.00	Sand	36.40	0.700		70
13	Costa et al. (2016)	F5	Slope	Wrapped Around	Geotextile	229	0.87	20	0.144	7.20	0.60	30.00	Sand	36.40	0.700		70
14	Costa et al. (2016)	F6	Slope	Wrapped Around	Geotextile	229	0.87	20	0.144	7.20	0.60	30.00	Sand	36.40	0.700		70

Table 5.6. Summary of the models used in the assessment of the effect of reinforcement spacing (Continued).

#	Reference	ID	Type	Facing Type	Reinforcement Type	H (mm)	L/H	S_v (mm)	T_f (kN/m)	T_f/S_v (kN/m/m)	J (kN/m)	J/S_v (kN/m/m)	Backfill Type	φ (deg)	D_{50} (mm)	γ (kN/m^3)	D_r (%)
15	Woodruff (2003)	5c	Wall	Wrapped Around	Geotextile	229	0.25	20	1.000	50.00	N/A	N/A	Sand	36.70	0.700	16.05	70
16	Woodruff (2003)	7a	Wall	Wrapped Around	Geotextile	229	0.25	10	1.000	100.00	N/A	N/A	Sand	36.70	0.700	16.05	70
17	Woodruff (2003)	7b	Wall	Wrapped Around	Geotextile	229	0.25	30	1.000	33.33	N/A	N/A	Sand	36.70	0.700	16.05	70
18	Woodruff (2003)	7c	Wall	Wrapped Around	Geotextile	229	0.25	40	1.000	25.00	N/A	N/A	Sand	36.70	0.700	16.05	70
19	Woodruff (2003)	7d	Wall	Wrapped Around	Geotextile	229	0.25	50	1.000	20.00	N/A	N/A	Sand	36.70	0.700	16.05	70
20	Viswanadham & Mahajan (2007)	RS4	Slope	Wrapped Around	Geotextile	270	0.85	30	0.042	1.40	N/A	N/A	Sand	34.00	0.021	N/A	55
21	Viswanadham & Mahajan (2007)	RS6a	Slope	Wrapped Around	Geotextile	270	0.85	40	0.216	5.40	N/A	N/A	Sand	34.00	0.021	N/A	55
22	Zhang et al. (2002)	M2	Wall	Wrapped Around	Geotextile	240	0.18	20	0.510	25.50	5080.00	254000.00	Sand	37.50	0.170	15.50	N/A
23	Zhang et al. (2002)	M4	Wall	Wrapped Around	Geotextile	240	0.18	40	0.300	7.50	4520.00	113000.00	Sand	37.50	0.170	15.50	N/A
24	Zhang et al. (2002)	M5	Wall	Wrapped Around	Geotextile	240	0.18	20	0.300	15.00	4520.00	226000.00	Sand	37.50	0.170	15.50	N/A
25	Zhang et al. (2002)	M6	Wall	Wrapped Around	Geotextile	240	0.18	20	0.550	27.50	6520.00	326000.00	Sand	37.50	0.170	15.50	N/A
26	Zhang et al. (2002)	M7	Wall	Wrapped Around	Geotextile	240	0.18	40	0.550	13.75	6520.00	163000.00	Sand	37.50	0.170	15.50	N/A
27	Zhang et al. (2002)	M8	Wall	Wrapped Around	Geotextile	240	0.18	60	0.550	9.17	6520.00	108666.67	Sand	37.50	0.170	15.50	N/A
28	Zhang et al. (2002)	M12	Wall	Wrapped Around	Geotextile	240	0.18	40	0.510	12.75	5080.00	127000.00	Sand	37.50	0.170	15.50	N/A
29	Zhang et al. (2002)	M13	Wall	Wrapped Around	Geotextile	240	0.18	40	0.510	12.75	5080.00	127000.00	Sand	37.50	0.170	15.50	N/A
30	Zhang et al. (2002)	M24	Wall	Wrapped Around	Geotextile	240	0.18	40	0.410	10.25	4460.00	111500.00	Sand	37.50	0.170	15.50	N/A

Table 5.6. Summary of the models used in the assessment of the effect of reinforcement spacing (Continued).

#	Reference	ID	Type	Facing Type	Reinforcement Type	H (mm)	L/H	S_v (mm)	T_f (kN/m)	T_f/S_v (kN/m/m)	J (kN/m)	J/S_v (kN/m/m)	Backfill Type	φ (deg)	D_{50} (mm)	γ (kN/m^3)	D_r (%)
31	Iacorossi et al. (2013)	L2S6	Wall	Modular Blocks	Geogrid	145	0.20	66	10.400	157.58	474.50	7189.39	Sand	28.20	0.015	15.75	N/A
32	Iacorossi et al. (2013)	L2S4	Wall	Modular Blocks	Geogrid	145	0.20	44	10.400	236.36	474.50	10784.09	Sand	28.20	0.015	15.75	N/A
33	Iacorossi et al. (2013)	L2S2	Wall	Modular Blocks	Geogrid	145	0.20	22	10.400	472.73	474.50	21568.18	Sand	28.20	0.015	15.75	N/A
34	Iacorossi et al. (2013)	L3S6	Wall	Modular Blocks	Geogrid	145	0.30	66	10.400	157.58	474.50	7189.39	Sand	28.20	0.015	15.75	N/A
35	Iacorossi et al. (2013)	L3S4	Wall	Modular Blocks	Geogrid	145	0.30	44	10.400	236.36	474.50	10784.09	Sand	28.20	0.015	15.75	N/A
36	Iacorossi et al. (2013)	L3S2	Wall	Modular Blocks	Geogrid	145	0.30	22	10.400	472.73	474.50	21568.18	Sand	28.20	0.015	15.75	N/A
37	Iacorossi et al. (2013)	L4S6	Wall	Modular Blocks	Geogrid	145	0.40	66	10.400	157.58	474.50	7189.39	Sand	28.20	0.015	15.75	N/A
38	Iacorossi et al. (2013)	L4S4	Wall	Modular Blocks	Geogrid	145	0.40	44	10.400	236.36	474.50	10784.09	Sand	28.20	0.015	15.75	N/A
39	Iacorossi et al. (2013)	L4S2	Wall	Modular Blocks	Geogrid	145	0.40	22	10.400	472.73	474.50	21568.18	Sand	28.20	0.015	15.75	N/A

A comparison has been conducted from compiled data retrieved from several studies in the technical literature (Zornberg et al. 1998 and Zhang et al. 2002). These studies involved testing structural models in geotechnical centrifuge; these structures included GRS walls (steep face batter) and GRS slopes (mild face batter). The performance of the structural models were compared based on their reinforcement strength to spacing (Tf/Sv) ratio. This parameter is believed to be the key controlling parameter of the behavior of GRS structures in many design guidelines (e.g. AASHTO, NCMA).

Zornberg et al. (1998) investigated the failure mechanisms of GRS slopes. Their study involved testing 8 centrifuge test models. Their testing program included varying several parameters reinforcement vertical spacing, reinforcement tensile strength, and backfill density reinforcement vertical spacing and reinforce-ment tensile strength. The characteristics of these test models are summarized in Table 5.6. It was observed that the location of the failure surface was not affected by the reinforcement spacing, reinforcement strength, or backfill density. In addition, crest settlement was independent of reinforcement spacing and strength, but was affected by backfill density.

Zhang et al. (2002) conducted a comprehensive study on the behavior of GRS walls. They studied the behavior of 24 centrifuge test models with various parameters. This included varying reinforcement tensile strength, reinforcement vertical spacing, reinforcement length, backfill material, foundation material. In their study, they addressed the effect of changing wall parameters on the deformation mechanisms, failure modes, and failure surfaces of GRS models. Nine test models were used in reinforcement spacing assessment herein are their characteristics are summarized in Table 5.6.

Figures 5.6a and 5.6b show the g-level at failure versus the T_f/S_v ratio for several models from Zornberg et al. (1998) and Zhang et al. (2002), respectively. Contour lines were established for models having the same reinforcement spacing and varying tensile strength (dashed lines) or the same reinforcement tensile strength and varying spacing (dotted lines) as shown in Figures 5.6a and 5.6b. These contour show the effect of increasing the reinforcement spacing (while maintaining the same reinforcement strength) or increasing of the reinforcement strength (while maintaining the same reinforcement spacing) on the behavior of GRS models. It was observed that the effect of reinforcement spacing overweighs that of the reinforcement tensile strength on the structural stability of GRS structures. This observation was found consistent among all the contour lines established for models from the same study and among models from different studies. Similarly, Figures 5.7a and 5.67b show the g-level at failure versus the J/S_v ratio for several models from Zornberg et al. (1998) and Zhang et al. (2002), respectively. These figures are more representative for the behavior of GRS structures at working stress levels. It was observed that the effect of reinforcement spacing also overweighs that of the reinforcement tensile stiffness on the structural stability of GRS structures.

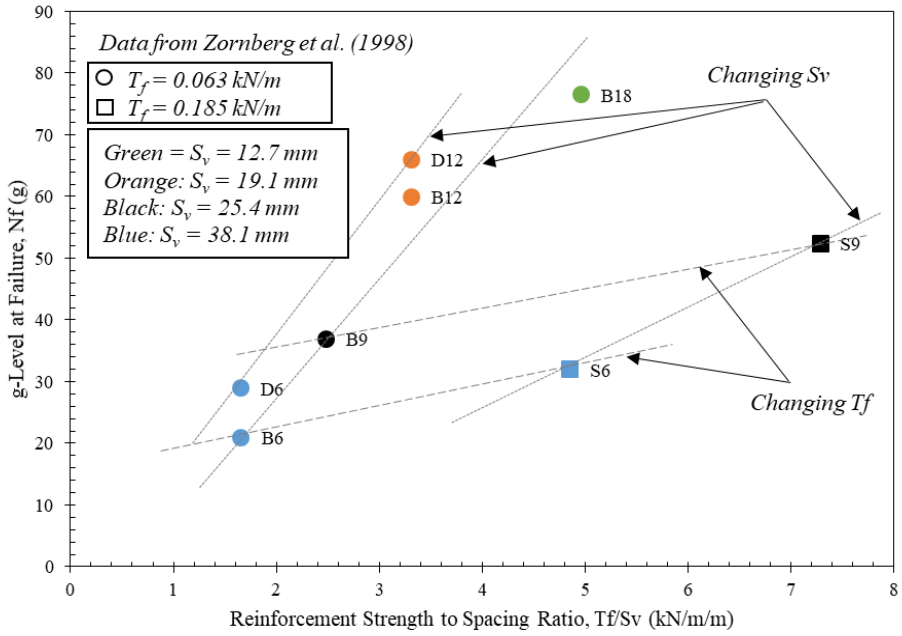

(a)

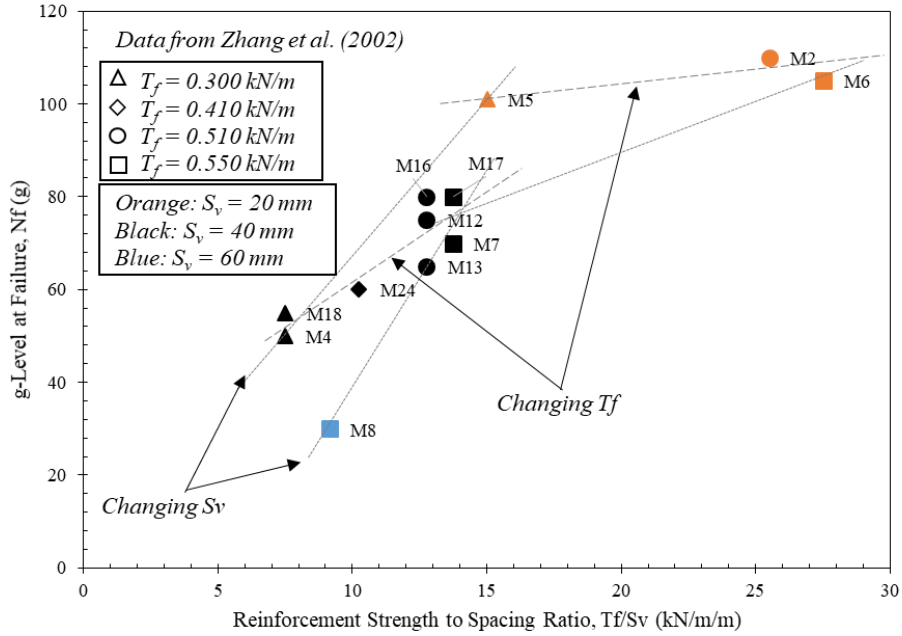

(b)

Figure 5.6. Effect of reinforcement spacing and tensile strength on the behavior of GRS structures: (a) GRS slopes; (b) GRS walls.

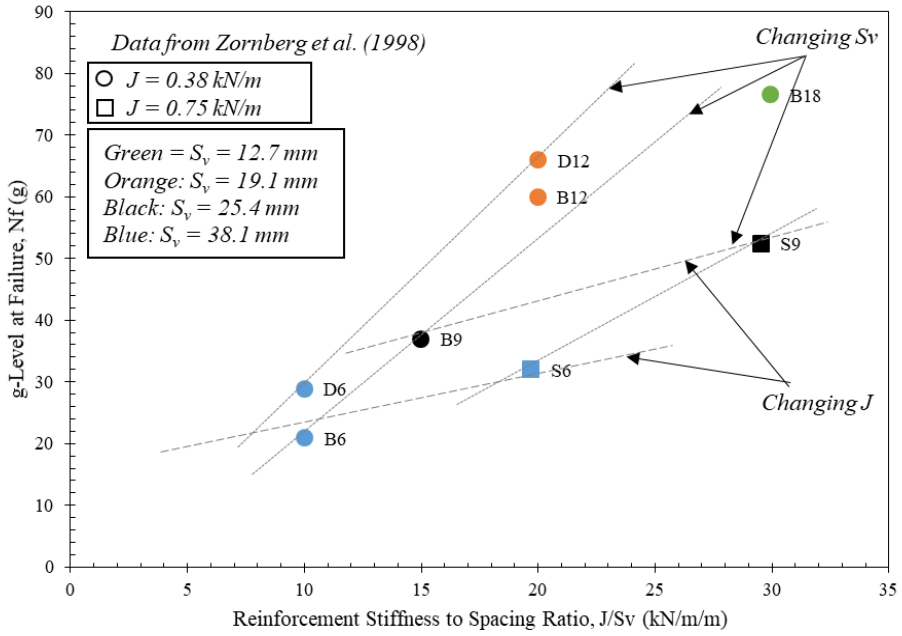

(a)

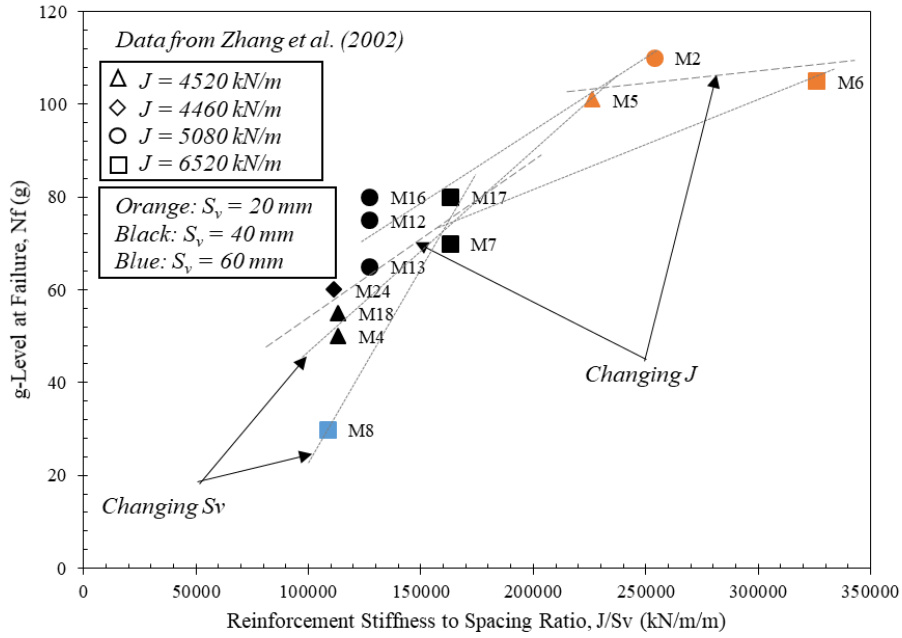

(b)

Figure 5.7. Effect of reinforcement spacing and tensile stiffness on the behavior of GRS structures: (a) GRS slopes; (b) GRS walls.

Models B18 and S6 are two GRS slope models with very close T_f/S_v ratios. The g-level at failure reported by Zornberg et al. (1998) was much higher for Model B18 (the model with smaller reinforcement spacing and weaker reinforcement) than that for Model S6 (the model with larger reinforcement spacing stronger reinforcement) as shown in Figure 5.8. That is, the reinforcement spacing has a higher effect on the model stability and strength than the reinforcement strength. However, the model with the smaller reinforcement spacing and weaker reinforcement exhibited a catastrophic failure unlike the other model which failed progressively. Note that the total stiffness of the reinforcement layers used in Model B18 (ΣJ) was higher than that of Model S6. In addition, the global soil-reinforcement interface for Model B18 (18 layers with peak friction angle of 30 deg) was higher than that for Model S6 (6 layers with peak friction angle of 31 deg).

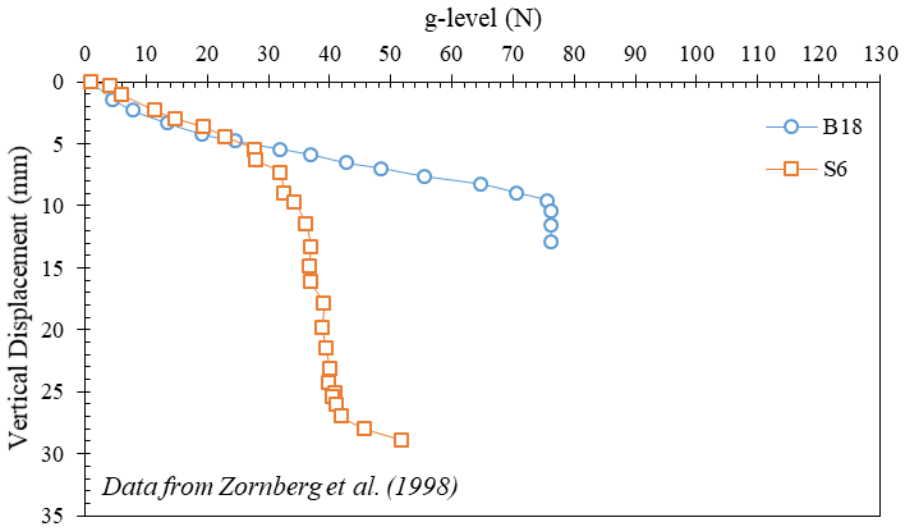

Figure 5.8. Vertical displacement on top of GRS models during centrifuge testing for GRS Slope Models with T_f/S_v 4.9-5.0

Models M8 and M24 are two GRS wall models with very close T_f/S_v and J/S_v ratios. The characteristics of these models are summarized in Table 5.6. The models were constructed using the same backfill material, sand with friction angle of 37.5 degrees. The reinforcement length used in both models was 0.18 of the wall height (i.e., L/H = 0.18) and were wrapped around at the facing. Reinforcements with different tensile strength and spacing were adopted. However, both models had similar T_f/S_v ratio, which was 9.17 and 10.25 kN/m/m for Models M8 and M24, respectively. The g-level at failure reported by Zhang et al. (2002) was much higher for Model M24 (the model with smaller reinforcement spacing and weaker reinforcement) than that for Model M8 (the model with larger reinforcement spacing stronger reinforcement) as shown in Figure 5.9. The total stiffness of the reinforcement layers used in both models was very close. However, Model M24 has more soil-reinforcement interfaces, and thus a stiffer behavior compared to that of Model M8 at working stress conditions as shown in Figure 5.9.

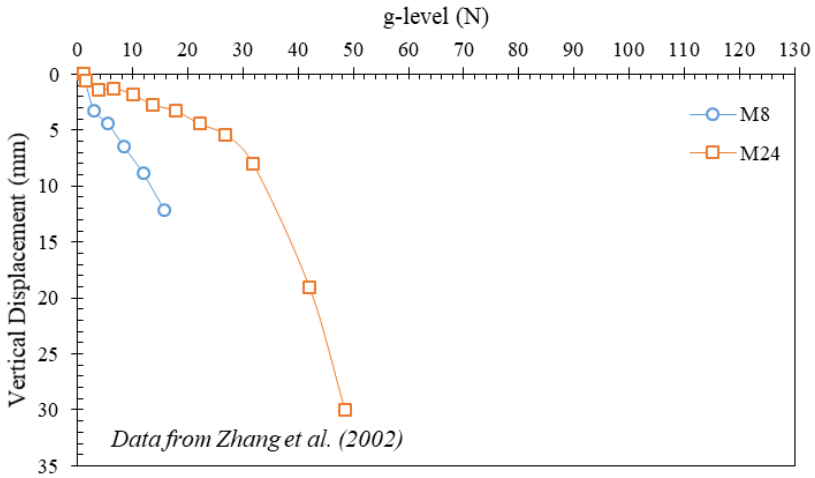

Figure 5.9. Vertical displacement on top of GRS models during centrifuge testing for GRS Wall Models with T_f/S_v 9.2-10.3

Models M5 and M7 also had very close T_f/S_v ratios, which are 15.00 and 13.75 kN/m/m, respectively. Both models have similar characteristics as summarized in Table 5.6. However, the reinforcement in Model M5 was placed at a smaller vertical spacing and had a weaker tensile strength compared to the reinforcement in Model M7. The g-level at failure reported by Zhang et al. (2002) was much higher for Model M5 (the model with smaller reinforcement spacing and weaker reinforcement) than that for Model M7 (the model with larger reinforcement spacing stronger reinforcement) as shown in Figure 5.10. Both the total stiffness of reinforcement layers and total interface friction in Model M5 were higher than those in Model M7. This resulted in a stiffer behavior for Model M5 in working stress conditions as shown in Figure 5.10.

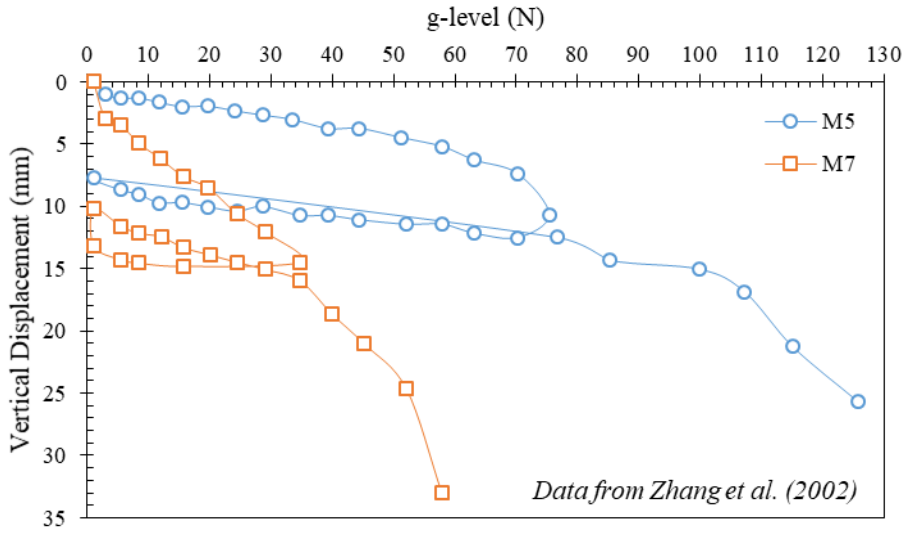

Figure 5.10. Vertical displacement on top of GRS models during centrifuge testing for GRS Wall Models with T_f/S_v 13.8-15.0

Figure 5.11 shows schematic diagrams for four wall pairs. Each pair discusses the effect of changing one reinforcement parameter. Figure 5.11a shows two walls with reinforcements placed at different vertical spacing and have the same total reinforcement tensile capacity (ΣT_f), the same total reinforcement tensile stiffness (ΣJ), the same soil-geosynthetic interface friction (δ_{sg}). That is, both walls have the same T_f/S_v and J/S_v; however, the number of interfaces in the wall reinforced at a smaller spacing is higher than that reinforced at a larger spacing. This provides more interaction with the reinforced soil mass rendering better performance at working stress conditions.

Figure 5.11b shows two walls with reinforcements placed at the same vertical spacing and have the same tensile strength and stiffness; however, the reinforcements of one wall have higher soil-geosynthetic interface friction than the other. Even though the T_f/S_v and J/S_v ratios are the same for both walls, the performance of the wall with higher soil-reinforcement interface friction would render a better performance at working stress conditions. This is due to the higher interaction the reinforcements have with the soil mass.

Figure 5.11c shows two walls with reinforcements placed at the same vertical spacing and have the same tensile strength and soil-geosynthetic interface friction; however, the reinforcements of one wall have higher tensile stiffness than the other. That is, the total reinforcement tensile capacity for both walls is the same and the total number of soil-reinforcement interfaces contributing in soil stabilization is the same. However, the performance of the wall with stiffener reinforcements would perform better at working load conditions. The reinforcement stiffness plays a role in controlling the deformation of the reinforced soil mass.

Figure 5.11d shows two walls with reinforcements placed at the same vertical spacing and have the same tensile stiffness and soil-geosynthetic interface friction; however, the reinforcements of one wall have higher tensile strength than the other. That is, the parameters that control the reinforcement deformation and soil-reinforcement deformation are the same. Both walls should exhibit the same performance at working stress conditions. However, the wall reinforced with stronger reinforcements can sustain higher stress at failure condition.

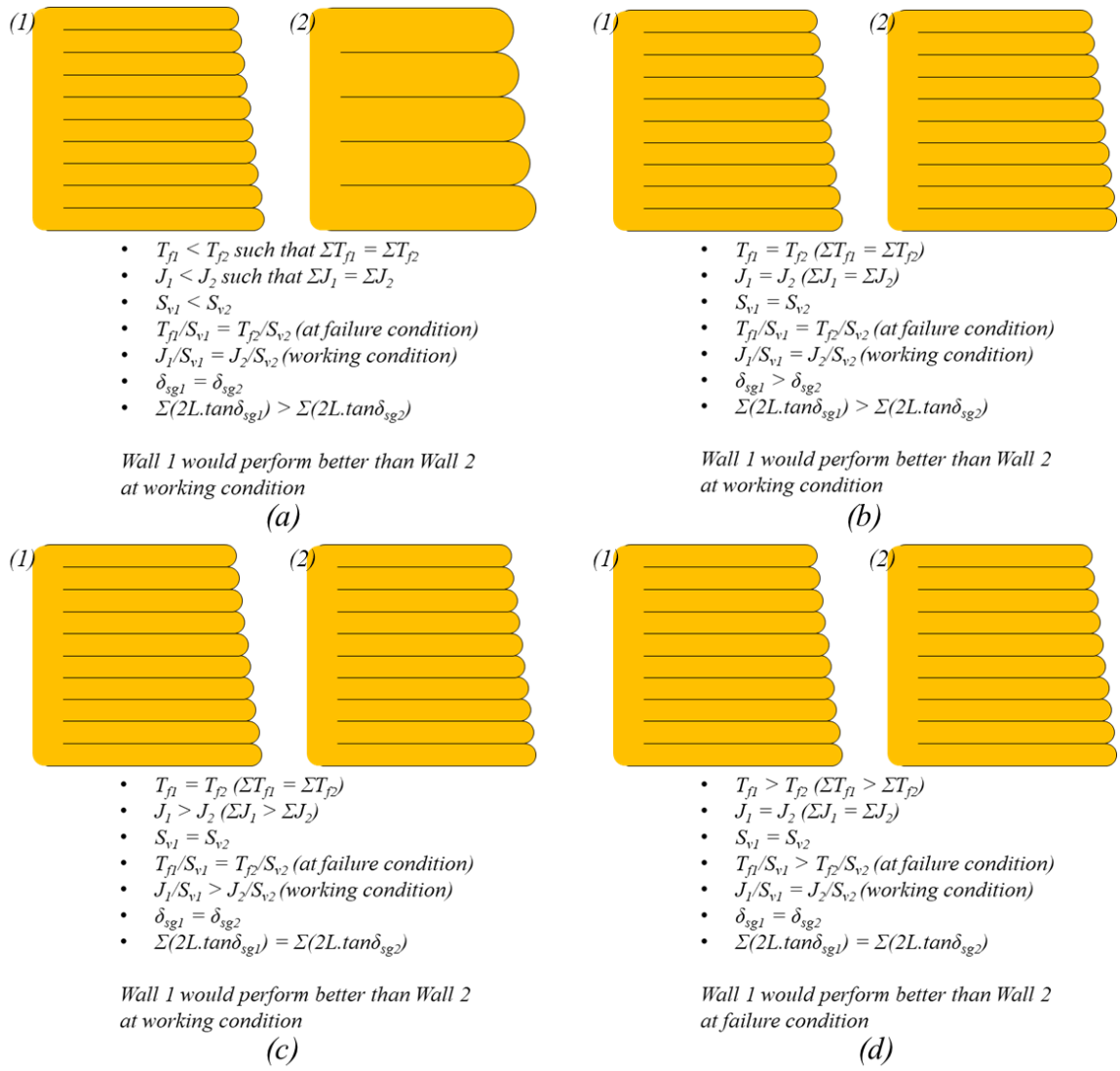

Figure 5.11. Parametric evaluation: (a) Effect of reinforcement spacing, S_v; (b) Effect of soil-geotextile interface friction, δ_{sg}; (c) Effect of reinforcement stiffness, J; (d) Effect of reinforcement tensile strength, T_f.

5.10. CONCLUSIONS

The geotechnical centrifuge technology is very powerful in modelling geosynthetic-reinforced structures. It allows simulating as-real conditions in reduced-scale models that would allow investigating the strain and stress states scaled to real structures. This provides crucial practical insights into the type of behavior expected from these structures and optimizing design accordingly. This study consolidated and analyzed a large number of GRS centrifuge models reported in literature with focus on models in which the reinforcement vertical spacing was varied. This study resulted in the following insights:

- Reducing the reinforcement vertical spacing increases the structural stability of the walls even with small L/H ratios.
- The reassessment of data indicated that decreasing the reinforcement spacing mitigates the lateral earth pressures on the facing resulting in less lateral deformation and thus less vertical deformation (settlement).
- The reassessment of data indicated that GRS structures constructed with the same total reinforcement tensile capacity ($\sum T_f$) and total reinforcement stiffness ($\sum J$) were found to perform differently if their reinforcements were placed at different vertical spacing.
- Using a comparatively large number of reinforcement layers of comparatively low tensile strength and stiffness but placed at a comparatively small vertical spacing can result in a better overall structural performance than a comparable structure with reinforcements of strong tensile strength and stiffness but placed at a large vertical spacing. This difference in performance is because of the large number of soil-reinforcement interfaces in structures with closely-spaced reinforcement.

The large number of interfaces enhances the compatibility between the soil and the reinforcement layers.

- Soil-reinforcement interaction plays a key role not only in resisting the pullout failure but also in controlling the deformation of the entire reinforced soil mass.
- GRS structural performance at working stress conditions shown by centrifuge data reassessment was found to be controlled by reinforcement vertical spacing, reinforcement stiffness, soil-reinforcement interface stiffness, and perhaps soil stiffness. All of which are needed to render proper design of GRS structures.

5.11. REFERENCES

AASHTO (2016). AASHTO LRFD Bridge Design Specifications. Seventh Edition, American Association of State Highway and Transportation Officials (AASHTO).

Arriaga, F. (2003). Response of Geosynthetic-Reinforced Structures under Working Stress and Failure Conditions. Ph.D. dissertation, Department of Civil Engineering, University of Colorado, Boulder, Colorado.

Bathurst, R.J., Nernheim, A., Walters, D.L., Allen, T.M., Burgess, P., and Saunders, D.D. (2009). "Influence of Reinforcement Stiffness and Compaction on the Performance of Four Geosynthetic-Reinforced Soil Walls." Geosynthetics International, Vol. 16, No. 1, pp. 43-59.

Bathurst, R.J., Walters, D., Vlachopoulos, N., Burgess, P., and Allen, T.M. (2000). "Full Scale Testing of Geosynthetic Reinforced Walls." Proceedings of GeoDenver Conference, pp. 1-17.

Bathurst, R.J., Vlachopoulos, N., Walters, D.L., Burgess, P.G., and Allen, T.M. (2006). "The Influence of Facing Stiffness of Two Geosynthetics Reinforced Soil Retaining Walls." Canadian Geotechnical Journal, pp. 1225-1237.

Boyle, S.R. and Holtz, R.D. (1994). "Deformation Characteristics of Geosynthetic-Reinforced Soil." Proceedings of the 5th International Conference on Geotextiles, Geomembranes and Related Products, September 1994, Vol. 1, pp. 361-364.

Costa, C.M.L. (2004). "Deformacoes Dependentes do Tempo em Muros de Solo Reforcado Com Geotexteis." Ph.D. Dissertation, Escola de Engenharia de Sao Carlos, da Universidade de Sao Paulo, 330p. (In Portuguese).

Costa, C.M.L., Zornberg, J.G., de Souza Bueno, B., and Costa, Y.D.J. (2016). "Centrifuge Evaluation of the Time-Dependent Behavior of Geotextile-Reinforced Soil Walls." Geotextiles and Geomembranes, Vol. 44, No. 2, pp. 188-200.

Goodings, D.J. (1990). "Research on Geosynthetics in Reinforced Cohesive Soil Retaining Walls at the University of Maryland." Geotechnical News, pp. 23-25.

Gomes, R.C., Palmeira, E.M., and Lanz, D. (1994). "Failure and Deformation Mechanisms in Model Reinforced Walls Subjected to Different Loading Conditions." Geosynthetics International, No. 1, No. 1, pp. 45-65.

Gourc, J.P., Gotteland, Ph., Haza, E., Perrier, H., and Baraize, E. (1995). "Geotextile Reinforced Structures as Bridge Abutments: Fullscale Experimentation." Proceedings of the 5th International Conference on Geosynthetics, Nashville, Tennessee, USA, pp. 79-92.

Güler, E. and Goodings, D.J. (1992). "Centrifuge Models of Clay-Lime Reinforced Soil Walls." Proceedings of Grouting, Soil Improvement and Geosynthetics, ASCE, pp. 1249-1260.

Hatami, K. and Bathurst, R.J. (2005). "Development and Verification of a Numerical Model for the Analysis of Geosynthetic-Reinforced Soil Segmental Walls Under Working Stress Conditions." Canadian Geotechnical Journal, Vol 42, No. 4, pp. 1066-1085.

Hatami, K. and Bathurst, R.J. (2006). "Numerical Model for Reinforced Soil Segmental Walls Under Surcharge Loading." Journal of Geotechnical and Geoenvironmental Engineering, Vol. 132, No. 6, pp. 673-684.

Haza, E., Gotteland, P., and Gourc, J.P. (2000). "Design Method for Local Load on a Geosynthetic Reinforced Soil Structure." Geotechnical & Geological Engineering, Vol. 18, No. 4, pp. 243-267.

Holtz, R.D. and Lee, W.F. (2002). Internal Stability Analyses of Geosynthetic Reinforced Retaining Walls. Washington State Department of Transportation, Report No. WA-RD 532.1, Olympia, Washington, USA.

Iacorossi, M. (2012). Earth Reinforced Retaining Structures. Report, Department of Civil Engineering, Columbia University, NY, USA.

Iacorossi, M., Ling, H.I., Gottardi, G., and Li, L. (2013). "Centrifuge Modeling of Earth-Reinforced Retaining Walls." Proceedings of International Symposium on Design and Practice of Geosynthetic-Reinforced Soil Structures. Bologna, Italy.

Jaber, M.B. (1989). Behavior of Reinforced Soil Walls in Centrifuge Model Tests. Berkeley. Ph.D. Dissertation, University of California, Berkeley, 239p.

Jewell, R.A. (1991). “Application of Revised Design Charts for Steep Reinforced Slopes.” Geotextiles and Geomembranes, Vol. 10, No. 3, pp. 203-233.

Juran, I. and Christopher, B. (1989). “Laboratory Model Study on Geosynthetic Reinforced Soil Retaining Walls.” Journal of Geotechnical Engineering, Vol. 115, No. 7, pp. 905-926.

Kniss, K.T., Yang, K.-H., Wright, S.G., and Zornberg, J.G. (2007). “Earth Pressures and Design Consideration of Narrow MSE Walls.” Proceedings of the Conference of Texas Section-ASCE Meeting, Taylor, Texas, April, 2007.

Ko, H.Y. (1988a). “The Colorado Centrifuge Facility.” Proceedings of International Conference of Centrifuges in Soil Mechanics, James and Schofield (eds.), pp. 319-324.

Ko, H.Y. (1988b). “Summary of the State-of-the-art in Centrifuge Model Testing.” Proceedings of International Conference of Centrifuges in Soil Mechanics, James and Schofield (eds.), pp. 11-18.

Lee, Y.-B. (2010). Deformation behavior of shored mechanically stabilized earth (SMSE) wall systems. PhD thesis, University of Colorado, Boulder, CO, USA.

Lee, K.L., Adams, B.D., and Vagneron, J.M.J. (1973). “Reinforced Earth Retaining Walls.” Soil Mechanics and Foundation Engineering, ASCE, Vol. SM10, pp. 745–764.

Lee, Y.-B., McCartney, J.S., and Ko, H.-Y. (2010a). “Centrifuge Modeling of Shored Mechanically Stabilized Earth Walls.” Proceedings of International Conference on Physical Modeling in Geotechnics, Zurich, Switzerland, pp. 481-486.

Lee, Y.-B., Ko, H.-Y., and McCartney, J.S. (2010b). "Deformation Response of Shored MSE Walls under Surcharge Loading in the Centrifuge." Geosynthetics International, Vol. 17, No. 6, pp. 389-402.

Leshchinsky, D. and Boedeker, R.H. (1989). "Geosynthetic Reinforced Soil Structures." Journal of Geotechnical Engineering, Vol. 115, No. 10, pp. 1459-1478.

Lin, H., Ling, H.I., Collin, J.G., Leshchinsky, D., and Rimoldi, P. (2013). "Centrifuge Modeling of Gabion Walls Reinforced with Geosynthetics." Proceedings of International Symposium on Design and Practice of Geosynthetic-Reinforced Soil Structures. Bologna, Italy.

Ling, H.I., Wu, J.T., and Tatsuoka, F. (1992). "Short-Term Strength and Deformation Characteristics of Geotextiles Under Typical Operational Conditions." Geotextiles and Geomembranes, Vol. 11, No. 2, pp. 185-219.

Malinowska, E.E. (2015). "Gabion Wall Testing during the Forced Overloading in the Geotechnical Centrifuge." Acta Scientiarum Polonorum. Architectura, Vol. 14, No. 3.

Mahajan, R.R. (2007). Centrifuge Model Studies on Geosynthetic Reinforced Soil Slopes. Ph.D. Dissertation. Indian Institute of Technology Bombay, India.

McGown, A., Andrawes, K.Z., and Kabir, M.H. (1982). "Load Extension Testing of Geotextiles Confined in Soil." Proceedings of the 2nd International Conference on Geotextiles, August 1982, Vol. 3, pp. 793-798. Roseville, Minnesota.

NCMA (1997). Design Manual for Segmental Retaining Walls. Second Edition, National Concrete Masonry Association (NCMA), Publication Number TR 127A.

Ovesen, N. (1975). “Centrifuge testing applied to bearing capacity problems of footings on sand.” Geotechnique, Vol. 25, No. 2, pp. 394-401.

Palmeira, E.M. and Lanz, D. (1994). “Stresses and Deformation in Geotextile Reinforced Model Walls.” Geotextiles and Geomembranes, Vol. 12, No. 5, pp. 331-348.

Porbaha, A. and Goodings, D.J. (1994). “Geotextile Reinforced Cohesive Slopes on Weak Foundations.” Proceedings of Centrifuge, Vol. 94, pp. 623-628.

Porbaha, A. and Goodings, D.J. (1996). “Centrifuge Modeling of Geotextile-Reinforced Cohesive Soil Retaining Walls.” Journal of Geotechnical Engineering, Vol. 122, No. 10, pp. 840-848.

Santamarina, J.C. (1984). Effect of adjacent soils on reinforced soil structures-centrifuge model testing. Ph.D. Dissertation, Purdue University, West Lafayette, Indiana, USA.

Schofield, A. (1980). “Cambridge Geotechnical Centrifuge Operation.” Geotechnique, Vol. 30, No. 3, pp. 227-268.

Sommers, A.N. and Viswanadham, B.V.S. (2009). “Centrifuge Model Tests on the Behavior of Strip Footing on Geotextile-reinforced Slopes.” Geotextiles and Geomembranes, Vol. 27, No. 6, pp. 497-505.

Springman, S.M., Bolton, M.D., Sharma, J., and Balachandran, S. (1992). “Modelling and Instrumentation of a Geotextile in the Geotechnical Centrifuge.” Proceedings of the International Symposium on Earth Reinforcement Practice, Kyushu, September 1992, Vol. 167, p. 172.

Thamm, B.R., Krieger, B., and Krieger, J. (1990). “Fullscale Test on Geotextile Reinforced Retaining Structure.” Proceedings of the 4th International Conference on

Geotextiles, Geomembranes and Related Products, Hague, The Netherlands, Vol. 1, pp. 3-8.

Vafaeian, M. and Abbaszadeh, R. (2006). "Laboratory Small Scale Tests to Study the Behaviour of Reinforced Soil Wall." Proceedings of 8th International Conference on Geosynthetics, Kuwano, J., Kuseki, J. (eds.), Millpress Science, Rotterdam, Vol. 4, pp. 1409-1412.

Viswanadham, B.V.S. and König, D. (2004). "Studies on Scaling and Instrumentation of a Geogrid." Geotextiles and Geomembranes, Vol. 22, No. 5, pp. 307-328.

Viswanadham, B.V.S. and Mahajan, R.R. (2007). "Centrifuge Model Tests on Geotextile-reinforced Slopes." Geosynthetics International, Vol. 4, No. 6, pp. 365-379.

Wichter, L., Risseeuw, P., and Gay, G. (1986). "Large Scale Test on Bearing Behaviour of a Woven Reinforced Earth." Proceedings of 3rd International Conference on Geotextiles, Vienna, Austria, pp. 1073-1078.

Woodruff, R. (2003). Centrifuge modeling for MSE-shoring composite walls. MS Thesis, University of Colorado, Boulder, CO, USA.

Wright, S.G. and Duncan, J.M. (1991). "Limit Equilibrium Stability Analyses for Reinforced Slopes." Transportation Research Record, No. 1330, pp. 40–46.

Wu, J.T.H., Lee, K., Helwany, S., and Ketchart, K. (2006). Design and Construction Guidelines for Geosynthetic-Reinforced Soil Bridge Abutments with a Flexible Facing System. NCHRP Report 556, Project 12-59, National Cooperative Highway Research Program, Transportation Research Board, National Research Council, Washington, DC.

Yang, K.-H., Kniss, K.K., Zornberg, J.G., and Wright, S.G. (2008). "Finite-Element Analyses for Centrifuge Modeling of Narrow MSE Walls." Proceedings of the First Pan American Geosynthetics Conference, GEOAMERICAS-2008 (CD-ROM), International Fabrics Association Int., Rosevile, MN, USA, pp. 1246–1255.

Yang, K.H., Zornberg, J.G., Hung, W.Y., and Lawson, C.R. (2011). "Location of Failure Plane and Design Considerations for Narrow Geosynthetic Reinforced Soil Wall Systems." Journal of GeoEngineering, Vol. 6, No. 1, pp. 27-40.

Zhang, W., Lai, Z., and Xu, G. (2002). "Centrifuge Model Tests of Geosynthetics Reinforced Retaining Walls." Proceedings of the International Conference on Physical Modelling in Geomechanics: ICPMG '02, Philips, Guo, and Popescu (eds.), pp. 999-1004.

Zornberg, J.G. (1994). Performance of Geotextile-reinforced Soil Structures. Ph.D. Dissertation, University of California, Berkeley, CA, USA.

Zornberg, J.G. and Arriaga, F. (2003). "Strain Distribution within Geosynthetic Reinforced Slopes." Journal of Geotechnical and Geoenvironmental Engineering, Vol. 129, No. 1, pp. 32-45.

Zornberg, J.G. and Mitchell, J.K. (1994). "Reinforced Soil Structures With Poorly Draining Backfills. Part I: Reinforcement Interactions and Functions." Geosynthetics International, Vol. 1, No. 2, pp. 103-147.

Zornberg, J.G., Mitchell, J.K., and Sitar, N. (1997). "Testing of Reinforced Slopes in a Geotechnical Centrifuge." Geotechnical Testing Journal, Vol. 20, No. 4, pp. 470-480.

Zornberg, J.G., Sitar, N., and Mitchell, J.K. (1998a). "Performance of Geosynthetic Reinforced Slopes at Failure." Journal of Geotechnical and Geoenvironmental Engineering, Vol. 124, No. 8, pp. 670-683.

Zornberg, J.G., Sitar, N., and Mitchell, J.K. (1998b). "Limit Equilibrium as Basis for Design of Geosynthetic Reinforced Slopes." Journal of Geotechnical and Geoenvironmental Engineering, Vol. 124, No. 8, pp. 684-698.

Chapter 6: Assessment of the Founders/Meadows Geosynthetic-Reinforced Soil Bridge Abutment Performance

6.1. ABSTRACT

Geosynthetic-reinforced soil (GRS) technology is now recognized as a construction alternative to bridge abutments. This technology has proven to provide the flexibility required to alleviate the bumps at the ends of bridges. The Founders/Meadows Bridge supported on GRS abutments, constructed near Denver, Colorado in 1999, is the first constructed on a major highway in the United States. Subsequently, several studies investigated the type of response to be expected from GRS structures. This study revisits and evaluates the field monitoring data collected from the Founders/Meadows abutments based on our current understanding of GRS technology. This evaluation assessed the data collected on the lateral and vertical deformation of the GRS abutments, reinforcement strains, differential settlement between the bridge superstructure and its approaching roadway structures, temperature and moisture changes, and vertical and lateral stresses within the GRS mass. The vertical stress distribution revealed the stress propagation and pattern within the GRS mass. In addition, the study found that the temperature variations, construction sequence, and construction season may have significant effect on the behavior of GRS abutments.

6.2. INTRODUCTION

The technology for geosynthetic reinforced soil (GRS) bridge-supporting abutments has been used in the United States since the 1990s. GRS abutments are used to support not only their own weight and to retain backfill, but also to support bridge superstructures and traffic loads. This kind of abutments supports the bridge superstructure

directly without employing any deep foundation. In addition, it has proven to alleviate the potential bumps at the ends of bridges by allowing compatible settlements between the bridge deck and the approaching roadway structures. The Founders/Meadows Bridge was the first in the United States to use GRS bridge-supporting abutments on a major highway. The structure is located in Castle Rock, 20 miles south of downtown Denver, Colorado, USA along Founders/Meadows Parkway crossing US Interstate Highway 25 (I-25). The structure replaced an out-of-service two-span bridge in which the abutments were supported by H-piles and the central pier was supported by a spread footing. The old central pier was reemployed in the new bridge. The behavior of the Founders/Meadows reinforced soil structures has been studied repeatedly since its opening to traffic in June 1999. These studies addressed the pressure distribution within the reinforced soil mass and reinforcement straining (e.g. Abu-Hejleh et al. 2001a; Helwany et al. 2003; Fakharian and Attar 2007; Zheng et al. 2015). However, these studies addressed only the short-term response of the bridge. Also, a thorough analysis of the pressure distribution and reinforcement straining has not yet been provided. This study evaluates the field monitoring data of the Founder/Meadows bridge abutments during construction and around four service years. Specifically, the evaluation conducted in this study assessed the data collected on (1) the lateral deformation the bridge abutments, (2) the settlement of the abutments, (3) the reinforcement straining, (4) the differential settlement between the bridge superstructure and the approaching roadway structures, which points towards the formation of the bumps at the ends of the bridge, (5) temperature and moisture changes and their effect on the behavior of the GRS mass, and (6) the vertical and lateral stresses

within the GRS mass. The study provides insightful conclusions into the behavior of the structure, which can also be generalized on similar reinforced soil structures.

6.3. DESCRIPTION OF THE FOUNDERS/MEADOWS BRIDGE

The Founders/Meadows Bridge is located in Castle Rock, Colorado to separate the two-way traffic of Founders/Meadows Parkway (Colorado State Highway 86) from that of the US Interstate Highway 25 (I-25). This highway is heavily packed with traffic; the total Annual Average Daily Traffic (AADT) recorded on Founder/Meadows Parkway in 2014 by traffic stations located at immediate west and immediate east of the bridge was approximately 39000 and 42000 vehicle/day, respectively (CDOT 2016). According to Highway Performance Monitoring System (HPMS), the AADT level of Founders/Meadows Parkway at this location classifies as Volume Group #7. In addition, CDOT (2016) records show that the AADT for trucks in 2014 at traffic stations west and east the bridge was 2600 and 1390 truck/day, respectively. The total projected AADT for 2023 as per CDOT (2016) is 75894 and 43386 vehicle/day at the west and east sides of the bridge, respectively. Also, the projected AADT for trucks 5060 and 1436 truck/day at the west and east sides of the bridge, respectively.

The bridge has six traffic lanes (three lanes per traffic direction), two sidewalks, and a median. The bridge consists of a two-span superstructure that rests on two GRS abutments and a central pier as shown in Figure 6.1. The bridge superstructure is 69-m long (each span is 34.5-m long) and 34.5-m wide (each direction is 17.25-m wide). The superstructure consists of 20 pre-stressed reinforced concrete box girders. Each of the GRS abutments consists of a reinforced concrete footing with U-shaped reinforced concrete walls (Figure 6.2) resting on a geosynthetic-reinforced soil mass constructed on bedrock.

The front walls of the GRS mass extend to the sides at a 90-degree angle forming wing walls on both sides (lower GRS walls) as shown in Figure 6.2. Another tier of side wing walls extends beyond the legs of the U-shaped reinforced concrete footing as shown in Figure 6.2. The central pier consists of five columns resting on a spread footing founded on bedrock. The construction was completed over two phases: (1) Phase I, which included the westbound direction of the bridge; and (2) Phase II, which included the eastbound direction of the bridge. Sections 200, 400, and 800 (locations are shown on Figure 6.2) were instrumented; Section 800 was heavily instrumented, while Sections 200 and 400 were lightly instrumented for the purpose of behavior verification. In addition, Sections 200, 300, 400, 800 and 900 (locations are shown on Figure 6.2) were surveyed to monitor the lateral deformation.

Figure 6.1. View of the Founders/Meadows Bridge in 2016.

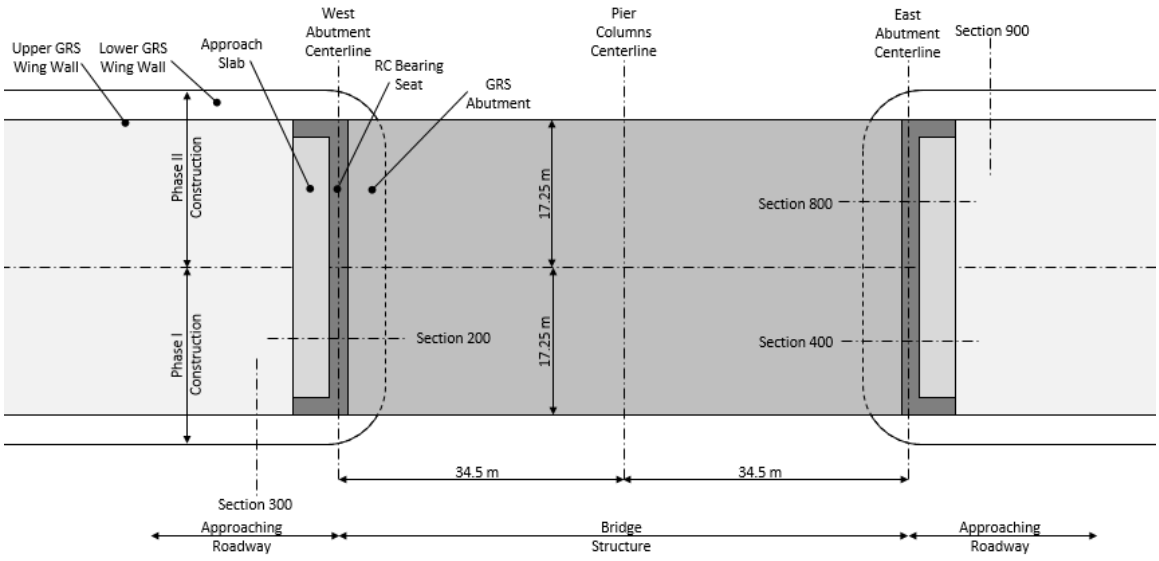

Figure 6.2. Top view of the Founders/Meadows Bridge (redrawn after Abu-Hejleh et al. 2002).

The main cause of differential settlements in typical bridge foundation systems is the use of different foundation types. Approaching roadway structures are typically founded on compacted backfill soil while bridge abutments are usually founded on deep foundations that convey the bridge loads to a stronger soil strata, which are less likely to settle. The Founders/Meadows Bridge rests on geosynthetic-reinforced soil abutments that provide flexible behavior and compatible deformations between the abutments and the approaching roadway structures alleviating any potential differential settlements. Differential settlements can also arise by erosion of the backfill material induced by the surface water runoff. In the Founders/Meadows abutments, precautions were adopted to prevent the surface water and the groundwater from reaching the reinforced soil mass and the bedrock at its base. These precautions included: (1) impervious membranes with

collector pipes placed underneath the roadway structures as shown in Figures 6.3a and 6.3b; and (2) drainage blankets with drainage pipes placed behind the reinforced soil mass to divert groundwater and infiltration as shown in Figure 6.3a. In addition, temperature changes can cause the bridge superstructure to expand and contract inducing lateral pressure on the abutments. In the Founders/Meadows abutments, compressible 75 mm-thick, low-density, expanded polystyrene sheets were placed vertically between the reinforced backfills and the abutment walls as shown in Figure 6.3a. These compressible sheets alleviate the lateral earth pressure on the back of the concrete wall due to thermal-induced movements of the bridge superstructure.

Table 6.1 summarizes the construction stages of the Founders/Meadows Bridge. Figure 6.4 shows the construction time history of the bridge for construction Phase I (which includes Sections 200 and 400) and construction Phase II (which includes Section 800). The bridge construction was completed in approximately 160 days (Stages I through VI). Note that Stage VII extended for up to four years after the bridge was inaugurated to traffic on 30 June 1999.

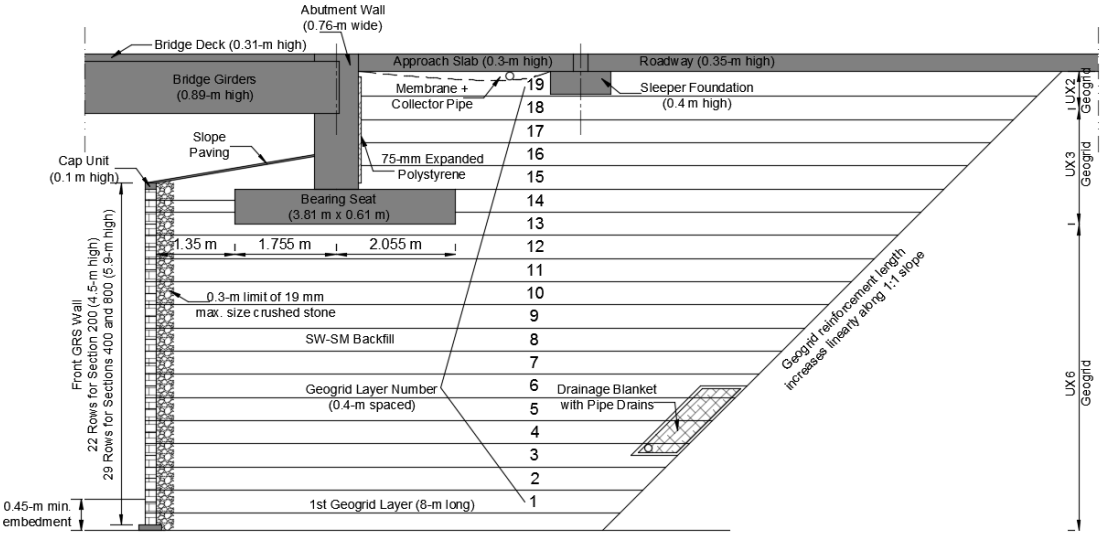

(a)

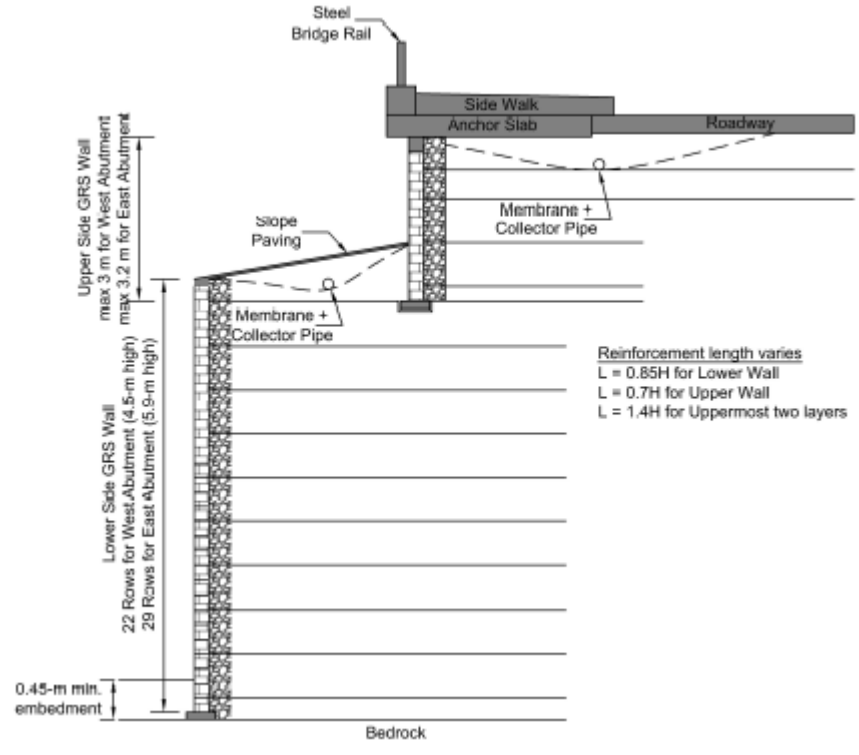

(b)

Figure 6.3. Typical cross-section of the Founders/Meadows Bridge abutment: (a) Sections 200, 400, and 800 (redrawn after Abu-Hejleh et al. 2002); and (b) Section 300 and 900 (redrawn after Abu-Hejleh et al. 2001a).

Table 6.1. Construction stages (Abu-Hejleh et al. 2001a).

Stage #	Description
0	Leveling pad placement
I	Construction of the front GRS wall up to the bridge footing elevation. The Stage I structure provides support for the bridge and approaching roadway structures
II	Placement of bridge footing and girders seats
III	Placement of girders
IV	Placement of the reinforced backfill behind the abutment wall from the bridge footing elevation to the bottom of the sleeper footing
V	Placement of bridge deck
VI	Placement of the approaching roadway structure (including approach slab) and other minor structures
VII	Post-construction after opening the structure to traffic

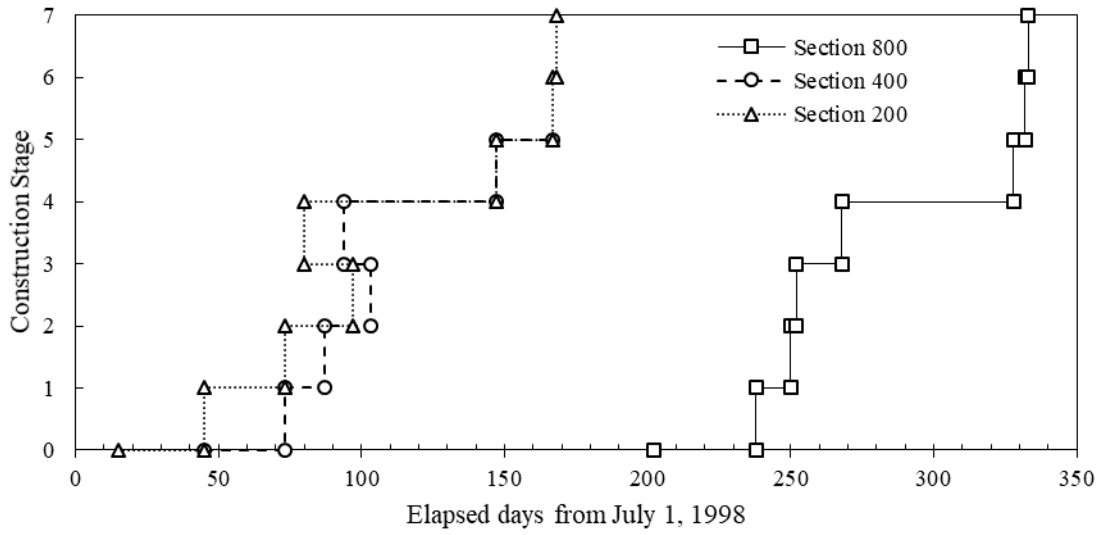

Figure 6.4. Time history of construction.

6.4. MATERIAL CHARACTERISTICS OF THE GRS ABUTMENTS

The reinforced soil mass of the Founders/Meadows Bridge abutments consist primarily of alternating layers of backfill material and reinforcement. The reinforced soil zone is covered by a facing system. The material characteristics of the abutments are summarized in the following subsections:

6.4.1. Backfill material

The backfill material used in the Founders/Meadows Bridge abutments was a mixture of gravel (35.0%), sand (54.4%), and fines (10.6%). The liquid limit and plasticity index for the fines content were 25 and 4, respectively. The soil classifies as SW-SM in accordance with ASTM 2487 and as A-1-B (0) in accordance with AASHTO M 145. The average unit weight, dry unit weight, and water content of the compacted backfill as measured during compaction were 22.1 kN/m3, 21.0 kN/m3, and 5.6%, respectively. The backfill was compacted to 95% of the maximum dry unit weight determined in accordance with AASHTO T-180A. A set of conventional direct shear tests were conducted in accordance with AASHTO T-236 on the backfill after excluding the 35% gravel portion. The maximum dry unit weight and optimum moisture content of the backfill without the gravel portion were 19.9 kN/m3 and 8.8% as per AASHTO T-99A. The specimens were compacted to 95% of the maximum unit weight and a moisture content of 9.6%. The peak friction angle and the cohesion intercept obtained for the tested specimens were 40.1 degrees and 17.0 kPa, respectively. Meanwhile, a set of large-scale direct shear and large-scale triaxial tests were conducted on the backfill including the gravel portion to evaluate the suitability of the measured strength parameters obtained from the conventional direct shear tests. The specimens where prepared at similar unit weight and moisture content to

those measured in the field. The large-scale direct shear tests were conducted on specimens compacted at dry unit weight of 21.0 kN/m3 and moisture content of 5.6% and tested in a large-size direct shear box in accordance with ASTM D3080. Figure 6.5a shows the test results for three different confinement levels. The peak friction angle and the cohesion intercept obtained for the tested specimens were 47.7 degrees and 110.5 kPa, respectively. The large-scale triaxial tests were conducted on specimens compacted at 20.6 kN/m3 dry unit weight and 5.7% moisture content. Figure 6.5b shows the test results for three different confinement levels. A peak friction angle of 39.5 degrees and 69.8 kPa cohesion intercept were obtained. In addition, Figure 6.6 shows the volumetric-axial strain relationship obtained from the three conducted triaxial tests.

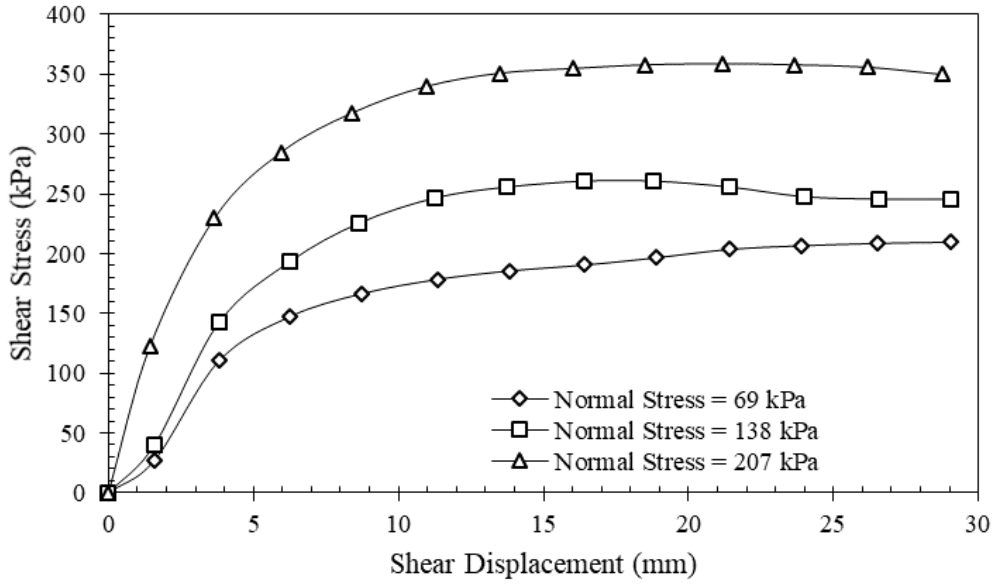

(a)

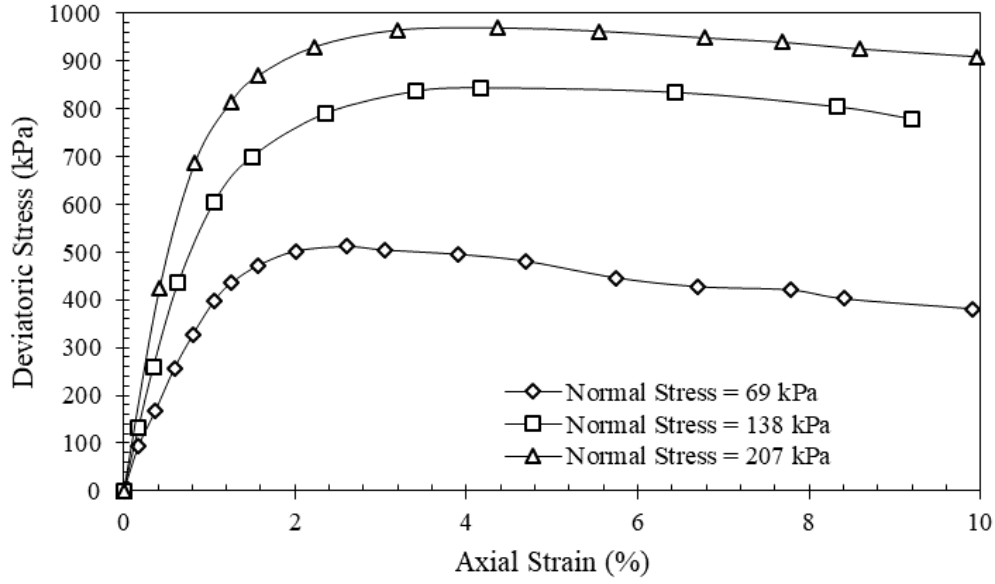

(b)

Figure 6.5. Shear strength test results: (a) large-scale direct shear; (b) large-scale triaxial (after Abu-Hejleh et al. 2001a).

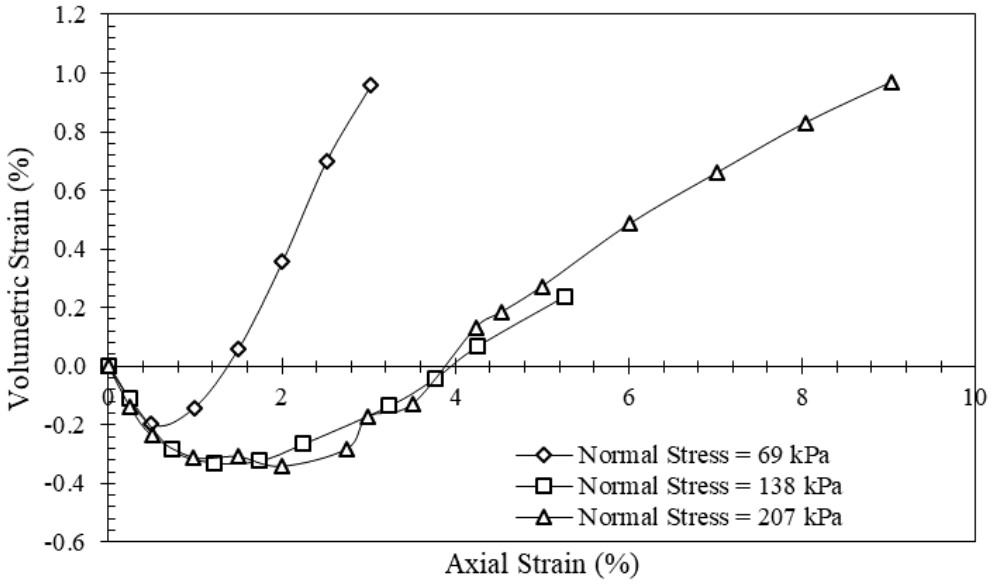

Figure 6.6. Volumetric strain versus axial strain relationship obtained from triaxial testing (after Abu-Hejleh et al. 2001a).

6.4.2. Reinforcement

The reinforcement used in the Founders/Meadows Bridge abutments was polyethylene geogrids from Tensar Earth Technologies. Tensar® Uniaxial UX6 geogrids were used beneath the bridge footing and Uniaxial UX3 and UX2 geogrids were used behind the abutment wall as shown in Figure 6.3. The ultimate tensile strengths of the employed geogrids in accordance with the ASTM D 4595 were 157.3, 64.2, and 39.3 kN/m for the UX6, UX3, and UX2 geogrids, respectively. The tensile stiffness of the UX6 and UX3 geogrids at the 0-2% tensile strain range were approximately 2000 and 1000 kN/m, respectively. The GRS mass was constructed in a trapezoidal shape that had 1:1 back slope as shown in Figure 6.3a. The reinforcement length was made long to support not only the bridge superstructure bearing seats but also the approaching roadway structures to mitigate

the possible differential settlement between the bridge deck and the approaching slabs. In addition, the extension of the reinforced soil mass intended to enhance the overall stability of the bridge abutments.

6.4.3. Concrete facing blocks

Mesa concrete facing blocks (Figure 6.7) were used with positive mechanical connectors between the blocks and the reinforcement layers, and between the blocks themselves (Figure 6.8). The Mesa facing blocks had a compressive strength of 28 MPa and were 0.457 m long, 0.279 m wide, and 0.203 m high. Crushed stone of 19-mm maximum size was placed behind the facing blocks for a distance of 0.3 m to facilitate the compaction process. This zone provided an internal drainage system and prevented the migration of fines to the wall facing.

(a) (b)

Figure 6.7. Mesa concrete facing blocks: (a) top view; and (b) bottom view (Abu-Hejleh et al. 2001a).

6.4.4. Facing connectors

The mechanical connectors used had a mobilized connection strength of 57.7 kN/m measured in accordance with the National Concrete and Masonry Association (NCMA) Test Method SRWU-1 at a horizontal movement of 19 mm (service state).

(a) (b)

Figure 6.8. Mechanical connectors: (a) general view; and (b) assembly view (Abu-Hejleh et al. 2001a).

6.5. INSTRUMENTATION PROGRAM

The Founders/Meadows Bridge abutments were heavily instrumented. Figure 6.9 shows the instrumentation layout of Section 800. The instrumentation included can be divided into two categories: (1) instrumentation to monitor the external deformation of the structure, which included surveying, a dipstick road profiler, and an inclinometer; and (2) instrumentation to monitor the internal response of the structure, which included verti`cal earth pressure cells, lateral contact pressure cells, reinforcement strain gages, temperature gages, and water content reflectometers. Information on the various instrumentation employed in the structure as detailed in Abu-Hejleh et al. (2001a) are summarized in the following subsections:

6.5.1. Instrumentation to monitor the external deformation of the structure

6.5.1.1.Surveying points

Reflective sign sheeting were mounted on the facing of the walls, girders, and abutments. Survey targets marked by nails were flushed into holes in the bridge deck, approaching slab, and roadway slab. The locations of the targets are shown in Figure 6.9. The targets were shot by a surveying total station.

6.5.1.2.Dipstick road profiler

A dipstick road profiler was utilized to profile the bridge deck and the approaching roadways. The road surface was profiled along the external edges of the bridge and into the roadway surface in both directions. The profiler was used to plot an accurate profile of a roadway surface. The profiler used has a digital level with two pivoting legs that are 0.3-m (1-foot) apart. That is, this profiler can acquire elevation data every 0.3-m increment.

6.5.1.3.Inclinometer

One Geokon Model 6000 inclinometer was installed vertically behind the facing to measure the lateral deformation of the reinforced soil mass. The inclinometer is divided into segments and measures the displacement of the junctions between the settlements. Consequently, displacement values from the inclinometer represent average displacements for multiple layers. The inclinometer was placed in Section 400.

6.5.2. Instrumentation to monitor the internal response of the structure

6.5.2.1.Vertical earth pressure cells

Geokon 4800 earth pressure cells with a range of 345 kPa were used to measure the localized vertical pressure within the reinforced soil mass. The array of the vertical earth

pressure cells installed for Section 800 is shown in Figure 6.9. This cell is designed to be placed in the soil and was positioned horizontally to measure vertical pressure.

6.5.2.2.Lateral earth pressure cells

Geokon 4810 contact pressure cells were used to measure the horizontal pressure exerted by the reinforced soil mass on the facing. The array of the vertical earth pressure cells installed for Section 800 is shown in Figure 6.9. These cells were placed vertically against the back of the block facing and the abutment wall to measure the horizontal pressure exerted by the reinforced soil.

6.5.2.3.Strain gages

Geokon 4050 strain gages with a gage length of 150 mm and range of 0.7% were used to measure the localized reinforcement strain. The array of the strain gages installed for Section 800 is shown in Figure 6.9. The strain gages were mounted using two brackets which clamp to the geogrid.

6.5.2.4.Resistive temperature probes

Geokon temperature probe was used to monitor the air temperature changes. The probe was placed on the top of front GRS wall and below the girders (Figure 6.9) to protect it against the direct sunlight and precipitation. Vibrating wire sensors associated with thermistors were buried within the reinforced soil mass to monitor the change in the backfill temperature. One sensor was placed under the girder at the elevation of Layer 16 to monitor the air temperature and two sensors were placed at Layer 10, Locations A and B to measure the difference in the temperature alterations near the facing and under the center of the bearing seat.

6.5.2.5.Water content reflectometers

Campbell Scientific CS615 water content reflectometers were used to monitor the change in moisture content within the reinforced soil mass. Two sensors were placed below the sleeper foundation at Section 800 as shown in Figure 6.9. Theses sensors determine the change in water content through the change in the dielectric constant of the soil.

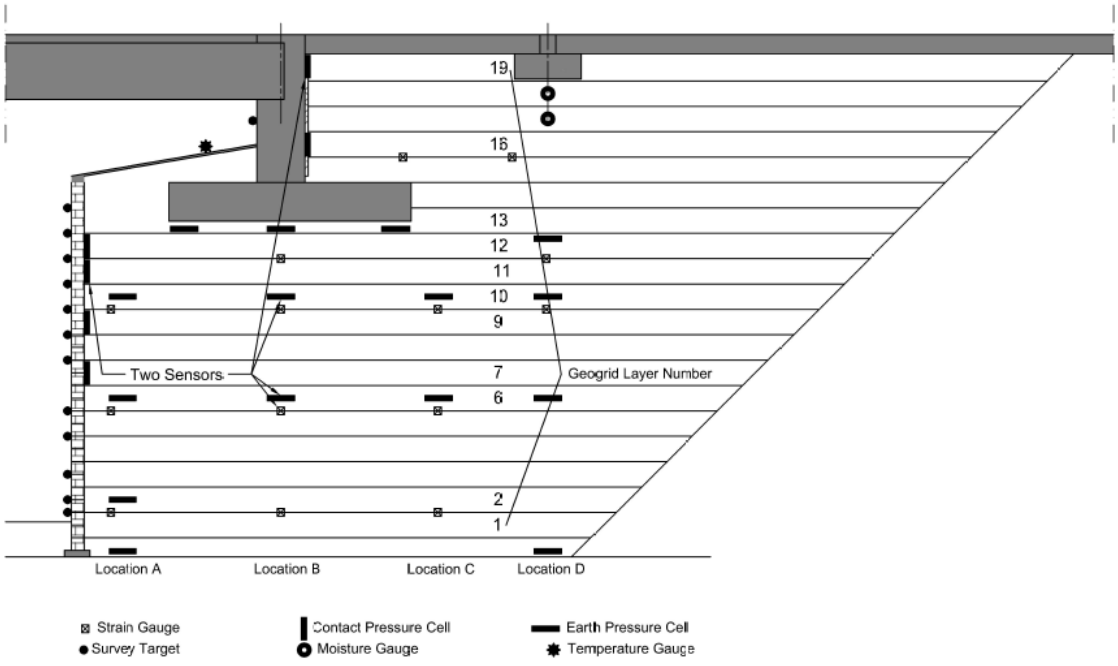

Figure 6.9. Layout of Instrumented Section 800 (redrawn after Abu-Hejleh et al. 2002).

6.6. ABUTMENT LATERAL DEFORMATION

The lateral deformation of the instrumented sections were measured by surveying occasionally during construction and after the bridge was opened to traffic. Figures 6.10a through 9.10e show the measured lateral deformation since the construction of the GRS backfill (i.e., since the completion of Stage II) at different dates for Sections 800, 400, 200, 300, and 900, respectively. Note that the bridge construction was completed and the bridge

was opened to traffic in June 1999. The lowermost 1 m was not surveyed since the embedment depth had been buried by the time the walls were surveyed except for the first reading for Sections 400, 200, and 300. In addition, the second meter was not surveyed for Sections 800, 400, and 200 due to the placement of the right-of-way jersey barriers in front of the abutment front walls.

The lateral deformation was found insignificant where the maximum value observed was 22.6 mm and was recorded for Section 400. However, the maximum lateral deformation that was experienced by the structure after its completion is 15.7 mm and was observed in Section 400 as well. Sections 400 and 200 showed very similar deformations in their early readings (during construction). However, Section 400 has shown slightly higher lateral deflection in the later readings. This is attributed to the difference in wall height, where Section 400 is 5.9-m high and Section 200 is 4.5-m high. Similarly, the lateral deformation at Section 300 was observed to be less than that at Section 900 due to the difference in wall heights. The difference in lateral deformation between the two sections was pronounced under higher loads. On the other hand, Section 800 exhibited less lateral deflection compared to Section 400, which has the same height as Section 800. This can be attributed to three possible reasons: (1) the construction season of the GRS walls. The construction of the GRS walls at Sections 400 and 200 (Phase I) was completed by November 1998 and the subsequent construction of the bridge was completed by December 1998 (i.e., during the warm season), whereas the construction of the GRS wall at Section 800 (Phase II) was completed by March 1999 and the subsequent construction of the bridge was completed by June (i.e., during the warm season). That is, the superstructure of Phase I was constructed and experienced possible contraction of the cold season. This resulted in

higher lateral deformation of the front walls. On contrary, the superstructure of Phase II was constructed and experienced possible expansion of the warm season. This resulted in less lateral deformation of the front walls; (2) an additional reason is that construction during the cold season in this district where temperature drops below the freezing temperature of water would have frozen the soil layers as they get covered. Note that as construction advanced layers are buried under their successive layers and reducing the possibility of thawing over short time period. That is, the frozen backfill by the end of the Phase II GRS wall construction (i.e., construction during the hot season) applied less lateral pressure on the facing than that applied by the backfill at the end of Phase I GRS wall construction (i.e., construction during the warm season); and (3) the construction sequence of Phase I and Phase II had a difference. In Phase I (represented in Section 400) the bridge girders were placed after the placement of the backfill behind the abutment wall. That is, a lateral load was applied on the abutment before it is probed by the bridge girders. On contrary, in Phase II (represented in Section 800) the bridge girder s were placed before the placement of the backfill behind the abutment wall. That is, the lateral load applied by the added backfill was after the abutment was probed by the girders. This resulted in a larger lateral deformation at Section 400 compared to that at Section 800. Note that the hypotheses mentioned herein contradicts with the hypotheses made by Abu-Hejleh et al. (2002), which was based on surveying data recorded for Stage I only.

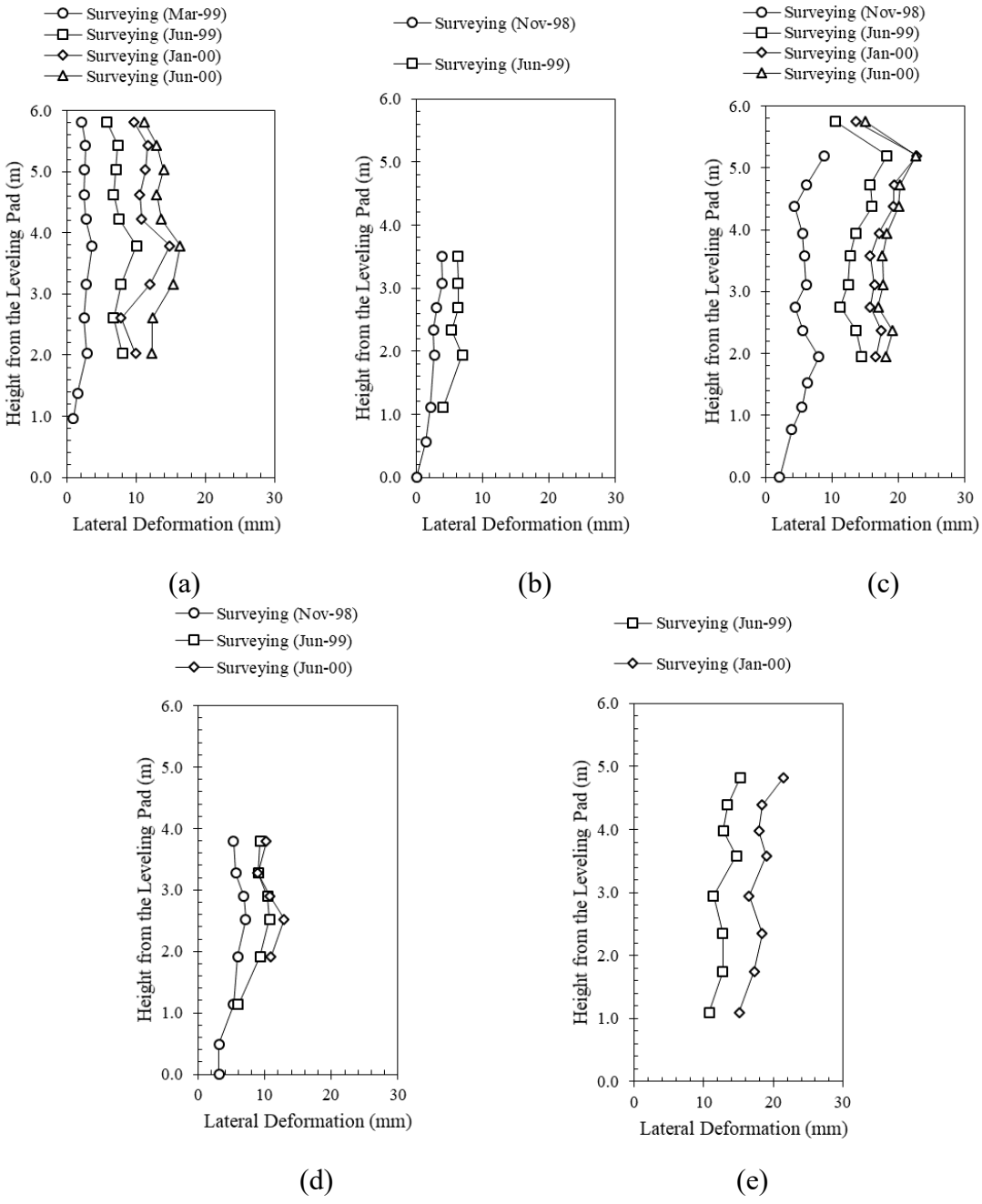

Figure 6.10. Lateral deformation measured during and after construction (i.e., Stages II to IV) from surveying for (a) Section 800, (b) Section 400, (c) Section 200, (d) Section 300, and (e) Section 900.

An inclinometer was placed right behind the facing at Section 400 to provide redundancy in the lateral deformation measurements. The inclinometer started recording its data after the bridge Phase I construction had completed and the measured lateral deformation is presented in Figure 6.11a. The data measured from the inclinometer can be compared to the lateral deformation measured by surveying after the completion of Phase I construction. Subsequently, the lateral deformation measured after construction by surveying was plotted and is presented in Figure 6.11b. While, the lateral deformation obtained from both surveying and the inclinometer are in the same order of magnitude, the inclinometer exhibited less deformation. This is because the inclinometer measured deformation based on a fixed reference point at its tail (the first point of its array). However, the surveying data showed that the lowermost point of the abutment has moved. This implies that the reference point of the inclinometer has moved laterally and its data is underestimating the lateral deformation. To correct the data measured by the inclinometer, the average of lowermost lateral deflection value (at elevation 2 m) measured from surveying was used to correct for the corresponding average deflection value measured from the inclinometer. The difference between these two values is 2.4 mm, which was added to all the inclinometer data to adjust its data. Note that average values was used since the data obtained by inclinometer and surveying was not for the same time periods, however it was over a similar time span. The corrected lateral deformation obtained from the inclinometer data was then plotted and is presented in Figure 6.11c. The lateral deformation measurement in the early years after construction and the vertical profiles of the wall show that the deformation occurred to the walls is primarily sliding deformation and there is no any overturning potential.

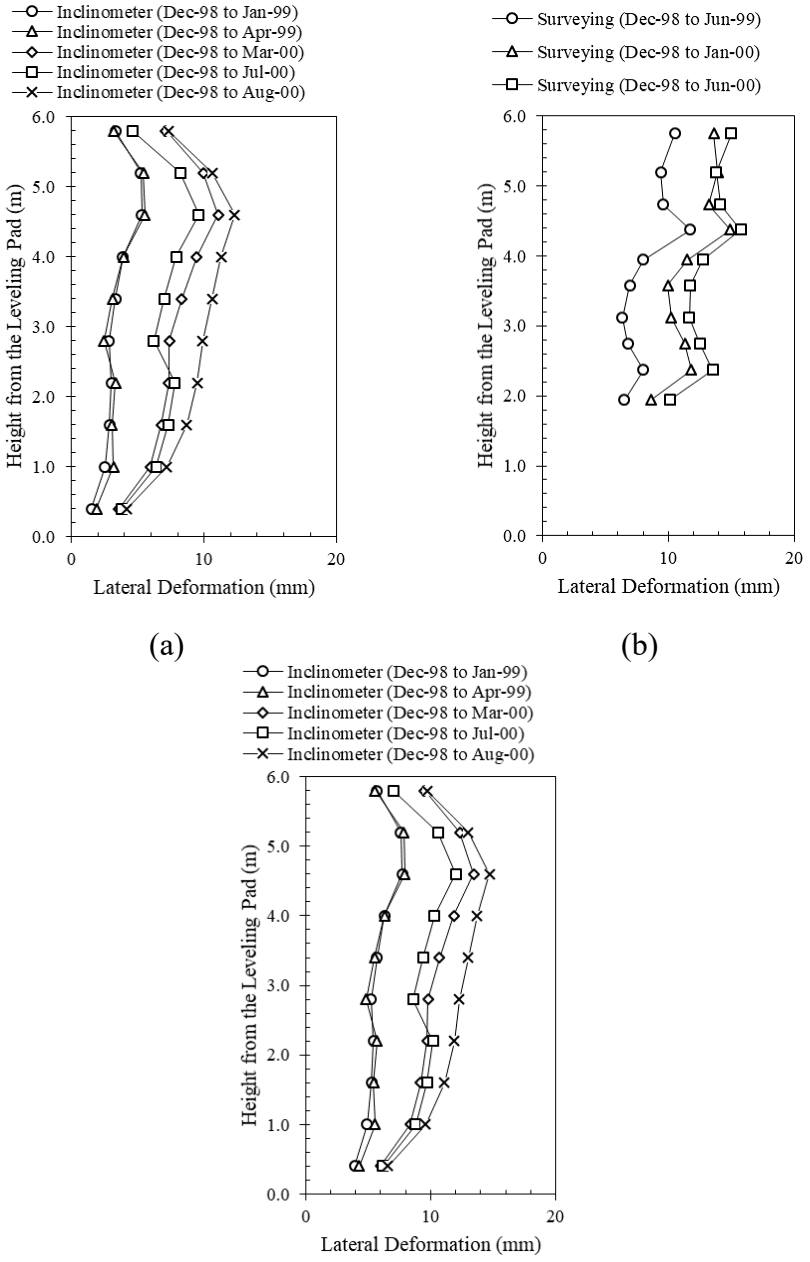

Figure 6.11. Lateral deformation measured after construction for Section 400: (a) from inclinometer; (b) from surveying; (c) from inclinometer corrected for surveying.

In order to evaluate the long-term performance of the GRS bridge abutments the walls for all the monitored sections were surveyed in March 2016 (approximately 17 years after construction). The vertical profiles of Sections 800, 400, and 200 are plotted as shown in Figure 6.12a, whereas those of Sections 300 and 900 are plotted in 12b. While the absolute lateral deformation could not be determined, the walls still exhibit a very satisfactory vertical profiles. The abutment front facing batter angle measured was approximately 4 degrees (14V:1H). This value is deemed very small compared to the maximum batter allowed as per original design, which was 15 degrees.

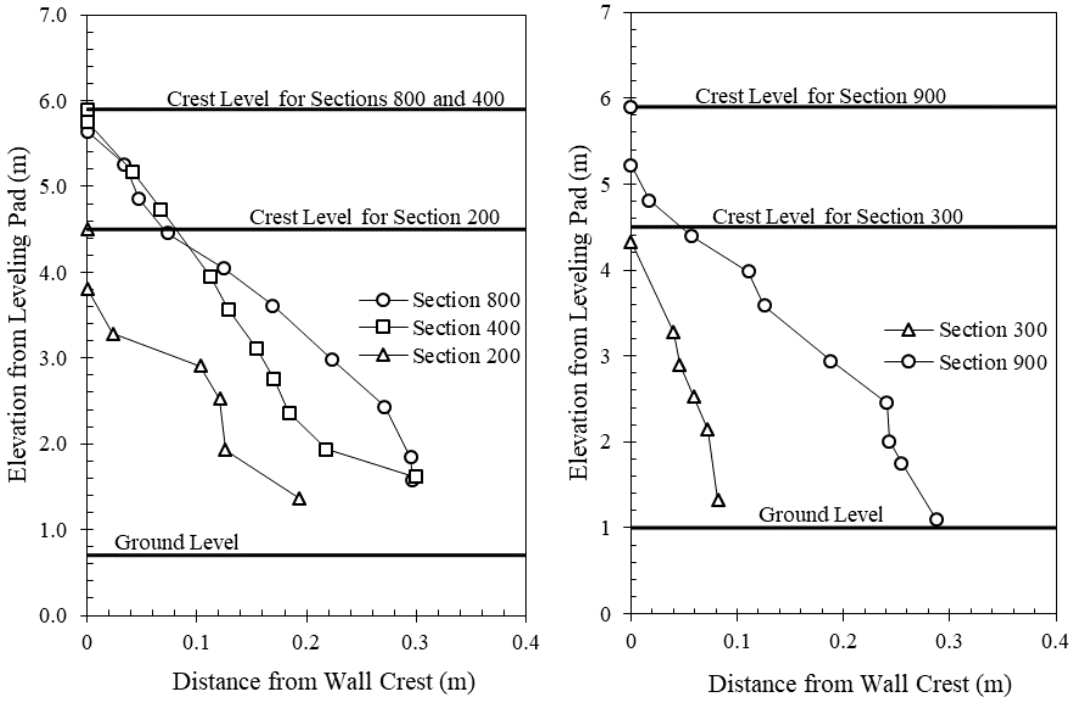

Figure 6.12. Vertical wall profiles in March 2016: (a) Sections 800, 400, and 200; and (b) Sections 300 and 900.

6.7. ROAD PROFILE

Differential settlements occur across the transition section from bridge deck to approaching roadway in typical bridges. This is due to the different foundation systems used for the bridge deck and the approaching roadway structures. Unlike the conventional bridges, Founders/Meadows was supported directly by the reinforced soil abutments. The reinforced soil extended to support the approaching roadway structures. The bridge elevation profiles along the transition from bridge deck to approaching roadway at was monitored along four lines: (1) at the east bridge abutment along eastbound direction; (2) at the east bridge abutment along westbound direction; (c) at the west bridge abutment along eastbound direction; and (d) at the west bridge abutment along westbound direction. Monitoring conducted in February 2000 and November 2001 using a digital road profiler and in March 2016 using a total station.

Figures 6.13a through 6.13d show the elevation profile relative to the abutment crest elevation along the four profiling lines, respectively. The distance is measured from the abutment location such that the positive values denote distances toward the approaching slab and the negative values denote distances towards the bridge deck. Note that the bridge deck is downhill towards the west. The expansion joints are located on the approach slabs around 4 m away from the bridge abutments as shown in Figure 6.3a. The profiles shown in Figure 6.13 indicate the absence of any differential settlements at the transition between the bridge and approaching roadway and the expansion joints. The data collected in March 2016, 17 years after the bridge construction and inaugurated to traffic, proves that the GRS technology can mitigate the bump-at-the-bridge problem and providing a smooth bridge ride.

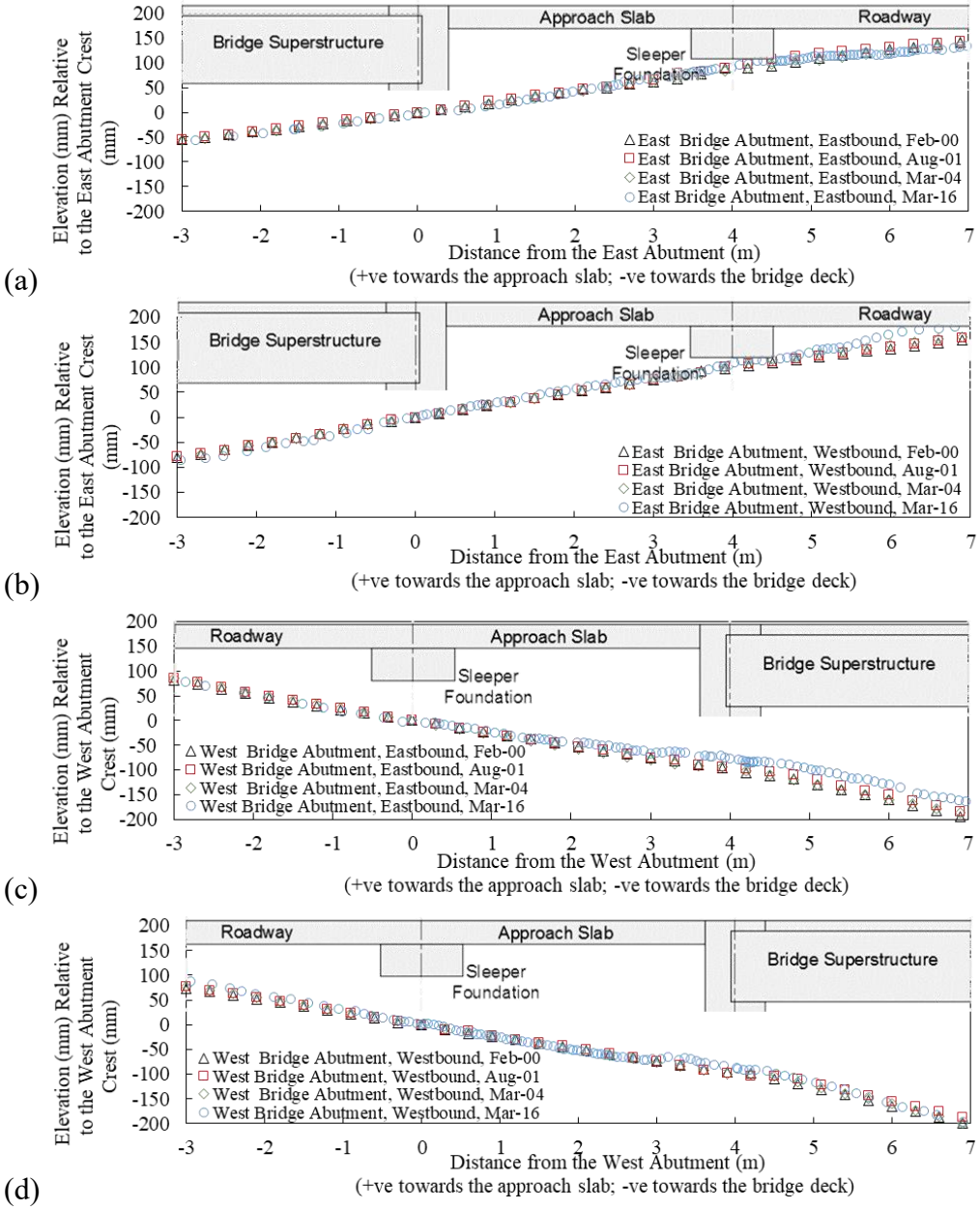

Figure 6.13. Elevation profiles along the transition from bridge deck to approaching roadway: (a) at the east bridge abutment, eastbound direction; (b) at the east bridge abutment, westbound direction; (c) at the west bridge abutment, eastbound direction; and (d) at the west bridge abutment, westbound direction.

6.8. TEMPERATURE MONITORING

Temperature was monitored at three locations during construction and after the construction completion and bridge inauguration to traffic. The temperature was monitored specifically at three different locations: (1) on the top of the GRS wall and under the bridge superstructure. This location was selected to monitor the air temperature change while protecting the sensor from the direct sunlight and the environmental events; (2) behind the facing (i.e., at Location A) at Layer 10. This sensor intended to monitor the temperature changes at a shallow region within the GRS mass (i.e., close to the GRS boundaries); and (3) under the footing (i.e., at Location B) at Layer 10. This sensor intended to monitor the change in temperature at a deep region within the GRS mass (i.e., far from the GRS boundaries). Figure 6.14 shows the time history of the recorded temperature at the three different locations. The sensors embedded within the GRS mass were stopped around 2.7 years after construction, while readings from the air temperature sensor lasted until the fifth year post construction. It is clear from the air temperature time history that the temperature was lowest at the top of the years (peak winter seasons) and was highest at the mid of the years (peak summer seasons). The temperature at the shallow regions followed the air temperature strongly in its time history and magnitude. However, the short-term fluctuations in the temperature was not as high as the air temperature. On the other hand, the temperature at the deep regions did not promptly change with the air temperature changes. This is clear in Figure 6.14 where the time history of the temperature recorded at Layer 10, Location B exhibits a phase difference by around 3 months in its seasonal cycles. The air temperature change did not fully alter the temperature at deep regions within the GRS mass. In addition, no short-term temperature fluctuations (daily temperature changes) were observed at the deep regions as presented in Figure 6.14.

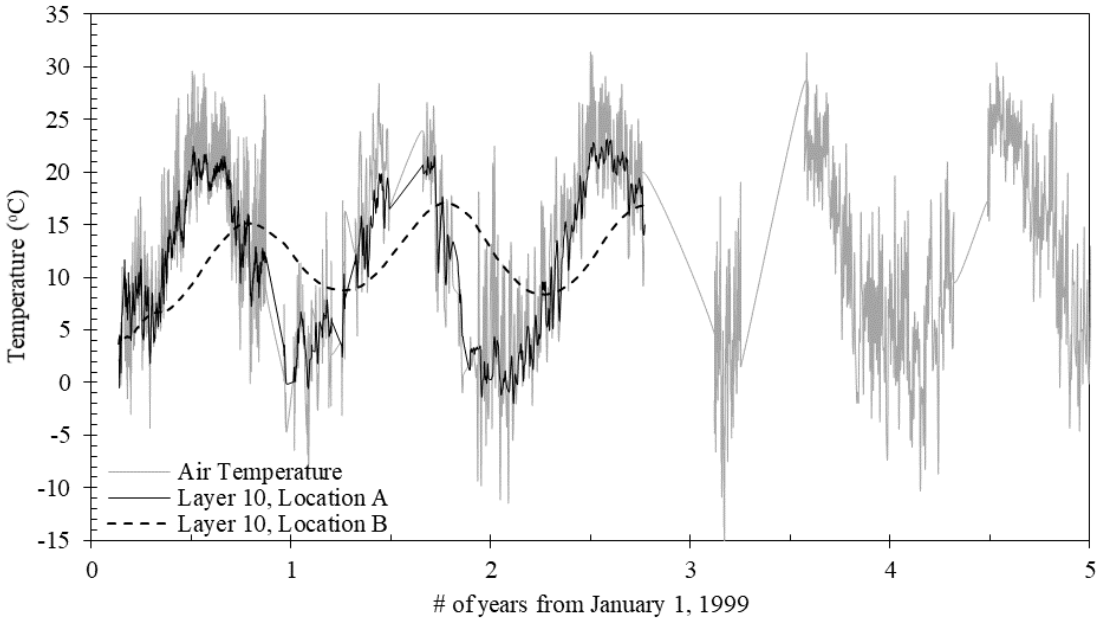

Figure 6.14. Temperature time history.

6.9. MOISTURE MONITORING

Two water content reflectometers were installed under the sleeper foundation (i.e., Location D), which was placed under the expansion joint between the concrete roadway structure and the concrete approach slab. The sensors were placed at Layer 17 (0.5-m deep) and Layer 18 (0.1-m deep). Figure 6.15 shows the moisture time history (gravitational and volumetric water contents) recorded at the two specified locations over five years after construction. The fluctuation in the moisture content was not very high due to dry environment of the bridge location. However, the fluctuation that was observed in the moisture at depth 0.1 m was less pronounced at depth 0.5 m as shown in Figure 6.15. That is, the drainage system placed underneath the approach slab worked efficiently.

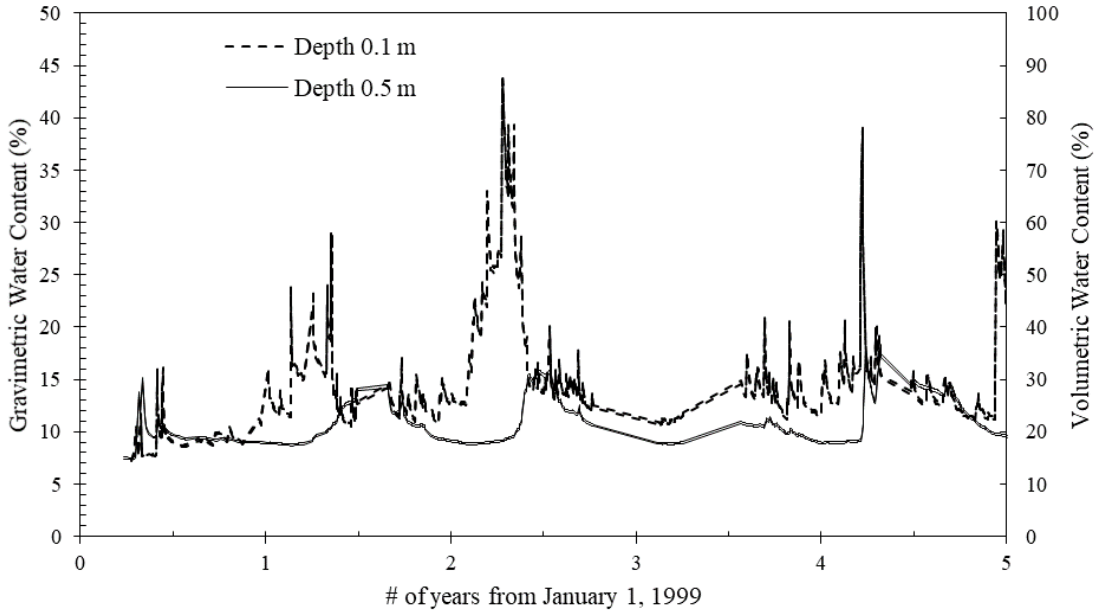

Figure 6.15. Moisture time history.

6.10. VERTICAL EARTH PRESSURES

Figure 6.16 shows average estimated vertical stress increase at the foundation level of the bearing seats and at the base of the GRS mass as the construction progressed. Figure 6.17 shows the vertical earth pressure distribution within the GRS mass at Section 800 for different elevations throughout the various bridge construction stages and after the bridge completion and inauguration to traffic. Figure 6.17a shows the earth pressure distribution across the base of the GRS mass. At this elevation, only two vertical pressure cells were placed at Locations A and D. The measured stresses showed that the vertical pressure at Location A was higher than that at location D in the early construction stages. This may be attributed to the locked-in compaction induced stresses close to the facing. It was also observed that the rate of increase in the vertical pressure was almost the same at both locations up to construction Stage III. Yet, beyond Stage IV, the vertical pressure at

Location A dropped. This can be attributed to the outward lateral movement of the facing after placement of the bridge superstructure. This lateral movement may have released the locked-in stresses behind the facing. The pressure at Location A built up again after Stage V and increased at a similar rate to that at Location D. The vertical pressure measured at Locations A and D maintained constant after the construction completion and until the monitoring has terminated 2.3 years after the traffic was allowed on the bridge. Figure 6.17a also shows the estimated earth pressure distribution at layer 0 in accordance to the integration of Boussinesq (1885) solution. The figure shows a good agreement in stress values. The predicted distribution pattern was verified due to the lack of pressure cells number at this elevation.

Figures 6.17b and 6.17c show the vertical earth pressure distribution across the GRS mass at Layers 6 and 10, respectively. It is clear that there was a general increase in the vertical earth pressure across the GRS mass as the construction progressed. The rate of increase in the vertical pressure at location B was observed to be the highest across the GRS mass at both Layers 6 and 10. This observation agrees with the fact that the vertical pressure below the center of the distributed load is the maximum and fades towards the edges. Figures 6.17b and 6.17c also show the estimated earth pressure distribution at layer 0 in accordance to the integration of Boussinesq (1885) solution. The predicted values consider that the increase in the overburden pressure at Locations C and D upon the construction of the reinforced backfill underneath the roadway approach structure. The figures show a good agreement in regards of the stress values and distribution patterns. Accordingly, the measured vertical earth pressure was extrapolated from Location A to the facing (over a distance of 0.6 m) by subtracting the difference in vertical stress estimated

by the integration of Boussinesq (1885) solution. Note that two pressure cells were placed at Location B on both Layers 6 and 10. The pressure cells showed very consistent and similar data for both layers; the data plotted is the average of the data recorded by each couple of sensors for the different layer. The vertical pressure measured beneath the footing was recorded by all sensors maintained constant after the construction completion and until the monitoring has terminated 2.3 years after the bridge inauguration to traffic.

A reverse trend in the vertical earth pressure was observed close to the facing for both Layers 6 and 10. The vertical earth pressure at Location A increased throughout the construction stages up to Stage IV. Then, following Stage IV, a reduction was observed in the vertical pressure. This may be attributed to the increase in the outward movement of the facing, which was clear beyond Stage IV. In addition, the down-drag force on the facing units may have contributed in the initial increase in the earth pressure readings in the early construction stages. Abu-Hejleh et al. (2001a) reported that the high pressure recorded behind the facing for Layers 0 and 6 could be attributed to the down-drag force. This down-drag force is induced by friction between the backfill material and the back surface of the facing units (Buttry et al. 1996; Hatami and Bathrust 2006). This down-drag force were mobilized during compaction and caused a higher pressure at Location A than at Location C resulting in some eccentricity at Layers 6 and 10. Hatami and Bathrust (2006) reported that generally there is a local reduction in the vertical earth pressure immediately behind the facing. This observation agrees with the behavior shown by the Founders/Meadows Bridge abutment. Helwany et al. (2003) conducted a numerical study on the Founder/Meadows Bridge abutment and reported predicted pressure values similar to the measured pressure at Layers 6 and 10. Fakharian and Attar (2007) argued that the drop in

vertical earth pressure behind the facing at Layer 6 was illogical and due to instrumentation and monitoring problems. However, this argument is not valid as the same trend was encountered in all the instrumented layers. Zheng et al. (2015) reported that the large lateral movement occurring during Stage V caused a drop in the lateral and vertical earth pressures near the facing (i.e., at Location A).

As the construction progressed, settlement and outward facing movement may have relieved the down-drag force, and thus reduced the vertical earth pressure behind the facing. In addition, Abu-Hejleh et al. (2001a) reported that the wall system might be rigid during winter and that deformations occurred mainly during the warm seasons. These deformations reduced the frictional down-drag force (Buttry et al. 1996) and also reduced the lateral earth pressure. Based on those studies, it can be concluded that as construction advanced, and the load increased, reinforcement layers started to strain allowing the facing units to move and reducing the pressure behind them. In turn, the pressure could have diffused inwards to the rest of the layer due to soil arching. This happened when the load increased enough to strain the reinforcement where the reinforcement strain rate increased after Stage IV (discussed later). Note that the reinforcement strains in Stage I occurred during backfill placement and compaction (before considerable pressure was applied). The load distributed uniformly over the layer with a rise behind the facing units. This can be attributed to soil arching as blocks were more confining than the retained native soil during the early construction stages and until the reinforcement strained. The drop in the readings of the strain gages at location A implies that these gauges were compressed. While this compression implies that the localized reinforcement strain decreased; however, the integration of the strain over the length of the reinforcement confirms that the total outward

movement increased. McGown et al. (1998) reported that if the lateral boundary of the wall is not allowed to yield, the resulting pressure equates or exceeds that obtained under at-rest conditions (upper limit). On the contrary, if the lateral boundary of the wall is allowed to yield sufficiently to mobilize a large tensile resistance in the reinforcement, and if the required forces and available forces balance, theoretically there should be no lateral earth pressure acting on the wall (lower limit). However, even in the case of the lower limit, the soil masses between the reinforcing layers may have a tendency to produce localized stresses near the facing. These stresses develop because each soil layer acts separately causing the wall to be subjected to active horizontal pressure over the depth of the layer.

Figure 6.17d shows the vertical earth pressure across the GRS below the concrete foundation. The pressure distribution is similar to that observed from the other layers in the early construction stages. Beyond Stage III, a different pressure distribution was observed, where the pressure increased below the edges of the foundation to be more than the pressure below the center. This pressure distribution is typical for rigid foundations on compacted granular soils. Boussinesq (1885) solution was not plotted for this layer since it assumes flexible foundation, which is not the case in this layer. Helwany et al. (2003) reported higher predicted pressure values than the measured pressure underneath the bridge footing. However, the predicted pressure values at lower elevations were in a good match with the measured ones. Note that the predicted data they reported showed that the pressure decreases towards the facing, which contradicts the measured data. They attributed that soil arching might be one of the reasons for the difference between predicted and measured soil pressure underneath the bridge footing. Abu-Hejleh et al. (2000b) suggested that the vertical pressure distribution had no overturning potential. They attributed this to the

flexibility of the reinforced soil structure which redistributed the overturning stresses. The vertical pressure measured beneath the footing was recorded by all sensors maintained constant after the construction completion and until the monitoring has terminated 2.3 years after the bridge was opened to traffic.

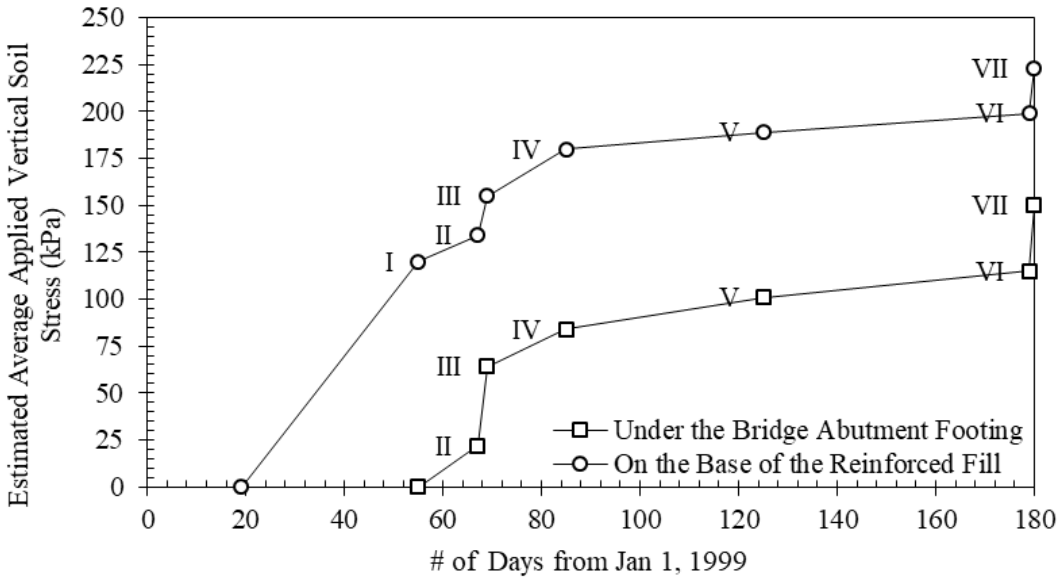

Figure 6.16. Estimated vertical stress increase under the bridge footing and at the base of the reinforced fill through the various construction stages

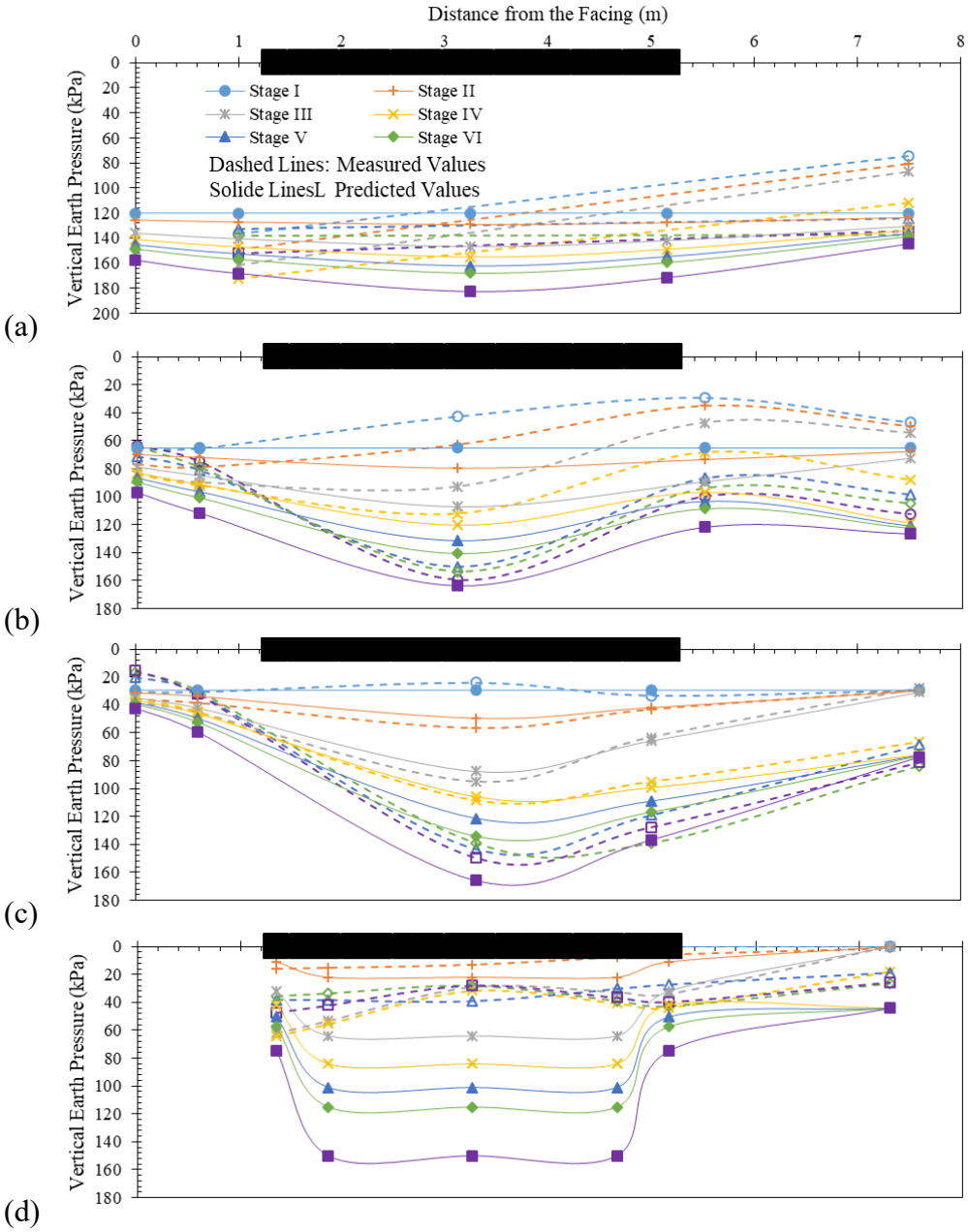

Figure 6.17. Vertical earth pressure across the front GRS structure: (a) at the base of the reinforced soil (layer 0); (b) between reinforcement layers 6 and 7; (c) between reinforcement layers 10 and 11; (d) between reinforcement layers 13 and 14 (at the foundation level of the abutment footing).

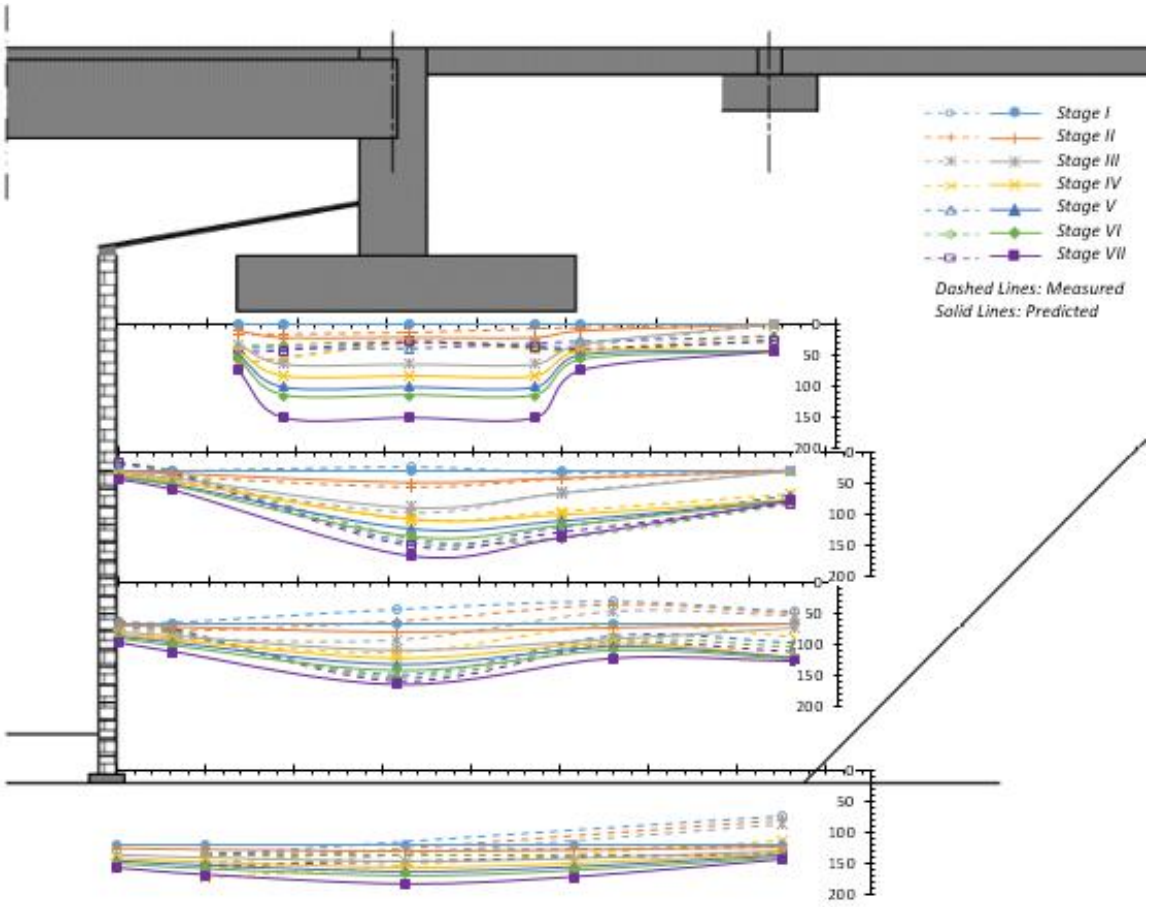

Figure 6.17. Vertical earth pressure across the front GRS structure (consolidated figure).

6.11. LATERAL EARTH PRESSURES

The lateral earth pressure was monitored on the back side of the facing and the backside of the concrete abutment wall throughout the various construction stages and after the bridge was opened to traffic. The lateral pressure was monitored at Section 800 at Layers 7, 9, 11, and 12 (on the facing of the front GRS wall), and at Layers 16 and 19 (on the backside of the concrete abutment wall). Note that two pressure cells were placed at Layers 11 and 19; while pressure cells at Layer 11 showed very consistent and similar data, one of the pressure cells at Layer 19 was faulty. Subsequently, the lateral pressure plotted

for Layer 11 resulted from the average of data recorded by its both sensors, whereas that plotted for Layer 19 resulted from the data recorded by the proper sensor. Figure 6.18 shows the lateral earth pressure on the front GRS wall facing during the various construction stages. The lateral earth pressure is much less than the estimated stresses by solutions derived from Rankine (1857), Boussinesq (1885), Scott (1963), or NAVFAC (1986) for conventional retaining structures.

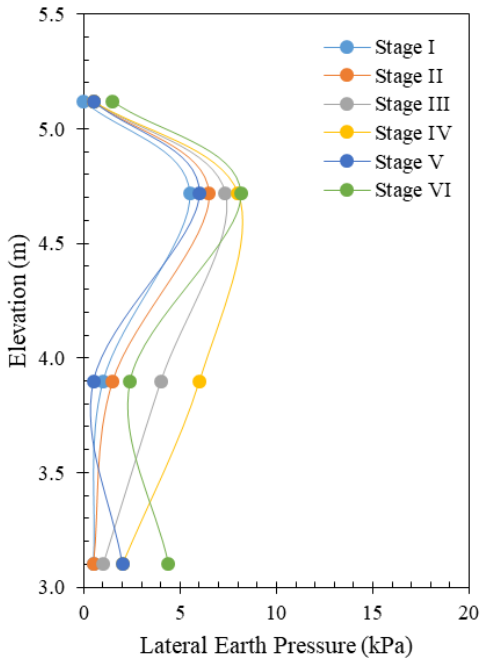

Figure 6.18. Measured lateral earth pressure on the front GRS wall facing during construction.

Figures 6.19a and 6.19b show the long-term lateral earth pressure on the front GRS wall facing and on the concrete abutment wall, respectively. The figures shows the lateral earth pressure every half a year from 1 January 1999. Note that the construction of the

bridge was completed and traffic was allowed to bridge in 30 June 1999 (i.e., after half a year and at the end of Stage VI). The figure shows a significant fluctuation in the lateral earth pressure that is very consistently synchronized with the temperature fluctuation (Figure 6.14). During the warm seasons (Stage VI and Stage VII 1.5, 2.5, 3.5, and 4.5 years) the bridge superstructure tended to expand pushing the concrete bearing seats against the backfill. On contrary, during the cold seasons (Stage VII 1, 2, 3, 4, and 5 years) the bridge superstructure tended to contract releasing the pressure exerted by the concrete bearing seats against the backfill. In addition, during the cold seasons the backfill tended to freeze which resulted less lateral pressure on the facing. Note that the temperature behind the facing can be represented by the sensor placed behind the facing whose recorded time history is presented in Figure 6.14. The seasonal fluctuation in temperature is very consistent with the air temperature. In addition, the backfill used in the GRS walls had a considerable amount of fines (10.6%) that can hold water until it freezes. Also, Figure 6.15 shows a consistent presence of water in the GRS mass. Note that the pressure cells reduced data considered temperature in accordance with the manufacturer datasheet. In addition, no fluctuation was observed for the vertical pressure cells, which were exposed to the same temperature alterations. The fluctuation in the lateral pressure was more pronounced on the abutment concrete wall than the facing of the front GRS wall since it is directly connected to the bridge superstructure.

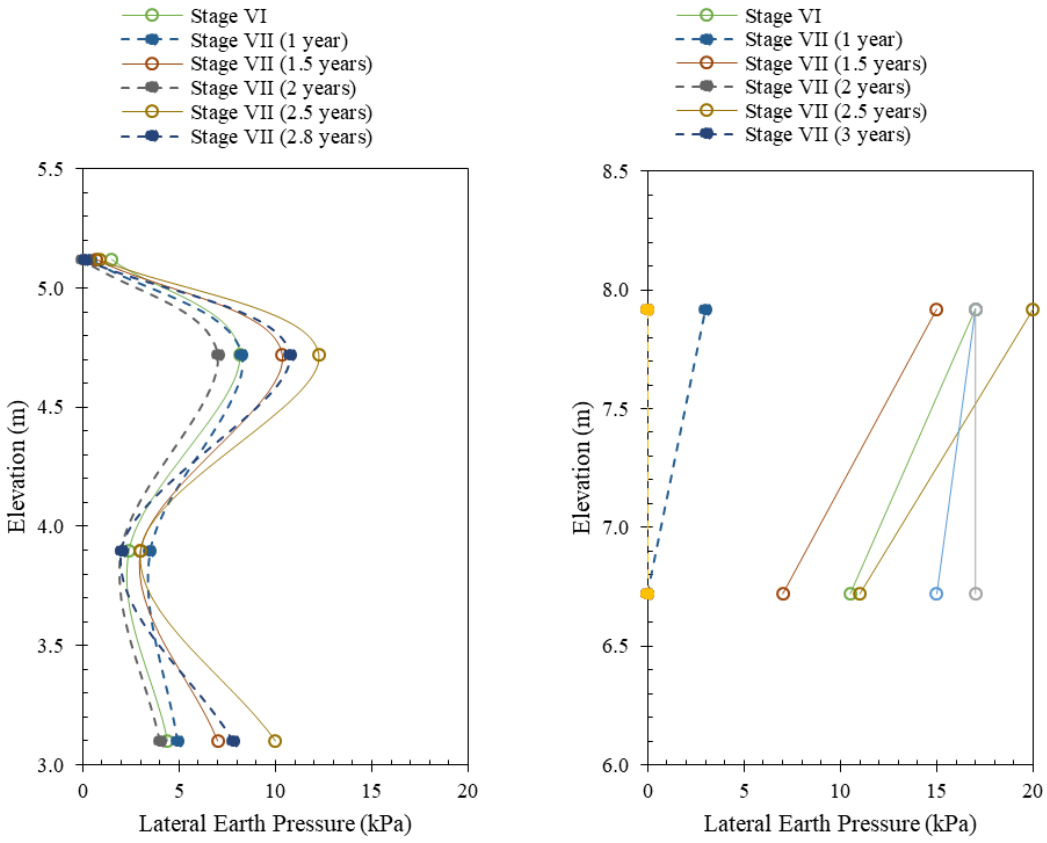

(a) (b)

Figure 6.19. Measured lateral earth pressure after construction completion: (a) on the front GRS wall facing; (b) on the concrete abutment wall.

6.12. REINFORCEMENT STRAINING

Figure 6.20 shows the reinforcement strains measured by the strain gauges along the reinforcement length across the front GRS wall at Section 800 for different reinforcement layers. Large reinforcement strains were recorded at all locations during Stage I. This can be attributed to the compaction effect and the compaction induced stress that might have stretched the reinforcement while the normal pressure on the reinforcement was negligible. Abu-Hejleh et al. (2001a) reported that 50% of the reinforcement strains

developed during the backfill placement and compaction stage (Stage I). Abu-Hejleh et al. (2000b) explained that the sharp increase in the reinforcement strains in Stage I were possibly because of the locked-in strains. McGown et al. (1998) reported that locked-in strains can happen during compaction where the soil particles are forced into the reinforcement apertures causing straining that are locked in after the compaction ends. Locked-in strains have a similar effect to a confining stress on the soil (i.e. they increase the strength of the soil and reduce lateral earth pressure). Abu-Hejleh et al. (2001a) suggested that the compaction methodology, construction season, and construction sequence may affect the deformations in the structure. Abu-Hejleh et al. (2002) reported that these large movements during Stage I were due to (1) soil compaction, (2) low normal pressure, and (3) reinforcement wrinkles.

Figure 6.20a shows the reinforcement strains along Layer 2 throughout the various construction stages. Three strain gages were installed at this layer: one at Location A, one at Location B, and one at Location C. The reinforcement strain recorded at Location A was greater than that recorded at Location B while the strains at Location D was the least. The same trend was observed during the construction stages. This might be due to the effect of the side boundary where Location D is close to a lateral confined mass and Location A is closer to a laterally open to displacement mass. The reinforcement strain increased as the construction advanced and the vertical load at the reinforcement layers increased. Note that the reinforcement strain at Location A (i.e., close to facing) dropped at Stage IV. This was due to the drop in the vertical pressure at the same location. Reinforcement strain was measured after construction every half a year and up to 1.5 years after bridge construction completion; however, data is available only at Location D.

Figure 6.20b shows the reinforcement strains along Layer 6 throughout the different construction stages. Four strain gages were installed at this layer: one at Location A, two at Location B, and one at Location C. It can be inferred that the strains at Location A are greater than the strains at Location C. This can be attributed to the side boundary, which is confined at Location C (inwards) and open to displacement at Location A (outwards). In addition, the strain accumulates to the open side of the structure which forces the movement outwards. At Location B, the strains increased with loading in which the reinforcement is expected to bow downwards at all times (Figure 6.17b) increasing the tensile stresses in the reinforcement. The reinforcement strain at Location C did not show a significant increase throughout the various construction stages except during Stage I. This can be attributed to the confinement of this zone, which has restricted the soil movement unlike Location A. Reinforcement strain was measured every half a year and up to 4 years after bridge construction completion (4.5 years from 1 January 1999). Figure 6.20b shows very slow rate of strain increase was observed during the long-term monitoring. Note that Figure 6.20b was reported in Abu-Hejleh et al. (2002) at an early stage of monitoring. However, after 4.5 years of monitoring it was realized from the time history that the strain data plotted for Location B was for a faulty strain gage. Consequently, the data plotted for Location B herein is from the other strain gage, which worked properly over the entire monitoring program.

Figure 6.20c shows the reinforcement strain along Layer 10 throughout the different construction stages. Four strain gages were installed at this layer: one at Location A, one at Location B, one at Location C, and one at Location D. In general, the trend is very similar to that observed for Layers 2 and 6, where the reinforcement strains at Location

A are higher than the strains at Location D. This observation is similar to that of Layers 2 and 6, which strengthens the argument mentioned earlier on the lateral confinement effect. The reinforcement strain increased as construction progressed; however, a drop in the strain was observed at Location A after Stage IV, upon adding the bridge superstructure. This is consistent with the drop in the vertical pressure at the same location and at the same construction stage. A similar trend has been observed in Kongkitkul et al. (2008) in which a drop in the reinforcement strain occurred upon construction completion. Abu-Hejleh et al. (2002) reported that the outward displacement at Layer 10 was higher than that of Layer 6. They attributed this to the increase in the width of the active zone combined with the elevation from the base of the reinforced mass. The active zone is defined by the locus of maximum tension in the reinforcement layer. They attributed movements during Stage VII to traffic loads, creep under constant applied load, and seasonal changes. Reinforcement strain was monitored every half a year and up to 4 years after bridge construction completion (4.5 years from 1 January 1999) and traffic was allowed on the bridge. It was observed that the strain increased at a very low rate. Note that Figure 6.20c was reported in Abu-Hejleh et al. (2002) at an early stage of monitoring. By the end of the 4.5-year monitoring program it was realized that the strain gage at Location C was faulty; subsequently, its data was discarded herein.

Figure 6.20d shows the reinforcement strain along Layer 12 (close to the concrete bearing seat foundation level) throughout the various construction stages. The reinforcement strains recorded only at Locations B and D; the strains recorded at Location B were greater than those recorded at Location D. This happened during Stages III and IV in which the vertical stresses at Location B was higher than that at Location D. However,

after Stage IV the vertical stresses at both Locations B and D were close resulting in similar reinforcement strains. Reinforcement strain was monitored every half a year and up to 4 years after bridge construction completion (4.5 years from 1 January 1999) and traffic was allowed on the bridge.

Figure 6.20e shows the reinforcement strain along Layer 16 behind the concrete abutment wall and below the sleeper of the approaching roadway structure (i.e., from Location C to Location D) throughout the various construction stages. Two strain gages were installed at this layer; one gage at each of Location C and Location D. Although a lower vertical pressure was applied on this portion than on the other portions of the GRS mass, the reinforcement experienced some strains. This is due to the reinforcement used in this area (UX3 for Layer 16) was of lower stiffness than the reinforcement used in below the bearing seat foundation level (UX6). In addition, the presence of the flexible polystyrene sheet that was placed behind the concrete abutment wall to alleviate the lateral earth pressure exerted on the abutment wall. This flexible sheet may have allowed movement of the reinforced fill behind the abutment wall. The reinforcement stain was almost uniform over the portion between location C and location D. Yet, as construction advanced the strain at Location D increased after the construction of the sleeper foundation, which is located at Location D.

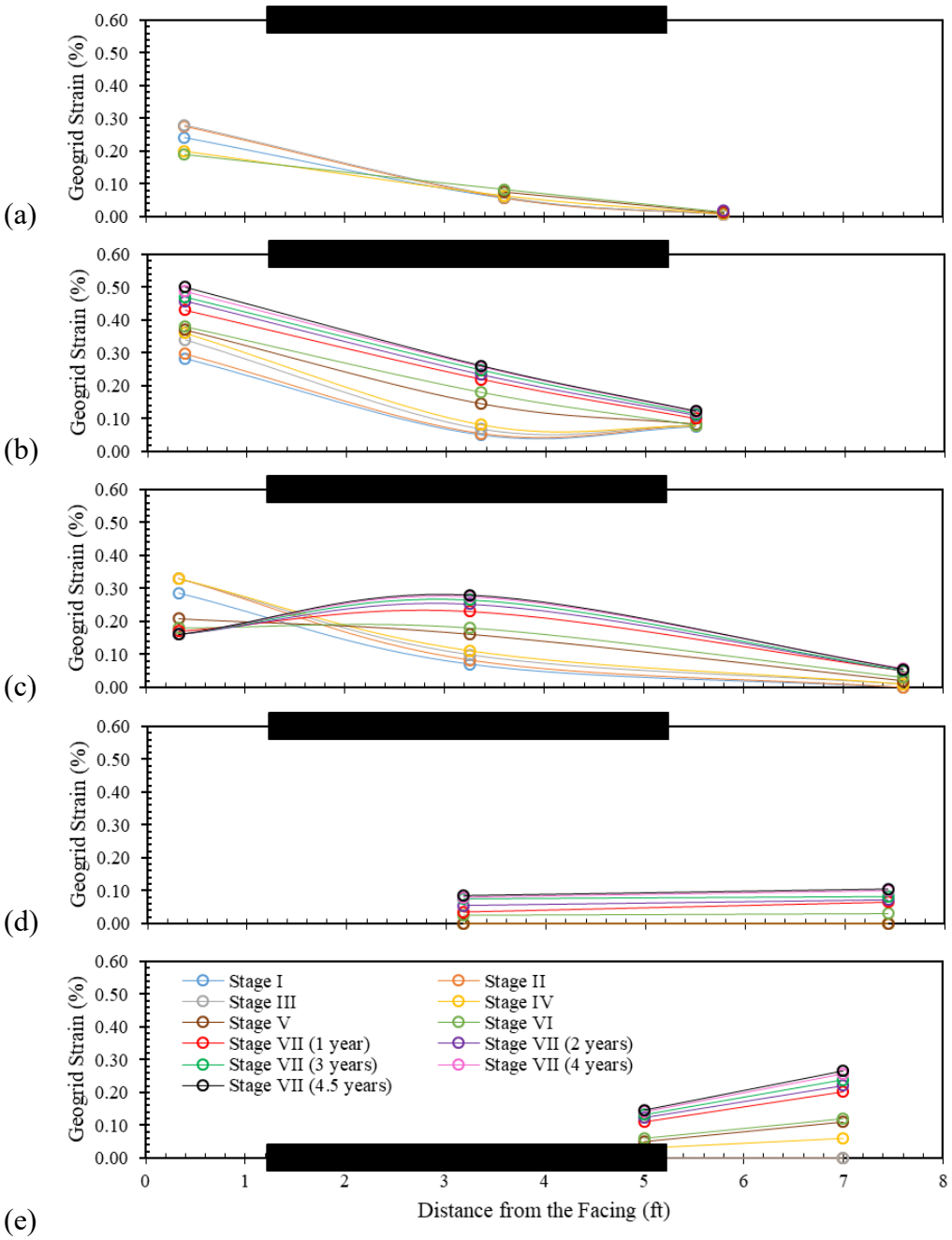

Figure 6.20. Measured reinforcement strain across the front GRS structure: (a) at reinforcement layer 2; (b) at reinforcement layer 6; (c) at reinforcement layer 10; (d) at reinforcement layer 13; and (e) at reinforcement layer 16.

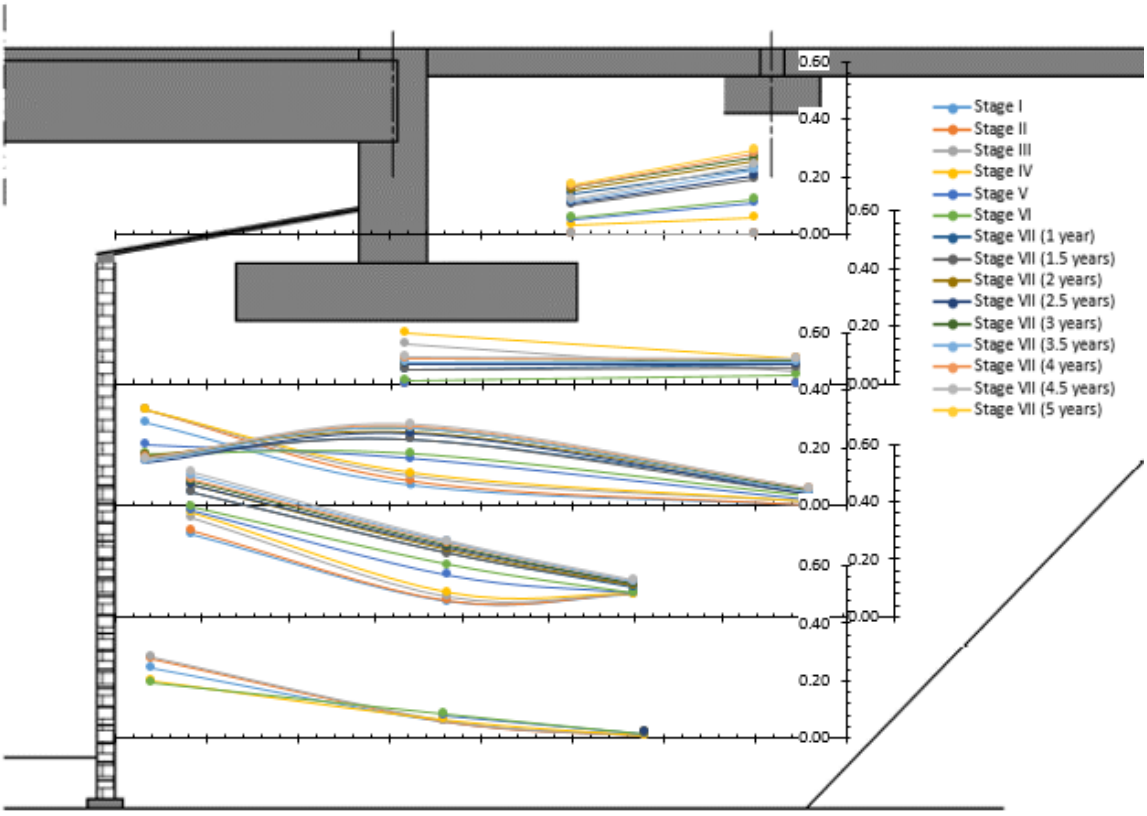

Figure 6.20. Measured reinforcement strain across the front GRS structure (consolidated figure).

It was observed from the time history of the strain gauges that the rate of strain increase during the cold seasons was higher than that in the warm seasons. This effect was more pronounced at the top layers (strain gauges placed at Layers 12 and 16), which are close to the surface and more susceptible to temperature changes as discussed earlier. This caused apparent strain fluctuation of approximately 0.05%. The readings from these gauges were corrected to negate the effect of temperature changes on the strain gauges.

Andraws and Yogarajah (1994) compared the stiff and flexible facing connections. They reported that the stiff connection causes a linear tensile strain distribution along the

reinforcement with maximum strains close to facing. In contrast, the flexible connection results in a maximum tensile strain far from the facing and results in a larger shear resistance mobilized in soil resulting in reduced lateral pressure on the facing units. This indicates that the behavior of the facing connections of the lower layers was more rigid than that of the upper layers. In addition, this explains why the vertical earth pressure behind the facing is higher at lower layers than that at upper layers. Also, Tatsuoka (1992) showed that the higher the connection strength, the higher the tensile stresses in the reinforcement near the facing. The distribution of the tensile stresses idealized by Tatsuoka (1992) for the no-connection strength showed that the stresses increase from the facing to the boundary of the unstable zone then decays towards the end of the reinforcement. On the other hand, the idealized distribution for the high-strength connection showed that the stresses is high over the entire unstable zone then decays towards the end of the reinforcement. The difference in the reinforcement strain distribution between Layer 10 and Layers 6 and 2 (see Figures 6.20a through 6.20c) implies that the facing connection near Layer 10 was weaker than that at Layers 6 and 2 with respect to their applied load. This is due to the higher lateral pressure at Layer 10 in comparison to Layer 6 (and most possibly Layer 2) as shown in Figure 6.18. It was observed that in maximum strain in Layer 10 was close to the facing during construction stages and then was shifted inwards. Similar observation was made by Bathrust et al. (2006) for segmental walls.

6.13. CONCLUSIONS

While the use of GRS abutments in supporting bridges has been recently recognized, their use is limited to the small low-traffic bridges due to the lack of understanding of their behavior. This study revisits the performance data of the

Founders/Meadows bridge case study, which is considered a major inspiration for the evolution of this technology in the United States of America. The study aimed at providing better understanding of the behavior of the GRS abutments. The evaluation of the data led to the following conclusions on the GRS bridge abutments:

- Down-drag forces generate on the back surface of the facing were found to result in an initial increase in the vertical earth pressure behind the facing in the early construction stages. This down-drag force is induced by the soil settlement behind the facing blocks dragging the reinforcement layers. These dragging forces pulls the facing units inwards and resulting in higher lateral earth pressure. The increase in lateral earth pressure near is the top is anticipated to exceed that near the bottom because the cumulative settlement magnitude near the top is larger than that near the bottom.
- Boussinesq (1885) earth pressure solution provides good estimation for the vertical pressure distribution except at shallow depths below the bridge bearing seat where loading rigidity is more pronounced. This is valid for GRS structures reinforced at a vertical spacing of 0.4 m (i.e., similar to Founders Meadows abutments).
- The GRS structure might be rigid during cold seasons and subsequent deformations occur mainly during warm seasons.
- The lateral earth pressure on the abutment facing is susceptible to seasonal temperature variation due to superstructure expansion and contraction.

- As construction advances and the load increases reinforcement layers strain allowing the facing to move. This results in a reduction in the vertical earth pressure behind the facing.
- The vertical earth pressure distribution showed no overturning potential as the overturning stresses redistribute due to the flexibility of the reinforced soil structure.
- A significant portion of the total reinforcement strains takes place during the backfill placement and compaction. This happens because of the locked-in strains where the soil particles are forced into the reinforcement apertures causing strains. These strains remain locked-in after the compaction ends.
- The compaction methodology, construction season, and construction sequence may affect the deformations occur to the structure.
- The behavior of the facing connections of the lower layers is more rigid than that of the upper layers.
- GRS bridge abutments are capable of eliminating the bumps at the ends of bridges by allowing even settlement for bridge superstructures and their approaching roadway structures.

6.14. REFERENCES

Abu-Hejleh, N., Wang, T., and Zornberg, J.G. (2000b). "Performance of Geosynthetic-reinforced Walls Supporting Bridge and Approaching Roadway Structures." Geotechnical Special Publication, pp. 218-243.

Abu-Hejleh, N., Zornberg, J.G., Elias, V., and Watcharamonthein, J. (2003). "Design Assessment of the Founders/Meadows GRS Abutment Structure." In Proceedings of the 82nd Annual TRB Meeting.

Abu-Hejleh, N., Zornberg, J.G., Wang, T., and McMullen, M. (2000a). Performance of Geosynthetic-Reinforced Walls Supporting the Founders/Meadows Bridge and Approaching Roadway Structures. Colorado Department of Transportation Report No. CDOT-DTD-R-2000-5.

Abu-Hejleh, N., Zornberg, J.G., Wang, T., and McMullen, M. (2001a). Performance of Geosynthetic-Reinforced Walls Supporting the Founders/Meadows Bridge and Approaching Roadway Structures. Colorado Department of Transportation Report No. CDOT-DTD-R-2001-13.

Abu-Hejleh, N., Zornberg, J. G., and Wang, T. (2001b). "Monitored Displacements of a Unique Geosynthetic-Reinforced Walls Supporting Bridge and Approaching Roadway Structures." In TRB annual meeting.

Abu-Hejleh, N., Zornberg, J.G., Wang, T., and Watcharamonthein, J. (2002). "Monitored Displacements of Unique Geosynthetic-reinforced Soil Bridge Abutments." Geosynthetics International, 9(1), 71-95.

Abu-Hejleh, N., Hanneman, D., White, D. J., Wang, T., and Ksouri, I. (2006). Flowfill and MSE Bridge Approaches: Performance, Coast, and Recommendations for Improvements. Colorado Department of Transportation Report No. CDOT-DTD-R-2006-2.

Adams, M. and Nicks, J. (2015). "Comparison of GMSE and GRS Design Methodology." In Proceedings of Geosynthetics 2015, February 15-18, Portland, Oregon.

Andrawes, K.Z., and Yogarajah, I. (1994). “Effects of Reinforcement Connections on the Behaviour of Reinforced Soil Retaining Walls.” Computer Methods and Advances in Geomechanics, Vol. 2, pp. 1313-1318.

Bathurst, R.J., Vlachopoulos, N., Walters, D.L., Burgess, P.G., and Allen, T.M. (2006). “The Influence of Facing Stiffness on the Performance of Two Geosynthetic Reinforced Soil Retaining Walls.” Canadian Geotechnical Journal, Vol. 43, No. 12, pp. 1225-1237.

Boussinesq, M.J. (1885). “Application des potentiels a l'etude de l'equilibre et du movement des solides elastiques, principalement au calculations des deformations et des pressions que produisent, dans ces solides, des efforts quelconques exerces sur une petite partie de leur surface ou de leur interieur: Memoire suivi de notes etendues sur divers points de physique mathematique et d'analyse,” GauthierVillars, Paris, pp. 722. (In French).

Buttry, K., McCullough, E., and Wetzel, R. (1996). “Temperatures and Related Behavior in Segmental Retaining Wall System.” Transportation Research Record: Journal of the Transportation Research Board, Vol. 1534, pp. 19-23.

CDOT (2014). Annual Average Daily Traffic. Colorado Department of Transportation.

Fakharian, K. and Attar, I.H. (2007). “Static and seismic numerical modeling of geosynthetic-reinforced soil segmental bridge abutments.” Geosynthetics International, 14(4), 228-243.

Hatami, K., and Bathurst, R.J. (2006). “Numerical Model for Reinforced Soil Segmental Walls under Surcharge Loading.” Journal of Geotechnical and Geoenvironmental engineering. Vol. 132, No. 6, pp. 673-684.

Helwany, S. M., Wu, J.T., and Froessl, B. (2003). "GRS Bridge Abutments—An Effective Means to Alleviate Bridge Approach Settlement." Geotextiles and Geomembranes, Vol. 21, No. 3, pp. 177-196.

Ingold, T.S. (1979). "The Effects of Compaction on Retaining Walls." Geotechnique, Vol. 29, No. 3, pp. 265-283.

Kongkitkul, W., Hirakawa, D., Sugimoto, T., Kawahata, S., Yoshida, T., Ito, S., and Tatsuoka, F. (2008). "Post-construction Time History of Tensile Force in the Geogrid Arranged in a Full-Scale High Wall." Proceedings of 4th GeoSynthetics Asia, Shanghai, pp. 64-69.

Lee, K.Z., and Wu, J.T. (2004). "A Synthesis of Case Histories on GRS Bridge-supporting Structures with Flexible Facing." Geotextiles and Geomembranes, Vol. 22, No. 4, pp. 181-204.

McGown, A., Andrawes, K.Z., Pradhan, S., and Khan, A.J. (1998). "Limit State Design of Geosynthetic Reinforced Soil Structures." Proceedings of the 6th International Conference on Geosynthetics, pp. 144-179.

NAVFAC (1986). Foundations and Earth Structures. Design Manual DM-7.02. Naval Facilities Engineering Command.

Rankine, W. (1857). "On the Stability of Loose Earth." Philosophical Transactions of the Royal Society of London, Vol. 147.

Scott, R.F. (1963). "Principles of Soil Mechanics." Addison Wesley, Reading, Mass, 550p.

Tatsuoka, F. (1992). "Roles of facing rigidity in soil reinforcing." Keynote Lecture, Proceedings of Earth Reinforcement Practice, IS-Kyushu '92, Ochiai et al. eds., Vol. 2, pp. 831−870.

Xiao, C., Han, J., and Zhang, Z. (2016). “Experimental Study on Performance of Geosynthetic-reinforced Soil Model Walls on Rigid Foundations Subjected to Static Footing Loading.” Geotextiles and Geomembranes, Vol. 44, No. 1, pp. 81-94.

Zheng, Y., Fox, P.J., and Shing, P.B. (2015). “Verification of Numerical Model for Static Analysis of Geosynthetic Reinforced Soil Bridge Abutments.” Proceedings Conference on Geosynthetics, pp. 152-160.

Zornberg, J.G., Abu-Hejleh, N., and Wang, T. (2001). “Geosynthetic-reinforced Soil Bridge Abutments.” Geotechnical Fabrics Report, Vol. 19, No. 2, pp. 52-55.

Zornberg, J.G. (2015). “Performance of a Geosynthetic-reinforced Bridge Abutment in the US.” Proceedings of the 2nd International GSI-Asia Geosynthetics Conference (GSI-Asia 2015), Seoul, Korea (Rep.), June 24-26, 2015.

SECTION II: EVALUATION OF SOIL-REINFORCEMENT COMPOSITE INTERACTION AND SHEAR BAND CHARACTERIZATION

The main objectives of the experimental component of this research included in Section II are to (1) design a novel experimental equipment that features the soil-reinforcement interaction experimental aspects suitable to properly characterize the interaction between soil and multiple reinforcement layers, and (2) implement a testing program that aimed at assessing the soil-reinforcement interaction that identifies and quantifies possible benefits of closely-spaced reinforcement. A detailed description is provided of a new testing equipment designed to comprehensively assess soil-reinforcement interaction under both working stress and failure conditions. The new equipment aims at assessing the mechanical behavior of a GRS mass considering variable reinforcement spacing. In addition, it allows investigation of the interface shear stress transfer mechanisms as well as direct visualization of the kinematic response of soil particles adjacent to reinforcement layers.

The equipment was extensively instrumented to allow: (1) evaluating of the effect of the shear stress generated at soil-reinforcement interfaces of one reinforcement layer on the neighboring reinforcement layers, (2) mapping the pressure within the reinforced soil mass in order to assess local changes in normal pressure on the soil-reinforcement interface with increasing shear stresses, (3) mapping the straining of reinforcements, (4) characterizing the evolution of shear band in the vicinity of the soil-reinforcement interface, (5) quantifying the stiffness of the soil-reinforcement interface, (6) evaluating the unit tension in the reinforcement at working stress and ultimate stress levels, (7) assessing the unconfined tensile properties of the tested reinforcement specimen

corresponding to every soil-reinforcement interaction test, (8) assessing the dilatancy in the reinforced soil mass upon shear stress mobilization at the soil-reinforcement interface when volume changes are allowed, and (9) assessing the pressure within the reinforced soil mass induced by shearing at the soil-reinforcement interface when dilation is restricted.

This section includes three chapters:

- Chapter 7: Experimental Material Identification
- Chapter 8: Development of Soil-Geosynthetic Composite Interaction Experimental Approach
- Chapter 9: Parametric Evaluation of Soil-Geosynthetic Composite Interaction

Chapter 7: Experimental Material Identification

7.1. INTRODUCTION

This chapter presents the properties of the materials used in the testing program of the experimental component of the study. Specifically, this chapter discusses the properties of the fill materials, reinforcements, and soil-reinforcement interface.

7.2. FILL MATERIALS

One baseline fill material was used in most of the tests conducted in this study. This material was selected to be a clean granular material that could be used in an air-dried condition to avoid the need to control the moisture content (and associated suction) that would be needed with the presence of fine materials. Specifically, to avoid the variability in the fill material properties that may result from the moisture condition. An additional granular material was used to evaluate the effect of grain size. The following sections describ the two materials used in the testing program.

7.2.1. General description

7.2.1.1.AASHTO Gravel No. 8

The baseline fill material used in most of the tests in this study was a washed river pea gravel deposited by the Colorado River near Austin, Texas. This material is a uniformly graded clean gravel that classifies as GP (poorly graded gravel) according to the Unified Soil Classification System (USCS) and classifies as A-1-a according to American Association of State Highway and Transportation Officials (AASHTO) classification (AASHTO M 145). The gravel gradation conforms to the standard range of AASHTO No. 8 grain size distribution. The material has sub-rounded to sub-angular particles and consists predominantly of quartz with traces of other minerals as shown in Figure 7.1a. The grain

size of this material ranges approximately from 1 to 13 mm with a mean grain size of 7 mm. The grain size distribution of the material used in this study and the AASHTO No.8 gradation bounds are presented in Figure 7.2.

7.2.1.2.Monterey Sand No. 30

Monterey Sand No. 30 was used in one soil-geosynthetic interaction test for comparison purposes to evaluate the effect of medium grain size on the soil-reinforcement composite behavior. This soil was procured from a quarry near Monterey, California. Monterey Sand No. 30 is uniformly graded clean sand classified as SP (poorly graded) according to the Unified Soil Classification System (USCS). This sand has rounded to sub-rounded particles and consists predominantly of quartz with a trace of feldspars and other minerals as shown in Figure 7.1b. The grain size of this Monterey Sand No. 30 ranges from 0.2 to 2 mm with a mean grain size of 0.7 mm; the grain size distribution is presented in Figure 7.2.

(a) (b)

Figure 7.1. Close up on the fill materials: (a) AASHTO Gravel No. 8; and (b) Monterey Sand No. 30.

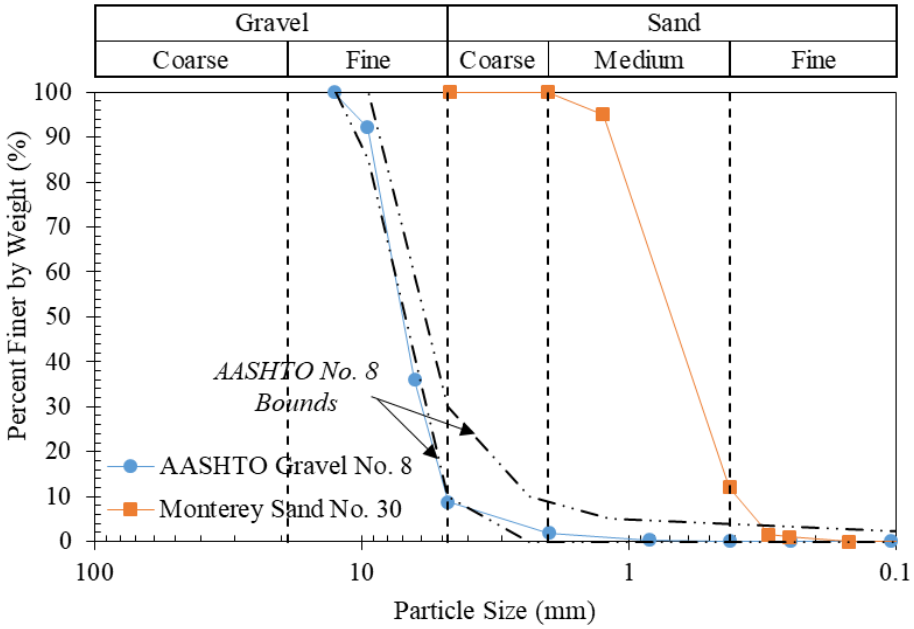

Figure 7.2. Grain size distribution of the soils used in this study.

7.2.2. Index properties

7.2.2.1.AASHTO Gravel No. 8

The coefficients of uniformity and curvature for AASHTO Gravel No. 8 are 1.6 and 0.9, respectively. Its specific gravity is 2.62 (ASTM D854) and its maximum and minimum void ratios are 0.73 and 0.50, respectively. The corresponding maximum and minimum dry unit weight values are 15.14 and 17.47 kN/m^3, respectively. These values were determined in accordance to ASTM D4253 and ASTM D4254, respectively. The backfill material was placed in 75-mm (3-in.) thick lifts and was gently hand tamped until reaching relative density of 70%, which corresponds to a dry unit weight of 16.67 kN/m^3 and a void ratio of 0.57.

7.2.2.2.Monterey Sand No. 30

The coefficients of uniformity and curvature for Monterey Sand No. 30 are 1.9 and 1.3, respectively. Its specific gravity is 2.65 (ASTM D854) and its maximum and minimum void ratios are 0.76 and 0.56, respectively. The corresponding maximum and minimum dry unit weight values are 14.76 and 16.70 kN/m^3, respectively. These values were determined in accordance to ASTM D4253 and ASTM D4254, respectively. Note that the maximum and minimum void ratios for Monterey No. 20 sand were reported by Marachi et al. (1969) to be 0.78 and 0.57, respectively, and those for Monterey No. 0 sand were reported by Lade and Duncan (1973) to be 0.86 and 0.57, respectively. Monterey Sand No. 30 was placed and compacted in 75-mm (3-in.) thick lifts at a moisture content of 3.5% to a relative density of 70%, which corresponds to a dry unit weight of 16.05 kN/m^3 and a void ratio of 0.62. Samples were taken from the every lift during compaction and during soil removal after the end of the test to confirm the homogeneity of the moisture content within the reinforced soil mass.

7.2.3. Shear strength

7.2.3.1.AASHTO Gravel No. 8

The shear strength of the backfill used in this study was evaluated by conducting a set of triaxial tests on specimens 152.4 mm (6 in.) in diameter and 330.2 mm (13 in.) in height (Figure 7.3). Three tests were conducted at three different confining stress levels of 35, 70, and 105 kPa and a relative density of 70%. The stress-strain curves for the conducted tests are presented in Figure 7.4a. Figure 7.4b shows the shear strength envelope, where the peak friction angle was 36.9 degrees with y-intercept of 15.6 kPa for the range of confining stresses at which the specimens were tested. An isotropic compression test

was conducted using AASHTO Gravel No. 8 to evaluate the volumetric strain at increasing isotropic confining stress. Figure 7.5 shows the obtained relationship between the isotropic stress and the volumetric strain.

In addition to the triaxial tests, two large-scale direct shear tests were conducted on AASHTO Gravel No. 8 samples 510-mm (20-in.) long, 510-mm (20-in.) wide, and 200-mm (8-in.) deep. Figure 7.6 shows the direct shear testing equipment used to perform these tests. The tests were conducted under normal stresses of 24 and 52 kPa at the shear plane. The samples were also prepared at relative density of 70%. The stress-displacement curves for these tests are presented in Figure 7.7a. Figure 7.7b shows the shear strength envelope, where the peak friction angle identified as 30.9 degrees, which is lower than that obtained from the triaxial tests.

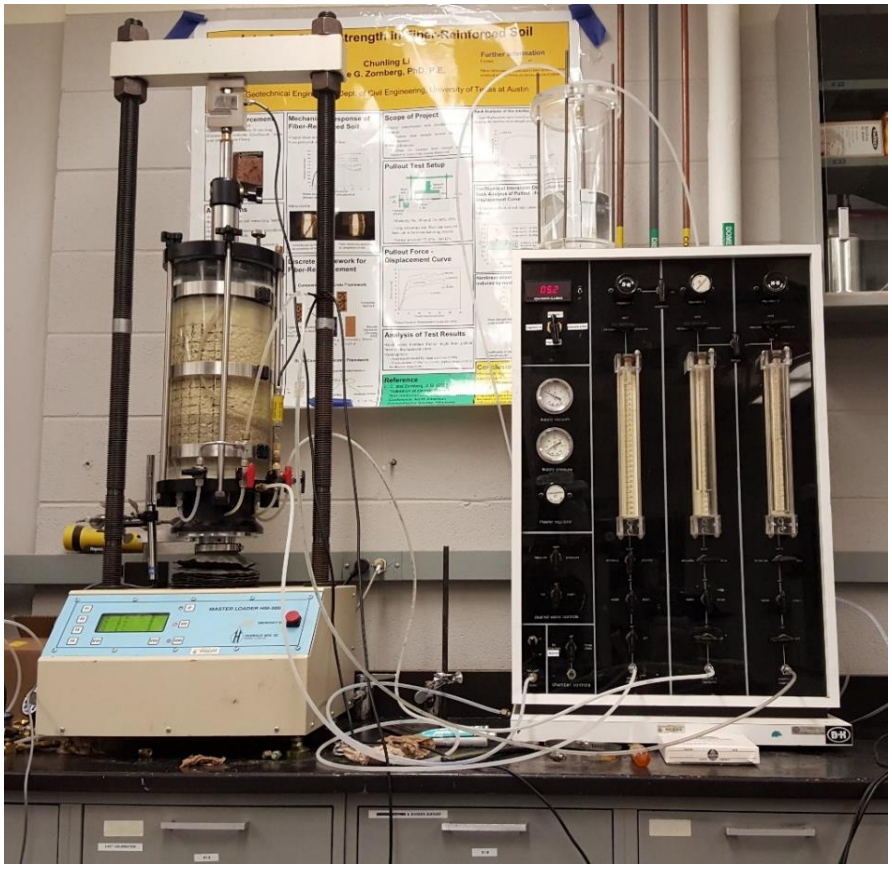

Figure 7.3. Triaxial setup.

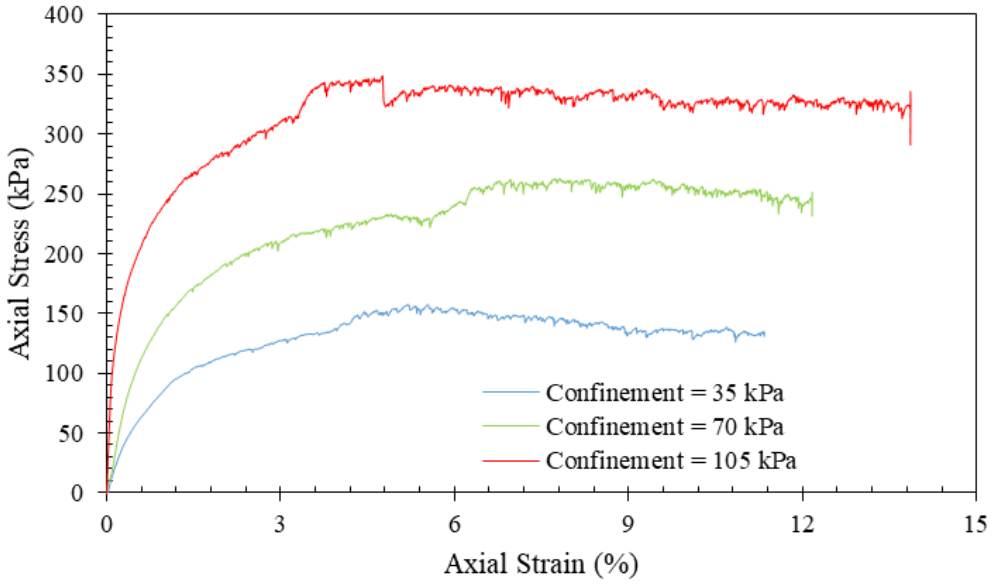

(a)

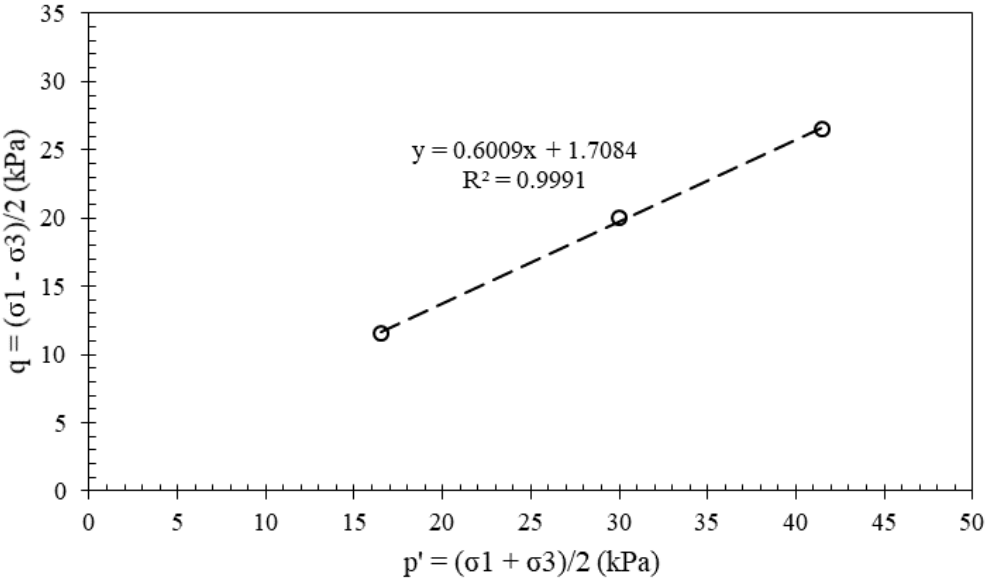

(b)

Figure 7.4. AASHTO Gravel No. 8 shear behavior from triaxial testing: (a) Shear stress-strain behavior; (b) Shear strength envelope.

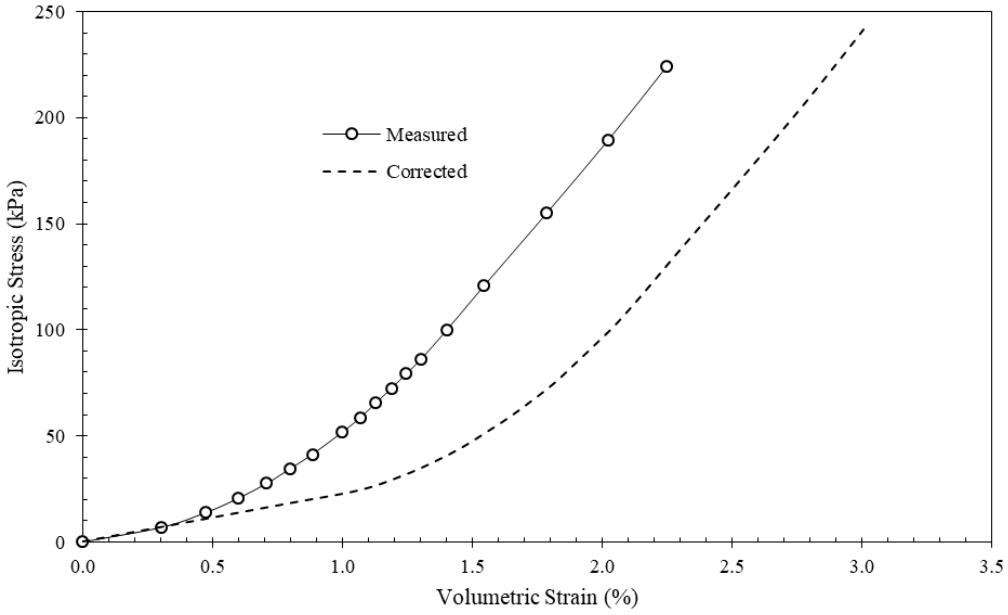

Figure 7.5. AASHTO Gravel No. 8 isotropic compression from triaxial testing.

Figure 7.6. Large-scale direct shear setup.

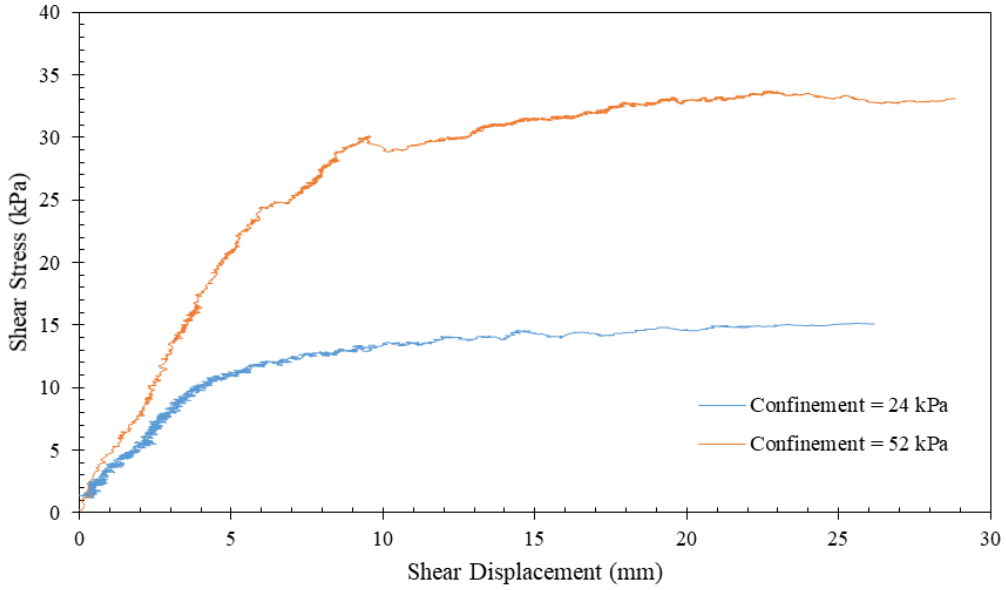

(a)

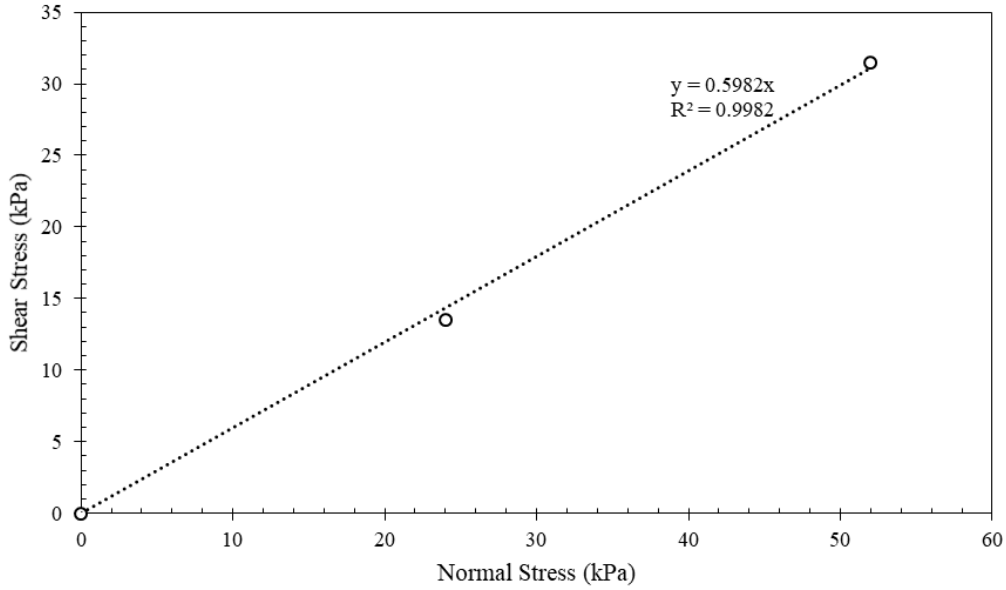

(b)

Figure 7.7. AASHTO Gravel No. 8 shear behavior from direct shear testing: (a) Shear stress-strain behavior; (b) Shear strength envelope.

7.2.3.2.Monterey Sand No. 30

The shear strength of Monterey Sand No. 30 used in this study was evaluated by a set of triaxial tests reported in Viratjandr (2000) and Li (2002). The stress-strain curves for the conducted tests are presented in Figure 7.8. Each study involved six tests that were conducted at three different confining stress levels and two relative densities. Figure 7.9 shows the peak friction angle at various relative densities for the same used in this study (Monterey Sand No. 30) reported in Viratjandr (2000), Li (2002), and Zornberg (2002). The report peak friction angle for Monterey Sand No. 30 at a relative density of 70% was estimated as 36.7 degrees.

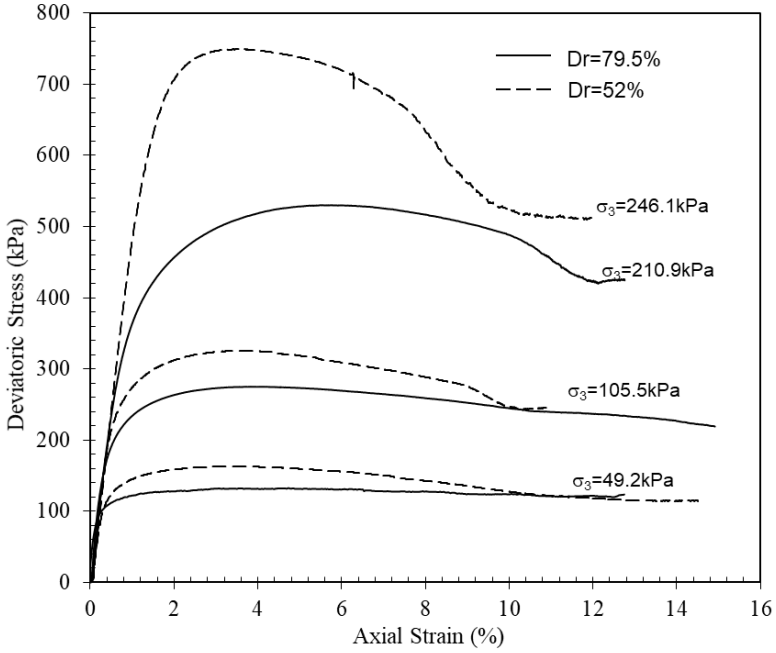

(a)

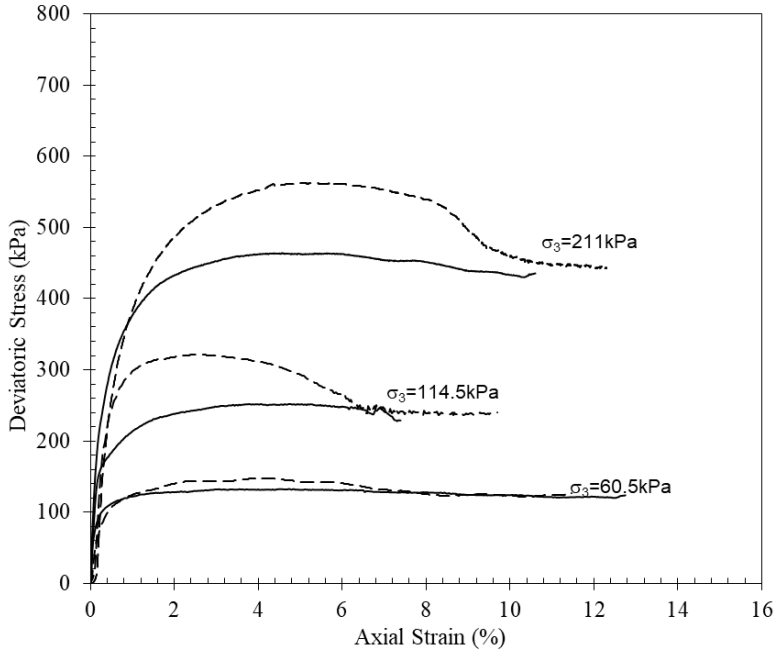

(b)

Figure 7.8. Stress-strain curves for Monterey Sand No. 30: (a) adapted from Viratjandr (2000); (b) adapted from Li (2002).

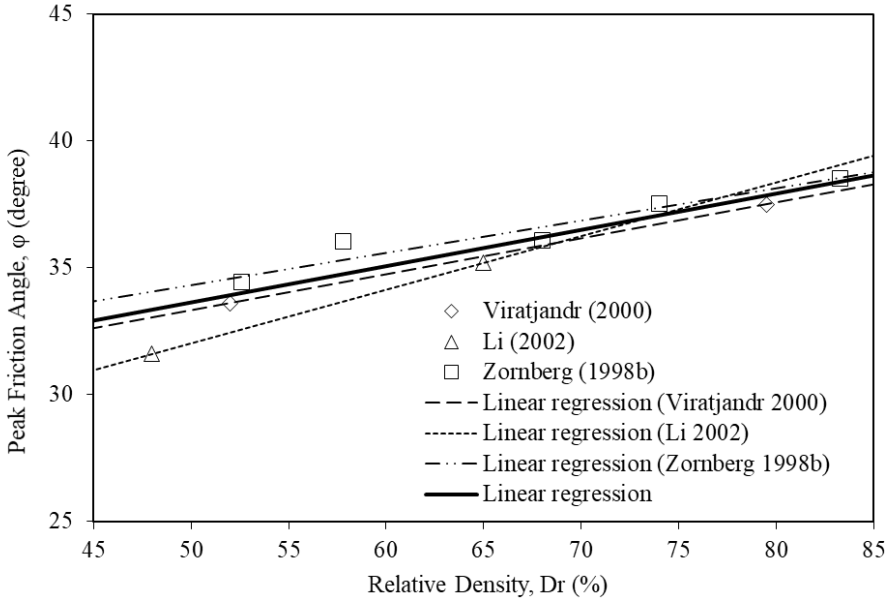

Figure 7.9. Peak friction angle for Monterey Sand No. 30 (adapted from Woodruff 2003).

7.3. REINFORCEMENT MATERIALS

Five geosynthetic reinforcement types were used in the soil-reinforcement interaction testing program conducted as part of this study: (1) HP570 woven polyester geotextile, which is the baseline reinforcement that was used in most of the tests. This specific reinforcement type was selected as the baseline because this material was extensively used in many GRS structures around the United States; (2) RS580i woven polyester geotextile; (3) BX1100 extruded (rigid) polypropylene geogrid; (4) BX1200 extruded (rigid) polypropylene geogrid; and (5) 80T knitted (flexible) polyester geogrid. The mechanical properties of the reinforcement materials in the direction where they were tested in the soil-geosynthetic interaction device are summarized in Table 7.1. Figure 7.10 shows the various reinforcement types, also showing the machine direction (rollway direction) for each reinforcement.

Table 7.1. Characteristics of the reinforcements used in this study.

Mechanical Properties	***HP570 (XMD[a])***	***RS580i (XMD[a])***	***BX1100 (XMD[a])***	***BX1200 (XMD[a])***	***80T (MD[b])***
T_{ult}[c] (kN/m)	70.0	70.0	19.0	28.8	89.6
$T_{@5\%}$[d] (kN/m)	39.4	70.0	13.4	19.6	45.7
J[e] (kN/m)	876	1400	268	392	914
Type	Woven Geotxtile	Woven Geotxtile	Extruded Biaxial Geogrid	Extruded Biaxial Geogrid	Knitted Uniaxial Geogrid
Material	Polyester	Polyester	Polypropylene	Polypropylene	Polyester

[a]XMD: Cross-machine direction (cross-rollway direction)
[b]MD: Machine direction (rollway direction)
[c]T_{ult}: Ultimate tensile strength
[d]$T_{@5\%}$: Tensile strength at 5% axial strain
[e]J: Approximate tensile stiffness defined as $J = T_{@5\%}/5\%$

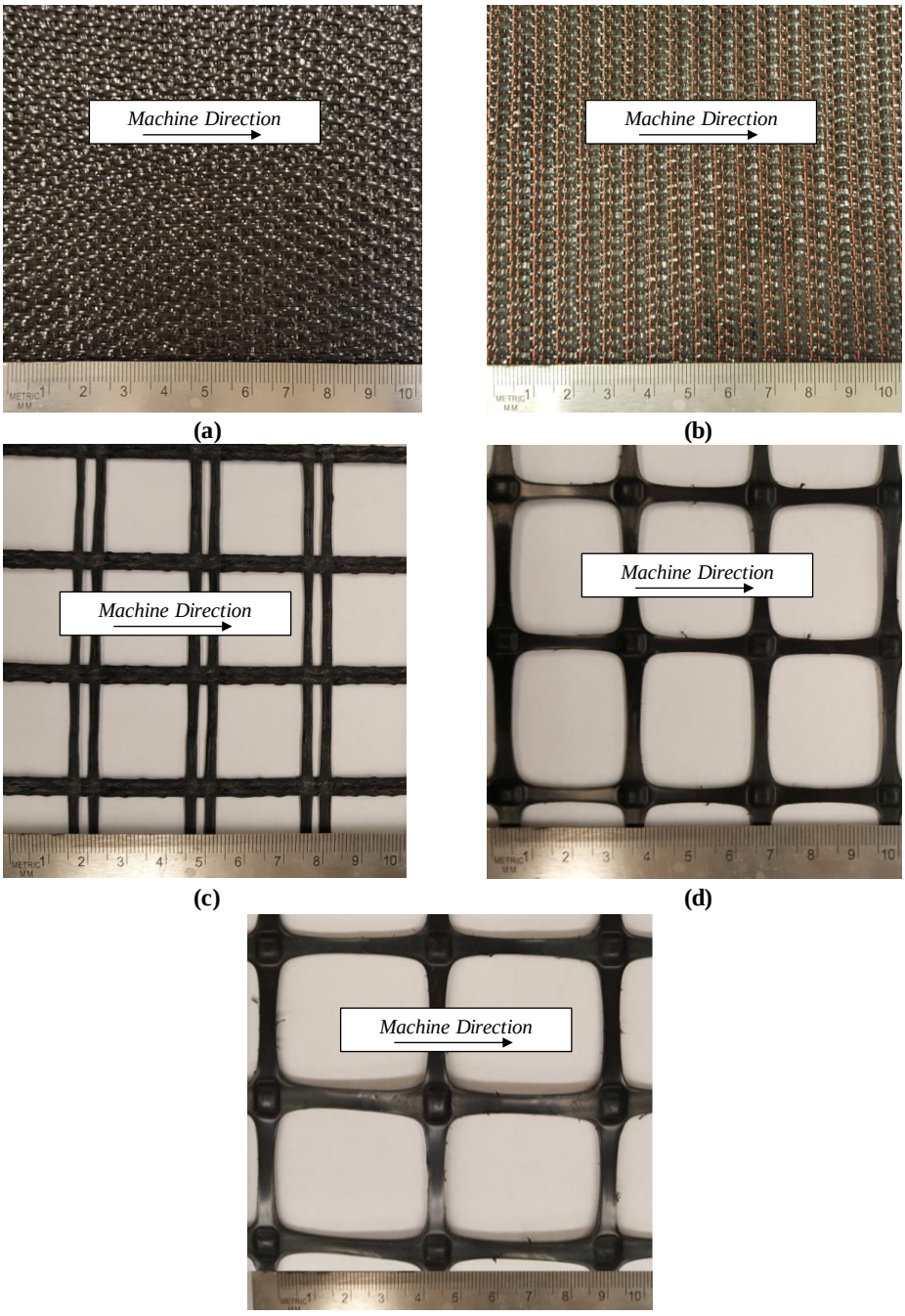

Figure 7.10. Photographs of the reinforcements used in this study: (a) HP570 geotextile; (b) RS580i geotextile; (c) 80T geogrid; (d) BX1100 geogrid; and (e) BX1200 geogrid.

7.4. SOIL-REINFORCEMENT INTERFACE

7.4.1. Description of the testing setup

A large-scale direct shear equipment originally designed to test large-sized soil samples with grain size up to 25 mm (Figure 7.6) was modified as a part of this study to evaluate the soil-reinforcement interface shear behavior. Two general criteria were required for testing soil samples in direct shear: (1) the width of the soil sample should be at least ten times larger than the maximum particle size (ASTM D 3080); and (2) the width-to-thickness (B/H) ratio of the specimen should be 2:1. The testing equipment used has a square shear box with interior dimensions of 510 mm in length, 510 mm in width, and 200 mm in height. The shear box consists of two halves with the bottom half being 125-mm high and 100-mm deep; while, the top half is 175-mm high in order to accommodate the normal pressure reaction frame shown in Figure 7.10a. The equipment has a reaction frame, as shown in Figure 7.10b, to allow application of the normal and shear forces. The frame is relatively stiff so that the machine deflection of the device was minimal during testing. The shear box is fixed at its bottom to a water reservoir (traveling cart).

Figures 7.11a and 7.11b show a schematic of the testing equipment before and after testing, respectively. During testing, the water reservoir was pulled by a large pneumatic actuator, which has a piston 305 mm in diameter and 125 mm in stroke length. The reservoir moves on four bearings and two linear guide rails, as shown in Figure 7.12. The bottom half of the shear box travels with the water reservoir monolithically during the test. The shear box halves slide over each other through two side v-rails and four v-grooved bearings. These v-rails allow a 3-mm gap between the two halves to eliminate friction. The 3-mm gap was selected so as not to allow soil particles to jam between the two box halves during testing.

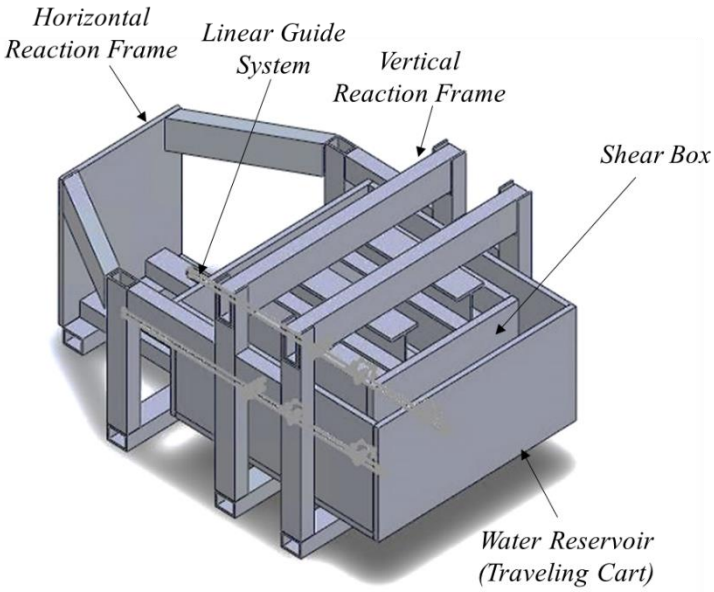

(a)

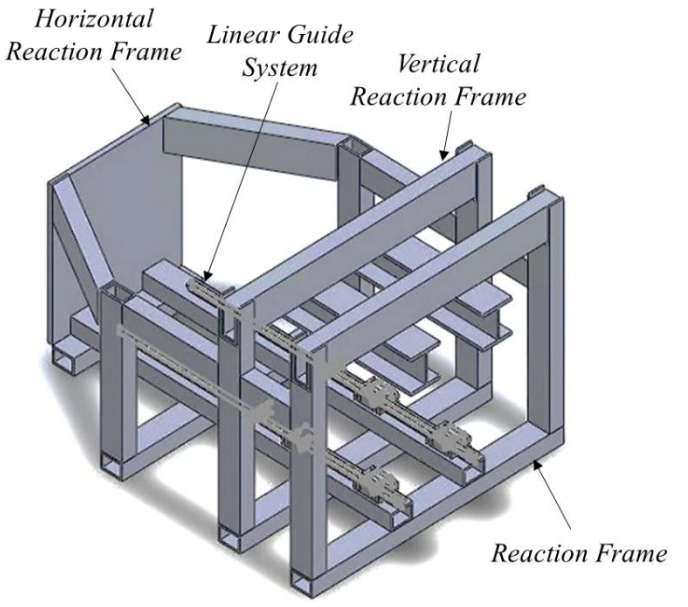

(b)

Figure 7.10. Schematic layout of the large-scale direct shear equipment: (a) shear box in the reaction frame (full assembly); (b) reaction frame.

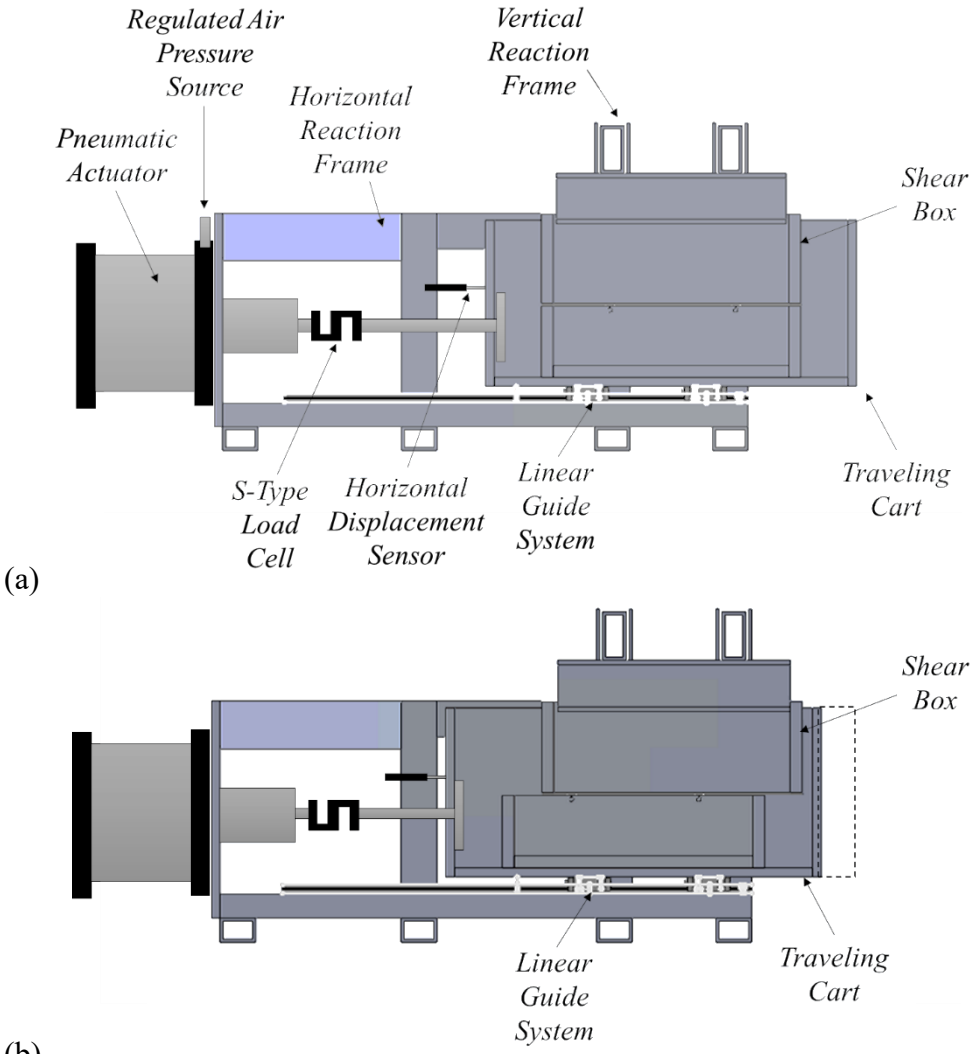

Figure 7.11. Schematic side view of the large-scale direct shear equipment: (a) before shearing; (b) after shearing.

Normal stresses are applied to the top of the specimen using an air pressure rubber bladder, which received a constant air pressure supply from a regulated air pressure line. The horizontal pneumatic actuator could be operated with pressures up to 1725 kPa and could deliver a horizontal shear force up to 120 kN. The equipment was used to conduct

displacement-controlled direct shear tests, where the shear force was applied by increasing air pressure to the actuator with an airflow control valve and constant inlet pressure.

For soil-reinforcement interface tests, the reinforcement layer was glued with heavy-duty epoxy to a smooth board that rested on hardwood located in the bottom half of the box. Figures 7.12a and 7.12b show schematic side and elevation views for the soil-reinforcement interface shear testing setup, respectively.

The vertical and horizontal displacements of the specimen were monitored by a system of three linear potentiometers: one to measure the horizontal displacements (relative displacement between the top and bottom box halves); and two to measure the vertical displacement at the front and rear sides of the test specimen. An S-type load cell was used to measure the applied horizontal shear force.

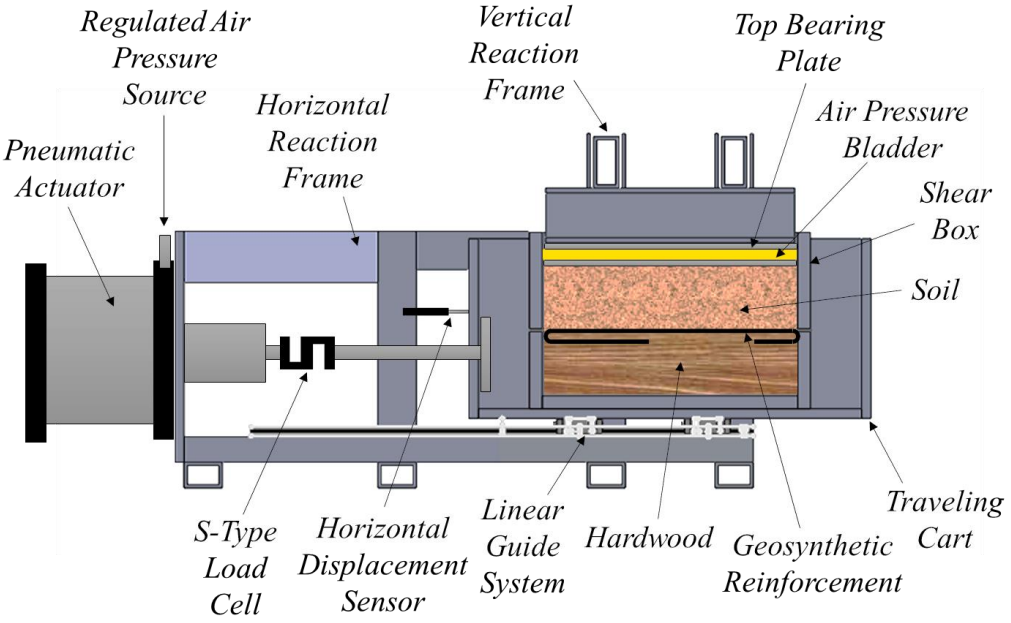

(a)

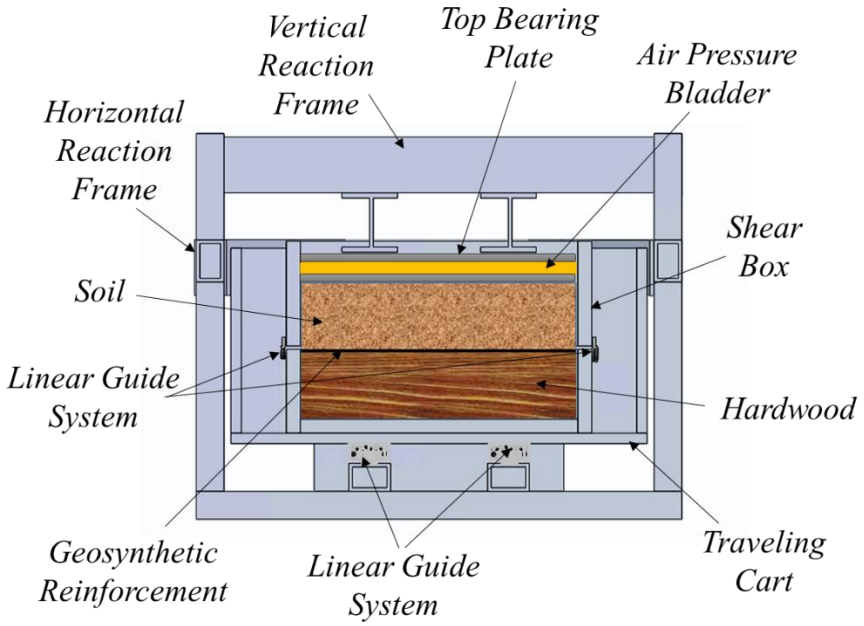

(b)

Figure 7.12. Schematic of the large-scale direct shear equipment in interface strength testing: (a) side view; (b) elevation view.

7.4.2. Testing program

An interface direct shear testing program was implemented to evaluate the interface shear behavior between the baseline fill material (AASHTO Gravel No. 8) and the baseline reinforcement type (HP570 geotextile). In addition, the interface shear behavior between AASHTO Gravel No. 8 and two smooth products was evaluated. Specifically, the interface behavior between the fill material and Mylar was evaluated to assess the use of Mylar sheeting as lining material for the interior walls of the box to minimize the boundary friction. The interface behavior between the fill material and Teflon was evaluated to compare to that between the fill material and Mylar. Note that Mylar is transparent and Teflon is opaque white. That is, Teflon cannot be used to line transparent walls. Table 7.2 summarizes the characteristics of the tests conducted in this testing program.

Table 7.2. Scope of the interface shear testing program.

Test Series	*Theme*	*Fill Material*	*Normal Stress (kPa)*	*Geosynthetic Type*
A	Interface Friction	AASHTO Gravel No. 8	24 38 52	HP570
B	Boundary Friction	AASHTO Gravel No. 8	24 38 52	Mylar
C	Boundary Friction	AASHTO Gravel No. 8	24 38 52	Teflon

7.4.3. Testing procedure

A series of displacement-controlled direct shear tests was performed on compacted gravel specimens with an applied normal stress ranging from 24 to 52 kPa. The two halves of the shear box were aligned and connected together by clamping screws before specimen

compaction. The geosynthetic reinforcement was glued to a smooth board using a heavy-duty epoxy. In case of the HP570 woven geotextile, the reinforcement specimen was glued such that the cross-rollway direction (corss-machine direction) was oriented towards the shear direction (same direction as in the soil-reinforcement interaction tests). The reinforcement was placed such that its plane was at the elevation of the shear plane (mid-height of the 3-mm gap between the two box halves), as shown in Figure 7.12. The 127-mm (5-in.) high soil specimen (in the upper half of the box) was compacted in two 63.5-mm (2.5-in.) thick lifts. All four consecutive layers were compacted using a hand tamper to to a unit weight of 16.67 kN/m^3.

After soil was placed, a top plate was placed on top of the sample, followed by an air bladder backed with a bearing plate (on top of the bladder), as shown in Figure 7.12. Two vertical linear potentiometers were positioned with their tips seating on two cantilever plates extending from the top plate (underneath the bladder) outside the shear box. These potentiometers allowed measurement of vertical displacements of the top surface of the sample (i.e., compression or dilation) during shearing. The relative horizontal displacement between the box halves during shearing (shear displacement) was measured by a linear potentiometer mounted on the water reservoir (traveling cart).

After assemblage, the normal stress was applied and the aligning screws connecting the two box halves were removed. The relative horizontal displacement between the two halves of the specimen, the vertical movements at the top of the specimen, and the applied horizontal shear force were recorded simultaneously during shearing.

7.4.4. Interface shear strength

Figures 7.13a and 7.13b present the interface shear stress-displacement behavior and interface shear strength envelope, respectively, from the tests conducted with AASHTO Gravel No. 8 and HP570 woven geotextile. The interface friction angle was identified to be 30 deg with zero y-intercept. Similarly, Figures 7.14a and 7.14b present the interface shear behavior and strength envelope, respectively, for the tests conducted with AASHTO Gravel No. 8 and Mylar. The peak interface friction angle obtained between AASHTO Gravel No. 8 and Mylar was 5.1 degrees. However, it can be observed from the results shown in Figure 7.14a that the effect of the normal stress magnitude on the interface shear strength against Mylar is negligible before yielding. Also, this displacement magnitude corresponding to yielding was never reached in the tests conducted in this study as will be presented later in Chapters 8 and 9 (Section II). Figure 7.14b shows the shear strength envelope at the yielding, which confirms that the effect of the normal stress on the interface behavior is negligible. Figures 7.15a and 7.15b present the interface shear behavior and shear strength envelope, respectively, for the tests conducted with AASHTO Gravel No. 8 and Teflon. The measured peak interface friction angle was 8.1 degrees, which is higher than that measured for Mylar. Unlike Mylar, the interface behavior involving Teflon was found to depend on the selected normal stresses.

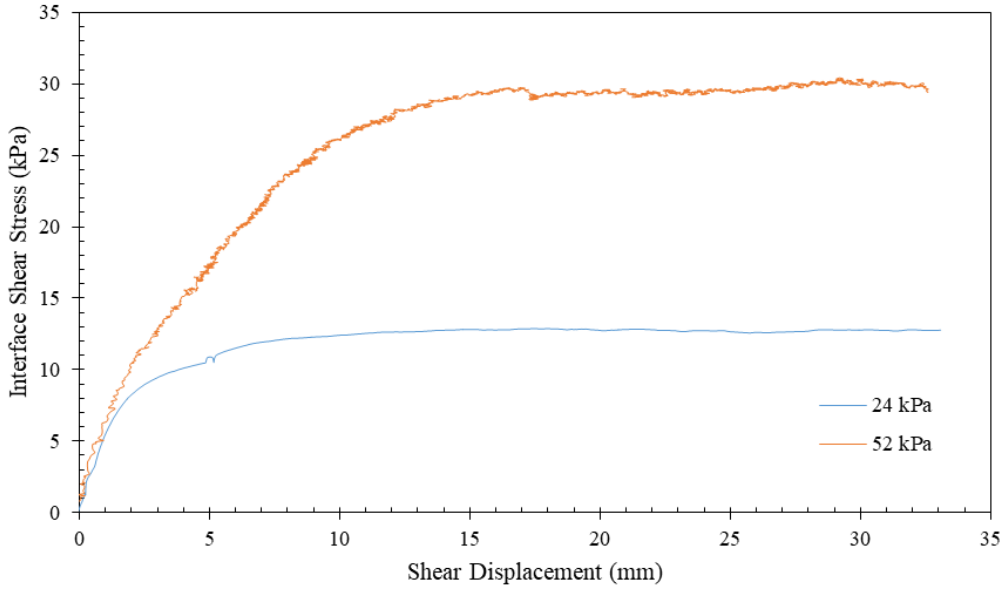

(a)

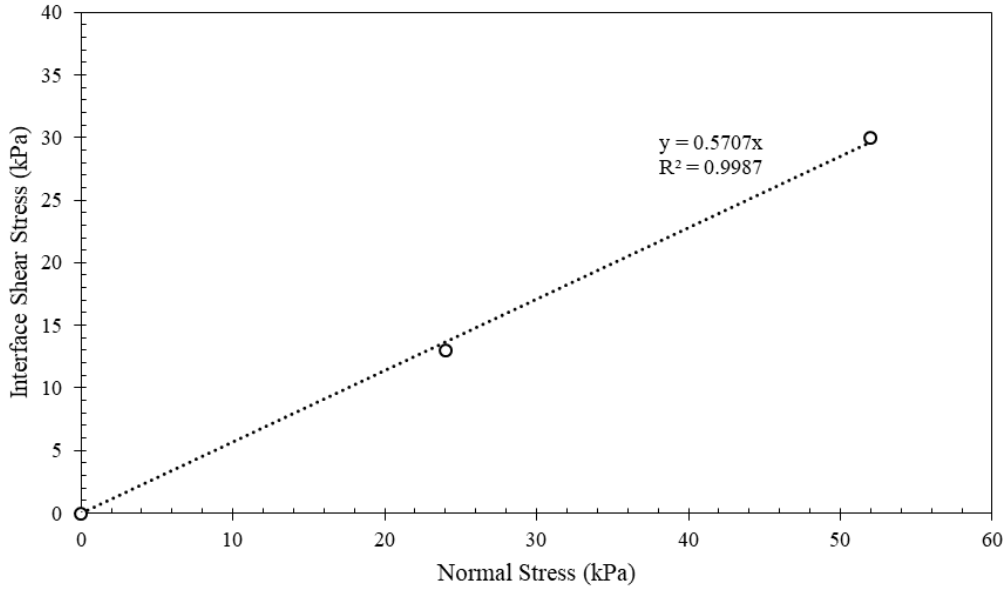

(b)

Figure 7.13. AASHTO Gravel No.8 against HP570 interface shear behavior from direct shear testing: (a) Interface shear stress-strain behavior; (b) Interface shear strength envelope.

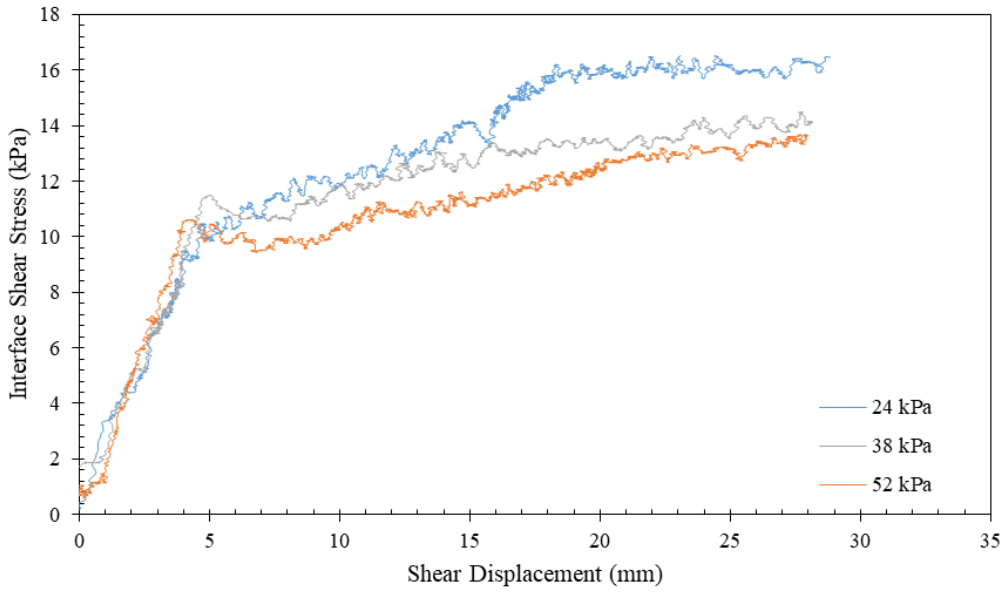

(a)

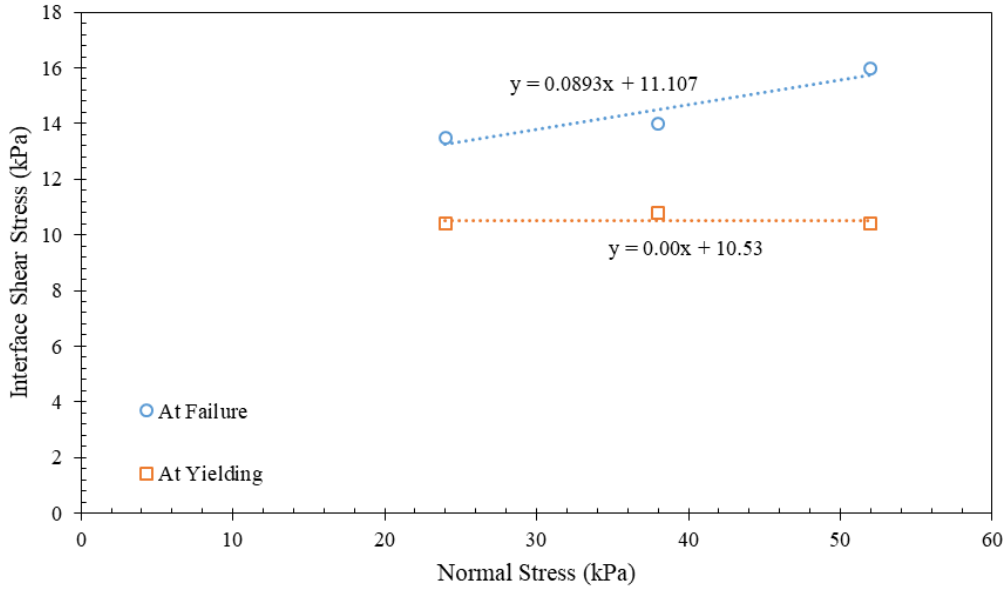

(b)

Figure 7.14. AASHTO Gravel No.8 against Mylar interface shear behavior from direct shear testing: (a) Interface shear stress-strain behavior; (b) Interface shear strength envelope.

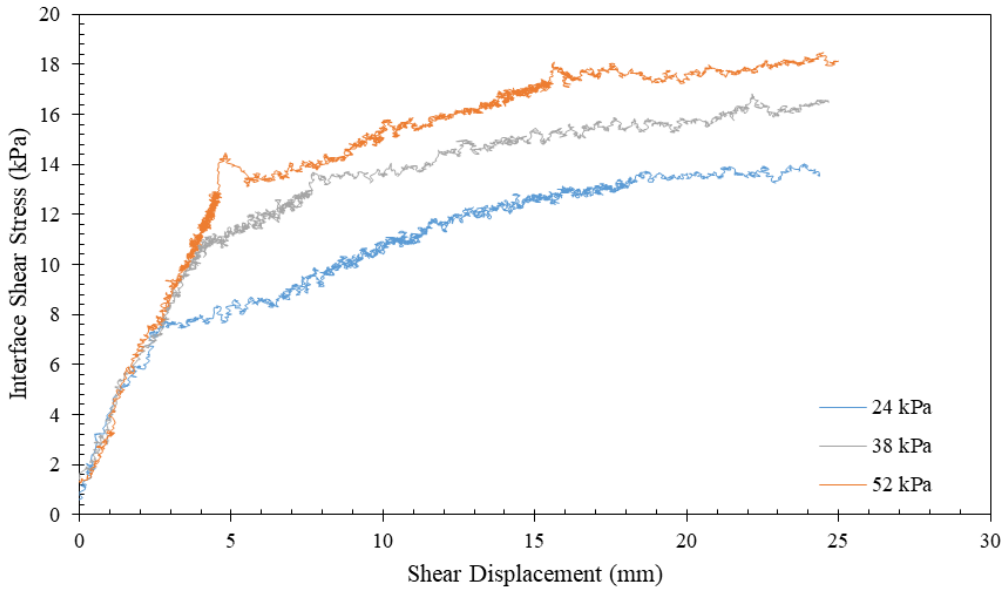

(a)

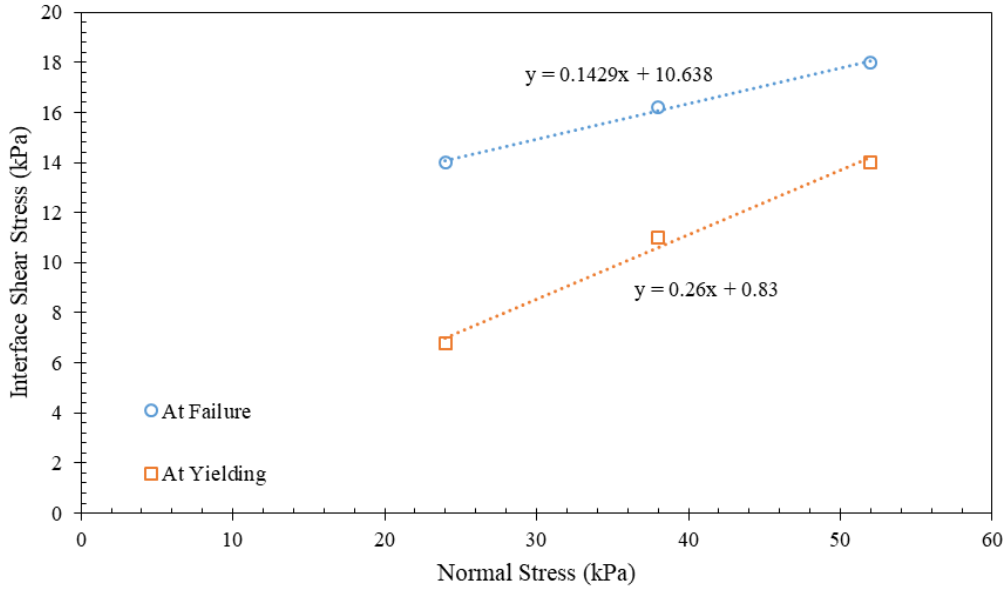

(b)

Figure 7.15. AASHTO Gravel No.8 against Teflon interface shear behavior from direct shear testing: (a) Interface shear stress-strain behavior; (b) Interface shear strength envelope.

7.5. CONCLUSIONS

This chapter presented the properties of the materials used in the testing program of Section II of this dissertation. Specifically, this chapter discussed the properties of the fill materials, reinforcements, and soil-reinforcement interface. The study in this chapter led to the following findings:

- The peak interface friction angle for AASHTO Gravel No. 8 and HP570 woven geotextile was 30 degrees.
- The peak interface friction angle for AASHTO Gravel No. 8 and Mylar sheeting was 5.1 degrees.
- No effect for the normal stress magnitude on the interface shear strength against Mylar up to the yielding stage for the normal stress range used in testing (24 to 52 kPa).
- Mylar sheeting is a great option for lining equipment to minimize boundary friction, especially for transparent surfaces that are used to provide direct visualization.
- The peak interface friction angle for AASHTO Gravel No. 8 and Teflon sheeting was 8.1 degrees (higher than that measured for Mylar).
- Unlike Mylar, the interface behavior involving Teflon was found to depend on the selected normal stresses.

7.6. REFERENCES

AASHTO, M. (2008). 145-91. Classification of soil and soil-aggregate mixtures for highway construction purposes, American Association of State Highway and Transportation Officials.

ASTM D3080–03 (2003). Standard Test Method for Direct Shear Test of Soils Under Consolidated Drained Conditions. Annual Book of ASTM Standards, ASTM.

Lade, P.V. and Duncan, J.M. (1973). "Cubical triaxial tests on cohesionless soil." Journal of Soil Mechanics and Foundations, Division of American Society of Civil Engineers, Vol. 99, No. 10, pp. 793-811.

Li, C. (2002). Experimental studies on fiber-reinforced soil University of Colorado. Research Report, University of Colorado, Boulder, Colorado, USA.

Marachi, N.D., Chan, C.K., Seed, H.B., and Duncan, J.M. (1969). Strength and Deformation Characteristics of Rockfill Materials. University of California Report TE-69-5, Berkeley, California, USA.

Viratjandre, C. (2000). "Shear strength of tire shred sand mixture." Master of Philosophy Thesis, University of Colorado, Boulder, Colorado, USA.

Woodruff, R. (2003). Centrifuge modeling for MSE-shoring composite walls. MS Thesis, University of Colorado, Boulder, CO, USA.

Zornberg, J. G. (2002). "Peak versus Residual Shear Strength in Geosynthetic-reinforced Soil Design." Geosynthetics International, Vol. 9, No. 4, pp. 301-318.

Chapter 8: Development of Soil-Geosynthetic Composite Interaction Experimental Approach

8.1. INTRODUCTION

The use of soil reinforcement has been widely recognized as an alternative in the design of many geotechnical systems. The interaction between the soil and reinforcement plays a key role in the load transfer forming a composite material that has the ability to resist the externally applied loads. The spacing between reinforcement layers governs the degree of interaction not only between the reinforcement layer and surrounding soil, but also between the soil-reinforcement interfaces of neighboring reinforcement layers. This complex interaction may play a key role in the overall mechanical response of the reinforced soil composite mass. Reinforcement spacing has been reported to have a greater effect on the reinforced soil composite behavior than that of the reinforcement tensile properties. This observation was reported as occurring in conditions where reinforcement spacing was small (e.g. Nicks et al. 2013; Morsy et al. 2017a, 2017b). However, the need remains for further understanding of the mechanisms and extent of such effect.

This study presents a new experimental approach to assess the behavior of reinforced soil structures. This evaluation includes: (1) a review of the soil-reinforcement interaction experimental modeling of reinforced soil structures based on reinforcement pullout equipment; (2) a description of newly developed testing approach and equipment used in soil-reinforcement interaction behavior assessment; and (3) a description of the experimental testing procedure implemented; and (4) typical testing results to illustrate the capabilities of the proposed testing approach.

8.2. REVIEW OF TECHNICAL LITERATURE

The interaction of geosynthetic reinforcements with the surrounding soil involves complex shear stress transfer mechanisms, the manifestation of which is a shear band that develops in the vicinity of the reinforcement (e.g. Palmeira 2009). Beyond this zone, the soil is no longer affected by the reinforcement. The thickness of this band may be affected by a number of factors, including the reinforcement tensile stiffness, the deformability and shear strength of the backfill material, and the characteristics of the soil-geosynthetic interface. A composite response is expected to result when the shear bands of two contiguous reinforcements interact with each other (Leshchinsky et al. 1994). Accordingly, the thickness of the shear band represents the limit beyond which the interaction between contiguous reinforcement layers no longer occurs. That is, the shear bands of closely-spaced reinforcements interfere with each other and change the interaction from a simple tie-back mechanism to a more complex, composite mechanism that may involve increased confinement, reduced lateral movements and reduced soil dilation (e.g. Adams et al. 2012).

This chapter includes a detailed literature review on pullout testing equipment, which is the device that served as basis for the development of the new equipment used in this investigation. This review focuses on the reported limitations of soil-geosynthetic interaction equipment (e.g. dimensions, materials, instrumentation) in order to benefit from the experience of other studies. While much of the focus in the evaluation of soil-reinforcement interaction corresponds to pre-failure conditions, pullout testing devices provide a good basis to a new setup to investigate the interaction behavior. Pullout tests have been proven to be suitable for different types of geosynthetics and soil types (ASTM D6706). The pullout resistance was found to be function of variables such as soil gradation, plasticity, relative compaction, moisture content, and geosynthetic characteristics (ASTM

D6706). Pullout tests involve embedding a geosynthetic within a soil mass and imposing axial loads to mobilize the different soil-geosynthetic interaction mechanisms. The soil mass is subjected to a normal pressure to reproduce state of stresses that is representative of the soil-reinforcement interface conditions in the field. Much of the previous research has been on different boundary effects, testing procedures, preparation methods, and compaction techniques (Juran et al. 1988; Farrag et al. 1993). The test was recently standardized in the latest revision of ASTM D6706 in a way to mimic the as-built conditions as closely as possible. The characteristics and limitations of pullout testing equipment, as reported in the technical literature, are summarized next.

8.2.1. Box dimensions

According to ASTM D6706, the length of a pullout box should exceed 600 mm, and should be larger than 5 times the maximum aperture size if a geogrid reinforcement is used. The width of the box should be larger than 750 mm in devices with rough side walls, and 450 mm in devices with smooth side walls. Also, the width should exceed 20 times the D_{85} of the soil and it should be at least 6 times the maximum soil particle size. The box depth should accommodate a soil layer with a thickness above and below the geosynthetic that exceeds 150 mm, and it should be at least six times the D_{85} of the soil and three times the maximum soil particle size. Ladeira (1995) developed a box measuring 1530 mm long by 1000 mm wide by 800 mm high, and demonstrated that these dimensions minimized lateral and horizontal boundary effects.

Considering the relevant literature on box dimensions, the soil-geosynthetic interaction device was designed having dimensions of 1500 mm (L) x 750 mm (W) x 1200 mm (H). The height was chosen to be 1200 mm to allow varying the vertical reinforcement

spacing up to 600 mm. The width of the equipment was chosen 750 mm to avoid any potential arching of the fill material with the side walls, especially when adopting the full-height configuration of the box and soils of relatively large-sized granules. The length of the equipment was chosen 1500 mm to reasonably fit the selected width. The aspect ratio of the device (length-to-width ratio) is particularly important to control the aspect ratio of the reinforcement specimens. Additional details are provided in Section 8.3 of this dissertation.

8.2.2. Reinforcement length

According to ASTM D6706, the reinforcement specimen length in pullout tests should extend 600 mm beyond the sleeve and measure at least twice the sample width (i.e., the length-to-width ratio should exceed two). Lopes and Ladeira (1996) investigated the effect of geogrid specimen length on pullout resistance and displacement at failure. They reported that the effect of the specimen length depended on the soil density. For dense sands, they reported that the pullout resistance decreased with increasing specimen length, whereas for loose sands, the pullout resistance increased with increasing specimen length. The decrease in pullout resistance observed for dense sands could be due to an increase in volumetric strain. This increase in strain resulted in an increase in the void ratio of dense sands, and thus increased the total reaction of the geogrid transverse ribs (Dyer 1985; Palmeira and Milligan 1989). Lopes and Ladeira (1996) defined an adherence factor as the ratio between the tangential stress at the soil-reinforcement interface to the product of normal stress at the interface and the tangent of the soil friction angle at the testing stress level. They reported a decrease in the adherence factor with increasing specimen length. However, they noted that the factor should have been greater than the values reported, as

the specimens failed because tension exceeded the tensile capacity, rather than because of a deficiency in adherence. Lopes (1992) demonstrated that the influence of specimen length on interface shear resistance was minimal beyond a certain length. However, Moraci and Recalcati (2006) reported that pullout behavior depended on specimen length. They indicated that the pullout interaction mechanism developed progressively along the length of the specimen, with a gradual increase in pullout resistance and displacement.

Considering the relevant literature on reinforcement dimensions, the reinforcement length and width in the soil-geosynthetic interaction device selected was 1000 and 750 mm, respectively (i.e., the length-to-width aspect ratio was 1.33). Additional details are provided in Section 8.3 of this dissertation.

8.2.3. Reinforcement width (influence of side boundaries)

According to ASTM D6706, there should be a clearance between the edge of the specimen and both side walls. This clearance should exceed 75 mm in devices with smooth side walls, and 150 mm in devices with rough side walls (ASTM D6706; Farrag et al. 1993). The width of the specimen should exceed 300 mm and include at least five tensile elements. The friction of the side walls was found to reduce the amount of the normal stresses applied at the soil-reinforcement interface (Farrag et al. 1993). Jewell (1980) recommended lining the side walls with lubricated membranes to minimize friction. Lopes and Ladeira (1996) studied the effect of specimen width on pullout resistance and did not observe a significant influence. However, the results showed a slight increase in pullout resistance and a slight decrease in the adherence factor with decreasing specimen width.

Considering the relevant literature on reinforcement width and the influence of side boundaries, the reinforcement width selected in the soil-geosynthetic interaction equipment

was the same as the box width (i.e., 750 mm). This was needed to allow the soil adjacent to the side walls to displace as the soil in middle. The box was lined with smooth material to minimize the firction of the side walls. Additional details on the selected reinforcement width are provided in Section 8.3 of this dissertation.

8.2.4. Soil thickness (influence of upper and lower boundaries)

ASTM D6706 requires that the box depth accommodate a soil thickness above and below the geosynthetic greater than 150 mm (6 in.), greater than 6 times the D_{85} of the soil, and greater than 3 times the maximum particle size of the soil (D_{max}). Interaction may develop between the upper and lower boundaries and the soil-reinforcement interface. Farrag et al. (1993) developed a box measuring 1520 mm (L) x 900 mm (W) x 760 mm (H). They reported that this interaction increased with decreasing soil thickness, and thus influenced the test results. They also reported the development of shear forces between the soil and the two horizontal boundaries (the bottom boundary in particular). Brand and Duffy (1987) studied the effect of the soil thickness on pullout resistance. Based on a limited number of tests, the authors observed that the pullout resistance decreased with increasing soil thickness, but only up to a certain value, beyond which there was no further change. Lopes and Ladeira (1996) showed that the predicted friction angle of the soil may increase beyond values measured using conventional techniques due to an increased normal pressure as a result of supressed soil dilatancy (Lopes and Ladeira 1996; Farrag et al. 1993). Lopes and Ladeira (1996) reported that the specimen length significantly affects the impact of the upper and lower boundaries on the test results. Palmeira and Milligan (1989) reported that increasing the ratio of specimen length to soil thickness led to greater influence of the pullout box upper and lower boundaries. Farrag et al. (1993) reported that

the soil thickness should exceed 300 mm both above and below the reinforcement layer to eliminate the effect of the horizontal boundaries (top and bottom box surfaces). Farrag et al. (1993), Ladeira (1995), and Lopes and Ladeira (1996) used a modular structured box to facilitate changes in soil thickness in various tests.

Considering the relevant literature on soil thicknkess and the influence of the horizontal upper and lower boundaries, the selected box height of the soil-geosynthtic interaction equipment was 225 mm and 600 mm in two different configurations. Additional details on the selected soil thicknesses are provided in Section 8.3 of this dissertation.

8.2.5. Sleeve length

According to ASTM D6706, the box should have a metal sleeve consisting of two thin plates less than 12.5 mm thick. Inside the box the sleeve should extend to a distance greater than 150 mm and preferably equal to the thickness of the soil above the geosynthetic. The interior sleeve end should be tapered to reach a maximum contact thickness of 3 mm. Palmeira and Milligan (1989) reported that interaction develops between the reinforced soil mass and the rigid front wall of the pullout box. They showed that this interaction increased with increasing friction along the front wall. During pullout tests, the lateral earth pressure developed on the front wall of the box increased, resulting in an increase in pullout resistance (Farrag et al. 1993). The sleeve allowed the pullout force application line to be transferred away from the soil adjacent to the front wall to the inner soil mass (Christopher 1993; Farrag et al. 1993). Williams and Houlihan (1987) used flexible front walls in an attempt to reduce the effect of rigid walls. Lopes and Ladeira (1996) investigated the effect of the sleeve on pullout resistance. They observed an increase of approximately 10% in the apparent pullout resistance in the absence of the sleeve. They

reported that the frictional stresses developed on the front wall of the box resulted in increased vertical stress acting on the reinforcement. Lateral pressure was measured in their study and in the absence of the sleeve, higher pressure on the front wall was observed during testing. This increased lateral pressure resulted in increased shear stresses developed at the soil-reinforcement interface at the front section of the specimen, and in decreased shear stresses developed at the back section of the specimen. They recommended using a 200 mm-long sleeve inside the box to reduce the frictional effects of the front wall boundary. Farrag et al. (1993) reported that a sleeve at least 30 cm long should be used to eliminate the front wall effect.

Considering the relevant literature on sleeve length, the sleeve in the soil-geosynthetic interaction device was designed to be 225-mm long with detachable cantilever to allow compaction of the soil underneath. Additional details about the designed sleeve are provided in Section 8.3 of this dissertation.

8.2.6. Reinforcement pullout loading system

The tensile axial force should be at the same level as the geosynthetic plane so as not to interfere with the soil-reinforcement shear surface (ASTM D6706). According to ASTM D6706, the pullout force should be applied at a constant displacement rate of 1 mm/min +/-10%. However, a constant stress loading approach can also be adopted. This approach could be achieved by three different methods. The first method involves a controlled stress rate, which simulates short-term conditions. In this method a uniform rate of loading is applied to a maximum value of 2 kN/m/min. The second method involves incremental stress, which is also suitable for short-term conditions. In this method, the pullout load is increased incrementally. The third method involves constant stress (creep),

which is suitable for evaluation of long-term conditions. In this method one of the two previous methods is adopted until the desired loading level is reached, and then constant stress is maintained for a period of time.

The pullout force has been reported to be applied using displacement rates ranging from 0.1 to 20 mm/min. The pullout force is typically applied at a controlled displacement rate (Farrag et al. 1993). However, some researchers have carried out pullout tests using load controlled systems (e.g. Tzong and Cheng-Kuang 1987). Farrag et al. (1993) also studied the effect of displacement rates on pullout resistance. They conducted tests using displacement rates of 2, 6, 10 and 20 mm/min, and concluded that high displacement rates affected the pullout force and displacement distribution. Specifically, it was reported that at high displacement rates, reinforcement strains were minimally mobilized, resulting in a higher contribution by the interface resistance than by the passive resistance of the transverse ribs. They recommended displacement rates below 6 mm/min to minimize the displacement rate effects. Fannin and Raju (1993) studied the influence of the pullout displacement rate on pullout resistance at low rate levels. They adopted displacement rates of 0.25, 0.50 and 1.00 mm/min. They reported that pullout resistance is independent of the pullout displacement rate at low rate values. Yet, their data showed a slight increase in pullout resistance with an increase in the displacement rate.

Considering the relevant literature, the pullout loading system for the soil-geosynthetic interaction device was designed to operate at constant displacement rates. The selected displacement rate was 0.15 mm/min. Additional details on the pullout loading system are provided in Section 8.3 of this dissertation.

8.2.7. Reinforcement clamping system

A clamp is used to attach the geosynthetic to the pulling system. The design should be such that the specimen is held without any slipping, breaking, or weakening due to stress concentrations. The clamp should ensure uniform load distribution along the width of the specimen so as not to interfere with the shear stress on the soil-reinforcement interface (ASTM D6706). The clamping system typically consists of two steel plates sandwiching the geosynthetic (Farrag et al. 1993; Stadler 2001). Roller grips have also been used to clamp geosynthetic specimens to pullout devices. Zornberg et al. (2009) used a roller grip consisting of a steel cylinder with a slit to which the specimen could be attached and bolted. Zornberg et al. (2009) reported that the roller grip design helped minimize stress concentration at a single plane throughout the specimen by distributing it uniformly over a wider area.

Considering the relevant literature, the clamping system of the soil-geosynthetic interaction equipment was designed with a roller grip lined with sandpaper and rubber edges to minimize reinforcement slippage, breakage, and weakening due to stress concentrations. Additional details on the design on the clamping system design are provided in Section 8.3 of this dissertation.

8.2.8. Unconfined reinforcement portion

Some studies reported clamping of the reinforcement outside the box, thus leaving a portion of the reinforcement unconfined outside the box (Koerner 1986; Brand and Duffy 1987; Stadler 2001; Zornberg et al. 2009). Other researchers have used clamps inside the sleeve to avoid having unconfined zones (e.g. Farrag et al. 1993; Ladeira 1995; Lopes and Ladeira 1996).

Considering the relevant literature, the clamping system of the soil-geosynthetic interaction equipment was designed to provide an unconfined reinforcement portion to allow evaluation of the unconfined tensile properties of the reinforcement specimens concurrently with their soil-geosynthetic interaction properties. Additional details are provided in Section 8.3 of this dissertation.

8.2.9. Normal stress loading system

Normal stress is applied to the top of the soil such that the soil-reinforcement interface reaches the target normal stress. The applied normal stress should be uniform and remain constant throughout the test. In order to maintain constant normal stress, ASTM D6706 recommends using a flexible pneumatic or hydraulic diaphragm-loading device that covers the entire area of the box. The normal stress has been commonly applied using an air-bag fixed to the interior top side of the box and covering the entire area to develop a constant uniform stress on top of the soil (Ingold 1983; Palmeira and Milligan 1989; Farrag et al. 1993). Lopes and Ladeira (1996) used a thick neoprene rubber layer and wooden plates to achieve uniform stress distribution on top of the soil. They applied normal stress to the wooden plates using 10 pressure cylinders. Zornberg et al. (2009) and Hanumasagar et al. (2014) used six air pressure cylinders jacking against a steel lid. Jayawickrama et al. (2014) utilized nine pressure plates hydraulically jacked against three wide flange cross beams.

Considering the relevant literature, the normal stress system was of the soil-geosynthetic interaction equipment was designed to include independent pneumatic actuators on wooden footings backed with neoprene rubber. This system was designed to allow measurement of vertical displacements (compression and dilation) of the reinforced

soil mass during shearing. Additional details on the design on the normal stress loading system design are provided in Section 8.3 of this dissertation.

8.2.10. Reinforcement straining measurements

To measure the internal displacements in reinforcement layers and assess their elongation along the specimen, inextensible wires are often attached to reinforcements at different locations. Attached to the other end of the inextensible wires are linear potentiometers (Lopes and Ladeira 1996; Zornberg et al. 2009), or LVDTs (ASTM D6706; Farrag et al. 1993), that are mounted outside the pullout box. Tubes have often been used to protect the wires from the normal pressure applied to the soil mass (ASTM D6706; Farrag et al. 1993). Movements that develop at different locations along the extensible reinforcement during pullout testing have been reported to involve two components: (1) displacement due to the shear strain of the soil-reinforcement interface; and (2) reinforcement elongation.

Considering the relevant literature, reinforcement displacements in the the soil-geosynthetic interaction tests were measured using tell-tales made of inextensilble music wires attached to reinforcements at various locations along their embedment lengths and connected to linear potentiometers. Special jackets were selected to protect the wires and minimize their interference with the surrounding soil. Additional details on the design of the tell-tales are provided in Section 8.3 of this dissertation.

8.2.11. Soil deformation measurements

Other research studies aimed at generally measuring internal displacements within the backfill. Some pullout testing devices have utilized transparent boundary surfaces to monitor soil grain trajectories (Fannin and Raju 1993; Leshchinsky et al. 1994; Zhou et al.

2012). Transparent boundaries were also used in a number of other devices that investigated soil-reinforcement interaction (Jacobs et al. 2002a, 2002b, 2003). These surfaces allow visualization of the kinematic response of soil particles in general, and those adjacent to the geosynthetic reinforcement layers in particular. In addition, Fannin and Raju (1993) used LVDTs on the top of a reinforced soil mass in pullout testing equipment, which allowed for the measurement of dilation.

Considering the relevant literature, the soil-geosynthetic interaction device was designed with a transparent side wall made of 25-mm (1-in.) thick acrylic sheet. This transparent wall allowed direct visualization of soil kinematics during testing. Additional details on the design of the transparent wall are provided in Section 8.3 of this dissertation.

8.2.12. Compaction and specimen preparation

During specimen preparation for a pullout test, the soil layers are placed and compacted in the box to its mid-height. The reinforcement specimen is then placed before placing the rest of the soil layers to the full height of the box. The required number of lifts and compaction effort depend on the type of the soil and the desired compaction moisture content (ASTM D6706). Farrag et al. (1993) and Lopes and Ladeira (1996) placed and compacted soil in 150-mm (6-in.) thick layers. Granular soils have also been placed in pullout boxes using pluviation techniques, which involve pouring from a constant height (Jewell 1980; Palmeira and Milligan 1989; Farrag et al. 1993; Min et al. 1995; Ochiai et al. 1996; Lopes and Ladeira 1996). Compaction has also been performed using electric vibratory hammers (Lopes and Ladeira 1996), electric jack hammers, standard proctor hammers (Saxena and Budiman 1985), mechanical compaction (Chang et al. 1977; Farrag et al. 1993; Alfaro et al. 1995a; Stadler 2001), and hand tamping (Elias 1979; Hanumasagar

et al. 2014). Relative density of the compacted layer has been verified using density gauges (Farrag et al. 1993; Lopes and Ladeira 1996), conducting sand cone tests (Stadler 2001), or weighing the box before and after soil placement (Alfaro et al. 1995a; Cuelho 1998).

Considering the relevant literature, the soil preparation and compaction method adopted in the tests conduced using the soil-geosynthetic interaction device was hand tamping. Additional information about the soil prepataion and compaction method used is provided in Section 8.3 of this dissertation.

Table 8.1 shows the characteristics of pullout equipment used in several studies along with the requirements documented by GRI GT6 (1991) and EN 13738 (2004).

Table 8.1. Reinforcement pullout test devices (Modified after Minažek and Mulabdić 2013).

Reference	Dimensions L (m) x W (m) x H (m)	Pullout force generation, with increase D – deformation (mm/min), N – stress (description)	Sleeve: exist (yes/no, description, width (cm))/clamping system (description)	Soil thickness bellow/above reinforcement (cm)	Force and displacement sensors	Compaction and density
Chang *et al.* (1977)	1.30 x 0.91 x 0.51	D	-	-	-	Mechanical compaction
Yuan and Chua (1985)	0.76 x 0.71 x 0.61	D (hydraulic)	-	30/30	Load cell, displacement transducers	-
Palmeira and Milligan (1989)	0.25 x 0.15 x 0.15 1.10 x 1.10 x 1.10	D (0.5 mm/min, hydraulic)	No (just opening in front box side) // clamps (connected with bolts and aluminum alloy to reinforcement)	-	Photo measurement of wires out of the box, 8 load cells on the front box side, LVDT – on the piston, load cell	Pluviation, vibrocompactor, cylinders in the box
Farrag *et al.* (1993)	1.52 x 0.90 x 0.76	D, N (max 6 mm/min, hydraulic)	Yes (width 30 cm) // clamps (plates inside sleeve and soil)	Min. 30/30	LVDT, velocity transducers and load cells, pressure cell on front box side	Pluviation, mechanical compaction, nuclear densimeter
Alfaro *et al.* (1995b)	1.60 x 0.70 x 0.50	D (1 mm/min)	Yes (width 20 cm) // clamps (plates inside sleeve)	25/15	LVDT, load cells	-
Fannin and Raju (1993)	1.30 x 0.64 x 0.60	D	No // clamps (there is upper and lower clamps)	-	Load cell, 2 displacement transducers, piezometers, 5 extensometers	-
Kharchafi and Dysli (1993)	-	-	-	-	x-ray records	-
Bergado *et al.* (1994)	1.30 x 0.80 x 0.50	D (1 mm/min, hydraulic)	-	-	Load cell, LVDT	-
Koerner (2005)	1.90 x 0.91 x 1.10	D, N (1 mm/min, hydraulic)	Yes // clamps (no)	Min. 30/30	Load and displacement transducers	-
Min *et al.* (1995)	0.60 x 0.60 x 0.20	N (hydraulic, electric, cyclic load, force increments for 24 h)	No // clamps (grid glues on metal plates which extend 10 cm in the box)	-	Load cells, LVDT at front, 4 extensometers on grid	Pluviation
Alfaro *et al.* (1995a)	1.60 x 0.50 x 0.60	D	Yes // clamps (inside the box)	25/15	Load cell, LVDT	Mechanical compaction, weighing
Lopes and Ladeira (1996)	1.53 x 0.80 x 1.00	D (hydraulic)	No or yes (width 20 cm) // clamps (exist)	30/30	Load cell. LVDT, vertical pressure cell LVDT on grid	Nuclear densimeter
Ochiai *et al.* (1996)	0.60 x 0.40 x 0.40	D (1 mm/min, reducer, cyclic)	Yes // -	-	Load cell, displacement transducers	Pluviation

Table 8.1. Reinforcement pullout test devices (Modified after Minažek and Mulabdić 2013) (Continued).

Reference	Dimensions L (m) x W (m) x H (m)	Pullout force generation, with increase D – deformation (mm/min), N – stress (description)	Sleeve: exist (yes/no, description, width (cm))/clamping system (description)	Soil thickness bellow/above reinforcement (cm)	Force and displacement sensors	Compaction and density
Bernal *et al.* (1997)	1.22 x 0.50 x 1.22	D (1 mm/min, 2 hydraulic cylinders)	Yes (width 15 cm) // clamps (reinforcement sample in resin, bolted to two plates)	20.5/20.5	Load cell, LVDT, 3 displacement transducers on sample, total cell on box bottom	Hand compaction
Cuelho (1998)	1.25 x 1.10 x 0.90	D, N (0-2 mm/min, electrical-reducer, 2 air cylinders)	Yes (width 26 cm) // clamps (plates with reinforcement samples glued)	-	Load cell, extensometers (5), glued deflectometers	Vibro-compactor, weighing
Teixeira (2003)	1.50 x 0.48 x 0.70	D (4,6 mm/min, electrical, reducer)	Yes (width 20 cm) // clamps (bolted to the reinforcement samples, passing through sleeve)	-	Load cell, 3 total cells, 6 extensometers on the sample, deflectometers	-
Alagiyawanna *et al.* (2001)	0.68 x 0.625 x 0.30	D (1 mm/min)	No, sponge to prevent soil loss, // -	-	Displacement transducer, laser sensors for grid displacements, load cell for vertical and horizontal direction	-
Bergado and Teerawattanasuk (2001)	1.27 x 0.76 x 0.51	D (1 mm/min, hydraulic)	-	-	-	Pluviation
Meyer *et al.* (2003)	1.50 x 0.70 x 0.60	D (2 mm/min, hydraulic, cyclic load up to 4 Hz)	Yes (width 20 cm) // clamps (reinforcement is rolled or pulled with two rods)	-	3 load cells on bottom, LVDT	Weighing, nondestructive methods
Marques (2005)	1.53 x 1.00 x 0.80	(hydraulic)	Yes (width 20 cm) // -	40/40	Different measuring instruments	Mechanical compaction, weighing system on the box bottom
Moraci and Gioffrè (2006)	1.70 x 0.60 x 0.68	(electrical)	Yes (width 25 cm) // clamps (inside soil)	-	RVDT (6 on grid sample), load cell	-
Abdelrahman *et al.* (2007)	1.20 x 1.16 x 0.70	(hydraulic, hand)	No // clamps (two steel plates with thickness of 6 mm)	-	2 sensors: 1 vertical, 1 horizontal, 2 LVDT on sample	Mechanical compaction
Aydogmus and Klapperich (2008)	0.60 x 0.50 x 0.20	D (0.000001-12 mm/min)	No // clamps (outside the box)	10/10	Load cell, pressure measurement at box bottom and in airbags	Pluviation, mechanical
Abdelouhab *et al.* (2008)	2.00 x 1.10 x 1.10	-	-	-	Load cell and total cell (front and bottom box side)	-
Requirements by EN 13738 (2004)	1.50 x 0.60 x 0.30	D, N (2+/-0.2 mm/min, hydraulic)	Yes (width 20 cm), clamps (articularly connected)	$6D_{max}/6D_{max}$	LVDT, load cells	-

Table 8.1. Reinforcement pullout test devices (Modified after Minažek and Mulabdić 2013) (Continued).

Reference	Dimensions L (m) x W (m) x H (m)	Pullout force generation, with increase D – deformation (mm/min), N – stress (description)	Sleeve: exist (yes/no, description, width (cm))/clamping system (description)	Soil thickness bellow/above reinforcement (cm)	Force and displacement sensors	Compaction and density
Requirements by GRI GT6 (1991)	1.20 x 0.75 x 0.60 or > $20D_{85}$	D (1 mm/min)	Yes (width 15 cm) // clamps (2 plates width 20 cm)	Min. 30/30	LVDT, measuring ring, load cells	-
Stadler (2001)	0.95-1.50 x 1.20 x 0.60 (adjustable length)	D (1 mm/min, hydraulic)	Yes (width 15 cm) // clamps (outside the box)	18/18	3 LVDTs for confined geosynthetic, 2 LVDT for pullout bar, 1 LVDT for unconfined geosynthetic, 2 pressure transducers for pullout actuators	Mechanical and hand compaction, sand cone test
Jayawickrama *et al.* (2014)	3.60 x 3.60 x 1.20	(hydraulic)	-	-	5 vertical pressure cells, pressure transducer for normal stress jacks, load cell for pullout jack, optical and digital measures for geosynthetic displacement	-
Hanumasagar *et al.* (2014)	1.50 x 0.60 x 0.30	D (1 mm/min, hydraulic)	Yes (width 7.5 cm) // clamps (roller grips outside the box)	15/15	-	Hand tamping and jack hammer
Zornberg *et al.* (2009); Roodi and Zornberg (2017)	1.50 x 0.60 x 0.30	D (1 mm/min, hydraulic)	Yes (width 7.5 cm) // clamps (roller grips outside the box)	15/15	Load cell for pullout force and LVDTs for geosynthetic displacement	Hand tamping and jack hammer

8.3. EXPERIMENTAL APPROACH

A new experimental device was designed and developed at the University of Texas at Austin to evaluate the soil-reinforcement composite behavior and to quantify the thickness of the soil shear band that develops in the vicinity of the soil-reinforcement interface upon shear stress generation. The box was designed to accommodate soil specimens up to 1200-mm deep, 150-mm long, and 750-mm wide. Six pneumatic actuators were placed on wooden pyramids that cover the top surface of the reinforced soil mass. The actuators react against a stiff reaction frame, which conveys the reaction load exerted by the actuators to the bottom of the reinforced soil box. This normal pressure system was designed to allow assessment of soil dilatancy. In addition, this system can maintain a controlled-dilation condition to allow for comparison of the soil-reinforcement interaction in free, reduced, and suppressed soil dilation conditions. The axial pullout loading system consists of two hydraulic actuators reacting against the front wall of the box. The pullout system is connected to a clamping system that conveys the applied tensile load to the active reinforcement. The embedded reinforcement layer is subjected to increasing loads, with particular focus on the responses under loads representative of working stress and ultimate stress conditions. In addition to the active reinforcement layer, two additional geosynthetic reinforcement layers of the same type are used as upper and lower boundaries to represent the presence of contiguous reinforcements. Soil was placed between the boundary reinforcements and the top and bottom boundaries of the box to properly model the behavior of the boundary reinforcements. A combination of collars (to heighten the box) was used to control the soil thickness. The equipment was heavily instrumented to monitor the potential interaction that takes place between the closely-spaced contiguous

reinforcement layers. The following sections provide a detailed description of the developed testing equipment and the adopted instrumentation and monitoring techniques.

8.3.1. Testing equipment

Figure 8.1 shows a schematic layout of the soil-geosynthetic interaction testing equipment developed as a part of this study. Many of its characteristics are based on those of large-scale pullout devices. A relevant feature is that this experimental system has the ability to accommodate multiple reinforcement layers at different vertical spacings. In addition, the characteristics of the materials used as top and bottom boundaries of the reinforced soil mass can be varied. The equipment included a geosynthetic-reinforced soil mass that contains three reinforcement layers as shown in the schematic cross-section in Figure 8.2. The soil-geosynthetic interaction equipment was extensively instrumented to provide comprehensive evaluation of the reinforced soil mass behavior: (1) evaluation of the effect of the shear stress generated by one of the reinforcement layers (active reinforcement) on the neighboring reinforcement layers; (2) mapping the pressure within the reinforced soil mass to assess local changes in normal pressure on the soil-reinforcement interface with increasing shear stresses; (3) mapping the straining of geosynthetic reinforcements; (4) characterizing the evolution of the shear band in the vicinity of the soil-reinforcement interface; (5) quantifying the stiffness of the soil-reinforcement interface; (6) evaluating the unit tension in the reinforcement at working stress and ultimate stress levels; (7) assessing the unconfined tensile properties of the tested reinforcement specimen corresponding to every soil-reinforcement interaction test; (8) assessing the dilatancy in the reinforced soil mass upon shear stress mobilization at the soil-reinforcement interface when volume changes are allowed; (9) assessing the

suppressed-dilation pressure within the reinforced soil mass upon shear stress generation at the soil-reinforcement interface when volume changes are restricted; and (10) evaluating the creep effect on soil-reinforcement interface strength. The equipment mainly consists of: (1) box in which the reinforced soil mass is placed; (2) normal loading system; (3) reinforcement clamping system; and (4) pullout loading system. Each of these components is described in detail in the following sub-sections.

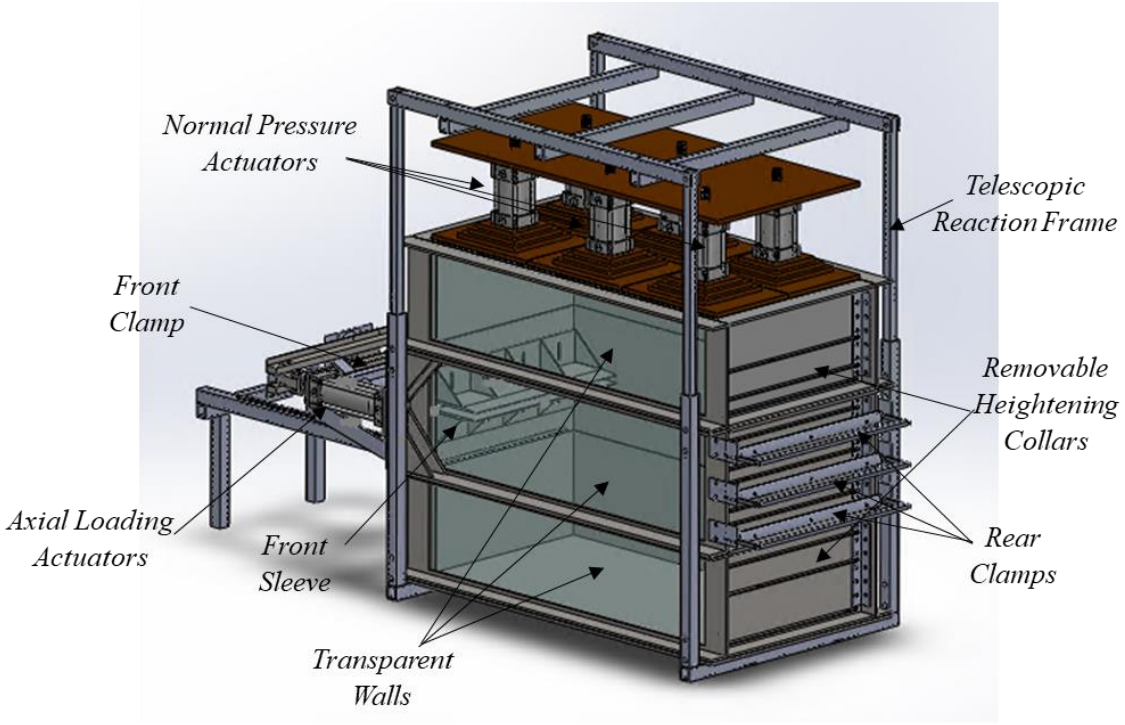

Figure 8.1. General layout of the soil-geosynthetic interaction equipment.

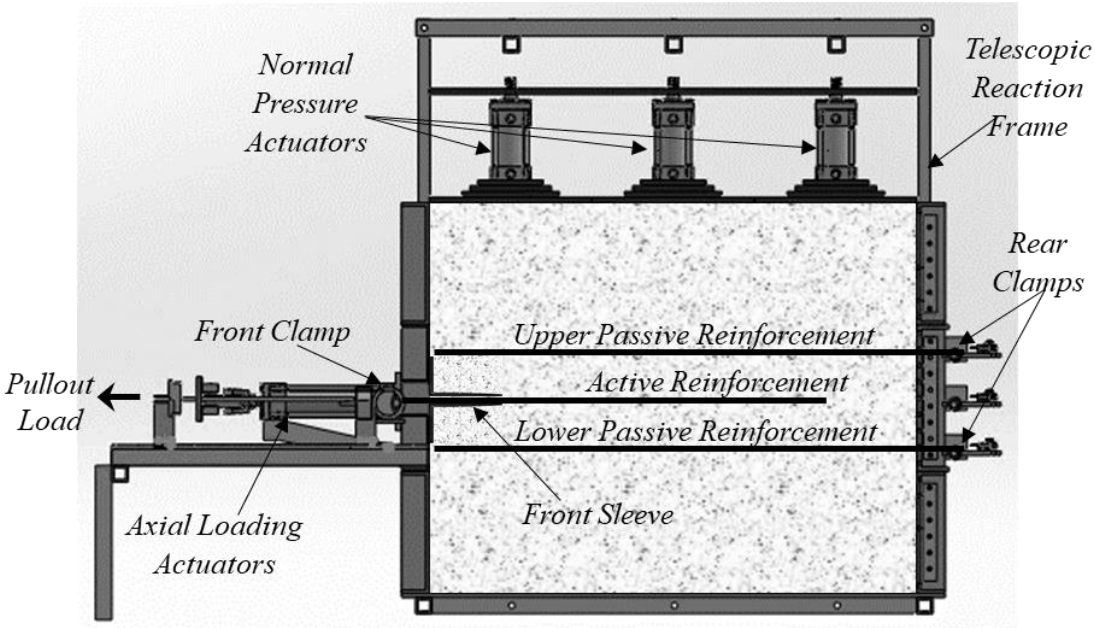

Figure 8.2. Schematic sectional side view of the soil-geosynthetic interaction equipment.

8.3.1.1.Reinforced soil box

The reinforced soil mass is accommodated in a steel box that is 1500-mm long, 750-mm wide, and up to 1200-mm deep. These dimensions are selected to allow varying the reinforcement vertical spacing from 50 to 600 mm. The box consists of three stacked collars; the middle collar (main collar) and is 450-mm deep, and the top and bottom collars are removable and are 375 mm deep. That is, the box depth can be either 1200 mm when the three collars are used or 450 mm when only the middle collar is used as shown in Figures 8.3a and 8.3b, respectively. Every collar consists of four steel channel beams forming its walls. One of the side walls of each collar is windowed to accommodate transparent acrylic walls. These transparent walls slide in fabricated grooves lined with rubber behind the windowed steel channels.

(a)

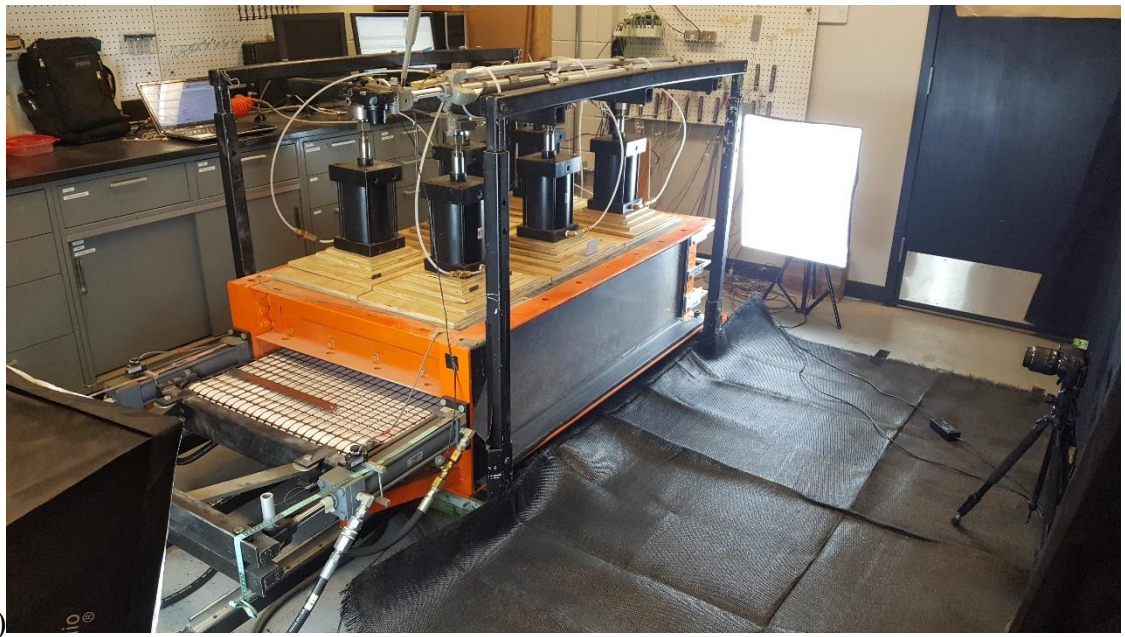

(b)

Figure 8.3. General view of the soil-geosynthetic interaction equipment: (a) 450-mm deep configuration (short); and (b) 1200-mm deep configuration (tall).

The front wall of the middle collar consists of two built-up steel channels 175-mm high forming a gap of 100 mm in the mid-height of the front wall. The height of this gap can be controlled by an adjustable sleeve such that the smallest gap height is 13 mm and the largest is 100 mm. This gap is adjusted according to the maximum grain size of the backfill material used in the tests. The bigger the particle size, the wider the gap has to be to avoid particle jamming during testing, hence avoiding apparent (false) increase in the pullout resistance. The front sleeve is attached to the inner side of the middle collar's front wall, as shown in Figure 8.4. The sleeve consists of two built-up steel angles 713-mm long. Each angle has a 225-mm long cantilevered leg and the other leg is 125-mm long that faces the front wall on which is is secured. The cantilevered legs are removable to allow for soil compaction underneath the sleeve. Five wedges are attached to each angle to stiffen the free legs and minimize bending when exposed to high normal pressure magnitudes. The free legs have tapered ends such that their thicknesses are reduced to 3 mm.

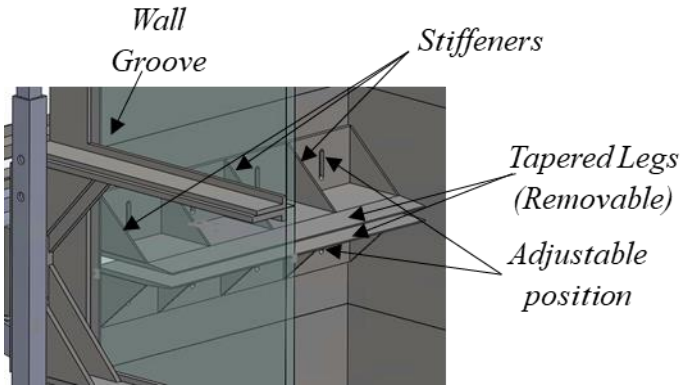

Figure 8.4. Front sleeve.

The rear wall of each collar has a number of slits which allow placement of instrumentations (e.g., telltales), seating loads, and rear clamping of the passive

reinforcement layers at various reinforcement spacings ranging from 50 to 600 mm, as shown in Figure 8.1.

The interior walls of the box are lined with Mylar sheets to minimize the interface friction that may develop between the backfill material and the interior side of the walls, particularly at high normal pressures. Mylar sheets were selected because of their very low roughness and for being transparent, two features that are important to allow visualization through the transparent side walls. The Mylar sheets placed on the steel walls had adhesive back sides. To confirm that the interface friction is low enough, interface shear tests were conducted to quantify the interface friction parameters between the baseline fill material used in this study (AASHTO Gravel No. 8) and Mylar sheets, as detailed in Chapter 7. Three interface tests were carried out using a large-scale direct shear machine at the normal stresses of 24, 38, and 52 kPa. Using the peak interface shear strength values from each test (Figure 8.5a), the interface shear strength envelope was defined as shown in Figure 8.5b. The interface friction angle was identified as 5.1 degrees. However, the friction angle was essentially zero for shear displacements less than 5 mm, as shown in Figure 8.5a, which is higher than the displacement range expected in testing.

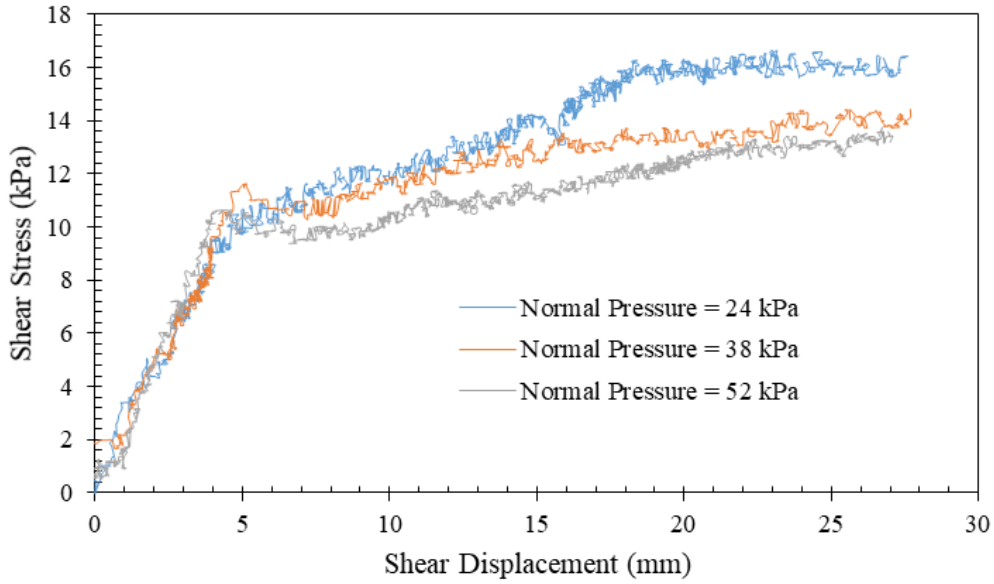

(a)

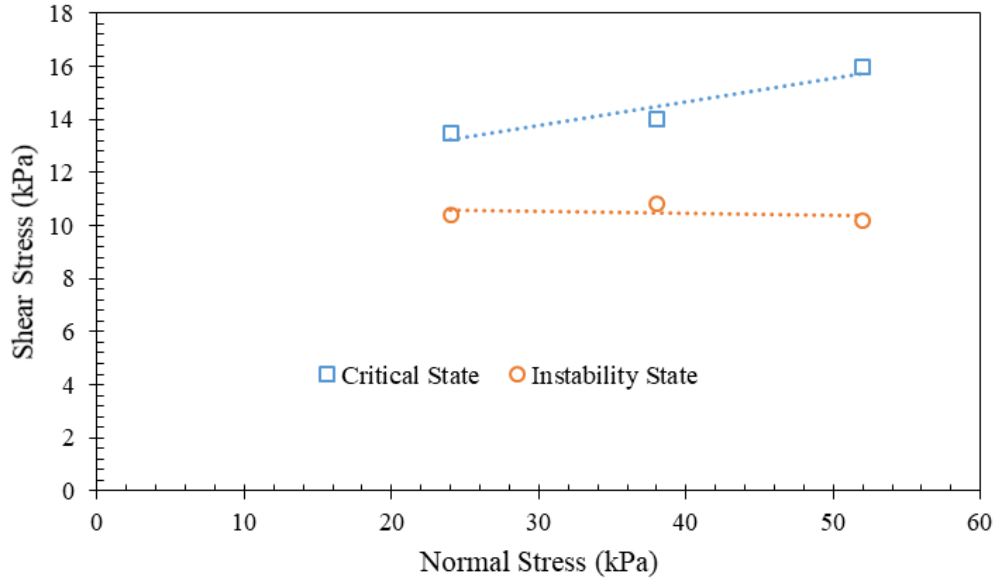

(b)

Figure 8.5. Soil-Mylar interface shear behavior: (a) Shear stress-displacement behavior; (b) Interface shear resistance envelopes.

8.3.1.2.Normal stress loading system

A normal stress loading system was designed to apply the target normal stresses on the top surface of the reinforced soil mass. The system consists of a set of six pneumatic actuators that exert pressure on the top surface of the reinforced soil mass, as shown in Figure 8.6. The actuatros react against three transverse beams that convey the load to two longitudinal beams, which in turn react against four columns located at the four corners of the box. The columns work in tension during testing and convey the load to two transverse beams mounted underneath the box where the load goes to the base plate of the box (i.e., the bottom surface of the reinforced soil mass). The bottom side of the box is stiffened by two other longitudinal beams to minimize possible bending at high normal pressure magnitudes. The reaction columns were designed to be telescopic in order to fit the two box configurations (i.e., 120-cm deep and 45-cm deep configurations).

Stepped wooden pyramids were used underneath each pneumatic actuator to uniformly distribute the pressure on the surface of the reinforced soil mass. The wooden pyramids sit on neoprene rubber mats to reduce the effect of load rigidity and to properly distribute uniform pressure on the top surface of the reinforced soil mass. This system provides a constant normal pressure, which requires that the pistons of the actuatros extend and retract to maintain the target normal pressure throughout the test. The pistons were adjusted initially at the mid-length of their stroke to allow both compression and heave. Thus, the system allows measurement of soil dilatancy and its sensitivity to changing the testing parameters without intervention of the top boundary. In addition, the system can control the amount of dilation during reinforcement pullout. That is, the system was designed to allow measurement of pressure changes due to reduced and suppressed soil

dilation. In the condition of suppressed dilation, the pistons were locked after applying the target initial normal pressure and full consolidation has taken place.

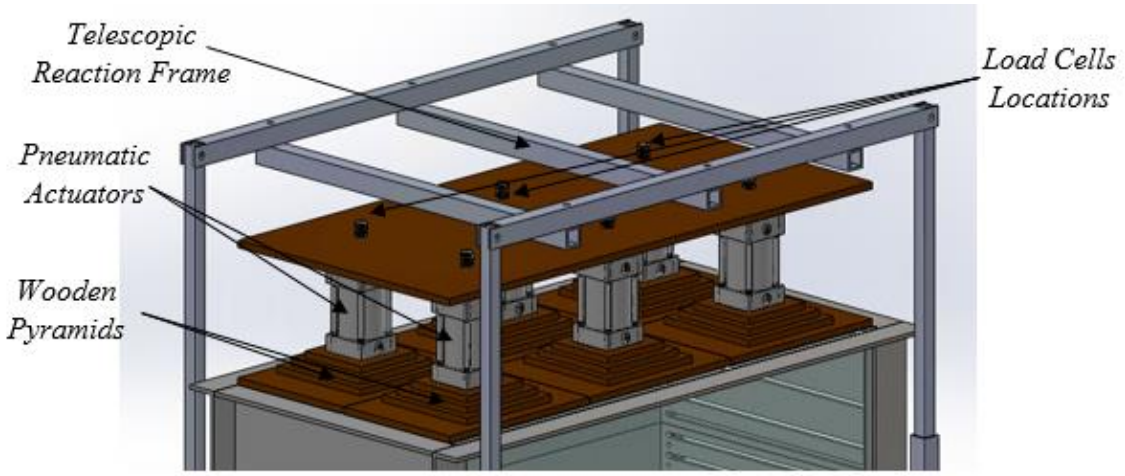

Figure 8.6. Normal stress loading system.

8.3.1.3.Reinforcement pullout loading system

Pullout loading of the active reinforcement layer is applied on the grip to which the reinforcement layer is clamped. The pullout loading system consists of two hydraulic actuators connected to a hydraulic pumping system. These actuators are connected by a stiffened beam which pushes against clamping system as shown in Figure 8.7. The clamping system is mounted on three ball bearing carriages that run on three linear guide motion rails. This linear guide system significantly reduces the friction against the movement of the clamping system, hence minimizing the contribution of the friction in the measured pullout loading. The total friction force for the linear guide system was identified to be approximately 0.010 kN. That is, the unit friction force added to the pullout force is 0.014 kN/m, which was within the accuracy level of the load cell used to measure the

pullout force. This value was found less than 0.03% of the average pullout force measured in typical tests conducted in this study. The loading system also allows maintaining a constact load to investigate creep effects on the soil-reinforcement interface behavior.

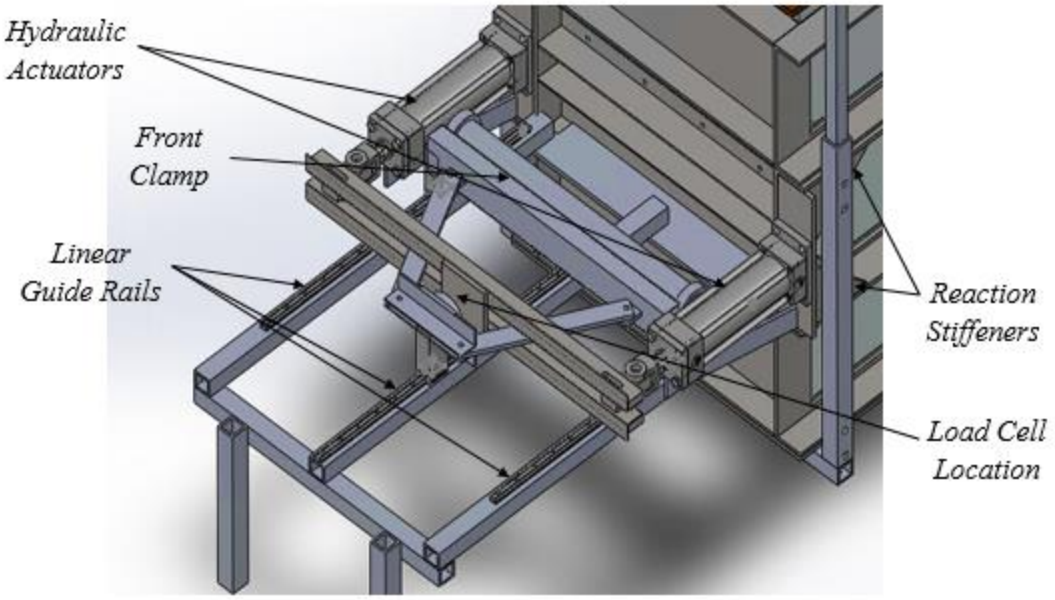

Figure 8.7. Reinforcement pullout loading system.

Figures 8.8 and 8.9 show a schematic diagram and a general view of the hydraulic system used for the pullout loading system, respectively. The system includes the following components: (1) a hydraulic pump, to provide the required pressure for the oil in the hydraulic circuit. The pump is accompanied with an oil tank to feed the system with hydraulic oil; (2) a pump flow control valve, to control the flow induced by the pump and return the excessive flow to the pump's oil tank; (3) an oil filter, mounted on the return inlet of the pump's oil tank to clarify the oil; (4) a 4-way directional hydraulic valve, to provide control on the oil flow direction either to the rear or the front side of the hydraulic

actuators (i.e., either to extend or retract the pistons of the actuators); (5) a hydraulic bridging meter valve to equate the pressure on both sides of the pistons in case of emergencies; (6) two flow control valves mounted on the rear side of the hydraulic actuators. These valves help controlling the rate of displacement of the pistons in the pushing direction (i.e., while loading the active reinforcement layer).

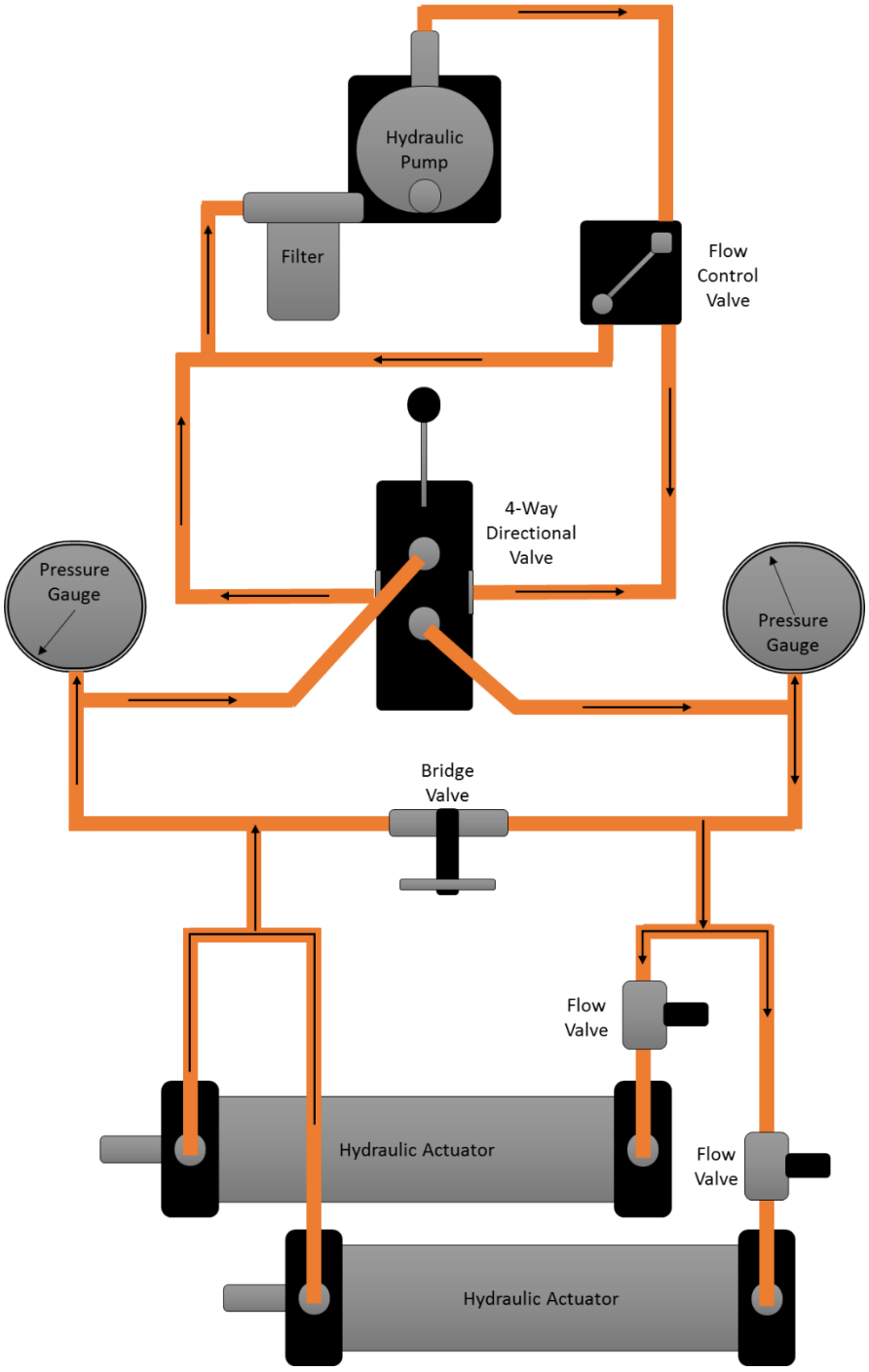

Figure 8.8. Schematic diagram for the hydraulic loading system (arrows denote direction of flow during loading).

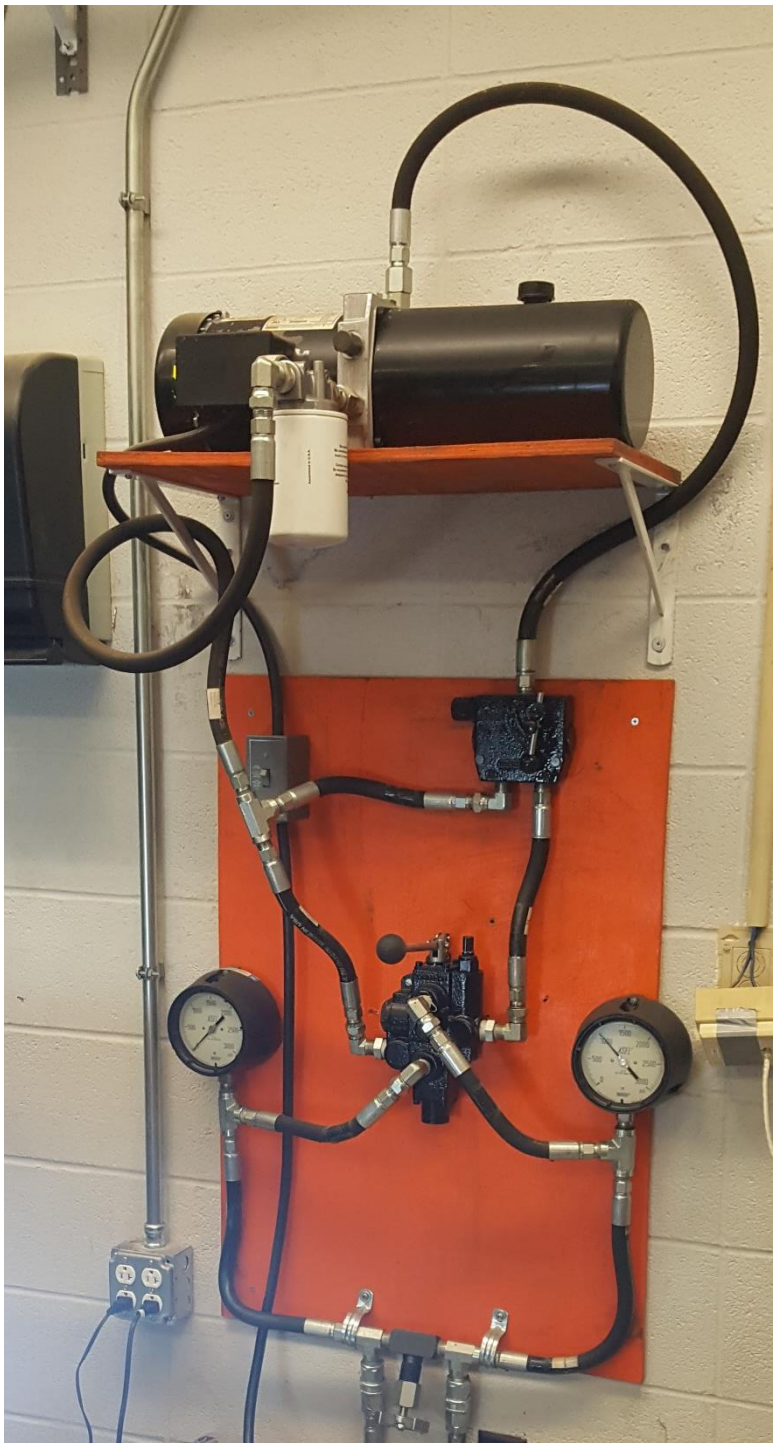

Figure 8.9. General view of the hydraulic loading system.

8.3.1.4.Reinforcement clamping system

The active reinforcement layer, which is placed in the middle of the box, is clamped from the front side to a movable clamp placed in front the box. This clamp is attached to the pullout loading system as shown in Figure 8.10. On the other hand, the passive (or boundary) reinforcement layers are clamped at the rear side of the box to stationary clamps. That is, the rear ends of the passive reinforcement are fixed.

(a)

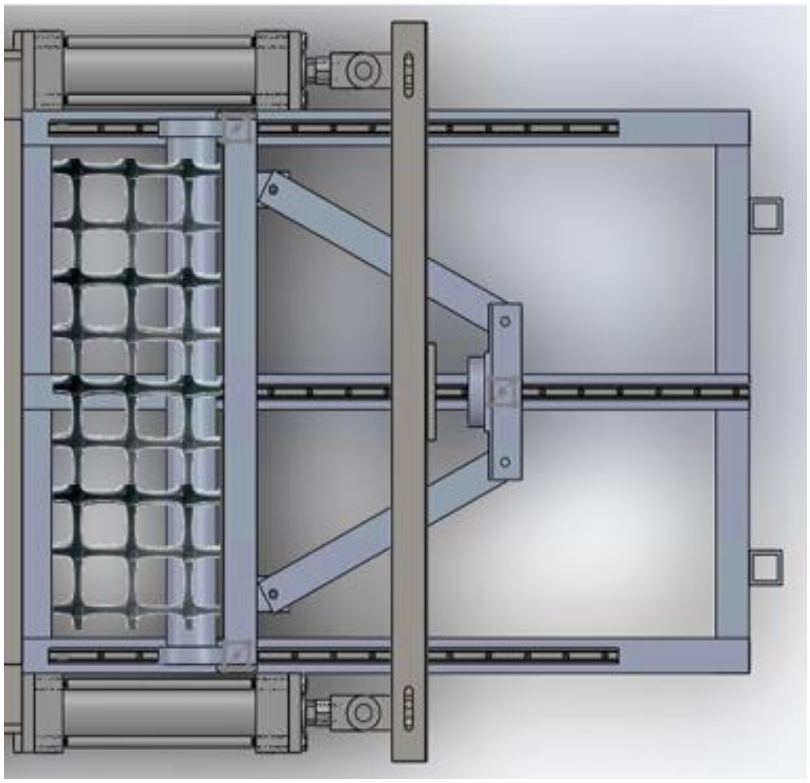

(b)

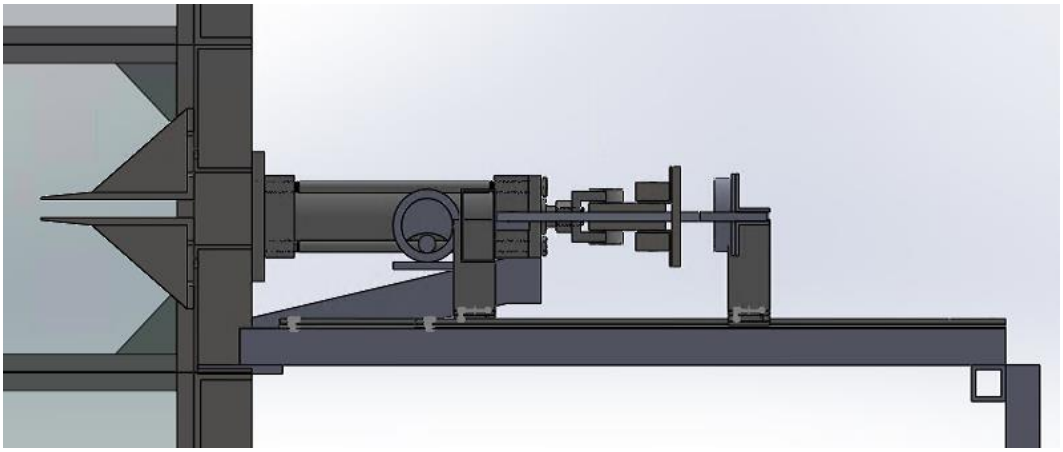

Figure 8.10. Front clamp and pullout loading system: (a) top view; (b) sectional side view.

8.3.1.4.1. Active reinforcement clamp

The active reinforcement is placed in the middle of the box and clamped to a roller grip, as shown in Figure 8.11a. The roller grip consists of a steel solid cylinder with a crescent cut. The reinforcement makes a 270-degree round around the cylinder and is clamped by a steel rod bolted to the steel cylinder by five screws against the crescent cut, such that the clamping line is facing towards the front wall of the box (Figure 8.11a). The grip is accommodated in a grip holder, which has two steel rings at both ends that are connected by a steel box tube. Two rods are connecting the box tube with a stiffened steel plate that is in direct contact with the pullout loading system, as shown in Figure 8.10. These rods are aligned with the top tangent plane of the grip (i.e., reinforcement plane) which is in turn aligned with the horizontal axial plane of the mid-height of the box. This alignement is important to ensure a perfect tensile loading on the reinforcement layer and to avoid generation of any moment on the clamping system.

For testing involving geogrid reinforcements, the geogrid is clamped such that a transverse rib is maintained beyond the clamping rod; whereas, for testing involving geotextile reinforcements, the geotextile is clamped such that a knitted double-layer strip is maintained beyond the clamping rod to avoid potential slippage. In addition, the clamp is lined with sandpaper to minimize reinforcement slippage. The edge of the crescent cut in contact with the reinforcement is lined with a neoprene foam strip to minimize stress concentration at this location. Evaluation was conducted after testing to ensure that no reinforcement slippage occurred during testing. Figures 8.12a and 8.12b show a clamped geotextile reinforcement and a clamped geogrid reinforcement, respectively, during testing. The clamping system allows a reinforcement unconfined portion (i.e., outside the

box). This allows evaluation unconfined tensile behavior characterization of each geosynthetic specimen used in the interaction tests.

8.3.1.4.2. Passive reinforcement clamp

The rear wall of each collar has a number of slits that allow clamping of the passive reinforcement layers at various reinforcement spacings ranging from 5 to 60 cm (2 to 24 in.). In addition, these slits allow placement of instruments and seating loads, as needed. The rear ends of the passive reinforcement layers are fixed so as to investigate their effect of the active reinforcement layer where interaction takes place. In addition, having the passive reinforcements fixed allows assessing of the effect on them by the shear stress generated at the soil-reinforcement interface of the active reinforcement layer. The passive reinforcement layers are clamped to roller grips mounted on the rear side of the box, as shown in Figure 8.1.

The elevation of these clamps can be changed according to the elevations of the passive reinforcement layers in the soil mass (i.e., to achieve the desired reinforcement vertical spacing). The clamps are accompanied with instrumentation holders as shown in Figure 8.11b. The clamps are also lined with sandpaper to avoid reinforcement slippage. A similar holder was used for the active reinforcement layer to secure its instrumentation and to enable placement of the seating load, as needed.

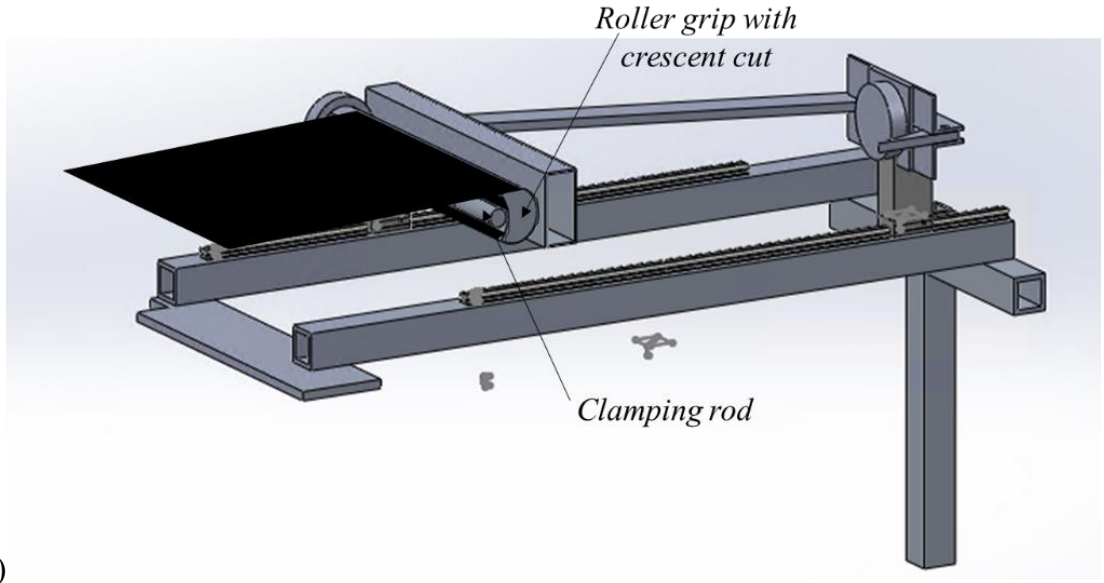

(a)

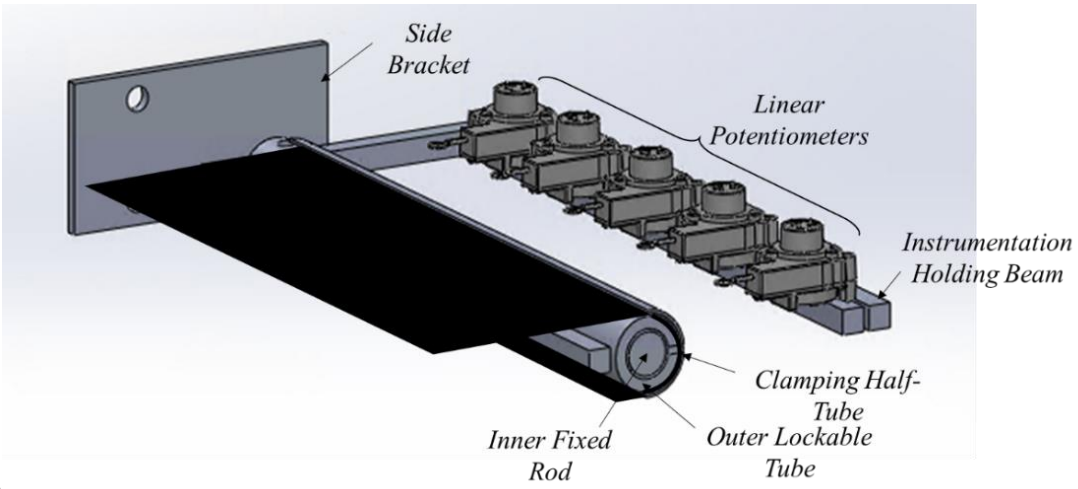

(b)

Figure 8.11. Reinforcement clamping systems: (a) Sectional view of the active reinforcement clamp; and (b) Sectional view of the passive reinforcement clamp.

(a)

(b)

Figure 8.12. View of clamped reinforcement during testing: (a) Geotextile reinforcement; and (b) Geogrid reinforcement.

8.3.2. Instrumentation and monitoring

The instrumentation of the soil-geosynthetic interaction device includes: (1) a load cell to measure the tensile load (pullout load) applied to the active reinforcement; (2) load cells at the normal pressure pneumatic actuators to monitor the actual applied normal pressure on top of the reinforced soil mass throughout the test; (3) a camera that captures the transparent side wall, allowing measurement of the soil displacement field as well as direct observation of the soil-reinforcement interaction. The width of the reinforcements was selected to extend to the sidewalls of the box. On the inner surface of the box, Mylar sheets were used to minimize side friction against the fill material. Markers are placed in the soil at the interface to facilitate tracking the soil movement with increasing tensile load in the geosynthetic reinforcement, especially with soils of poor pattern (i.e., uniform color intensity); (4) artifical gravel particles buried within the soil mass that are connected to displacement sensors via horizontal telltales, to allow for comparison of internal displacements with those obtained through the transparent wall; (5) artifical gravel particles placed on the surface of the reinforced soil mass that are connected to displacement sensors via vertical telltales to measure vertical displacements and to assess the dilatancy angle of of the reinforced soil mass; (6) an earth pressure mat, placed on the floor of the box, to evaluate the normal pressure magnitude and distribution conveyed through the reinforced soil mass; (7) lateral earth pressure sensors, fixed to the interior of the front wall, to monitor the change in lateral earth pressure against the front wall during testing to evaluate the effect of hacing a rigid front wall on the generated soil-reinforcement shear stresses; (8) displacement sensors to measure displacements at multiple locations within the active reinforcement, as well as within the passive reinforcements; and (9) a camera that measures displacement within the unconfined portion of the active reinforcement to simultaneously

evaluate the tensile behavior of the geosynthetic specimen used to evaluate the soil-reinforcement interaction.

8.3.2.1.Reinforcement axial load

Pullout loading on the active reinforcement layer is applied by the hydraulic loading system acting on the roller grip on which the reinforcement layer is clamped. The clamping system is mounted on three ball bearing carriages that run on three linear guide motion rails. This linear guide system significantly reduces the friction against the movement of the clamping system, hence minimizing the contribution of the friction in the measured pullout loading as discussed earlier. The applied load is measured in real time by a load cell placed at the only contact point between the clamp and the loading system, as shown in Figure 8.10. The load cell that was used in the system was a high-accuracy low-profile cell shown in Figure 8.13. The load cell is boosted with a load button to provide single-point contact. The clamp displacement was monitored using two linear potentiometers.

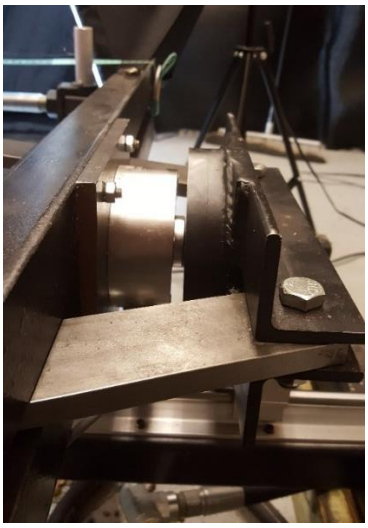

Figure 8.13. Low-profile load cell for pullout load measurement.

8.3.2.2.Reinforced soil normal pressure

Monitoring the normal pressure within the soil mass was achieved by monitoring the normal pressure imposed on the top of the reinforced soil mass and the distributed pressure within the reinforced soil mass.

8.3.2.2.1. Applied normal pressure

Six load cells were mounted at the reaction points of the six pneumatic actuators to measure the real-time load exerted by each actuator during the test. The load cells used in the system are high-accuracy low-profile cells (Figure 8.14). Note that ball bearings were used at the contact points of each piston and its coressponding load cell to accommodate possible tilting of actuators during testing and to maintain a single point load on each load cell (i.e., the load cells were not attached to the pistons of the actuators). This set of load cells allows measuring the pressure exerted on the surface of the reinforced soil mass by each actuator throughout the test in real time. In turn, this approach verifies the magnitude of the exerted normal pressure and its uniformity on top of the reinforced soil mass during testing. In addition, the load cells allow assessing the reinforced soil dilatancy in testing conditions of free, reduced, and supressed dialtion. That is, the system allows quantification of the increase in soil normal stress induced by dilation reduction or suppression.

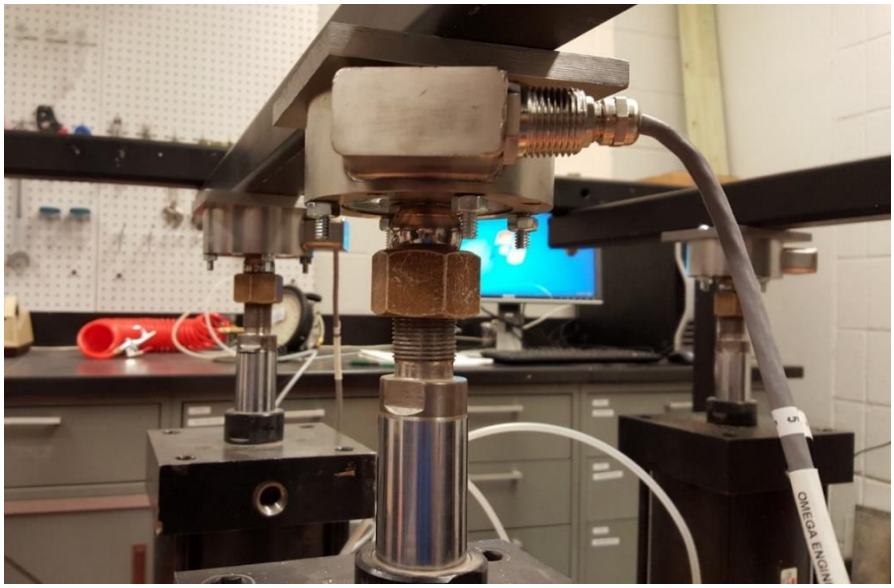

Figure 8.14. Load cells for applied normal pressure measurement.

8.3.2.2.2. Distributed normal pressure

A pressure sensing mat was placed on the floor of the reinforced soil box to monitor the pressure changes during the test. The pressure mat was placed on a compacted sand layer (Figure 8.15a) and was covered by another compacted sand layer (Figure 8.15b). The sand was subsequently covered by a latex membrane to separate it from the reinforced fill material (Figures 8.15c and 8.15d). In addition, pressure cells were added within the reinforced soil mass and on the box internal surfaces at different locations to monitor real-time changes in stress during testing. This included sensors to monitor both vertical and lateral earth pressure. The lateral earth pressure sensors were fixed to the inner surface of the front wall to monitor the change in lateral earth pressure on the front wall during testing. This allows evaluation of the effect of rigid front wall on the generated soil-reinforcement shear stresses.

(a) (b)

(c) (d)

Figure 8.15. Pressure mat placement: (a) Placing the mat on top of compacted sand layer; (b) Placing another compacted sand layer on top of the mat; (c) Placing a latex membrane on top of the sand; and (d) Placing the fill material on top of the latex membrane.

8.3.2.3.Reinforcement straining

While the active reinforcement layer was pulled out through the front side of the box, the rear ends of the passive reinforcement layers were fixed in place to investigate their effect on the active reinforcement layer where interaction takes place. The straining of the three reinforcement layers was monitored by tell-tales connected to draw-wire linear potentiometers mounted on holders at the rear side of the box. The tell-tales are attached to multiple locations along the embedment length of the reinforcement layers. The passive reinforcement layers are also instrumented to quantify the load transferred from the active

reinforcement layer. Different location patterns of tell-tales were adopted to different reinforcement types based on their geometry and testing conditions.

The tell-tales used involved spring-back music wires (also known as piano wires), which are made of tempered stainless steel. The music wires were 0.4064 mm (0.016 in.) in diameter and their mechanical properties follow ASTM A313 and ASTM A555 standards; their tensile strength is 1413.4 MPa (205 ksi). The wires were run through special tubes, generally used for bike cables. These tubes involve smooth jackets covering steel coils that in turn cover lubricated plastic inner pipes. These tubes are radially very stiff so they can accommodate high normal normal pressures without being squeezed. On the other hand, they are very flexible that can easily be straightened out after being released from their spool, which minimizes waving during installation and avoids any resistance to bending during testing. Ten tell-tales were installed on the middle reinforcement layer (i.e., active reinforcement layer) to monitor displacements using ten linear potentiometers; whereas, five tell-tales were installed on each of the passive reinforcement layers to monitor displacements using five linear potentiometers each. The locations of the tell-tales varied slightly when geogrid reinforcements were used so that the tell-tales matched grid junctions. Figure 8.16 shows a geotextile reinforcement layer with connected tell-tales already placed in the reniforced soil box.

If geogrid reinforcements were used, the music wires were knotted to the grid junctions. This knots have to be as tight as possible so as not to deform during testing resulting in underestimated displacement values of the grid junctions. On the other hand, when geotextile reinforcements were used, a rapid adhesive was employed at the locations of the tell-tales attachments. The music wires formed hooks and rested by solidifying areas

of approximately 1 cm^2 of the geotextile fabric at which the hooks of the tell-tales were centered. The adhesive included a powder and a liquid components. The reinforcement surface on which the adhesive was applied was initially cleaned. The hardening time for the adhesive was 20 to 30 minutes under a temperature of 20 Celsius.

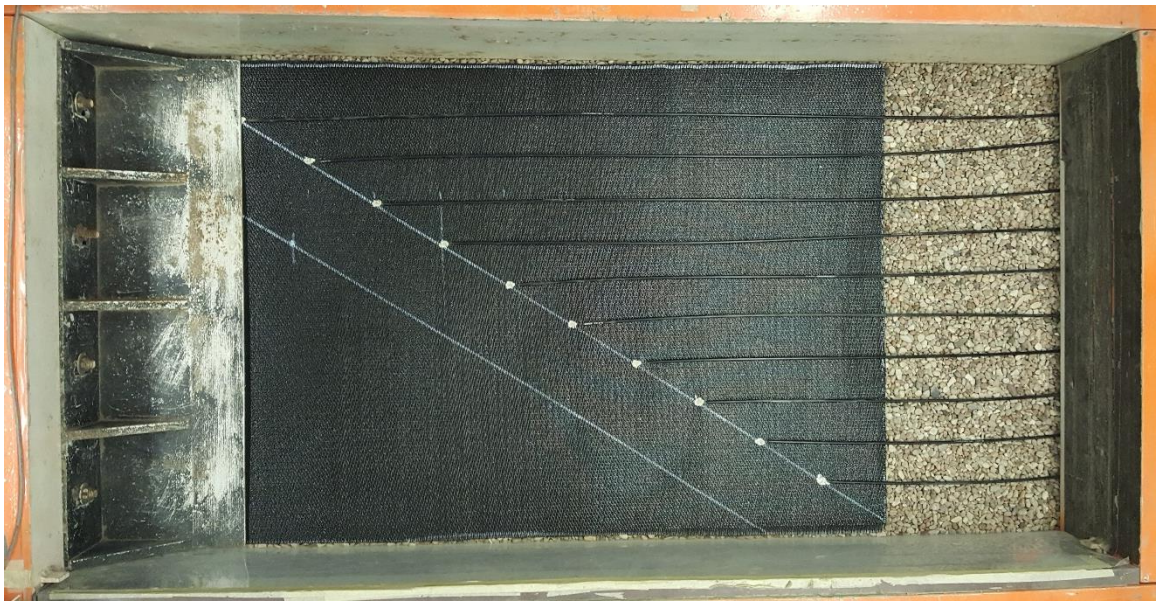

Figure 8.16. Tell-tales attached to an active reinforcement placed on the central horizontal plane of the reinforced soil mass.

8.3.2.4.Soil mass deformation

Deformation of the reinforced soil mass was monitored over the vertical plane adjacent to the transparent side of the box. The setup for real-time imaging of the transparent side of the box during testing is shown in Figure 8.17. Post-processing of the tethered images ultimately provided the full soil displacement field at any time during testing. Visualization of the development of the shear band at the soil-reinforcement interface provided particularly valuable insight into the mechanisms that may explain the

effect of vertical reinforcement spacing on the soil-reinforcement interaction. A camera connected to an image tethering software program was placed vertically to capture the transparent side of the box. Blackouts were used behind the camera and on the floor under the camera to reduce reflections on the transparent windows. Lighting equipment was placed on the sides of the window to enhance the light intensity and uniformity. A measuring tape was mounted behind the window to allow calibration of the image pixels, which accounts for camera distance and any refraction through the acrylic sidewall.

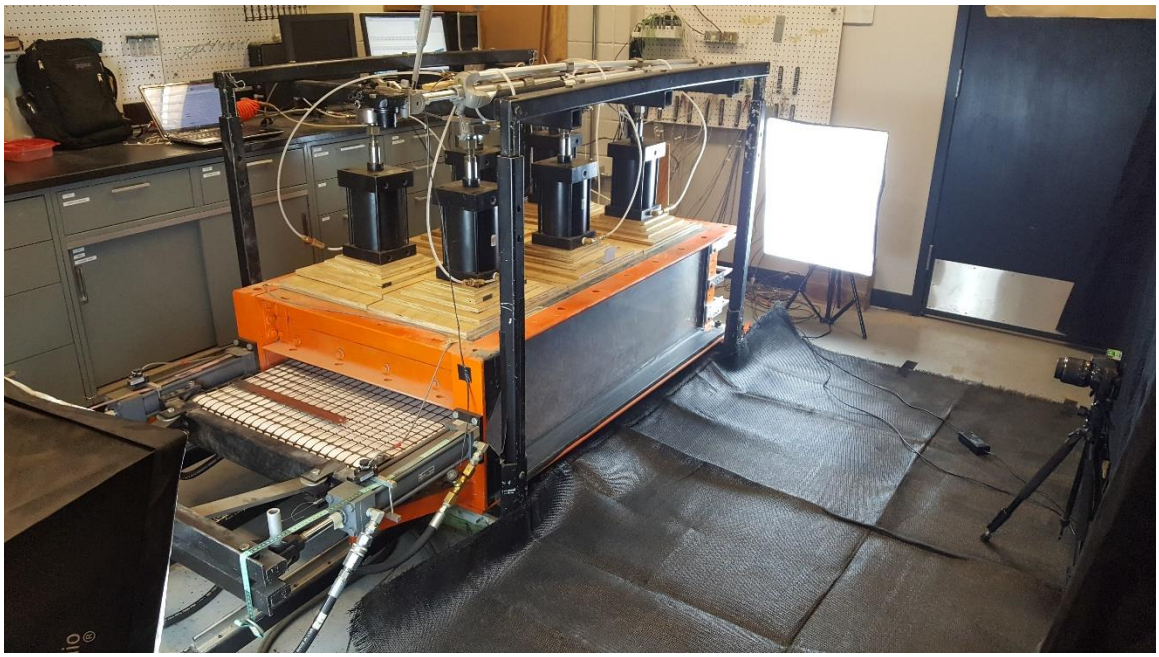

Figure 8.17. Camera shooting against the transparent side of the box containing the reinforced soil mass.

In addition, artificial gravel particles of similar characteristics as the real AASHTO Gravel No. 8 were buried in the soil at the center of the box. These artificial particles were connected to tell-tales, which were in turn connected to draw-wire linear potentiometers.

This allowed real-time monitoring of the horizontal or vertical displacements of soil particles at specific locations within the reinforced soil mass, as shown in Figures 8.18a and 8.18b, respectively.

(a)

(b)

Figure 8.18. Artificial gravel particle connected to a tell-tale: (a) Horizontal tell-tale; and (b) Vertical tell-tale.

8.3.2.5. Unconfined reinforcement tensile behavior

The clamping system used in the soil-geosynthetic interaction device allowed a part of the reinforcement to be unconfined (i.e., outside the box). This allowed evaluation of

the tensile behavior of the geosynthetic specimen concurrently with evaluation of the soil-reinforcement interaction as mentioned earlier. Also, it allowed evaluation of potential creep deformations in the reinforcements. A camera was mounted to capture the top view of the reinforcement unconfined portion during testing in real time. For continuous reinforcements (e.g., geotextiles), the exposed portion of the reinforcement was speckled using spray paint and randomly dappled with a white paint marker, as shown in Figure 8.19a. For gridd reinforcements (e.g., geogrids), a white sheet was placed underneath the geosynthetic to provide added contrast and facilitate image analysis, as shown in Figure 8.19b. A metal ruler was placed on the unconfined zone to allow calibration of the image pixels.

(a)

(b)

Figure 8.19. Unconfined reinforcement zone: (a) Geotextile reinforcement; and (b) Geogrid reinforcement.

8.4. DIGITAL IMAGE ANALYSIS

Digital Image Correlation (DIC) is a widely used technique for surface displacement analysis in solid mechanics. Particle Image Velocimetry (PIV) technique, a similar technique to DIC, has been used mostly in fluid mechanics. DIC invovles cross-correlation between successive images in an image stack. This cross-correlation provides the best match of targets (sub-image or group of pixels) in successive images compared to their preceding ones. The matching allows motion detection (movement, deformation, velocity, and acceleration profiles). A cross-correlation function C(x) can be applied on any two real functions F and G in 1D and 2D problems. For image correlation, which is a 2D problem, F(m,n) and G(m,n) functions can be a quantifiable property of the images. Grayscale intensity [0,255] was the quantifiable property adopted in this study. The correlation function C(x,y) scans the G function over the x,y space in a rotational motion around sub-image (m,n) in image (k+1). This scan searches for the sub-image in image (k+1) of G(m+Δx,n+Δy) that best matches the F(m,n) of sub-image (m,n) in image (k). This is accomplished by computing the integral of F(m,n)*G(m+Δx,n+Δy) using values associated with the corresponding pixels in the sub-images. F and G matching is the best when the integral value is maximum, and the corresponding Δx and Δy are the 2D displacement of the sub-image (m,n) from image (k) to image (k+1). Note that the search zone can be limited to specific domain to optimize the search process. This process is schematically illustrated in Figure 8.20.

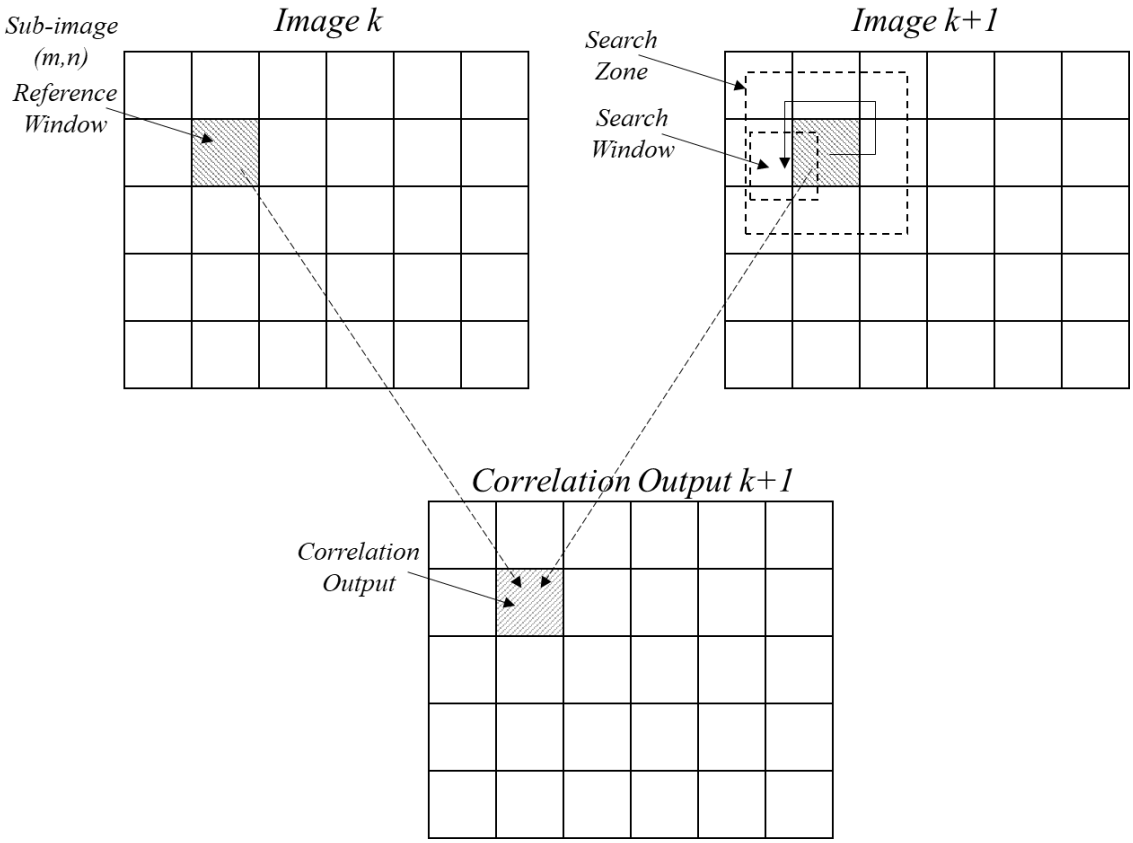

Figure 8.20. Schematic for cross-correlation process.

8.5. ILLUSTRATIVE TEST

This section describes the testing configuration of an illustrative test that was selected to illustrate the abilities of the newly developed soil-geosynthetic interaction equipment. The configuration of the test was chosen to magnify the capabilities of the new proposed experimental approach. In this test, the equipment was set in its short configuration; i.e., the height of the reinforced soil mass was 450 mm (18 in.). Three reinforcement layers were placed at a comparatively small vertical spacing of 50 mm (2 in.). The target normal pressure at the elevation of the active reinforcement layer was 21 kPa (3 psi). This normal pressure was selected to be low enough so that pullout failure

occurs for a comparatively long reinforcement before tensile rupture to allow for considerable reinforcement and soil displacements.

The backfill material was a gravel to exaggerate on the capabilities of the newly proposed approach. The backfill material used in the illustrative test was AASHTO Gravel No. 8. The backfill material was placed in lifts 7.5-cm (3-in.) thick and gently hand tamped until satisfying relative density of 70%, which is corresponding to dry unit weight of 16.67 kN/m^3 and void ratio of 0.57. Details on the properties of the backfill material are provided in Chapter 7.2 of this dissertaion.

The reinforcement was a woven geotextile, which is commonly employed in geosynthetic-reinforced soil structures where the reinforcement spacing is comparatively small. The embedment length of the active reinforcement layer was 1016 mm (40 in.). The passive reinforcement layers were extended to the end of the reinforced soil mass, where they were clamped. The reinforcement material used in the illustrative test was HP570 polyester woven geotextile. This geotextile has multi-filament yarns oriented in the rollway direction (i.e., machine direction) and mono-filament yarns oriented in the cross-rollway direction (i.e., cross-machine direction). The unconfined tensile properties reported by the geotextile manufacturer are summarized in Table 8.2. It was reported that the tensile strength properties were obtained in accordance with ASTM D4595. As will be presented in Section 8.6.5, these tensile properties were verified by test results obtained in this study.

Table 8.2. Reinforcement tensile properties (TenCate 2015).

Mechanical Properties	***Minimum Average Roll Value (MARV)***	
	Machine Direction	***Cross-machine Direction***
Ultimate Tensile Strength	70.0 kN/m	70.0 kN/m
Tensile Strength at 2% Strain	14.0 kN/m	19.3 kN/m
Tensile Strength at 5% Strain	35.0 kN/m	39.4 kN/m
Tensile Strength at 10% Strain	70.0 kN/m	Not applicable

The notations for the various instruments used in the illustrative test and the notations for their corresponding measurements are summarized in Table 8.3. The locations of the instruments will be provided in detail in Section 8.6 of this dissertation.

Table 8.3. Instruments and measurements notations.

Measurement	*Instrument Notation*	*Measurement Notation*
Nodal displacements of the active reinforcement layer	LP1	u1
	LP2	u2
	LP3	u3
	LP4	u4
	LP5	u5
	LP6	u6
	LP7	u7
	LP8	u8
	LP9	u9
	LP10	u10
Nodal displacements of the upper passive reinforcement layer	LP11	v1
	LP12	v2
	LP13	v3
	LP14	v4
	LP15	v5
Nodal displacements of the lower passive reinforcement layer	LP16	w1
	LP17	w2
	LP18	w3
	LP19	w4
	LP20	w5
Horizontal displacements of 7 artificial gravel particles	LP21	N/A*
	LP22	N/A*
	LP23	N/A*
	LP24	N/A*
	LP25	N/A*
	LP26	N/A*
	LP27	N/A*
Vertical displacements of 3 artificial gravel particles	LP28	N/A*
	LP29	N/A*
	LP30	N/A*
Clamp displacement	S1	uc1
	S2	uc2
Frontal pullout load	LC1	P
Front normal stress	LC2	σ_{front}
	LC3	σ_{front}
Middle normal stress	LC4	σ_{middle}
	LC5	σ_{middle}
Rear normal stress	LC6	σ_{rear}
	LC7	σ_{rear}

*N/A: Not applicable.

8.6. TYPICAL RESULTS AND ANALYSIS

This section presents the typical results the illustrative test. The results are presented to illustrate the capabilities of the developed experimental equipment. Note that this experimental approach involves significant redundancy in a number of varibles to validate the reported values.

8.6.1. Pullout resistance

Figure 8.21 shows the frontal load-displacement behavior of the active reinforcement layer. The frontal load is the total pullout force applied per unit width on the active reinforcement layer. The frontal load was measured using the load cell mounted in the loading system. The frontal displacement is the movement of the front end of the confined portion of the active reinforcement layer. The frontal displacement was measured using a linear potentiometer attached to a tell-tale, which was placed at the front end of the confined reinforcement zone. The failure mode observed in the illustrative test was pullout failure, which enabled evaluation of the soil-reinforcement interface behavior over the various interaction levels of interest (i.e., working stresses and failure conditions).

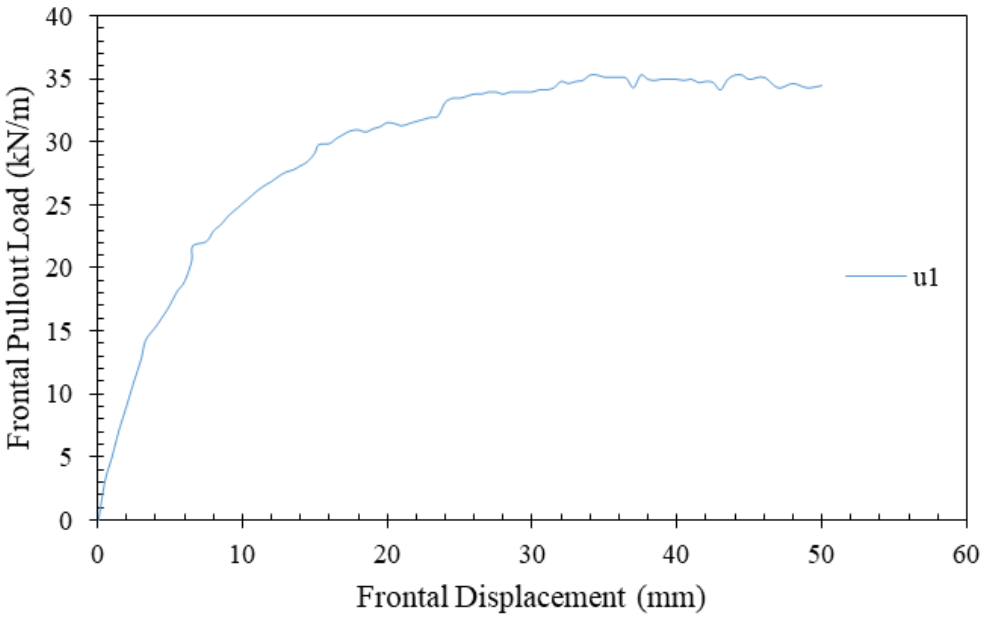

(a)

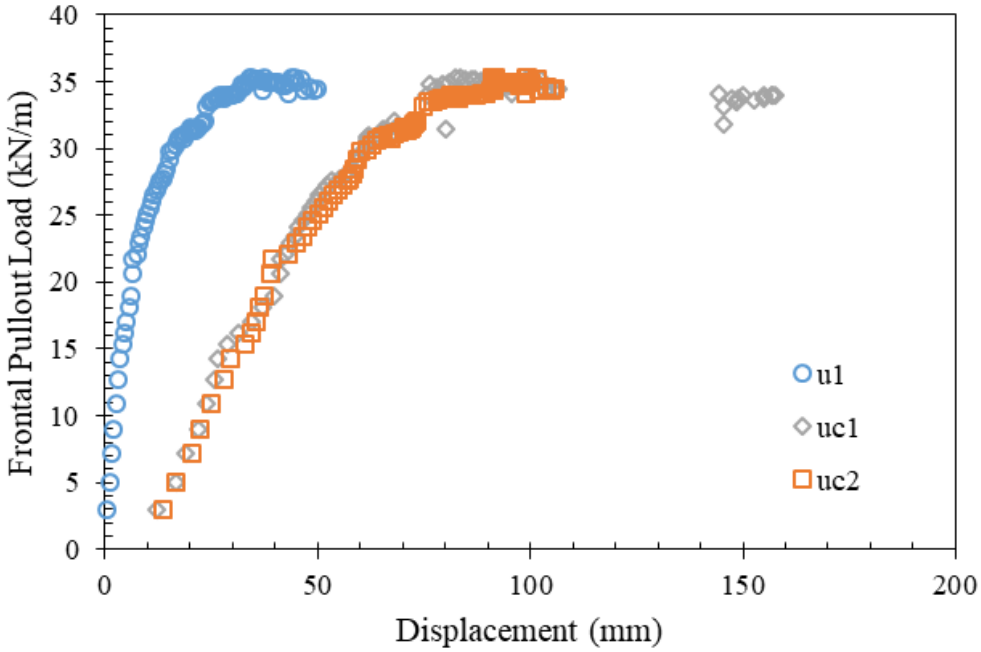

(b)

Figure 8.21. Frontal pullout load-displacement behavior: (a) Frontal load-displacement curve; and (b) Frontal and clamp load-displacement curves.

8.6.2. Confined reinforcement straining

Reinforcement displacements were measured at various nodes along its embedment length. These nodes were connected to tell-tales, which were in turn connected to linear potentiometers at the rear side of the box. The locations of these nodes are illustrated in Figures 8.22a, 8.22b, and 8.22c for the active, upper passive, and lower passive reinforcement layers, respectively. The figures show the locations of the nodes on a plan view of the reinforcement layers, where the locations of the sleeve and the rear bound of the active reinforcement layer are also showed. Note that the location of the monitored nodes in the passive reinforcement layers coincide with some of the nodes in the active reinforcement layer.

Figure 8.23 shows the displacements measured at the various nodes of the reinforcement layers as the frontal load increased. Specifically, Figure 8.23a shows the nodal displacements in the active reinforcement layer, whereas Figures 8.23b and 8.23c show the nodal displacements in the upper and lower passive reinforcement layers, respectively. To generate displacement profiles, the discretized values at specific frontal displacement values u1 were used. Figure 8.24a shows the nodal displacement profiles for the active reinforcement layers at increasing values of the frontal displacement. Figures 8.24b and 8.24c show the nodal displacement profiles for the upper and lower passive reinforcement layers, respectively. Note that the stresses generated at the soil-reinforcement interface of the active reinforcement layer sheds at an angle. This results in maximum displacement magnitudes near the middle of the passive reinforcement layers. That is, the displacements observed at the frontal portions of the passive reinforcement layers do not cause tensile strains as the displacements at the rear portions.

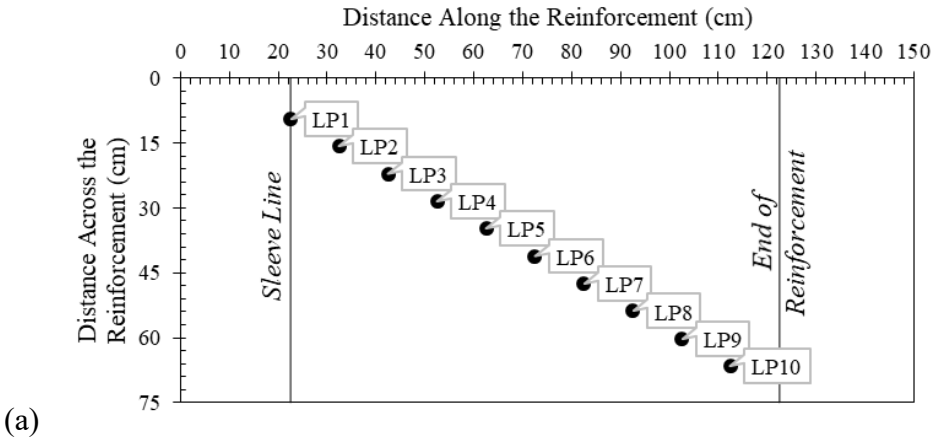

(a)

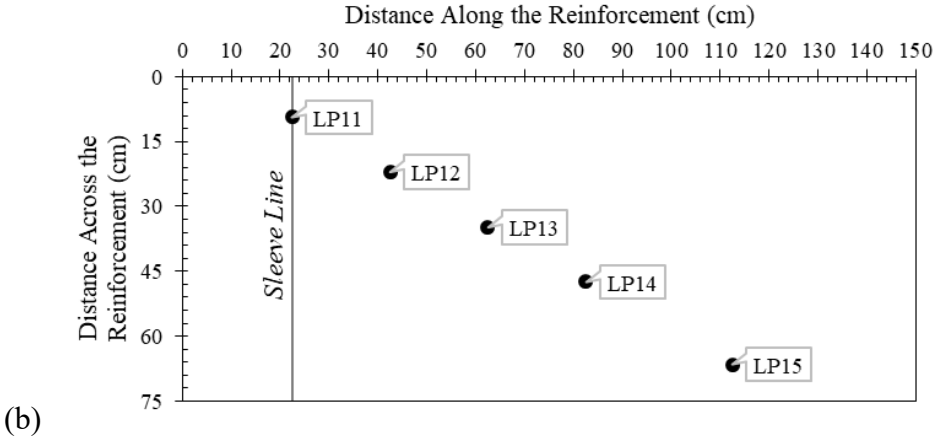

(b)

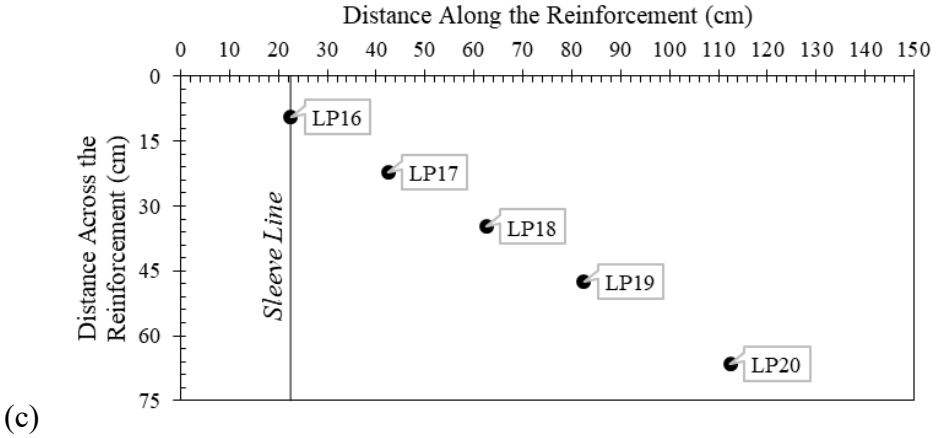

(c)

Figure 8.22. Locations of telltale connections: (a) Active reinforcement layer; (b) Upper passive reinforcement layer; and (c) Lower passive reinforcement layer.

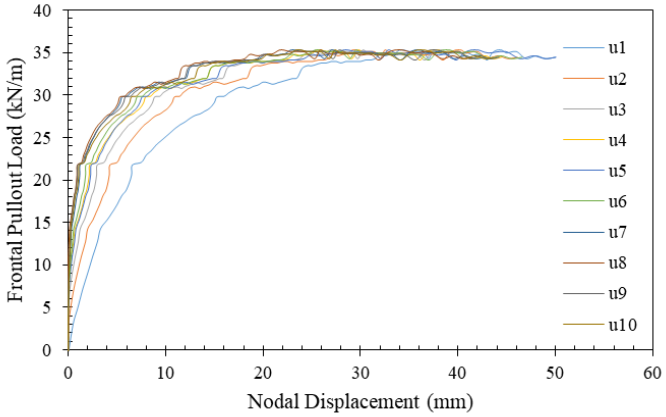

(a)

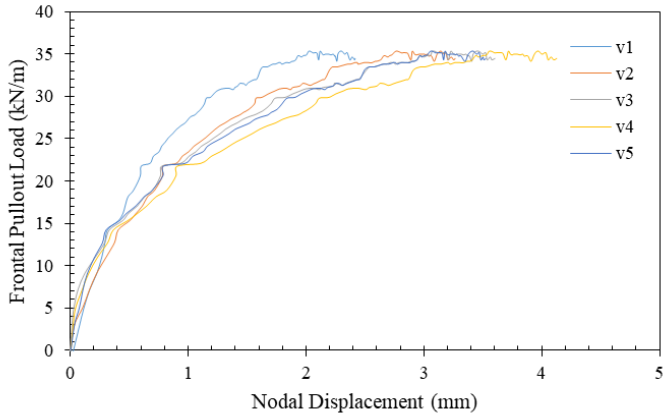

(b)

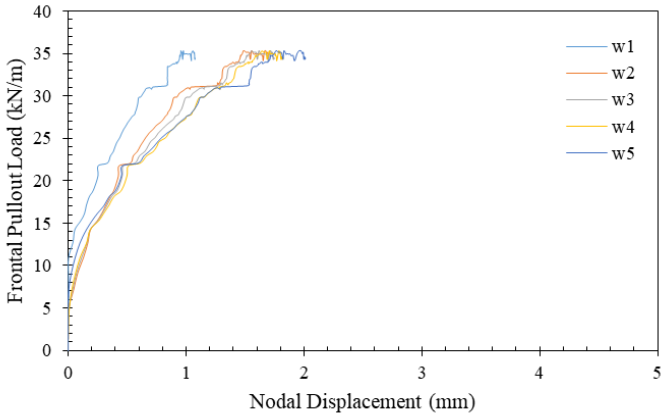

(c)

Figure 8.23. Reinforcement frontal load versus nodal displacement behavior: (a) Upper passive reinforcement layer; (b) Active reinforcement layer; and (c) Bottom passive reinforcement layer.

The displacement profiles were fit to their best parabolic function to faciltate calculating reinforcement strains. The parapolic function was found to be a good representation of the displacement profiles for the active and passive reinforcement layers in all the tests conducted in this study. Figure 8.25a shows the strain profiles. Figures 8.25b and 8.25c show the strain profiles for the upper and lower passive reinforcement layers, respectively. These figures also show the displacement and strain profiles for increasing values of frontal displacement of the active reinforcement layer. The parapbolic fit that was adopted for the displacement profiles of the active reinforcement resulted in linear strain profiles (strains are dervitaives of displacement with respect to length). The linear strain profiles were found to be a reasonable approximation and has been adopted in many design specifications (e.g. FHWA GEC-11). Similarly, the strain profiles of the passive reinforcement layers were linear too. Note that the strain profiles were limited to the rear reinforcement portions only, which exhibit the real tensile strain evolved in the reinforcement layers. These strain profiles allowed calculation of the tensile stresses transferred from the active reinforcement layer to the passive reinforcement layers and their percentage.

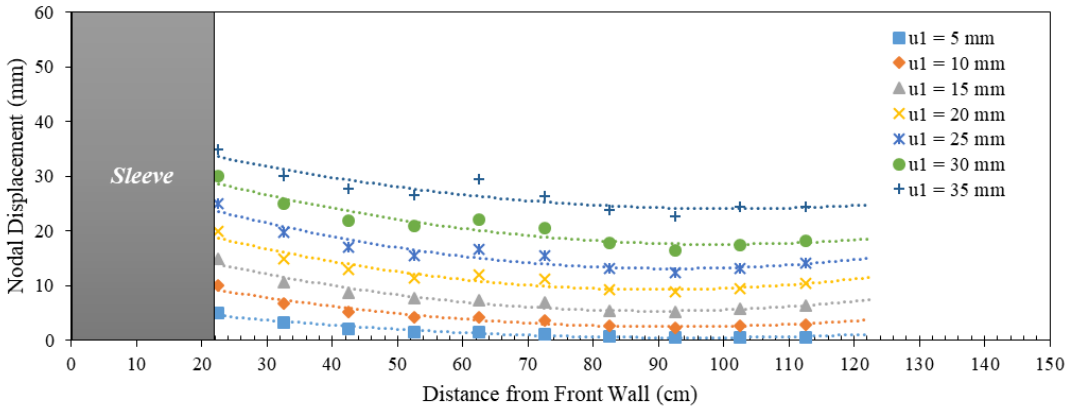

(a)

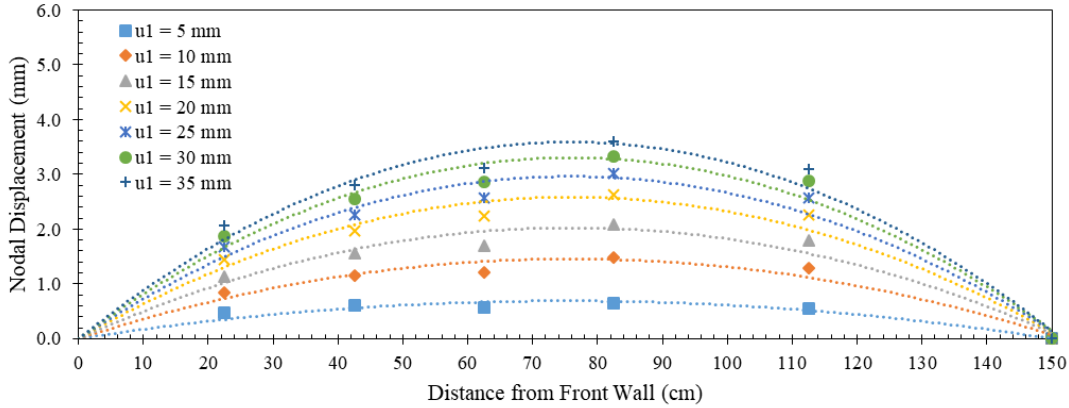

(b)

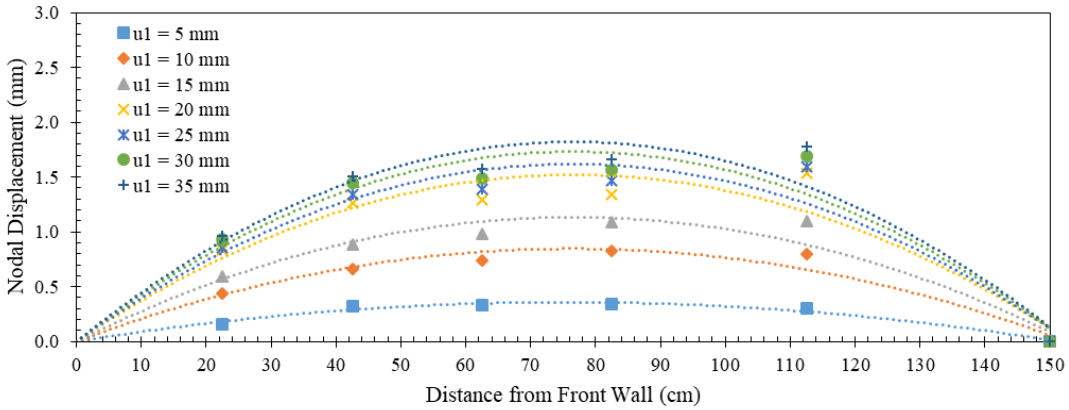

(c)

Figure 8.24. Reinforcement nodal displacement profiles: (a) Upper passive reinforcement layer; (b) Active reinforcement layer; and (c) Bottom passive reinforcement layer.

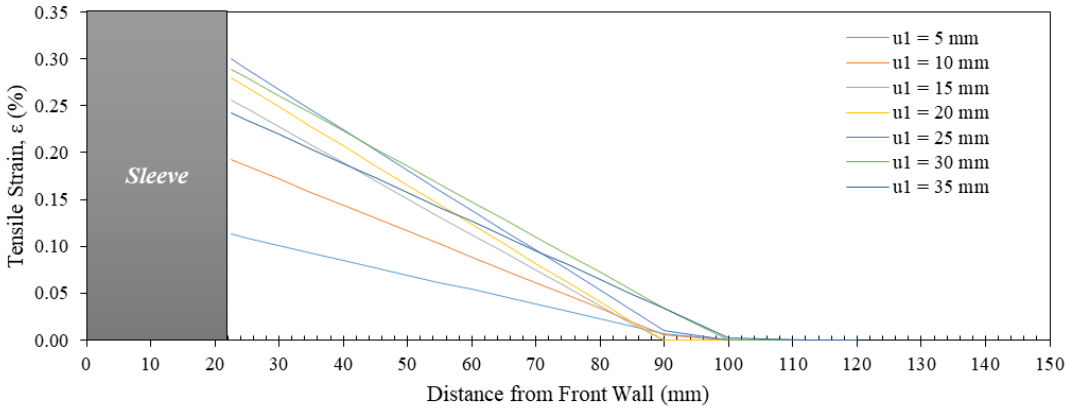

(a)

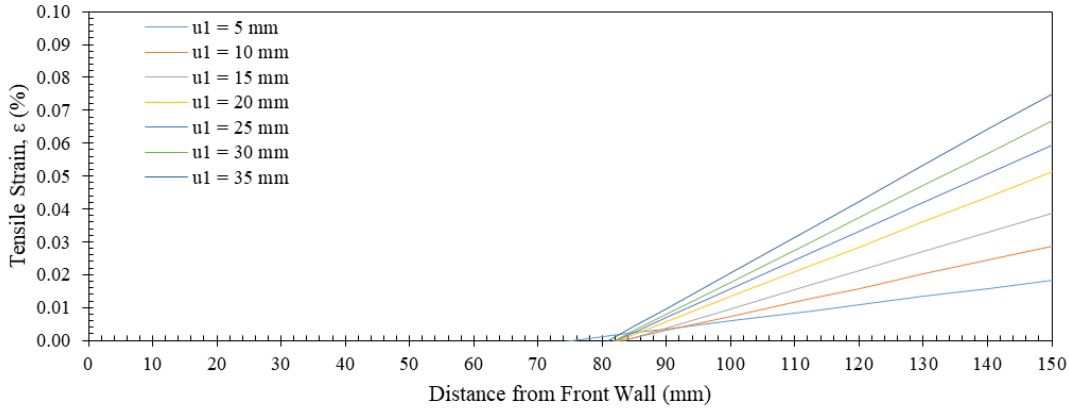

(b)

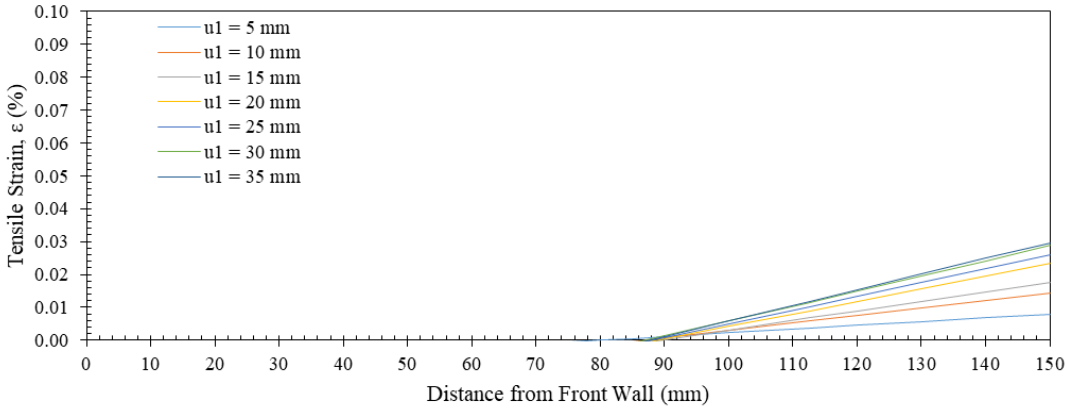

(c)

Figure 8.25. Reinforcement strain profiles: (a) Upper passive reinforcement layer; (b) Active reinforcement layer; and (c) Bottom passive reinforcement layer.

8.6.3. Reinforced soil mass displacements

Displacements within the reinforced soil mass were measured through the transparent side of the equipment, which allowed for direct visualization of the displacements of soil particles at a vertical section of the reinforced soil mass. Figures 8.26 through 8.34 show the displacement fields of the reinforced soil mass in the horizontal and vertical directions for increasing values of frontal displacement of the active reinforcement layer 5, 10, 15, 20, 25, 30, 35, 40, 45 mm, respectively. Each figure consists two subfigures a and b that present the horizontal and verical soil displacement fields, respectively. Tracable artificial gravel particles of similar size and shape to those of the gravel backfill material were used to validate the accuracy of displacement measurements taken at the boundary wall of the reinforced soil mass. These particles were attached to tell-tales, which were then attached to linear potentiometers to measure the artificial particle displacements in real time during testing. Figure 8.35 shows the locations of the artificial particles buried in the reinforced soil mass. Note that for the illustrative test, which was conducted using the short equipment configuration, particles LP32 and LP33 were not included.

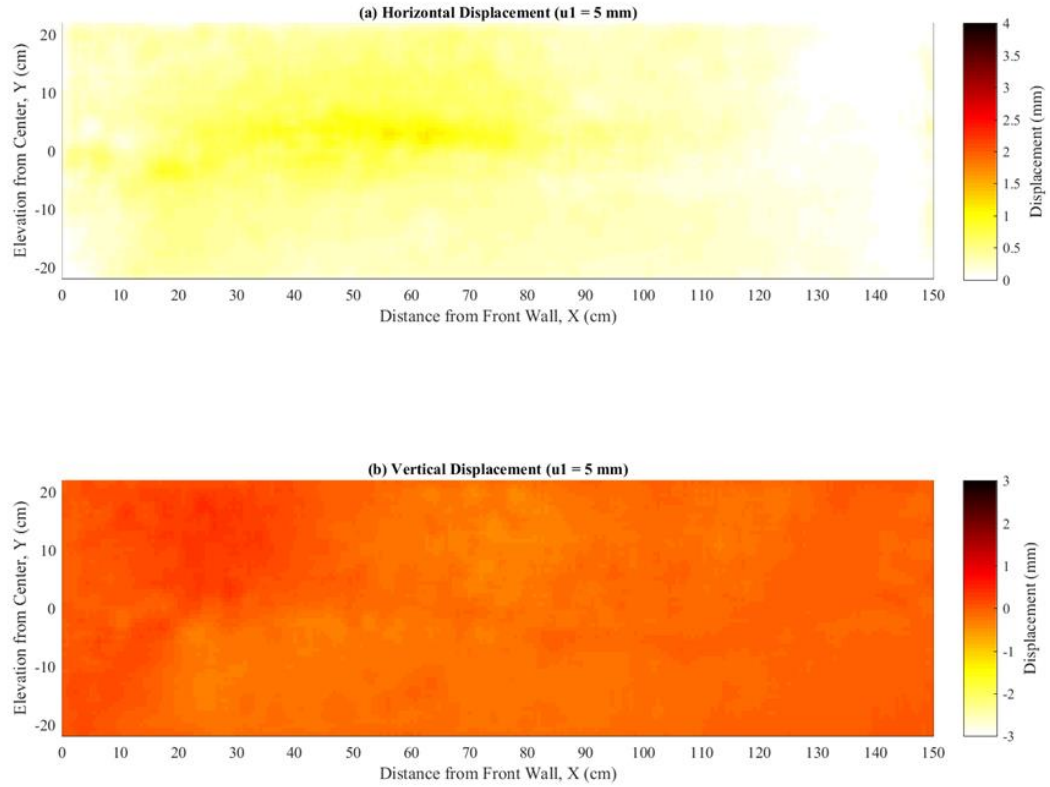

Figure 8.26. Displacement maps at 5-mm frontal displacement: (a) Horizontal displacements; and (b) Vertical displacements.

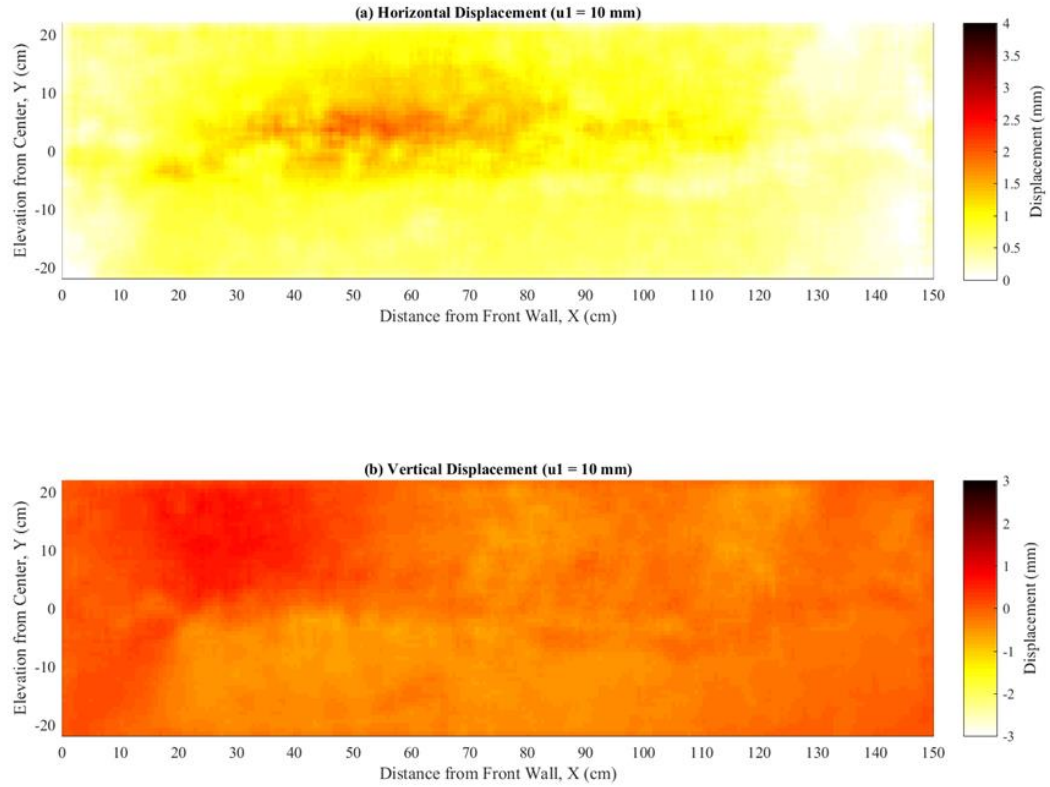

Figure 8.27. Displacement maps at 10-mm frontal displacement: (a) Horizontal displacements; and (b) Vertical displacements.

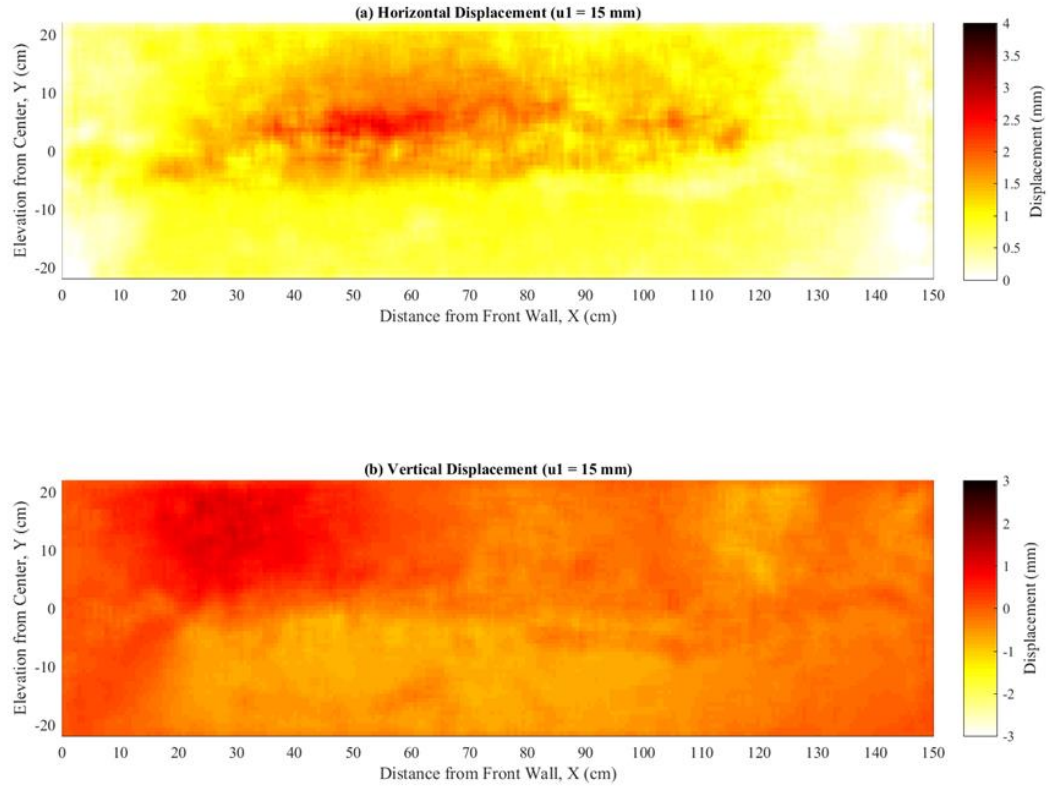

Figure 8.28. Displacement maps at 15-mm frontal displacement: (a) Horizontal displacements; and (b) Vertical displacements.

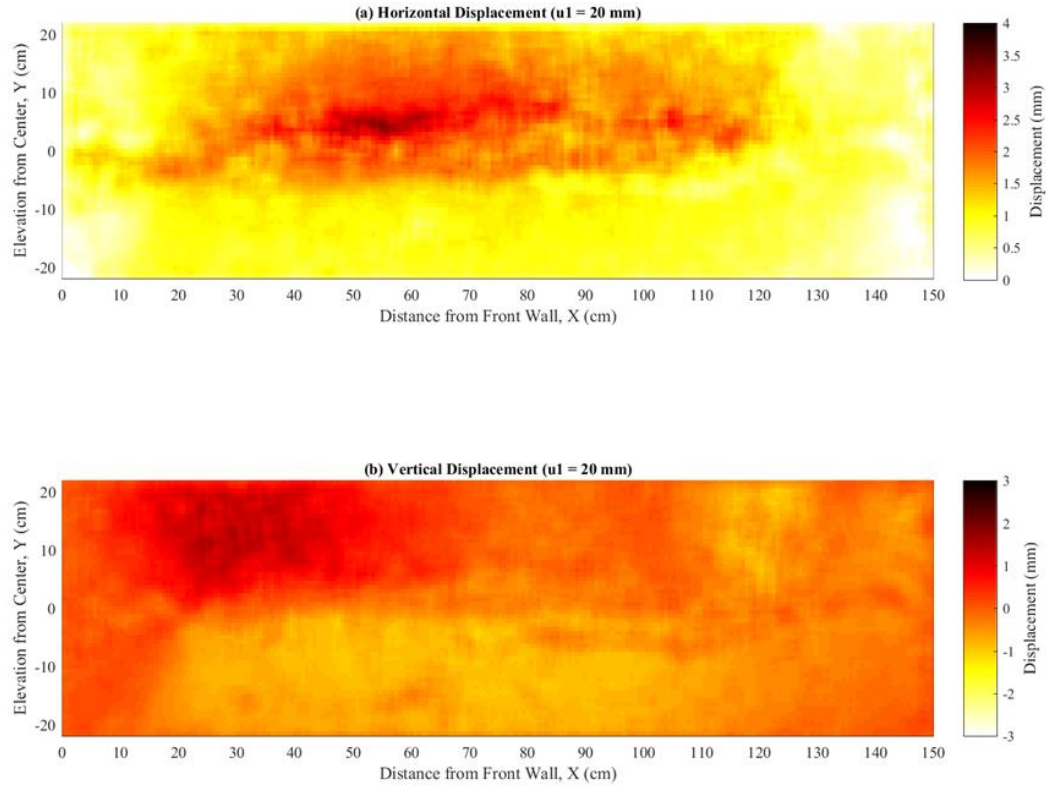

Figure 8.29. Displacement maps at 20-mm frontal displacement: (a) Horizontal displacements; and (b) Vertical displacements.

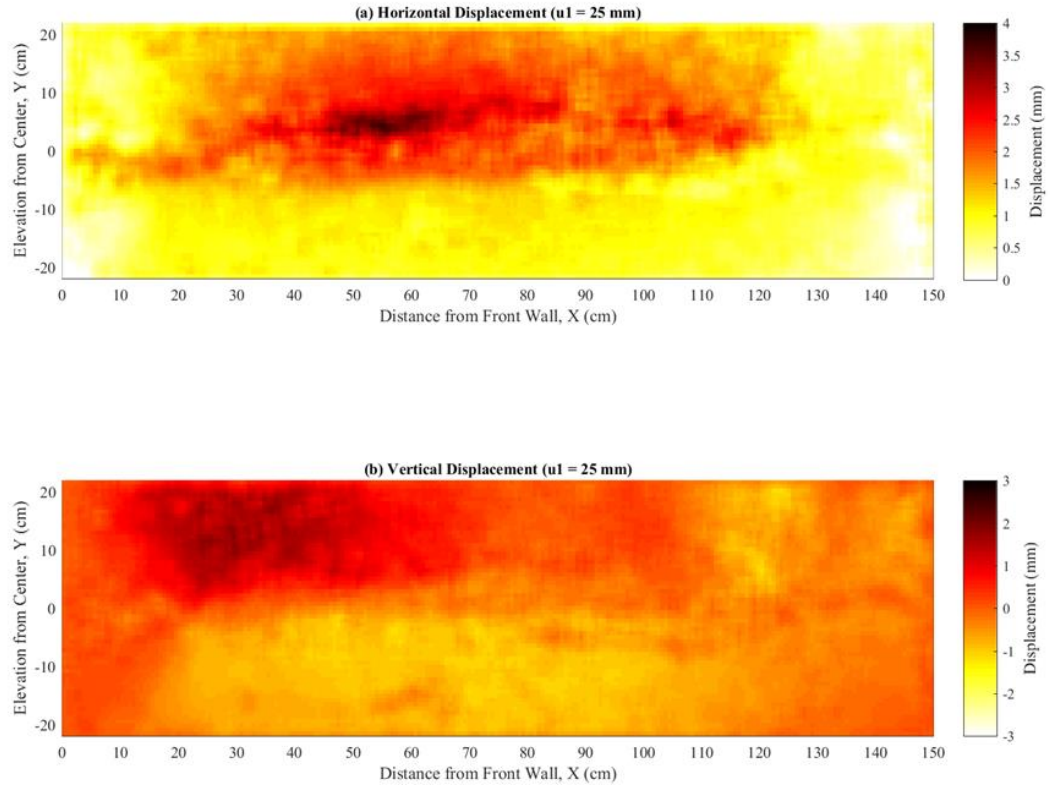

Figure 8.30. Displacement maps at 25-mm frontal displacement: (a) Horizontal displacements; and (b) Vertical displacements.

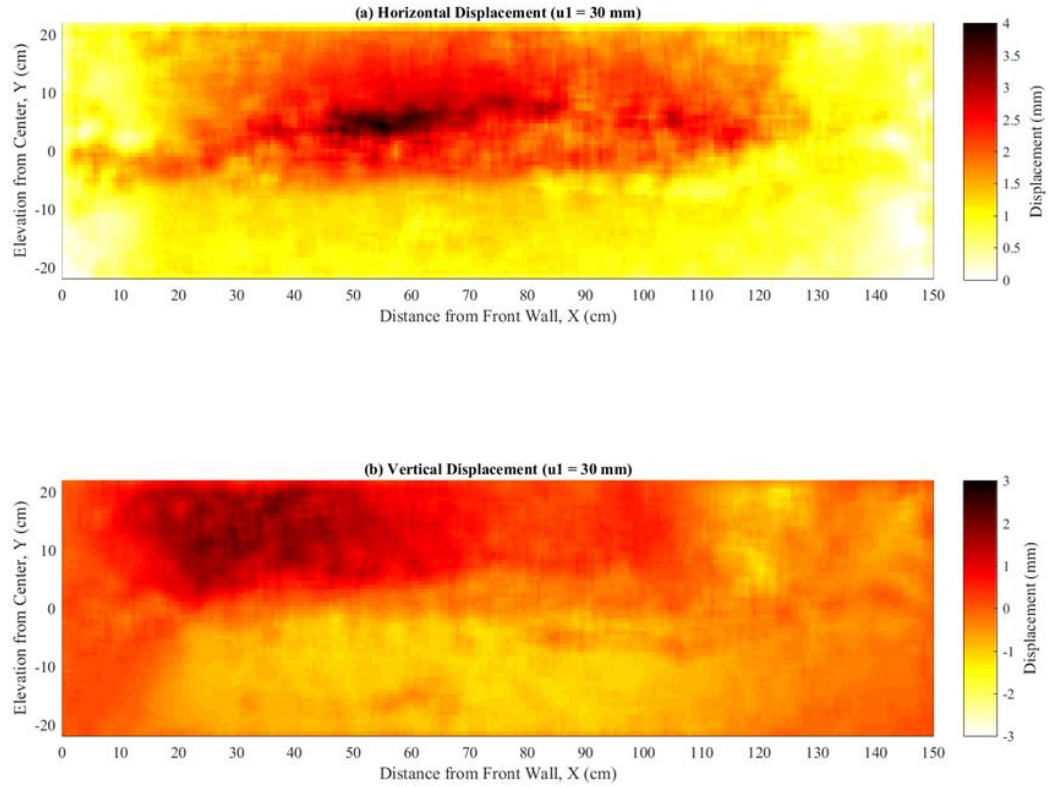

Figure 8.31. Displacement maps at 30-mm frontal displacement: (a) Horizontal displacements; and (b) Vertical displacements.

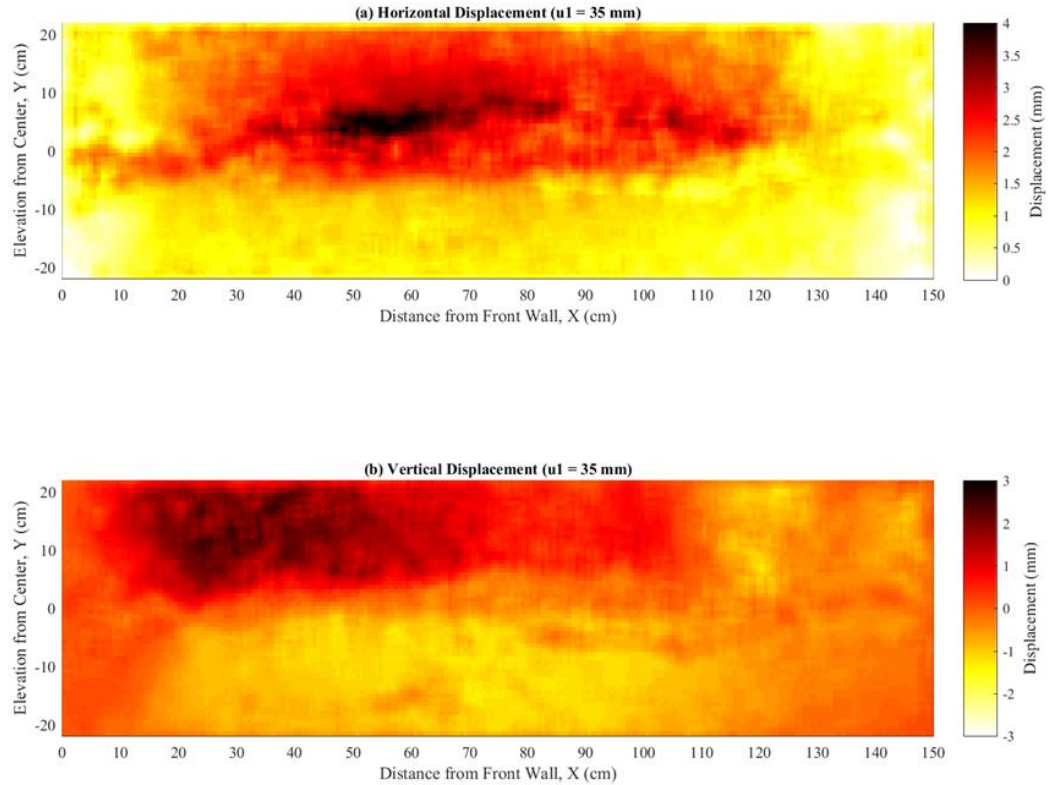

Figure 8.32. Displacement maps at 35-mm frontal displacement: (a) Horizontal displacements; and (b) Vertical displacements.

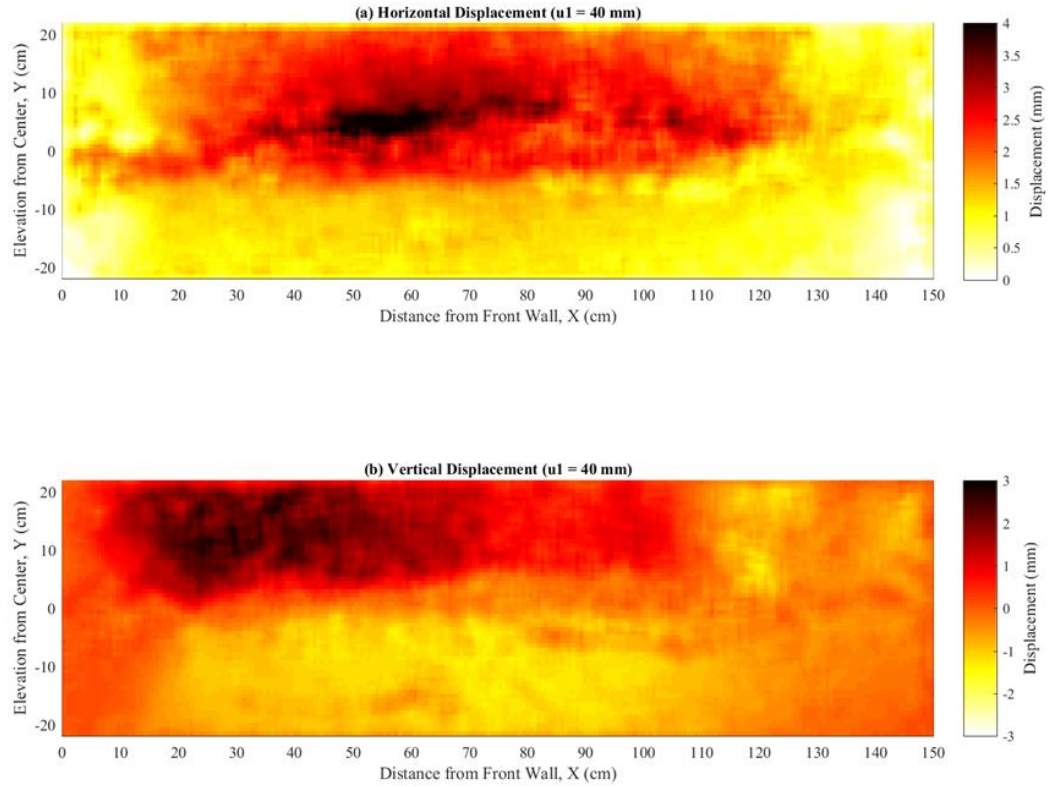

Figure 8.33. Displacement maps at 40-mm frontal displacement: (a) Horizontal displacements; and (b) Vertical displacements.

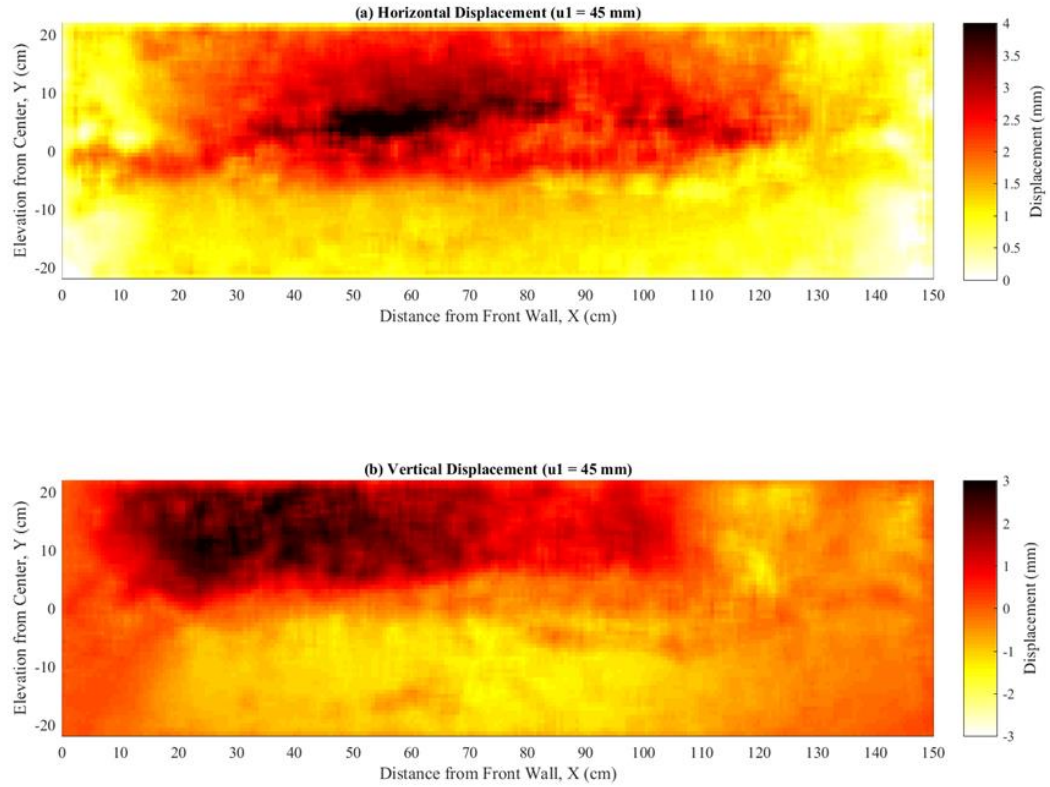

Figure 8.34. Displacement maps at 45-mm frontal displacement: (a) Horizontal displacements; and (b) Vertical displacements.

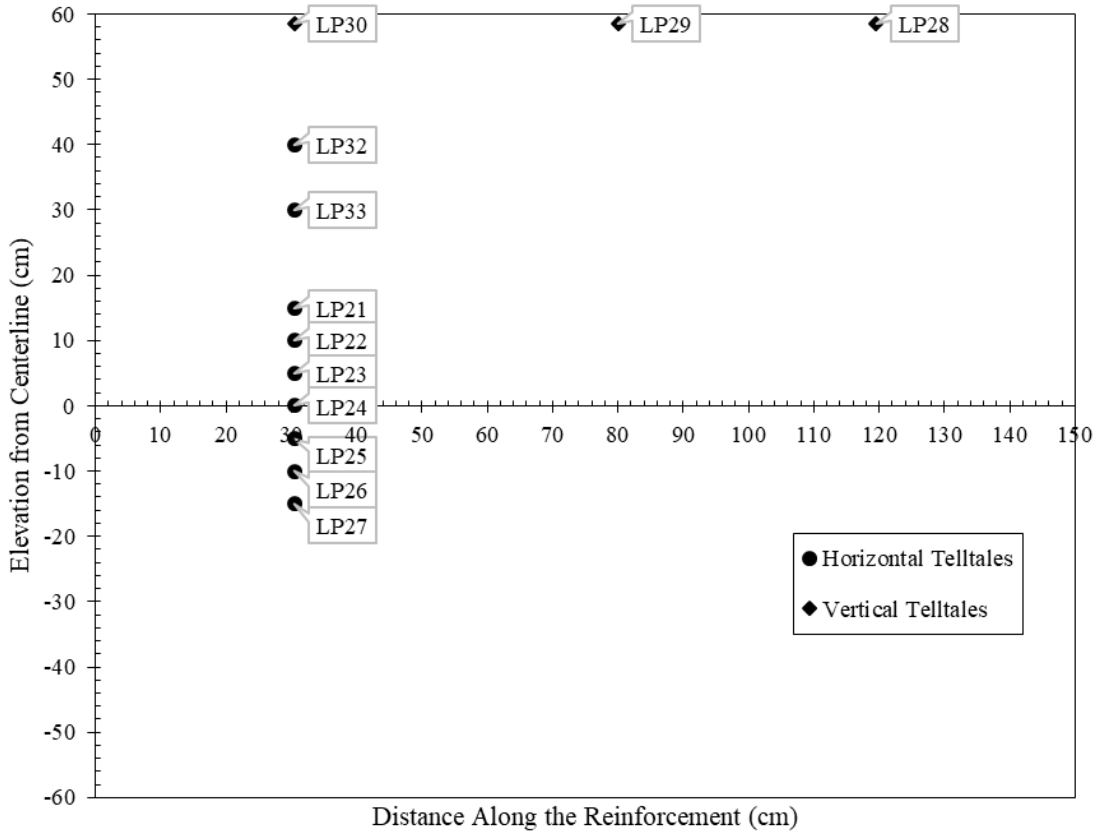

Figure 8.35. Locations of the artificial gravel particles within the reinforced soil mass.

8.6.3.1.Soil-reinforcement interface shear band

Seven artificial gravel particles were stacked along a vertical line located 30.5 cm (X = +30.5 cm) from the front wall. These particles were attached to linear potentiometers using tell-tales. This array of particles aimed at measuring the horizontal displacement of an originally vertical line, as shown in Figure 8.36. The figure also shows the horizontal displacements obtained at the boundary of the box after analyzing of the images tethered for the transparent sidewall. The two profiles show a good agreement at the various load levels. Specifically, evolution of the shear band with increasing frontal load can be

observed by analyzing images tethered from the side of the reinforced soil mass. In addition, the observed displacement at the front wall of the box (X = 0) were negligible over the depth of the reinforced soil (Figures 8.26a through 8.34a). This shows that the sleeve used almost essentially minimizes the effect of the front wall rigidity on the shear stresses generated at the soil-reinforcement interface.

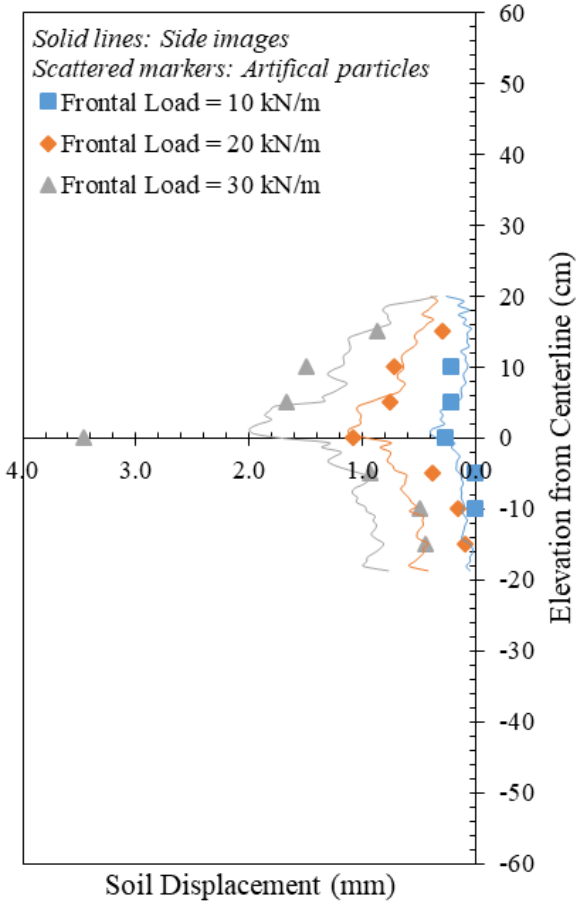

Figure 8.36. Horizontal displacement at X = +30.5 cm from the front wall of the box.

The horizontal soil displacement profile could be modeled using a sigmoid function as shown in Equation 8.1. Figure 8.37a shows a comparison between the modeled displacement and that measured using the artificial gravel particles and digital imaging. The soil shear strain could then be estimated by differentiating the horizontal displacement with respect to the elevation as shown in Equation 8.2. Figure 8.37b shows the shear strain profile.

$$\boldsymbol{\delta = \frac{2\delta_{max}}{1 + e^{bY}}\, u}$$

Equation 8.1

$$\gamma = \boldsymbol{\frac{d\delta}{dY}\, x100\%} = \left|\boldsymbol{\frac{2\delta_{max} b e^{bY}}{(1 + e^{bY})^2}\, u}\right| \boldsymbol{x100\%}$$

Equation 8.2

where δ and u are the soil and reinforcement displacements, respectively. δ_{max} is the maximum soil displacement at a given reinforcement displacement u (i.e., the soil displacement at the soil-reinforcement interface). This interface displacement depends on the soil-reinforcement interaction, normal stress, and reinforcement spacing. The constant b is a constant that depends on the shear stiffness of the soil, which depend on several parameters such as normal stress, void ratio, and particle characteristics.

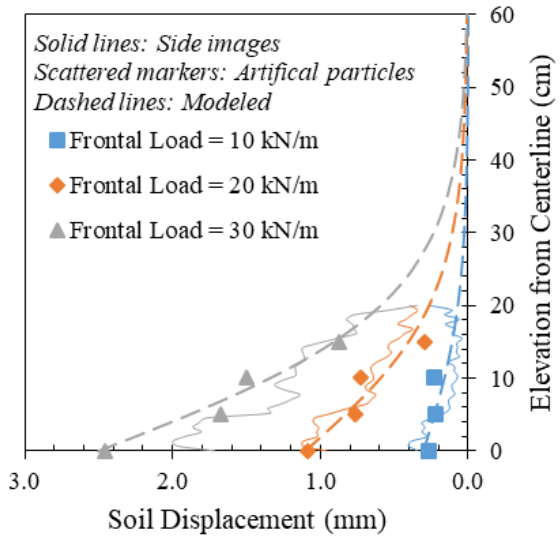

(a)

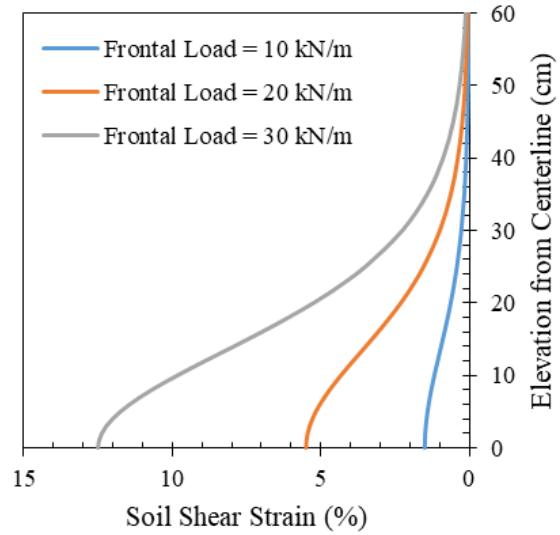

(b)

Figure 8.37. (a) Modeled horizontal displacement; and (b) Modeled shear Strain.

8.6.3.2.Soil-reinforcement interface differential displacement (relative displacement)

Understanding of the soil-reinforcement interface shear is essential for proper design of soil-geosynthetic systems under both working and ultimate stress conditions.

Most soil-reinforcement interface shear models assume that the interface shear mobilization is a function of the relative soil-reinforcement displacements along the interface. Such relative displacement is often assumed to be equal to the reinforcement displacement. However, this assumption may not be adequate since the soil displacements adjacent to the reinforcement may not be negligible. The relative displacement is the difference between the displacements of the reinforcement and those of the adjacent soil (i.e., soil slippage on the reinforcement).

Figure 8.38 shows the horizontal displacement profiles of the three reinforcement layers and of their adjacent soil planes. Specifically, Figures 8.38a through 8.38c present the displacement profiles for the active reinforcement, upper passive reinforcement, and lower passive reinforcement layers, respectively. For the active reinforcement, the difference between the reinforcement displacement and the soil displacement increased as the frontal load increased. In addition, the relative displacement along the reinforcement embedment length increased as the soil-reinforcement interface stresses propagated along the active reinforcement embedment length. Unlike the active reinforcement, the displacements of the passive reinforcements were similar to the displacements in their adjacent soil, as shown in Figures 8.38b and 8.38c. Note that the passive reinforcements displace only due to load transfer from the active reinforcement as conveyed through the soil mass between the active and passive reinforcement layers.

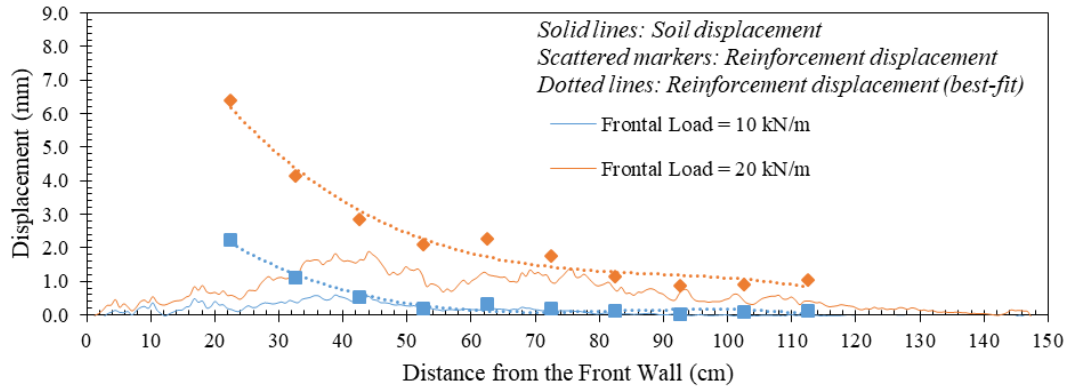

(a)

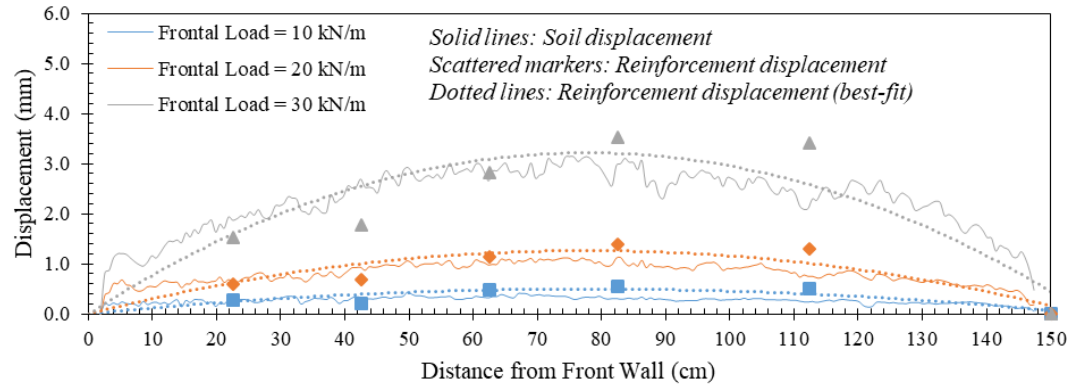

(b)

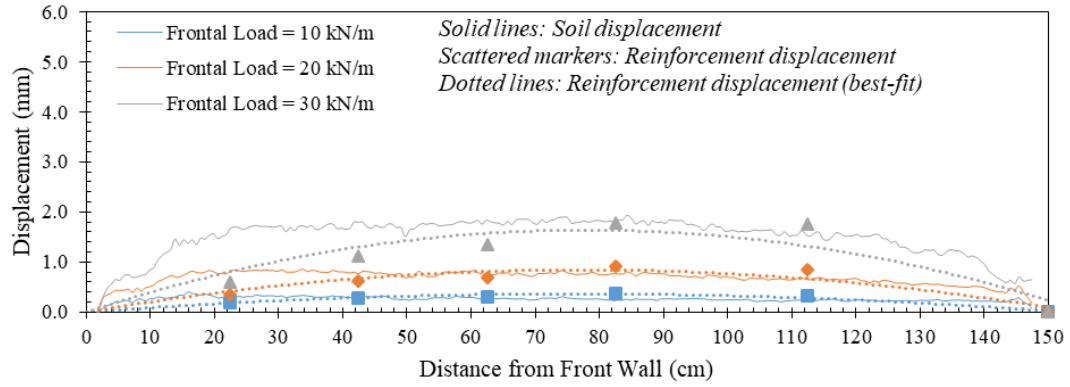

(c)

Figure 8.38. Reinforcement nodal displacement profiles and their adjacent soil displacement profiles: (a) Active reinforcement layer; (b) Upper passive reinforcement layer; and (c) Bottom passive reinforcement layer.

Figure 8.39 shows the horizontal displacement of the three reinforcement layers and of their adjacent artificial gravel particle displacement at X = +30.5 m. Specifically, Figures 8.39a through 8.39c present the displacement magnitudes for the active reinforcement, upper passive reinforcement, and lower passive reinforcement layers, respectively. Similar observation was made where the difference between the active reinforcement displacement and the soil displacement increased as the frontal load increased. On contrary, the displacements of the passive reinforcements were similar to the displacements in their adjacent soil.

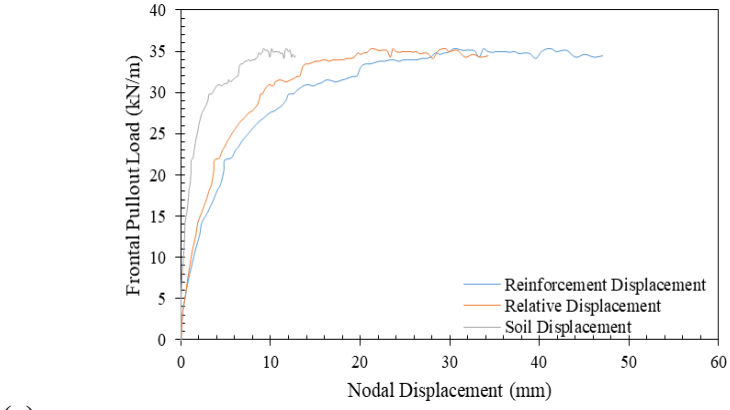

(a)

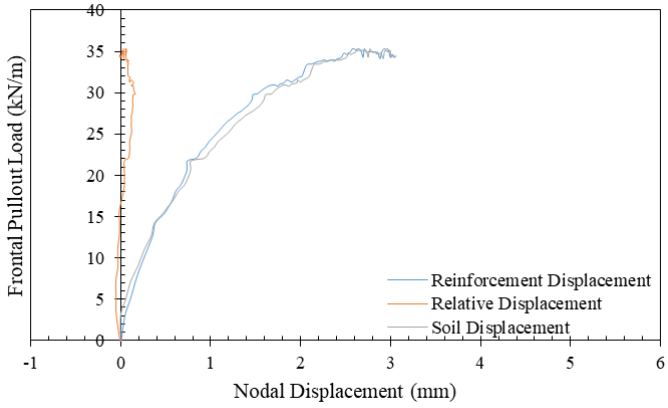

(b)

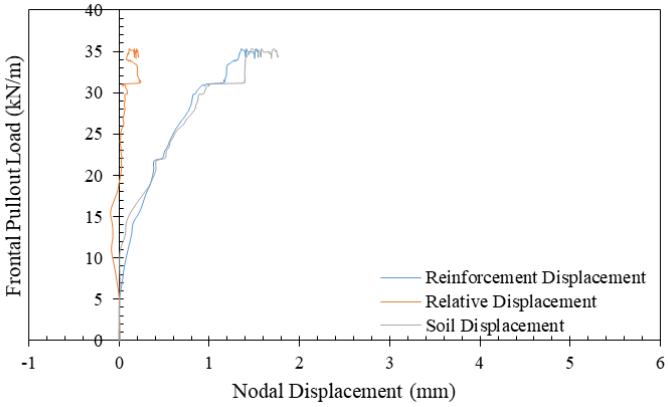

(c)

Figure 8.39. Reinforcement displacement and their adjacent artificial soil displacement at X = 30.5 m from the front wall: (a) Active reinforcement layer; (b) Upper passive reinforcement layer; and (c) Bottom passive reinforcement layer.

8.6.3.3.Dilatancy in the reinforced soil mass

Three artificial gravel particles were placed in the illustrative test on top of the reinforced soil mass, immediately underneath the normal pressure system (at Y = +21.5 cm). These particles were attached to linear potentiometers using tell-tales. This setup aimed at measuring the soil vertical displacement of an originally horizontal line centered in the box and located at the top of the reinforced soil mass (Figure 8.40). Figure 8.40 also shows the vertical displacement determined at the boundary of the box at Y = +20.0 cm after analyzing the images tethered from the transparent sidewall. The two profile show a reasonable agreement at various load levels. That is, the dilative/compressive behavior can be assessed with increasing frontal load as identified through analysis of the images tethered from the side of the reinforced soil mass.

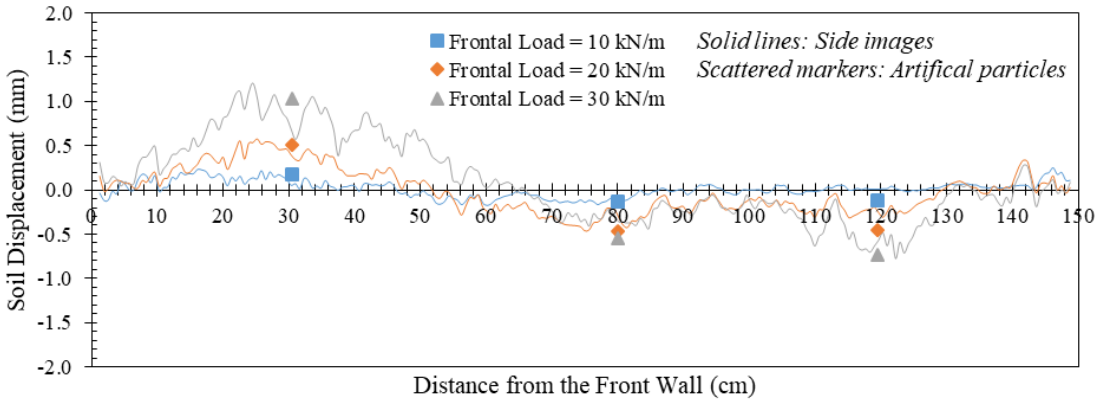

Figure 8.40. Vertical displacement at the surface of the reinforced soil mass.

8.6.4. Normal pressure

Figure 8.41 shows the normal pressure estimated at the elevation of the active reinforcement plane during the illustrative test. This pressure was defined using the load

measured by the load cells mounted on the reaction frame at the reaction point of each pneumatic actuator. These measured loads were added to the pressure exerted by the backfill self-weight and the normal pressure system self-weight. Figure 8.41 shows that normal pressure remained essentially constant until approximately 30% of the ultimate frontal pullout load (i.e., approximately 12 kN/m) was reached. However, beyond this load level, the normal pressure towards the front of the reinforced soil mass increased up to about 30% of the original normal pressure. Note that limited dilation was allowed during testing to highlight the capabilities of the equipment in assessing the free, reduced, and suppressed dilation conditions. The investigation of conditions corresponding to partially suppressed dilation may be consistent with the volume changes that may occur in real structures.

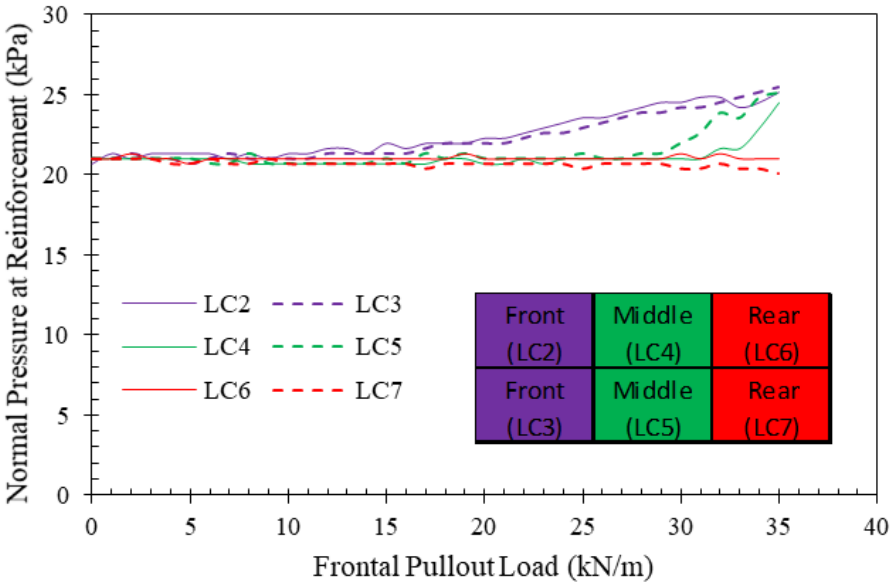

Figure 8.41. Normal pressure on the top of the reinforced soil mass.

8.6.5. Reinforcement unconfined tensile behavior

The new experimental device was designed to allow simultaneous determination of both the confined and the unconfined tensile behavior of the reinforcement specimen used in each soil-reinforcement interaction test. The evaluation of the unconfined tensile response was achieved by analyzing images tethered for the unconfined portion of the reinforcement. The exposed portion of the reinforcement had been speckled using spray paint and randomly dappled with a white paint marker. This served to create two levels of pattern that enhanced the accuracy of the image analysis. Indeed, the average strain rate was deliberately maintained below 0.1%/min throughout testing. The average strain rate in the illustrative test was approximately 0.02%/min. Figure 8.42 shows the strain data measured from images at various locations along the reinforcement unconfined zone, as well as the average of the measured points. Figure 8.42 also shows two data points reported by the reinforcement manufacturer in the technical specifications. Good agreement can be observed between the specified values and the values measured in the unconfined portion of the illustrative test.

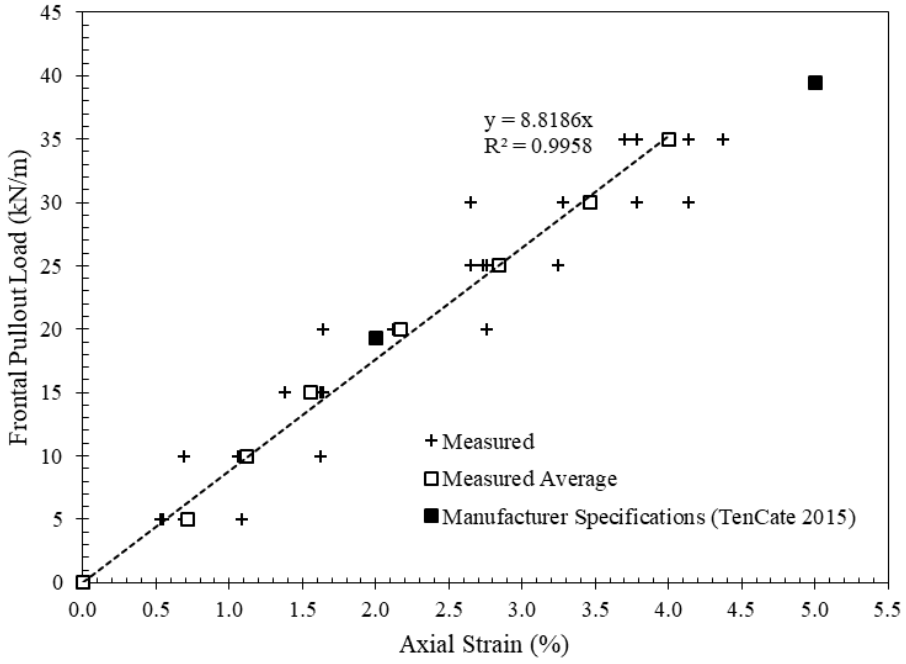

Figure 8.42. Reinforcement unconfined tensile behavior.

8.7. CONCLUSIONS

This chapter includes assessment of the multiple aspects that should be taken into consideration to establish an experimental approach that accounts for the interaction between adjacent reinforcement layers. The chapter includes a comprehensive review of soil-reinforcement interaction experimental aspects that should be considered to properly characterize the interaction between soil and multiple geosynthetic reinforcements. It also includes a detailed description of a novel experimental approach and a newly developed testing equipment designed to comprehensively assess soil-reinforcement interaction and its effect on neigbouring reinforcements under both working and ultimate stress conditions. In addition, typical testing results were presented to illustrate the capabilities of the proposed experimental approach.

The equipment uses a geosynthetic-reinforced soil mass that contains three reinforcement layers. This study led to the following findings:

- The new device was found capable of assessing the composite interaction in a geosynthetic-reinforced soil mass considering variable reinforcement vertical spacing.
- The device was found to provide suitable measurements of straining in both the loaded and the adjacent reinforcement layers.
- The device allows the investigation of the interface shear stress transfer mechanisms as well as visualization of the kinematic response of soil particles adjacent to the geosynthetic reinforcements.
- The device allowed measurement of soil displacement field via digital image analysis, which was found to provide good basis for determination of the shear band.
- The equipment was found to be able to successfully monitor the dilatant behavior of the reinforced soil mass, which is expected to provide significant insight into the effect of reinforcement vertical spacing on the performance of geosynthetic-reinforced soil structures.
- The artificial gravel particles were found to efficiently measure internal displacements of soil.
- Good match was observed between redundant measurements of soil displacements determined using the artificial gravel particles and images from the transparent sidewall. This included horizontal and vertical soil displacements.

- Good match was observed between the tensile properties obtained from the unconfined reinforcement meaurements and the properties specified by the reinforcement manufacturer in the technical specifications.

8.8. REFERENCES

Abdelouhab, A., Dias, D., and Freitag, N. (2010). "Physical and Analytical Modelling of Geosynthetic Strip Pull-out Behaviour." Geotextiles and Geomembranes, Vol. 28, No. 1, pp. 44–53.

Abdel-Rahman, A.H., Ibrahim, M.A., and Ashmawy, A.K. (2007). "Utilization of a Large-Scale Testing Apparatus in Investigating and Formulating the Soil/Geogrid Interface Characteristics in Reinforced Soils." Australian Journal of Basic and Applied Sciences, Vol. 1, No. 4, pp. 415-430.

Adams, M.T., Nicks, J.E., Stabile, T., Wu, J.T.H., Schlatter, W., and Hartmann, J. (2012). Geosynthetic Reinforced Soil Integrated Bridge System Interim Implementation Guide. Report No. FHWA-HRT-11-026, Federal Highway Administration, McLean, VA.

Alagiyawanna, A.M.N., Sugimoto, M., Sato, S., and Toyota, H. (2001). "Influence of Longitudinal and Transverse Members on Geogrid Pullout Behavior during Deformation." Geotextiles and Geomembranes, Vol. 19, No. 8, pp. 483–507.

Alfaro, M.C., Hayashi, S., Miura, N., and Watanabe, K. (1995a). "Pullout Interaction Mechanism of Geogrid Strip Reinforcement." Geosynthetics International, Vol. 2, No. 4, pp. 679-698.

Alfaro, M.C., Miura, N., and Bergado, D.T. (1995b). "Soil-Geogrid Reinforcement Interaction by Pullout and Direct Shear Tests." Geotechnical Testing Journal, GTJODJ, Vol. 18, No. 2, pp. 157-167.

ASTM D4595-11 (2011). "Standard Test Method for Tensile Properties of Geotextiles by the Wide-Width Strip Method." ASTM Standards, American Society for Testing and Materials (ASTM), West Conshohocken, PA.

ASTM D6706-01 (2013). "Standard Test Method for Measuring Geosynthetic Pullout Resistance in Soil." ASTM Standards, American Society for Testing and Materials (ASTM), West Conshohocken, PA.

Aydogmus, T. and Klapperich, H. (2008). "Design and Evaluation of an Enhanced Shear and Pull-Out Testing Device." Proceedings of the 4th European Geosynthetics Conference, paper 170.

Bergado, D.T. and Chai, J.-C. (1994). "Pullout Force/Displacement Relationship of Extensible Grid Reinforcements." Geotextiles and Geomembranes, Vol.13, No.5, pp. 295-316.

Bergado, D.T. and Teerawattanasuk, C. (2001). "Analytical Models for Predicting the Pullout Capacity and Interaction between Hexagonal Wire Mesh and Silty Sand Backfill." Tamakang Journal of Science and Engineering, Vol. 4, No. 4, pp. 227-238.

Bernal, A., Salgado, R., Swan Jr., R.H., and Lovell C.W. (1997). "Interaction between Tire Shreds, Rubber-Sand and Geosynthetics." Geosynthetics International, Vol. 4, No. 6, pp. 623-643.

Brand, S.R. and Duffy, D.M. (1987). "Strength of Pull-Out Testing of Geogrids." Proceedings of Geosynthetics 1987, Vol. 1, New Orleans, LA, pp. 226-236.

Chang, J.C., Hannon, J.B., and Forsyth, R.A. (1977). "Pullout Resistance and Interaction of Earthwork Reinforcement and Soil." Transportation Research Record 640, National Research Council, Washington, DC, pp. 1-7.

Christopher, B.R. (1993). Deformation Response and Wall Stiffness in Relation to Reinforced Soil Wall Design. Ph.D. Dissertation, Department of Civil Engineering, Purdue University, West Lafayette, IN, 354 p.

Cuelho, E.V. (1998). Determination of Geosynthetic Constitutive Parameters and Soil/Geosynthetic Interactions by In-Air and In-Soil Experiments. MS Thesis, Montana State University, MT.

Dyer, M.R. (1985). Observation of the Stress Distribution in Crushed Glass with Applications to Soil Reinforcement. Ph.D. Thesis, The University of Oxford, UK.

Elias, V. (1979). "Friction in Reinforced Earth Utilizing Fine Grained Backfills." International Conference on Soil Reinforcement, Paris, France, pp. 435-8.

European Standards (2004). Geotextiles and Geotextile-related Products. Determination of Pullout Resistance in Soil. European Standards EN 13738:2004.

Fannin, R.J. and Raju, D.M. (1993). "On the Pullout Resistance of Geosynthetics." Canadian Geotechnical Journal, Vol. 30, No. 3, pp. 409-417.

Farrag, K., Acar, Y.B., and Juran, I. (1993). "Pull-Out Resistance of Geogrid Reinforcements." Geotextiles and Geomembranes, Vol. 12, No. 2, pp. 133-159.

Geosynthetic Institute (1991). Geogrid Pullout. GRI Test Methods GRI GG5. Geosynthetic Institute (GRI).

Hanumasagar, S.S., Roodi, G.H., and Zornberg, J.G. (2014). "Pullout Characterization of Geogrids Embedded in Blends of Dredged Material and Steel Slag Fines." Proceedings of the 10th ICG Conference, Berlin, Germany.

Ingold, T.S. (1983). "A Laboratory Investigation of Grid Reinforcements in Clay." Geotechnical Testing Journal, Vol. 6, No. 3, pp. 112-119.

Jacobs, F., Ruiken, A., and Ziegler, M. (2012a). "Experimental Investigation of Geogrid Reinforced Soil under Plane Strain Conditions." Geosynthetics Asia 2012, 5th Asian Regional Conference on Geosynthetics, 10 to 14 December 2012, Bangkok, Thailand.

Jacobs, F., Ruiken, A., and Ziegler, M. (2012b). "Investigation of Geogrid Reinforced Soil with Large Scale “Element” Testing." GeoAmericas 2012, Lima, Perú, May 2012.

Jacobs, F., Ziegler, M., and Ruiken, A. (2013). "Experimental Investigation of the Stress-Strain Behaviour of Geogrid Reinforced Soil." GeoAfrica 2013, Accra, Ghana, 18–20 November 2013.

Jayawickrama, P.W., Lawson, W.D., Wood, T.A., and Surles, J.G. (2014). "Pullout Behavior of Welded Grid Reinforcements Embedded in Coarse Granular Backfill." ASCE Geo-Congress, Atlanta, GA, February 2014.

Jewell, R.A. (1980). Some Effects of Reinforcement on the Mechanical Behavior of Soils. Ph.D. Dissertation, Cambridge University, Cambridge, UK.

Juran, I., Guermazi, A., Chen, C.L., and Ider, M.H. (1988). "Modelling and Simulation of Load Transfer in Reinforced Soil: Part 1." International Journal for Numerical and Analytical Methods in Geomechanics, Vol. 12, No. 2, pp. 141-155.

Kharchafi, M. and Dysli, M. (1993). "Study of Soil-Geotextile Interaction by an X-Ray Method." Geotextiles and Geomembranes, Vol. 12, No. 4, pp. 307-325.

Koerner, R.M. (2005). Designing with Geosynthetics, Fifth Edition. Pearson Prentice Hall.

Koerner, R.M. (1986). Direct Shear/Pull-Out Tests on Geogrids. Report No. 1, Department of Civil Engineering, Drexel University, Philadelphia, PA.

Ladeira, M.A.S.A. (1995). Estudo dos Fenômenos de Interação Solo-Geossintetico Através de Ensaios de Arranque. (In Portuguese) MS Thesis, University of Porto, Portugal.

Leshchinsky, D., Kaliakin, V., Bose, P., and Collin, J. (1994). "Failure Mechanism in Geogrid-Reinforced Segmental Walls: Experimental Implications." Soils and Foundations, Vol. 34, No. 4, pp. 33-41.

Lopes, M.L. (1992). Walls Reinforced with Geosynthetics. (In Portuguese) Ph.D. Thesis, University of Porto, Portugal, 335 p.

Lopes, M.L. and Ladeira, M. (1996). "Role of Specimen Geometry, Soil Height and Sleeve Length on the Pull-Out Behaviour of Geogrids." Geosynthetic International, Vol. 3, No. 6, pp. 701-719.

Marques, J.M.M.C. (2005). "Finite Element Modelling of the Pull-Out Test of Geosynthetics." VIII International Conference on Computation Plasticity, E. Onate and D.R. Owen (eds.).

McGown, A., Andrawes, K.Z., and Kabir, M.H. (1982). “Load Extension Testing of Geotextiles Confined in Soil.” In Proceedings of the 2nd International Conference on Geotextiles, Vol. 3, pp. 793-798. Roseville, Minnesota, August 1982.

Meyer, N., Nernheim, A., and Emersleben, A. (2003). "Influence of Normal pressure, Soil Density and Types of Geogrids on Soil-Geogrid Interaction Coefficient." E-Conference "Modern Trends in Foundation Engineering: Geotechnical Challenges and Solutions", IITM, India.

Min, Y., Leshchinsky, D., Ling, H.I., and Kaliakin, V.N. (1995). "Effects of Sustained and Repeated Tensile Loads on Geogrid Embedded in Sand." Geotechnical Testing Journal, Vol. 18, No. 2, pp. 204-225.

Minažek, K. and Mulabdić, M. (2013). "A Review of Soil and Reinforcement Interaction Testing in Reinforced Soil by Pullout Test." Građevinar 2013, Vol. 65, No. 3, pp. 235-250.

Moraci, N. and Gioffre, D. (2006). "A Simple Method to Evaluate the Pullout Resistance of Embedded in a Compacted Granular Soil Extruded Geogrids." Geotextiles and Geomembranes, Vol. 24, No. 2, pp. 116–128.

Moraci, N. and Recalcati, P. (2006). "Factors Affecting the Pullout Behaviour of Extruded Geogrids Embedded in a Compacted Granular Soil." Geotextiles and Geomembranes, Vol. 24, No. 4, pp. 220–242.

Morsy, A.M., Leshchinsky, D., and Zornberg, J.G. (2017a), “Effect of Reinforcement Spacing on the Behavior of Geosynthetic-Reinforced Soil,” In Proceedings of Geotechnical Frontiers 2017, American Society of Civil Engineers (ASCE), March 12-15, 2017 | Orlando, Florida, USA, pp. 112-125.

Morsy, A.M., Zornberg, J.G., Christopher, B.R., Leshchinsky, D., Tanyu, B.F., and Han, J. (2017b), “Experimental Approach to Characterize Soil-Reinforcement Composite Interaction,” In Proceedings of the 19th International Conference on

Soil Mechanics and Geotechnical Engineering (19th ICSMGE), International Society for Soil Mechanics and Geotechnical Engineering (ISSMGE), September 17-22, 2017 | Seoul, Korea, pp. 451-454.

Myles, B. (1982) “Assessment of Soil Fabric Friction by Means of Shear.” Proceedings 2nd International Conference on Geotextiles, Las Vegas, p. 787-791.

Ochiai, H., Otani, J., Hayashic, S., and Hirai, T. (1996). "The Pull-Out Resistance of Geogrids in Reinforced Soil." Geotextiles and Geomembranes, Vol. 14, No. 1, pp. 19-42.

Palmeira, E.M. (2009). "Soil-Geosynthetic Interaction: Modelling and Analysis." Geotextiles and Geomembranes, Vol. 27, No. 5, pp. 368–390.

Palmeira, E.M. and Milligan, G.W.E. (1989). "Scale and Other Factors Affecting the Results of Pull-Out Tests of Grids Buried in Sand." Geotechnique, Vol. 39, No. 3, pp. 511-524.

Roodi, G. H., & Zornberg, J. G. (2017). “Stiffness of soil-geosynthetic composite under small displacements. II: Experimental evaluation.” Journal of Geotechnical and Geoenvironmental Engineering, ASCE, Vol. 143, No. 10.

Saxena, S.K. and Budiman, J.S. (1985). "Interface Response of Geotextiles." Proceedings of the 11th International Conference on Soil Mechanics and Foundation Engineering.

Schuettpelz, C., Fratta, D., and Edil, T. (2009). "Evaluation of the zone of influence and stiffness improvement from geogrid reinforcement in granular materials." Transportation Research Record: Journal of the Transportation Research Board, Vol. 2116, pp. 76-84.

Stadler, A.T. (2001). Geogrid Reinforcement of Piedmont Residual Soil. Report No. HWY-2001-02, North Carolina Department of Transportation, Raleigh, NC.

Teixeira, S.H.C. (2003). Estudo da Interação Solo-Geogrelha em Testes de Arrancamento e a sua Aplicação na Análise e Dimensionamento de Maciços Reforçados. (In Poruguese) Ph.D. Thesis, School of Engineering, Univerity of São Paulo, São Carlos.

TenCate Geosynthetics (2015). Mirafi® HP570 Specifications. Nicolon Corporation.

Tzong, W.H. and Cheng-Kuang, S. (1987). "Soil-Geotextile Interaction Mechanism in Pullout Test." Proceedings of Geosynthetics 1987, Vol. 1, New Orleans, LA, pp. 250-259.

Williams, N.D. and Houlihan, M.F. (1987). "Evaluation of Interface Friction Properties between Geosynthetics and Soils." Proceedings of Geosynthetics 1987, Vol. 2, New Orleans, LA, pp. 616-627.

Yuan, Z. and Chua, K.M. (1991). "Numerical Evaluation of the Pullout Box Method for Studying Soil-Reinforcement Interaction." Transportation Research Record 1278, Transportation Research Board, Washington, D.C., pp. 116-124.

Zhou, J., Chen, Chen, J.-F., Xue, J.-F., and Wang, J.-Q. (2012). "Micro-Mechanism of the Interaction between Sand and Geogrid Transverse Ribs." Geosynthetics International, 2012, Vol. 19, No. 6, pp. 1072-6349.

Zornberg, J.G., Ferreira, J.A.Z., Gupta, R.V., Joshi, R.V., and Roodi, G.H. (2009). Geosynthetic-Reinforced Unbound Base Courses: Quantification of the Reinforcement Benefits. Center for Transportation Research (CTR), Report No.

FHWA/TX-10/5-4829-1, Austin, Texas, December 2009, Revised February 2012, 170 p.

Zornberg, J.G. and Mitchell, J.K. (1994). "Reinforced Soil Structures with Poorly Draining Backfills. Part I: Reinforcement Interactions and Functions." Geosynthetics International, Vol. 1, No. 2, pp. 103-147.

Zornberg, J.G., Roodi, G.H., Ferreira, J.Z., and Gupta, R. (2013). "Characterization of Soil-geosynthetic Interaction under Small Displacement Conditions." Proceedings of the 18th International Conference on Soil Mechanics and Geotechnical Engineering, 02-06 September, Paris, France, pp. 1385-1388.

Chapter 9: Parametric Evaluation of Soil-Geosynthetic Composite Interaction

9.1. INTRODUCTION

A comprehensive testing program was conducted using the newly developed experimental approach and equipment detailed in Chapter 8. The testing program was designed to evaluate the following aspects: (1) test repeatability; (2) effect of reinforced soil normal stress on the soil-reinforcement composite interaction behavior; (3) effect of reinforcement vertical spacing on the soil-reinforcement composite interaction behavior; (4) effect of reinforcement properties on the soil-reinforcement composite interaction behavior; (5) effect of boundary type on the soil-reinforcement composite interaction behavior; and (6) effect of backfill properties on the soil-reinforcement composite interaction behavior. This chapter provides a parametric evaluation and discussion of results in light of these aspects.

9.2. TESTING PROGRAM

This section describes the testing scheme adopted to fulfil the objectives of this dissertation. The following subsections include the testing configurations for the various tests and the characteristics of the materials used in the testing program.

The equipment is designed to have two configuration: (1) 450-mm (1.5-ft Configuration, whose dimensions are 1500 mm (L) x 300 mm (W) x 450 mm (H), as shown in Figure 9.1a; and (2) 120-mm (4-ft) Configuration, whose dimensions are 1500 mm (L) x 300 mm (W) x 1200 mm (H), as shown in Figure 9.1b. Three reinforcement layers were placed at a vertical spacing ranging from 0.05 m (2 in.) to 0.15 mm (6 in.) in the first configuration and ranging from 0.20 m (8 in.) to 0.40 m (16 in.) for the second

configuration. The target normal pressure ranged from 15 kPa (2.25 psi) to 50 kPa (7 psi) at the level of the main (middle) reinforcement layer. This normal pressure was intended to be low enough to allow pullout failure to occur before reinforcement rupture. This, particularly, allows excessive deformation to take place in the reinforcement and the surrounding soil (mostly pullout failure). This allows complete understanding of the soil-reinforcement load-transfer mechanisms and assessment of the soil-reinforcement composite interaction behavior. The embedment length of the main reinforcement layer was 1016 mm (40 in.). On the other hand, the boundary reinforcement layers were extended to the rear end of the reinforced soil mass, where they were clamped.

Table 9.1 shows the detailed experimental program adopted in this study. The program is divided into seven series A through G: Series (A) includes a baseline test that was used in most of comparisons. This test was conducted with the baseline materials AASHTO Gravel No. 8 and HP570 woven geotextile reinforcements, and baseline reinforcement spacing and normal stress; Series (B) includes tests conducted at various reinforcement spacings for two different normal stresses; Series (C) includes a test conducted using different passive reinforcement condition; Series (D) includes tests conducted using different reinforcement types; Series (E) includes tests conducted at different normal stresses; Series (F) includes a test conducted using different fill material; and Series (G) includes a test conducted using different dilation condition.

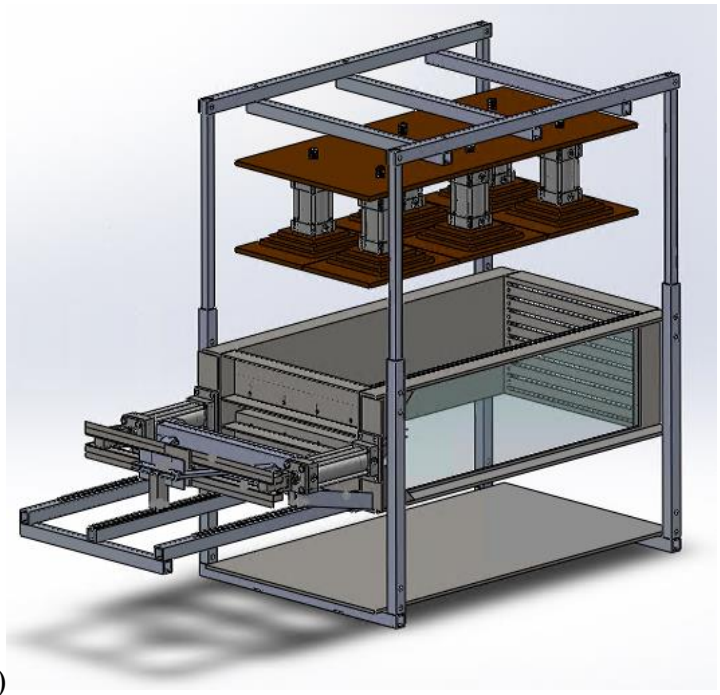

(a)

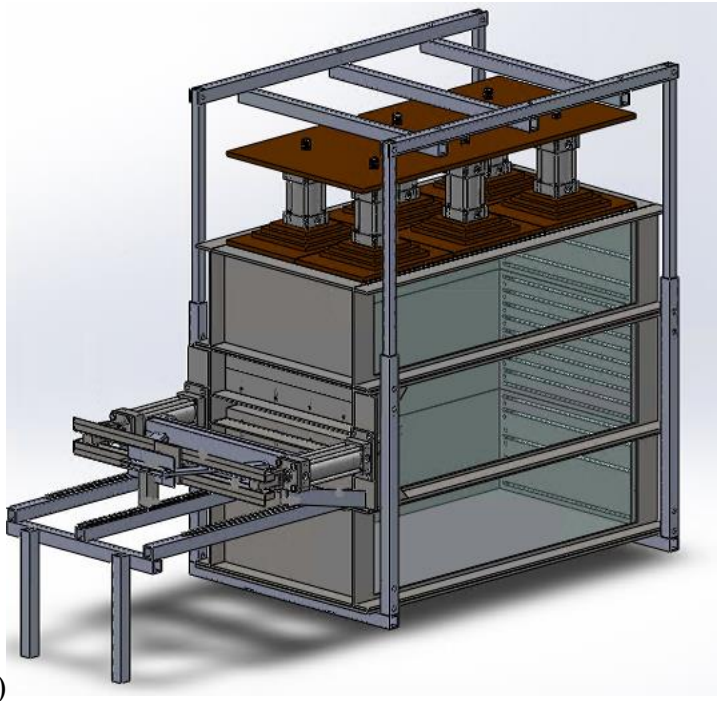

(b)

Figure 9.1. Equipment testing configurations: (a) 45-cm configuration (short); and (b) 120-cm configuration (tall).

Table 9.1. Testing scheme.

Test Series	*Theme of the Series*	*Test Number*	*Test ID*	*Testing Variables*					
				Fill Material	*Reinforcement Spacing, S_v*	*Normal Stress, σ_v*	*Geosynthetic Type*	*Boundary Type*	*Dilation Control*
A	***Baseline***	1	GP-06-03-G1-G	AASHTO Gravel No. 8	0.15 m	21 kPa	HP570	Geosynthetic	Allowed
B	***Reinforcement Spacing, S_v***	2	GP-02-03-G1-G	AASHTO Gravel No. 8	0.05 m	21 kPa	HP570	Geosynthetic	Allowed
		3	GP-04-03-G1-G		0.10 m				
		4	GP-02-07-G1-G		0.05 m	50 kPa			
		5	GP-04-07-G1-G		0.10 m				
		6	GP-04-07-G1-G(R)		0.10 m				
		7	GP-06-07-G1-G		0.15 m				
		8	GP-08-07-G1-G		0.20 m				
		9	GP-12-07-G1-G		0.30 m				
		10	GP-16-07-G1-G		0.40 m				
C	***Boundary Type***	11	GP-06-03-G1-S	AASHTO Gravel No. 8	0.15 m	21 kPa	HP570	Mylar	Allowed
D	***Geosynthetic Type***	12	GP-06-03-G2-G	AASHTO Gravel No. 8	0.15 m	21 kPa	RS580i	Geosynthetic	Allowed
		13	GP-06-02-G3-G			15 kPa	BX1100		
		14	GP-06-03-G4-G			21 kPa	BX1200		
		15	GP-06-03-G5-G			21 kPa	80T		
E	***Normal Stress, σ_v***	16	GP-06-02-G1-G	AASHTO Gravel No. 8	0.15 m	15 kPa	HP570	Geosynthetic	Allowed
		17	GP-06-05-G1-G			35 kPa			
F	***Fill Material***	18	SP-06-03-G1-G	Montery Sand No. 30	0.15 m	21 kPa	HP570	Geosynthetic	Allowed
G	***Dilation Control***	19	GP-06-03S-G1-G	AASHTO Gravel No. 8	0.15 m	21 kPa	HP570	Geosynthetic	Reduced

9.3. PARAMETRIC EVALUATION

9.3.1. Test repeatability

A comparison was conducted to assess the repeatability of the test. Two identical tests were conducted at the same conditions. Table 9.2 summarizes the properties of the tests involved in this comparison. Specifically, two tests were conducted using HP570 polyester woven geotextile reinforcements. The reinforcement has ultimate tensile strength 70 kN/m and tensile stiffness of 876 kN/m at 5% tensile strain in the cross-rollway direction (i.e., cross-machine direction). Three reinforcement layers, one active and two passive reinforcements were used in each test. The reinforcements were placed at a vertical spacing of 0.10 m. The passive reinforcement layers are of the same type as the active layers. Both tests used AASHTO Gravel No. 8 fill material and were conducted at normal stress of 50 kPa at the active reinforcement level (i.e., central horizontal plane of the reinforced soil mass).

Table 9.2. Summary of repeated tests.

Test ID	***Testing Variables***					
	Fill Material	***S_v***	***σ_v***	***Active GS***	***Passive GS***	***Dilation***
GP-04-03-G1-G GP-04-03-G1-G(R)	AASHTO No. 8	0.10 m	50 kPa	HP570	HP570	Allowed

Figure 9.2 shows the frontal pullout load-displacement experimental curves for both tests. Good agreement can be between the two curves. Figures 9.3 through 9.6 show the displacement profiles for the active and passive reinforcement layers at active reinforcement frontal displacements (u1) of 5, 10, 15, and 20 mm, respectively. Good match can be observed between the displacement profiles obtained from both tests at the various loading stages. Similar observation can be made regarding the displacement profiles of the passive reinforcement layers. Figures 9.7a through 9.7d present the

horizontal soil displacement measured for nodal displacements of 5, 10, 15, and 20 mm, respectively. These displacement were measured at specific locations by tracking artificial gravel particles making a vertical array within the soil at 30.5 cm from the front wall. It was observed that the soil displacements are very similar for both tests at the various loading stages.

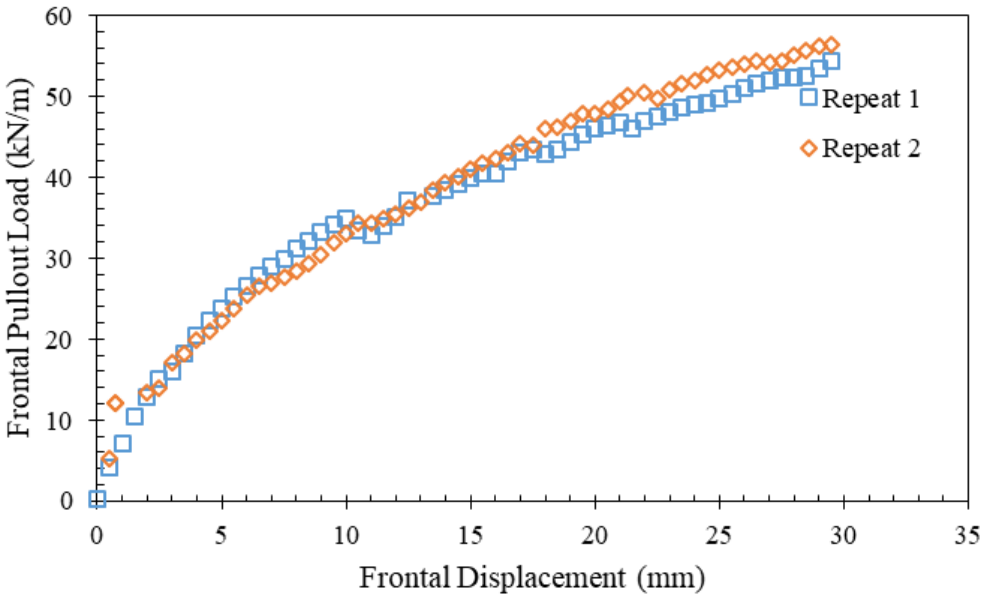

Figure 9.2. Frontal pullout load-displacement curves.

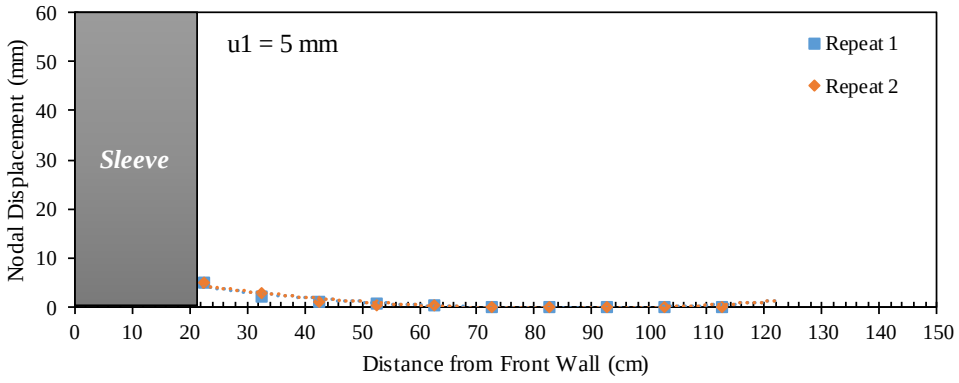

(a)

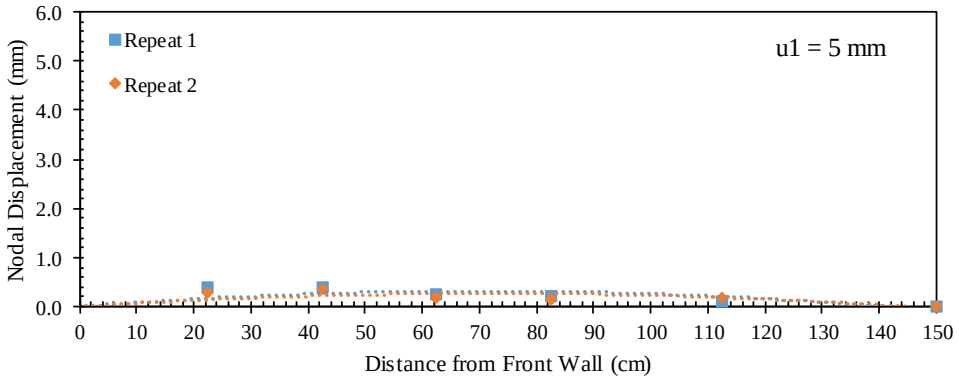

(b)

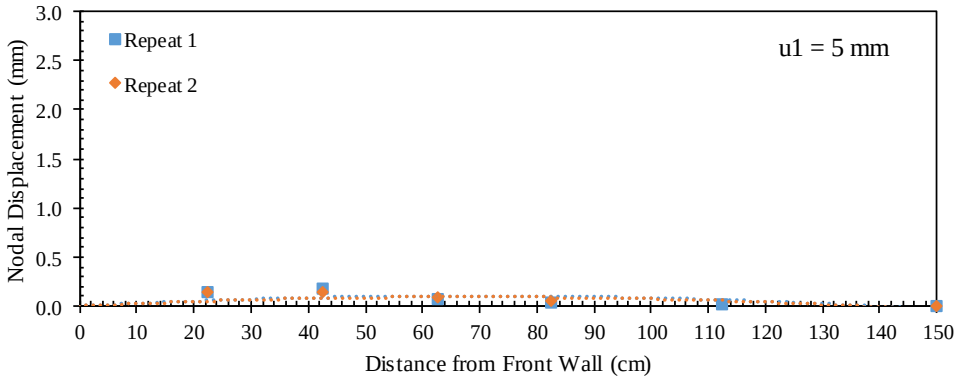

(c)

Figure 9.3. Reinforcement displacement profiles at frontal displacement u1 = 5 mm: (a) Active reinforcement; (b) Upper passive reinforcement; and (c) Lower passive reinforcement.

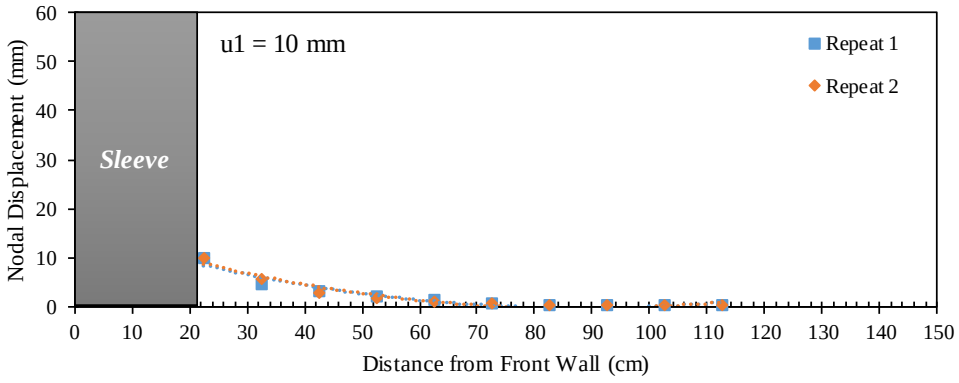

(a)

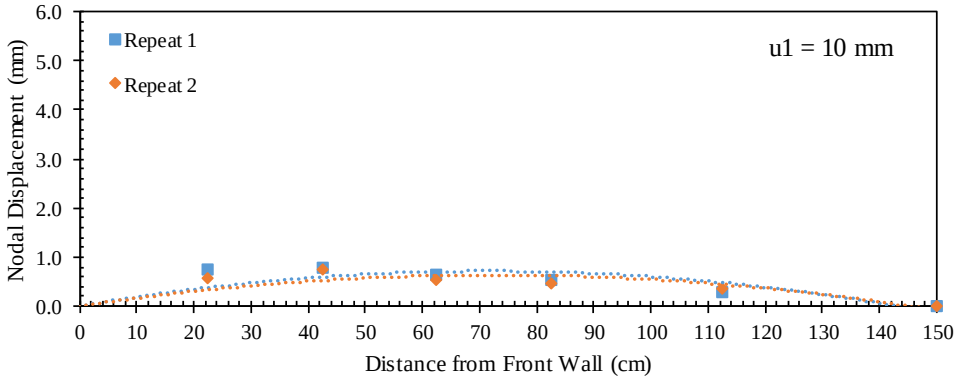

(b)

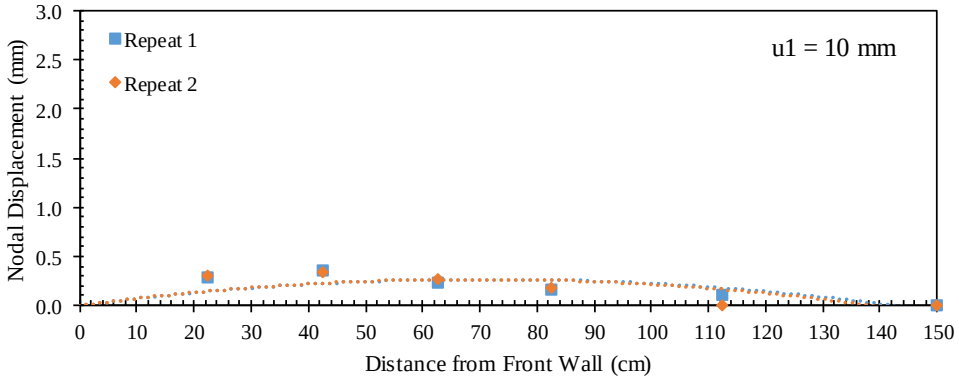

(c)

Figure 9.4. Reinforcement displacement profiles at frontal displacement u1 = 10 mm: (a) Active reinforcement; (b) Upper passive reinforcement; and (c) Lower passive reinforcement.

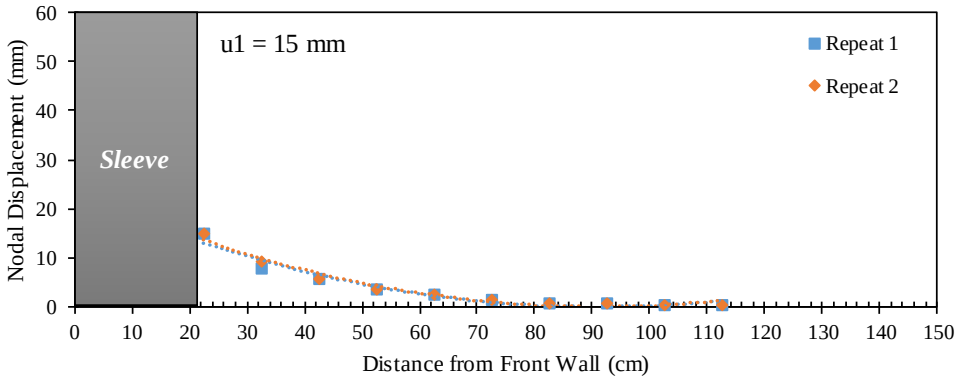

(a)

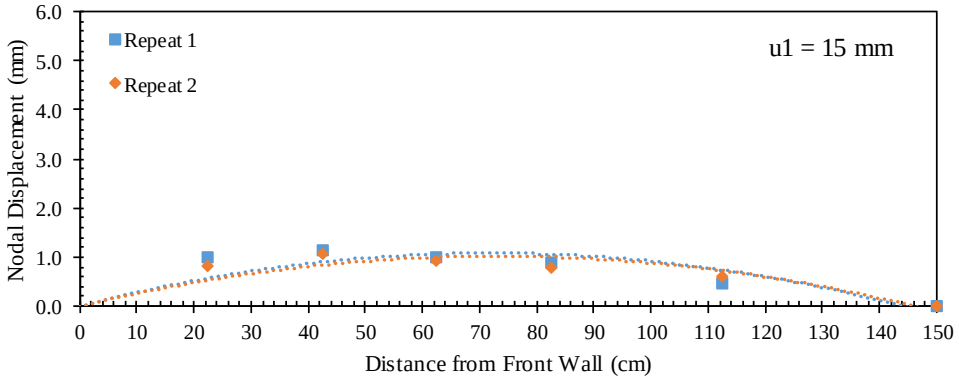

(b)

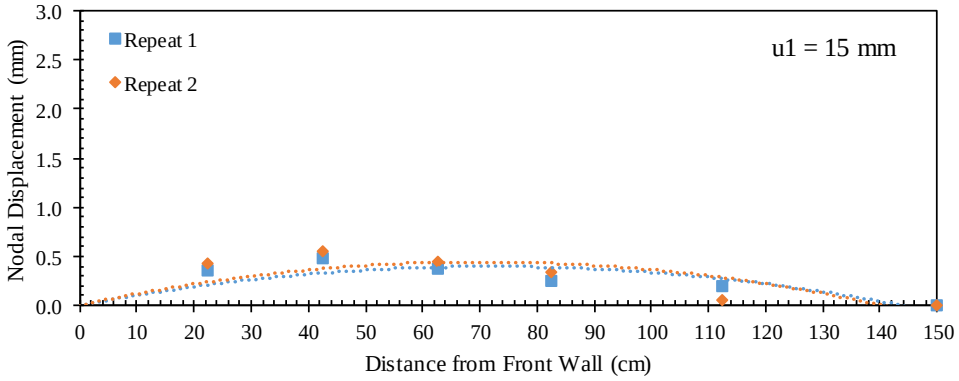

(c)

Figure 9.5. Reinforcement displacement profiles at frontal displacement u1 = 15 mm: (a) Active reinforcement; (b) Upper passive reinforcement; and (c) Lower passive reinforcement.

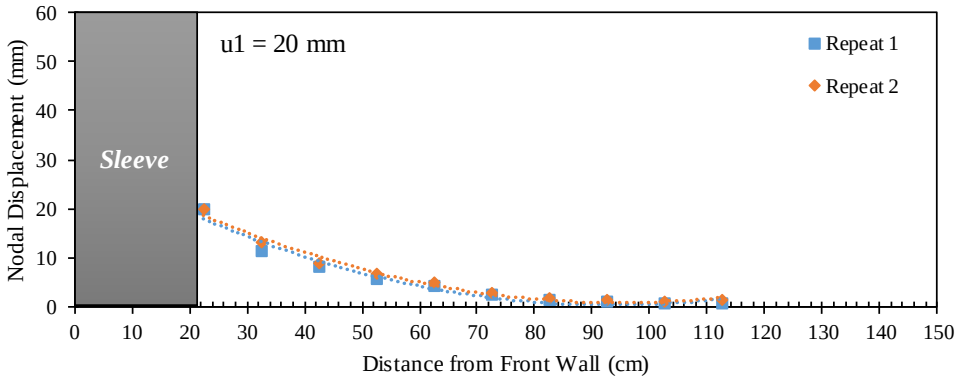

(a)

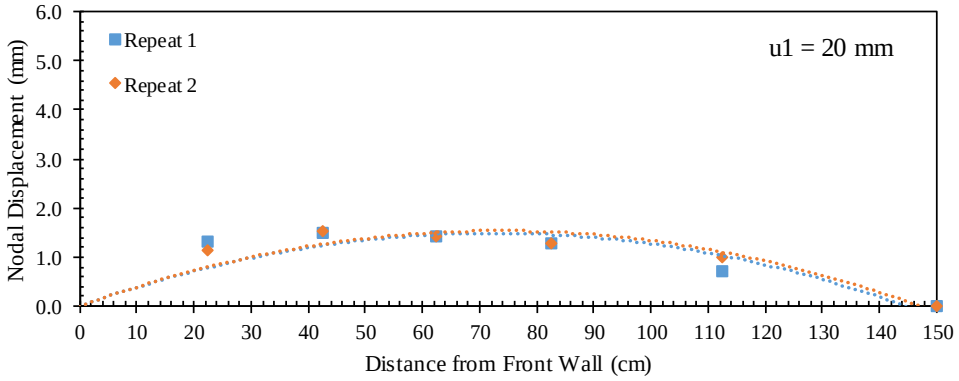

(b)

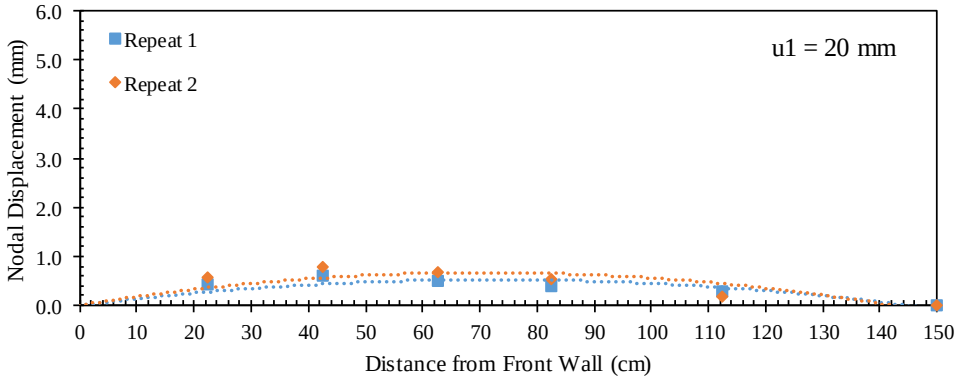

(c)

Figure 9.6. Reinforcement displacement profiles at frontal displacement u1 = 20 mm: (a) Active reinforcement; (b) Upper passive reinforcement; and (c) Lower passive reinforcement.

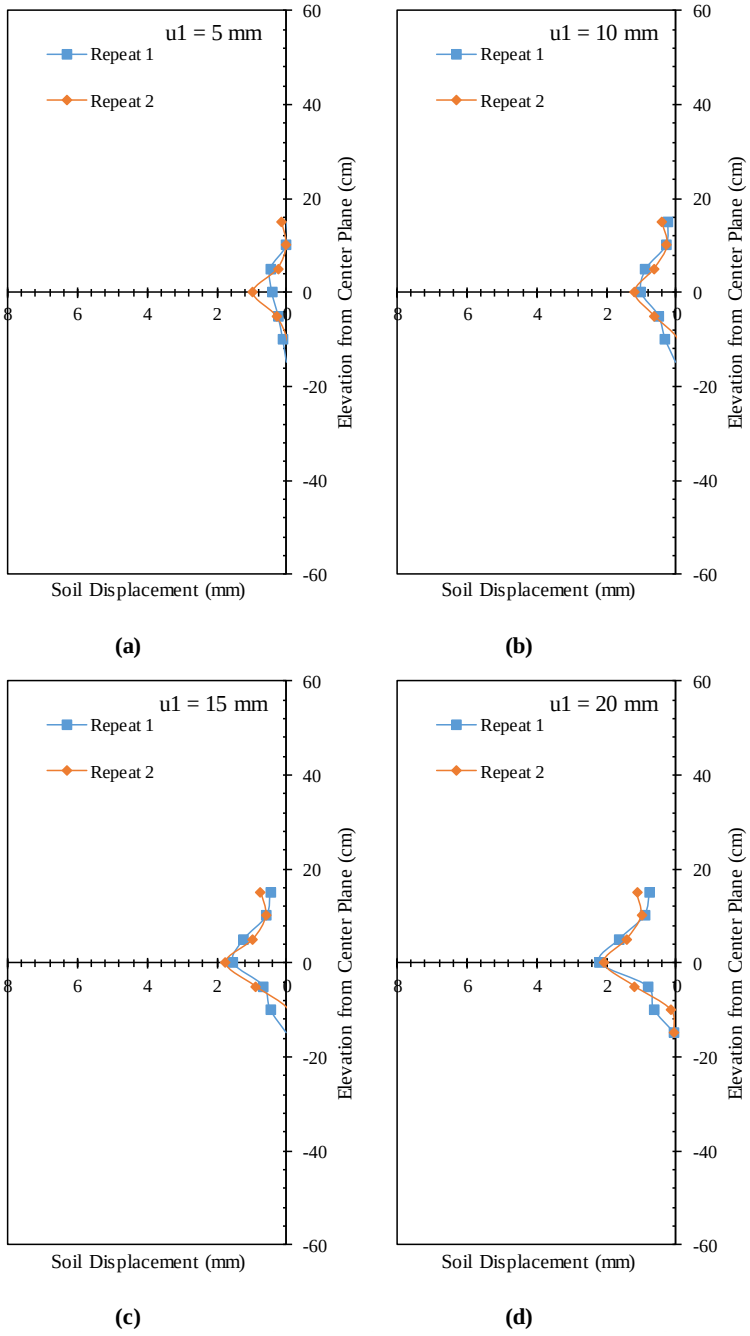

Figure 9.7. Horizontal soil displacement profiles (measured by means of artificial gravel particles): (a) At frontal displacement u1 = 5 mm; (b) At frontal displacement u1 = 10 mm; (b) At frontal displacement u1 = 15 mm; and (d) At frontal displacement u1 = 20 mm.

9.3.2. Effect of reinforced soil normal stress

In order to assess the effect of overburden pressure on the interaction between the contiguous reinforcement layers in GRS structures, the testing program included tests conducted at the same testing configuration but various normal stress levels. Table 9.3 summarizes the tests that allow assessment of the effect of normal stress on the soil-geosynthetic interaction. Specifically, four tests were conducted using reinforcements spaced at 0.15 m (6 in.), two tests were conducted for reinforcements spaced at 0.10 m (4 in.), and two tests were conducted for reinforcements spaced at 0.05 m (2 in.). The normal stress levels in the tests conducted in this study ranged from 15 to 50 kPa (2.25 to 7 psi) at the level of main reinforcement layer. This normal stress range was adopted so that the majority of the tests in the experimental program would fail in pullout. This allows assessing the full range of soil-reinforcement interaction, specifically including working stress and ultimate strength conditions.

Table 9.3. Summary of tests in which normal stress was varied.

Test ID	***Testing Variables***					
	Fill Material	***S_v***	***σ_v***	***Active GS***	***Passive GS***	***Dilation***
GP-06-02-G1-G	AASHTO No. 8	0.15 m	15 kPa	HP570	HP570	Allowed
GP-06-03-G1-G			21 kPa			
GP-06-05-G1-G			35 kPa			
GP-06-07-G1-G			50 kPa			
GP-04-03-G1-G	AASHTO No. 8	0.10 m	21 kPa	HP570	HP570	Allowed
GP-04-07-G1-G			50 kPa			
GP-02-03-G1-G	AASHTO No. 8	0.05 m	21 kPa	HP570	HP570	Allowed
GP-02-07-G1-G			50 kPa			

Three comparisons were made between the results from tests conducted at various normal stress levels and with reinforcements placed at different vertical spacing: (1) a comparison between four tests conducted at normal stresses of 15, 21, 35, and 50 kPa at the active reinforcement level (i.e., central horizontal plane of the reinforced soil mass). These tests were conducted with reinforcements placed at vertical spacing of 0.15 m (6

in.); (2) a comparison between two tests conducted at normal stresses of 21 and 50 kPa at the active reinforcement level. These tests were conducted with reinforcements placed at vertical spacing of 0.10 m (4 in.); and (3) a comparison between two tests conducted at normal stresses of 21 and 50 kPa at the active reinforcement level. These tests were conducted with reinforcements placed at vertical spacing of 0.05 m (2 in.). Note that tests of the same comparison group were carried out using the same testing conditions, including the same reinforcement type and fill material. The active and passive reinforcements for all tests were HP570 geotextiles, and the fill material was AASHTO Gravel No. 8. That is, the only difference among tests of the same comparison group was the normal stress level.

Figures 9.8a through 9.8c show the frontal pullout load-displacement experimental curves for the tests conducted with reinforcements placed at vertical spacing of 0.15, 0.10, and 0.05 m, respectively. The results indicate that the resistance of the active reinforcement to pullout increases with increasing normal stress. This trend is the same for tests conducted with reinforcements placed at different vertical spacings. In addition, the soil-reinforcement interface shear strength was found to increase with increasing normal stress.

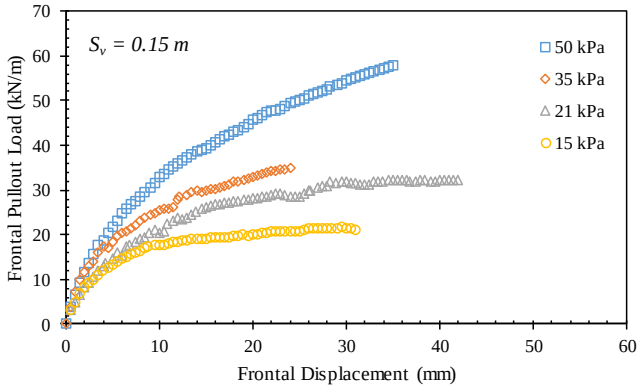

(a)

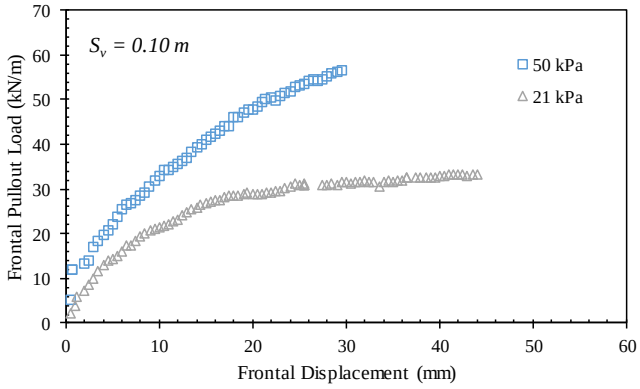

(b)

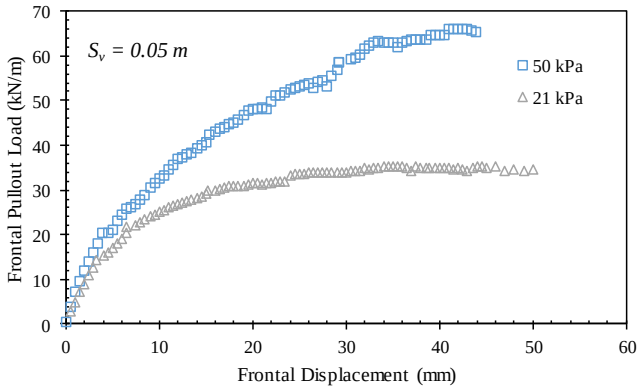

(c)

Figure 9.8. Frontal pullout load-displacement curves: (a) Tests conducted with S_v = 0.15 m; (b) Tests conducted with S_v = 0.10 m; and (c) Tests conducted with S_v = 0.05 m.

Figures 9.9 through 9.11 present the average displacements for the passive reinforcement layers with respect to the average displacements of the active reinforcement layer for tests conducted with reinforcements spaced at 0.15, 0.10, and 0.05 m, respectively. Each figure consists of two subfigures a and b that show the average displacements for the upper and lower passive reinforcement layers, respectively. Figures 9.9 through 9.11 reflect the load transfer from the active reinforcement to the passive reinforcements at the same nodal reinforcement of the active reinforcement; i.e., the same soil-reinforcement interface shear displacement. The average displacement represents the area under displacement profile normalized by the reinforcement length. Assuming the interface shear stress-displacement constitutive behavior is linear and of close stiffness at the normal stress range tested, the results shown in Figures 9.9 through 9.11 provide insight into the effect of normal stress on the interaction between neighboring reinforcements.

The results indicate that the relationship between the displacements of the passive reinforcements is linear with the displacements of the active reinforcement at early loading stages. This relationship then becomes non-linear as the load-displacement relationship of the active reinforcement curves. That is, Figures 9.9 through 9.11 reflect the effect of interface condition of the passive reinforcement on the interaction between the contiguous reinforcement layers. At early pullout loading stages, the tests conducted at low normal stresses tend to mobilize displacements in the passive reinforcements more than those conducted at higher normal stresses. This is because the flexibility of soil to deform at low normal stresses resulting in higher load transfer and thus higher interaction between reinforcements. However, as pullout progressed the soil-reinforcement interface stiffness yielded more in the tests conducted at low normal stresses compared to this of the tests conducted at higher normal stresses. In general, the normal stress, for the range tested, did

not show an impact on the degree of interaction the active reinforcement layer can have on the passive reinforcement layers before the yielding of interface strength (i.e., at working stresses). However, it was concluded that increasing normal stress lead to higher interaction between neighboring reinforcements at higher interface stresses. This is because the interface strength is higher at higher normal stresses at yields at larger interface displacements. In addition, at high normal pressures, the soil, which is the medium responsible for transfering the shear stresses, is stiffer and can transfer more stresses before yielding either internally or at the soil-reinforcement interface.

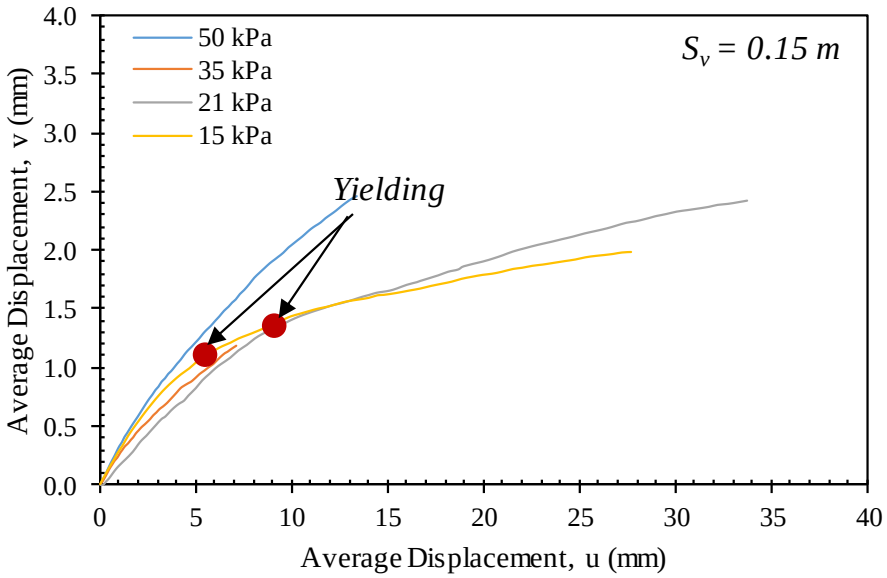

(a)

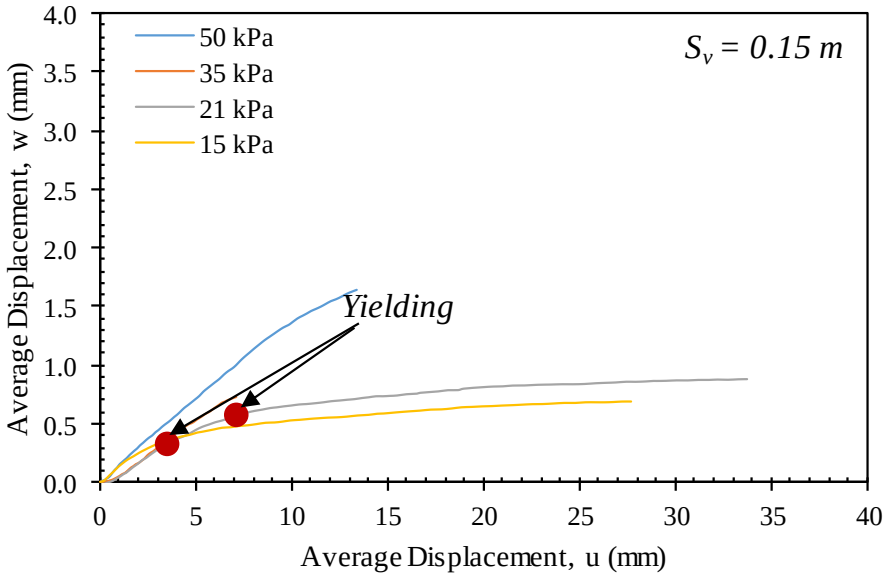

(b)

Figure 9.9. Average displacements at the passive reinforcement layers with respect to average displacements at the active reinforcement layer: (a) Upper passive reinforcement layer; and (b) Lower passive reinforcement layer (tests conducted at S_v = 0.15 m).

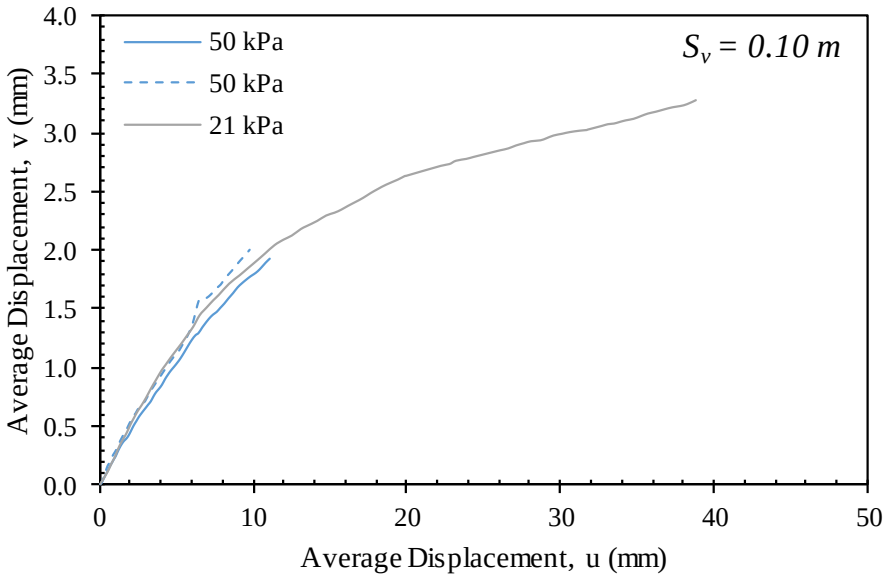

(a)

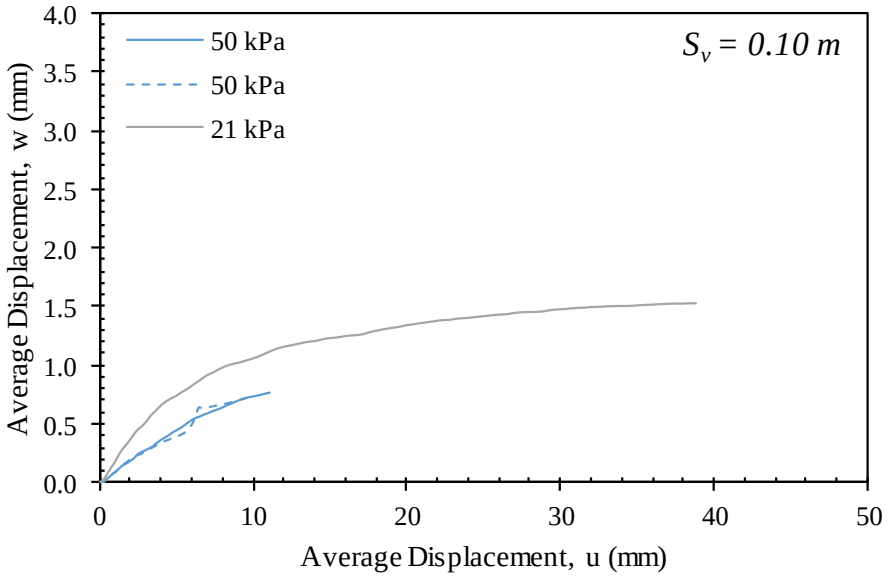

(b)

Figure 9.10. Average displacements at the passive reinforcement layers with respect to average displacements at the active reinforcement layer: (a) Upper passive reinforcement layer; and (b) Lower passive reinforcement layer (tests conducted at S_v = 0.10 m).

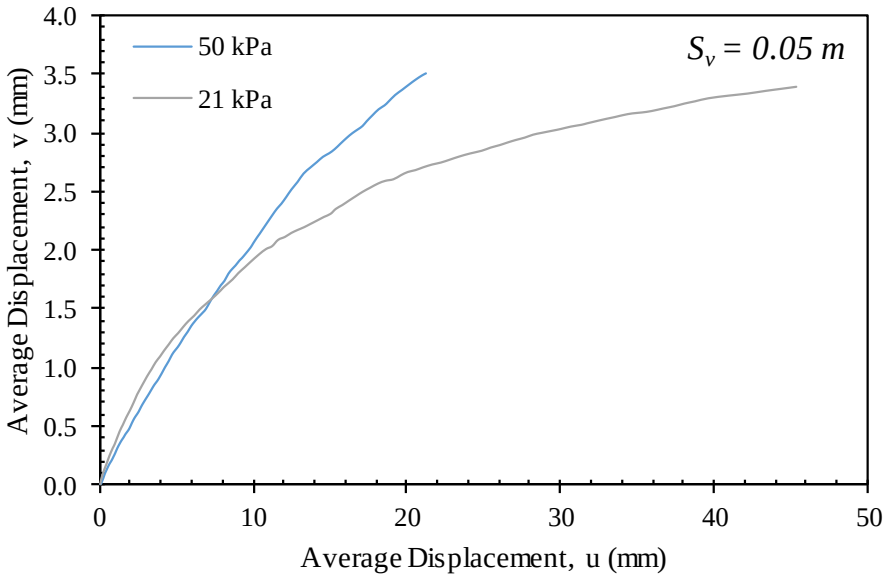

(a)

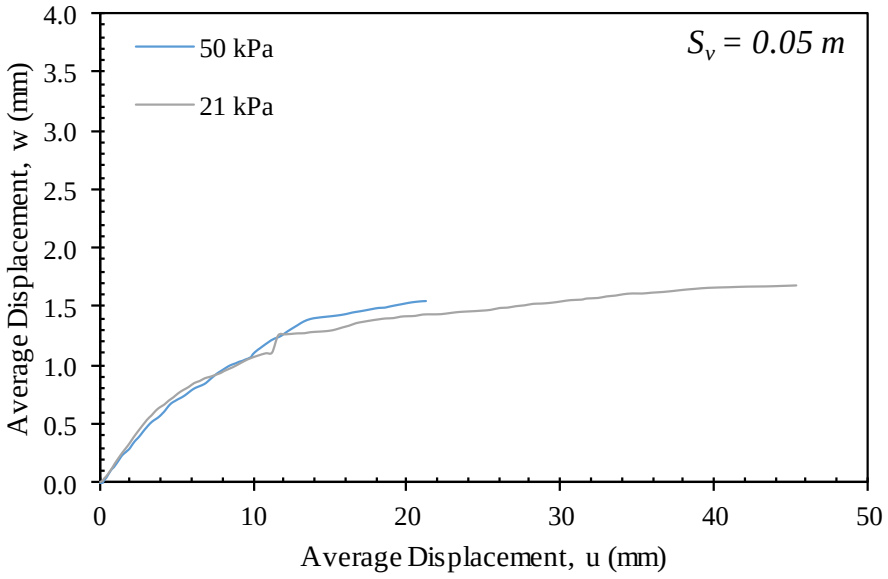

(b)

Figure 9.11. Average displacements at the passive reinforcement layers with respect to average displacements at the active reinforcement layer: (a) Upper passive reinforcement layer; and (b) Lower passive reinforcement layer (tests conducted at S_v = 0.05 m).

Figures 9.12 through 9.16 show the displacement profiles for the active and passive reinforcement layers spaced at 0.15 m at active reinforcement frontal displacements (u1) of 5, 10, 15, 20, and 30 mm, respectively. Figures 9.17 through 9.20 show the displacement profiles for reinforcement layers spaced at 0.10 m at active reinforcement frontal displacements (u1) of 5, 10, 15, and 20 mm, respectively. Figures 9.21 through 9.25 show the displacement profiles for reinforcement layers spaced at 0.05 m at active reinforcement frontal displacements (u1) of 5, 10, 15, 20, and 30 mm, respectively. Note that the comparison is based on the same frontal displacement for the different reinforcements rather than the same pullout frontal load. The profiles of tests conducted at low normal stress show higher displacements along the length of the active reinforcement compared to those conducted at high normal stress. This difference increased as pullout progressed (i.e., with increasing values of u1). The profiles of the passive reinforcement layers also showed higher displacement values for the tests conducted at low normal stress compared to those conducted at high normal stress. The differences tend to decrease and even reverse at high pullout loads. This is explained by the displacement profile of the active reinforcement. The reinforcement tested at low normal pressure could mobilize more soil to transfer load for the same frontal displacement value. That is, the comparison between displacement profiles of passive reinforcements at same u1 values for tests conducted at different normal stresses cannot distinguish the effect of normal stress on the interaction between neighboring reinforcements.

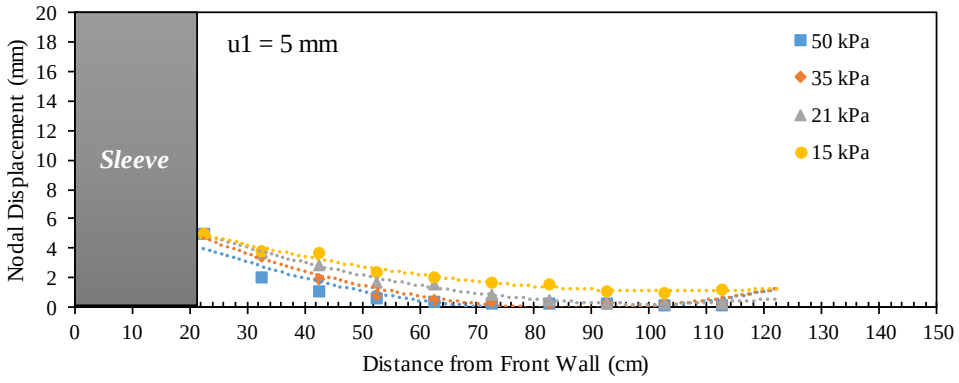

(a)

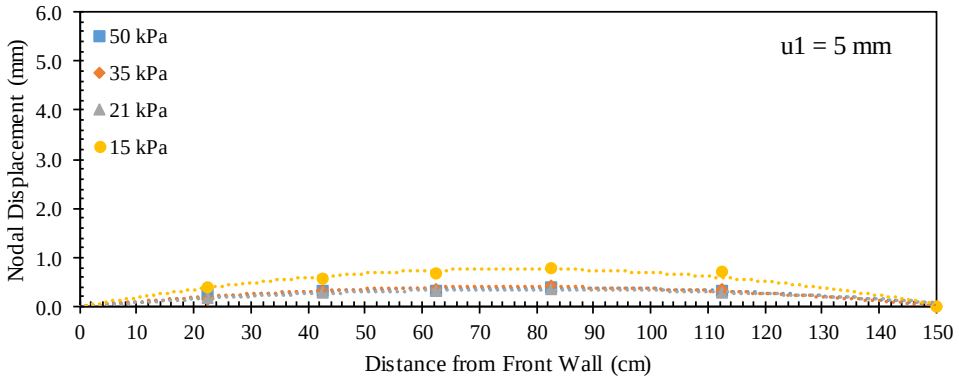

(b)

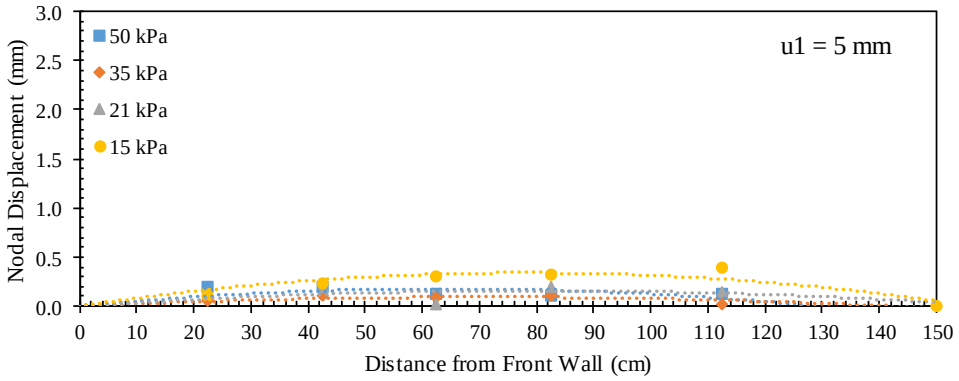

(c)

Figure 9.12. Reinforcement displacement profiles at frontal displacement u1 = 5 mm: (a) Active reinforcement; (b) Upper passive reinforcement; and (c) Lower passive reinforcement (S_v = 0.15 m).

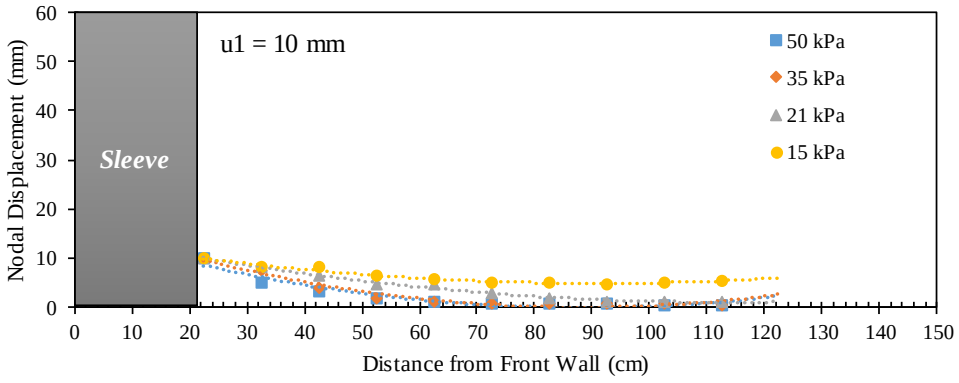

(a)

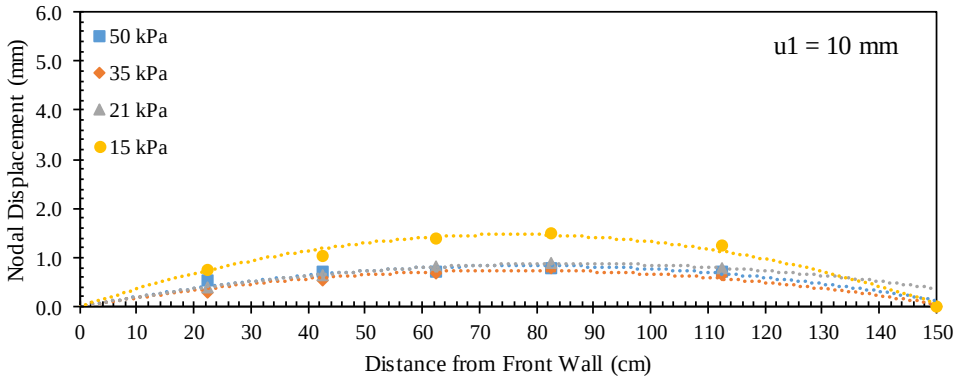

(b)

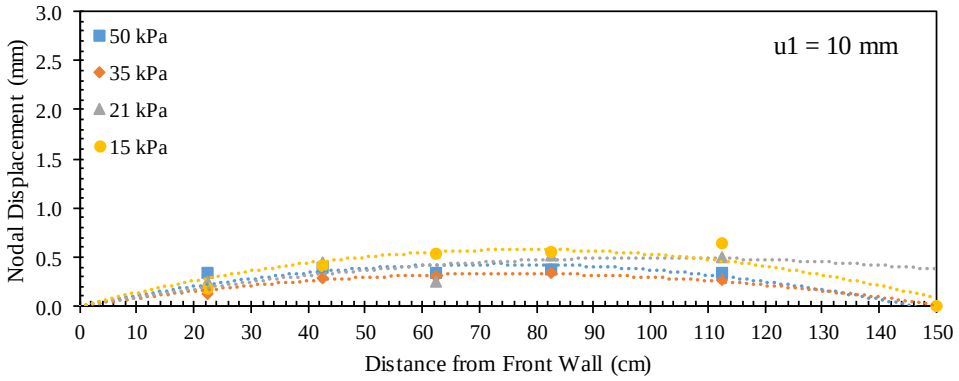

(c)

Figure 9.13. Reinforcement displacement profiles at frontal displacement u1 = 10 mm: (a) Active reinforcement; (b) Upper passive reinforcement; and (c) Lower passive reinforcement (S_v = 0.15 m).

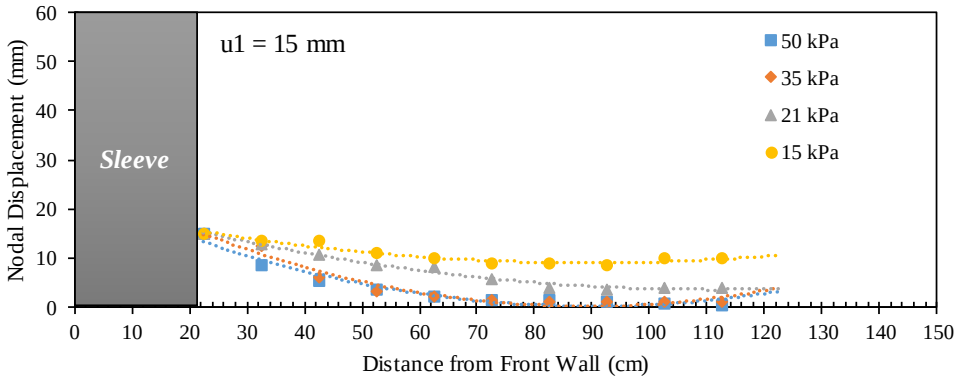

(a)

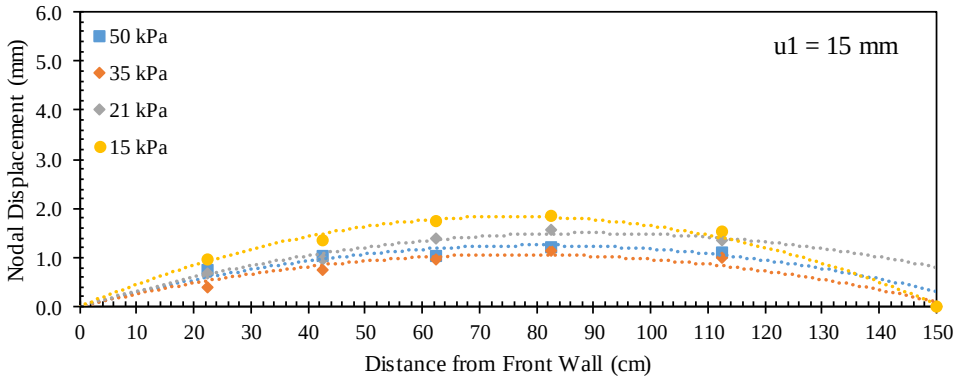

(b)

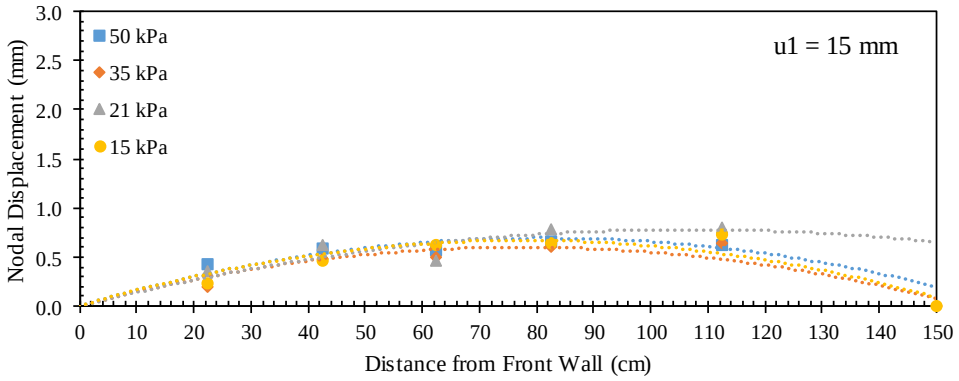

(c)

Figure 9.14. Reinforcement displacement profiles at frontal displacement u1 = 15 mm: (a) Active reinforcement; (b) Upper passive reinforcement; and (c) Lower passive reinforcement (S_v = 0.15 m).

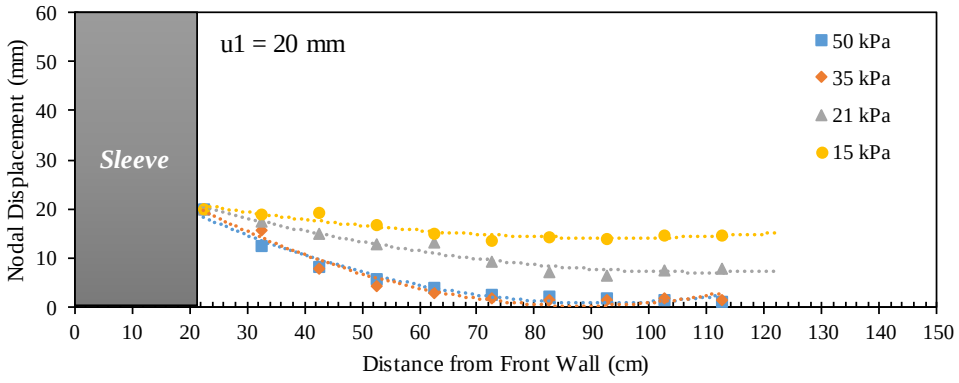

(a)

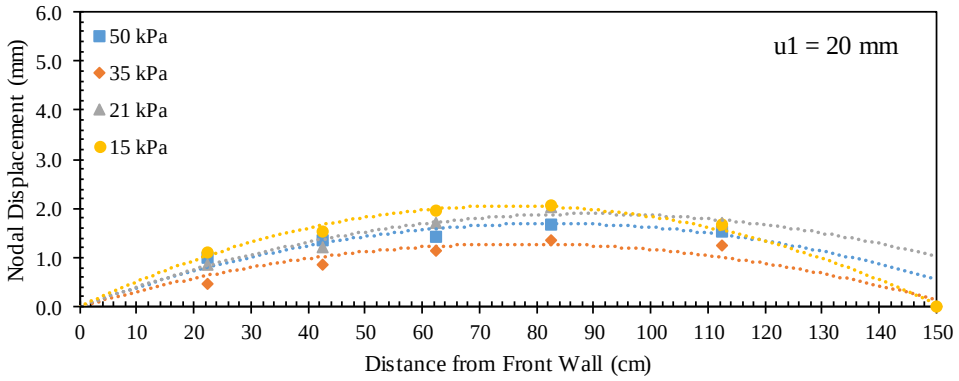

(b)

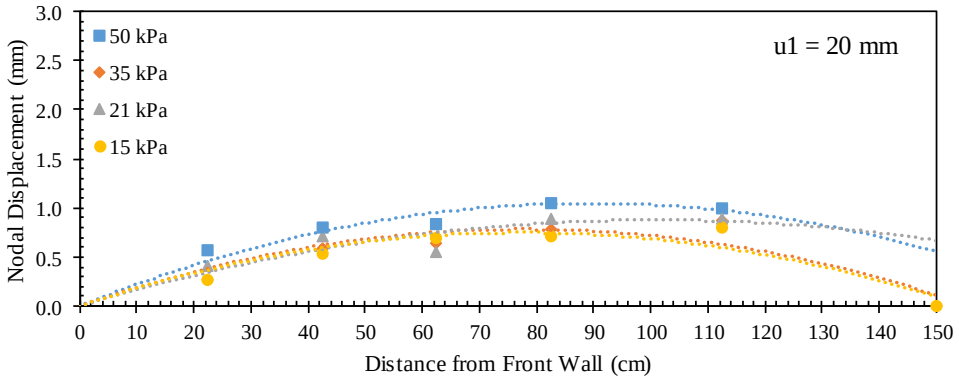

(c)

Figure 9.15. Reinforcement displacement profiles at frontal displacement u1 = 20 mm: (a) Active reinforcement; (b) Upper passive reinforcement; and (c) Lower passive reinforcement (S_v = 0.15 m).

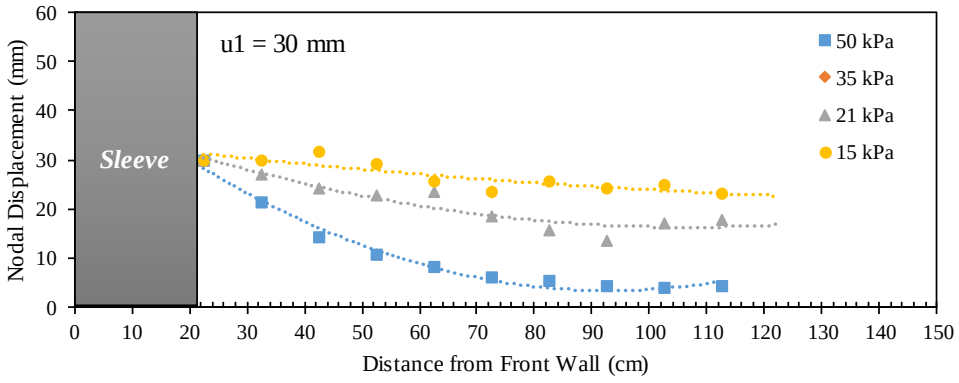

(a)

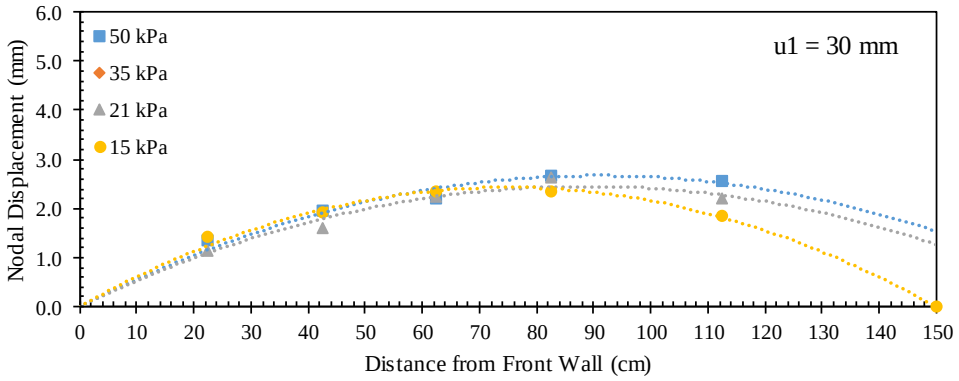

(b)

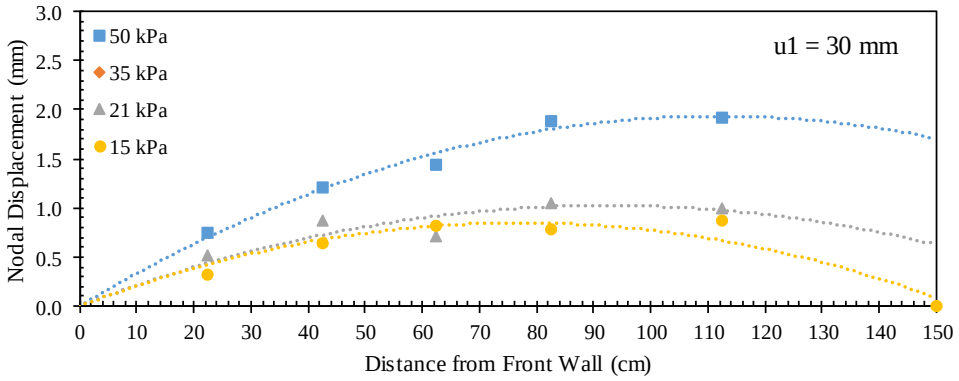

(c)

Figure 9.16. Reinforcement displacement profiles at frontal displacement u1 = 30 mm: (a) Active reinforcement; (b) Upper passive reinforcement; and (c) Lower passive reinforcement (S_v = 0.15 m).

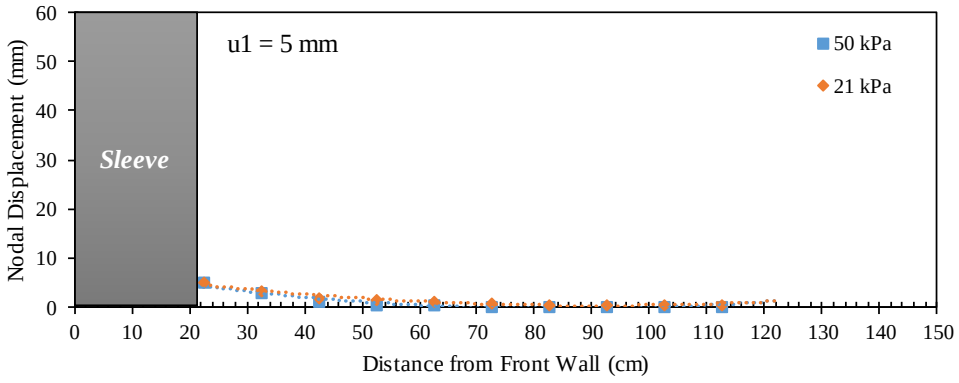

(a)

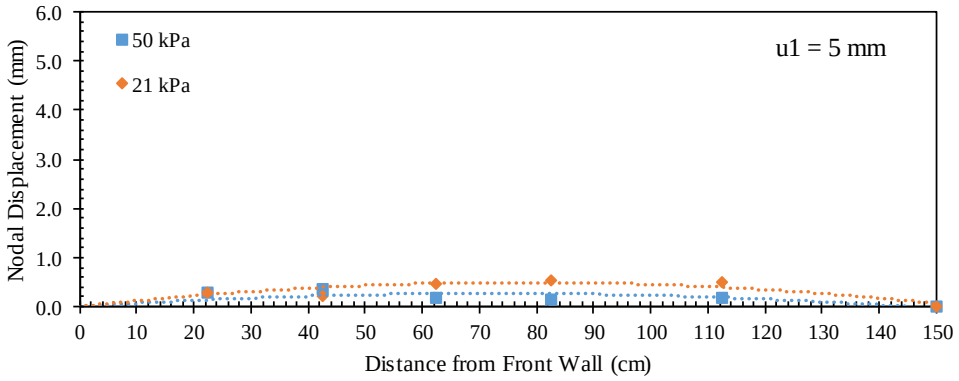

(b)

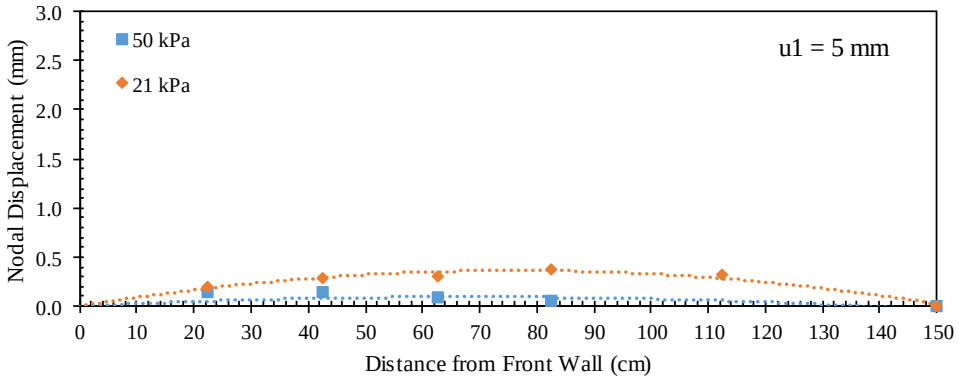

(c)

Figure 9.17. Reinforcement displacement profiles at frontal displacement u1 = 5 mm: (a) Active reinforcement; (b) Upper passive reinforcement; and (c) Lower passive reinforcement (S_v = 0.10 m).

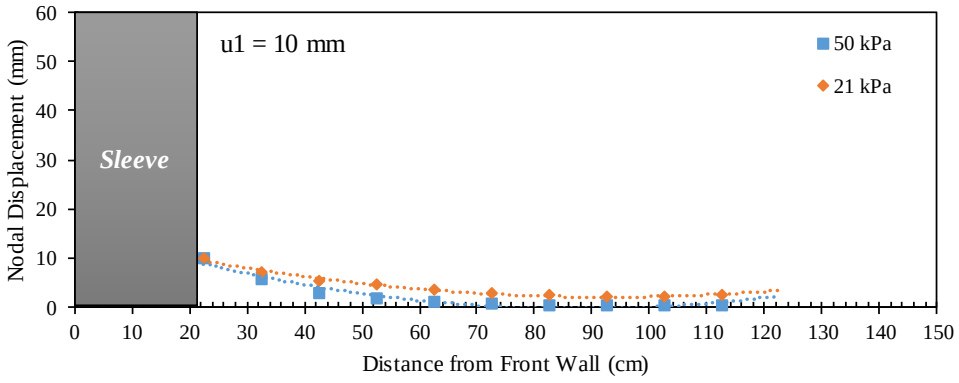

(a)

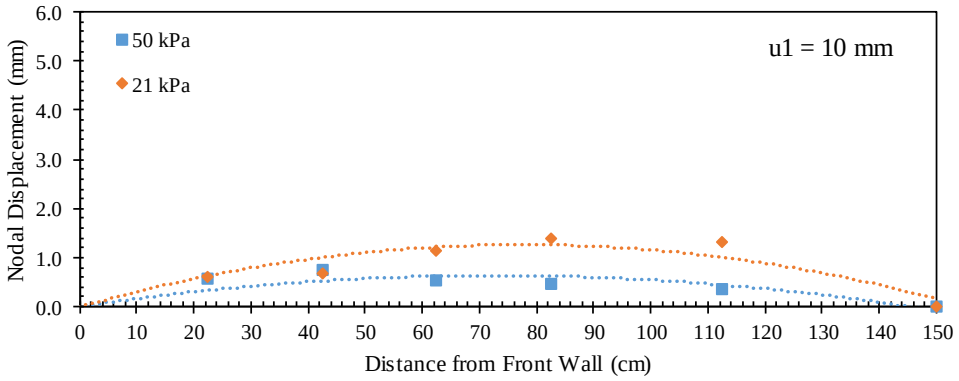

(b)

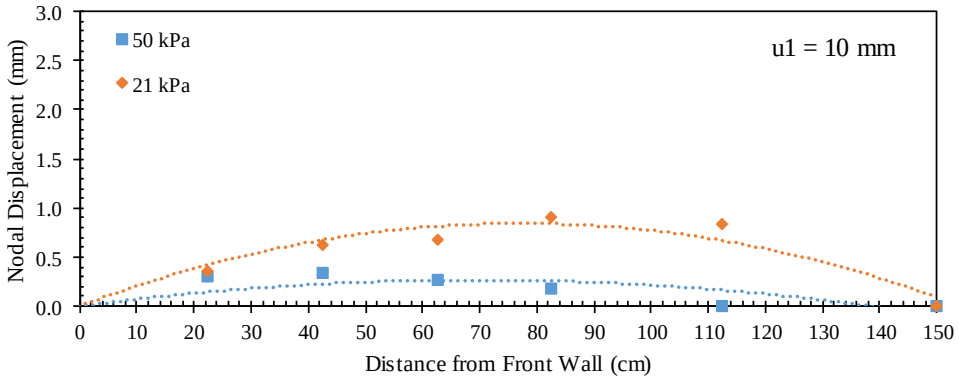

(c)

Figure 9.18. Reinforcement displacement profiles at frontal displacement u1 = 10 mm: (a) Active reinforcement; (b) Upper passive reinforcement; and (c) Lower passive reinforcement (S_v = 0.10 m).

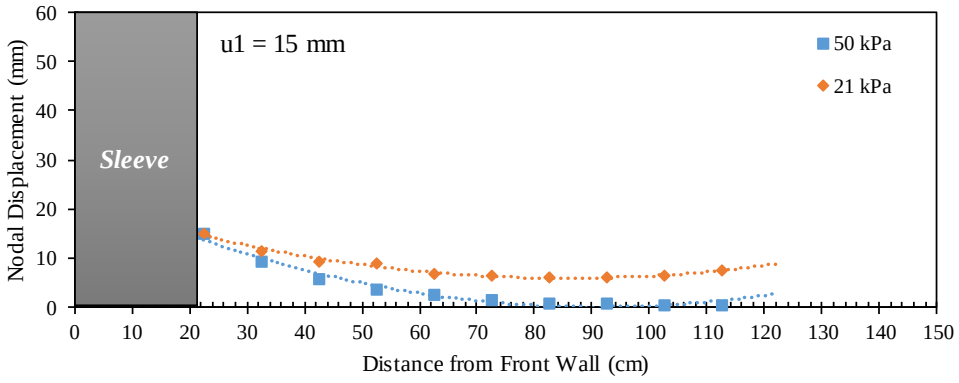

(a)

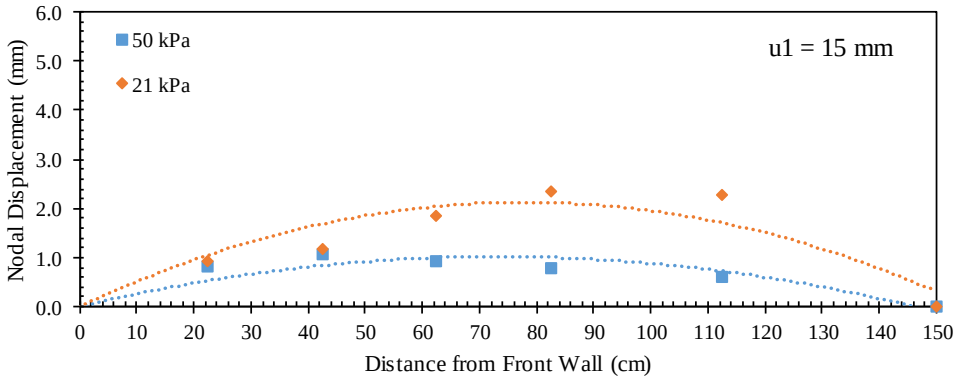

(b)

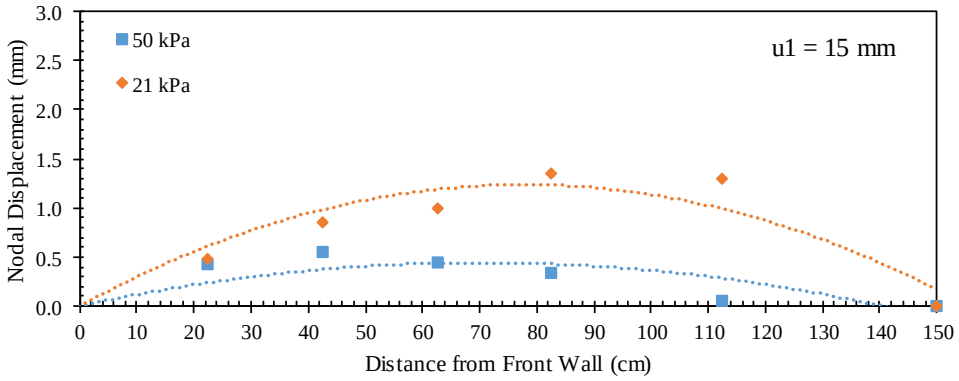

(c)

Figure 9.19. Reinforcement displacement profiles at frontal displacement u1 = 15 mm: (a) Active reinforcement; (b) Upper passive reinforcement; and (c) Lower passive reinforcement (S_v = 0.10 m).

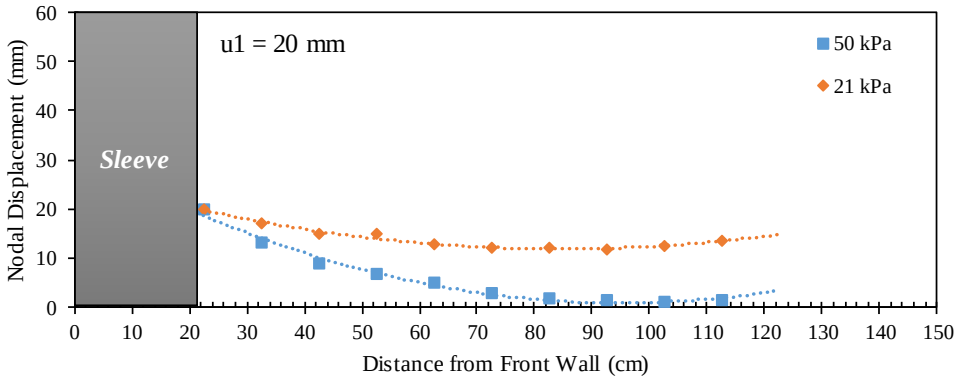

(a)

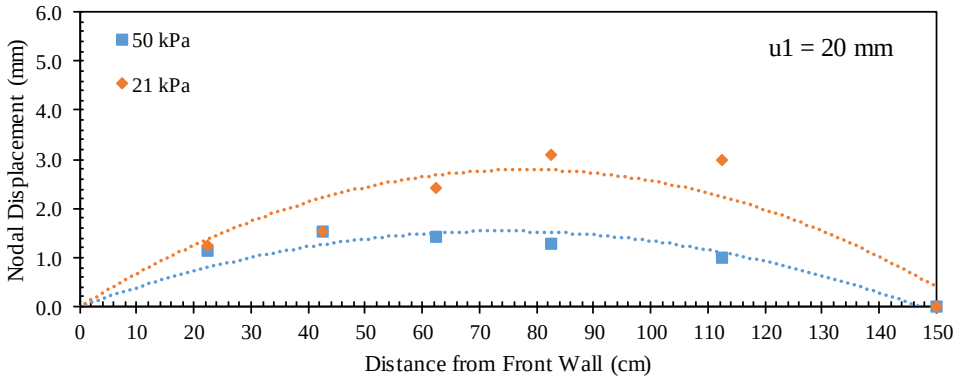

(b)

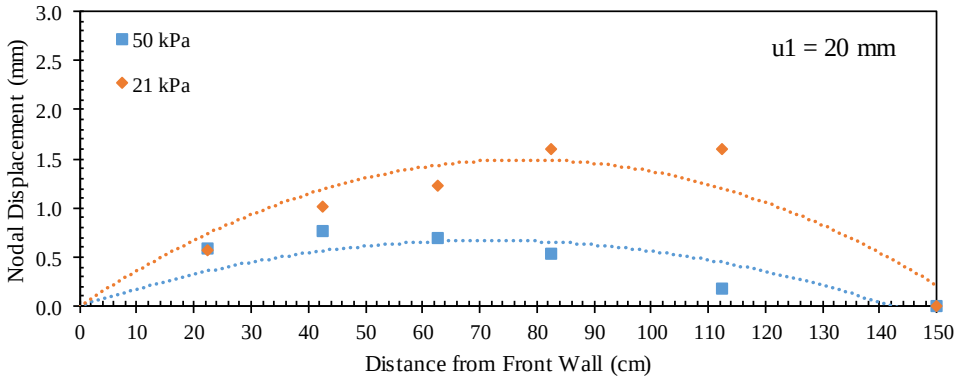

(c)

Figure 9.20. Reinforcement displacement profiles at frontal displacement u1 = 20 mm: (a) Active reinforcement; (b) Upper passive reinforcement; and (c) Lower passive reinforcement (S_v = 0.10 m).

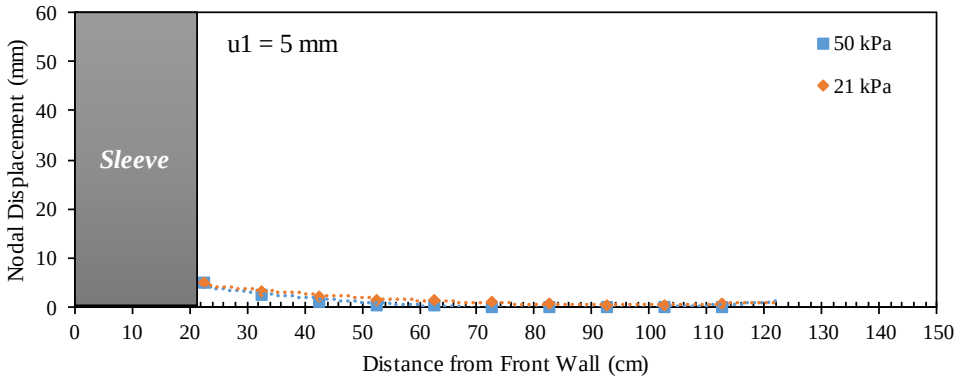

(a)

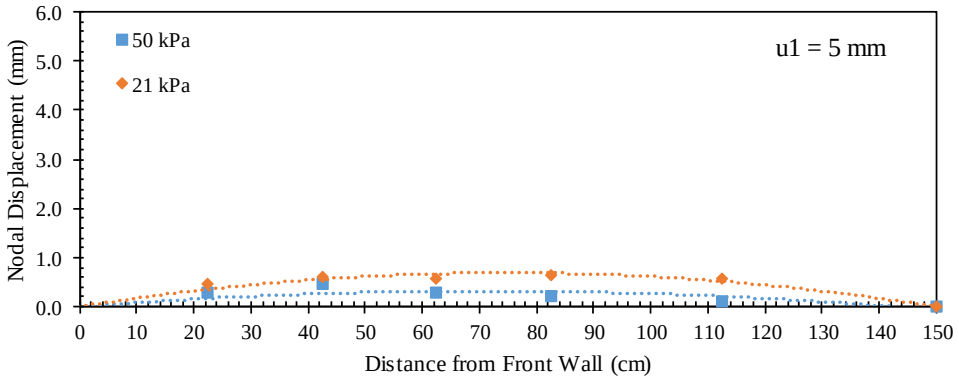

(b)

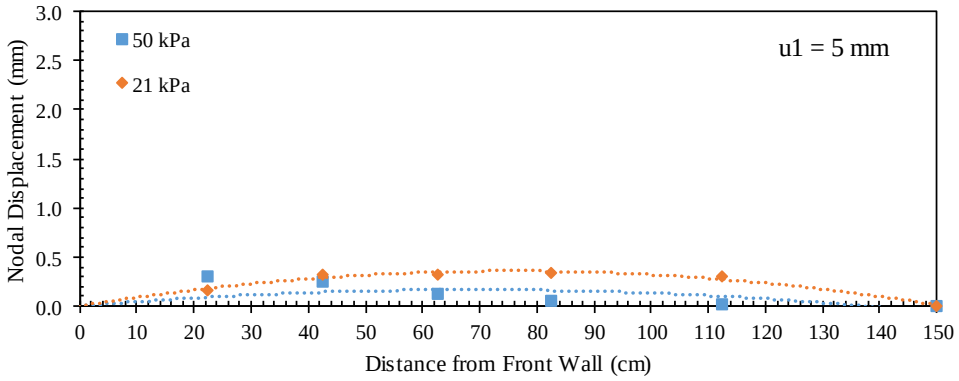

(c)

Figure 9.21. Reinforcement displacement profiles at frontal displacement u1 = 5 mm: (a) Active reinforcement; (b) Upper passive reinforcement; and (c) Lower passive reinforcement (S_v = 0.05 m).

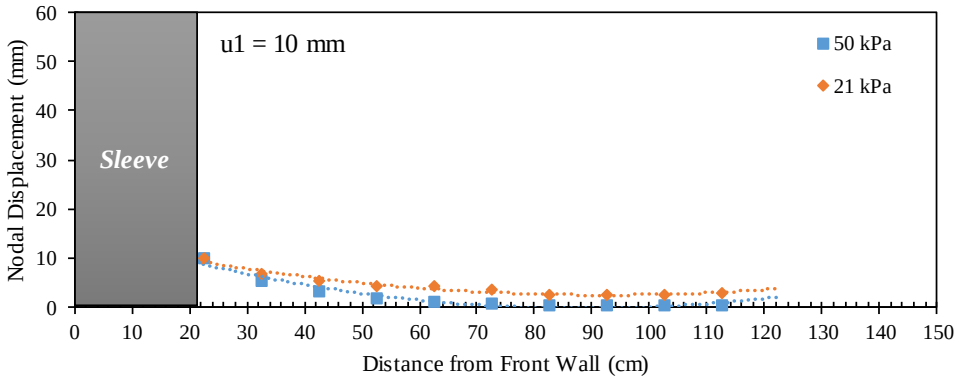

(a)

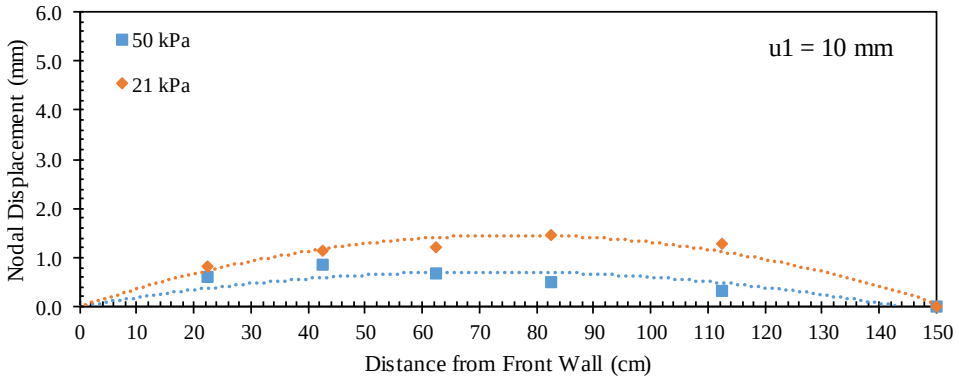

(b)

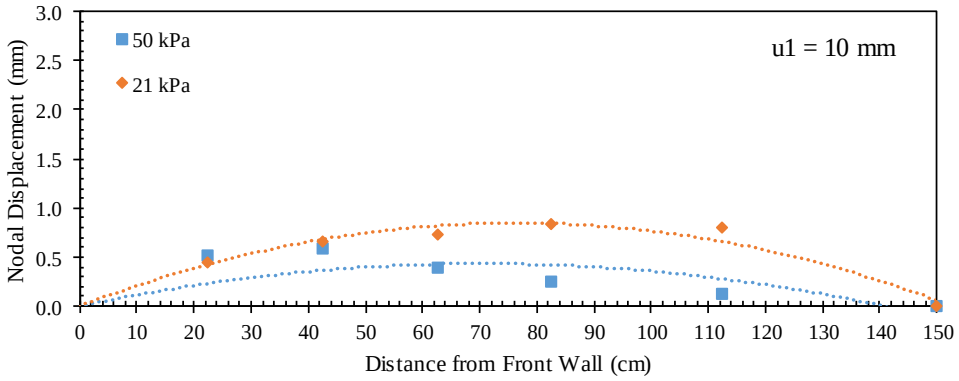

(c)

Figure 9.22. Reinforcement displacement profiles at frontal displacement u1 = 10 mm: (a) Active reinforcement; (b) Upper passive reinforcement; and (c) Lower passive reinforcement (S_v = 0.05 m).

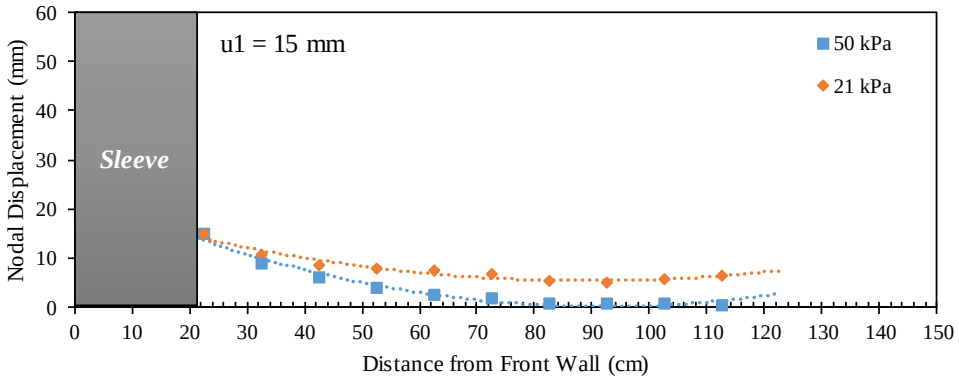

(a)

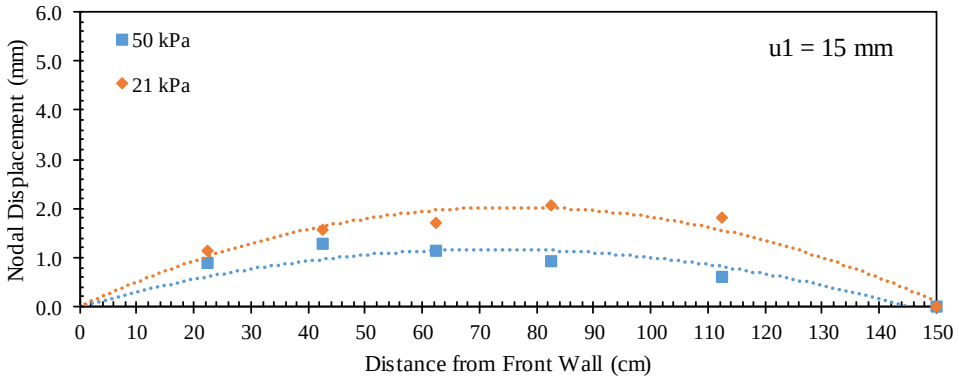

(b)

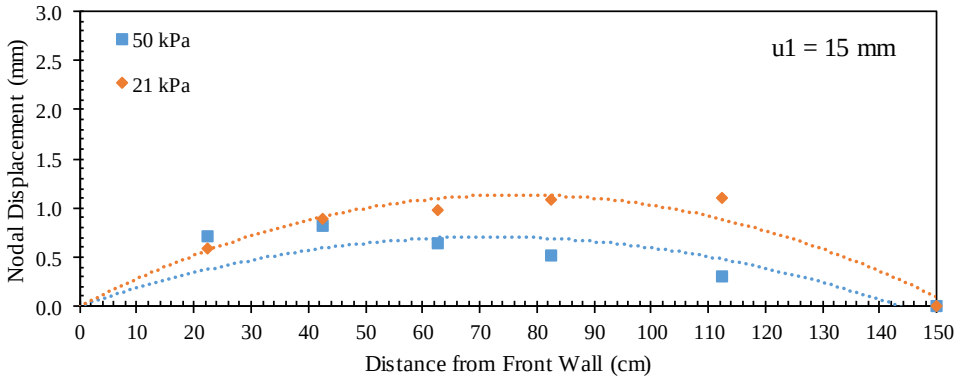

(c)

Figure 9.23. Reinforcement displacement profiles at frontal displacement u1 = 15 mm: (a) Active reinforcement; (b) Upper passive reinforcement; and (c) Lower passive reinforcement (S_v = 0.05 m).

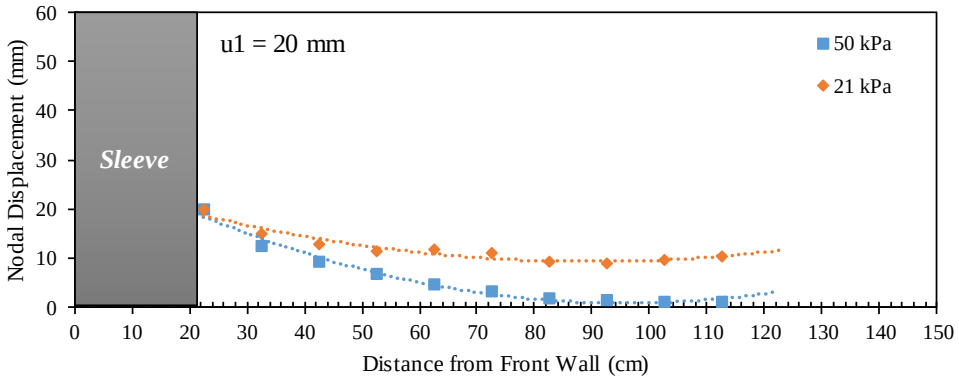

(a)

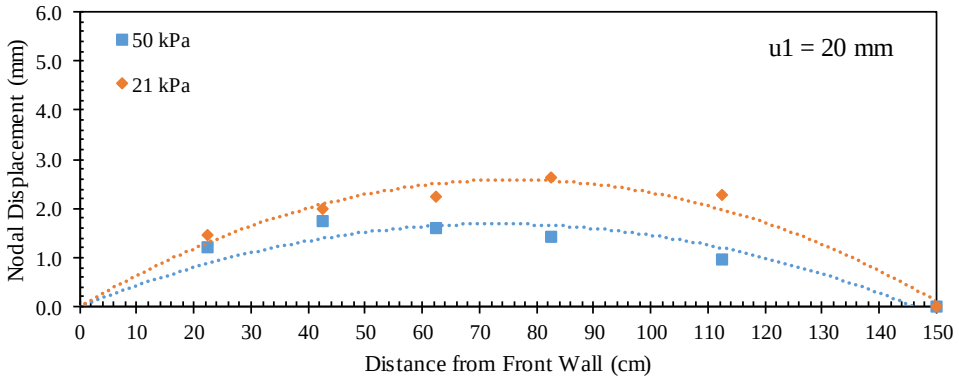

(b)

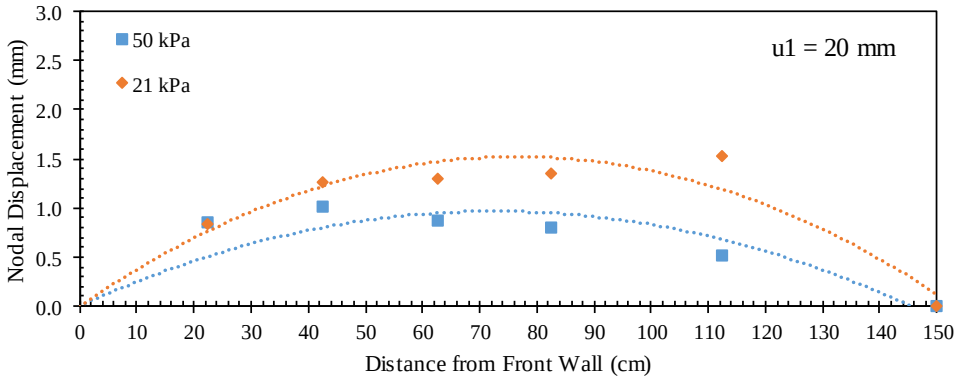

(c)

Figure 9.24. Reinforcement displacement profiles at frontal displacement u1 = 20 mm: (a) Active reinforcement; (b) Upper passive reinforcement; and (c) Lower passive reinforcement (S_v = 0.05 m).

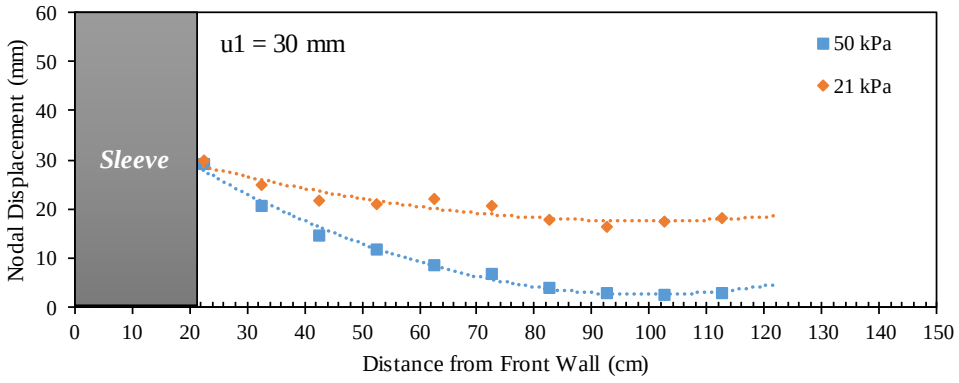

(a)

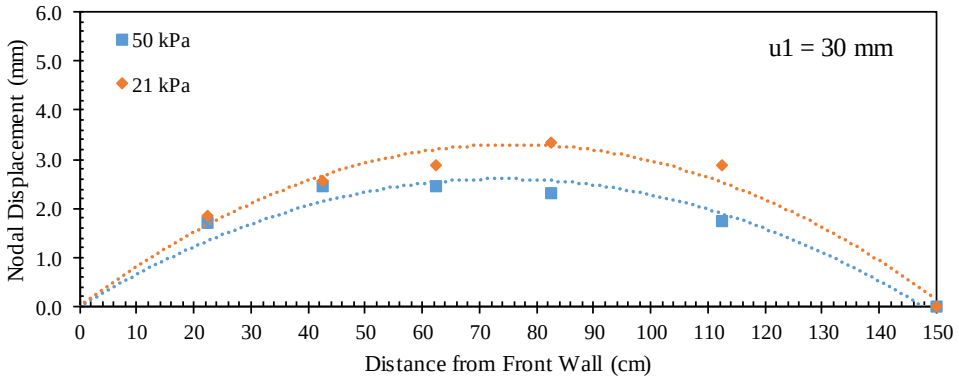

(b)

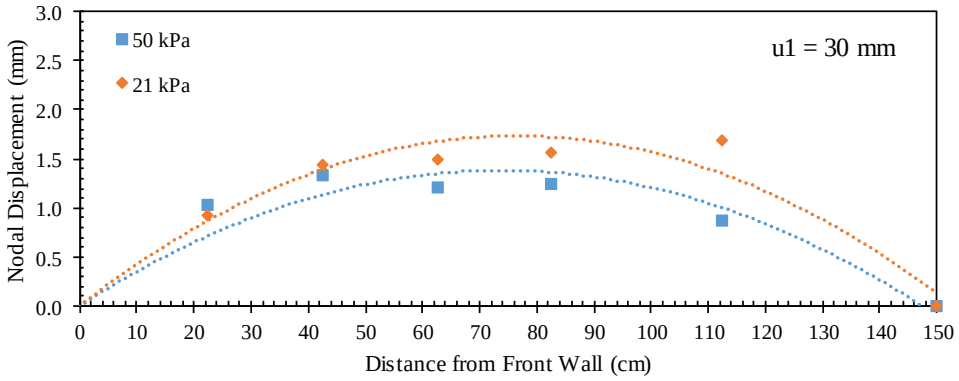

(c)

Figure 9.25. Reinforcement displacement profiles at frontal displacement u1 = 30 mm: (a) Active reinforcement; (b) Upper passive reinforcement; and (c) Lower passive reinforcement (S_v = 0.05 m).

For a proper comparison, Figures 9.26 through 9.28 show the upper passive reinforcement displacement profiles for tests conducted with reinforcements spaced at 0.15 m for intermediate nodal displacement values of the active reinforcement of 5, 10, and 15 mm, respectively. Specifically, each figure consists of a, b, c, and d subfigures that provide comparisons of the upper passive reinforcement profiles for same nodal displacements u1, u3, u5, and u7, respectively. Note that some subfigures are missing since the nodal displacements u3, u5, and u7 did not reach the values 5, 10, 15, and 20 mm in all tests.

Figures 9.29 through 9.32 show the upper passive reinforcement displacement profiles for tests conducted with reinforcements spaced at 0.10 m for various intermediate nodal displacements of the active reinforcement of 5, 10, 15, and 20 mm, respectively. Figures 9.33 through 9.36 show the upper passive reinforcement displacement profiles for tests conducted with reinforcements spaced at 0.05 m for various intermediate nodal displacements of the active reinforcement of 5, 10, 15, and 20 mm, respectively.

That is, the comparisons were conducted for the similar soil-reinforcement induced reinforcement displacement. This provides more insight into the comparison regarding the ability of the neighboring reinforcements to interact at different normal stress level for a given soil medium and reinforcement type. It was observed from Figures 9.26 through 9.36 that the interaction between the reinforcement layers is higher at high normal stresses. In addition, reinforcement vertical spacing has no effect on the sensitivity of the reinforcement interaction to the normal stress magnitude.

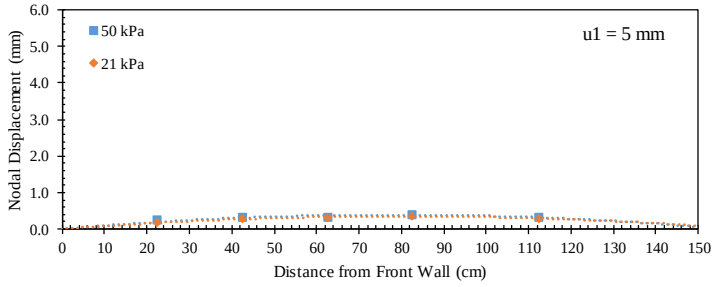

(a)

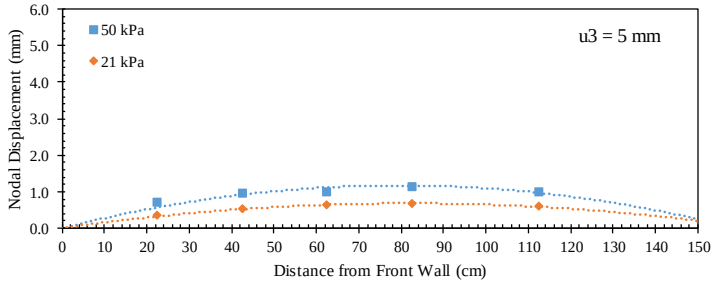

(b)

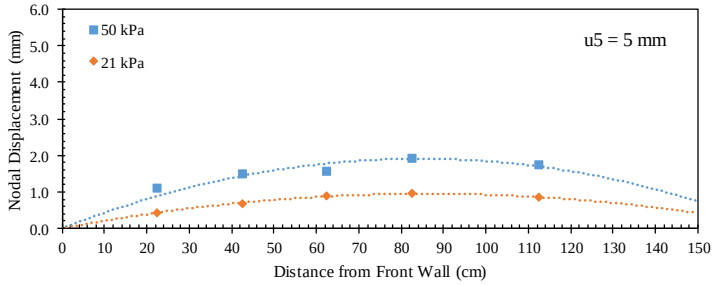

(c)

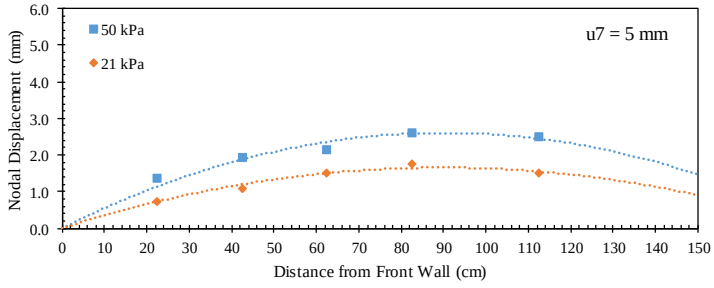

(d)

Figure 9.26. Upper passive reinforcement displacement profiles: (a) At nodal displacement u1 = 5 mm; (b) At nodal displacement u3 = 5 mm; (c) At nodal displacement u5 = 5 mm; and (d) At nodal displacement u7 = 5 mm (S_v = 0.15 m).

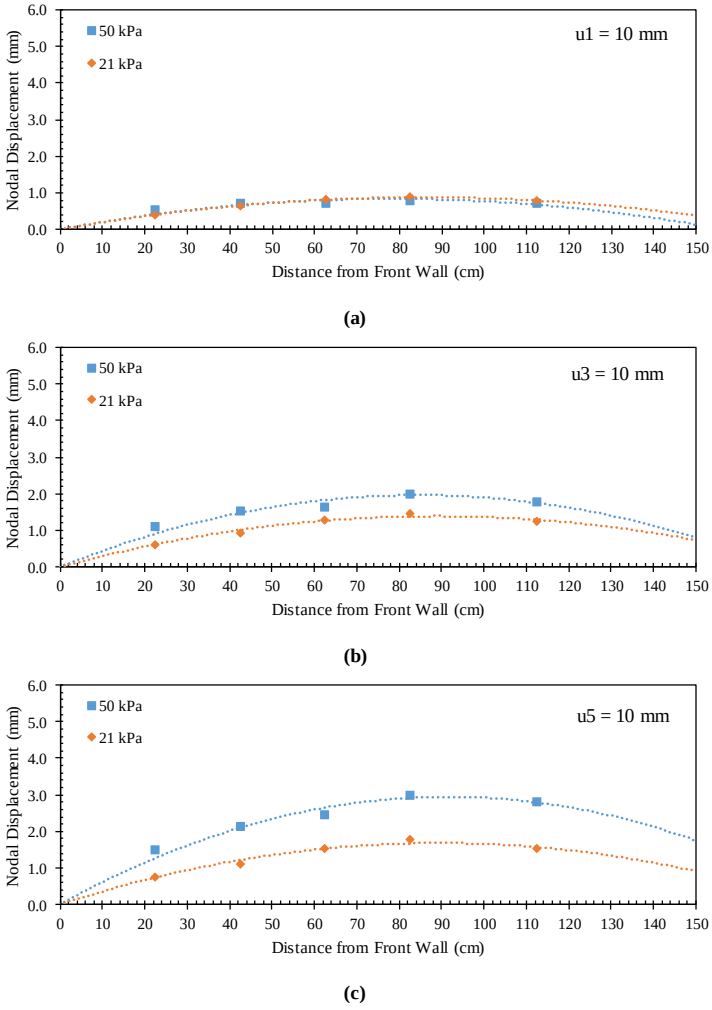

Figure 9.27. Upper passive reinforcement displacement profiles: (a) At nodal displacement u1 = 10 mm; (b) At nodal displacement u3 = 10 mm; and (c) At nodal displacement u5 = 10 mm (S_v = 0.15 m).

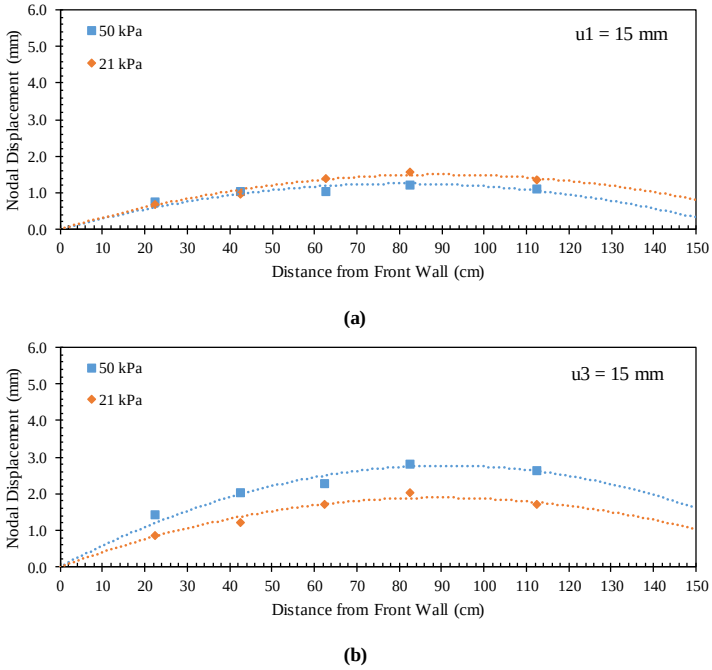

Figure 9.28. Upper passive reinforcement displacement profiles: (a) At nodal displacement u1 = 15 mm; and (b) At nodal displacement u3 = 15 mm (S_v = 0.15 m).

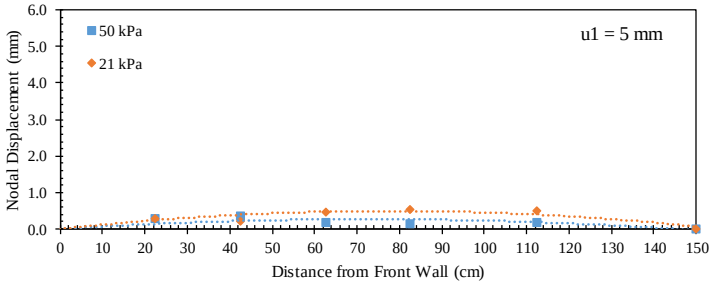

(a)

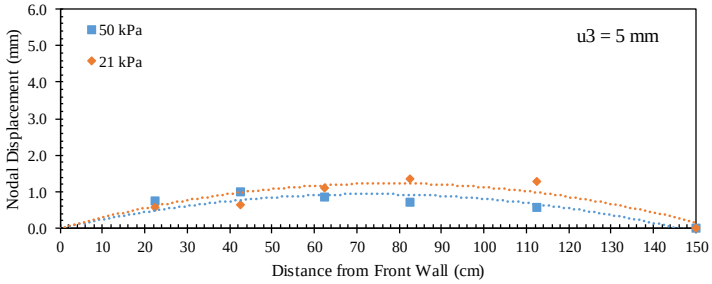

(b)

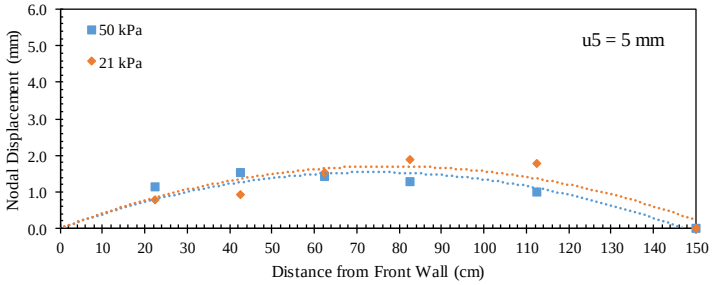

(c)

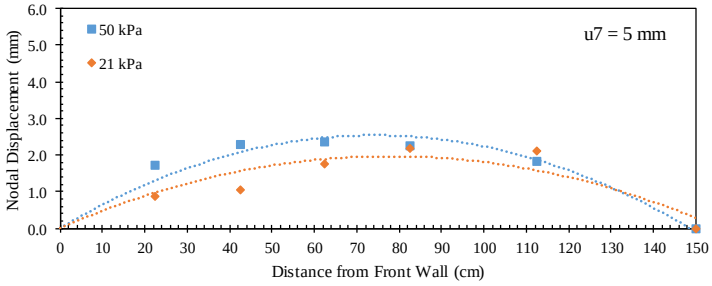

(d)

Figure 9.29. Upper passive reinforcement displacement profiles: (a) At nodal displacement u1 = 5 mm; (b) At nodal displacement u3 = 5 mm; (c) At nodal displacement u5 = 5 mm; and (d) At nodal displacement u7 = 5 mm (S_v = 0.10 m).

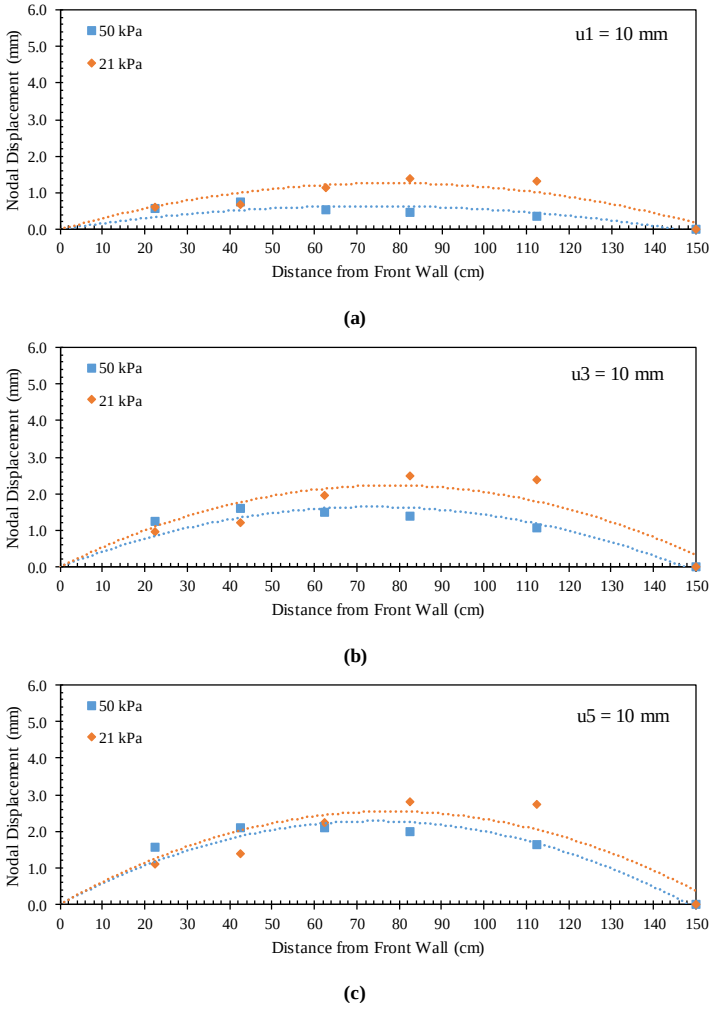

Figure 9.30. Upper passive reinforcement displacement profiles: (a) At nodal displacement u1 = 10 mm; (b) At nodal displacement u3 = 10 mm; and (c) At nodal displacement u5 = 10 mm (S_v = 0.10 m).

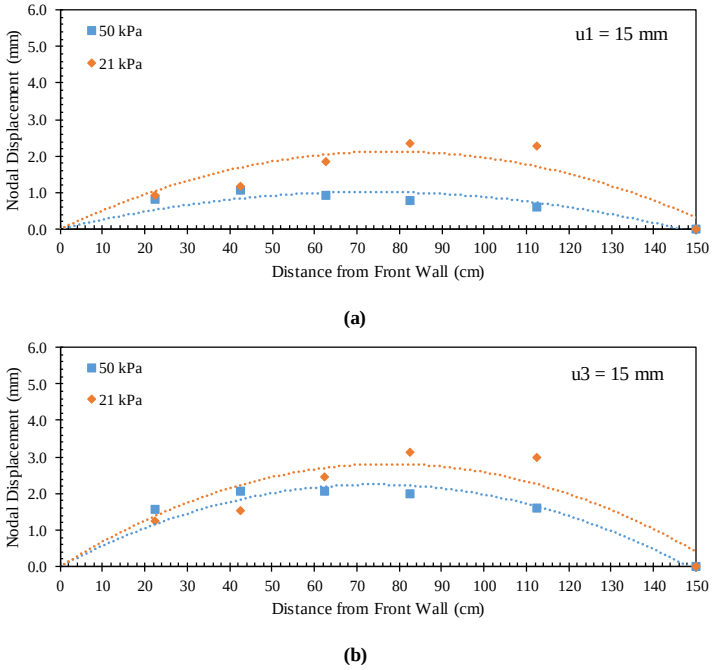

Figure 9.31. Upper passive reinforcement displacement profiles: (a) At nodal displacement u1 = 15 mm; and (b) At nodal displacement u3 = 15 mm (S_v = 0.10 m).

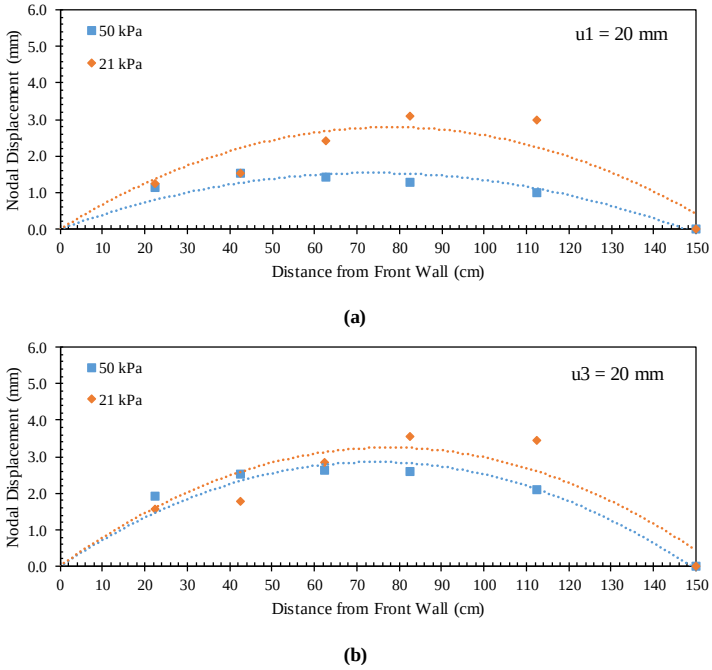

Figure 9.32. Upper passive reinforcement displacement profiles: (a) At nodal displacement u1 = 20 mm; and (b) At nodal displacement u3 = 20 mm (S_v = 0.10 m).

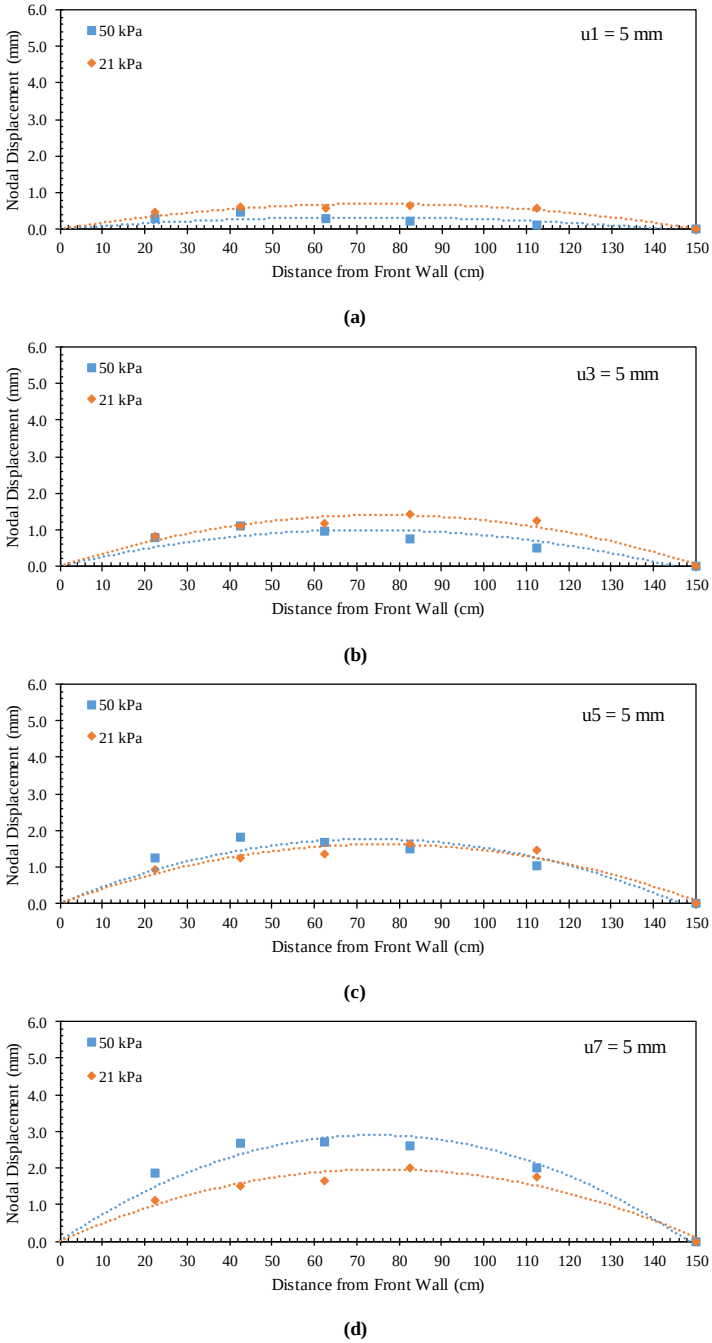

Figure 9.33. Upper passive reinforcement displacement profiles: (a) At nodal displacement u1 = 5 mm; (b) At nodal displacement u3 = 5 mm; (c) At nodal displacement u5 = 5 mm; and (d) At nodal displacement u7 = 5 mm (S_v = 0.05 m).

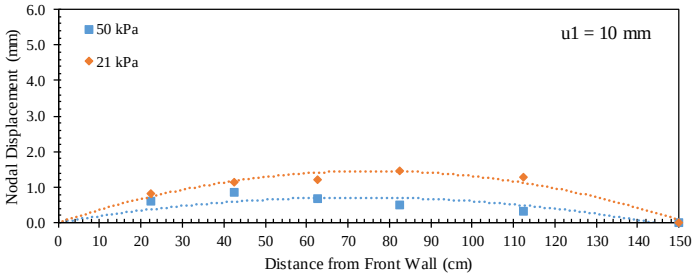

(a)

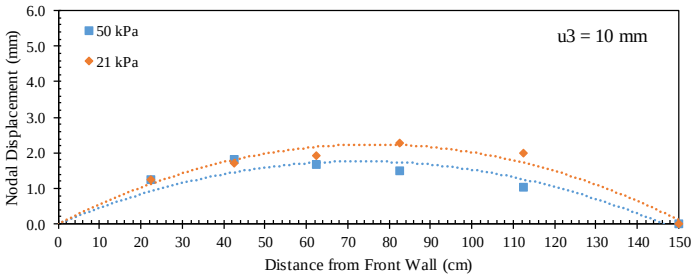

(b)

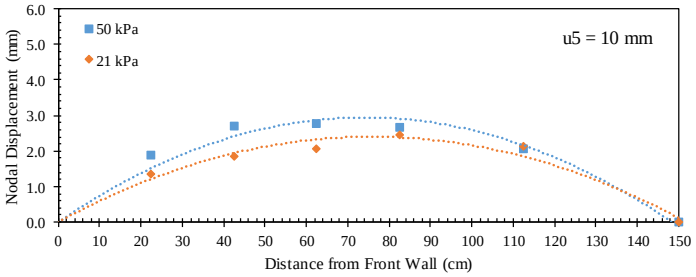

(c)

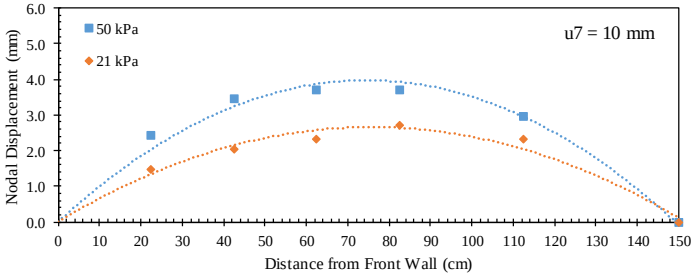

(d)

Figure 9.34. Upper passive reinforcement displacement profiles: (a) At nodal displacement u1 = 10 mm; (b) At nodal displacement u3 = 10 mm; (c) At nodal displacement u5 = 10 mm; and (d) At nodal displacement u7 = 10 mm (S_v = 0.05 m).

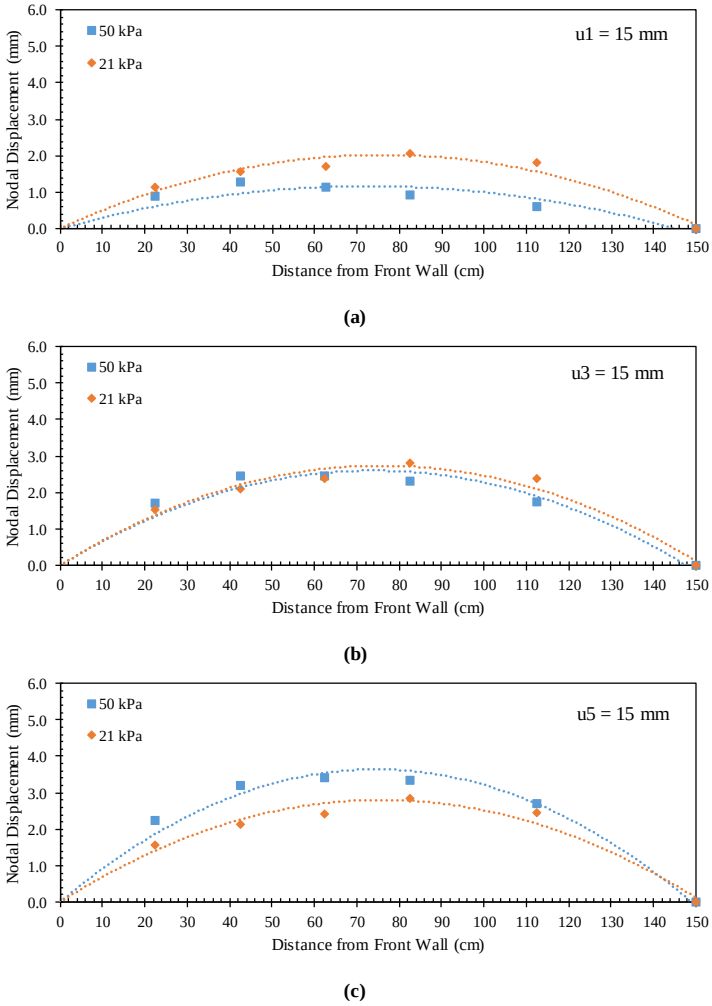

Figure 9.35. Upper passive reinforcement displacement profiles: (a) At nodal displacement u1 = 15 mm; (b) At nodal displacement u3 = 15 mm; and (c) At nodal displacement u5 = 15 mm (S_v = 0.05 m).

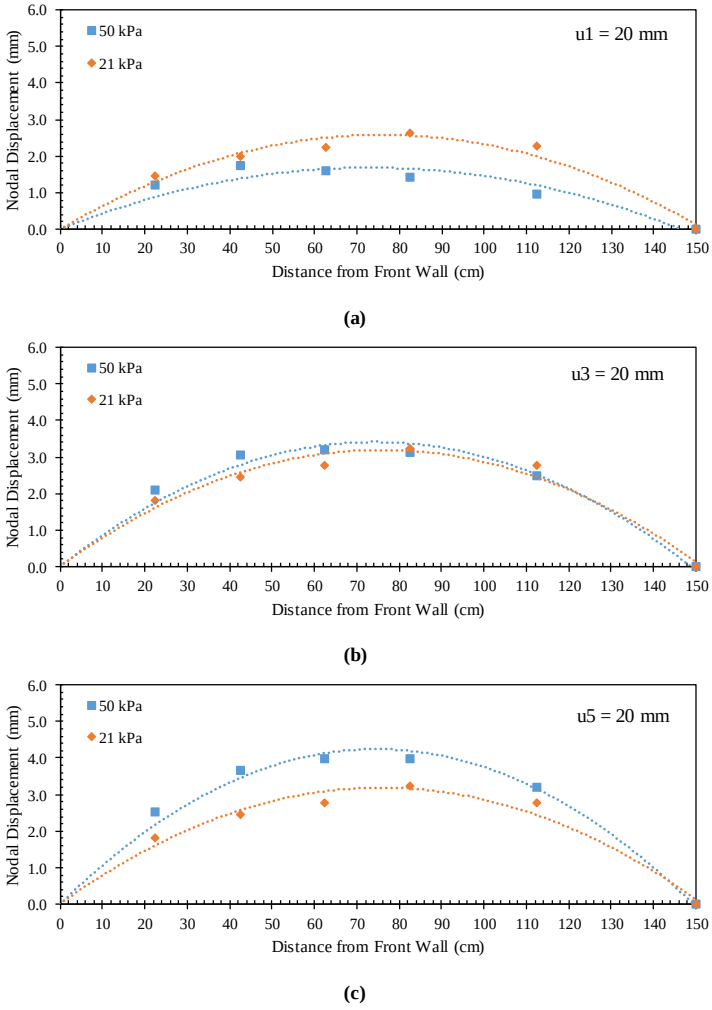

Figure 9.36. Upper passive reinforcement displacement profiles: (a) At nodal displacement u1 = 20 mm; (b) At nodal displacement u3 = 20 mm; and (c) At nodal displacement u5 = 20 mm (S_v = 0.05 m).

Figures 9.38a through 9.38c show the soil-reinforcement relative displacement magnitude at 30.5 cm from the front wall for tests conducted with reinforcements spaced at 0.15, 0.10, and 0.05 m, respectively. This relative displacement was obtained by subtracting the reinforcement displacement at this location (by interpolation between u1 and u3) and the soil displacement measured by the artificial gravel particle adjacent to the reinforcement (LP24). The results indicate that the relative displacement at the interface of the active reinforcement was higher in the tests conducted at low normal stresses than in those conducted at high normal stresses. The effect of vertical reinforcement spacing on the dependency of the soil-reinforcement relative displacement magnitude on normal stress will be discussed later in Section 9.3.3 in this dissertation.

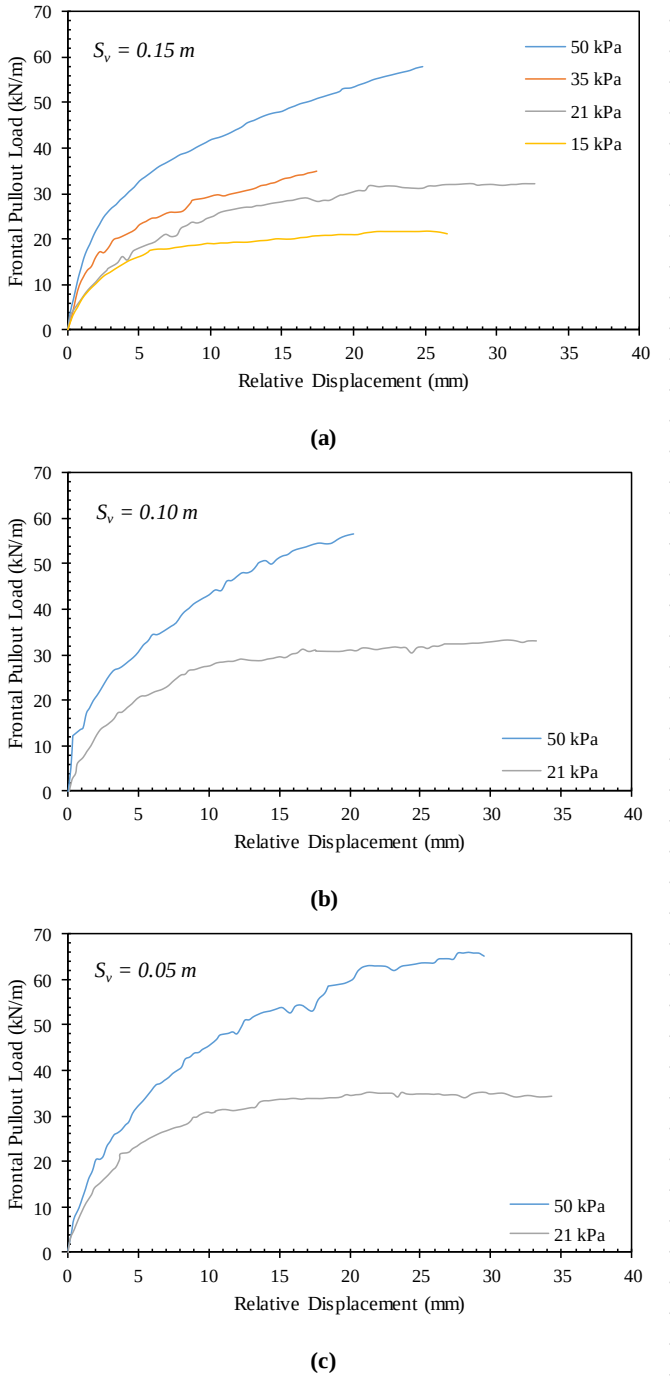

Figure 9.37. Soil-reinforcement relative displacement magnitude for tests conducted with reinforcement placed at different spacings: (a) S_v = 0.15 m; (b) S_v = 0.10 m; and (c) S_v = 0.05 m.

Figure 9.39 shows the vertical soil displacement measured by means of the artificial gravel particles placed on top of the reinforced soil mass. Figures 9.39a through 9.39c show the soil displacement with respect to reinforcement frontal displacement of the active reinforcement u1 for the back, middle, and front of the reinforced soil mass. The figures include tests conducted at normal stresses of 15, 21, and 35 kPa at the active reinforcement level (i.e., central horizontal plane of the reinforced soil mass). The results indicate that the soil tends to dilate near the front and settle near the back as pullout loading progressed. The results indicate that the dilation is higher in tests conducted at low normal stresses compared to those conducted at high normal stresses. The trends are consistent with the expected increase in dilatancy with decreaseing normal stresses. Similar trends were obtained for tests conducted using reinforcements placed at different reinforcement vertical spacings.

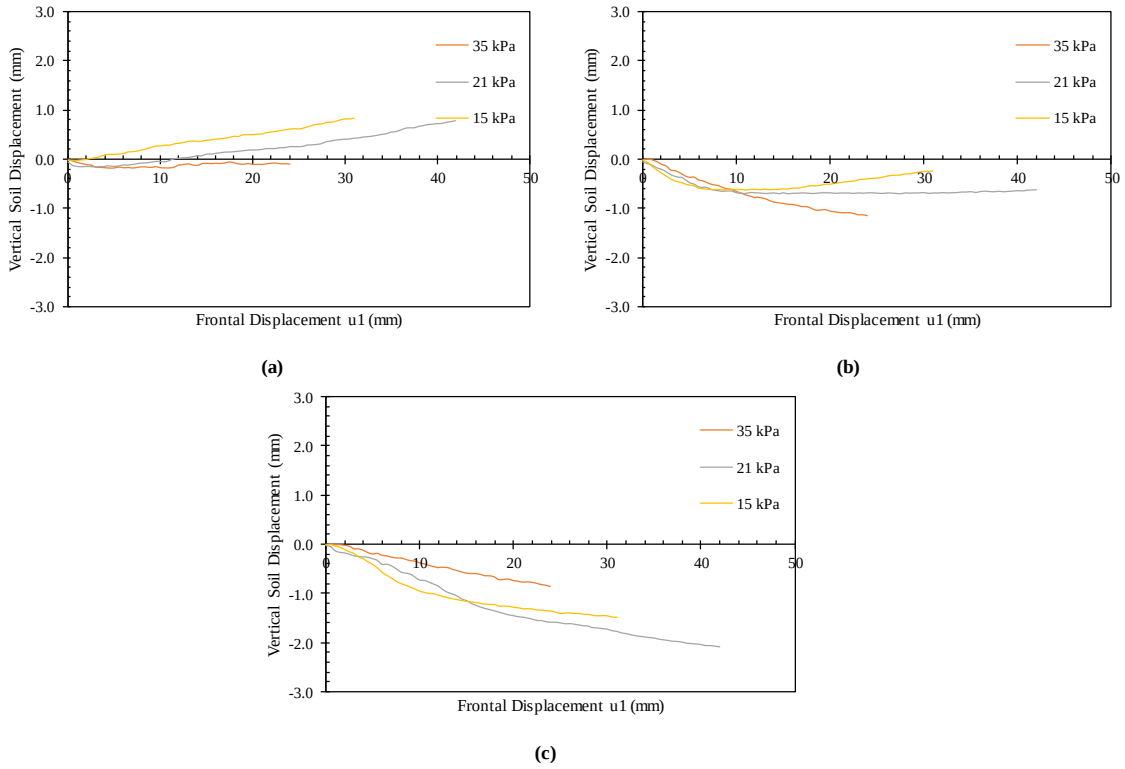

Figure 9.38. Vertical soil displacements (measured by means of artificial gravel particles) with respect to frontal displacement at the active reinforcement: (a) At the front of the soil mass; (b) At the middle of the soil mass; and (c) At the rear of the soil mass.

9.3.3. Effect of reinforcement vertical spacing

Two comparisons were made among the results from tests conducted using reinforcement layers placed at different vertical spacing. Table 9.4 summarizes the testing conditions of the tests involved in the two comparisons. Three reinforcement layers were used in each test, one active and two passive reinforcement layers, all of which were of the same type. The same reinforcement type was used in tests, polyester woven geotextile reinforcements. This reinforcement has ultimate tensile strength of 70 kN/m and tensile stiffness of 876 kN/m at tensile strain of 5% in the cross-rollway direction (i.e., cross-machine direction). The fill material used in these tests was AASHTO Gravel No. 8. Two comparisons were made among tests conducted at the same normal stress but with reinforcements placed at different vertical spacings: (1) a comparison between six tests conducted at normal stress of 50 kPa at the level of active reinforcement layer (i.e., central horizontal plane of the reinforced soil mass); and (2) a comparison between three tests conducted at normal stress of 21 kPa at the level of active reinforcement. The findings from both comparisons were compared to assess the effect of normal stress on the trends observed with varying the reinforcement vertical spacing within the reinforced soil mass.

Table 9.4. Summary of tests in which reinforcement vertical spacing was varied.

Test ID	*Testing Variables*					
	Fill Material	S_v	σ_v	*Active GS*	*Passive GS*	*Dilation*
GP-02-07-G1-G	AASHTO No. 8	0.05 m	50 kPa	HP570	HP570	Allowed
GP-04-07-G1-G		0.10 m				
GP-06-07-G1-G		0.15 m				
GP-08-07-G1-G		0.20 m				
GP-12-07-G1-G		0.30 m				
GP-16-03-G1-G		0.40 m				
GP-02-03-G1-G	AASHTO No. 8	0.05 m	21 kPa	HP570	HP570	Allowed
GP-04-03-G1-G		0.10 m				
GP-06-03-G1-G		0.15 m				

Figures 9.39a and 9.39b show the frontal pullout load-displacement experimental curves tests conducted at normal pressure of 50 and 21 kPa, respectively. It can be observed that the curves match well, particularly at early pullout loading stages. The agreement at higher pullout loading levels is still very good, although with comparatively higher scatter. This trend shows that the reinforcement vertical spacing has negligible effect on pullout resistance when using HP570 woven geotextile active and passive reinforcements. A minor difference in the maximum pullout resistance can be observed in Figure 9.39b, which shows the comparison made among tests conducted at low normal stress (21 kPa). For the tests reported in this figure, the reinforced soil tended to dilate more than the tests conducted at high normal pressure (50 kPa). The results indicate that for tests conducted using comparatively smaller reinforcement vertical spacing, the dilation tendency was smaller. That is, a decrease in vertical spacing results in reduction in the reinforced soil mass dilation, which is consistent with the effect of increased confinement and increased soil-reinforcement interface strength.

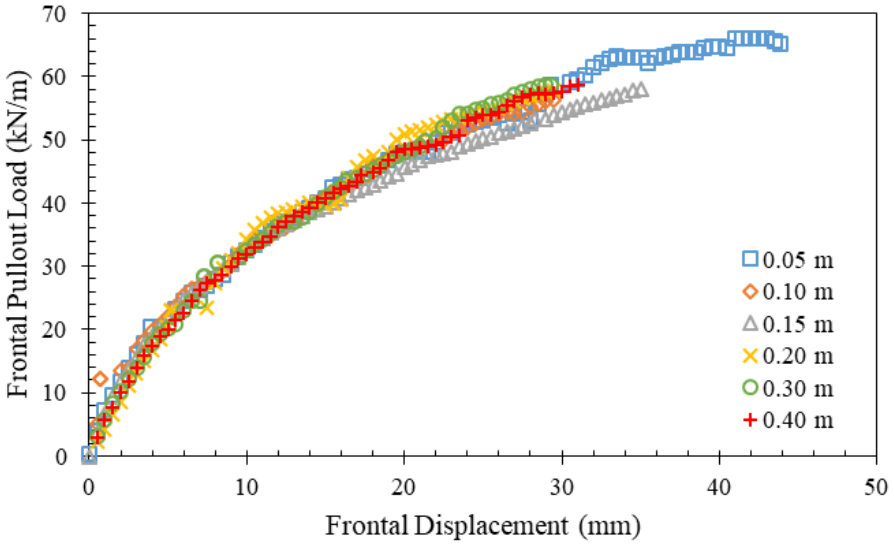

(a)

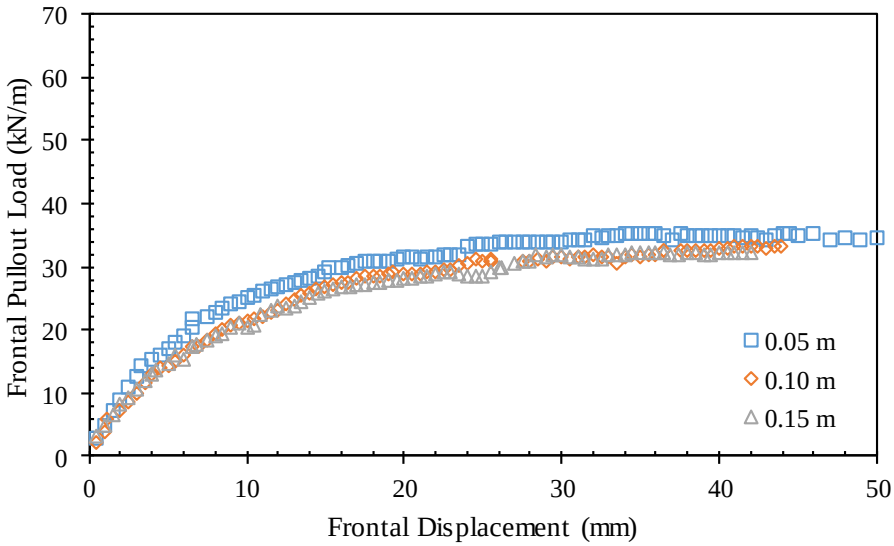

(b)

Figure 9.39. Frontal pullout load-displacement curves: (a) At normal stress, σ_v = 50 kPa; and (b) At normal stress, σ_v = 21 kPa.

Figures 9.40 and 9.41 show the average displacements measured for the active reinforcement and the corresponding average displacements for the passive reinforcements for tests conducted at normal stresses of 50 and 21 kPa, respectively. Every figure consists of a and b showing the average displacements measured for the upper and lower passive reinforcement layers, respectively. Note that the average displacement is the area under displacement profile normalized by the reinforcement length. Assuming the constitutive behavior for the interface shear behavior, Figures 9.40 and 9.41 provide insight into the effect of the normal stress on the interaction between neighboring reinforcements. It was concluded that the tests conducted with reinforcements placed at larger vertical spacing resulted in small interaction between neighboring reinforcements. The effect of the reinforcement spacing may have a bigger impact at high normal stresses.

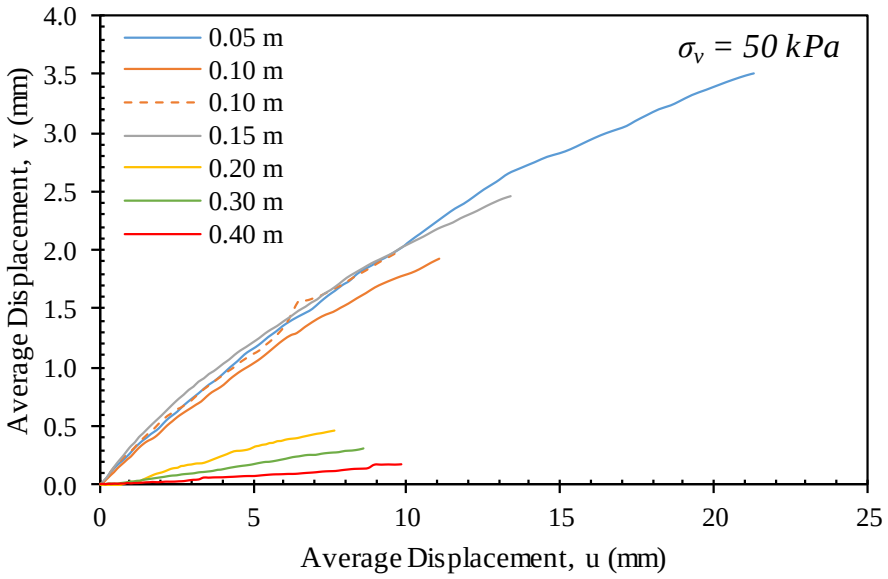

(a)

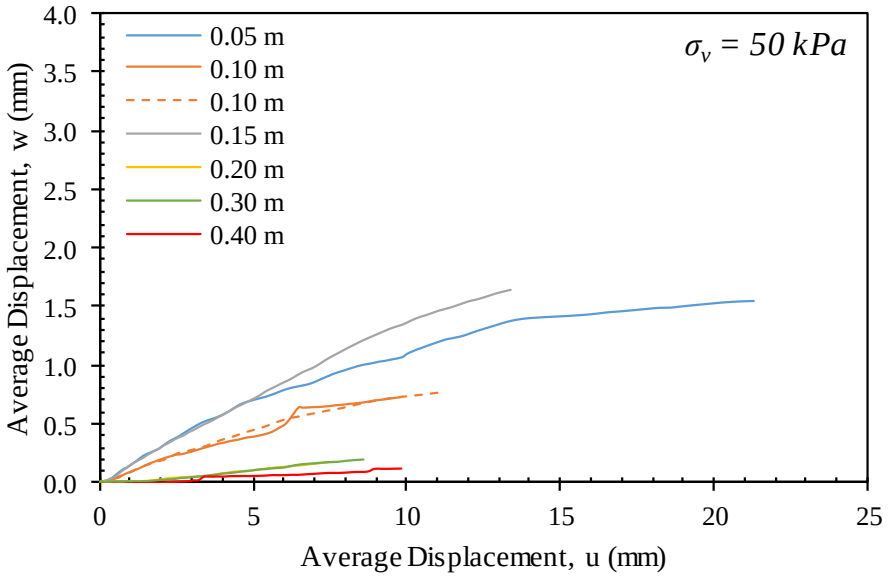

(b)

Figure 9.40. Average displacements of passive reinforcements with respect to average displacements of active reinforcement: (a) Upper passive reinforcement; and (b) Lower passive reinforcement (σ_v = 50 kPa).

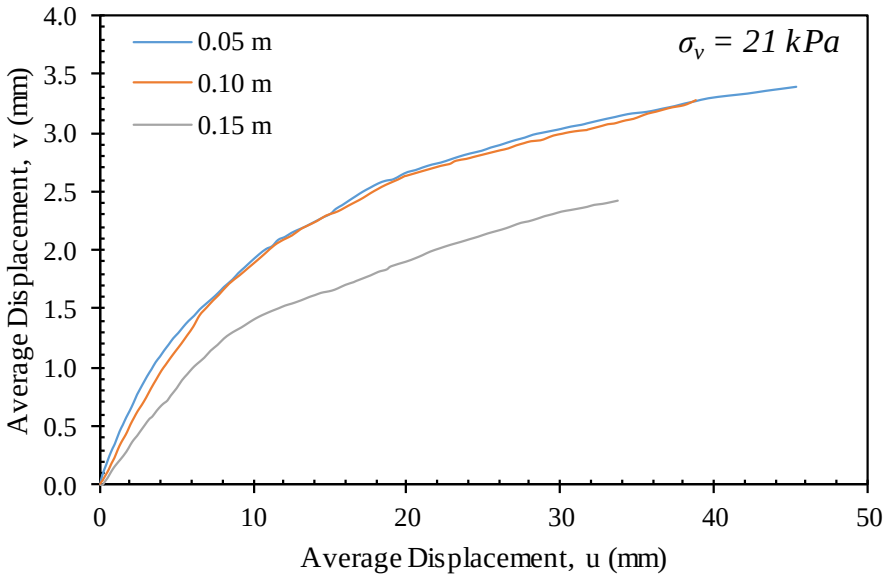

(a)

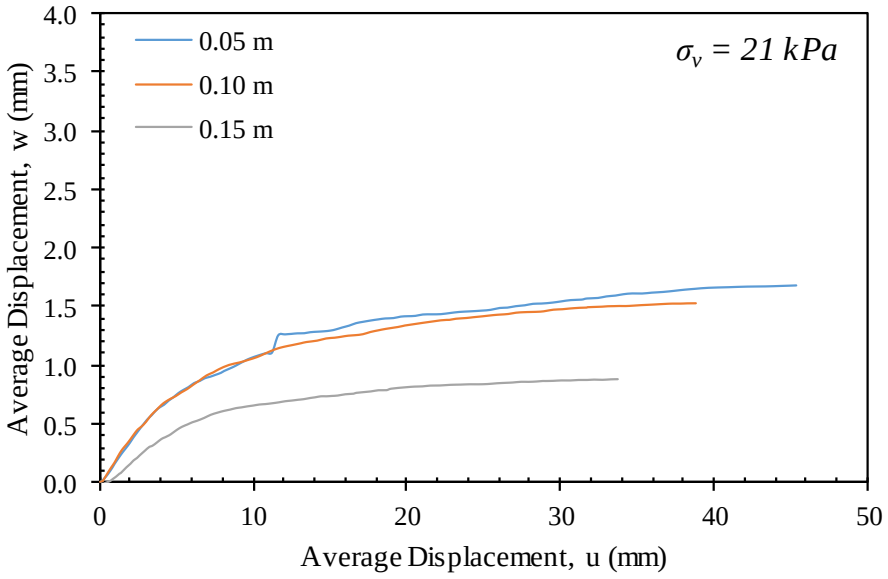

(b)

Figure 9.41. Average displacements of passive reinforcements with respect to average displacements of active reinforcement: (a) Upper passive reinforcement; and (b) Lower passive reinforcement (σ_v = 21 kPa).

Figure 9.42 shows a comparison between the interface shear strength back-calculated from the soil-geosynthetic interaction test results under ultimate condition and that obtained from large-scale direct shear testing. Note that the ultimate pullout values for the tests conducted at normal stresses of 35 and 50 kPa were determined by extrapolating the frontal pullout load-displacement curves. Since no trend could be distinguished for the ultimate pullout resistance values for tests conducted using reinforcements placed at different vertical spacings, average values at normal stresses of 21 and 50 kPa were used to construct the interface strength envelope. The results indicate that the interface friction angle resulting from the pullout testing is higher than that resulting from direct shear testing. This can be attributed to additional passive resistance that could be mobilized in pullout tests with flexible fabrics. Forensic investigation of the reinforcement layers after test completion revealed the presence of punch holes in the HP570 fabric that resulted from the adjacent gravel particles. This type of interaction may be similar to the interaction taking place due to passive resistance of transverse ribs in geogrid reinforcements.

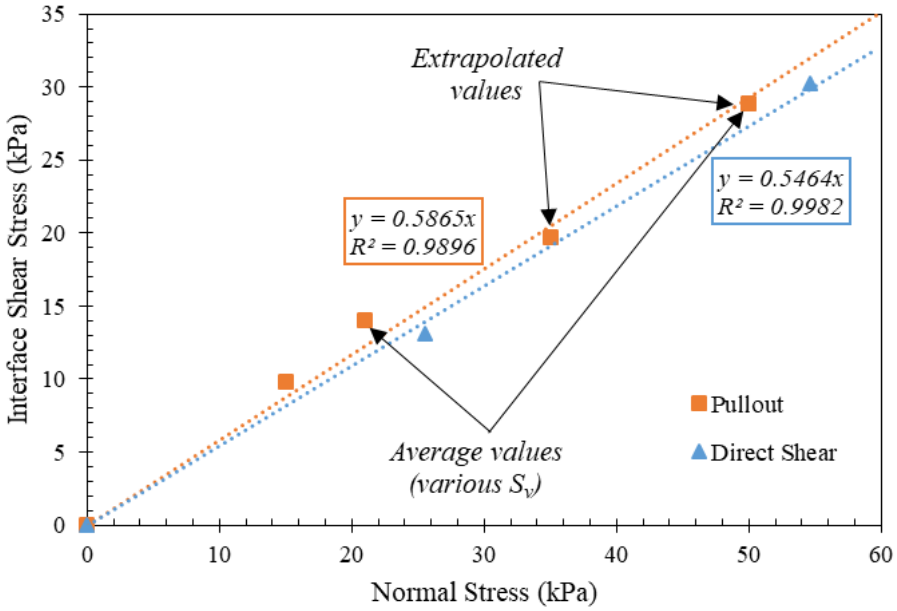

Figure 9.42. Soil-reinforcement interfaced shear strength envelopes (AASHTO Gravel No. 8 and HP570 geotextile interface).

Figures 9.43a through 9.43c show the ratio between the average displacements measured in the upper passive reinforcement layers to those measured in the active reinforcement layers at average displacements of the active reinforcement layers of 2, 5, and 10 mm, respectively. These figures reflect the degree of interaction between the active and the upper passive reinforcement layers for tests conducted at various normal stress and with reinforcements placed at various vertical spacings. The results point towards a threshold vertical spacing below which the effect of the spacing is maximum for specific normal stress range, soil medium, and reinforcement. This threshold vertical spacing can be reasonably identified as 0.10 m for normal stress range of 15 to 50 kPa. In addition, the interaction between reinforcement layers is essentially negligible beyond vertical spacing of 0.30 m for tests conducted at normal stress of 50 kPa. This observation points to another

boundary beyond which there is no longer an effect for the reinforcement spacing on the interaction between neighboring reinforcements for specific normal stress, soil medium, and reinforcement. This value can be can be reasonably identified as 0.30 m for normal stress range of 15 to 50 kPa.

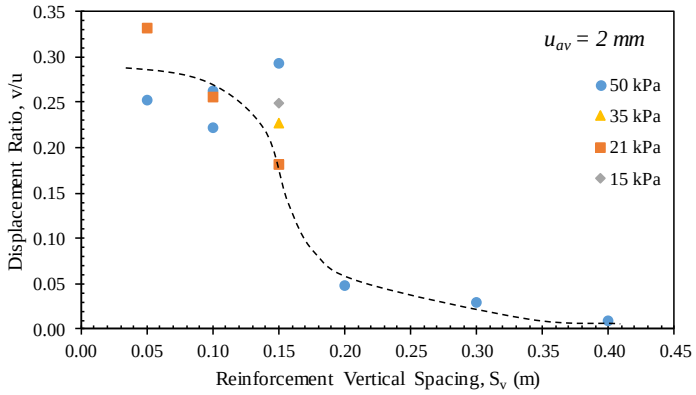

(a)

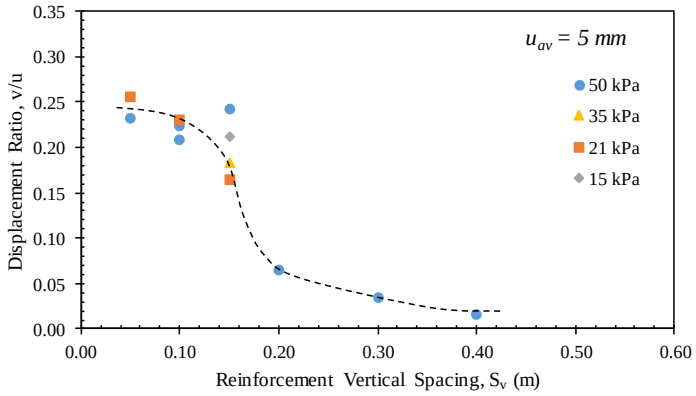

(b)

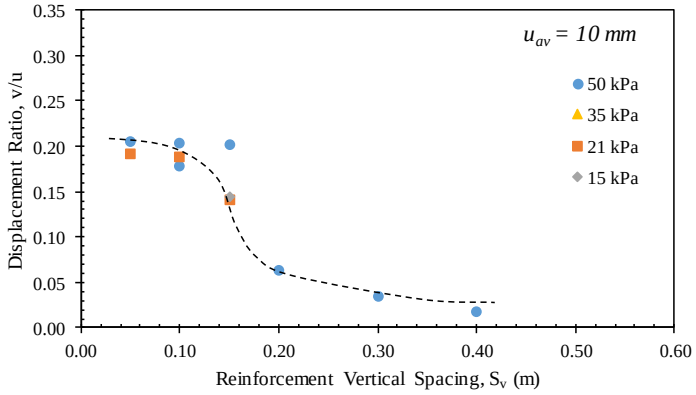

(c)

Figure 9.43. Average displacement ratio of the upper passive reinforcement layers at various average displacements of the active reinforcement layers: (a) u_{av} = 2 mm; (b) u_{av} = 5 mm; and (c) u_{av} = 10 mm.

Figures 9.44 through 9.48 show the displacement profiles for the active and passive reinforcement layers at active reinforcement frontal displacements (u1) of 5, 10, 15, 20, and 30 mm, respectively, for tests conducted at normal stress of 50 kPa. Similarly, Figures 9.49 through 9.53 show the displacement profiles for reinforcement layers at active reinforcement frontal displacements (u1) of 5, 10, 15, 20, and 30 mm for tests conducted at normal stress of 21 kPa. The profiles for the active reinforcements show the displacement for all tests conducted at the same normal stress. That is, the reinforcement vertical spacing has insignificant impact on the soil-reinforcement interaction behavior of the active reinforcement. On the other hand, the profiles of the passive reinforcements showed higher displacements for tests conducted with reinforcements placed at small vertical spacings compared to those conducted with reinforcements placed at larger spacings. The difference in displacement increased as the pullout loading progressed. Note that, however, there was no significant difference between the displacements measured for passive reinforcements in the tests conducted with reinforcements spaced at 0.05, 0.10, and 0.15 m at normal stress of 50 kPa. Similar observation was made in tests conducted with reinforcements spaced at 0.05 and 0.10 m at normal stress of 21 kPa.

It should be noted that the passive reinforcements in tests conducted with reinforcements placed at different spacings are subject to different normal stress due to the difference in the overburden pressure (different elevation from the central horizontal plane of the reinforced soil mass). If a comparison is made between passive reinforcements placed at the same elevation in soil masses reinforced at different vertical spacing, the effect of the spacing on the interaction among the neighboring reinforcements would increase. In such comparison, more layers are placed in the soil mass with closely-spaced reinforcements than that of with largely-spaced reinforcements. In the closely-spaced

reinforced system, the intermediate reinforcement layers would reduce the interaction between the active reinforcement and the passive reinforcements layers placed at the same elevation as that in the largely-spaced reinforced system.

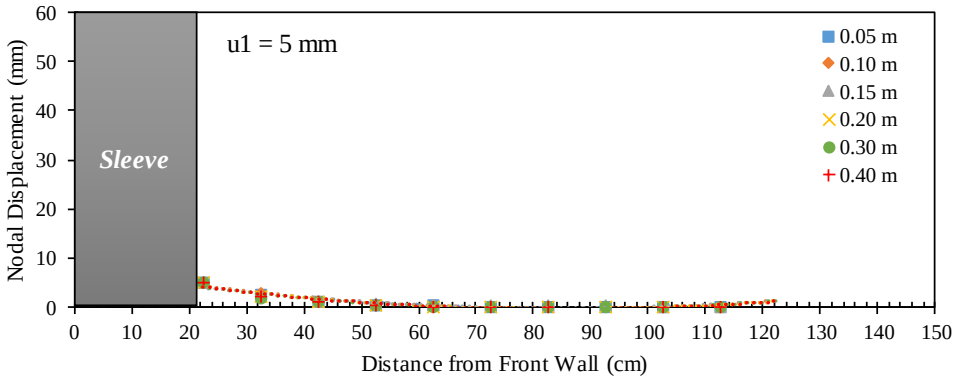

(a)

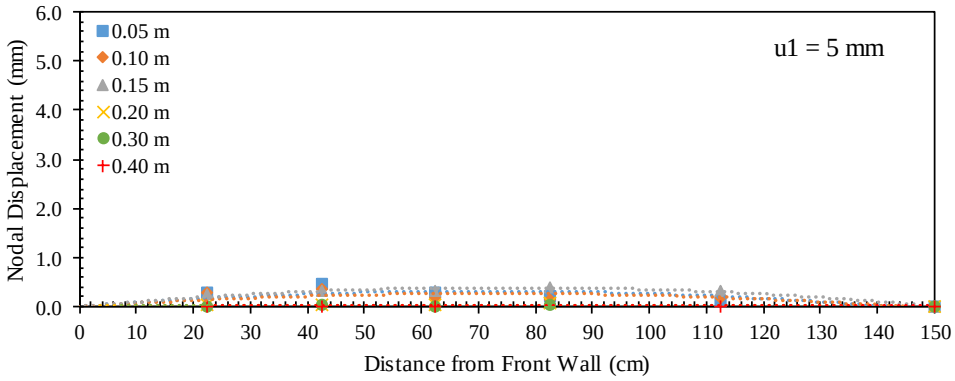

(b)

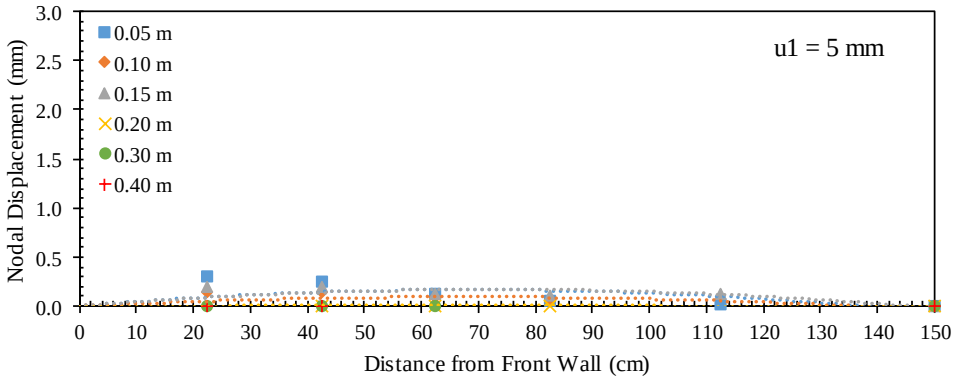

(c)

Figure 9.44. Reinforcement displacement profiles at frontal displacement u1 = 5 mm: (a) Active reinforcement; (b) Upper passive reinforcement; and (c) Lower passive reinforcement (σ_v = 50 kPa).

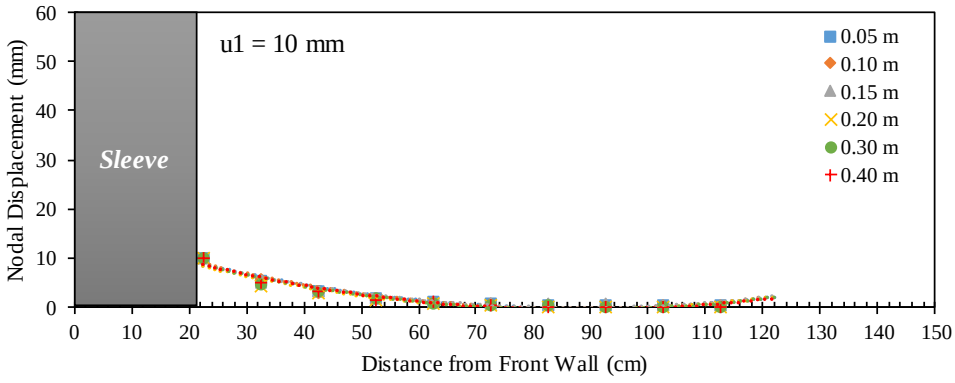

(a)

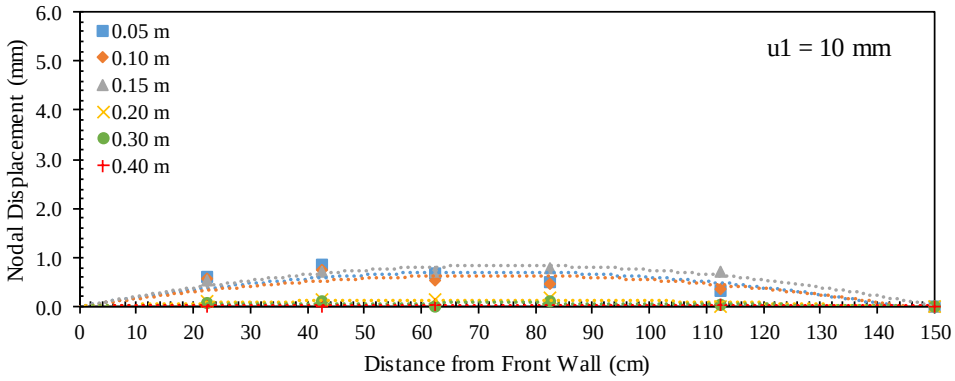

(b)

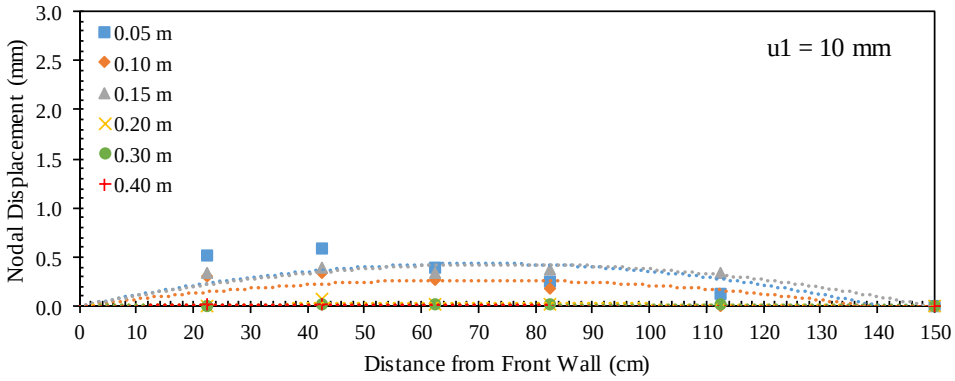

(c)

Figure 9.45. Reinforcement displacement profiles at frontal displacement u1 = 10 mm: (a) Active reinforcement; (b) Upper passive reinforcement; and (c) Lower passive reinforcement (σ_v = 50 kPa).

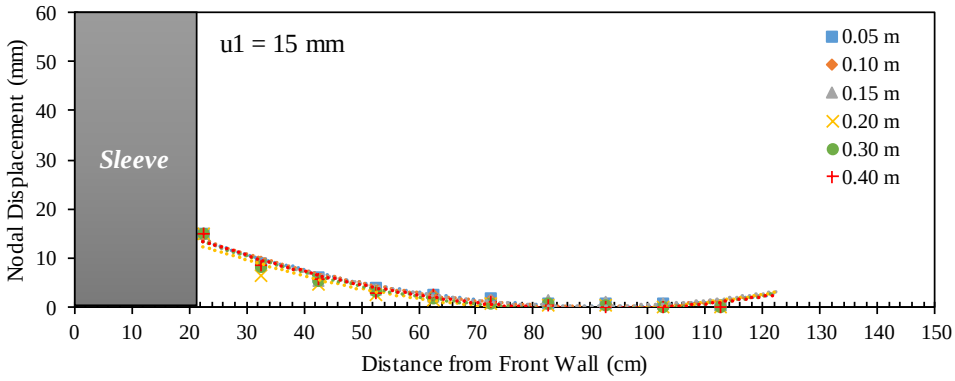

(a)

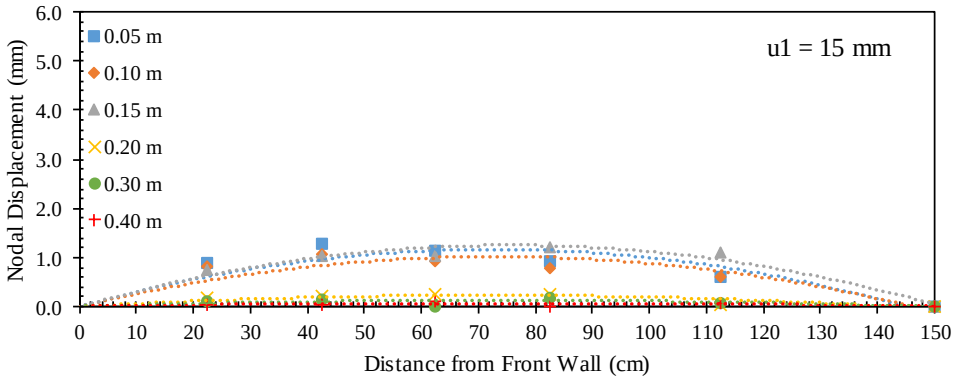

(b)

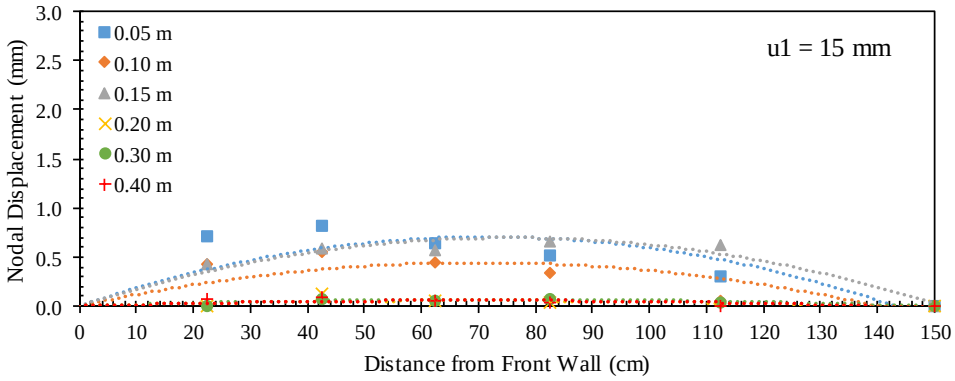

(c)

Figure 9.46. Reinforcement displacement profiles at frontal displacement u1 = 15 mm: (a) Active reinforcement; (b) Upper passive reinforcement; and (c) Lower passive reinforcement (σ_v = 50 kPa).

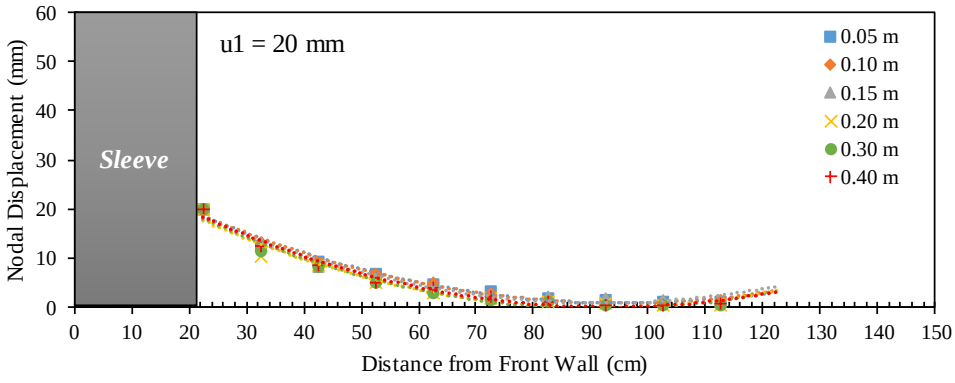

(a)

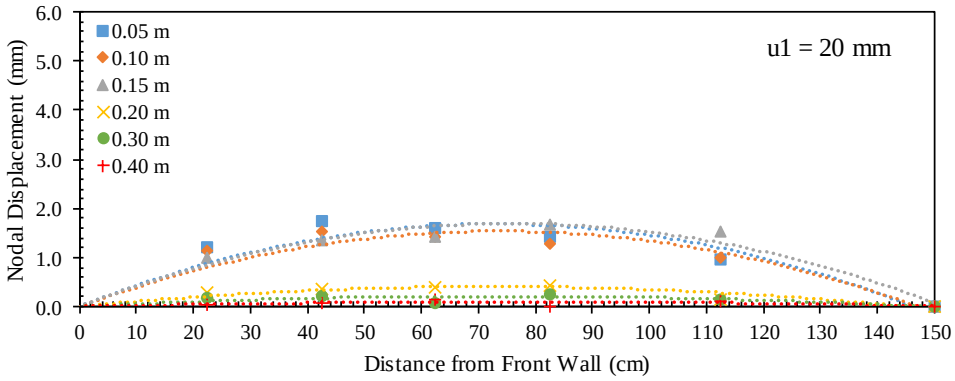

(b)

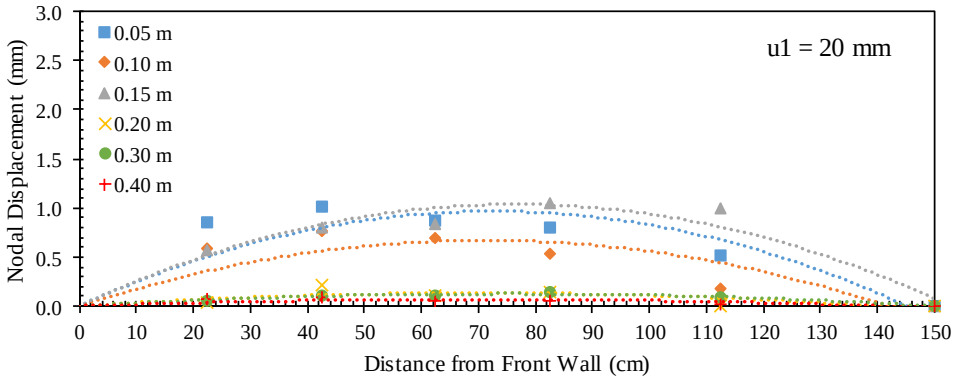

(c)

Figure 9.47. Reinforcement displacement profiles at frontal displacement u1 = 20 mm: (a) Active reinforcement; (b) Upper passive reinforcement; and (c) Lower passive reinforcement (σ_v = 50 kPa).

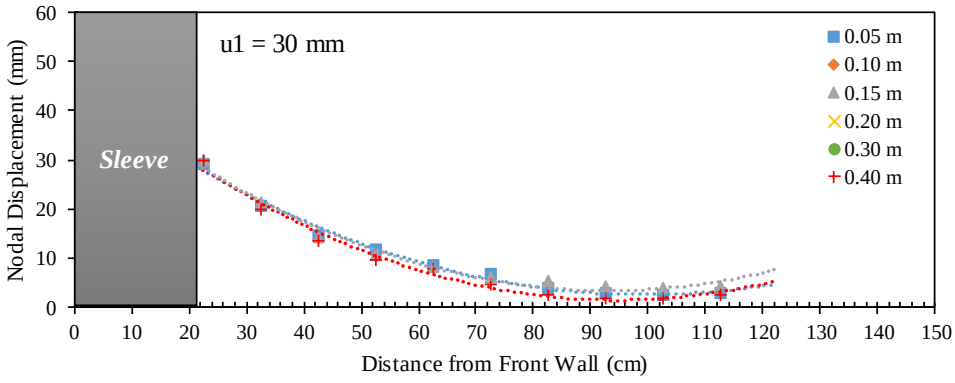

(a)

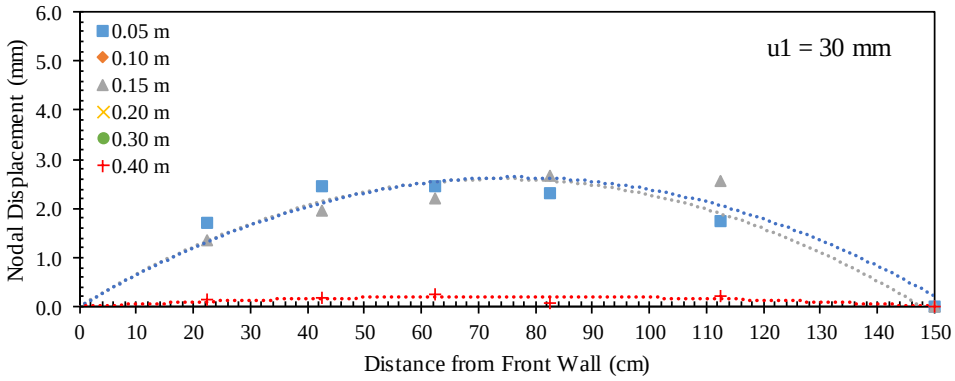

(b)

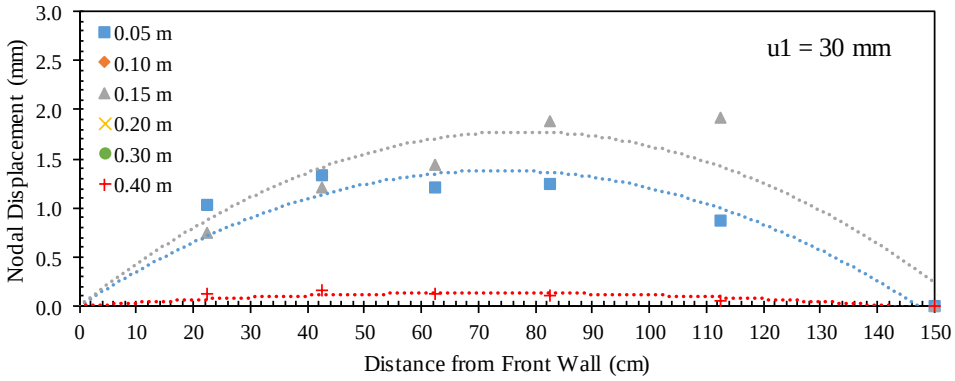

(c)

Figure 9.48. Reinforcement displacement profiles at frontal displacement u1 = 30 mm: (a) Active reinforcement; (b) Upper passive reinforcement; and (c) Lower passive reinforcement (σ_v = 50 kPa).

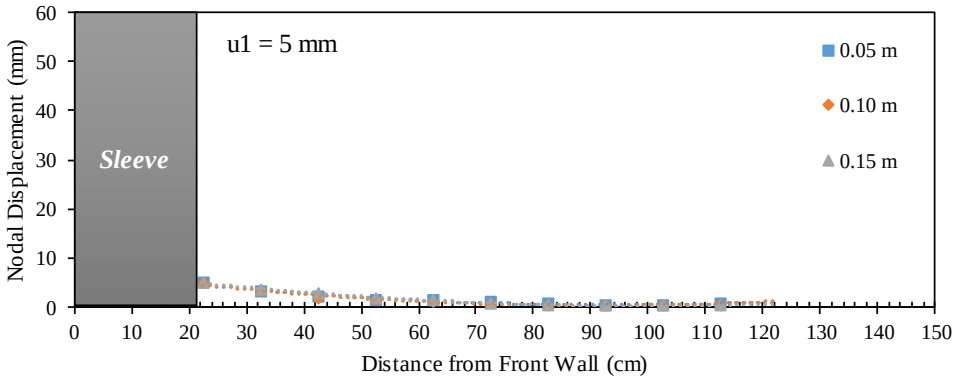

(a)

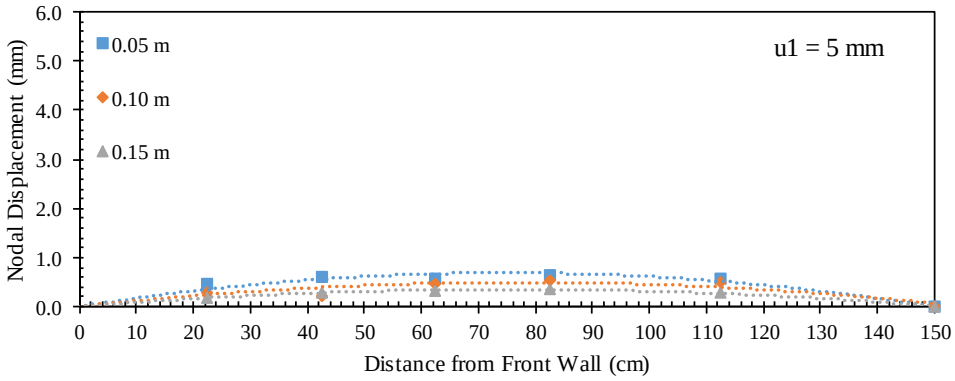

(b)

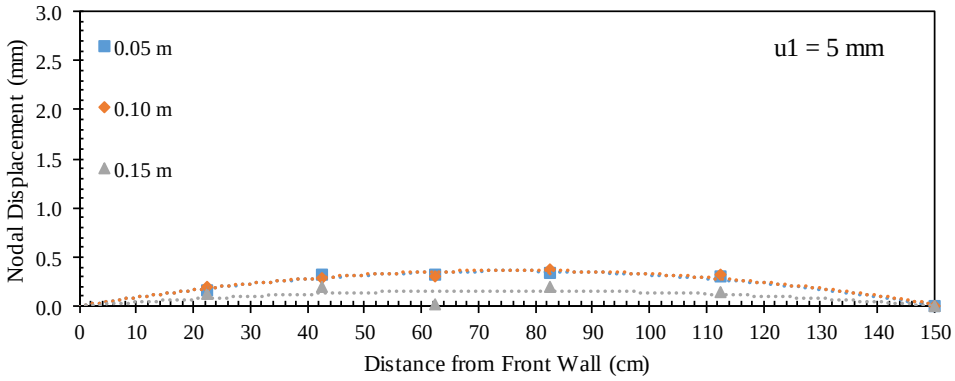

(c)

Figure 9.49. Reinforcement displacement profiles at frontal displacement u1 = 5 mm: (a) Active reinforcement; (b) Upper passive reinforcement; and (c) Lower passive reinforcement (σ_v = 21 kPa).

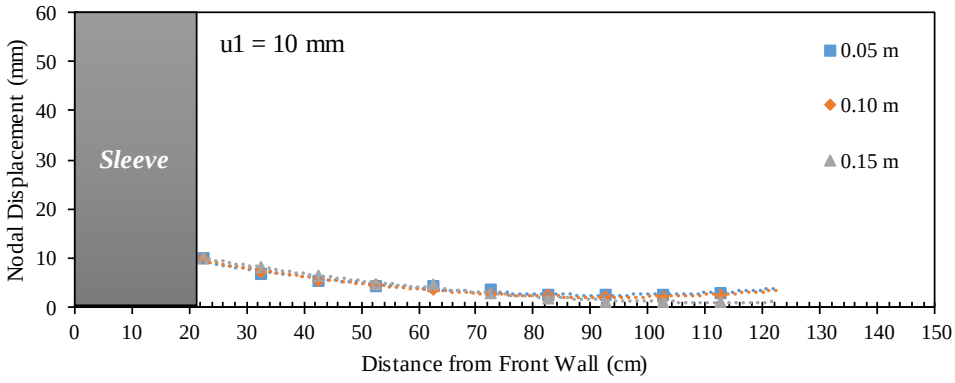

(a)

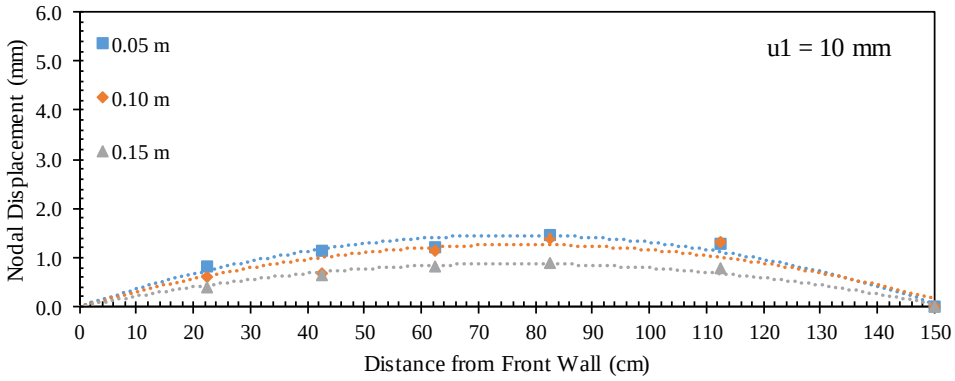

(b)

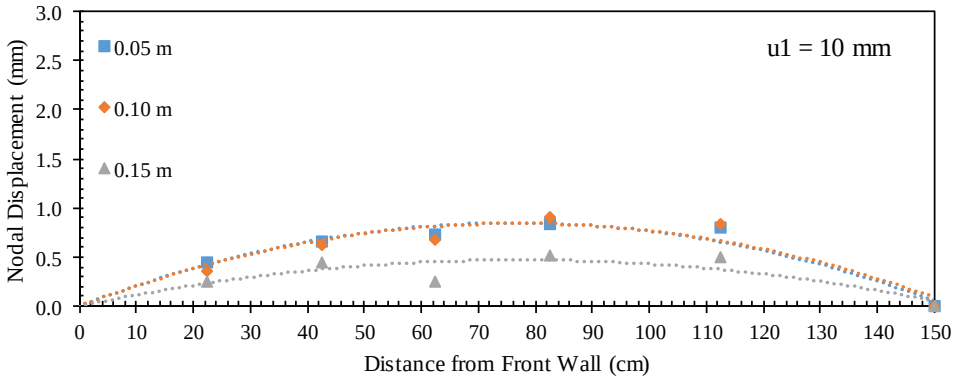

(c)

Figure 9.50. Reinforcement displacement profiles at frontal displacement u1 = 10 mm: (a) Active reinforcement; (b) Upper passive reinforcement; and (c) Lower passive reinforcement (σ_v = 21 kPa).

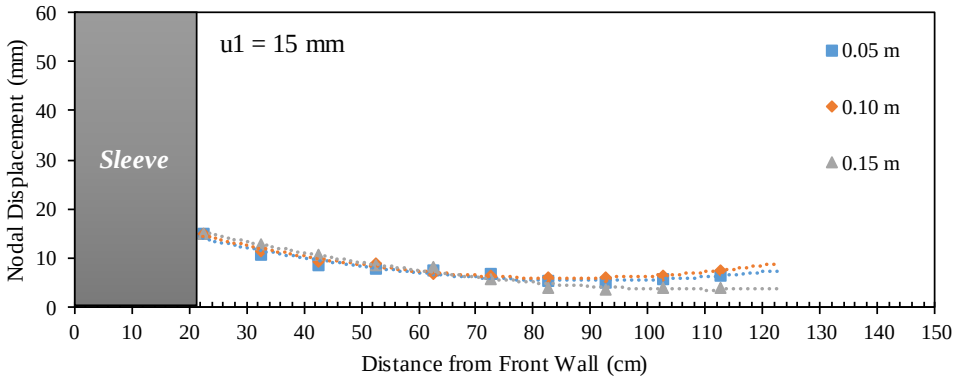

(a)

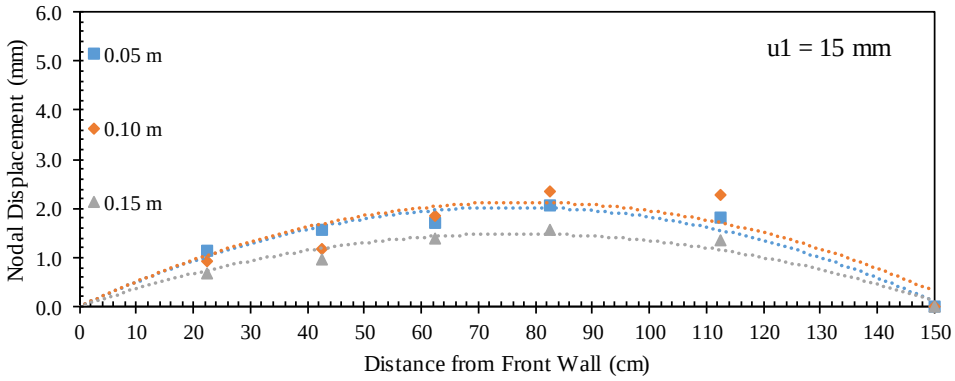

(b)

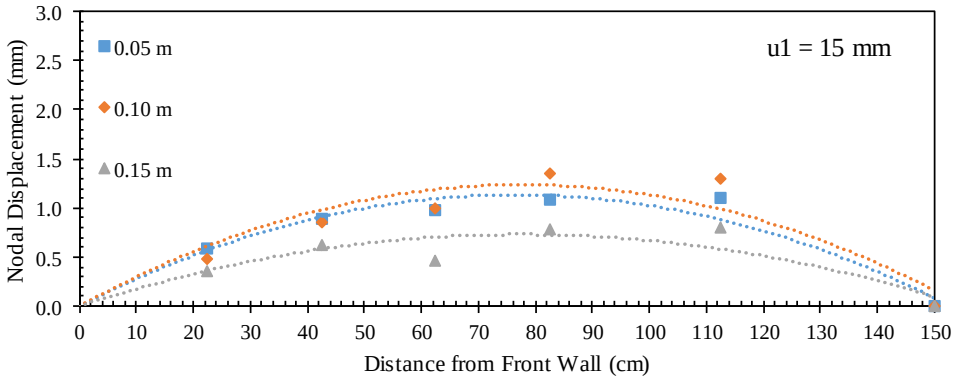

(c)

Figure 9.51. Reinforcement displacement profiles at frontal displacement u1 = 15 mm: (a) Active reinforcement; (b) Upper passive reinforcement; and (c) Lower passive reinforcement (σ_v = 21 kPa).

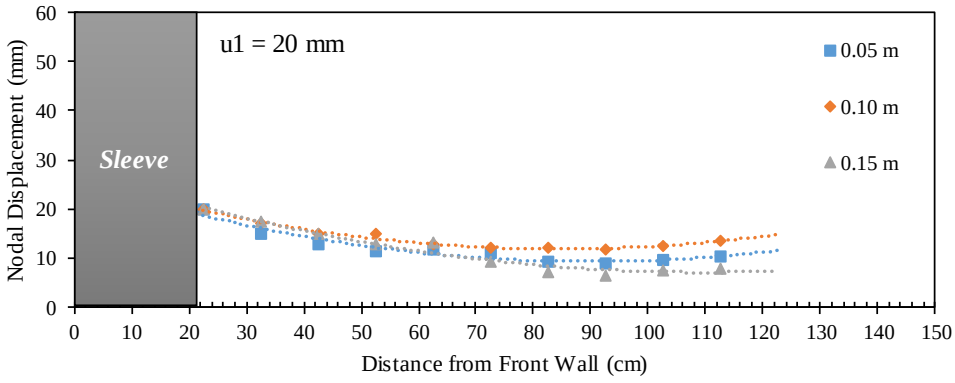

(a)

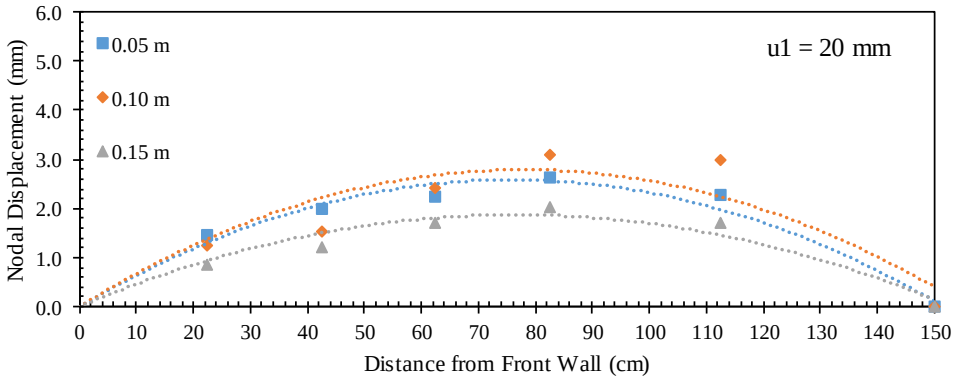

(b)

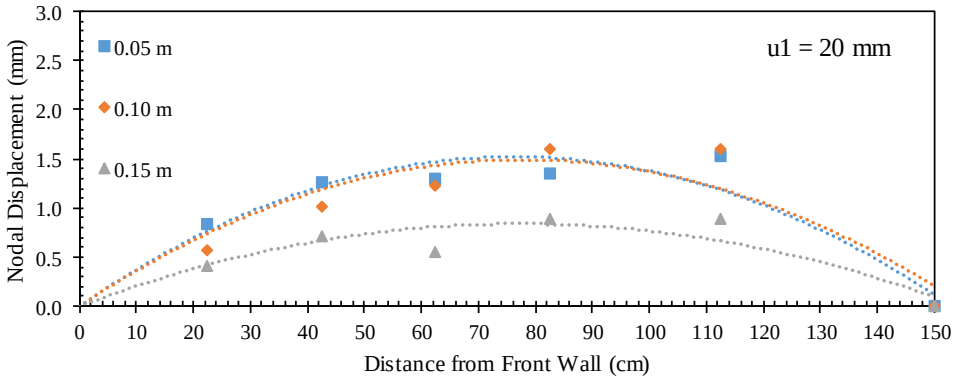

(c)

Figure 9.52. Reinforcement displacement profiles at frontal displacement u1 = 20 mm: (a) Active reinforcement; (b) Upper passive reinforcement; and (c) Lower passive reinforcement (σ_v = 21 kPa).

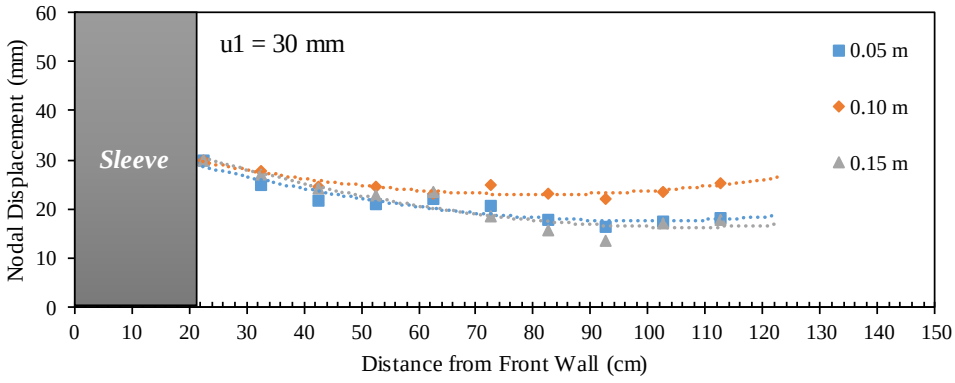

(a)

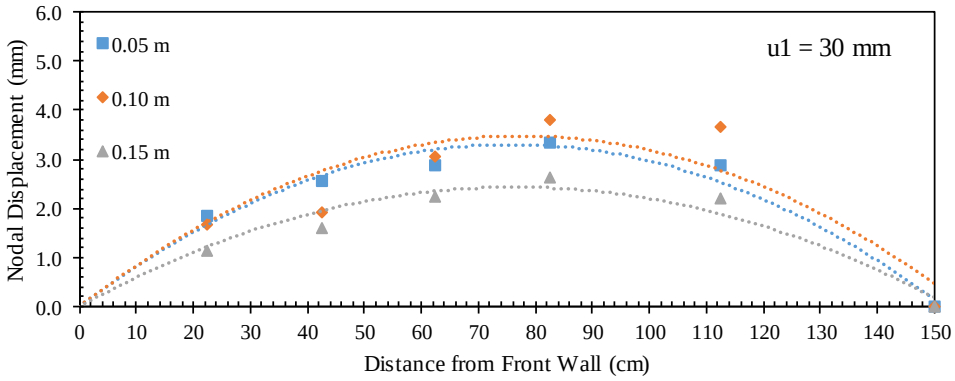

(b)

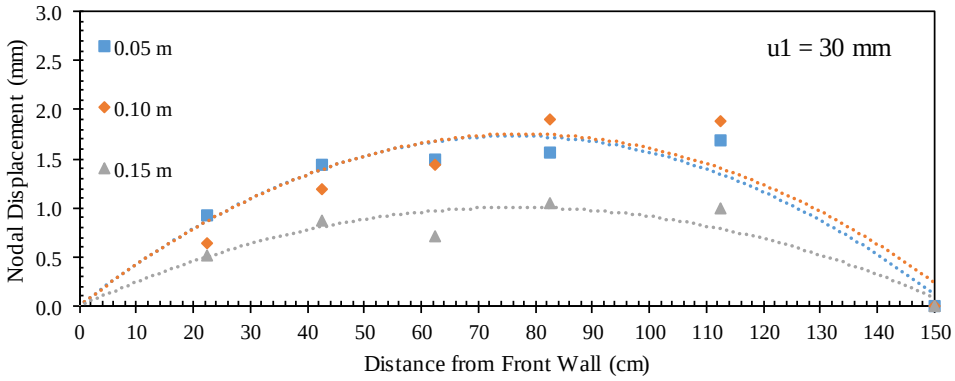

(c)

Figure 9.53. Reinforcement displacement profiles at frontal displacement u1 = 30 mm: (a) Active reinforcement; (b) Upper passive reinforcement; and (c) Lower passive reinforcement (σ_v = 21 kPa).

Figures 9.54 through 9.58 present the horizontal soil displacement measured for nodal displacements of 5, 10, 15, 20, and 30 mm, respectively, for the tests conducted with normal stress of 50 kPa. Similarly, Figures 9.59 through 9.63 present the horizontal soil displacement measured for nodal displacements of 5, 10, 15, 20, and 30 mm, respectively, for the tests conducted with normal stress of 21 kPa. Each figure consists of a and b that show the soil displacement with respect nodal displacements u1 and u3, respectively. These displacement were measured at specific locations by tracking artificial gravel particles making a vertical array within the soil at 30.5 cm from the front wall. Note that the soil adjacent to the reinforcement exhibited higher rate of displacement, which is due to yielding in the internal shear strength of the fill material that limits the load transfer from the reinforcement to larger distance away from the reinforcement.

The results indicate that the horizontal soil displacement was higher in the tests conducted with reinforcements spaced at small spacings that that measured in the tests conducted with reinforcements spaced at large spacings. The active reinforcement delivers the load to the surrounding soil medium, which is then transferred to the passive reinforcements. The soil-reinforcement interfaces of the passive reinforcements have weaker shear strength than the internal strength of the soil. These weaker interfaces allow the soil in between the reinforcement layers to displace more than in the case of no passive reinforcements. However, the passive reinforcements reduce the load transfer from the active reinforcement to the soil masses on the other sides of the passive reinforcements.

Note that the active reinforcement in each test delivers the same load to the surrounding soil since the reinforcement spacing was found not to affect the soil-reinforcement interaction behavior of active reinforcements as discussed earlier. That is, the same energy is delivered to the soil and the passive reinforcements in each test. For the

tests conducted with reinforcements placed at small vertical spacings, the soil mass in between the active and passive reinforcements displaces more compared to that in the tests conducted with reinforcements placed at large vertical spacings as it receives more energy per unit soil volume from the active reinforcement. On contrary, the soil masses on the other sides of the passive reinforcements displaces less than that in the tests conducted with reinforcements placed at small vertical spacings.

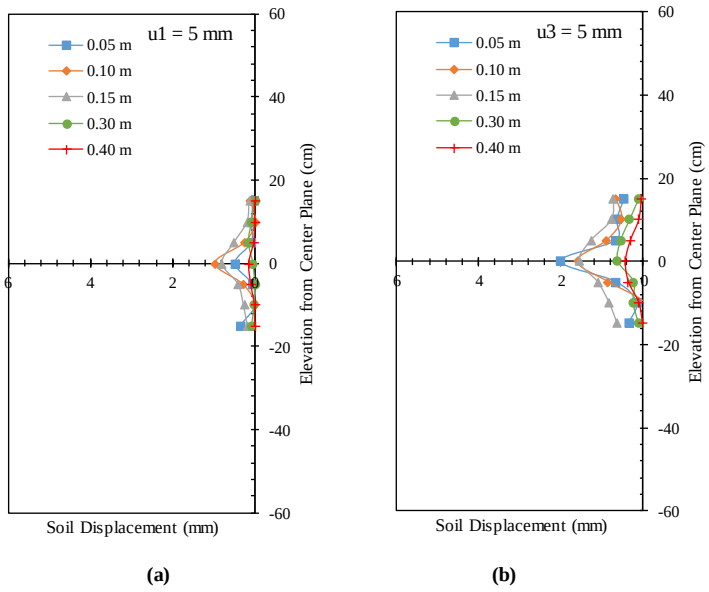

Figure 9.54. Horizontal soil displacement profiles (measured by means of artificial gravel particles): (a) At nodal displacement u1 = 5 mm; and (b) At nodal displacement u3 = 5 mm (σ_v = 50 kPa).

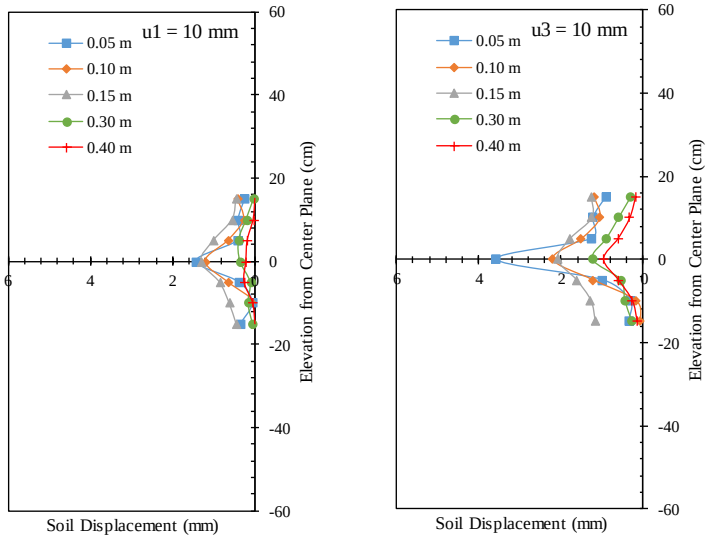

(a) **(b)**

Figure 9.55. Horizontal soil displacement profiles (measured by means of artificial gravel particles): (a) At nodal displacement u1 = 10 mm; and (b) At nodal displacement u3 = 10 mm (σ_v = 50 kPa).

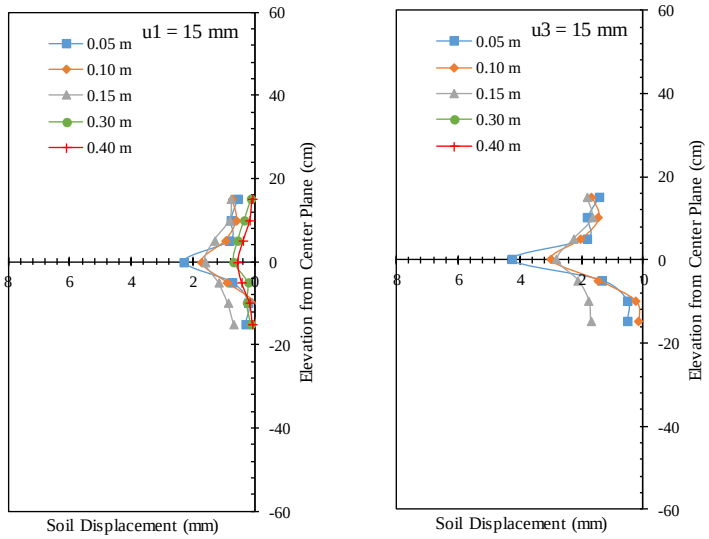

(a) **(b)**

Figure 9.56. Horizontal soil displacement profiles (measured by means of artificial gravel particles): (a) At nodal displacement u1 = 15 mm; and (b) At nodal displacement u3 = 15 mm (σ_v = 50 kPa).

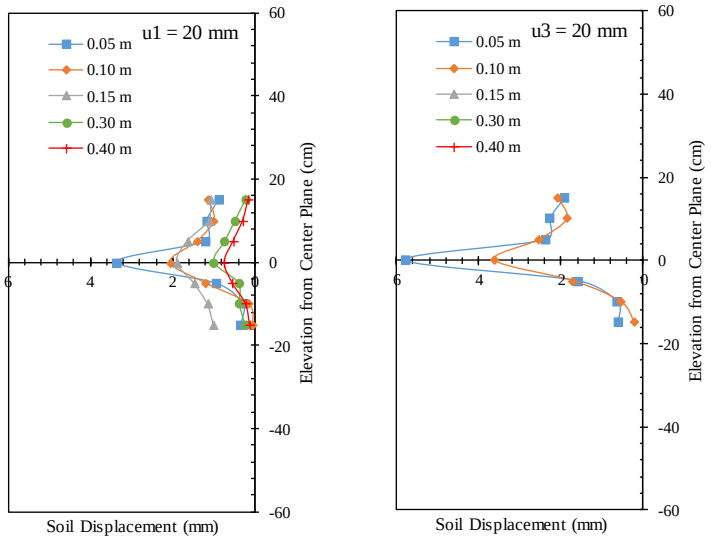

Figure 9.57. Horizontal soil displacement profiles (measured by means of artificial gravel particles): (a) At nodal displacement u1 = 20 mm; and (b) At nodal displacement u3 = 20 mm (σ_v = 50 kPa).

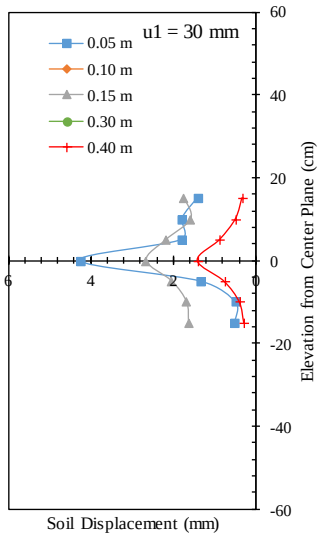

Figure 9.58. Horizontal soil displacement profiles (measured by means of artificial gravel particles) at nodal displacement u1 = 30 mm (σ_v = 50 kPa).

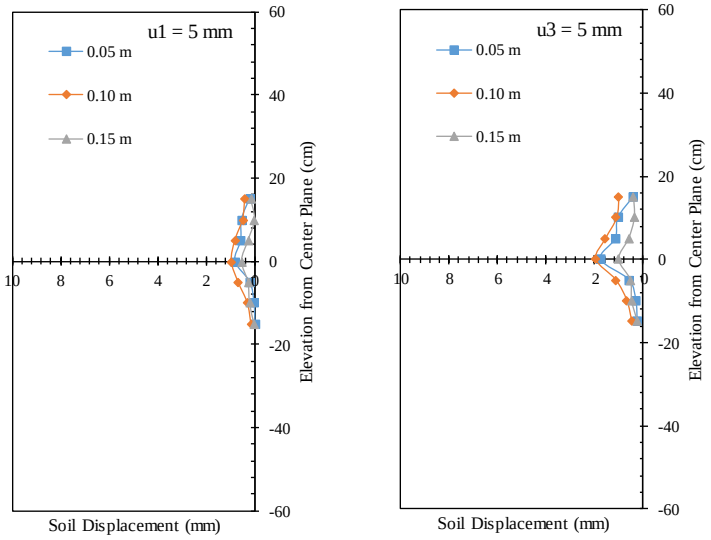

(a) **(b)**

Figure 9.59. Horizontal soil displacement profiles (measured by means of artificial gravel particles): (a) At nodal displacement u1 = 5 mm; and (b) At nodal displacement u3 = 5 mm (σ_v = 21 kPa).

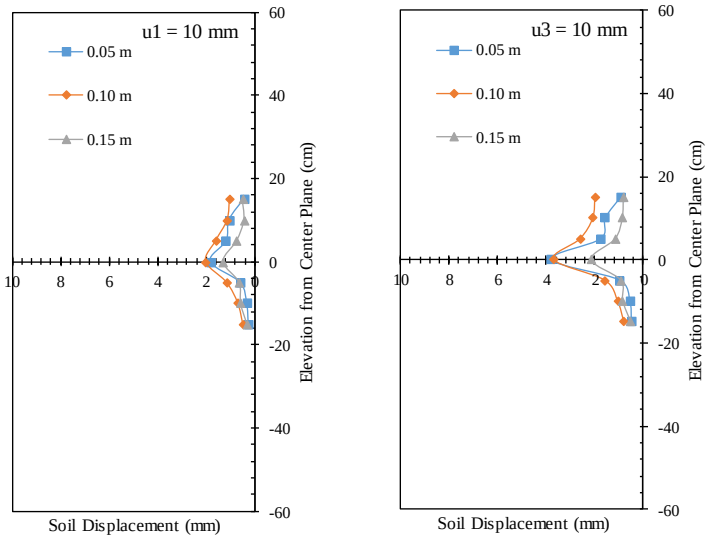

(a) **(b)**

Figure 9.90. Horizontal soil displacement profiles (measured by means of artificial gravel particles): (a) At nodal displacement u1 = 10 mm; and (b) At nodal displacement u3 = 10 mm (σ_v = 21 kPa).

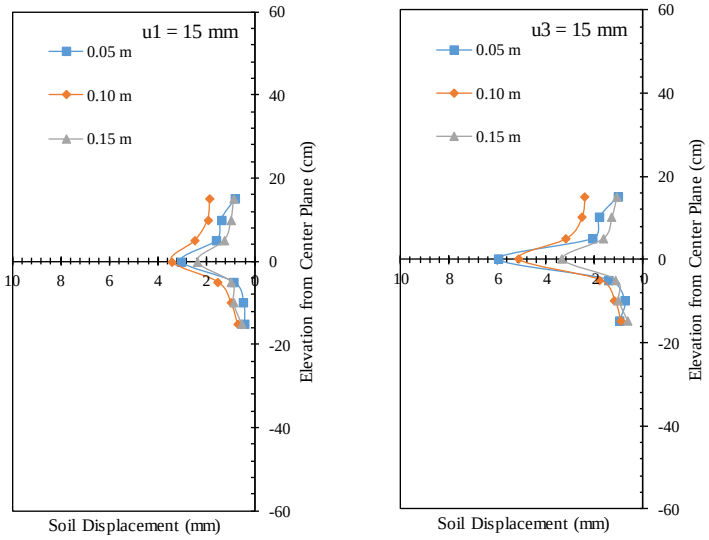

(a) **(b)**

Figure 9.61. Horizontal soil displacement profiles (measured by means of artificial gravel particles): (a) At nodal displacement u1 = 15 mm; and (b) At nodal displacement u3 = 15 mm (σ_v = 21 kPa).

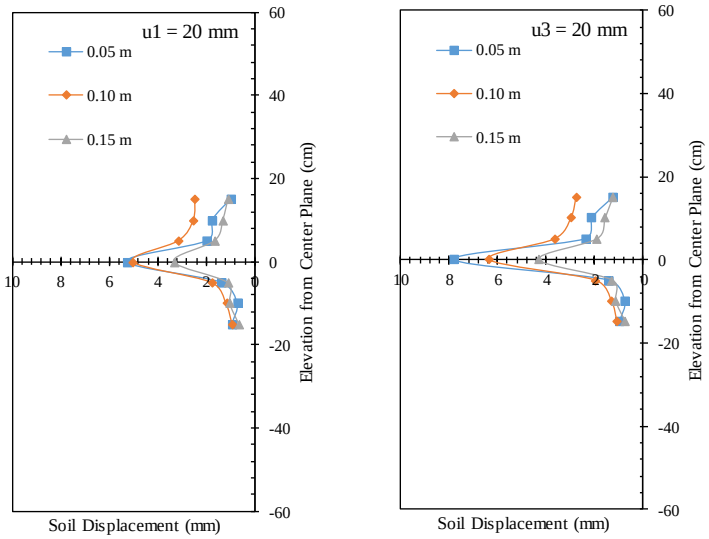

(a) **(b)**

Figure 9.62. Horizontal soil displacement profiles (measured by means of artificial gravel particles): (a) At nodal displacement u1 = 20 mm; and (b) At nodal displacement u3 = 20 mm (σ_v = 21 kPa).

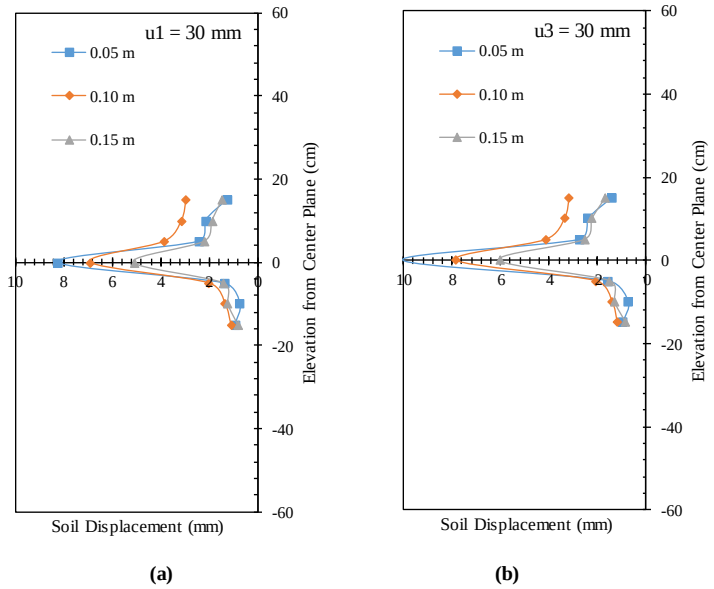

Figure 9.63. Horizontal soil displacement profiles (measured by means of artificial gravel particles): (a) At nodal displacement u1 = 30 mm; and (b) At nodal displacement u3 = 30 mm (σ_v = 21 kPa).

Figures 9.64a and 9.64b show the soil-reinforcement relative displacement magnitude at 30.5 cm from the front wall for tests conducted at normal stress of 50 and 21 kPa, respectively. This relative displacement was obtained by subtracting the reinforcement displacement at this location (by interpolation between u1 and u3) and the soil displacement measured by the artificial gravel particle adjacent to the reinforcement (LP24). This figure exhibits the reduction in the soil-reinforcement interface shear stiffness during the test. The results indicate that the relative displacement was higher in the tests conducted with reinforcements placed at large vertical spacings compared to that in tests conducted with reinforcements placed at small vertical spacings. The displacement of the soil adjacent to the reinforcements in the tests conducted with reinforcements placed at small vertical spacings was higher than that in the tests conducted with reinforcements placed at large vertical spacings. Meanwhile, the reinforcement displacement was the same

in all tests regardless the reinforcement vertical spacing. Figure 9.65 shows the effect of reinforcement vertical spacing on the sensitivity of soil-reinforcement relative displacement to normal stress. No difference in relative displacement was observed at early pullout loading stages between tests conducted at normal stress of 50 kPa.

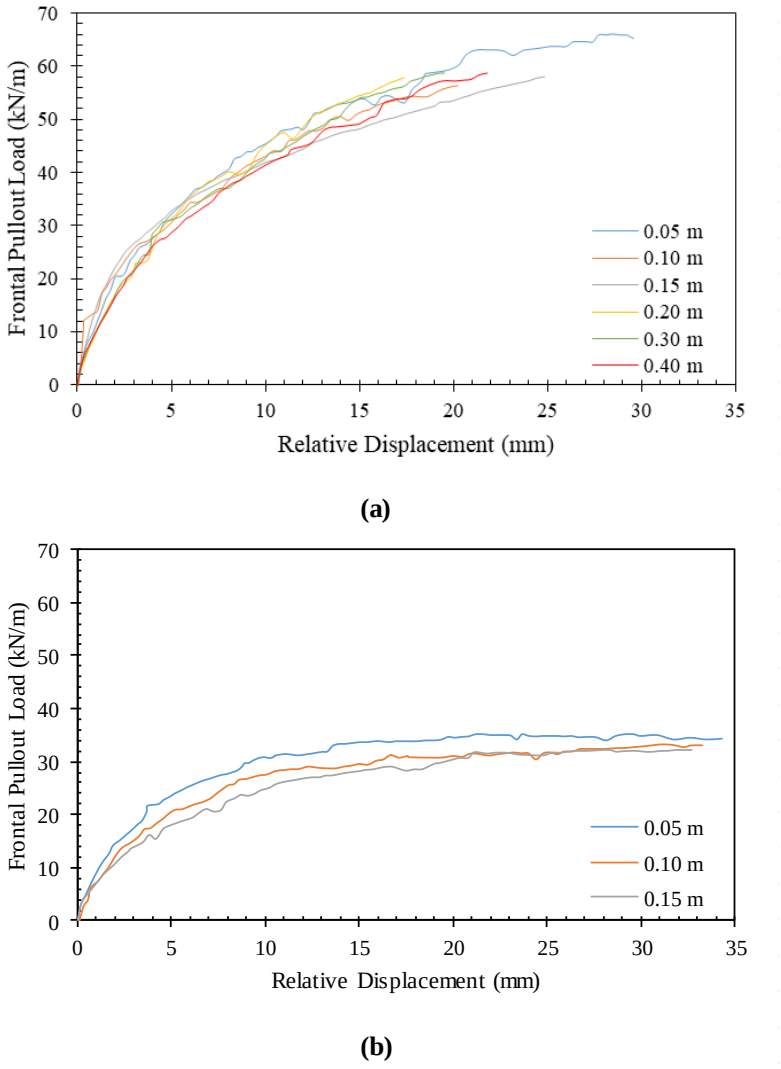

Figure 9.64. Soil-reinforcement relative displacement magnitude for tests conducted with reinforcement placed at different spacings: (a) σ_v = 50 kPa; and (b) σ_v = 21 kPa.

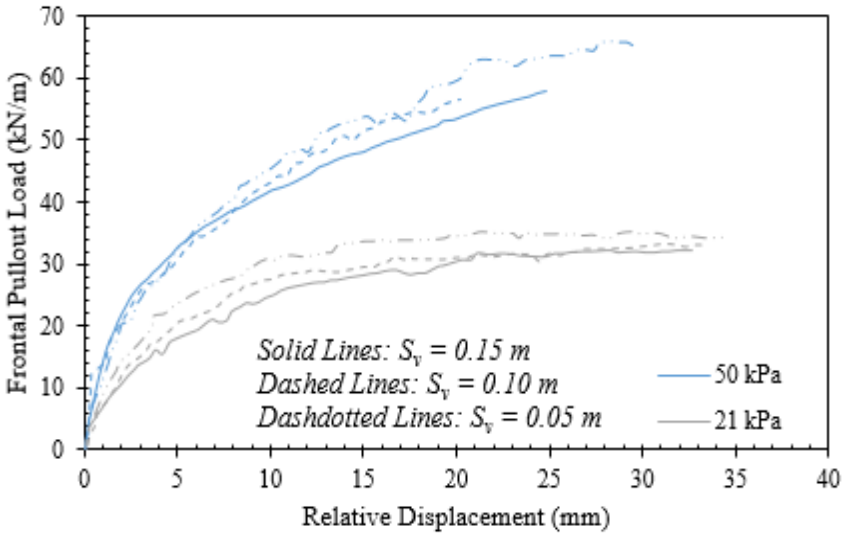

Figure 9.65. Soil-reinforcement relative displacement magnitude.

Figures 9.66 and 9.67 show the vertical soil displacement measured by means of the artificial gravel particles placed on top of the reinforced soil mass for tests conducted at normal stress of 50 and 21 kPa, respectively. Each figure consists of a, b, and c subfigures that show the soil displacement with respect to reinforcement frontal displacement of the active reinforcement u1 for the back, middle, and front of the reinforced soil mass, respectively. The figures include tests conducted with reinforcements placed at various vertical spacings. The results indicate that the soil tended to dilate near the front and settle near the back as pullout loading progressed. The dilation tendency near the front took place after settlement in early loading stages as shear stresses were generated at the soil-reinforcement interface. The results indicate that the dilation tendency was higher in the tests conducted with reinforcements placed at small spacings compared to that in the tests conducted with reinforcements placed at large spacings. Note that the dilation tendency was high in tests conducted at low normal stresses compared to those conducted at high normal stresses. That is, the impact of reinforcement vertical spacing on the soil-

reinforcement interface behavior was more pronounced in the tests conducted at 21 kPa normal stress.

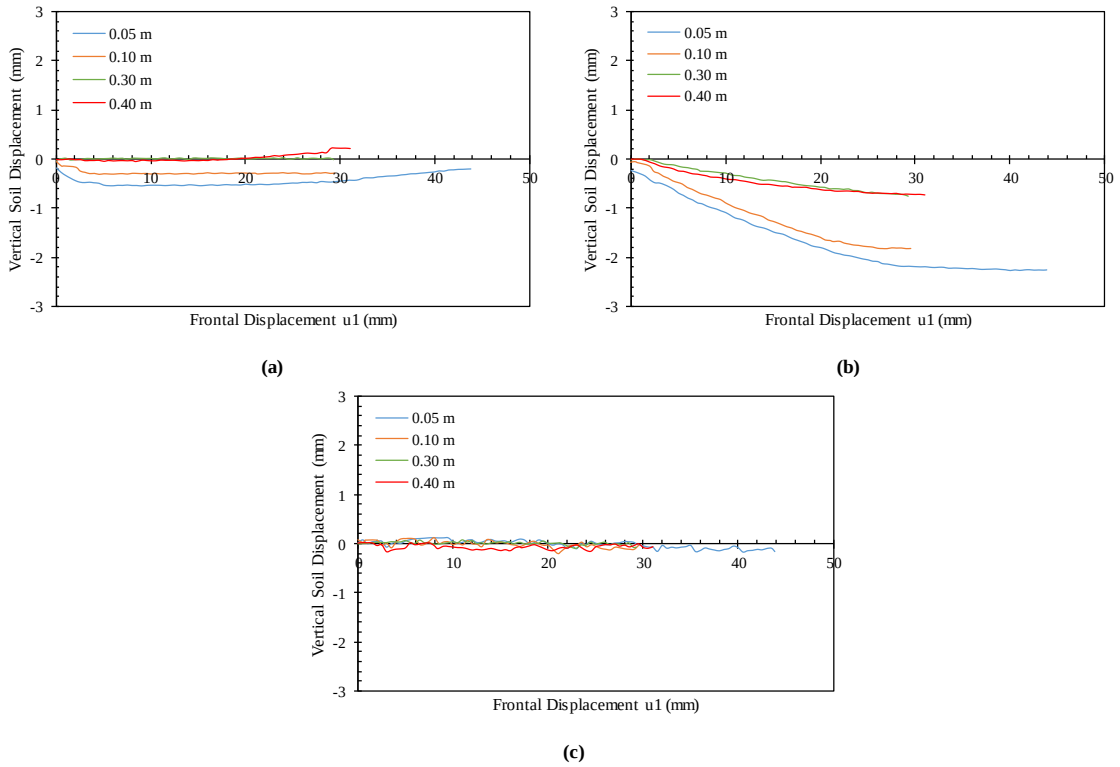

Figure 9.66. Vertical soil displacements (measured by means of artificial gravel particles) with respect to frontal displacement at the active reinforcement: (a) At the front of the soil mass; (b) At the middle of the soil mass; and (c) At the back of the soil mass (σ_v = 50 kPa).

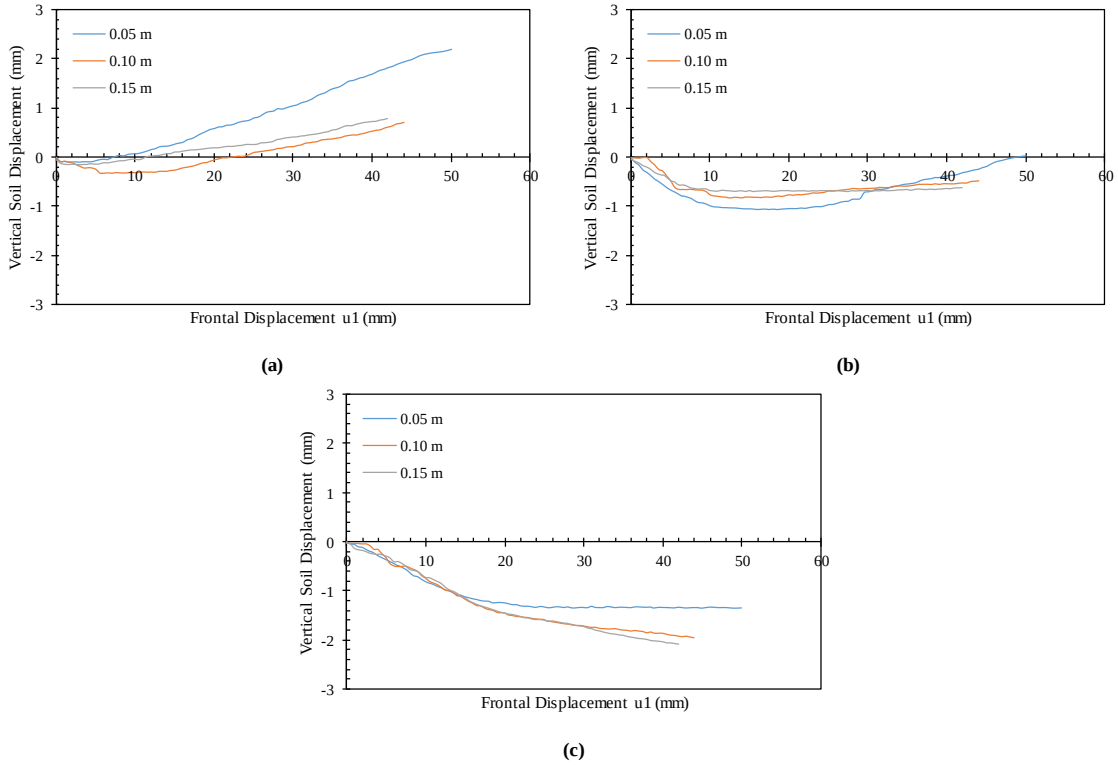

Figure 9.67. Vertical soil displacements (measured by means of artificial gravel particles) with respect to frontal displacement at the active reinforcement: (a) At the front of the soil mass; (b) At the middle of the soil mass; and (c) At the back of the soil mass (σ_v = 21 kPa).

9.3.4. Effect of reinforcement properties

In order to assess the effect of reinforcement properties (type, tensile stiffness, soil-reinforcement interaction, and ultimate strength) on the interaction between the contiguous reinforcement layers in GRS structures, the testing program included tests conducted at the same testing conditions using various reinforcement types. Table 9.5 summarizes the tests in which reinforcement type was varied. Specifically, six tests were conducted using AASHTO #8 fill material and three reinforcement layers placed at a vertical spacing of 0.15 m (6 in.). The normal stress at the active (middle) reinforcement layer was 15 kPa (2.25 psi) for two tests and 21 kPa (3 psi) for the other four tests. This normal stress range was selected to allow the majority of the tests conducted with various reinforcement types to fail under ultimate tensile stress condition. This allowed investigating the soil-reinforcement interaction over a wider range of deformation up to (or close to) pullout failure.

The reinforcements involved in the six tests were (1) HP570 woven polyester geotextile; (2) RS580i woven polyester geotextile with T_u = 70 kN/m at 5% tensile strain (approximately, J = 1400 kN/m); (3) BX1100 extruded (rigid) polypropylene biaxial geogrid with T_u = 13.4 kN/m at 5% tensile strain (approximately, J = 268 kN/m) and 19.0 kN/m at failure; (4) BX1200 extruded (rigid) polypropylene geogrid with T_u = 19.6 kN/m at 5% tensile strain (approximately, J = 392 kN/m) and 28.8 kN/m at failure; and (5) 80T knitted (flexible) polyester uniaxial geogrid with T_u = 45.7 kN/m at 5% tensile strain (approximately, J = 914 kN/m) and 89.6 kN/m at failure. The properties of the reinforcement types are summarized earlier in Table 7.1 Reinforcements (1) and (3) were tested at 15-kPa (2.25-psi) normal stress and reinforcements (1), (2), (4), and (5) were tested at 21-kPa (3-psi) normal stress.

Table 9.5. Summary of tests in which reinforcement type was varied.

Test ID	*Testing Variables*					
	Fill Material	S_v	σ_v	*Active GS*	*Passive GS*	*Dilation*
GP-06-03-G1-G	AASHTO No. 8	0.15 m	21 kPa	HP570	HP570	Allowed
GP-06-03-G2-G				RS580i	RS580i	
GP-06-03-G4-G				BX1200	BX1200	
GP-06-03-G5-G				80T	80T	

The comparisons were conducted to evaluate one reinforcement property. Three comparisons were made: (1) a comparison between HP570 and RS580i reinforcements to evaluate the effect of reinforcement tensile stiffness; (2) a comparison between HP570 and 80T reinforcements to compare the behavior of geotextiles and geogrids; and (3) a comparison between 80T and BX1200 to evaluate the effect of reinforcement rigidity.

9.3.4.1.HP570 geotextile versus RS580i geotextile

This comparison was conducted between two woven geotextile reinforcements made of polyester (same material) and produced by the same manufacturer. Both materials have the same ultimate tensile strength 70 kN/m. The major difference between both materials is the tensile stiffness and the fabric rigidity. The tensile stiffness for HP570 (XMD) and RS580i (XMD) is 876 and 1400 kN/m at 5% tensile strain, respectively. In addition, RS580i is more rigid and its longitudinal and transversal yarns are more integrated compared to HP570. Figure 9.68 shows the frontal pullout load-displacement experimental curves for both tests. The results indicate that both curves coincide up to 10-mm frontal displacement. However, beyond the 10-mm frontal displacement, RS580i exhibited lower pullout resistance. This observation revealed information about the soil-reinforcement interface shear behavior for both reinforcement with the AASHTO Gravel No. 8 used in the tests. The interface shear stiffness might be very similar for both reinforcements, however, the interface shear strength is larger for the HP570 compared to the RS580i. This is attributed to the fabric rigidity that plays a significant role in the

interaction between the fabric and the surrounding soil medium that adds additional resistance to the interface friction. Forensic investigation of the reinforcement layers after the test completion revealed many punch holes in the HP570 fabric that resulted from the adjacent gravel particles. This type of interaction resembles the interaction takes place due to passive resistance of transverse ribs in geogrid reinforcements. On contrary, such holes were not clear in the RS580i fabric due to the high integration and fabric rigidity it possess.

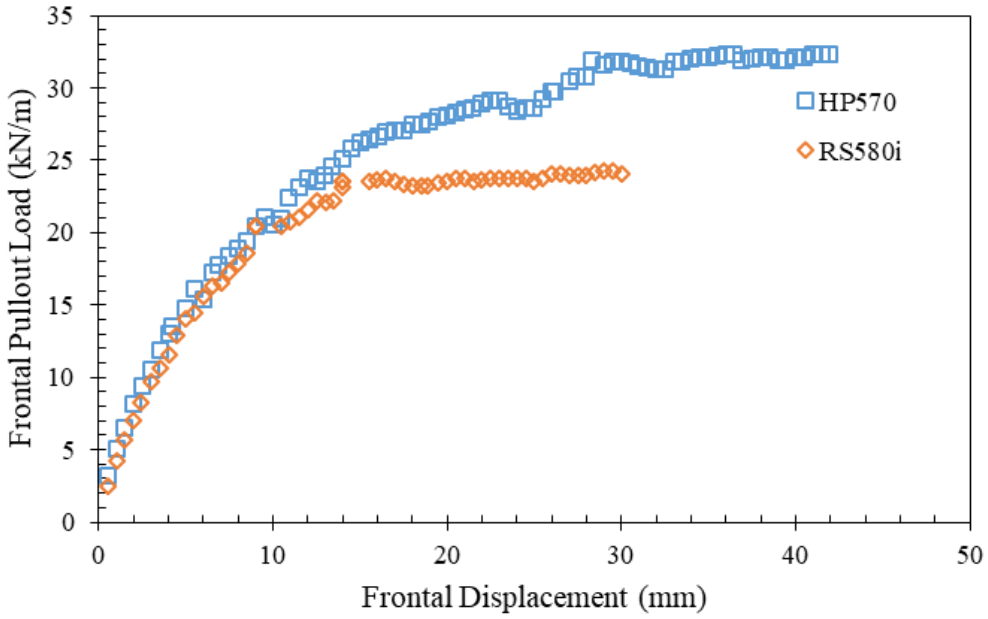

Figure 9.68. Frontal pullout load-displacement curves.

Figures 9.68 and 9.69 present the nodal displacement for the upper and lower passive reinforcement layers, respectively. Specifically, Figures 9.68a through 9.69d show the nodal displacements in the upper passive reinforcement corresponding to nodal displacements in the active reinforcement u1, u3, u5, and u7, respectively. Similarly, Figures 9.69a through 9.69d show the nodal displacements in the lower passive

reinforcement corresponding to nodal displacements in the active reinforcement u1, u3, u5, and u7, respectively. Figures 9.69 and 9.70 reveal the load transfer from the active reinforcement to the passive reinforcements at the same nodal reinforcement of the active reinforcement; i.e., the same soil-reinforcement interface shear displacement.

It was observed that the relationship between the nodal displacements for of the passive reinforcements are linear with the nodal displacements of the active reinforcement at early loading stages. This relationship then become non-linear as the load-displacement relationship of the active reinforcement curves. That is, Figures 9.68 and 9.69 reflect the reduction in shear stiffness at the soil-reinforcement interface. The results indicate that HP570 has a lower rate of interface shear stiffness reduction, which result in reduction of interaction with the neighboring reinforcement layers, compared to that of RS508i.

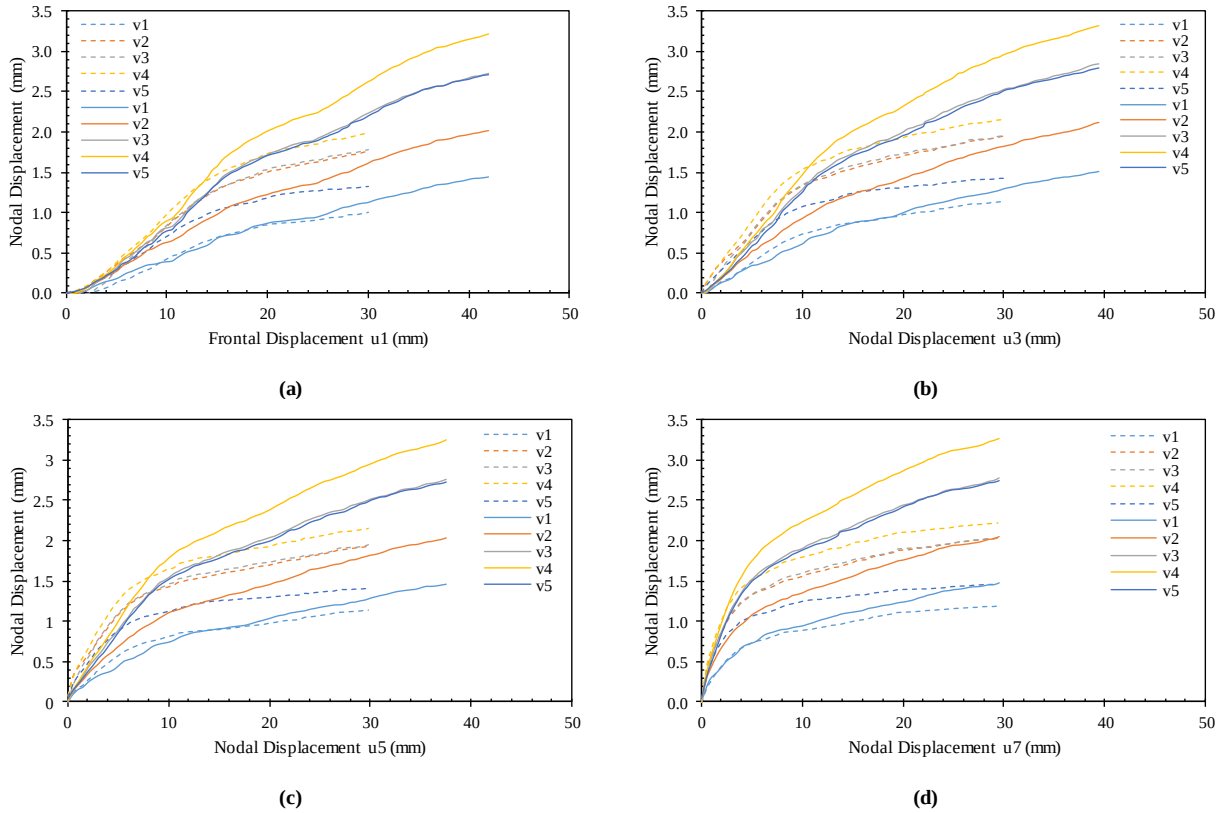

Figure 9.69. Nodal displacements at the upper passive reinforcement with respect to various nodal displacements at the active reinforcement: (a) nodal displacement u1; (b) nodal displacement u3; (c) nodal displacement u5; and (d) nodal displacement u7 (solid lines belong to HP570 and dashed lines belong to RS580i).

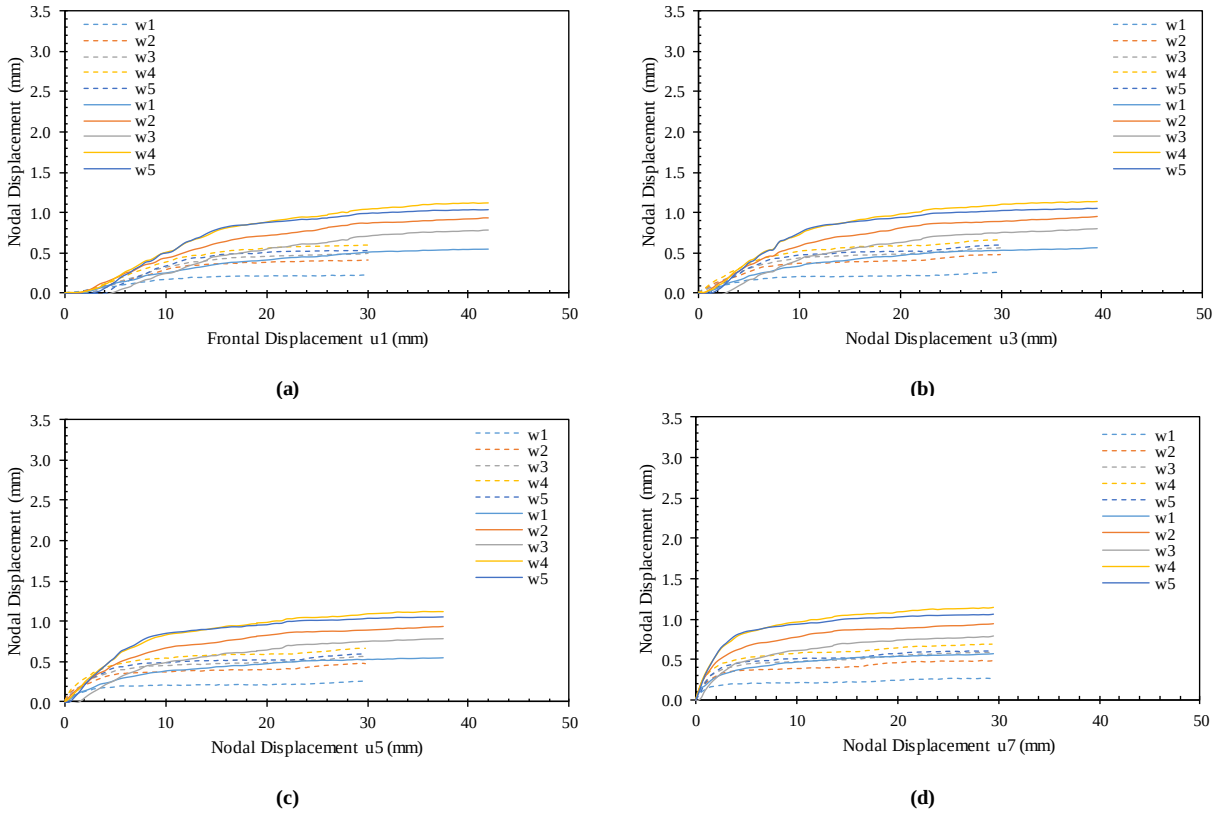

Figure 9.70. Nodal displacements at the lower passive reinforcement with respect to various nodal displacements at the active reinforcement: (a) Nodal displacement u1; (b) Nodal displacement u3; (c) Nodal displacement u5; and (d) Nodal displacement u7 (solid lines belong to HP570 and dashed lines belong to RS580i).

Figures 9.71 through 9.75 show the displacement profiles for the active and passive reinforcement layers at active reinforcement frontal displacements (u1) of 5, 10, 15, 20, and 30 mm, respectively. The displacement profiles for both reinforcement types, HP570 and RS580i, are very similar up to frontal displacement of 30 mm. Similar observation was made for the displacement profiles of the passive reinforcement layers. However, the measured displacements of the passive reinforcements were higher in case of HP570 reinforcement compared to those measured for the RS580i reinforcement. This is because the reduction in the soil-reinforcement interface shear strength in the case of RS580i reinforcement beyond frontal displacement of 10 mm. That is, the higher the soil-reinforcement interface shear strength, the higher the ability of the reinforcement to transfer load to the soil and the neighboring reinforcement layers for a given soil medium and normal stress level.

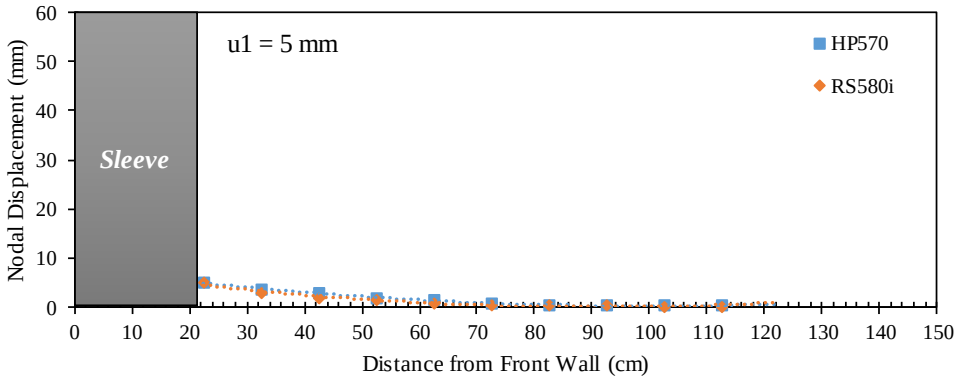

(a)

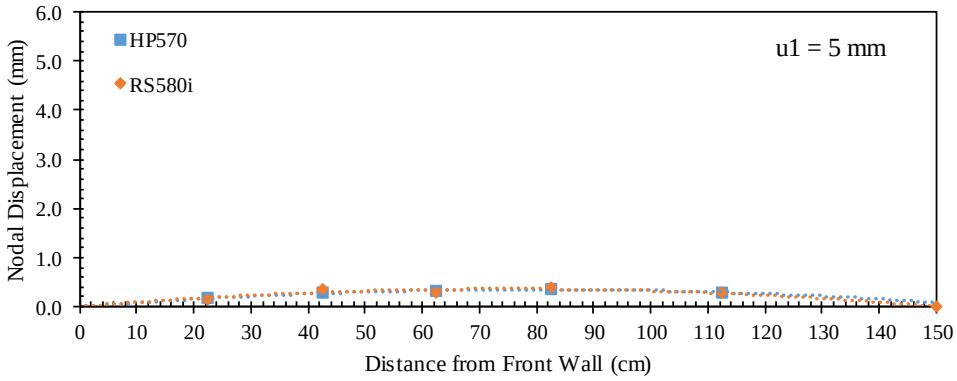

(b)

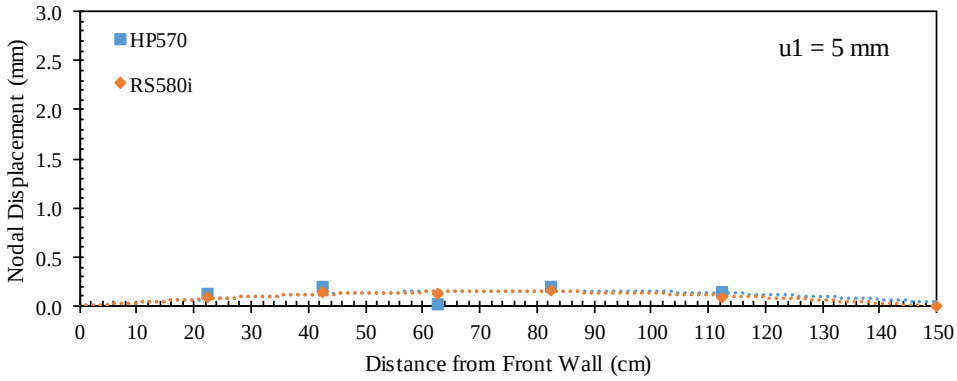

(c)

Figure 9.71. Reinforcement displacement profiles at frontal displacement u1 = 5 mm: (a) Active reinforcement; (b) Upper passive reinforcement; and (c) Lower passive reinforcement.

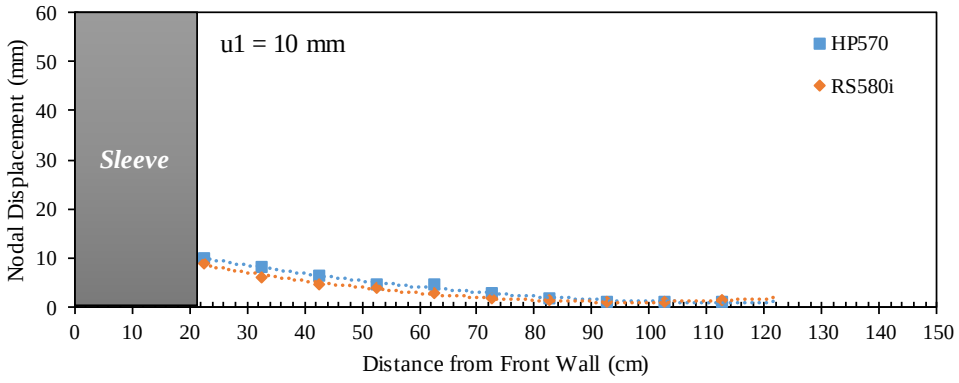

(a)

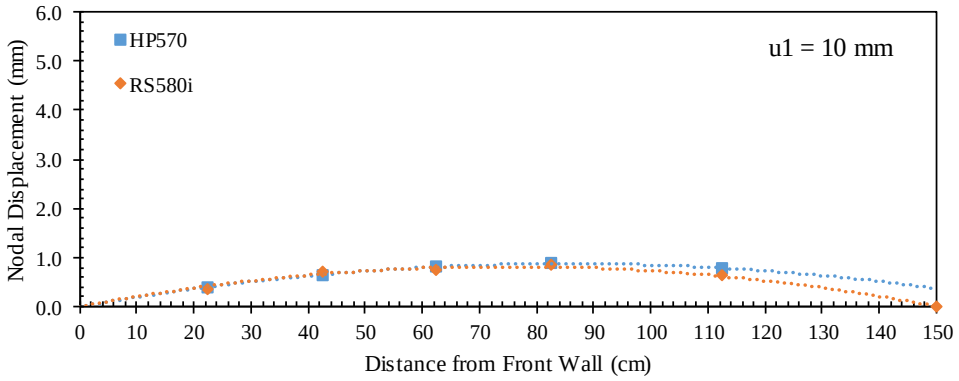

(b)

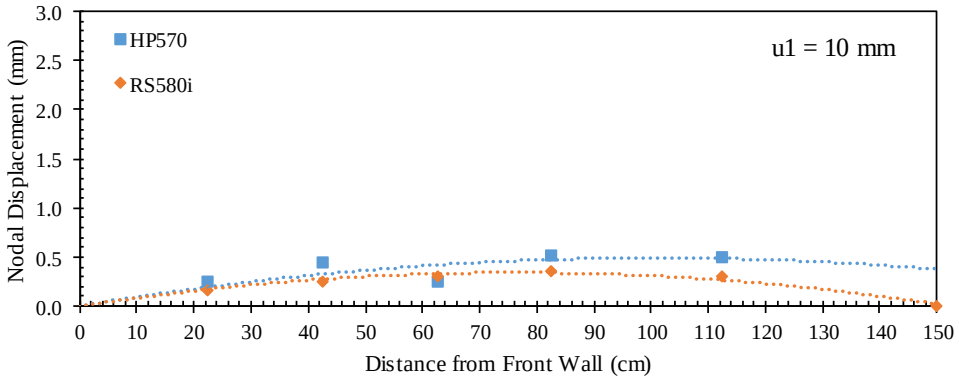

(c)

Figure 9.72. Reinforcement displacement profiles at frontal displacement u1 = 10 mm: (a) Active reinforcement; (b) Upper passive reinforcement; and (c) Lower passive reinforcement.

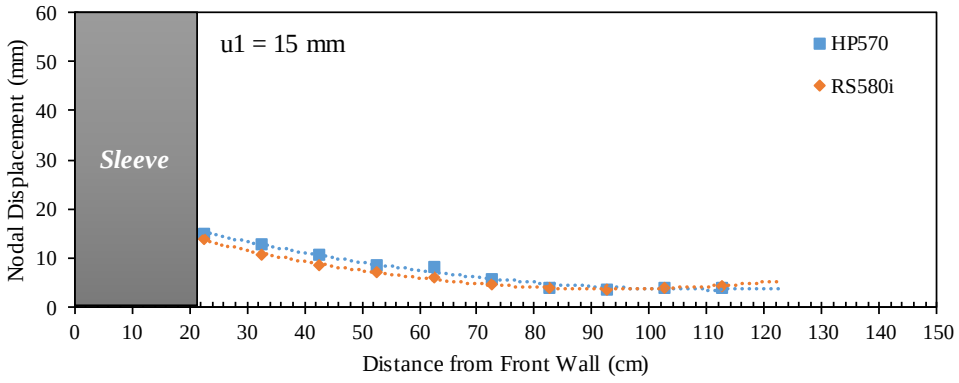

(a)

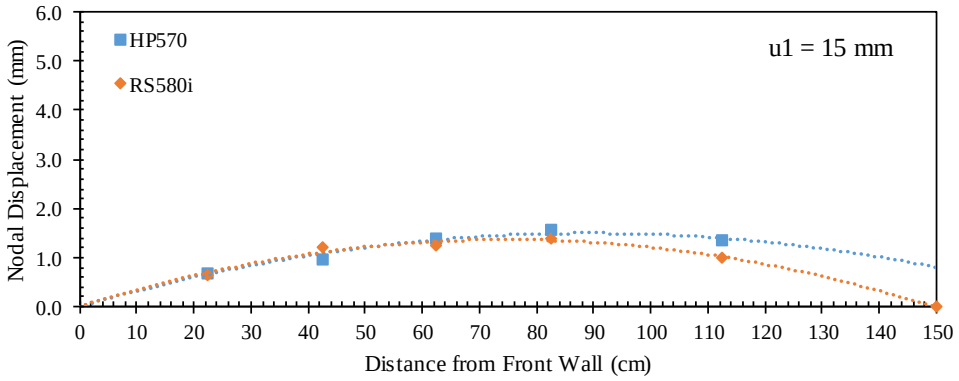

(b)

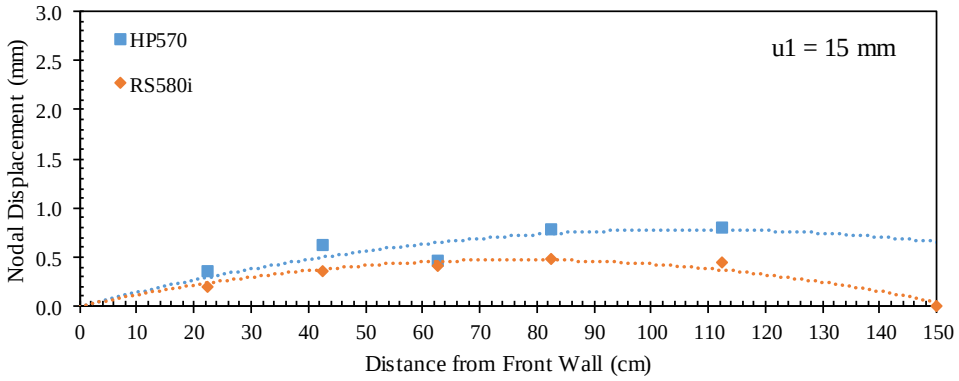

(c)

Figure 9.73. Reinforcement displacement profiles at frontal displacement u1 = 15 mm: (a) Active reinforcement; (b) Upper passive reinforcement; and (c) Lower passive reinforcement.

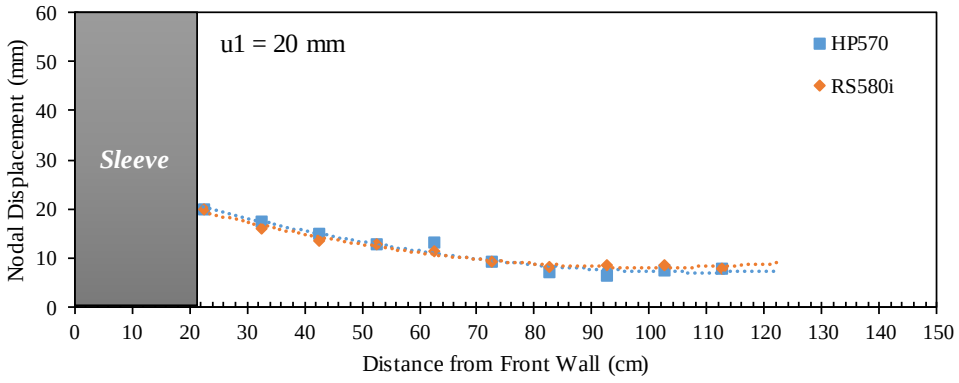

(a)

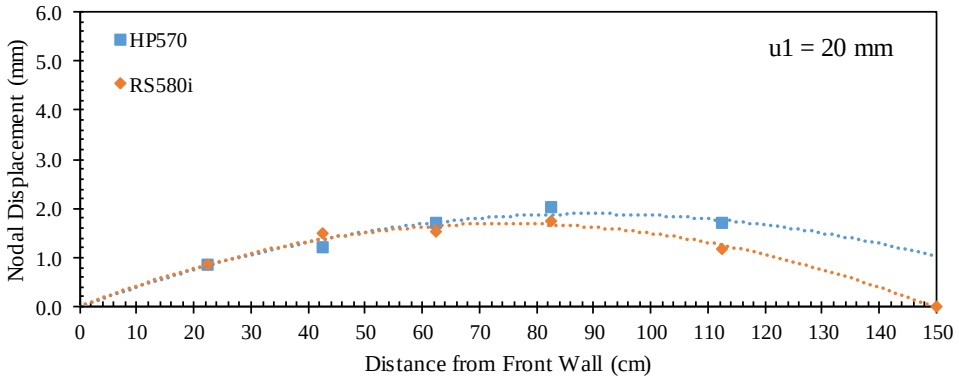

(b)

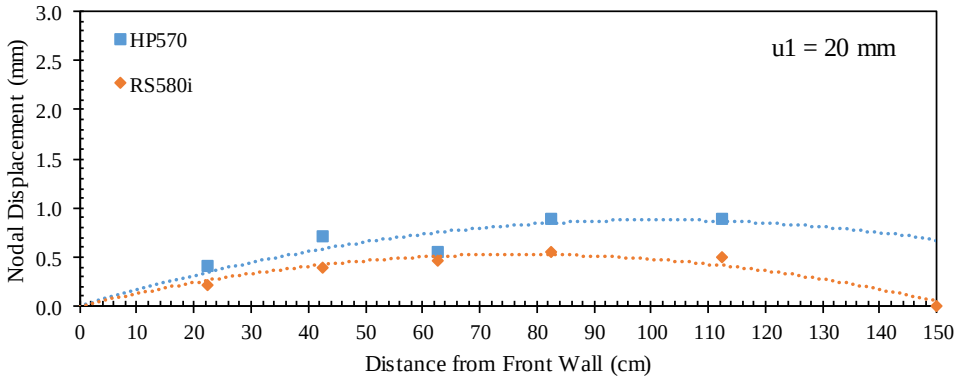

(c)

Figure 9.74. Reinforcement displacement profiles at frontal displacement u1 = 20 mm: (a) Active reinforcement; (b) Upper passive reinforcement; and (c) Lower passive reinforcement.

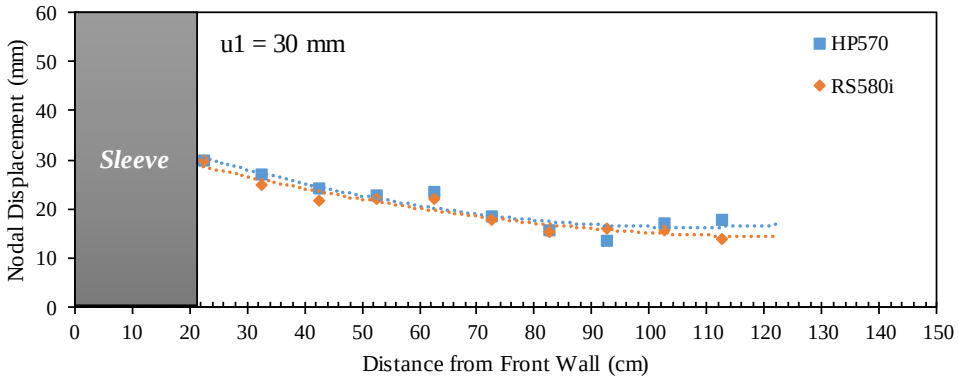

(a)

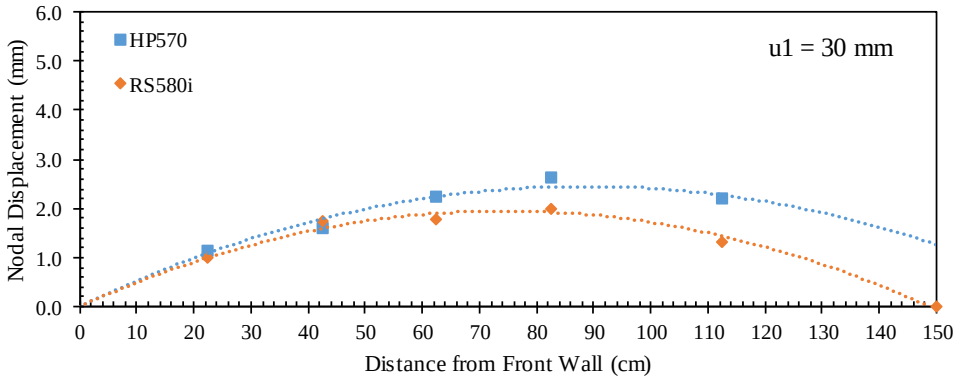

(b)

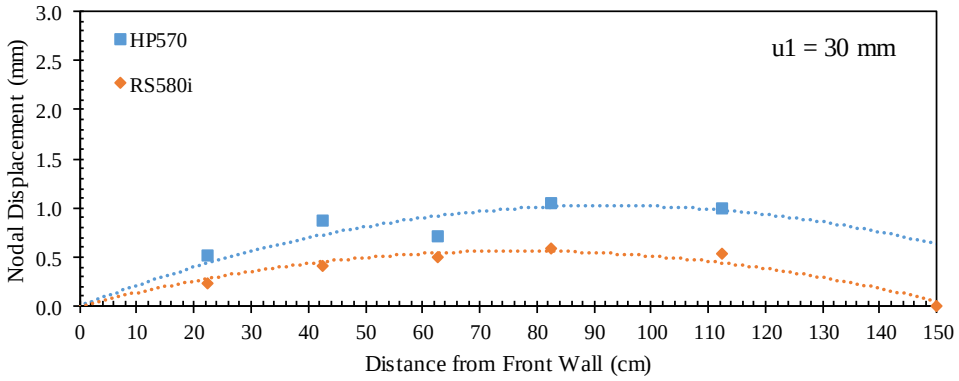

(c)

Figure 9.75. Reinforcement displacement profiles at frontal displacement u1 = 30 mm: (a) Active reinforcement; (b) Upper passive reinforcement; and (c) Lower passive reinforcement.

Figures 9.76 through 9.80 present the horizontal soil displacement measured for nodal displacements of 5, 10, 15, 20, and 30 mm, respectively. Each figure consists of a and b that show the soil displacement with respect nodal displacements u1 and u3, respectively. These displacement were measured at specific locations by tracking artificial gravel particles making a vertical array within the soil at 30.5 cm from the front wall. The results indicate that the soil displacement is very similar for the HP570 and RS580i reinforcements at early stages, up to nodal displacements of 10 mm, until a difference appeared in the soil-reinforcement interface shear strength. Thereafter, soil displacements measured in case of the HP570 were higher than those measured in case of the RS580i. Note that the soil adjacent to the reinforcement exhibited higher rate of displacement, which is due to yielding in the internal shear strength of the fill material that limits the load transfer from the reinforcement to larger distance away from the reinforcement.

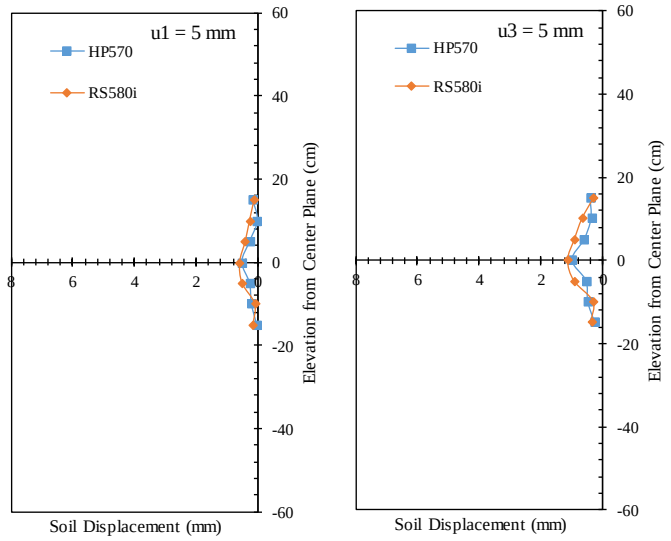

(a) **(b)**

Figure 9.76. Horizontal soil displacement profiles (measured by means of artificial gravel particles): (a) At nodal displacement u1 = 5 mm; and (b) At nodal displacement u3 = 5 mm.

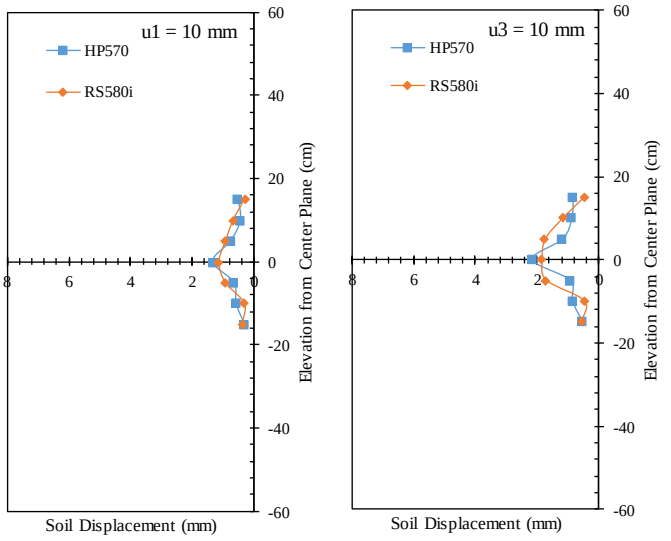

(a) **(b)**

Figure 9.77. Horizontal soil displacement profiles (measured by means of artificial gravel particles): (a) At nodal displacement u1 = 10 mm; and (b) At nodal displacement u3 = 10 mm.

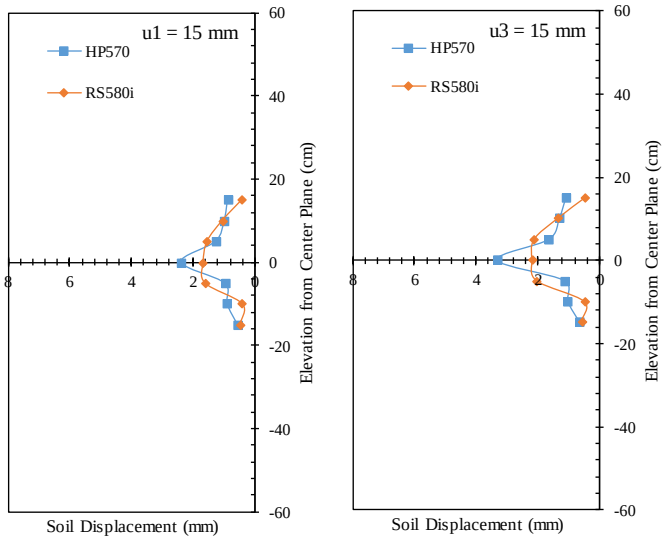

(a) **(b)**

Figure 9.78. Horizontal soil displacement profiles (measured by means of artificial gravel particles): (a) At nodal displacement u1 = 15 mm; and (b) At nodal displacement u3 = 15 mm.

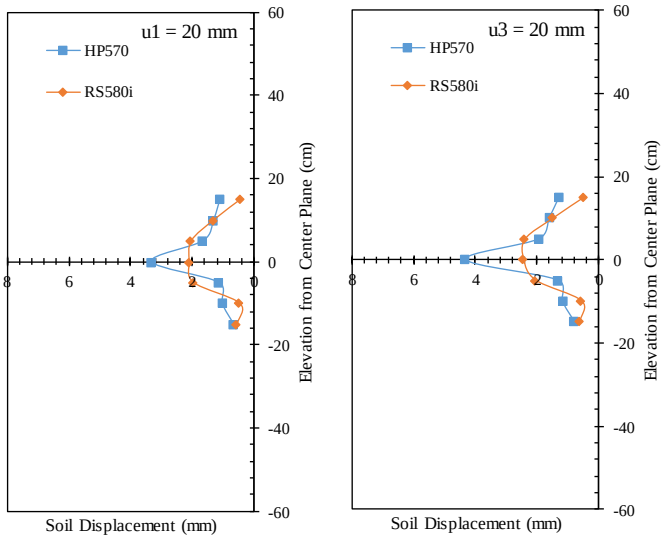

(a) **(b)**

Figure 9.79. Horizontal soil displacement profiles (measured by means of artificial gravel particles): (a) At nodal displacement u1 = 20 mm; and (b) At nodal displacement u3 = 20 mm.

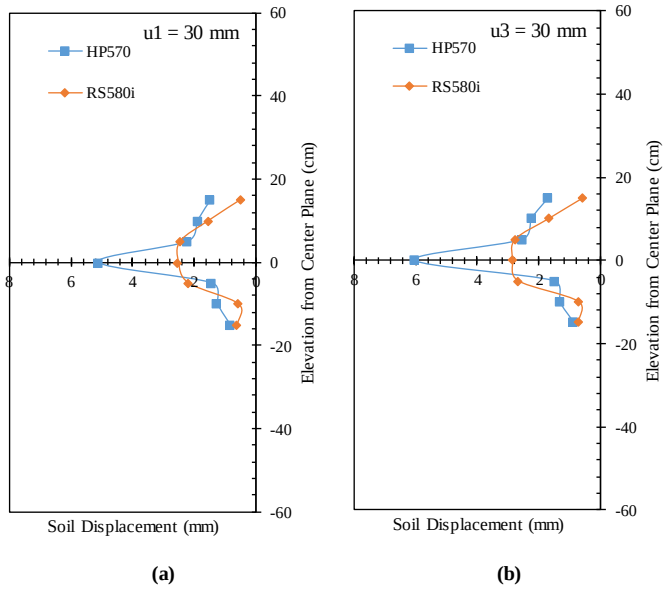

Figure 9.80. Horizontal soil displacement profiles (measured by means of artificial gravel particles): (a) At nodal displacement u1 = 30 mm; and (b) At nodal displacement u3 = 30 mm.

Figure 9.81 shows the soil-reinforcement relative displacement magnitude at 30.5 cm from the front wall. This relative displacement was obtained by subtracting the reinforcement displacement at this location (by interpolation between u1 and u3) and the soil displacement measured by the artificial gravel particle adjacent to the reinforcement (LP24). This figure exhibits the reduction in the soil-reinforcement interface shear stiffness during the test. The results indicate that the relative displacement at the HP570 interface was similar to that at the RS580i interface up to 10-mm frontal displacement. However, a significant difference appeared beyond 10-mm displacement due to the difference in the soil-reinforcement interaction between the two reinforcements, mainly which comes from the passive resistance in the HP570 fabric.

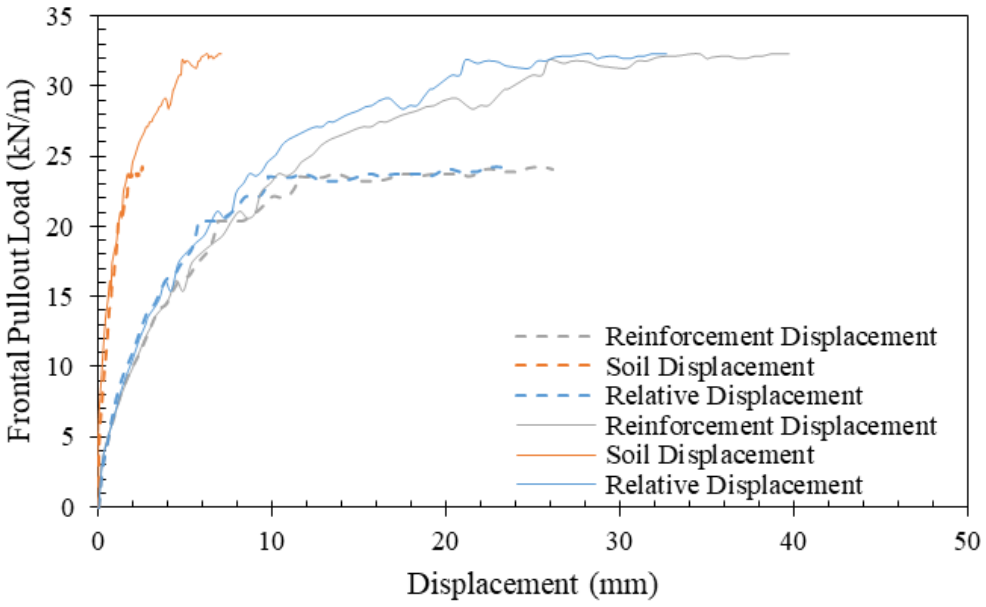

Figure 9.81. Soil-reinforcement relative displacement magnitude (solid lines belong to HP570 and dashed lines belong to RS580i).

Figure 9.82 shows the vertical soil displacements measured by means of the artificial gravel particles placed on top of the reinforced soil mass. Figures 9.82a through 9.82d show the soil displacements with respect to reinforcement nodal displacements u1, u3, u5, and u7. Both tests showed dilation near the front side of the reinforced soil mass and settlement near the rear side. The results indicate that the dilation at the front was higher in case of HP570 than that in case of RS580i. At the back, settlement was higher in case of HP570 compared to that in case of RS580i.

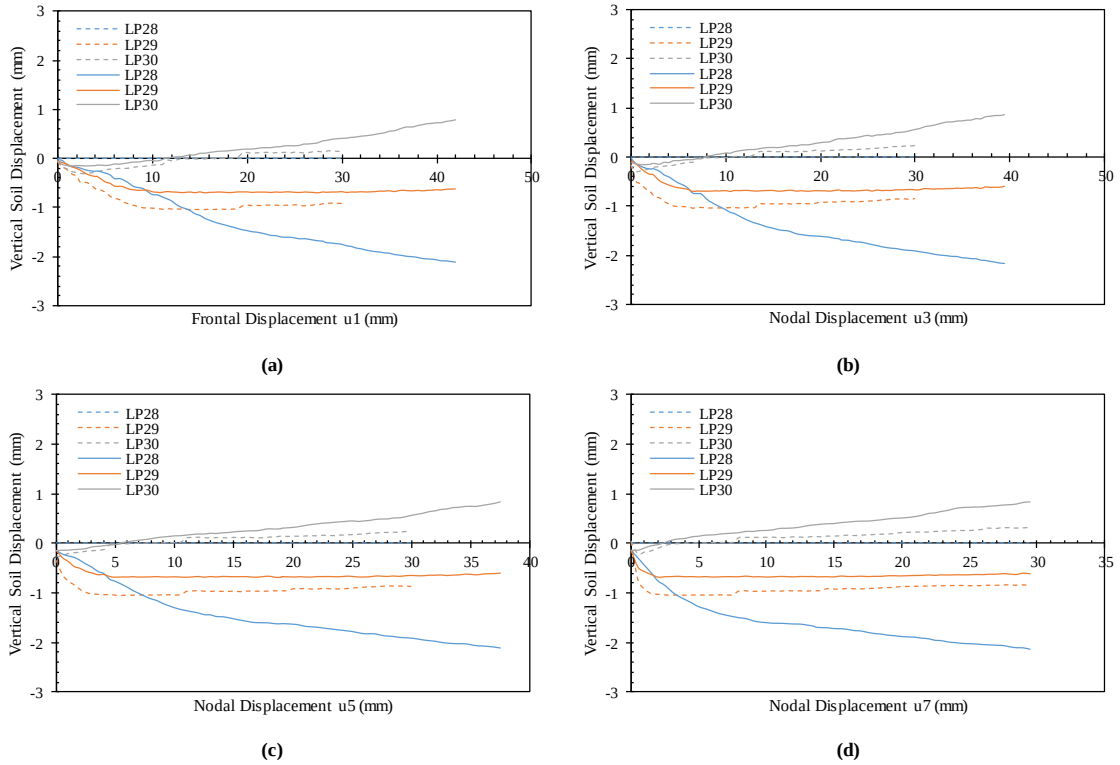

Figure 9.82. Vertical soil displacements (measured by means of artificial gravel particles) with respect to various nodal displacements at the active reinforcement: (a) Nodal displacement u1; (b) Nodal displacement u3; (c) Nodal displacement u5; and (d) Nodal displacement u7 (solid lines belong to HP570 and dashed lines belong to RS580i).

9.3.4.2.HP570 geotextile versus 80T geogrid

This comparison was conducted between HP570 woven geotextile and 80T knitted uniaxial geogrid reinforcements. Both reinforcements made of polyester (same material) and have very similar tensile stiffness. The tensile stiffness for HP570 (XMD) and 80T (MD) is 876 and 914 kN/m at 5% tensile strain, respectively. Figure 9.83 shows the frontal pullout load-displacement experimental curves for both tests. The results indicate that the resistance to pullout for the 80T geogrid was higher than that of HP570 geotextile. The difference in resistance increased as the pullout progressed. This observation revealed information about the soil-reinforcement interaction.

Note that the soil-reinforcement interaction here comprises two components: (1) the passive resistance that can be mobilized by the transverse members. The members can be transverse ribs in geogrids or transverse yarns in geotextiles if particles were able to interfere with the geotextile fabric as mentioned earlier in Section 9.3.3; and (2) the soil-reinforcement interface friction (interface shear resistance). The soil-reinforcement interaction was observed to be higher in the 80T geogrid compared to that of the HP570 geotextile.

While the 80T reinforcement is a uniaxial geogrid that has a weak junction (longitudinal and transverse ribs knitted forming square-aperture grid), the contribution of the passive resistance in the soil-reinforcement interaction was considerable. Forensic investigation of the reinforcement after that test revealed good integrity between the longitudinal and transverse ribs. This passive resistance in the 80T geogrid was found to outweigh the interface friction and the associated passive resistance that comes from the interlocking of punching soil particles in the case of HP570 geotextile.

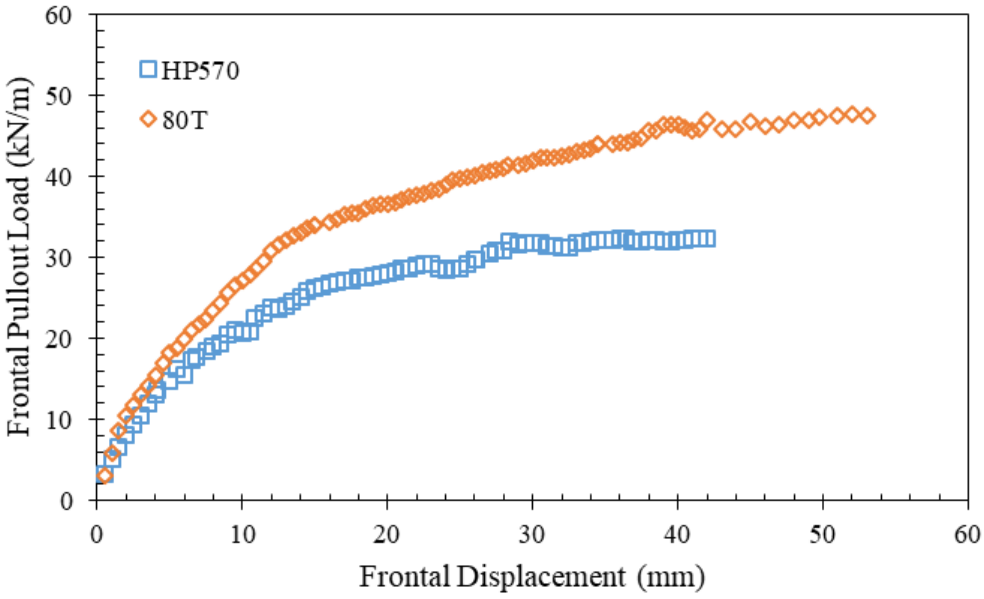

Figure 9.83. Frontal pullout load-displacement curves.

Figures 9.84 and 9.85 present the nodal displacement for the upper and lower passive reinforcement layers, respectively. Specifically, Figures 9.84a through 9.83d show the nodal displacements in the upper passive reinforcement corresponding to nodal displacements in the active reinforcement u1, u3, u5, and u7, respectively. Similarly, Figures 9.85a through 9.85d show the nodal displacements in the lower passive reinforcement corresponding to nodal displacements in the active reinforcement u1, u3, u5, and u7, respectively. Figures 9.84 and 9.85 reflect the load transfer from the active reinforcement to the passive reinforcements at the same nodal reinforcement of the active reinforcement (the same soil-reinforcement interface shear displacement). The results indicate that the relationship between the nodal displacements for of the passive reinforcements are linear with the nodal displacements of the active reinforcement at early loading stages. This relationship then become non-linear as the load-displacement

relationship of the active reinforcement curves. That is, Figures 9.84 and 9.85 reflect the reduction in soil-reinforcement interaction stiffness. The results indicate that HP570 geotextile has a higher rate of interaction stiffness reduction, which result in reduction of interaction with the neighboring reinforcement layers, compared to that of 80T geogrid.

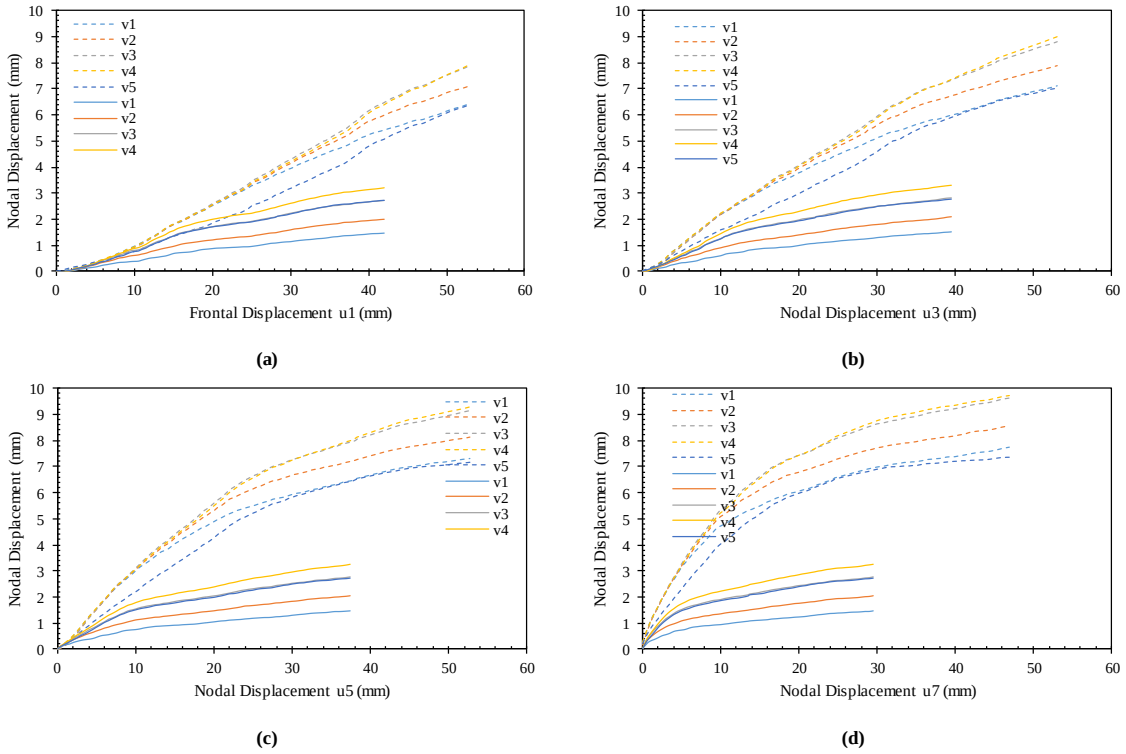

Figure 9.84. Nodal displacements at the upper passive reinforcement with respect to various nodal displacements at the active reinforcement: (a) nodal displacement u1; (b) nodal displacement u3; (c) nodal displacement u5; and (d) nodal displacement u7 (solid lines belong to HP570 and dashed lines belong to 80T).

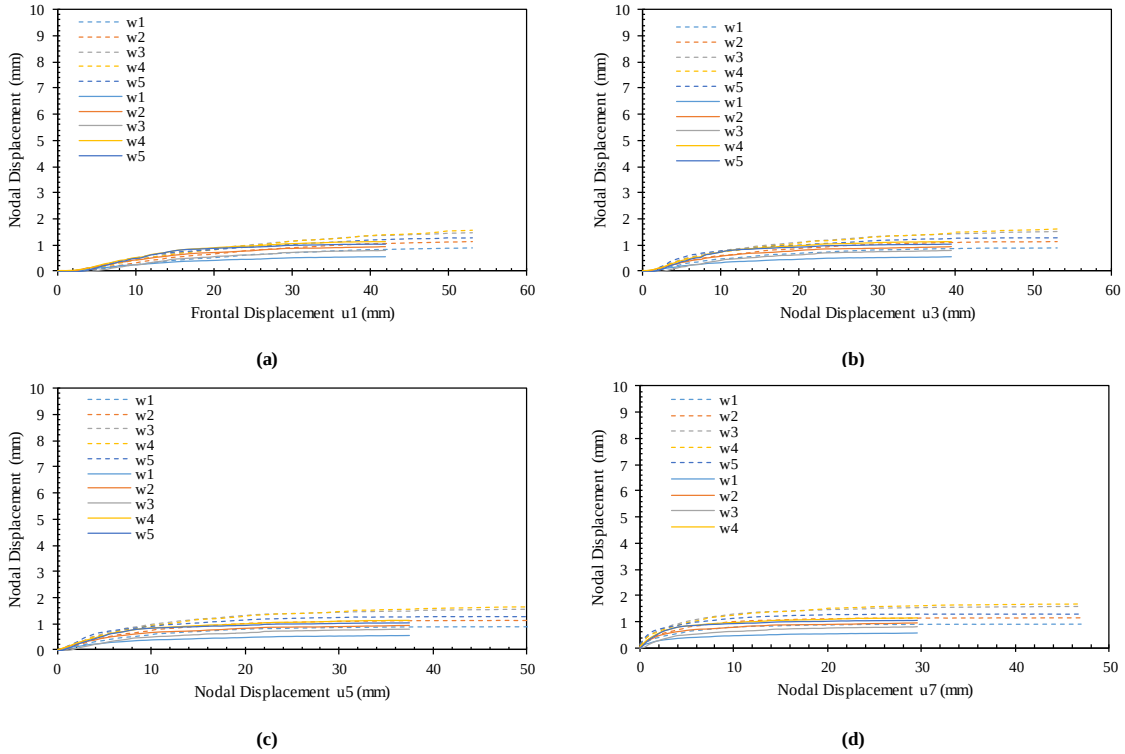

Figure 9.85. Nodal displacements at the lower passive reinforcement with respect to various nodal displacements at the active reinforcement: (a) Nodal displacement u1; (b) Nodal displacement u3; (c) Nodal displacement u5; and (d) Nodal displacement u7 (solid lines belong to HP570 and dashed lines belong to 80T).

Figures 9.86 through 9.90 show the displacement profiles for the active and passive reinforcement layers at active reinforcement frontal displacements (u1) of 5, 10, 15, 20, and 30 mm, respectively. Note that the comparison is based on the same frontal displacement for the different reinforcements rather than the same pullout frontal load. The profiles of HP570 geotextile show higher displacement along the length of the active reinforcement compared to those of 80T geogrid. This difference increased as pullout progressed. On contrary, the profiles of the passive reinforcement layers showed lower displacement values for the HP570 geotextile compared to those measured for the 80T geogrid. This observation points towards higher reinforcement interaction with the neighboring layers in case of the 80T geogrid compared to the HP570 geotextile. This is a result of the higher soil-reinforcement interaction of the 80T that resulted in a higher load transfer ability and a bigger zone of influence. Note that, although, the reinforcement displacement in the active reinforcement was smaller in the case of 80T geogrid, it showed a bigger interaction than that of HP570 geotextile, which has a bigger reinforcement displacement.

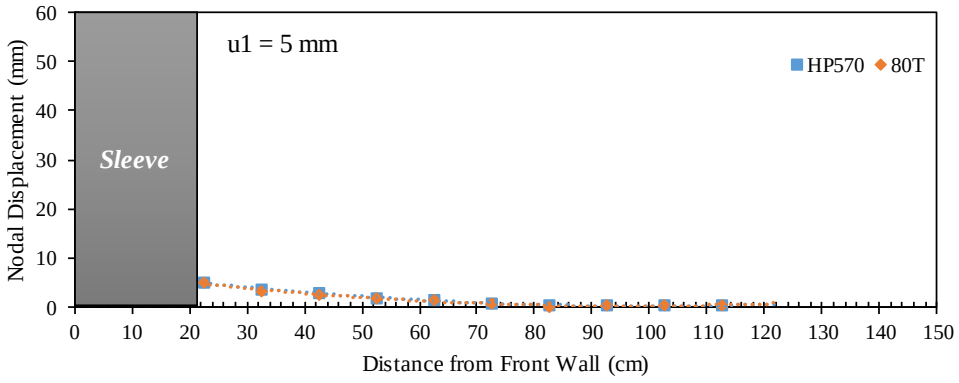

(a)

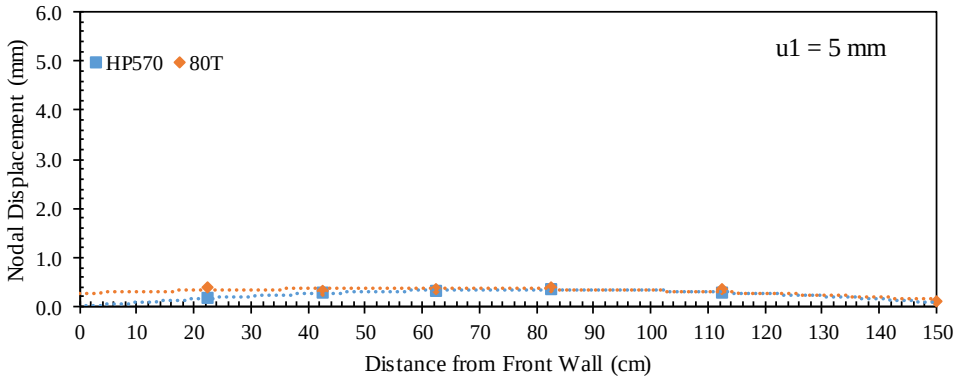

(b)

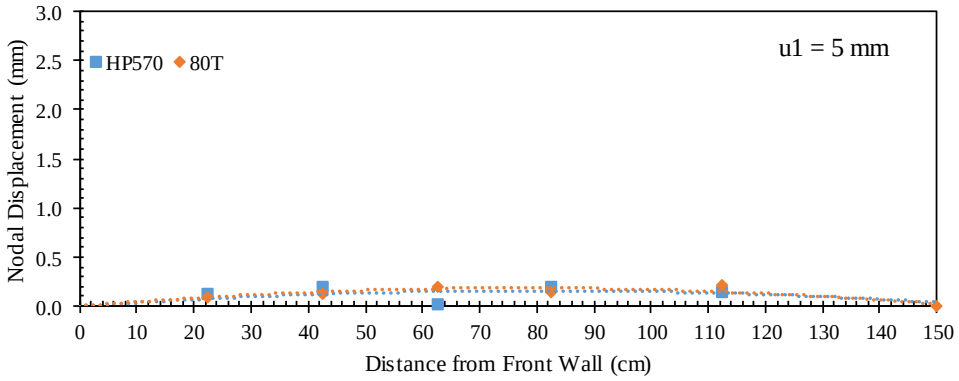

(c)

Figure 9.86. Reinforcement displacement profiles at frontal displacement u1 = 5 mm: (a) Active reinforcement; (b) Upper passive reinforcement; and (c) Lower passive reinforcement.

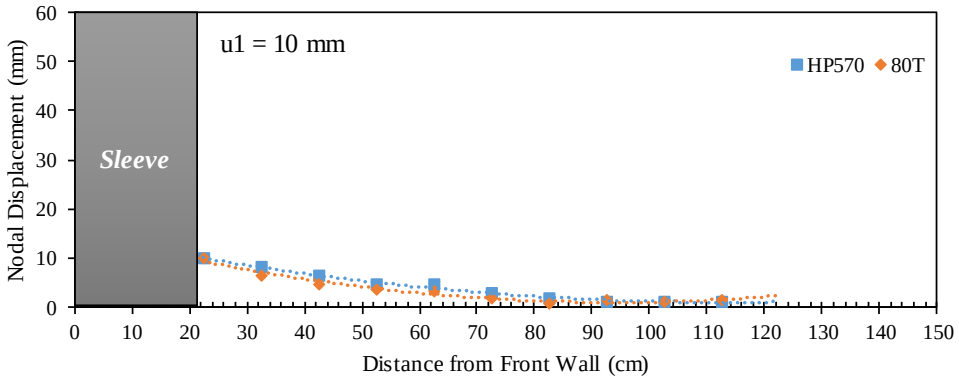

(a)

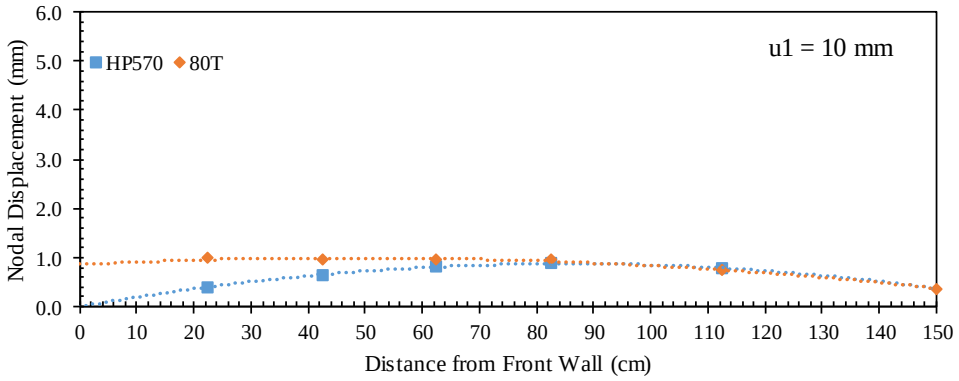

(b)

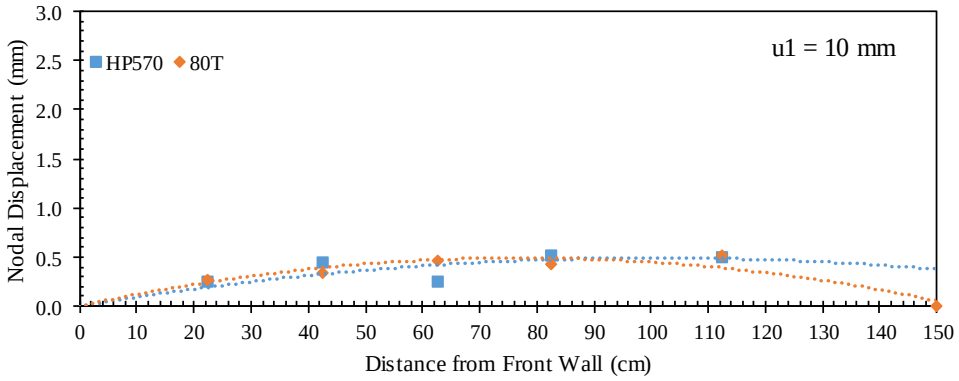

(c)

Figure 9.87. Reinforcement displacement profiles at frontal displacement u1 = 10 mm: (a) Active reinforcement; (b) Upper passive reinforcement; and (c) Lower passive reinforcement.

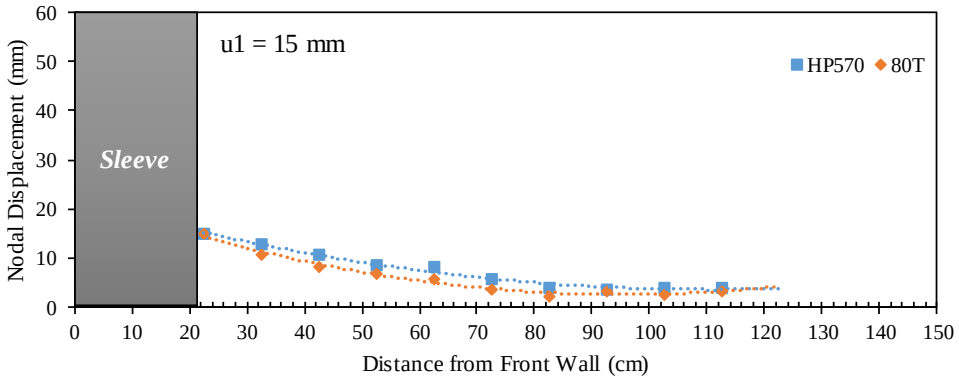

(a)

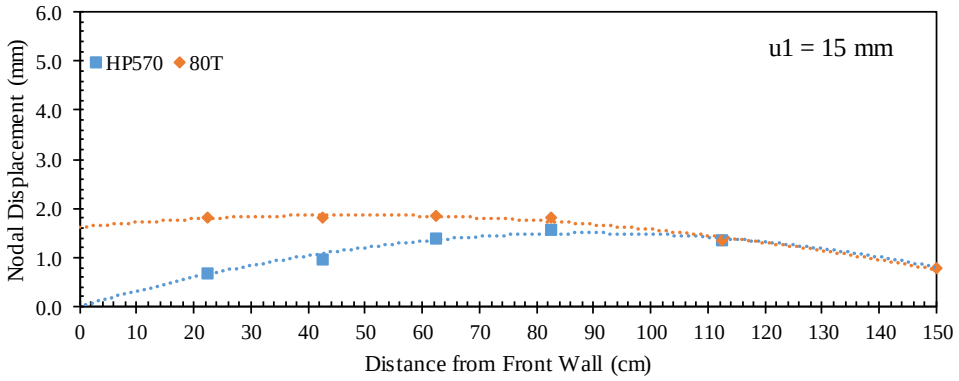

(b)

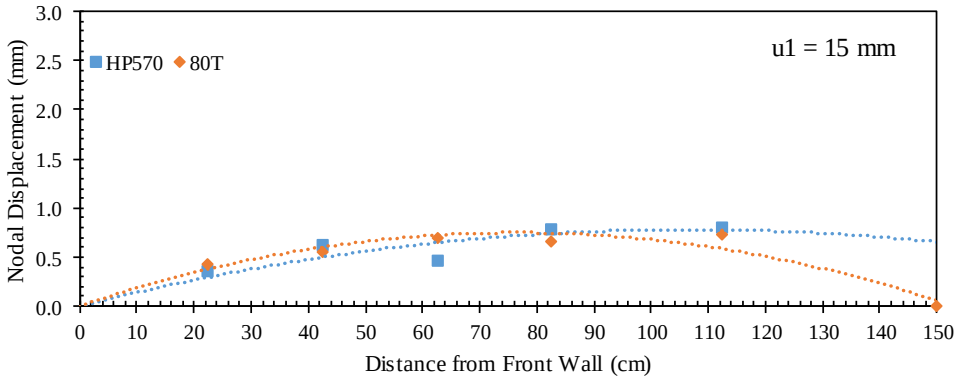

(c)

Figure 9.88. Reinforcement displacement profiles at frontal displacement u1 = 15 mm: (a) Active reinforcement; (b) Upper passive reinforcement; and (c) Lower passive reinforcement.

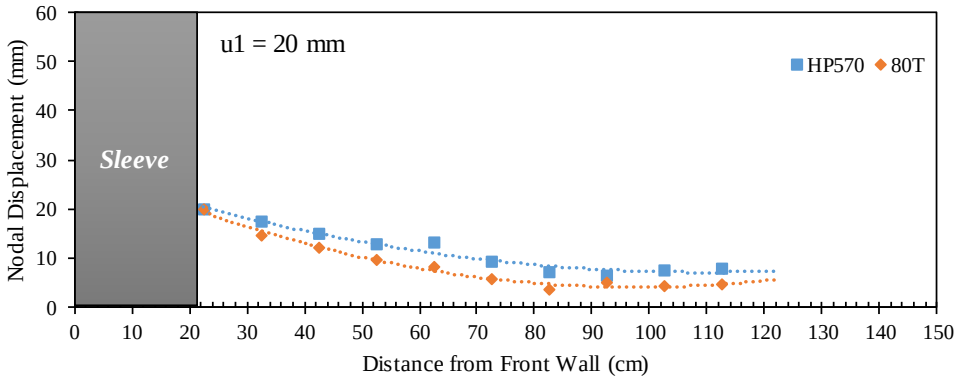

(a)

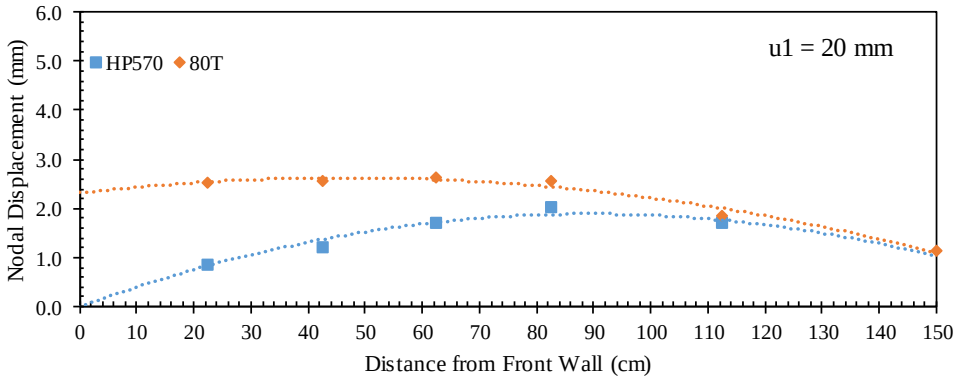

(b)

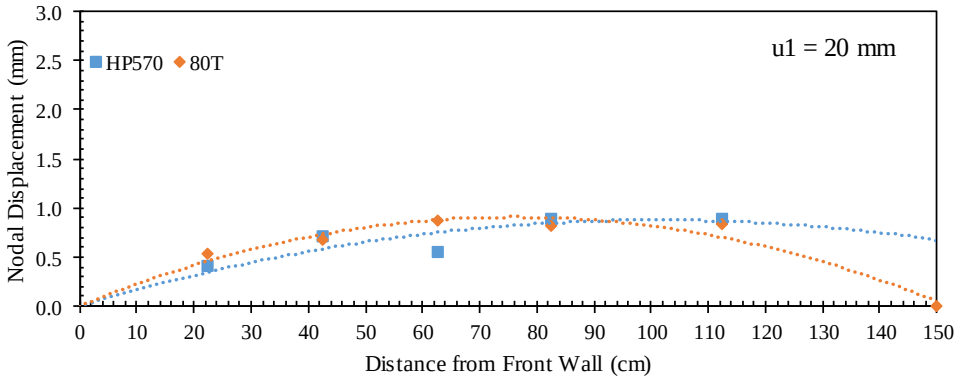

(c)

Figure 9.89. Reinforcement displacement profiles at frontal displacement u1 = 20 mm: (a) Active reinforcement; (b) Upper passive reinforcement; and (c) Lower passive reinforcement.

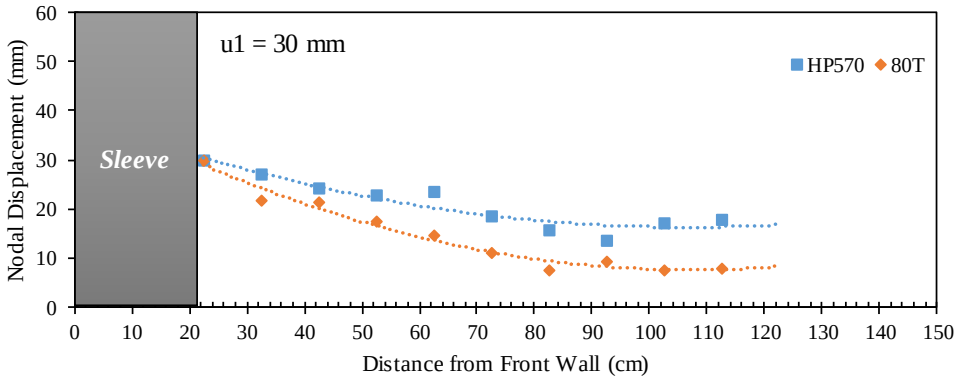

(a)

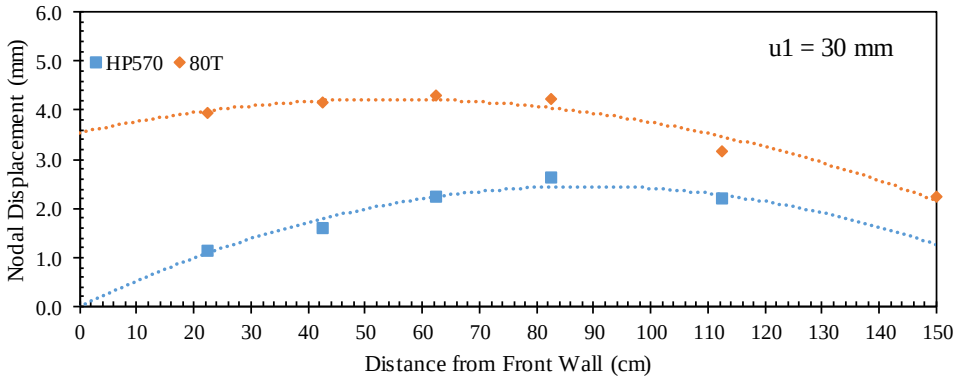

(b)

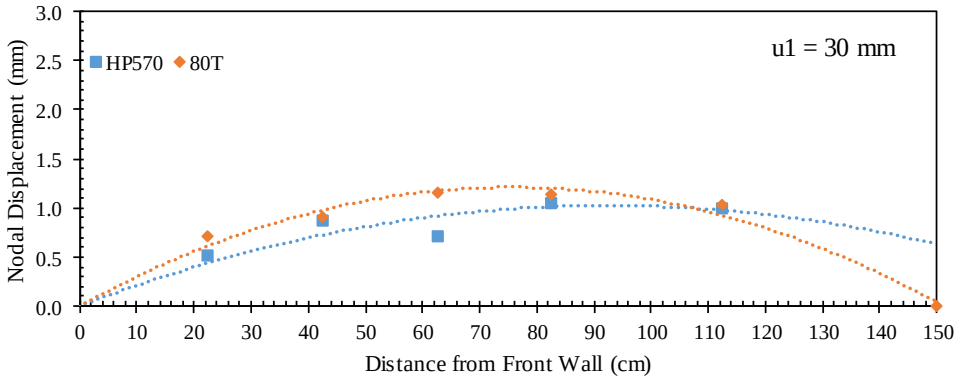

(c)

Figure 9.90. Reinforcement displacement profiles at frontal displacement u1 = 30 mm: (a) Active reinforcement; (b) Upper passive reinforcement; and (c) Lower passive reinforcement.

For a better comparison, Figures 9.91 through 9.95 show the passive reinforcement displacement profiles for various intermediate nodal displacements of the active reinforcement of 5, 10, 15, 20, and 30 mm, respectively. Specifically, each figure consists of a, b, c, and d subfigures that provide comparisons of the upper passive reinforcement profiles for same nodal displacements u1, u3, u5, and u7, respectively. That is, the comparisons were conducted for the similar soil-reinforcement induced interface displacement. This provides more insight into the comparison between the different reinforcement types in their ability to interact with their neighboring reinforcement layers for a given soil medium and normal stress level. It was observed from Figures 9.91 through 9.95 that the interaction between the reinforcement layers in case of the 80T geogrid is significantly higher than that in case of the HP570 geotextile.

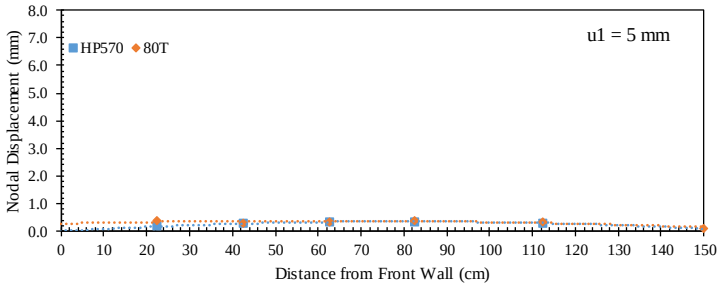

(a)

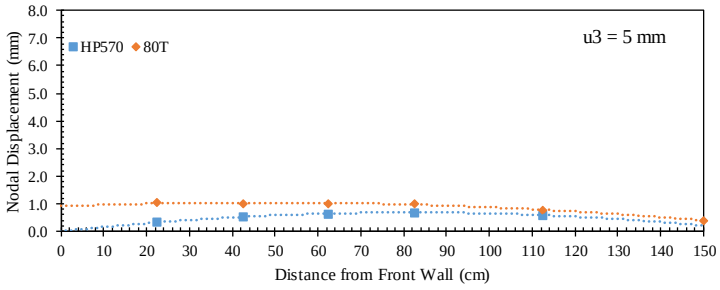

(b)

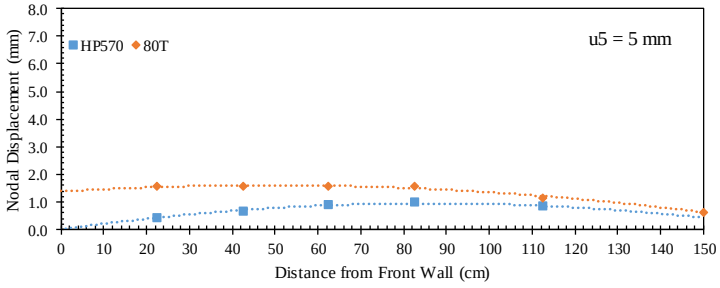

(c)

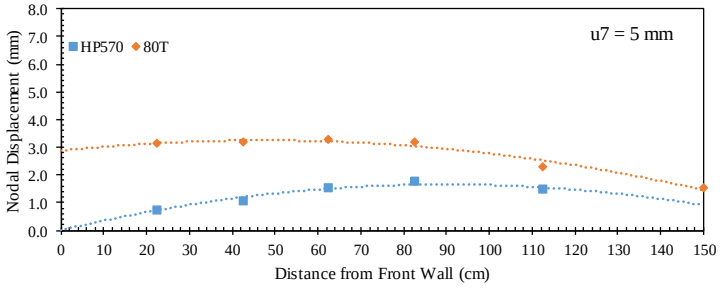

(d)

Figure 9.91. Upper passive reinforcement displacement profiles: (a) At nodal displacement u1 = 5 mm; (b) At nodal displacement u3 = 5 mm; (c) At nodal displacement u5 = 5 mm; and (d) At nodal displacement u7 = 5 mm.

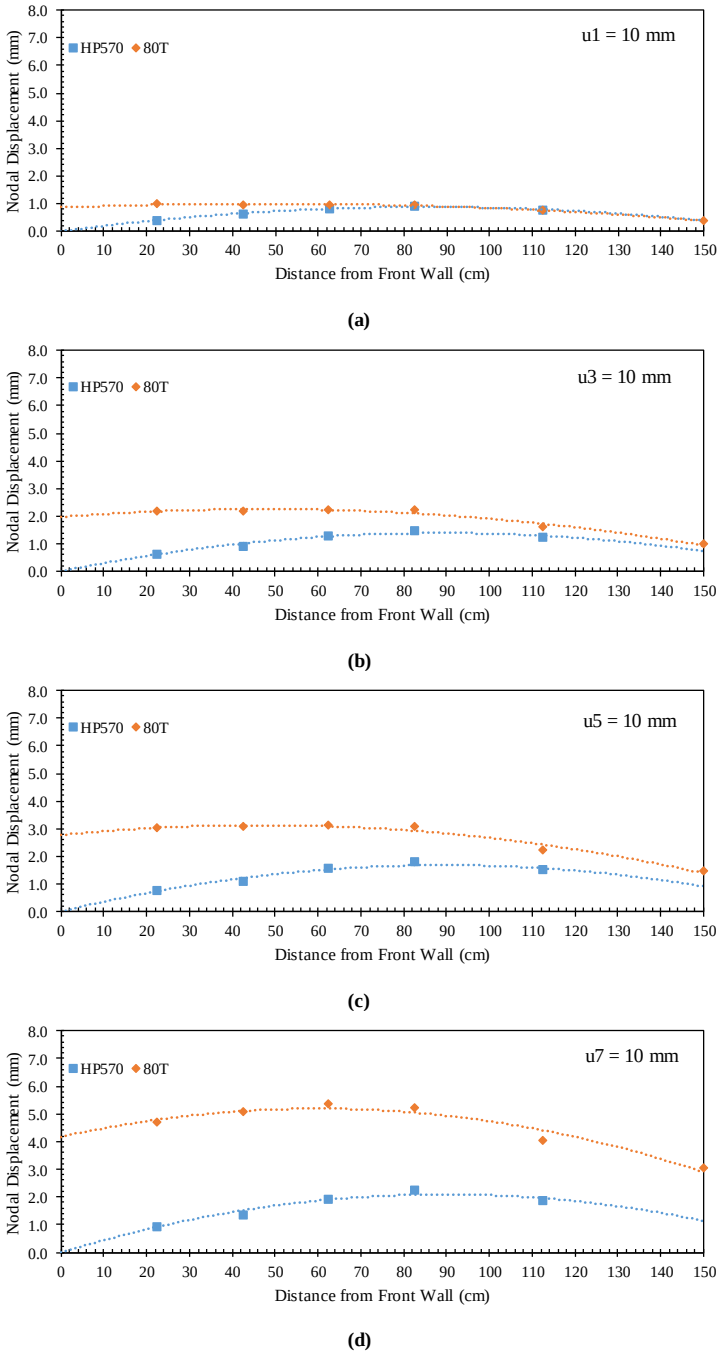

Figure 9.92. Upper passive reinforcement displacement profiles: (a) At nodal displacement u1 = 10 mm; (b) At nodal displacement u3 = 10 mm; (c) At nodal displacement u5 = 10 mm; and (d) At nodal displacement u7 = 10 mm.

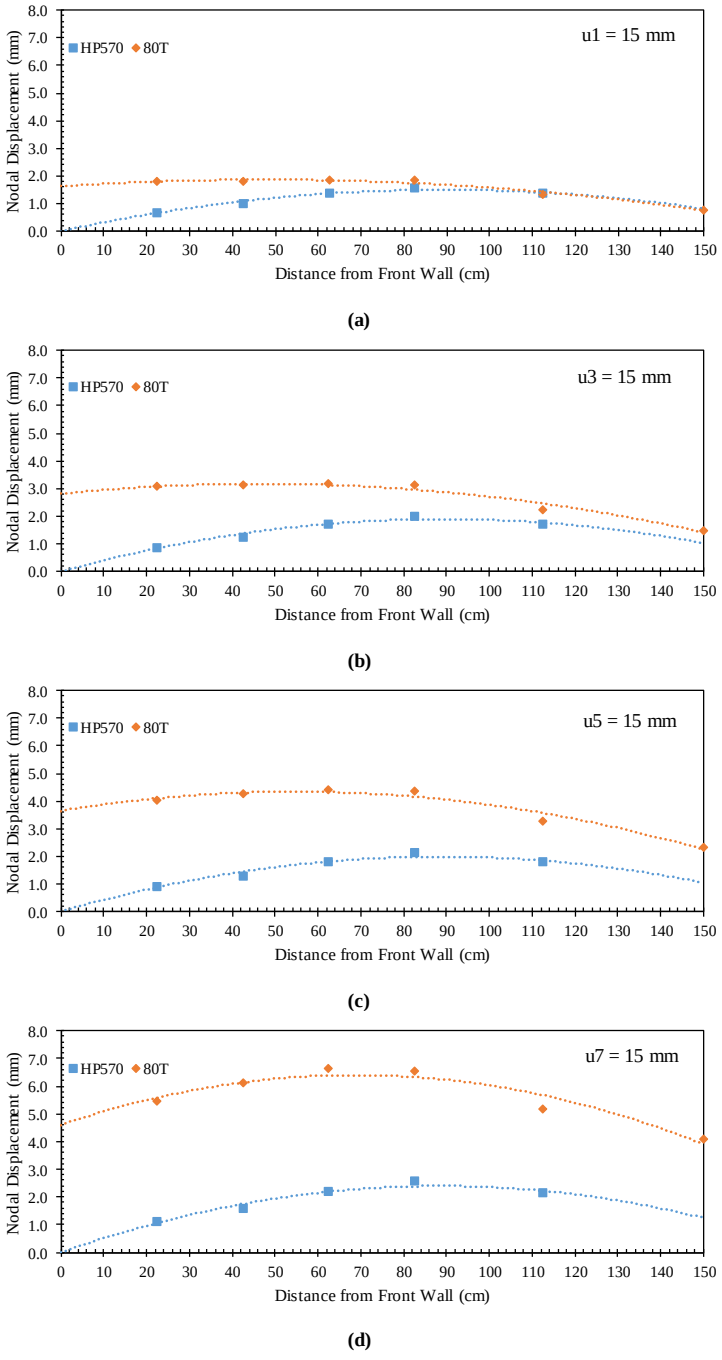

Figure 9.93. Upper passive reinforcement displacement profiles: (a) At nodal displacement u1 = 15 mm; (b) At nodal displacement u3 = 15 mm; (c) At nodal displacement u5 = 15 mm; and (d) At nodal displacement u7 = 15 mm.

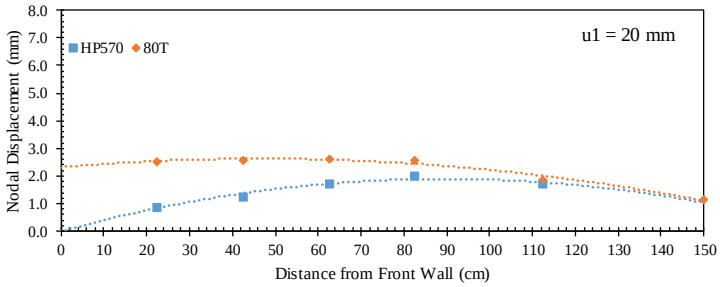

(a)

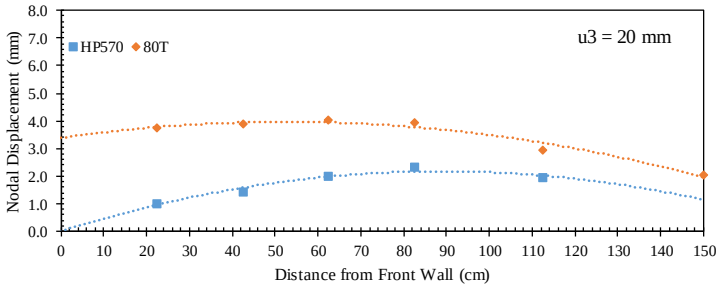

(b)

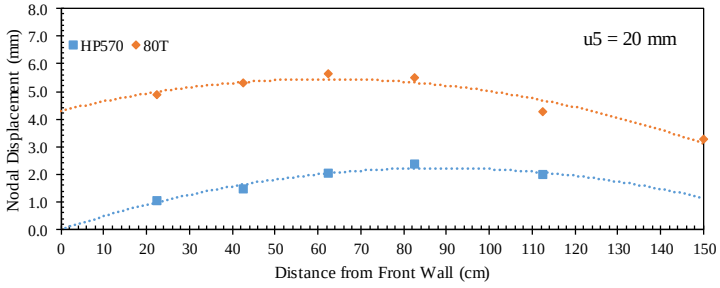

(c)

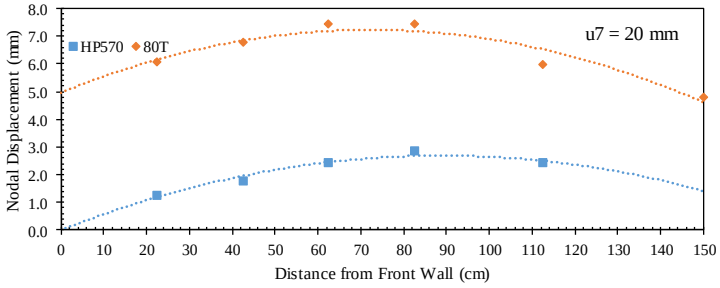

(d)

Figure 9.94. Upper passive reinforcement displacement profiles: (a) At nodal displacement u1 = 20 mm; (b) At nodal displacement u3 = 20 mm; (c) At nodal displacement u5 = 20 mm; and (d) At nodal displacement u7 = 20 mm.

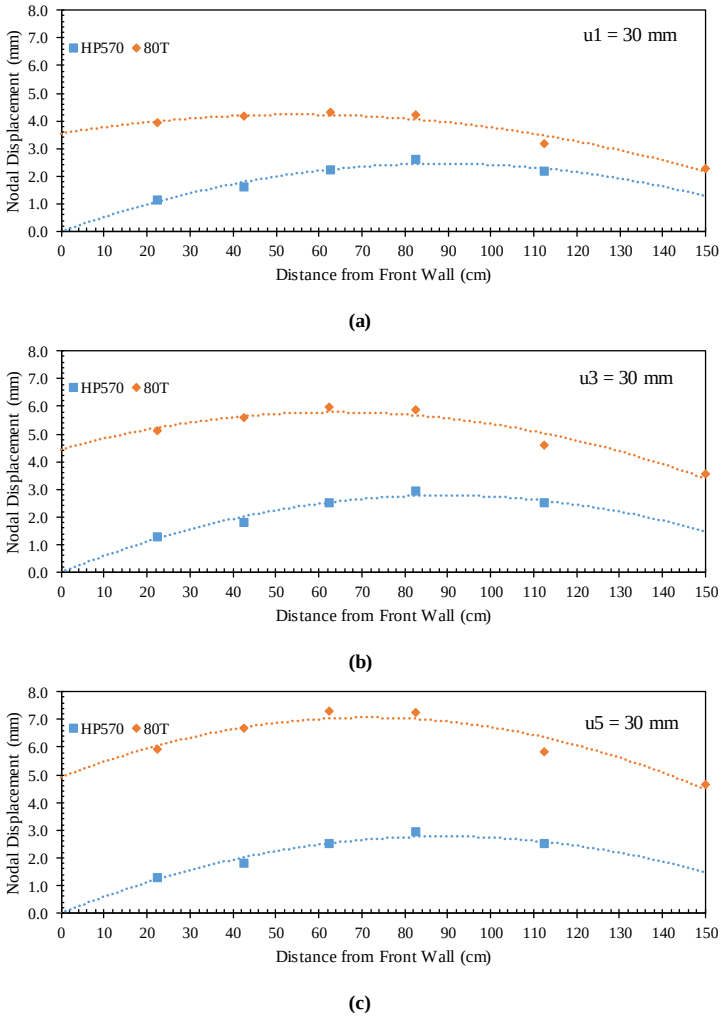

Figure 9.95. Upper passive reinforcement displacement profiles: (a) At nodal displacement u1 = 30 mm; (b) At nodal displacement u3 = 30 mm; and (c) At nodal displacement u5 = 30 mm.

Figures 9.96 through 9.100 present the horizontal soil displacement measured for nodal displacements of 5, 10, 15, 20, and 30 mm, respectively. Each figure consists of a and b that show the soil displacement with respect nodal displacements u1 and u3, respectively. These displacement were measured at specific locations by tracking artificial gravel particles making a vertical array within the soil at 30.5 cm from the front wall. The

results indicate that the soil displacement is smaller in case of HP570 geotextile compared to that of 80T geogrid. This difference was observed to increase as pullout progressed due to the difference the soil-reinforcement interaction between the two reinforcements. Note that the soil adjacent to the reinforcement exhibited higher rate of displacement compared to those away from the reinforcement. This is due to yielding in the internal shear strength of the fill material that limits the load transfer from the reinforcement to larger distance away from the reinforcement.

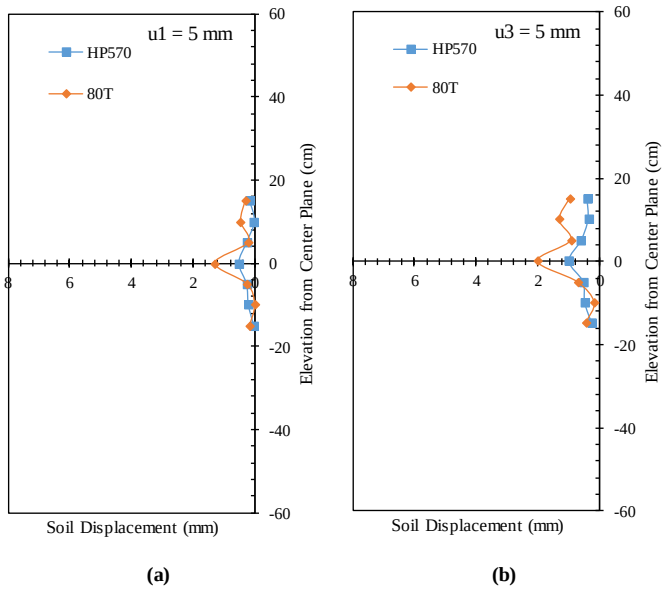

Figure 9.96. Horizontal soil displacement profiles (measured by means of artificial gravel particles): (a) At nodal displacement u1 = 5 mm; and (b) At nodal displacement u3 = 5 mm.

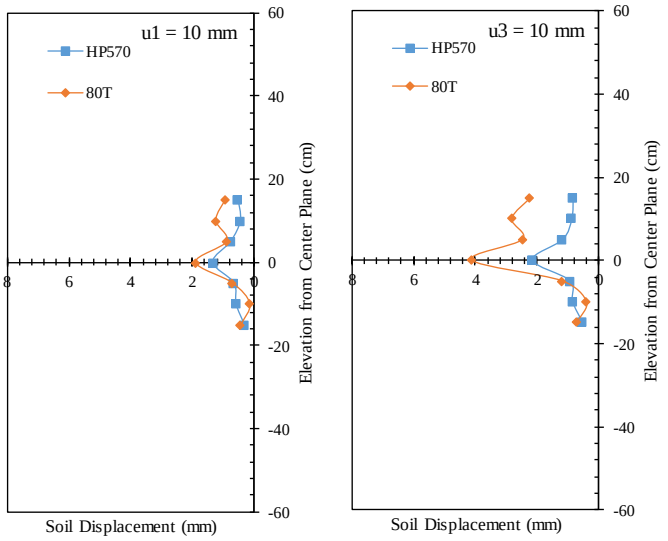

Figure 9.97. Horizontal soil displacement profiles (measured by means of artificial gravel particles): (a) At nodal displacement u1 = 10 mm; and (b) At nodal displacement u3 = 10 mm.

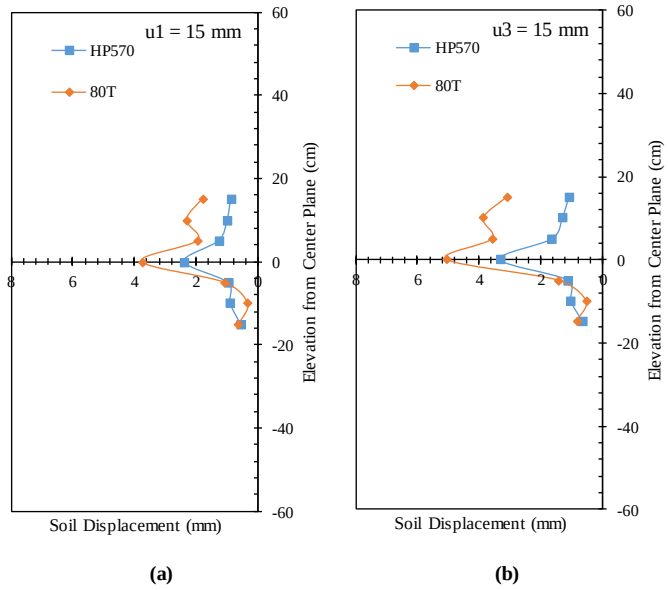

Figure 9.98. Horizontal soil displacement profiles (measured by means of artificial gravel particles): (a) At nodal displacement u1 = 15 mm; and (b) At nodal displacement u3 = 15 mm.

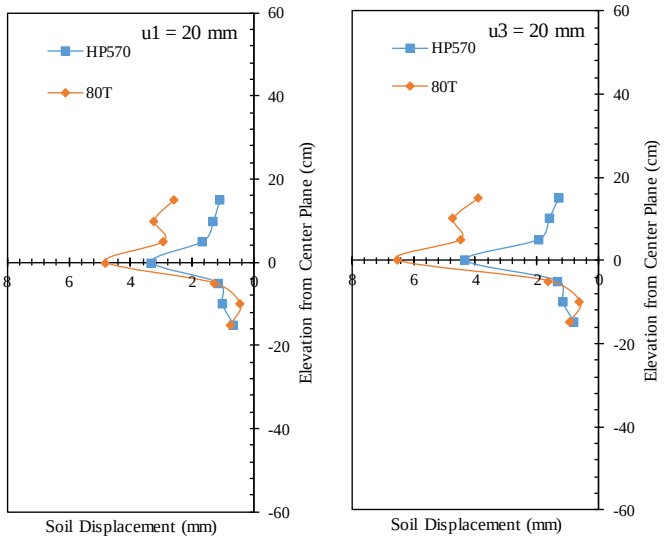

(a) **(b)**

Figure 9.99. Horizontal soil displacement profiles (measured by means of artificial gravel particles): (a) At nodal displacement u1 = 20 mm; and (b) At nodal displacement u3 = 20 mm.

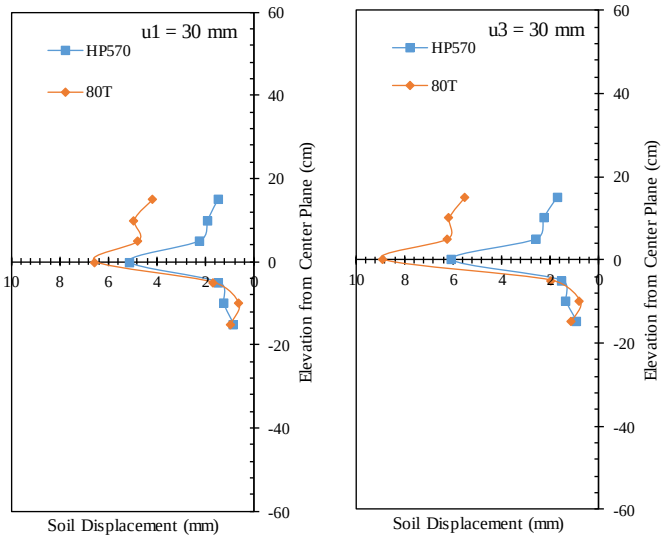

(a) **(b)**

Figure 9.100. Horizontal soil displacement profiles (measured by means of artificial gravel particles): (a) At nodal displacement u1 = 30 mm; and (b) At nodal displacement u3 = 30 mm.

Figure 9.101 show the soil-reinforcement relative displacement magnitude at 30.5 cm from the front wall. This relative displacement was obtained by subtracting the reinforcement displacement at this location (by interpolation between u1 and u3) and the soil displacement measured by the artificial gravel particle adjacent to the reinforcement (LP24). This figure exhibits the reduction in the soil-reinforcement interface shear stiffness during the test. The results indicate that the relative displacement at the HP570 interface was higher than that at the 80T interface due to the difference in the soil-reinforcement interaction between the two reinforcements.

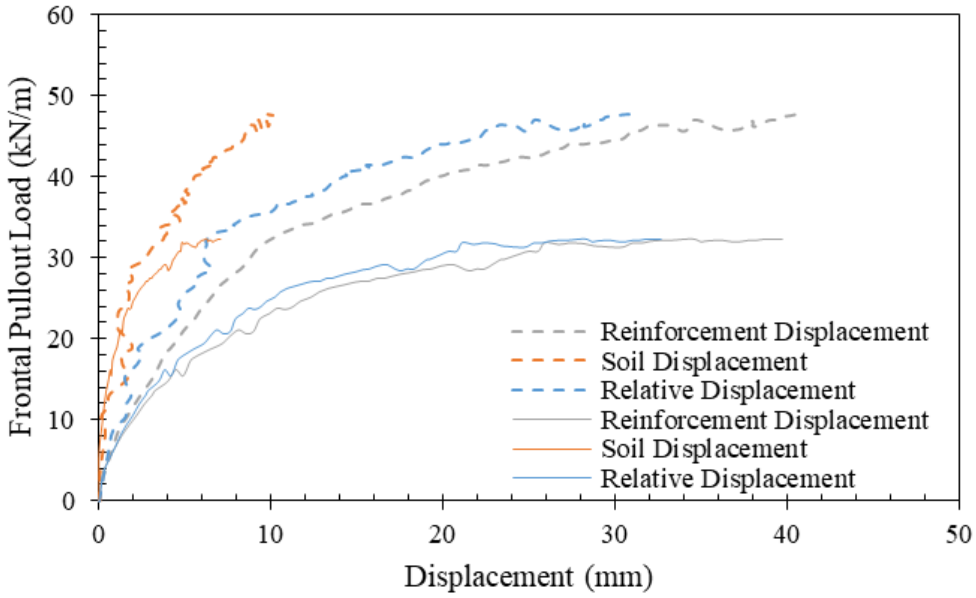

Figure 9.101. Soil-reinforcement relative displacement magnitude (solid lines belong to HP570 and dashed lines belong to 80T).

Figure 9.102 shows the vertical soil displacements measured by means of the artificial gravel particles placed on top of the reinforced soil mass. Figures 9.102a through 9.102d show the vertical soil displacements with respect to reinforcement nodal

displacements u1, u3, u5, and u7. Both tests showed dilation near the front side of the reinforced soil mass and settlement near the rear side. The results indicate that the dilation at the front was lower in case of HP570 geotextile than that in case of 80T geogrid, which was significantly high. At the back, settlement was higher in case of HP570 geotextile compared to that in case of 80T geogrid. In addition, in case of the 80T geogrid, settlement was observed at the middle of the reinforced soil mass followed by dilation as shear stresses increased at the soil-reinforcement interface.

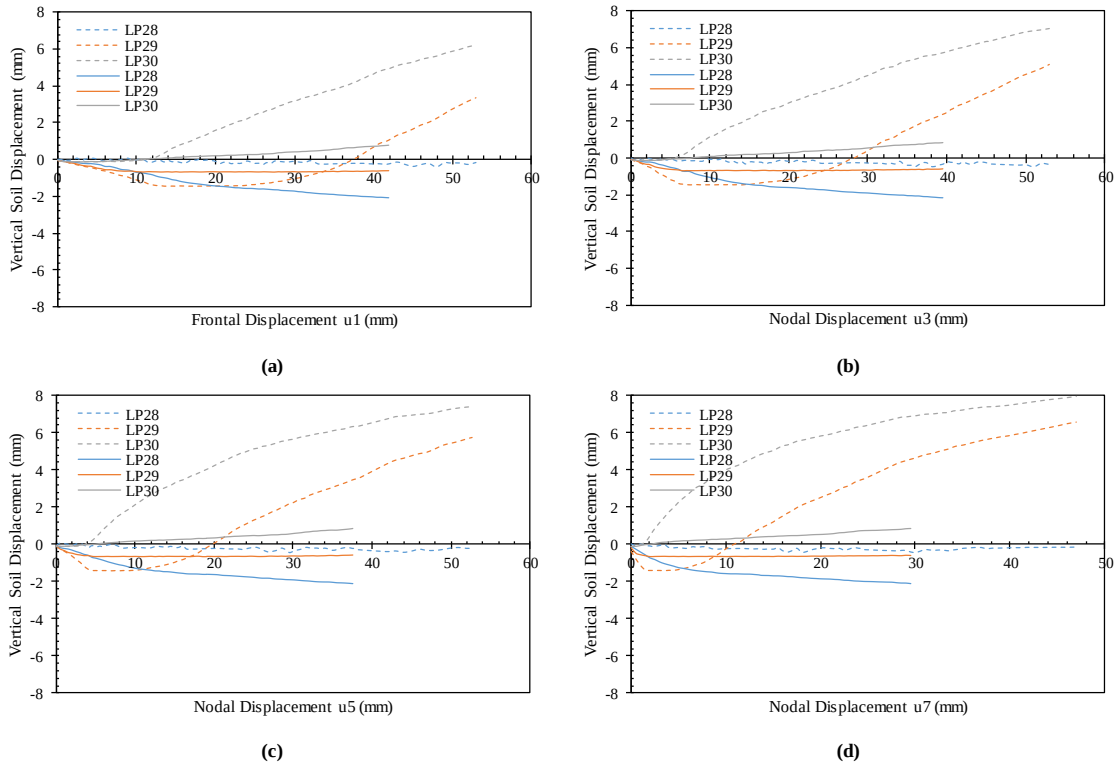

Figure 9.102. Vertical soil displacements (measured by means of artificial gravel particles) with respect to various nodal displacements at the active reinforcement: (a) Nodal displacement u1; (b) Nodal displacement u3; (c) Nodal displacement u5; and (d) Nodal displacement u7 (solid lines belong to HP570 and dashed lines belong to 80T).

9.3.4.3.80T geogrid versus BX1200 geogrid

This comparison was conducted between BX1200 extruded biaxial geogrid and 80T knitted uniaxial geogrid reinforcements. BX1200 is made of polypropylene and 80T is made of polyester. The tensile stiffness for BX1200 (XMD) and 80T (MD) is 392 and 914 kN/m at 5% tensile strain, respectively. Figure 9.103 shows the frontal pullout load-displacement experimental curves for both tests. The results indicate that the resistance to pullout for the 80T geogrid was higher than that of BX1200 geogrid. The difference in resistance increased as the pullout progressed. However, due to the low tensile strength and stiffness of the BX1200 geogrid, it failed in rupture before considerable soil-reinforcement interface displacement unlike the 80T geogrid. The comparison between the frontal pullout load-displacement curves in this case cannot provide full understanding of the soil-reinforcement interaction between both reinforcements. This is because the tensile stiffness is quite different between both reinforcements. A deeper look into the behavior of each reinforcement along their embedment length is needed to complement the information retrieved about the front.

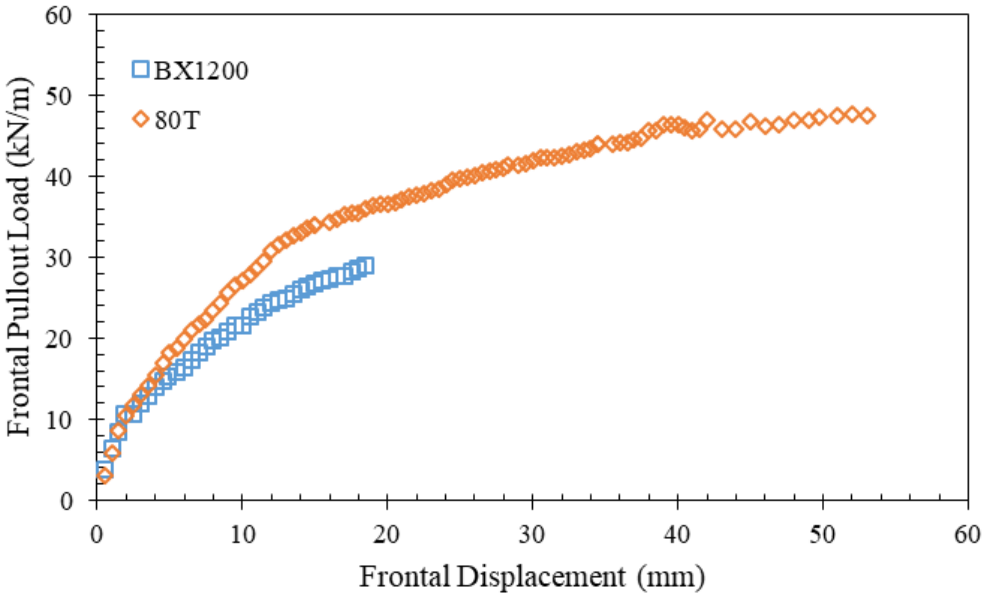

Figure 9.103. Frontal pullout load-displacement curves.

A comparison of the behavior at the early loading stage, up to failure of BX1200, was conducted. Figures 9.104 and 9.105 present the nodal displacement for the upper and lower passive reinforcement layers, respectively. Specifically, Figures 9.104a through 9.104d show the nodal displacements in the upper passive reinforcement corresponding to nodal displacements in the active reinforcement u1, u3, u5, and u7, respectively. Similarly, Figures 9.105a through 9.105d show the nodal displacements in the lower passive reinforcement corresponding to nodal displacements in the active reinforcement u1, u3, u5, and u7, respectively. Figures 9.104 and 9.105 reflect the load transfer from the active reinforcement to the passive reinforcements at the same nodal reinforcement of the active reinforcement.

Figures 104a, 104b, 105a, and 105b show that the interaction 80T has on its neighboring reinforcements is higher than that of BX1200. However, Figures 104c, 104d,

105c, and 105d show similar effect for both reinforcements. This observation is a result of the higher elongation BX1200 had compared to that of 80T. Overall, the comparison revealed information about the soil-reinforcement interaction stiffness. It was concluded that BX1200 geogrid has a slightly lower soil-reinforcement interaction stiffness, which resulted in a slightly less interaction with the neighboring reinforcement layers, compared to that of 80T geogrid.

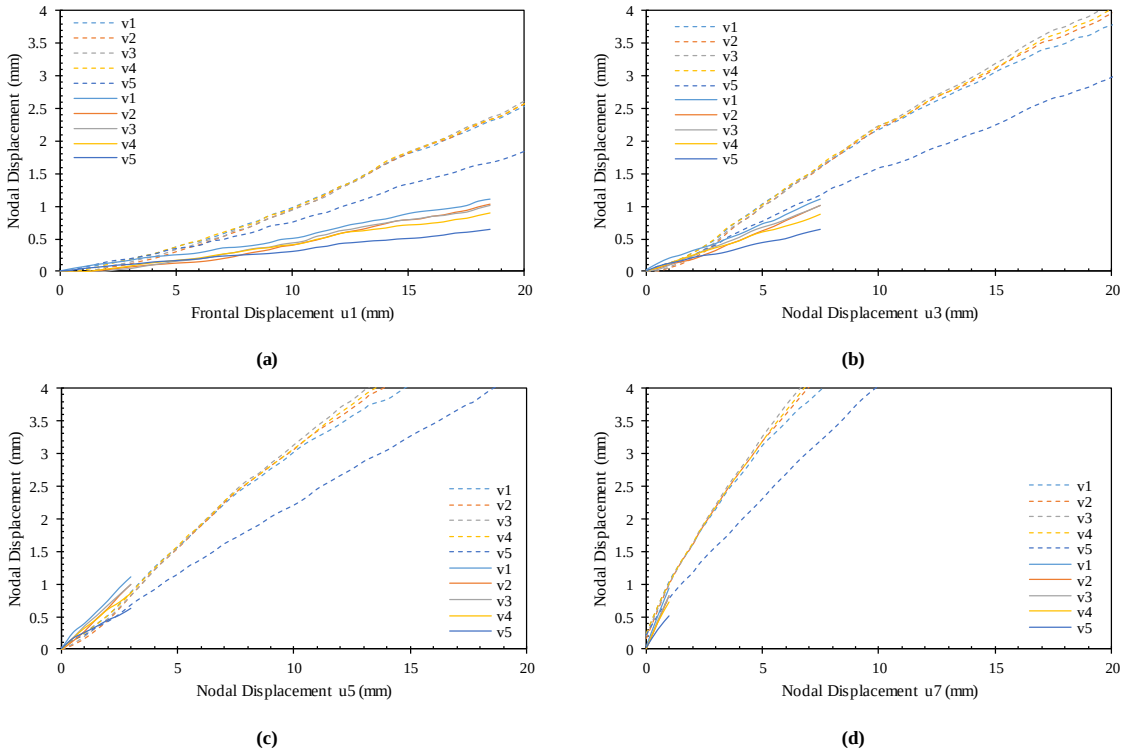

Figure 9.104. Nodal displacements at the upper passive reinforcement with respect to various nodal displacements at the active reinforcement: (a) nodal displacement u1; (b) nodal displacement u3; (c) nodal displacement u5; and (d) nodal displacement u7 (solid lines belong to BX1200 and dashed lines belong to 80T).

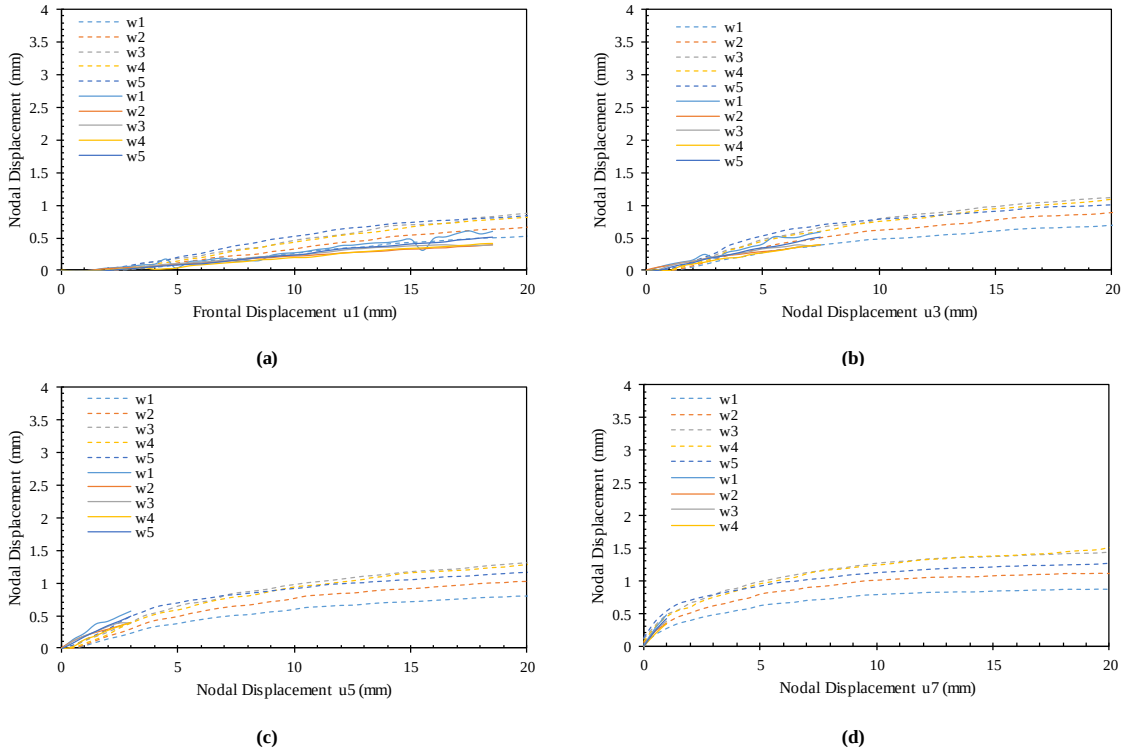

Figure 9.105. Nodal displacements at the lower passive reinforcement with respect to various nodal displacements at the active reinforcement: (a) Nodal displacement u1; (b) Nodal displacement u3; (c) Nodal displacement u5; and (d) Nodal displacement u7 (solid lines belong to BX1200 and dashed lines belong to 80T).

Figures 9.106 through 9.108 show the displacement profiles for the active and passive reinforcement layers at active reinforcement frontal displacements (u1) of 5, 10, and 15 mm, respectively. Note that the comparison is based on the same frontal displacement for the different reinforcements rather than the same pullout frontal load. The profiles of BX1200 geogrid show slightly lower displacement along the reinforcement length compared to those of 80T geogrid. This was observed for both active and passive reinforcement layers.

For a proper comparison, Figure 9.109 show the passive reinforcement displacement profiles for intermediate nodal displacements of the active reinforcement of 5 mm. Specifically, Figures 9.109a and 9.109b provide comparisons of the upper passive reinforcement profiles for same nodal displacements u1 and u3, respectively. That is, the comparisons were conducted for the similar soil-reinforcement induced interface displacement. The results indicate that the interaction between the reinforcement layers in case of the 80T geogrid is slightly higher than that in case of the BX1200 geogrid.

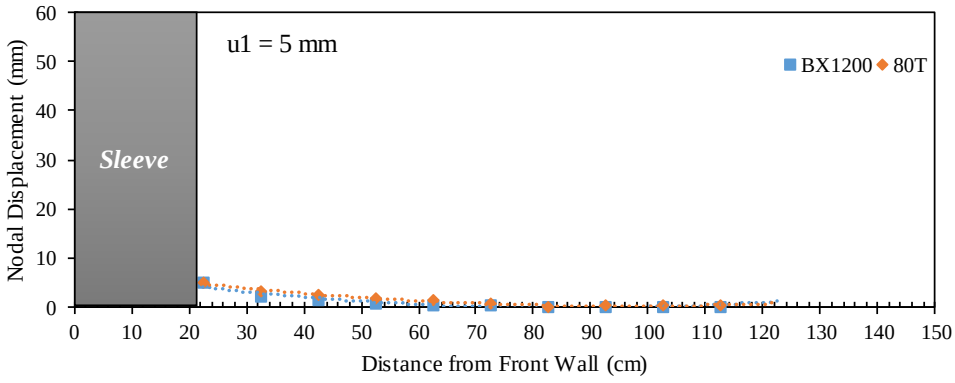

(a)

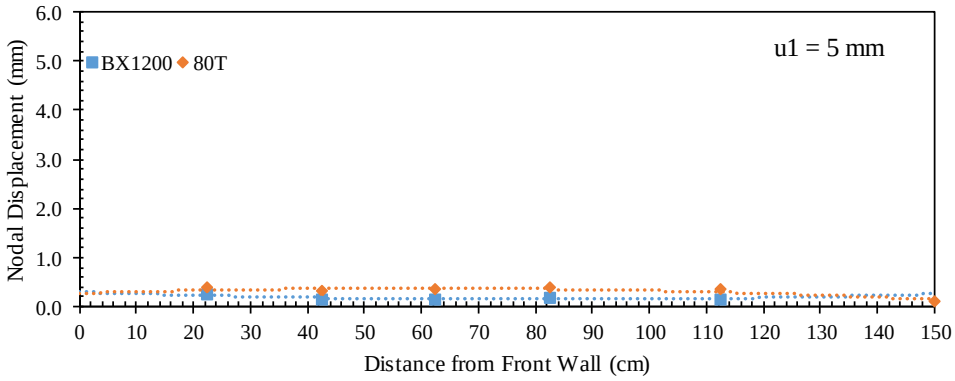

(b)

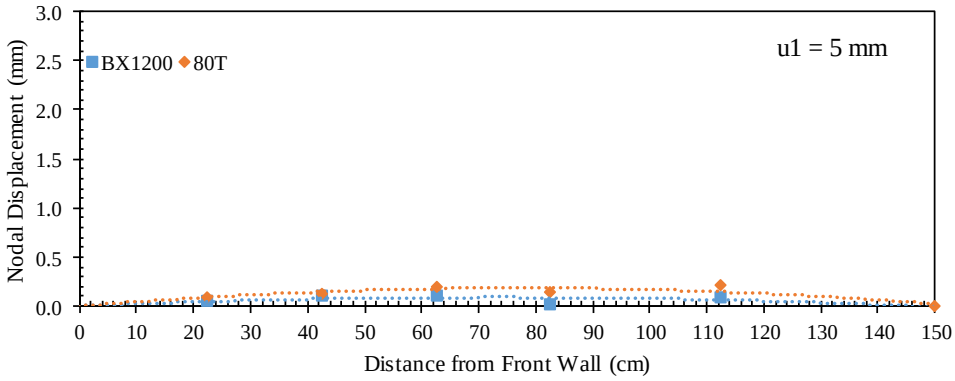

(c)

Figure 9.106. Reinforcement displacement profiles at frontal displacement u1 = 5 mm: (a) Active reinforcement; (b) Upper passive reinforcement; and (c) Lower passive reinforcement.

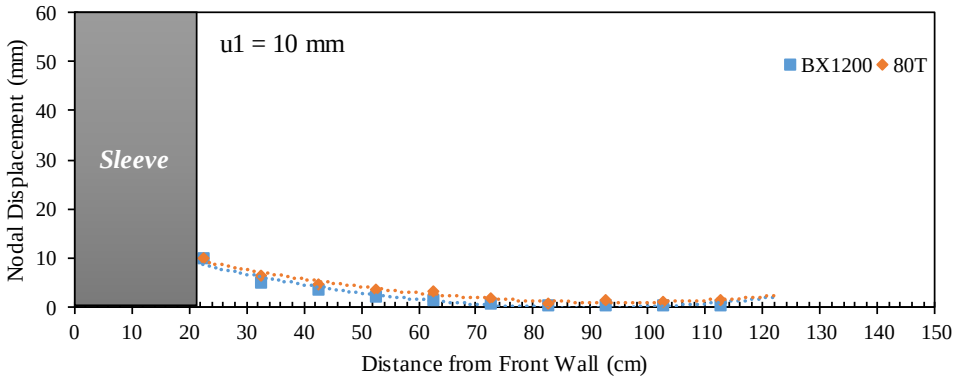

(a)

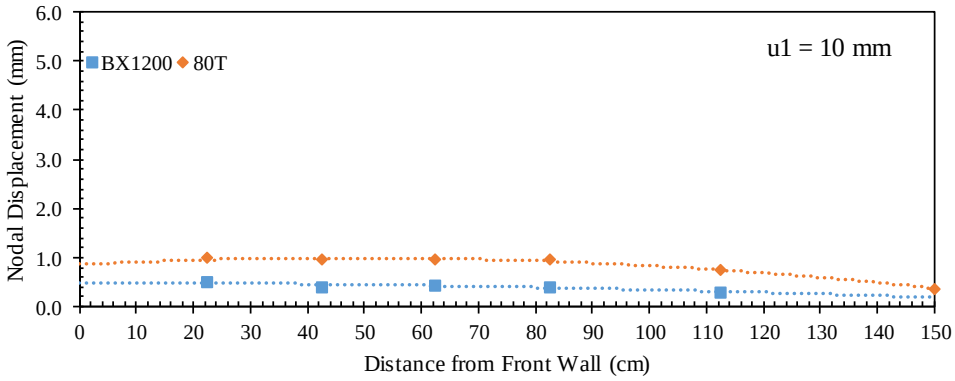

(b)

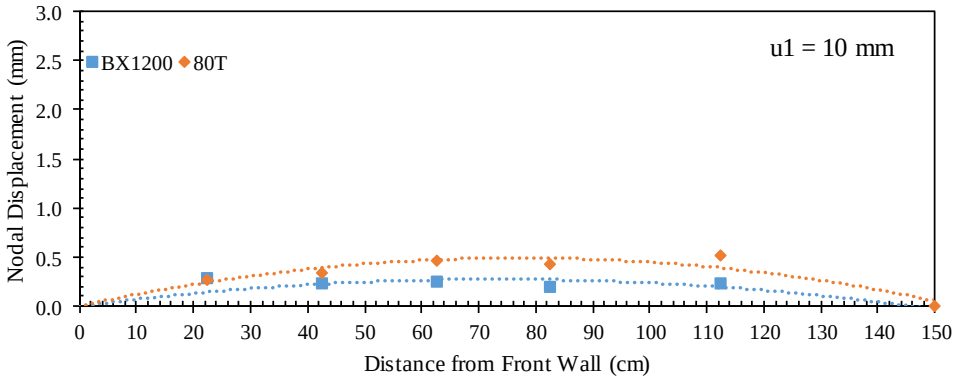

(c)

Figure 9.107. Reinforcement displacement profiles at frontal displacement u1 = 10 mm: (a) Active reinforcement; (b) Upper passive reinforcement; and (c) Lower passive reinforcement.

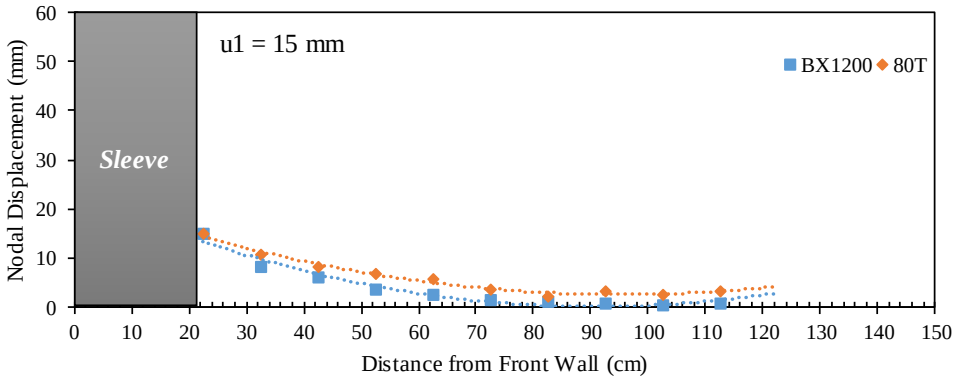

(a)

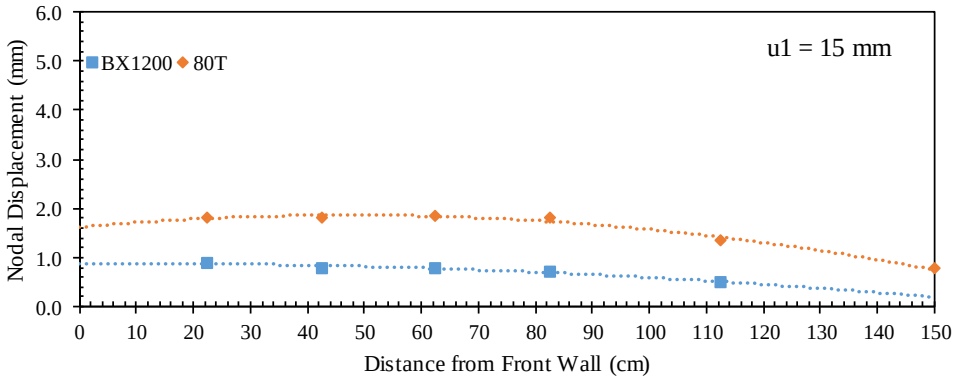

(b)

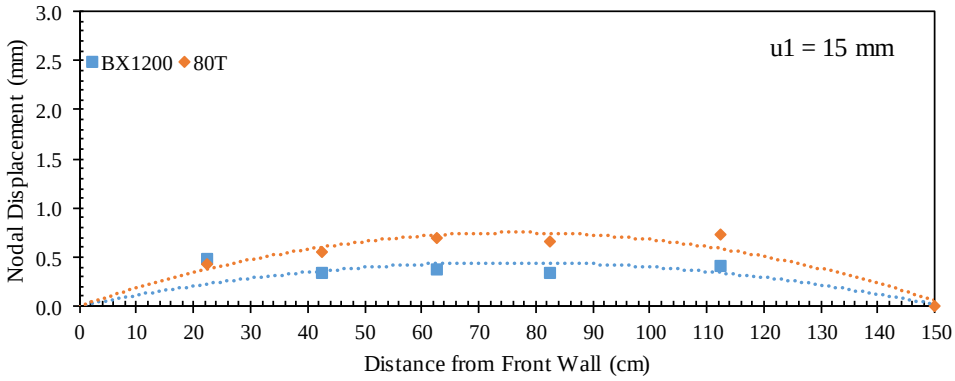

(c)

Figure 9.108. Reinforcement displacement profiles at frontal displacement u1 = 15 mm: (a) Active reinforcement; (b) Upper passive reinforcement; and (c) Lower passive reinforcement.

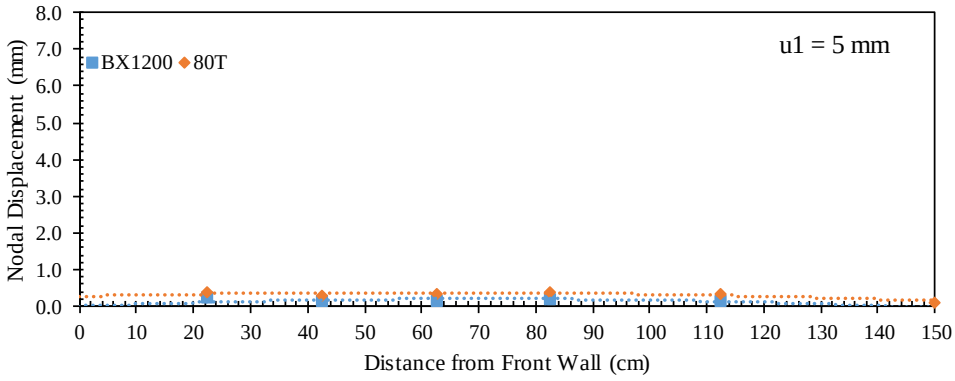

(a)

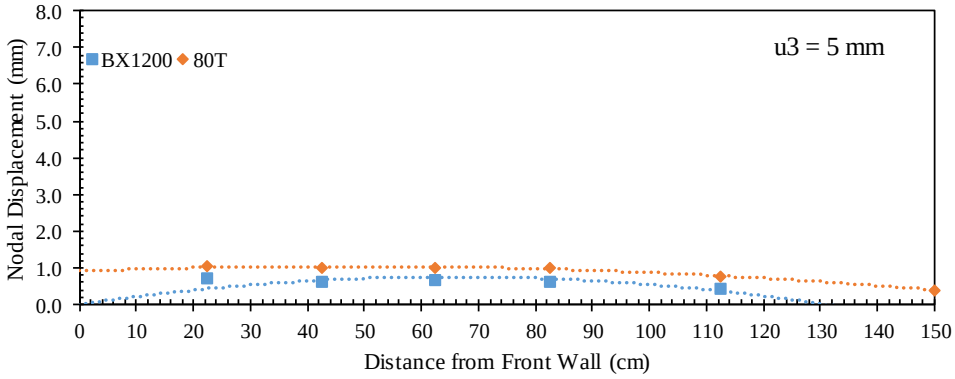

(b)

Figure 9.109. Upper passive reinforcement displacement profiles: (a) At nodal displacement u1 = 5 mm; and (b) At nodal displacement u3 = 5 mm.

Figures 9.110 through 9.111 present the horizontal soil displacement measured for nodal displacements of 5 and 15 mm, respectively. Each figure consists of a and b that show the soil displacement with respect nodal displacements u1 and u3, respectively. These displacement were measured at specific locations by tracking artificial gravel particles making a vertical array within the soil at 30.5 cm from the front wall. The results indicate that the soil displacement is smaller in case of BX1200 geogrid compared to that of 80T geogrid. This difference was observed to increase as pullout progressed due to the difference the soil-reinforcement interaction between the two reinforcements.

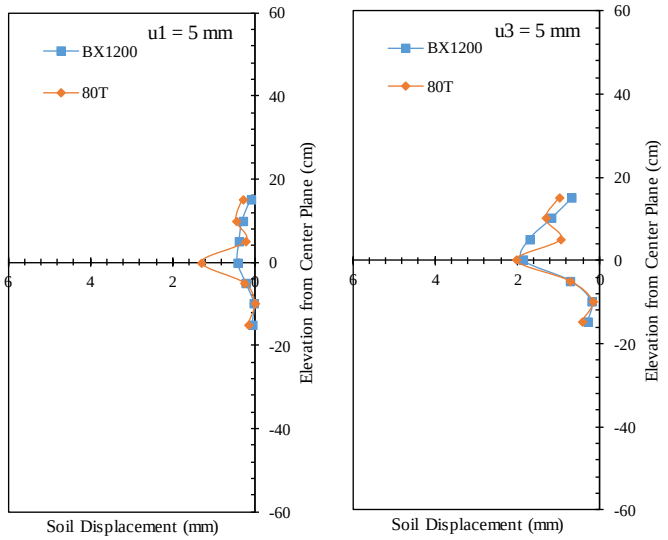

Figure 9.110. Horizontal soil displacement profiles (measured by means of artificial gravel particles): (a) At nodal displacement u1 = 5 mm; and (b) At nodal displacement u3 = 5 mm.

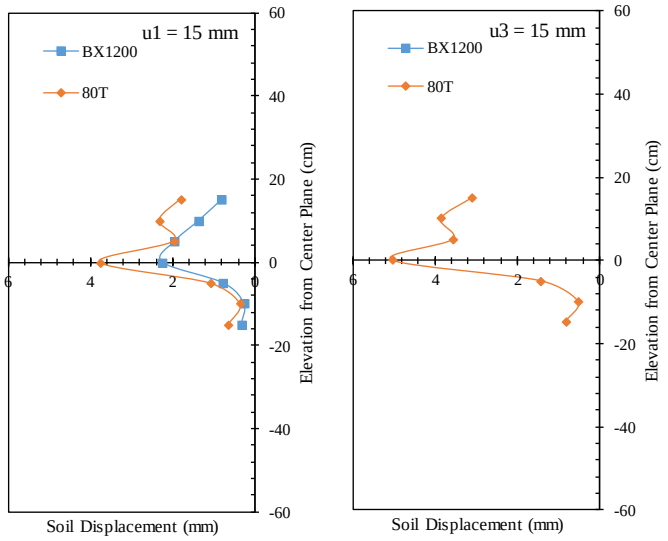

(a) **(b)**

Figure 9.111. Horizontal soil displacement profiles (measured by means of artificial gravel particles): (a) At nodal displacement u1 = 15 mm; and (b) At nodal displacement u3 = 15 mm.

Figure 9.112 show the soil-reinforcement relative displacement magnitude at 30.5 cm from the front wall. This relative displacement was obtained by subtracting the reinforcement displacement at this location (by interpolation between u1 and u3) and the soil displacement measured by the artificial gravel particle adjacent to the reinforcement (LP24). The results indicate that the relative displacement at the BX1200 interface was higher than that at the 80T interface due to the difference in the soil-reinforcement interaction between the two reinforcements.

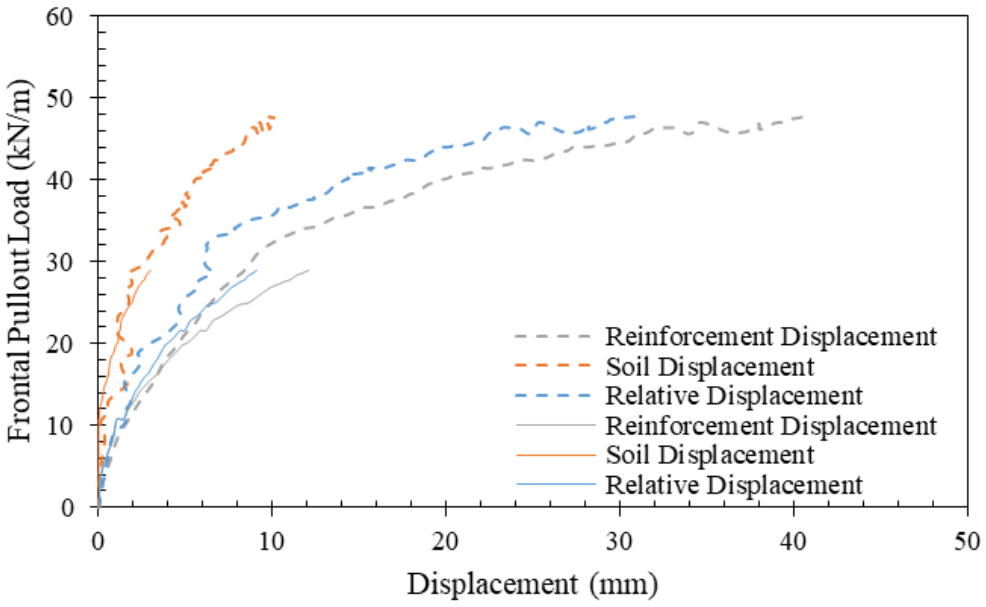

Figure 9.112. Soil-reinforcement relative displacement magnitude (solid lines belong to BX1200 and dashed lines belong to 80T).

Figure 9.113 shows the vertical soil displacement measured by means of the artificial gravel particles placed on top of the reinforced soil mass. Figures 9.113a through 9.113d show the soil displacement with respect to reinforcement nodal displacement u1, u3, u5, and u7. Both tests showed very similar dilation near the front side of the reinforced soil mass and similar settlement near the rear side.

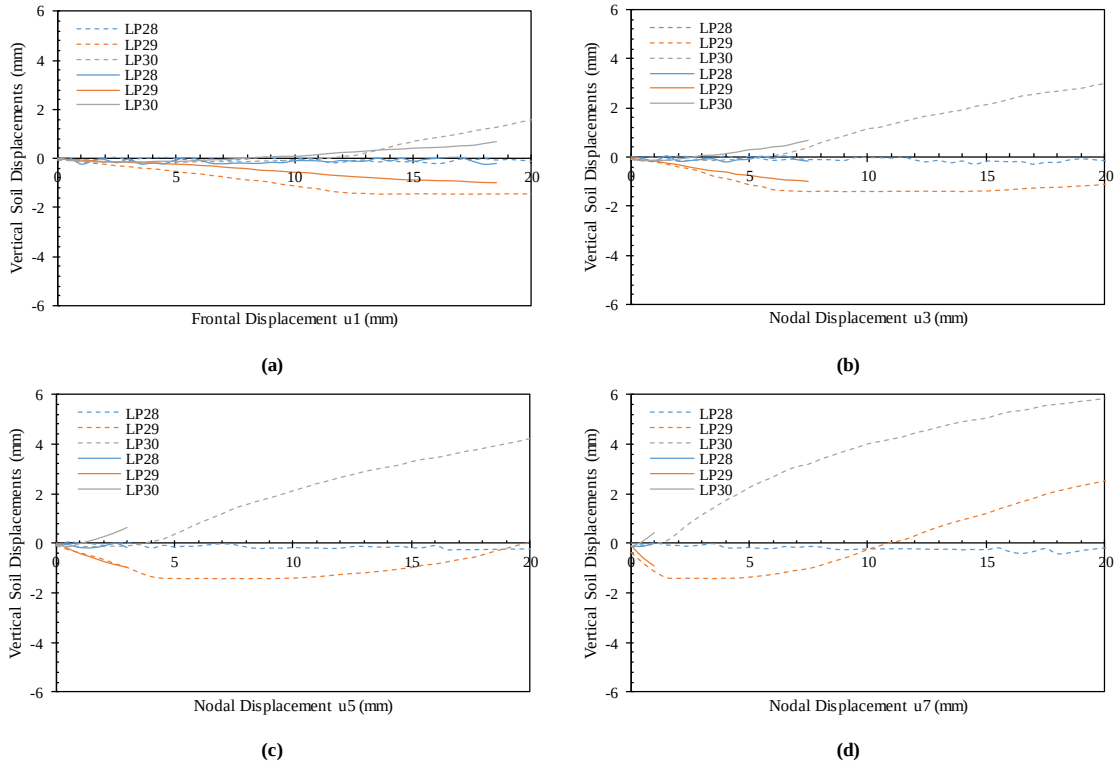

Figure 9.113. Vertical soil displacements (measured by means of artificial gravel particles) with respect to various nodal displacements at the active reinforcement: (a) Nodal displacement u1; (b) Nodal displacement u3; (c) Nodal displacement u5; and (d) Nodal displacement u7 (solid lines belong to BX1200 and dashed lines belong to 80T).

9.3.5. Effect of boundary type

This comparison was conducted between two tests conducted at the same testing conditions and using the same active reinforcement and fill material. The active reinforcement for both tests was HP570 geotextile. However, the passive reinforcements used were HP570 geotextiles for one test and Mylar sheets for the other. Note that Mylar sheets of 1-mm thickness have tensile strength of approximately 20 kN/m. that can typically reach up to . That is, this comparison shows the effect of the interface condition of passive reinforcements on the soil-reinforcement interaction and the interaction between the neighboring reinforcement layers. Table 9.6 summarizes the properties of the two tests involved in this comparison.

Table 9.6. Summary of tests in which boundary type was varied.

Test ID	***Testing Variables***					
	Fill Material	***S_v***	***σ_v***	***Active GS***	***Passive GS***	***Dilation***
GP-06-03-G1-G GP-06-03-G1-S	AASHTO No. 8	0.15 m	21 kPa	HP570	HP570 Mylar	Allowed

Figure 9.114 shows the frontal pullout load-displacement experimental curves for both tests. It was observed that both tests showed very similar curves with slight difference close to pullout failure. This observation showed that the soil-reinforcement interface shear behavior remained unchanged upon changing the interface condition of the passive reinforcements.

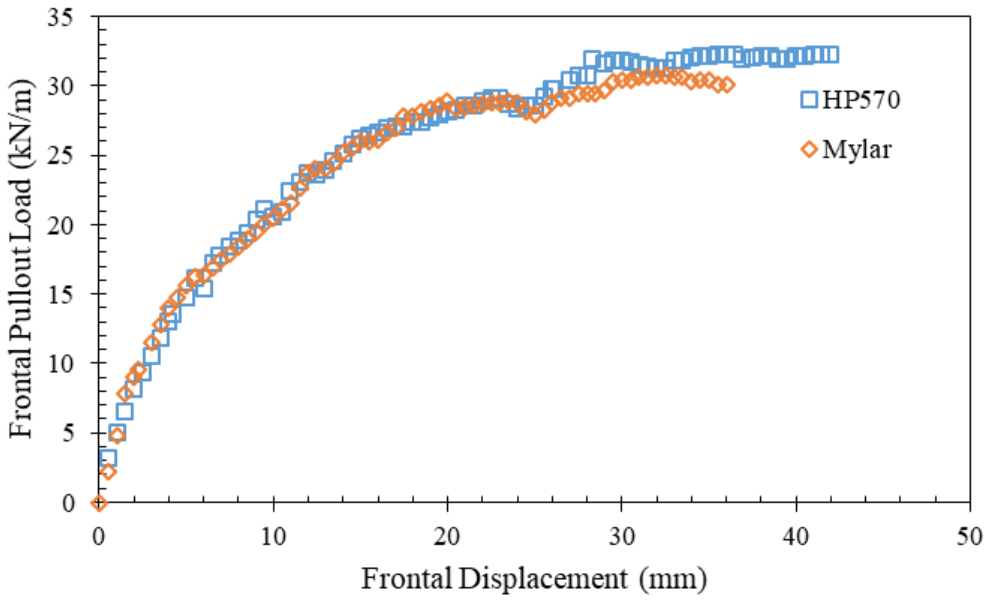

Figure 9.114. Frontal pullout load-displacement curves.

Figures 9.115 and 9.116 present the nodal displacement for the upper and lower passive reinforcement layers, respectively. Specifically, Figures 9.115a through 9.115d show the nodal displacements in the upper passive reinforcement corresponding to nodal displacements in the active reinforcement u1, u3, u5, and u7, respectively. Similarly, Figures 9.116a through 9.116d show the nodal displacements in the lower passive reinforcement corresponding to nodal displacements in the active reinforcement u1, u3, u5, and u7, respectively. Figures 9.115 and 9.116 reveal the load transfer from the active reinforcement to the passive reinforcements at the same nodal reinforcement of the active reinforcement.

It was observed that the relationship between the nodal displacements for of the passive reinforcements are linear with the nodal displacements of the active reinforcement at early loading stages. This relationship then become non-linear as the load-displacement

relationship of the active reinforcement curves. However, both tests were conducted using the same reinforcement type (HP570 geotextile) and showed similar pullout resistance and interface behavior. That is, Figures 9.115 and 9.116 reflect the effect of interface condition of the passive reinforcement on the interaction between the contiguous reinforcement layers. The results indicate that the test conducted using Mylar passive reinforcements showed higher interaction between the neighboring reinforcement layers compared to that conducted using geotextile passive reinforcements. This can be explained by the creation of the weak layer in the reinforced soil mass that allowed soil to slide on as the load of the active reinforcement is being transferred.

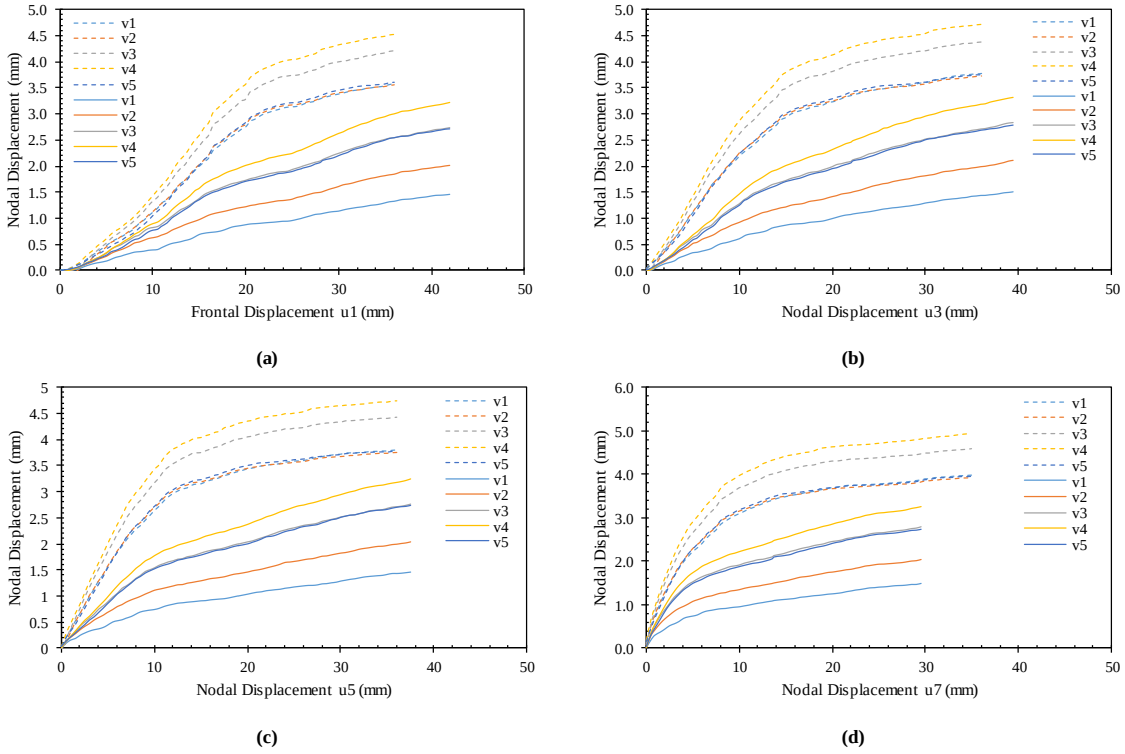

Figure 9.115. Nodal displacements at the upper passive reinforcement with respect to various nodal displacements at the active reinforcement: (a) nodal displacement u1; (b) nodal displacement u3; (c) nodal displacement u5; and (d) nodal displacement u7 (solid lines belong to HP570 and dashed lines belong to Mylar).

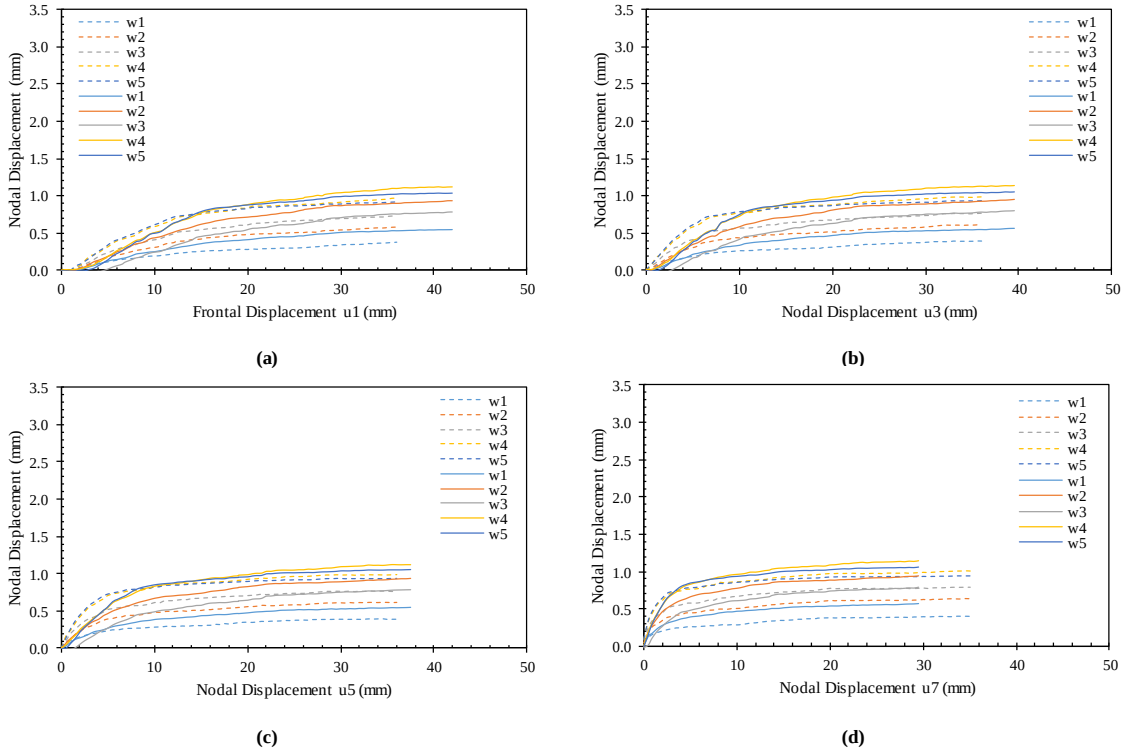

Figure 9.116. Nodal displacements at the lower passive reinforcement with respect to various nodal displacements at the active reinforcement: (a) Nodal displacement u1; (b) Nodal displacement u3; (c) Nodal displacement u5; and (d) Nodal displacement u7 (solid lines belong to HP570 and dashed lines belong to Mylar).

Figures 9.117 through 9.121 show the displacement profiles for the active and passive reinforcement layers at active reinforcement frontal displacements (u1) of 5, 10, 15, 20, and 30 mm, respectively. The displacement profiles for active reinforcement layers for both tests were very similar over up to frontal displacement of 30 mm. On contrary, the profiles of the passive reinforcements for the test conducted with Mylar passive layers showed higher displacement magnitudes compared to that conducted with geotextile passive layers. The difference increased as pullout progressed. This difference in reinforcement displacements is due to the weak interface of the Mylar layers. This weak interface allowed more soil to slide allowing more load to be transferred from the active reinforcement to the passive reinforcements with less energy loss in the in between soil medium. Note that if the active reinforcement layer in the test conducted with Mylar layers was also Mylar with weak interface shear resistance, the results are anticipated to be totally different. Specifically, very small load transfer would transfer from the active reinforcement to the passive reinforcements.

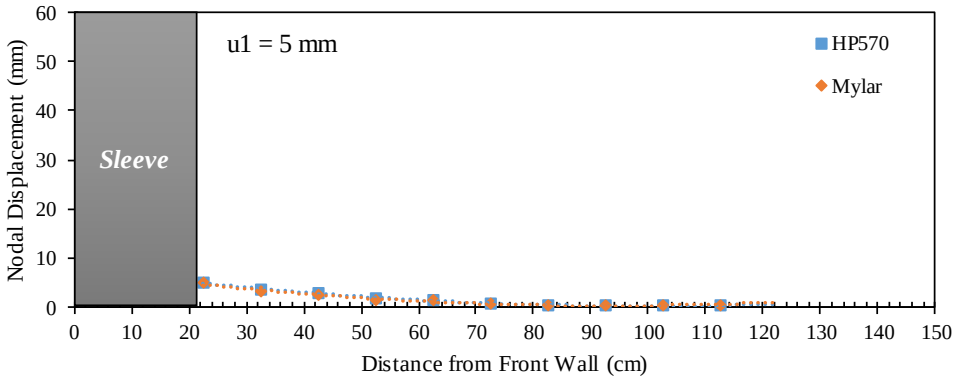

(a)

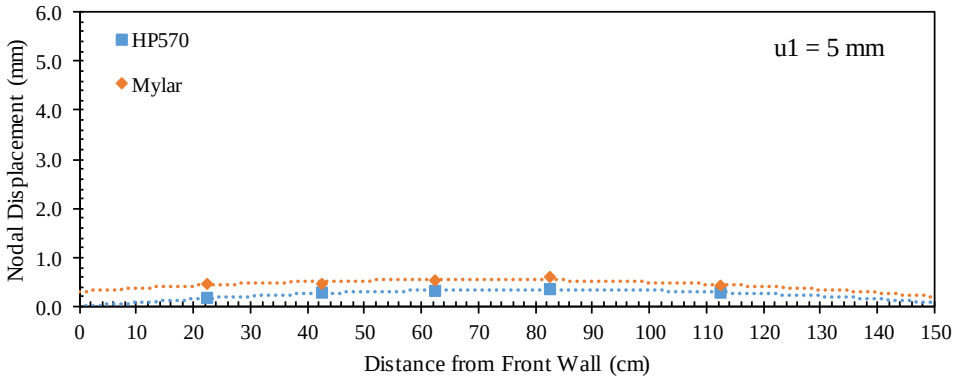

(b)

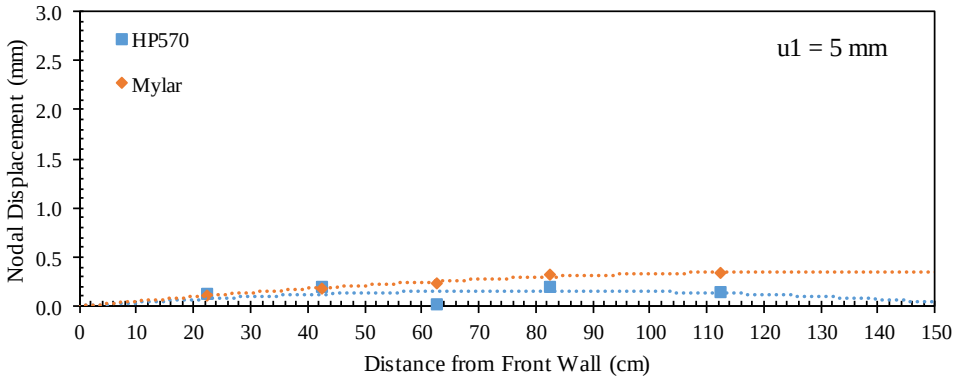

(c)

Figure 9.117. Reinforcement displacement profiles at frontal displacement u1 = 5 mm: (a) Active reinforcement; (b) Upper passive reinforcement; and (c) Lower passive reinforcement.

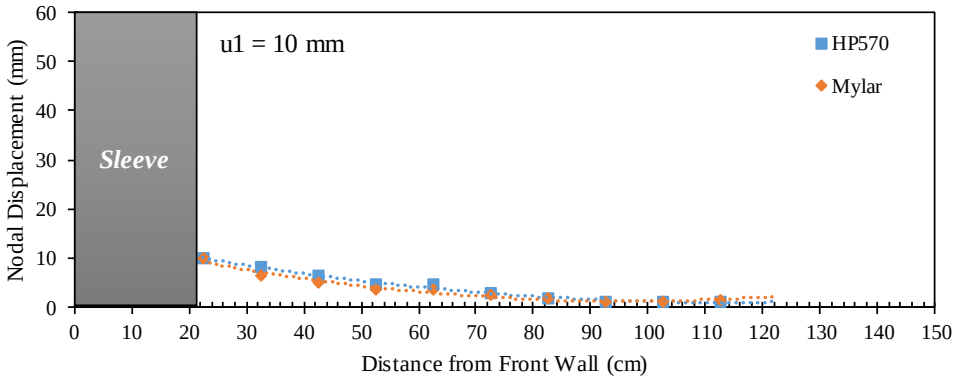

(a)

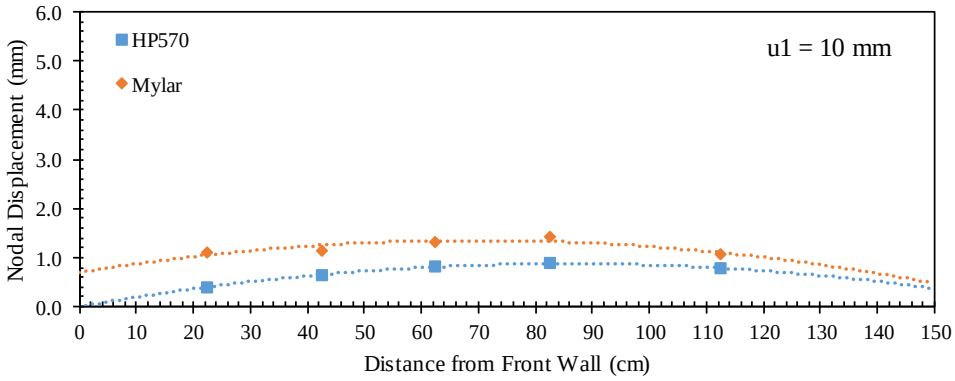

(b)

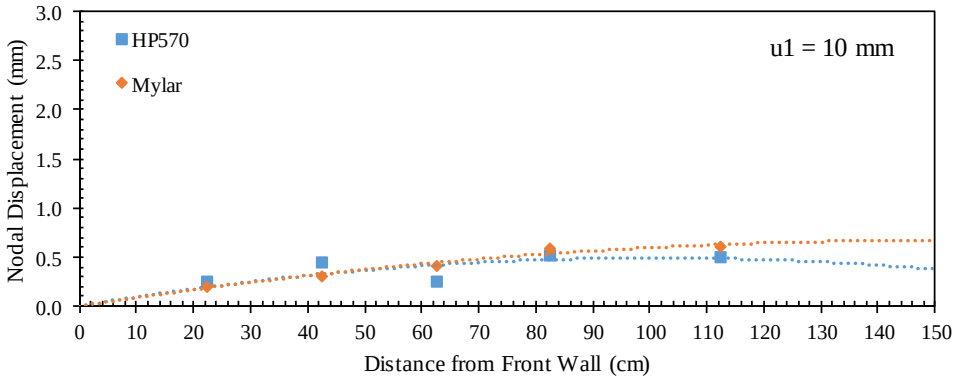

(c)

Figure 9.118. Reinforcement displacement profiles at frontal displacement u1 = 10 mm: (a) Active reinforcement; (b) Upper passive reinforcement; and (c) Lower passive reinforcement.

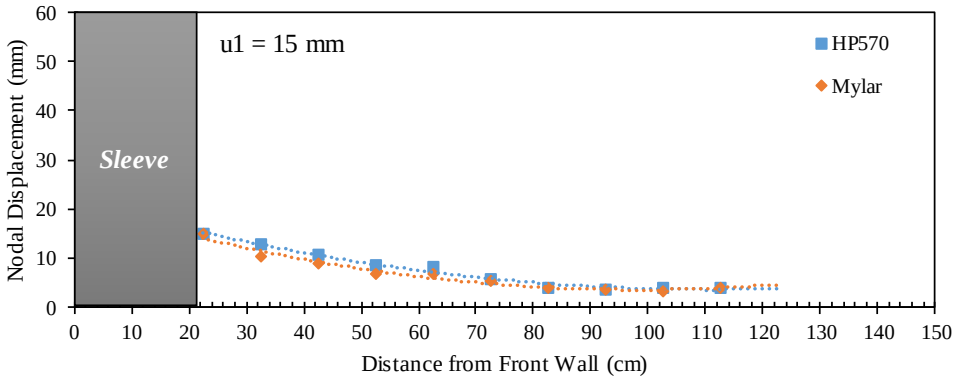

(a)

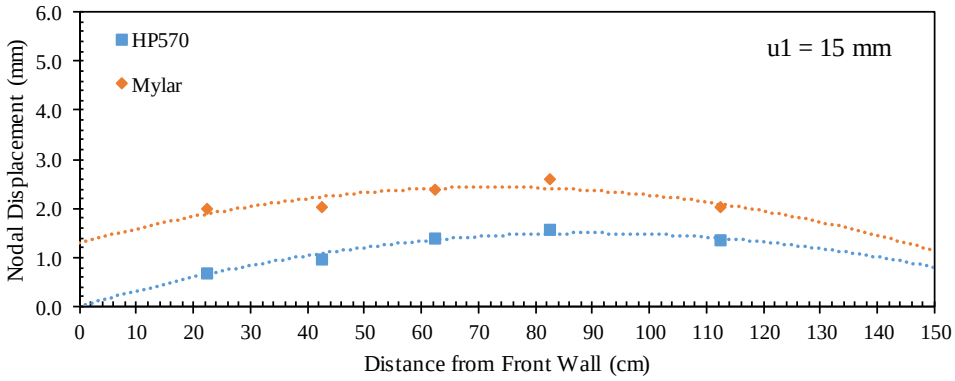

(b)

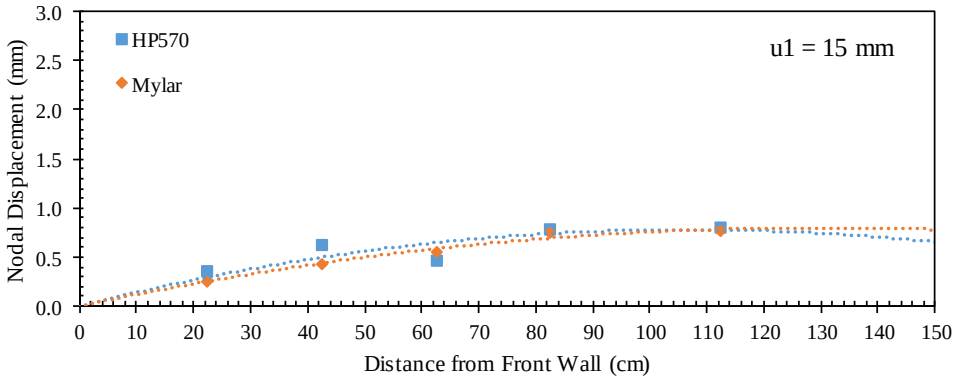

(c)

Figure 9.119. Reinforcement displacement profiles at frontal displacement u1 = 15 mm: (a) Active reinforcement; (b) Upper passive reinforcement; and (c) Lower passive reinforcement.

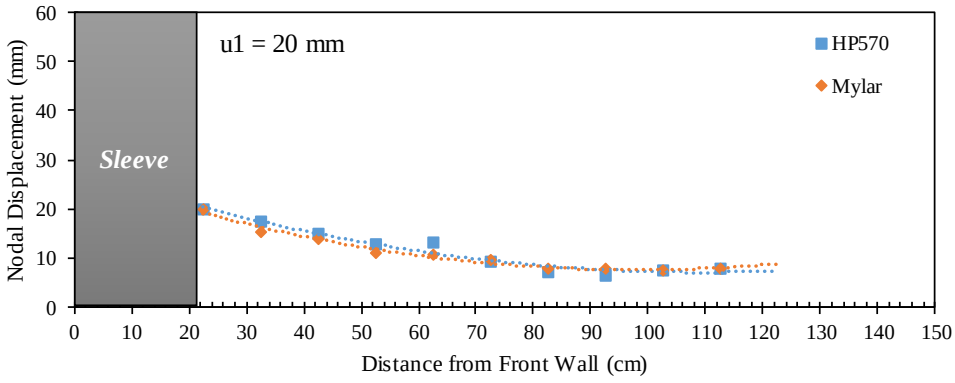

(a)

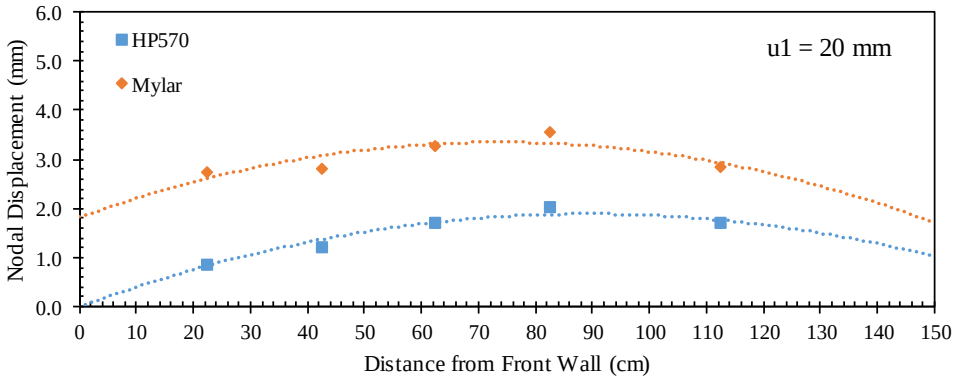

(b)

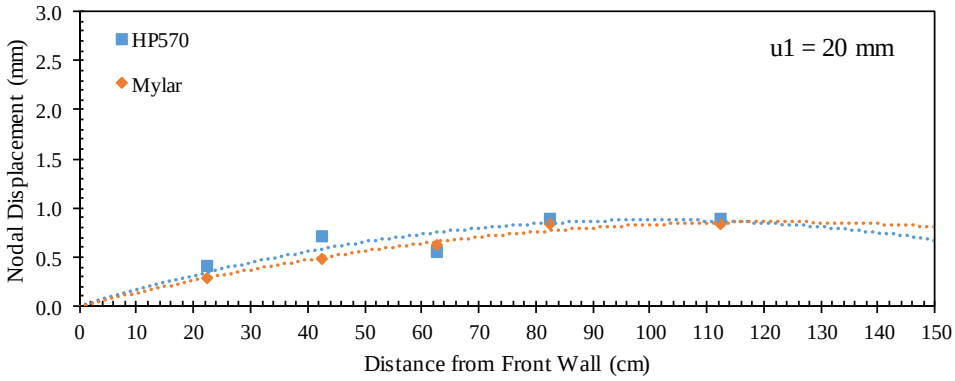

(c)

Figure 9.120. Reinforcement displacement profiles at frontal displacement u1 = 20 mm: (a) Active reinforcement; (b) Upper passive reinforcement; and (c) Lower passive reinforcement.

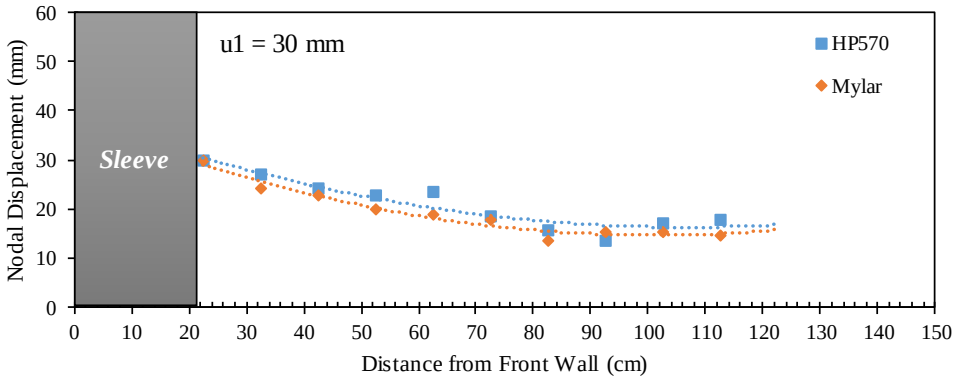

(a)

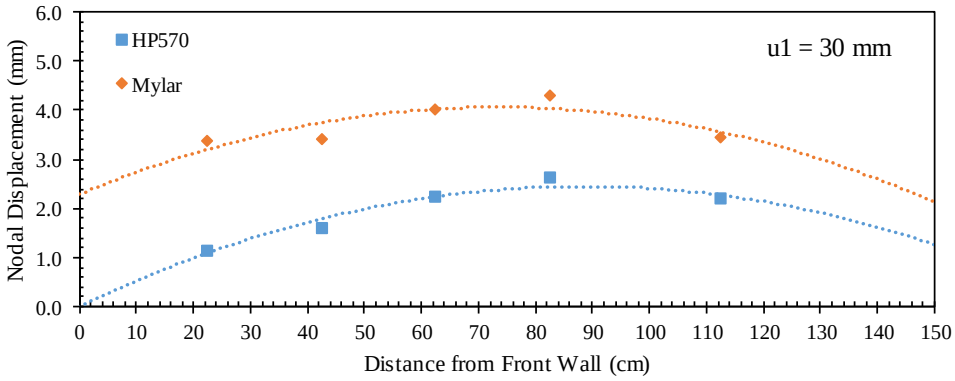

(b)

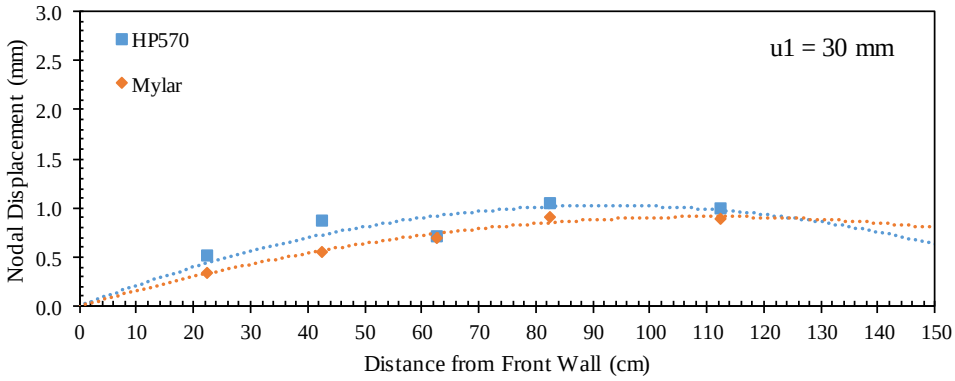

(c)

Figure 9.121. Reinforcement displacement profiles at frontal displacement u1 = 30 mm: (a) Active reinforcement; (b) Upper passive reinforcement; and (c) Lower passive reinforcement.

Figures 9.122 through 9.126 present the horizontal soil displacement measured for nodal displacements of 5, 10, 15, 20, and 30 mm, respectively. Each figure consists of a and b that show the soil displacement with respect nodal displacements u1 and u3, respectively. These displacement were measured at specific locations by tracking artificial gravel particles making a vertical array within the soil at 30.5 cm from the front wall.

The profiles for the test conducted using Mylar passive reinforcements showed higher soil displacements compared to that conducted with geotextile passive reinforcements. Note that the soil adjacent to the reinforcement in the test conducted with Mylar reinforcement did not exhibit significant difference in displacement compared to the soil away from the reinforcement. The reduction in interface stiffness occurred along the weak Mylar interface before occurring in the soil medium. On contrary, the test conducted with geotextile reinforcement showed a larger difference in the displacement rate between the soil adjacent to the reinforcement and the soil away from the reinforcement, which is due to yielding in the internal shear strength of the fill material. This observation was made only for the upper soil mass. For the lower soil mass, no much difference was observed in the soil displacement between the two tests.

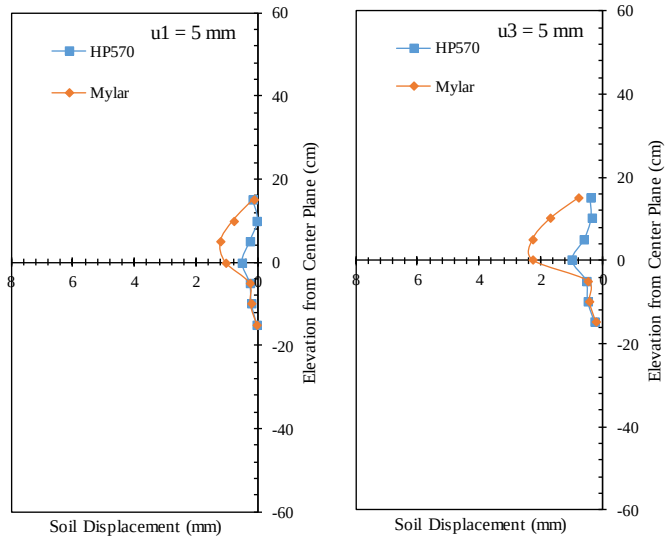

(a) **(b)**

Figure 9.122. Horizontal soil displacement profiles (measured by means of artificial gravel particles): (a) At nodal displacement u1 = 5 mm; and (b) At nodal displacement u3 = 5 mm.

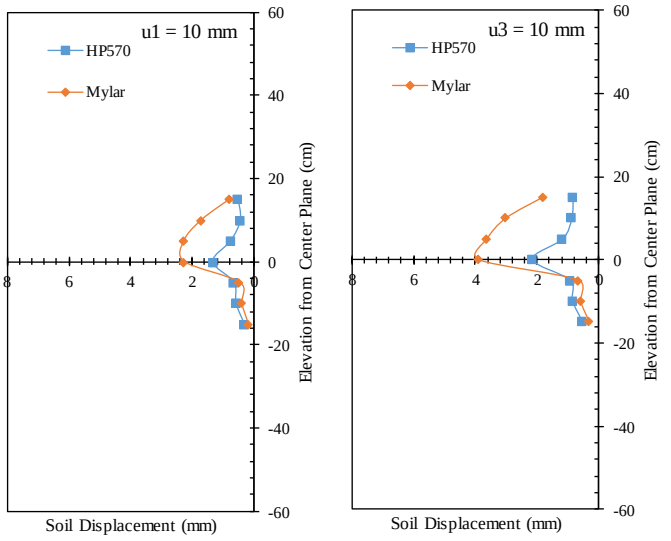

(a) **(b)**

Figure 9.123. Horizontal soil displacement profiles (measured by means of artificial gravel particles): (a) At nodal displacement u1 = 10 mm; and (b) At nodal displacement u3 = 10 mm.

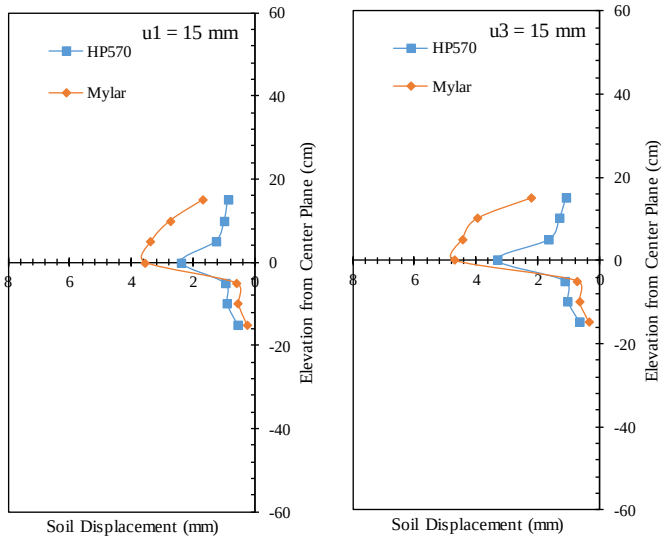

(a) **(b)**

Figure 9.124. Horizontal soil displacement profiles (measured by means of artificial gravel particles): (a) At nodal displacement u1 = 15 mm; and (b) At nodal displacement u3 = 15 mm.

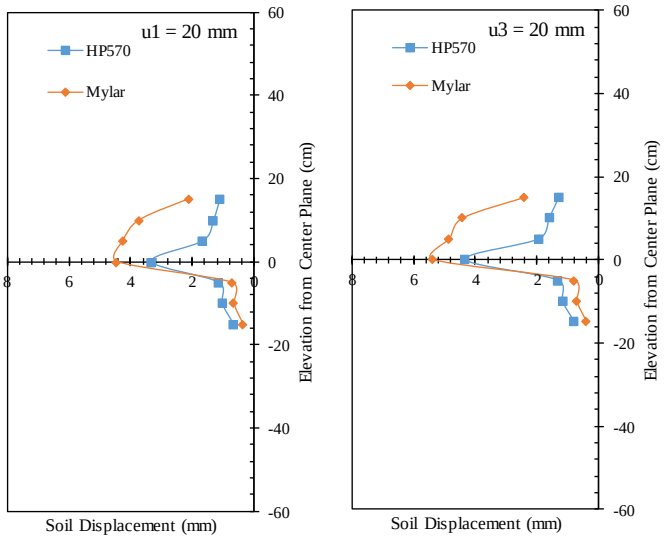

(a) **(b)**

Figure 9.125. Horizontal soil displacement profiles (measured by means of artificial gravel particles): (a) At nodal displacement u1 = 20 mm; and (b) At nodal displacement u3 = 20 mm.

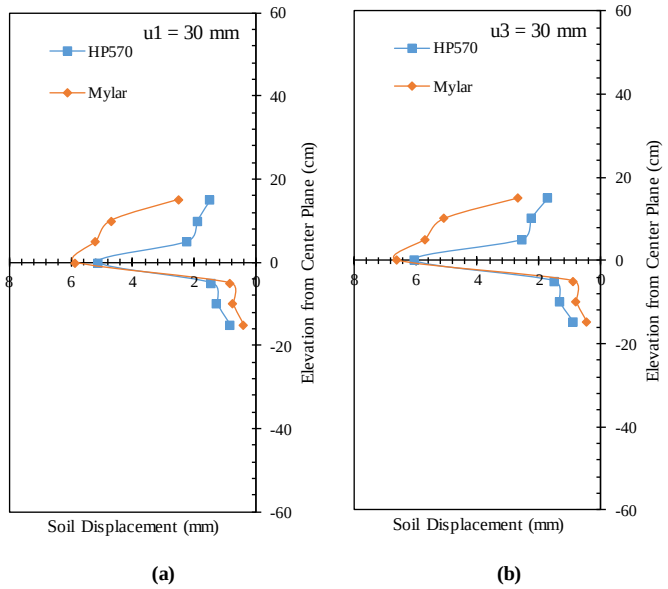

Figure 9.126. Horizontal soil displacement profiles (measured by means of artificial gravel particles): (a) At nodal displacement u1 = 30 mm; and (b) At nodal displacement u3 = 30 mm.

Figure 9.127 shows the soil-reinforcement relative displacement magnitude at 30.5 cm from the front wall. This relative displacement was obtained by subtracting the reinforcement displacement at this location (by interpolation between u1 and u3) and the soil displacement measured by the artificial gravel particle adjacent to the reinforcement (LP24). The results indicate that the relative displacement at the interface of the active reinforcement was lower in the test conducted with the Mylar passive layers compared to that conducted with the geotextile passive layers. That is, creating a weak plane inside the reinforced soil mass reduces the friction that causes the relative displacement between the active reinforcement and the surrounding soil. If this weak plane did not exist, the internal soil friction would have increased the relative displacement magnitude.

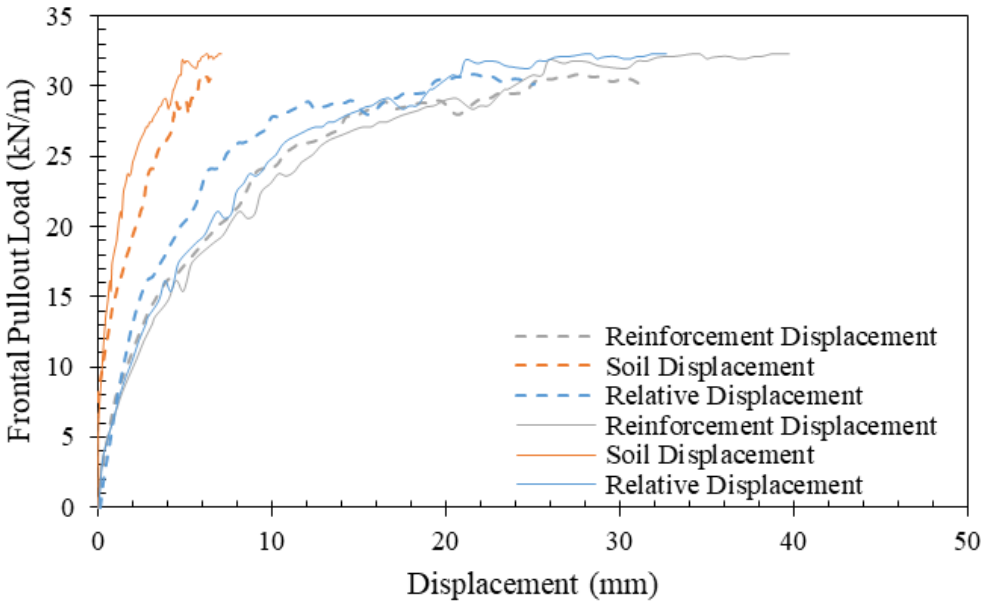

Figure 9.127. Soil-reinforcement relative displacement magnitude (solid lines belong to HP570 and dashed lines belong to Mylar).

Figure 9.128 shows the vertical soil displacement measured by means of the artificial gravel particles placed on top of the reinforced soil mass. Figures 9.128a through 9.128d show the soil displacement with respect to reinforcement nodal displacement u1, u3, u5, and u7. Both tests showed dilation near the front side of the reinforced soil mass and settlement near the rear side. Larger dilation and at the front was observed in case of the test conducted with the Mylar passive layers compared to that compared with the geotextile passive layers. This is because more soil was affected by the load transferred from the active reinforcement layer mobilizing more deformation in the soil. Similar settlement was measured at the back for both tests.

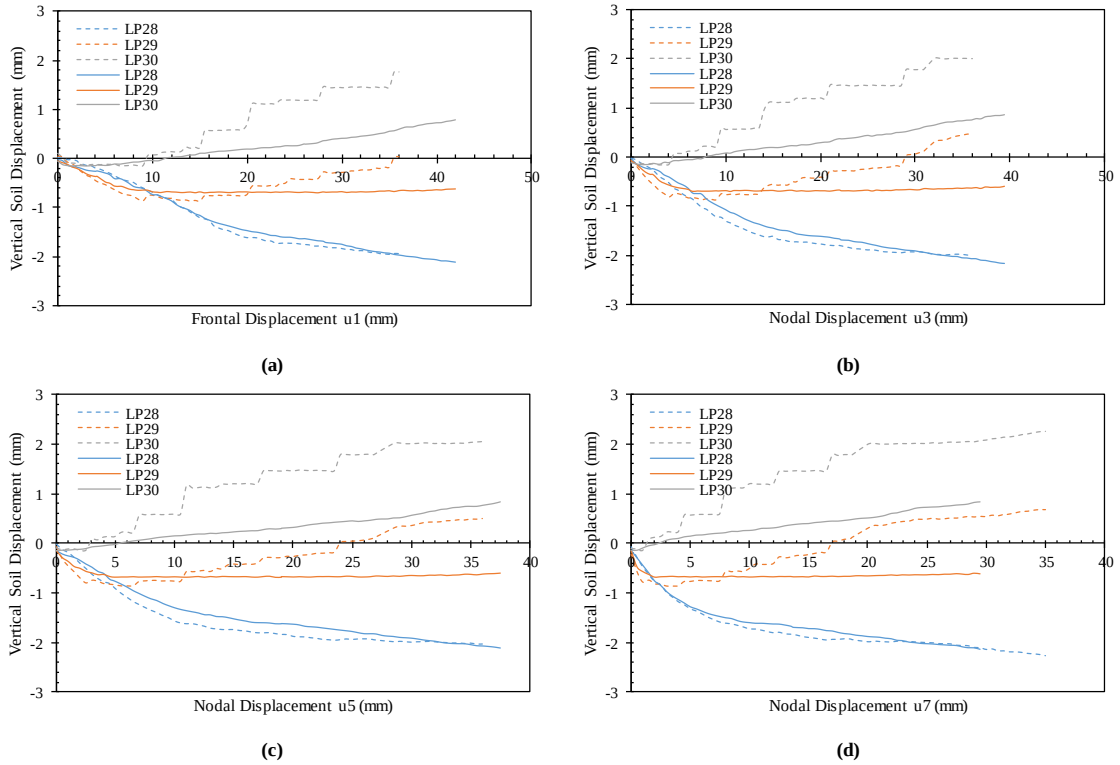

Figure 9.128. Vertical soil displacements (measured by means of artificial gravel particles) with respect to various nodal displacements at the active reinforcement: (a) Nodal displacement u1; (b) Nodal displacement u3; (c) Nodal displacement u5; and (d) Nodal displacement u7 (solid lines belong to HP570 and dashed lines belong to Mylar).

9.3.6. Effect of fill material properties

In order to assess the effect of backfill properties (type, angle of internal resistance, cohesion, gradation, and particle characteristics) on the interaction between the contiguous reinforcement layers in GRS structures, tests should be conducted at the same testing conditions using various backfill types of wide range of properties to capture their effects. This assessment is deemed tedious and very time demanding as it requires a large number of tests to provide reliable conclusions. Such assessment can, however, be conducted using numerical analysis methods to extrapolate the finding from this study. The testing program included two tests were conducted using different soils and three HP570 woven geotextile reinforcement layers placed at a vertical spacing of 0.15 m (6 in.) and normal normal pressure of 21 kPa (3 psi) at the level of the active reinforcement layer. This section presents a comparison between two backfill materials that were used in these tests: AASHTO Gravel # 8 and Monterey Sand No. 30. Both soils are uniformly graded but with a large different in the particle size classified as GP and SP according to the Unified Soil Classification System (USCS), respectively. Detailed information about the properties of these materials is in Chapter 7. This comparison can provide information about the effect of particle size the soil deformation patters around a loaded reinforcement layer. Table 9.7 summarizes the tests in which fill material type was varied.

Table 9.7. Summary of tests in which fill material type was varied.

Test ID	*Testing Variables*					
	Fill Material	S_v	σ_v	*Active GS*	*Passive GS*	*Dilation*
GP-06-03-G1-G SP-06-03-G1-G	AASHTO No. 8 Monterey No. 30	0.15 m	21 kPa	HP570	HP570	Allowed

Figure 9.129 shows the frontal pullout load-displacement experimental curves for both tests. The results indicate that both the pullout resistance obtained from the test conducted using Monterey Sand No. 30 was higher that obtained from the test conducted

using AASHTO Gravel No. 8 at working stress and ultimate stress conditions. This observation showed that the soil-reinforcement interface shear strength was higher between HP570 woven geotextile and sand than that between HP570 woven geotextile and gravel. This is not essentially true other reinforcement type was used. For instance, reinforcements with high bearing resistance (e.g., geogrids) may provide between interaction with gravel that with sand depending on several parameters such as bearing rib thickness and grid aperture size relative to particle size. For geotextile reinforcements in which the main contribution in the pullout resistance is the interface friction, the contact total area the soil make with the reinforcement plays an important role in mobilizing the interface strength. Note that the friction angles of both fill materials used in this study are very close. However, sands (small grain size) can provide a high contact with the geotextile that gravels (large grain size). In addition, small particles can enter between the yarns of the geotextile enhancing the leverage the soil can have on the reinforcement. This happens to lower extent with gravel because of the less number of particles in contact with the reinforcement. Note that, however, at high pullout loads gravel particles can punch holes into the reinforcement enhances its grip to the soil.

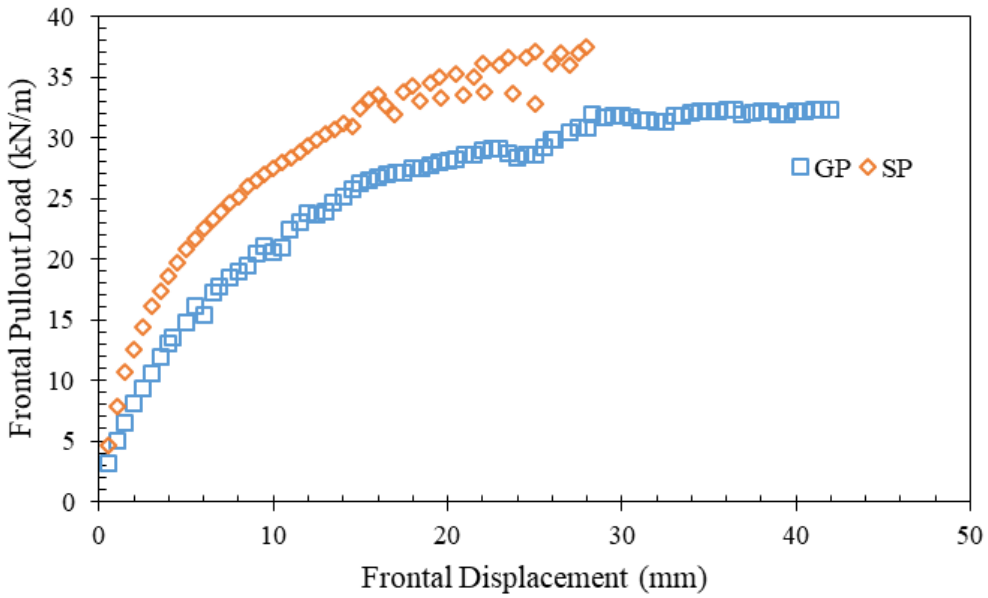

Figure 9.129. Frontal pullout load-displacement curves.

In order to compare the interaction between the reinforcement layers in the two different soil media, the interface shear displacement imposed should be similar. This could be done by comparing the integrated displacement of the active reinforcement to those of the passive reinforcements. This integrated displacement can be represented by the average reinforcement displacement. Figures 9.130a and 9.130b show that average displacements of upper and lower passive reinforcements, respectively, with respect to average displacements of active reinforcement.

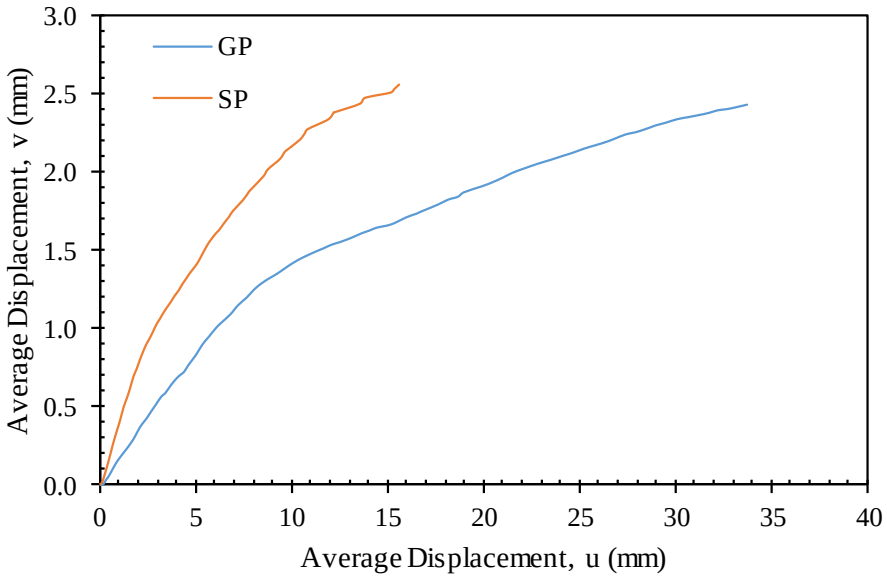

(a)

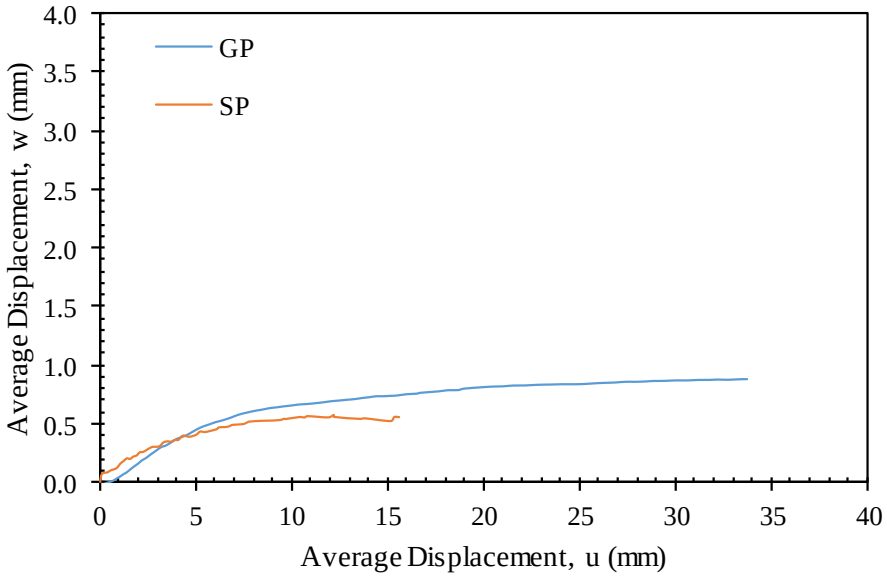

(b)

Figure 9.130. Average displacements of passive reinforcements with respect to average displacements of active reinforcement: (a) Upper passive reinforcement; and (b) Lower passive reinforcement.

Figures 9.131 through 9.134 show the displacement profiles for the active and passive reinforcement layers at active reinforcement frontal displacements (u1) of 5, 10, 15, and 20 mm, respectively. Note that the comparison is based on the same frontal displacement for the active reinforcement layer rather than the same pullout frontal load. The displacements measured for the active reinforcement layer for the test conducted with Monterey Sand No. 30 were lower than those measured for the test conducted with AASHTO Gravel No. 8. This difference increased as pullout progressed. On the other hand, the profiles of the passive reinforcement layers showed higher displacement values for the test conducted with Monterey Sand No. 30 than that conducted with AASHTO Gravel No. 8. The difference tend to vanish and reverse at high pullout loads. This is explained by the displacement profile of the active reinforcement. The reinforcement gripped with gravel mobilized more soil to transfer load for the same frontal displacement value. That is, the comparison between the displacement profiles of passive reinforcements tested at different normal stresses cannot evaluate the effect of normal stress magnitude on the interaction among neighboring reinforcements.

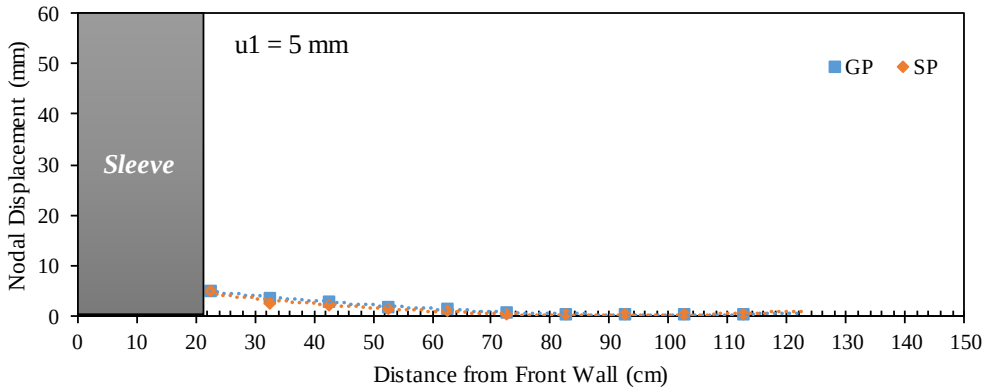

(a)

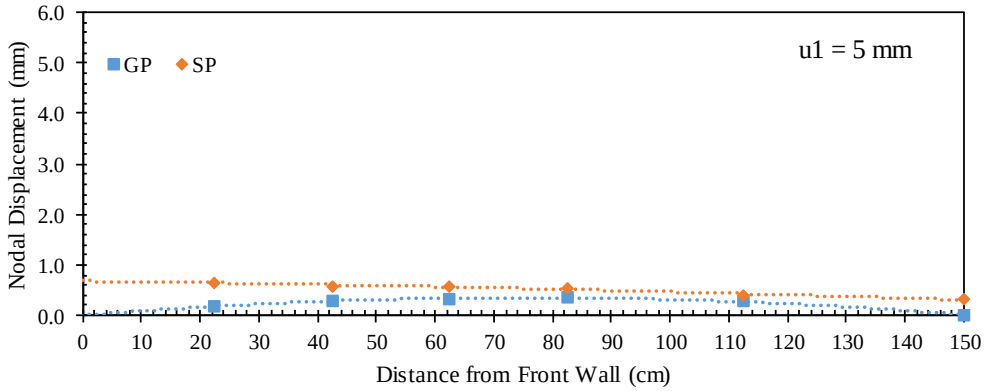

(b)

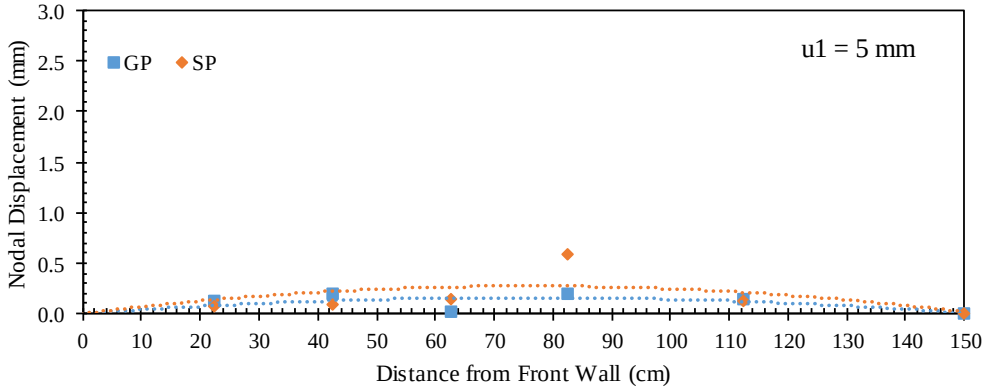

(c)

Figure 9.131. Reinforcement displacement profiles at frontal displacement u1 = 5 mm: (a) Active reinforcement; (b) Upper passive reinforcement; and (c) Lower passive reinforcement.

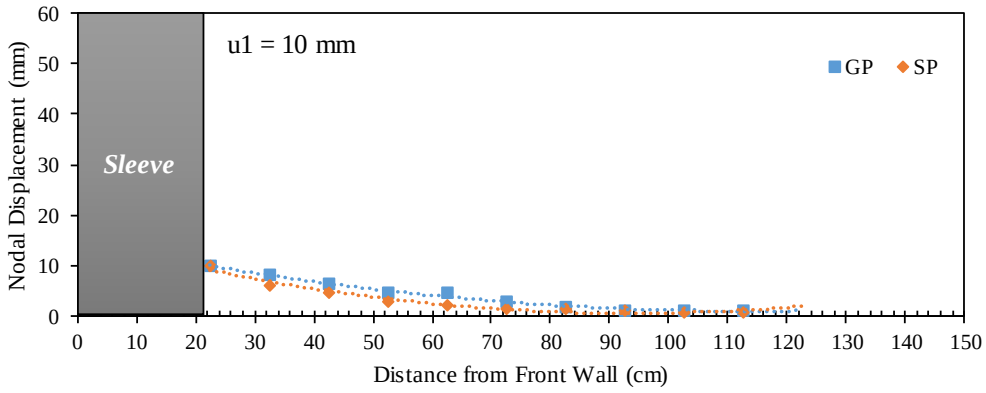

(a)

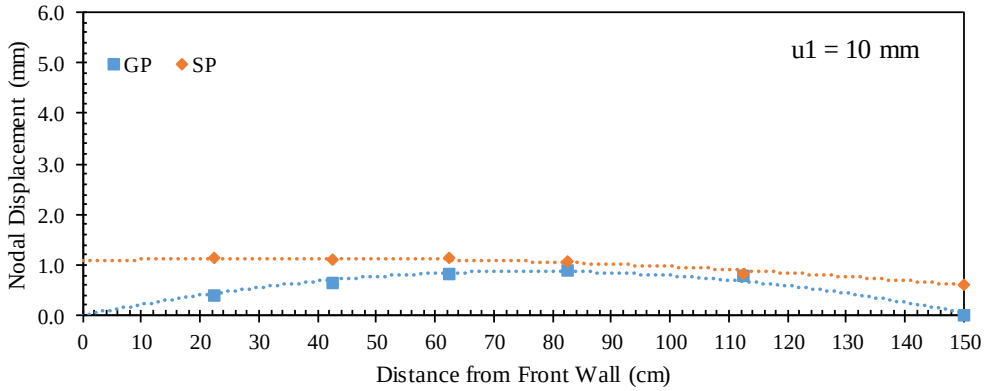

(b)

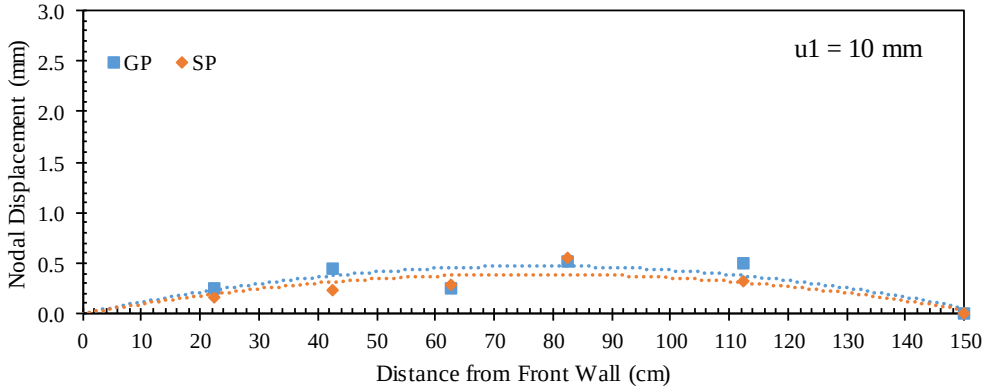

(c)

Figure 9.132. Reinforcement displacement profiles at frontal displacement u1 = 10 mm: (a) Active reinforcement; (b) Upper passive reinforcement; and (c) Lower passive reinforcement.

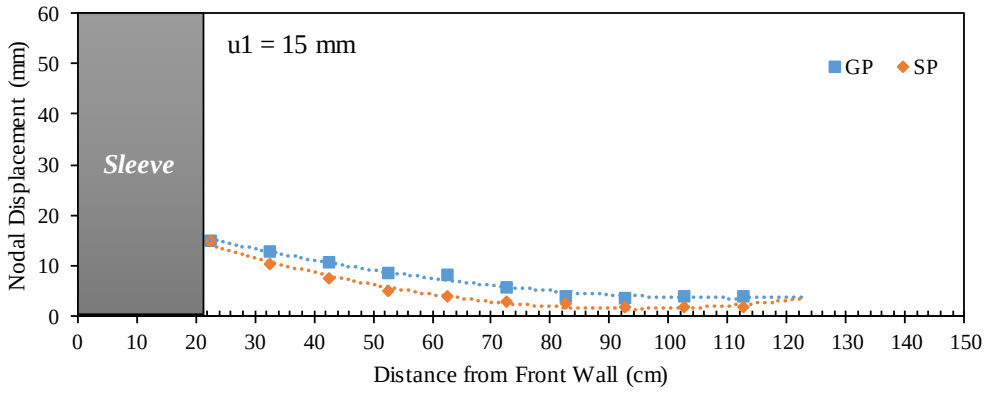

(a)

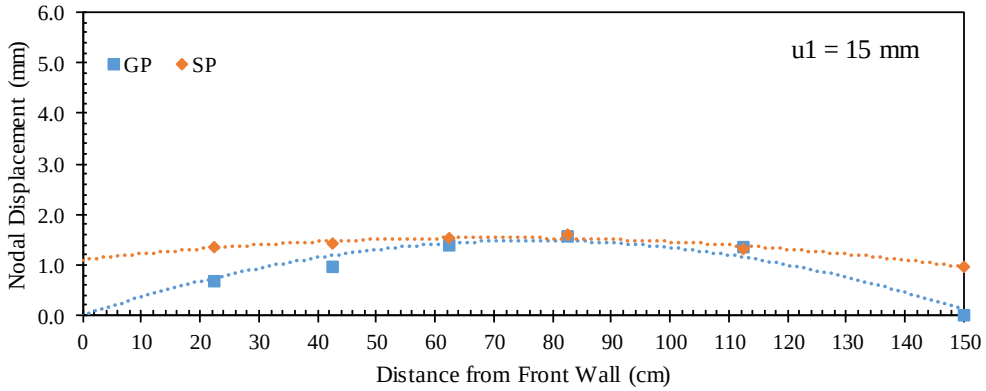

(b)

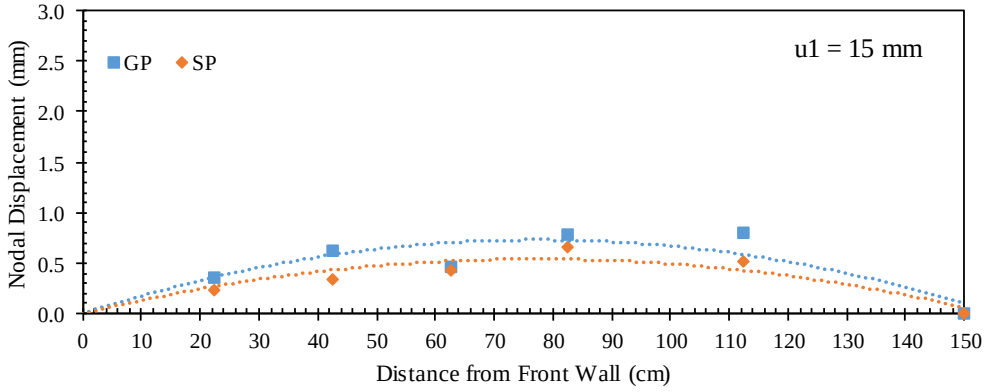

(c)

Figure 9.133. Reinforcement displacement profiles at frontal displacement u1 = 15 mm: (a) Active reinforcement; (b) Upper passive reinforcement; and (c) Lower passive reinforcement.

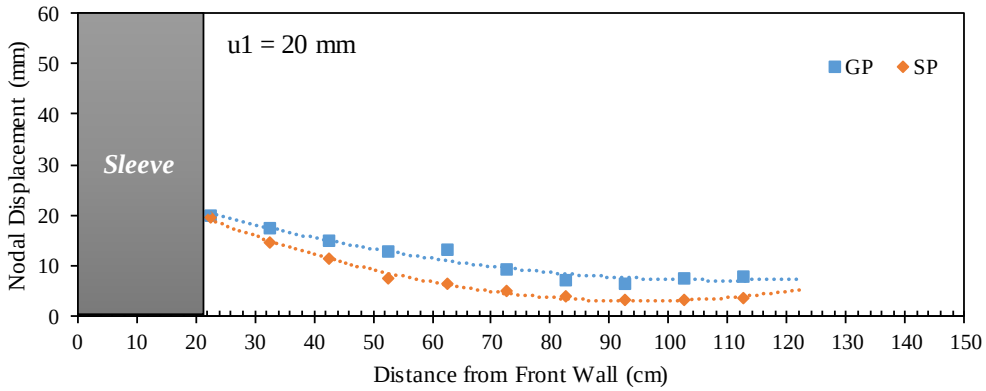

(a)

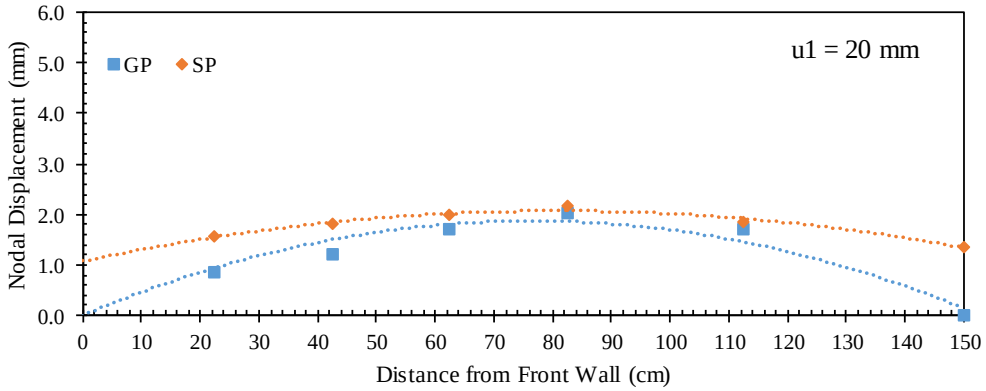

(b)

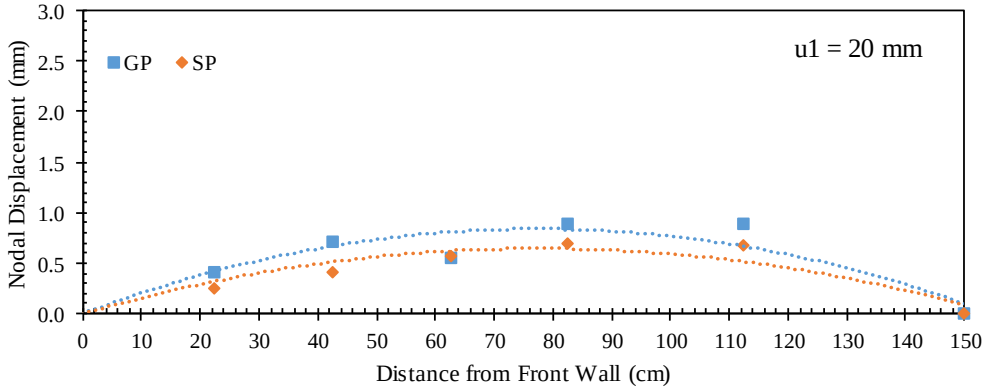

(c)

Figure 9.134. Reinforcement displacement profiles at frontal displacement u1 = 20 mm: (a) Active reinforcement; (b) Upper passive reinforcement; and (c) Lower passive reinforcement.

Figures 9.135 through 9.137 present the horizontal soil displacement measured for nodal displacements of 5, 10, and 15 mm, respectively. Each figure consists of a and b that show the soil displacement with respect nodal displacements u1 and u3, respectively. These displacement were measured at specific locations by tracking artificial gravel particles making a vertical array within the soil at 30.5 cm from the front wall. The results indicate that the soil displacements measured in case of Monterey Sand No. 30 was higher than those measured in case of the AASHTO Gravel No. 8. However, the soil adjacent to the reinforcement exhibited higher rate of displacement in case of the AASHTO Gravel No. 8 that the displacement magnitudes surpassed those in case of Monterey Sand No. 30. This was due to yielding in the internal shear strength of the AASHTO Gravel No. 8 fill material, which had a slightly lower friction angle that that of Monterey Sand No. 30. This yielding limited the load transfer from the reinforcement to larger distance away from the reinforcement.

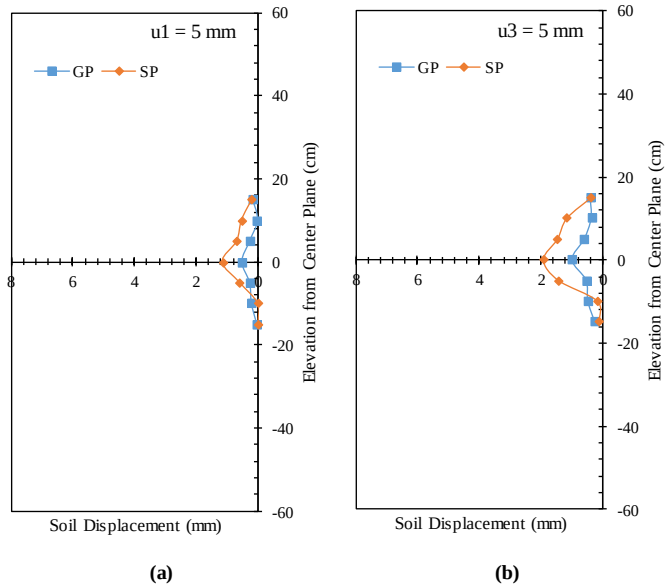

Figure 9.135. Horizontal soil displacement profiles (measured by means of artificial gravel particles): (a) At nodal displacement u1 = 5 mm; and (b) At nodal displacement u3 = 5 mm.

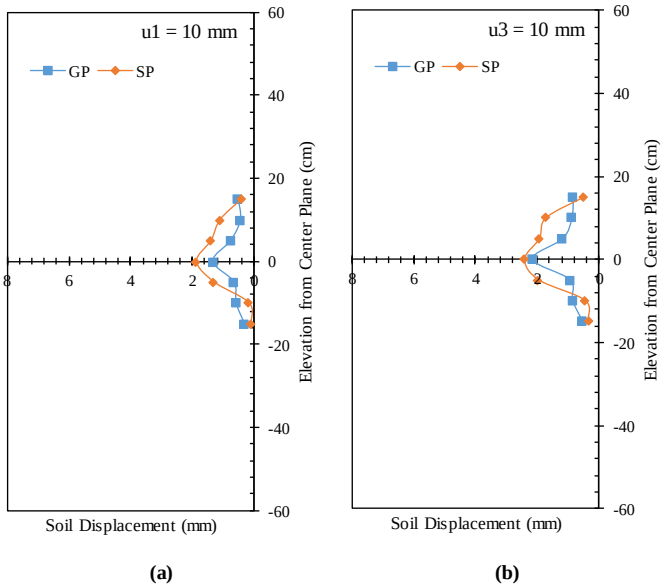

Figure 9.136. Horizontal soil displacement profiles (measured by means of artificial gravel particles): (a) At nodal displacement u1 = 10 mm; and (b) At nodal displacement u3 = 10 mm.

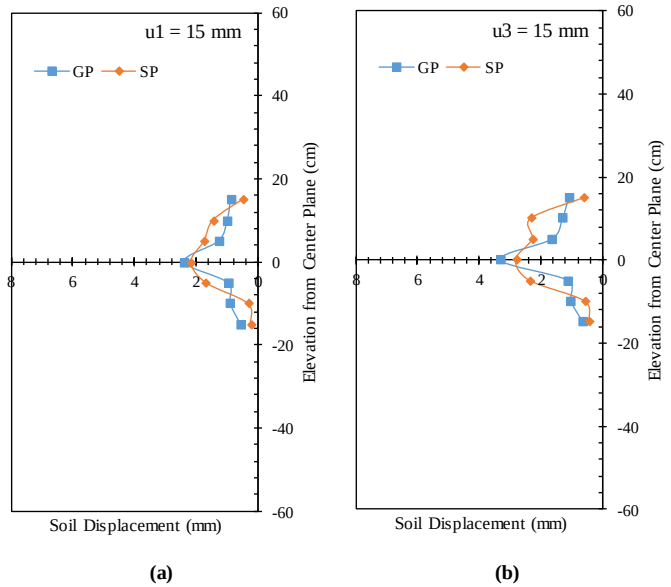

(a) **(b)**

Figure 9.137. Horizontal soil displacement profiles (measured by means of artificial gravel particles): (a) At nodal displacement u1 = 15 mm; and (b) At nodal displacement u3 = 15 mm.

Figure 9.138 shows the soil-reinforcement relative displacement magnitude at 30.5 cm from the front wall. This relative displacement was obtained by subtracting the reinforcement displacement at this location (by interpolation between u1 and u3) and the soil displacement measured by the artificial gravel particle adjacent to the reinforcement (LP24). The results indicate that the relative displacement at the reinforcement interface was higher in the case AASHTO Gravel No. 8 compared to that in the case Monterey Sand No. 30. This difference was due to the difference in the soil-reinforcement interaction between the two fill materials with the reinforcement.

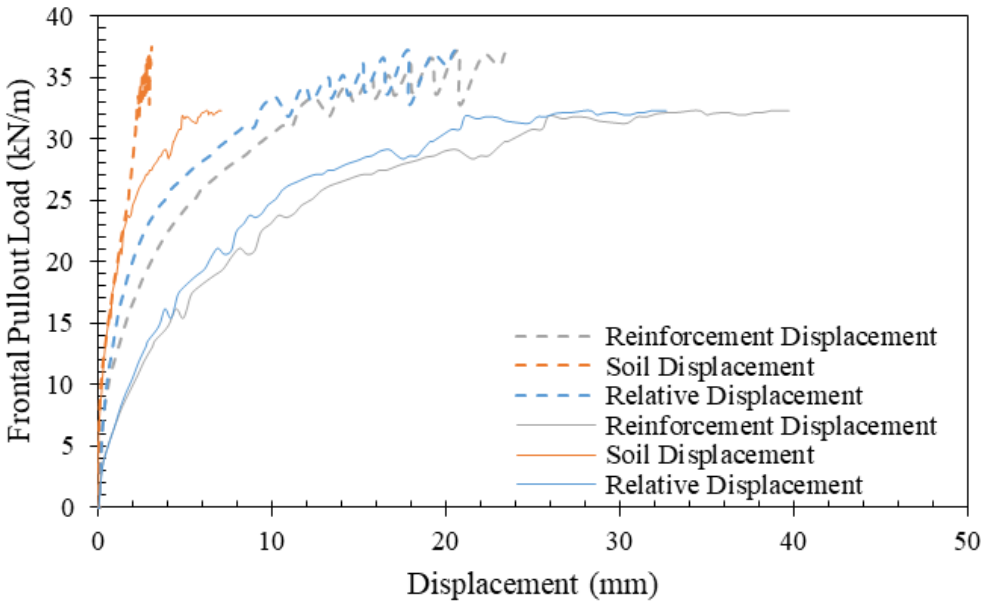

Figure 9.138. Soil-reinforcement relative displacement magnitude (solid lines belong to GP and dashed lines belong to SP).

9.4. CONCLUSIONS

A comprehensive testing program has been conducted adopting the developed experimental approach and equipment detailed in Chapter 8. The testing program was tailored to evaluate the following aspects: (1) test repeatability; (2) effect of reinforced soil normal stress; (3) effect of reinforcement vertical spacing; (4) effect of reinforcement properties; (5) effect of boundary type; and (6) effect of backfill properties. The findings from this study are summarized in the following subsections:

9.4.1. Evaluation of test repeatability

Two identical tests were conducted to evaluate the test repeatability of the developed experimental approach and equipment. This evaluation led to the following findings:

- The frontal pullout load-displacement experimental curves for both tests almost coincided.
- The displacement profiles for the active and passive reinforcement layers were found to match well at the various loading stages. Similar observation was made for the displacement profiles of the passive reinforcement layers.
- The horizontal soil displacement was very similar for both tests at the various loading stages.

9.4.2. Evaluation of the effect of reinforced soil normal stress

This evaluation was carried out through three comparisons for test groups having different reinforcement vertical spacing: (1) a comparison between four similar tests conducted at different normal stresses with reinforcements spaced at 0.15 m (6 in.); (2) a comparison between two similar tests conducted at different normal stresses with reinforcements spaced at 0.10 m (4 in.); and (3) a comparison between two tests conducted at different normal stresses with reinforcements spaced at 0.05 m (2 in.). This evaluation led to the following findings:

- The frontal pullout load-displacement experimental curves showed that the resistance of the active reinforcement to pullout increases with the increase in the normal stress. Same observation was made for test groups of different reinforcement vertical spacing.
- The soil-reinforcement interface shear strength increases with increasing normal stress.
- The tests conducted at low normal stresses tend to mobilize displacement in the passive reinforcements more those conducted at higher normal stresses at early pullout loading stages. This is because the flexibility of soil to

deform at low normal stresses resulting in higher load transfer and thus higher interaction between reinforcements. However, as pullout progressed the soil-reinforcement interface stiffness yielded more in the tests conducted at low normal stresses compared to this of the tests conducted at higher normal stresses.

- By comparing the integrated nodal displacement measured for the passive reinforcements occurring at the same corresponding integrated nodal displacement for the active reinforcement, it was concluded that the higher the normal stress the higher the interaction between neighboring reinforcement layers. This, however, was pronounced only after the interface strength yields, which occurs earlier at low normal stresses.
- At high normal pressures, the soil, which is the medium responsible to transfer the load, is stiffer and can more transfer load before yielding either internally or at the interface with reinforcements.
- The reinforcement vertical spacing has insignificant effect on the sensitivity of the reinforcement interaction to the normal stress level.
- The relative displacement at the interface of the active reinforcement was higher in the tests conducted at low normal stresses compared to those conducted at high normal stresses.
- The vertical soil displacement measured at the top of the reinforced soil mass showed that the soil tended to dilate near the front and settle near the back as pullout loading progressed. It was observed that the dilation was higher in tests conducted at low normal stresses. At low normal stresses soils tend to dilate more when subjected to shear compared to soils at high

normal stresses. Similar observation were made for tests conducted with reinforcements placed at different reinforcement vertical spacing.

9.4.3. Evaluation of the effect of reinforcement vertical spacing

Two comparisons were carried out between test groups having different normal stress: (1) a comparison between six tests conducted at normal stress of 50 kPa and with reinforcements placed at different vertical spacings; and (2) a comparison between three tests conducted at normal stress of 21 kPa and with reinforcements placed at different vertical spacings. This evaluation led to the following findings:

- At high normal stress, the frontal pullout load-displacement experimental curves coincided well at early pullout loading stages and then fairly agree with slight scatter near pullout failure. This observation shows that the reinforcement vertical spacing has insignificant interference with the soil-reinforcement interaction. However, at low normal stress, the frontal pullout load-displacement experimental curves, tests conducted at smaller reinforcement vertical spacing.
- The interface shear strength back-calculated from the pullout test results at ultimate condition were found higher than that resulting from direct shear testing conducted as a part of the study detailed in Chapter 7. This was attributed to the additional passive resistance that mobilizes in pullout tests with flexible reinforcements through punch holes by adjacent gravel particles. These holes were absent in case of the direct shear testing.
- The tests conducted with reinforcements placed at larger vertical spacing resulted in small interaction between neighboring reinforcements.

- The reinforcement vertical spacing has insignificant impact on the soil-reinforcement interaction behavior of the active reinforcement.
- A lower threshold bound for reinforcement vertical spacing below which the effect of the spacing is maximum was identified. This spacing is specific for a normal stress, soil medium properties, reinforcement properties, soil-reinforcement interaction properties. For the testing program implemented in this study, the lower threshold vertical spacing was reasonably identified as 0.10 m for normal stress range of 15 to 50 kPa.
- An upper threshold bound for reinforcement vertical spacing beyond which the interaction between reinforcement layers almost vanished was identified. Similarly, this spacing is specific for a normal stress, soil medium properties, reinforcement properties, soil-reinforcement interaction properties. For the testing program implemented in this study, the upper threshold vertical spacing was reasonably identified as 0.3 m for normal stress range of 15 to 50 kPa.
- The horizontal soil displacement was higher in the tests conducted with reinforcements placed at small spacings. That was because the soil-reinforcement interfaces of the passive reinforcements have weaker shear strength than the internal strength of the soil. These weaker interfaces allowed the soil in between the reinforcement layers to displace more than in the case of no passive reinforcements. However, the passive reinforcements reduced the load transfer from the active reinforcement to the soil masses on the other sides of the passive reinforcements.

- For each testing group, the same energy was delivered from the active reinforcement to the soil and the passive reinforcements. For the tests conducted with reinforcements placed at small vertical spacings, the soil mass in between the active and passive reinforcements displaced more as it received more energy per unit soil volume from the active reinforcement. On contrary, the soil masses on the other sides of the passive reinforcements displaces less than that in the tests conducted with reinforcements placed at small vertical spacings.
- The relative displacement at the soil-reinforcement interface was smaller in tests conducted with reinforcements placed at small vertical spacings. That was because the displacement of the soil adjacent to the reinforcements in tests conducted with reinforcements placed at small vertical spacings was higher.
- The vertical soil displacement measured at the top of the reinforced soil mass showed that the soil tended to dilate near the front and settle near the back as pullout loading progressed. The dilation tendency near the front takes place after settlement in early loading stages as shear stresses were generated at the soil-reinforcement interface. The dilation tendency was higher in the tests conducted with reinforcements placed at smaller spacings.
- The dilation tendency was high in tests conducted at low normal stresses compared to those conducted at high normal stresses. That is, the impact of reinforcement vertical spacing on the soil-reinforcement behavior was more pronounced in the tests conducted at 21-kPa normal stress.

9.4.4. Evaluation of the effect of reinforcement properties

Three comparisons were carried out to evaluate various reinforcement properties: (1) a comparison between HP570 and RS580i reinforcements to evaluate the effect of reinforcement tensile stiffness; (2) a comparison between HP570 and 80T reinforcements to compare the behavior of geotextiles and geogrids; and (3) a comparison between 80T and BX1200 to evaluate the effect of reinforcement rigidity. This evaluation led to the following findings:

- The frontal pullout load-displacement curves cannot provide full understanding about the soil-reinforcement interaction. A deeper look into the behavior of each reinforcement along their embedment length is needed to complement the information retrieved about the front.
- The higher the soil-reinforcement interaction, the higher the ability of the reinforcement to transfer load to the soil and the neighboring reinforcement layers for a given soil medium and normal stress level.
- The soil-reinforcement interaction comprises two components: (1) the passive resistance that can be mobilized by the transverse members. The members can be transverse ribs in geogrids or transverse yarns in geotextiles if particles were able to interfere with the geotextile fabric; and (2) the soil-reinforcement interface friction (interface shear resistance).
- Geotextile reinforcements with similar soil-reinforcement interface friction may have different soil-reinforcement interaction. The fabric rigidity plays a significant role in the interaction between the fabric and the surrounding soil medium that adds additional resistance to the interface friction. Passive resistance against adjacent soil particles punching in the fabric can

contribute to the soil-reinforcement interaction. This interaction resembles the interaction takes place due to passive resistance of transverse ribs in geogrid reinforcements.

- The contribution of the passive resistance to the soil-reinforcement interaction is likely to outweigh the contribution of the interface friction.
- The higher the soil-reinforcement interaction, the lower the relative displacement at the soil-reinforcement interface.
- The higher the soil-reinforcement interaction, the larger the horizontal soil displacement.
- The soil adjacent to active reinforcements exhibited higher rate of displacement than the soil away from reinforcements. This is because of the yielding in internal shear strength of the fill material that limits the load transfer from the reinforcement to larger distance away from the reinforcement.
- The vertical soil displacement measured at the top of the reinforced soil mass showed dilation near the front side of the reinforced soil mass and settlement near the rear side. The higher the soil-reinforcement interaction, the higher the dilation at the front and the settlement at the back.

9.4.5. Evaluation of the effect of boundary type

Two similar tests were conducted with the same active reinforcement layer and different passive layers. One tests employed the same reinforcement type as the active layer and the other employed layers of smooth material. This evaluation led to the following findings:

- The frontal pullout load-displacement experimental curves were very similar curves with slight difference close to pullout failure. That is, the soil-reinforcement interface shear behavior remained unchanged upon changing the interface condition of passive reinforcements.
- Smooth layers were found to create weak planes in the reinforced soil mass that allowed soil to slide on as the load of the active reinforcement was transferred with less energy loss in the in between soil medium.
- Higher displacements were measured for the smooth passive reinforcements.
- The horizontal soil displacement was higher for the test conducted with smooth boundaries. The soil adjacent to the reinforcement in the test conducted with smooth boundaries did not exhibit significant difference in displacement compared to the soil away from the active reinforcement. The reduction in interface stiffness occurred along the weak smooth interface before occurring in the soil medium.
- The relative displacement magnitude at the soil-reinforcement interface was lower in the test conducted with smooth boundaries.
- The vertical soil displacement measured at the top of the reinforced soil mass showed larger dilation tendency for the test conducted with smooth boundaries. This was because more soil was affected by the load transferred from the active reinforcement layer mobilizing more deformation in the soil.

Chapter 10: Conclusions and Recommendations for Future Studies

10.1. GENERAL REMARKS

This chapter includes the conclusions and recommendations for future studies. The conclusions section synthesizes the findings from the different studies involved in this dissertation. The recommendations for future studies section proposes expansion to the conducted study to enrich its findings.

10.2. CONCLUSIONS

10.2.1. Conclusions from Section I: Reevaluation of Data from the Literature

Given the individual objectives and the specific background of each study involved in this section, the information in each chapter is presented in a self-contained manner. Specifically, the objectives, background, conclusions, and references were separately indicated in each chapter. A summary of the main findings reached in each study of Section I are summarized below.

10.2.1.1. Evaluation of the Performance of Large-Scale Experimental Geosynthetic-Reinforced Soil Structures

Chapter 3 aimed at evaluating the design models reported in the FHWA GRS-IBS design guidelines. It should be noted that the experimental data reported in the reviewed research studies points towards the effect of reinforcement vertical spacing in reducing the lateral deformation and settlement, and increasing the bearing capacity of the reinforced soil mass.

The empirical design proposed by FHWA using the vertical stress-strain envelopes from a representative GRS Performance Test (Mini-Pier) was reevaluated at working stress levels (vertical stresses below 200 kPa). While the proposed envelopes were found to provide a very good repeatability on the full range of vertical stress-strain relationship,

reassessment of the data was found not to be repeatable at working stress levels. In addition, the comparison conducted on the behavior of GRS structures of comparable materials and different boundary conditions revealed differences in performance (structural vertical and lateral deformation). A relevant outcome of the reassessment is that the difference in the boundary conditions between test piers and actual abutments may need to be taken into consideration to predict the behavior of GRS structures.

The FHWA design guidelines do not account for the possible failure that can take place at the facing connection because the expected lateral earth pressures are small when the reinforcement layers are placed at comparatively close vertical spacings. However, reassessment of the collected data revealed that the reduction of lateral earth pressure due to the decrease in the reinforcement spacing could still be considered, although as a function in the reinforcement spacing and the type of backfill material used in the GRS structure.

10.2.1.2. Soil Arching in Geosynthetic-Reinforced Soil Structures

The study presented in Chapter 4 involved compilation and reevaluation of data from studies conducted on the possible composite nature of geosynthetic-reinforced soil masses. The outcome of the reassessment of the data indicated that the interaction of reinforcement layers in a geosynthetic-reinforced structure may be significant and could render a composite material behavior. It was reported in the reviewed studies that the soil mass between closely-spaced reinforcements can strain monolithically with the reinforcements without mobilizing interface shear stresses due to soil arching. It was also learned that the critical failure planes in geosynthetic-reinforced soil structures with closely-spaced reinforcement are likely to occur behind the reinforced soil zone and not internally, i.e., the reinforced soil mass is likely to act as a composite mass (one big block).

It was also learned that closely-spaced reinforcements can significantly reduce the lateral stresses acting against the wall facing.

10.2.1.3. Effect of Reinforcement Spacing on the Behavior of Geosynthetic-Reinforced Soil Centrifuge Models

The study presented in Chapter 5 consolidated and analyzed data from a large number of GRS centrifuge models reported in literature. While various aspects may have been the focus of the original data, the focus of this reassessment was on models in which the reinforcement vertical spacing was varied. The reassessment of data indicated that reducing the reinforcement vertical spacing increases the overall structural stability of the GRS walls even with small L/H ratios. Specifically, the reassessment of data indicated that decreasing the reinforcement spacing mitigates the lateral earth pressures on the facing resulting in less lateral deformation and thus less vertical deformation (settlement). The reassessment of data indicated that GRS structures constructed with the same total reinforcement tensile capacity ($\sum T_f$) and total reinforcement stiffness ($\sum J$) were found to perform differently if their reinforcements were placed at different vertical spacing. Specifically, using a comparatively large number of reinforcement layers of comparatively low tensile strength and stiffness but placed at a comparatively small vertical spacing can result in a better overall structural performance than a comparable structure with reinforcements of strong tensile strength and stiffness but placed at a large vertical spacing. This difference in performance is because of the large number of soil-reinforcement interfaces in structures with closely-spaced reinforcement. The large number of interfaces enhances the compatibility between the soil and the reinforcement layers. Overall, GRS structural performance at working stress conditions shown by centrifuge data reassessment was found to be controlled by reinforcement vertical spacing, reinforcement stiffness, soil-

reinforcement interface stiffness, and perhaps soil stiffness. All of which are needed to render proper design of GRS structures.

10.2.1.4. Assessment of the Founders/Meadows Geosynthetic-Reinforced Soil Bridge Abutment Performance

The study presented in Chapter 6 revisits the performance data of the Founders/Meadows bridge case study, which is considered a major milestone for the evolution of this technology in the United States of America. The study aimed at providing better understanding of the behavior of GRS abutments. The reassessment of data indicated that found that GRS abutments can efficiently alleviate the bumps at the ends of bridges by allowing even settlement for bridge superstructures and their approaching roadway structures. The reassessment of data indicated that the footings resting on GRS abutments were found not to tend to overturn as they are capable of accommodating eccentricity through redistribution of the vertical earth pressure due to the flexibility of geosynthetic-reinforced soil masses.

Down-drag forces generate on the back surface of the facing were found to result in an initial increase in the vertical earth pressure behind the facing in the early construction stages. This down-drag force is induced by the soil settlement behind the facing blocks dragging the reinforcement layers. These dragging forces pulls the facing units inwards and resulting in higher lateral earth pressure. The increase in lateral earth pressure near is the top is anticipated to exceed that near the bottom because the cumulative settlement magnitude near the top is larger than that near the bottom. The reassessment of data indicated that the lateral earth pressure on the abutment facing is susceptible to seasonal temperature variation due to superstructure expansion and contraction, especially in regions with large temperature difference between summer and winter.

10.2.2. Conclusions from Section II: Evaluation of Soil-Reinforcement Composite Interaction and Shear Band Characterization

The study presented in Section II involved the development of a new soil-geosynthetic interaction device to assess the soil-reinforcement interaction and its effect on neighboring reinforcements under both working and ultimate stress conditions. This new device used a geosynthetic-reinforced soil mass that contains three reinforcement layers. The study also involved a comprehensive testing program tailored to evaluate the following aspects: (1) test repeatability; (2) effect of reinforced soil normal stress; (3) effect of reinforcement vertical spacing; (4) effect of reinforcement properties; (5) effect of boundary type; and (6) effect of backfill properties.

The developed soil-geosynthetic device was found to successfully assess the composite interaction in a geosynthetic-reinforced soil mass considering variable reinforcement vertical spacing. Specifically, the device could measure the load transfer from an active (loaded) reinforcement layer to its two passive reinforcement layers. The device allowed direct visualization of the kinematic response of soil particles adjacent to the geosynthetic reinforcements via digital imaging, which facilitated identifying the shear band (zone of shear stress influence) of the soil-reinforcement interface. The device could measure the soil dilatancy of the reinforced soil mass, which can provide significant insight into the effect of reinforcement vertical spacing on the performance of geosynthetic-reinforced soil structures. The soil-geosynthetic interaction device was found to produce repeatable results of reinforcement and soil displacements. The main findings from the experimental component of this study can be summarized as follows:

- Increasing normal stress resulted in increased interaction between neighboring reinforcement layers. This increase, however, was pronounced only after yielding of the interface strength, which occurs earlier at low

normal stresses than at high normal stresses. At high normal pressures, the soil, which is the medium responsible to transfer the load, is stiffer than at low normal pressures and can more transfer load before yielding either internally or at the interface with reinforcements. In addition, the relative displacements at the interface were found to decrease with increasing normal stresses (higher soil-reinforcement displacement compatibility).

- The interlayer reinforcement interaction was found to increase with decreasing the reinforcement spacing. A lower threshold bound for reinforcement vertical spacing ($S_{v,cr,l}$) below which the effect of the spacing is maximum could be quantified in this study. This spacing depends on normal stress, soil medium mechanical properties, reinforcement mechanical properties, soil-reinforcement interaction mechanical properties. For the testing program implemented in this study, the lower threshold vertical spacing was reasonably identified as 0.10 m for normal stresses ranging from 15 to 50 kPa. In addition, an upper threshold bound for reinforcement vertical spacing ($S_{v,cr,u}$) beyond which the interaction between reinforcement layers became negligible (no load was identified to have been transferred from active reinforcement to passive reinforcements) could be quantified in this study. Also in this case, this spacing depends on normal stress, soil medium mechanical properties, reinforcement mechanical properties, soil-reinforcement interaction mechanical properties. For the testing program implemented in this study, the upper threshold vertical spacing was reasonably identified as 0.3 m for normal stresses ranging from 15 to 50 kPa.

- As the reinforcement spacing decreases the soil mass between the reinforcements tends to displace more with the displacement of the reinforcement. At small reinforcement spacing the soil between the reinforcement layers received more stresses from the load being transfer from the soil-reinforcement interface. In addition, the relative displacement at the soil-reinforcement interface was found to decrease with decreasing reinforcement spacings. That is, the displacement compatibility between the soil and the reinforcement was found to increase with decreasing the reinforcement vertical spacing.
- The dilatancy of the reinforced soil mass upon shearing the soil-reinforcement interface was found to increase with decreasing normal stresses. In addition, the dilatancy was found to increase with decreasing reinforcement spacing as the soil tended to displace with the reinforcement increasing the shear stresses in the soil mass between the reinforcement layers.
- The higher the soil-reinforcement interaction, the higher the soil-reinforcement displacement compatibility (and lower relative displacement at the soil-reinforcement interface), and the higher the ability of the reinforcement to transfer load to the soil and the neighboring reinforcement layers for a given soil medium and normal stress level.
- The soil-reinforcement interaction comprises two components: (1) the passive resistance that can be mobilized by transverse members. The members can be transverse ribs in geogrids or transverse yarns in geotextiles if particles were able to interfere with the geotextile fabric; and (2) the soil-

reinforcement interface friction (interface shear resistance). The contribution of the passive resistance to the soil-reinforcement interaction was found to outweigh the contribution of the interface friction. That is, geogrids are more likely to have higher soil-reinforcement interaction than geotextiles.

- Geotextile reinforcements with similar soil-reinforcement interface friction were found not to be necessarily have the same soil-reinforcement interaction. Specifically, the fabric rigidity was found to play a significant role in the interaction between the fabric and the surrounding soil medium that adds additional resistance to the interface friction. Passive resistance against adjacent soil particles punching in the fabric can contribute to the soil-reinforcement interaction. This interaction resembles that taking place in geogrid reinforcements due to passive resistance of transverse ribs.
- The zone of soil-reinforcement interaction influence (shear stress transfer extent) was found to increase with decreasing the soil grain size.

10.3. RECOMMENDATIONS FOR FUTURE STUDIES

This section proposes possible extensions to this study, in order to further extend the research findings and enrich the topic of soil-reinforcement composite interaction.

10.3.1. Extension of findings through experimentation

The shear band thickness, or the zone of influence of soil-reinforcement interaction, was found to be affected by a number of conditions, including the reinforcement tensile stiffness, the deformability and shear strength of the backfill, and the characteristics of the soil-geosynthetic interface. Further experimentation can be conducted to involve wider

ranges of parameters and testing configurations. This shall complement the findings of this study and capture the sensitivity of each testing parameter on the effects other parameters may have on the soil-reinforcement composite interaction (soil-reinforcement interaction and interaction between neighboring reinforcement layers).

10.3.2. Extension of findings through numerical modelling

Numerical modelling is recommended to extrapolate the findings from Section II of this study. This can further investigate the mechanisms of shear development as well as on the effect of influence factors (e.g., reinforcement characteristics, soil properties, soil-reinforcement interface behavior, normal stress) on the geosynthetic-soil interaction and the development of the interface shear band. Specifically, a comprehensive parametric study can be conducted to investigate the effects of influence factors, such as fill material properties (e.g., strength, modulus, dilation angle), reinforcement vertical spacing, normal stress, reinforcement properties (e.g., type, stiffness, interface), and boundary conditions. The study should assess the soil-reinforcement interaction under both working and ultimate conditions.

10.3.3. Extension of findings through field monitoring

It is recommended to evaluate the behavior of full-scale GRS structures. Well-instrumented field structures with instrumentation programs focusing on capturing the behavior soil-reinforcement of neighboring reinforcement layers is expected to lead to data suitable to validate the findings this study and link them to practice. GRS structures that can be instrumented involve single-layered and multi-layered GRS systems. In single-layered systems (e.g., GRS pavements), information about the shear band development can be gathered which can enhance the understanding of soil-reinforcement interaction. In

multi-layered systems (e.g., GRS walls, GRS bridge abutments, GRS platform foundations), information about the shear band interaction between neighboring reinforcement layers can be gathered which can enhance the understanding of the complex composite interactions takes place in GRS structures.

Bibliography

AASHTO (2016). AASHTO LRFD Bridge Design Specifications. Seventh Edition, American Association of State Highway and Transportation Officials (AASHTO).

AASHTO, M. (2008). 145-91. Classification of soil and soil-aggregate mixtures for highway construction purposes, American Association of State Highway and Transportation Officials.

Abdelouhab, A., Dias, D., and Freitag, N. (2010). "Physical and Analytical Modelling of Geosynthetic Strip Pull-out Behaviour." Geotextiles and Geomembranes, Vol. 28, No. 1, pp. 44–53.

Abdel-Rahman, A.H., Ibrahim, M.A., and Ashmawy, A.K. (2007). "Utilization of a Large-Scale Testing Apparatus in Investigating and Formulating the Soil/Geogrid Interface Characteristics in Reinforced Soils." Australian Journal of Basic and Applied Sciences, Vol. 1, No. 4, pp. 415-430.

Abernathy, C. (2013). Geosynthetic-reinforced Soil – Integrated Bridge System (GRS-IBS). Experimental Projects Construction Report. Montana Department of Transportation Research Programs. November 2013.

Abernathy, C. (2014). "Montana DOT Rebuilds an Old Bridge with a New System." Geosynthetics, April 2014, Vol. 32, No. 2.

Abernathy, C. (2015). Geosynthetic-reinforced Soil - Integrated Bridge System (GRS-IBS). Experimental Projects Construction and Site Inspection Report. Montana Department of Transportation Research Programs, June 2015.

Abu-Hejleh, N., Hanneman, D., White, D. J., Wang, T., and Ksouri, I. (2006). Flowfill and MSE Bridge Approaches: Performance, Coast, and Recommendations for Improvements. Colorado Department of Transportation Report No. CDOT-DTD-R-2006-2.

Abu-Hejleh, N., Wang, T., and Zornberg, J.G. (2000b). "Performance of Geosynthetic-reinforced Walls Supporting Bridge and Approaching Roadway Structures." Geotechnical Special Publication, pp. 218-243.

Abu-Hejleh, N., Zornberg, J. G., and Wang, T. (2001b). "Monitored Displacements of a Unique Geosynthetic-Reinforced Walls Supporting Bridge and Approaching Roadway Structures." In TRB annual meeting.

Abu-Hejleh, N., Zornberg, J.G., Elias, V., and Watcharamonthein, J. (2003). "Design Assessment of the Founders/Meadows GRS Abutment Structure." In Proceedings of the 82nd Annual TRB Meeting.

Abu-Hejleh, N., Zornberg, J.G., Wang, T., and McMullen, M. (2001a). Performance of Geosynthetic-Reinforced Walls Supporting the Founders/Meadows Bridge and

Approaching Roadway Structures. Colorado Department of Transportation Report No. CDOT-DTD-R-2001-13.

Abu-Hejleh, N., Zornberg, J.G., Wang, T., and Watcharamonthein, J. (2002). "Monitored displacements of unique geosynthetic-reinforced soil bridge abutments." Geosynthetics International, Vol. 1, pp. 71-95.

Adams, M. and Nicks, J. (2015). "Comparison of GMSE and GRS Design Methodology." In Proceedings of Geosynthetics 2015, February 15-18, Portland, Oregon.

Adams, M., Ketchart, K., Ruckman, A., DiMillio, A.F., Wu, J.T.H., and Satyanarayana, R. (1999). "Reinforced Soil for Bridge Support Applications on Low-Volume Roads." Transportation Research Board, Washington, D.C.

Adams, M., Nicks, J., Stabile, T., Wu, J., Schlatter, W., and Hartmann, J. (2011). Geosynthetic-reinforced Soil Integrated Bridge System, Synthesis Report. Report No. FHWA-HRT-11-027, Federal Highway Administration, McLean, VA.

Adams, M., Nicks, J., Stabile, T., Wu, J., Schlatter, W., and Hartmann, J. (2012). Geosynthetic-reinforced Soil Integrated Bridge System, Interim Implementation Guide. Report No. FHWA-HRT-11-026, Federal Highway Administration, McLean, VA.

Adams, M., Schlatter, W., and Stabile, T. (2007b). "Geosynthetic-Reinforced Soil Integrated Abutments at the Bowman Road Bridge in Defiance County, Ohio." Geosynthetics in Reinforcement and Hydraulic Applications (GSP 165), Gabr, and Bowders (Eds.). ASCE, Reston, VA, pp. 119-129.

Adams, M.T. (1997). "Performance of a Prestrained Geosynthetic-reinforced Soil Bridge Pier," Proceedings of the International Symposium on Mechanically Stabilized Backfill, J.T.H. Wu (Ed.), Balkema, Rotterdam, Netherlands.

Adams, M.T., Ketchart, K., and Wu, J.T. (2007a). "Mini pier experiments–geosynthetic reinforcement spacing and strength as related to performance." Proceedings of Geo-Denver.

Adams, M.T., Lillis, C.P., Wu, J.T.H., and Ketchart, K. (2002). "Vegas GRS Mini Pier Experiment and the Postulate of Zero Volume Change." Proceedings of Geosynthetics 7th ICG, Delmas, Gourc and Girad (eds.), pp. 389-394.

Adams, M.T., Nicks, J.E., Stabile, T., Wu, J.T.H., Schlatter, W., and Hartmann, J. (2012). Geosynthetic Reinforced Soil Integrated Bridge System Interim Implementation Guide. Report No. FHWA-HRT-11-026, Federal Highway Administration, McLean, VA.

Adams, M.T., Schlatter, W., and Stabile, T. (2007b). "Geosynthetic Reinforced Soil Integrated Abutments at the Bowman Road Bridge in Defiance County, Ohio." Proceedings of Geo-Denver, 2007, pp. 01-11.

Alagiyawanna, A.M.N., Sugimoto, M., Sato, S., and Toyota, H. (2001). "Influence of Longitudinal and Transverse Members on Geogrid Pullout Behavior during Deformation." Geotextiles and Geomembranes, Vol. 19, No. 8, pp. 483–507.

Albert, G.R. (2012). Unpublished monitoring data for the Huston Township, Clearfield 585 County Mount Pleasant Road Bridge.

Alexiew and Detert (2008). "Analytical and Numerical Analyses of a Real Scaled Geogrid Reinforced Bridge Abutment Loading Test." EuroGeo4 Paper number 257.

Alexiew, D. (2007) "Belastungsversuch an einem 1:1 Modell eines geogitterbewehrten Bruckenwiderlagers." Proceedings of KGeo 2007, Munich, Germany. (In German).

Alexiew, D. (2008). "Ultimate bearing capacity tests on an experimental geogrid-reinforced vertical bridge abutment without stiffening facing." New Horizons in Earth Reinforcement, Taylor and Francis Group, London, pp. 507-511.

Alexiew, D., Sobolewski, J., and Pohlmann, H. (2000). "Projects and Optimized Engineering with Geogrids from 'Non-Usual' Polymers." EuroGeo 2000: Proceedings of the 2nd European Geosynthetics Conference. Volume 1: Mercer Lecture, Keynote Lectures, Geotechnical Applications.

Alfaro, M.C., Hayashi, S., Miura, N., and Watanabe, K. (1995a). "Pullout Interaction Mechanism of Geogrid Strip Reinforcement." Geosynthetics International, Vol. 2, No. 4, pp. 679-698.

Alfaro, M.C., Miura, N., and Bergado, D.T. (1995b). "Soil-Geogrid Reinforcement Interaction by Pullout and Direct Shear Tests." Geotechnical Testing Journal, GTJODJ, Vol. 18, No. 2, pp. 157-167.

Allen, T. M., Bathurst, R. J., Holtz, R. D., Walters, D., and Lee, W. F. (2003). "A new working stress method for prediction of reinforcement loads in geosynthetic walls." Canadian Geotechnical Journal, Vol. 40, No. 5, pp. 976-994.

Allen, T.M., Christopher, B.R., and Holtz, R.D. (1992). "Performance of a 12.6 m High Geotextile Wall in Seattle, Washington." International Symposium on Geosynthetic-Reinforced Soil Retaining Walls, Balkema Publishers, Netherlands, pp. 81-100.

Allersma, H., (1982). Photoelastic Investigation of the Stress Distribution during Penetration. Proceedings of the 2nd European Symposium on Penetration Testing, Amsterdam, May 24–27, ESOPT-II, Netherlands, pp. 79–83.

Andrawes, K.Z., and Yogarajah, I. (1994). "Effects of Reinforcement Connections on the Behaviour of Reinforced Soil Retaining Walls." Computer Methods and Advances in Geomechanics, Vol. 2, pp. 1313-1318.

Arriaga, F. (2003). Response of Geosynthetic-Reinforced Structures under Working Stress and Failure Conditions. Ph.D. dissertation, Department of Civil Engineering, University of Colorado, Boulder, Colorado.

ASTM D4595-11 (2011). "Standard Test Method for Tensile Properties of Geotextiles by the Wide-Width Strip Method." ASTM Standards, American Society for Testing and Materials (ASTM), West Conshohocken, PA.

ASTM D6706-01 (2013). "Standard Test Method for Measuring Geosynthetic Pullout Resistance in Soil." ASTM Standards, American Society for Testing and Materials (ASTM), West Conshohocken, PA.

ASTM D3080–03 (2003). Standard Test Method for Direct Shear Test of Soils Under Consolidated Drained Conditions. Annual Book of ASTM Standards, ASTM.

Athanasopoulos, G.A. (1993). "Effect of Particle Size on the Mechanical Behavior of Sand-Geotextile Composite." Geotextiles and Geomembranes, Vol. 12, pp. 255-273, International Geosynthetics Society, West Palm Beach, FL.

Athanasopoulos, G.A. (1994). "On the Enhanced Normal pressure Approach to the Mechanics of Reinforced Soil." Geotechnical and Geological Engineering Vol. 12, pp. 122-132, Springer, Netherlands.

Aydogmus, T. and Klapperich, H. (2008). "Design and Evaluation of an Enhanced Shear and Pull-Out Testing Device." Proceedings of the 4th European Geosynthetics Conference, paper 170.

Bassett, A.K. and Last, N.C. (1978). "Reinforcing Earth below Footings and Embankments." Proceedings of the ASCE Spring Convention and Exhibit, Pittsburgh, PA.

Bathurst, R.J. and Benjamin, D.J. (1990). "Failure of a Geogrid-Reinforced Soil Wall." Transportation Research Record, Vol. 1288, pp. 109-116.

Bathurst, R.J., Nernheim, A., Walters, D.L., Allen, T.M., Burgess, P., and Saunders, D.D. (2009). "Influence of Reinforcement Stiffness and Compaction on the Performance of Four Geosynthetic-Reinforced Soil Walls." Geosynthetics International, Vol. 16, No. 1, pp. 43-59.

Bathurst, R.J., Vlachopoulos, N., Walters, D.L., Burgess, P.G., and Allen, T.M. (2006). "The Influence of Facing Stiffness of Two Geosynthetics Reinforced Soil Retaining Walls." Canadian Geotechnical Journal, pp. 1225-1237.

Bathurst, R.J., Walters, D., Vlachopoulos, N., Burgess, P., and Allen, T.M. (2000). "Full Scale Testing of Geosynthetic Reinforced Walls." Proceedings of GeoDenver Conference, pp. 1-17.

Benigni, C., Bosco, G., Cazzuffi, D., Col, R.D., 1996. “Construction, performance of an experimental large-scale wall reinforced with geosynthetics.” In: Ochiai, H., Yasufuku, N., Omine, K. (Eds.), Earth Reinforcement, Vol. 1. A. A. Balkema Publisher, Rotterdam, pp. 315-320.

Berg, R.R., Christopher, B.R., and Samtani, N.C. (2009a). Design of Mechanically Stabilized Earth Walls and Reinforced Soil Slopes–Volume I. Report No. FHWA-NHI-10-024, Federal Highway Administration. National Highway Institute.

Berg, R.R., Christopher, B.R., and Samtani, N.C. (2009b). Design of Mechanically Stabilized Earth Walls and Reinforced Soil Slopes–Volume II. Report No. FHWA-NHI-10-025, Federal Highway Administration. National Highway Institute.

Bergado, D.T. and Chai, J.C. (1994). "Pullout Force-Displacement Relationship of Extensible Grid Reinforcement." Geotextiles and Geomembranes, Vol. 13, No. 5, pp. 295–316.

Bergado, D.T. and Teerawattanasuk, C. (2001). "Analytical Models for Predicting the Pullout Capacity and Interaction between Hexagonal Wire Mesh and Silty Sand Backfill." Tamakang Journal of Science and Engineering, Vol. 4, No. 4, pp. 227-238.

Bergado, D.T., Chai, J.C., Alfaro, M.C., and Balasubramaniam, A.S. (1994). Improvement Techniques of Soft Ground in Subsiding and Lowland Environment. A. A. Balkema, Rotterdam, Netherlands.

Bergado, D.T., Shivashankar, R., Alfaro, M.C., Chai, J.C., and Balasubramaniam, A.S. (1993). “Interaction Behavior of Steel Grid Reinforcements in Clayey Sand.” Géotechnique, Vol. 43, No. 4, pp. 589–603.

Bernal, A., Salgado, R., Swan Jr., R.H., and Lovell C.W. (1997). "Interaction between Tire Shreds, Rubber-Sand and Geosynthetics." Geosynthetics International, Vol. 4, No. 6, pp. 623-643.

Bloser, S., Shearer, D., Corradini, K., and Scheetz, B. (2012). Geosynthetically Reinforced Soil-Integrated Bridge Systems (GRS-IBS) Specification Development for PennDOT Publication 447. Pennsylvania Department of Transportation Bureau of Planning and Research.

Boulanger, R.W., Bray, J.D., Chew, S.H., Seed, R.B., Mitchell, J.K., & Duncan, J.M. (1991). SSCOMPPC: Finite element analysis program for evaluation of soil-structure interaction and compaction efforts. Report No. UCB/GT/91-02, Univ of California, Berkeley.

Boussinesq, M.J. (1885). “Application des potentiels a l'etude de l'equilibre et du movement des solides elastiques, principalement au calculations des deformations et des pressions que produisent, dans ces solides, des efforts quelconques exerces sur une petite partie de leur surface ou de leur interieur: Memoire suivi de notes etendues sur divers points de physique mathematique et d'analyse,” GauthierVillars, Paris, pp. 722. (In French).

Boyle, S.R. and Holtz, R.D. (1994). “Deformation Characteristics of Geosynthetic-Reinforced Soil.” Proceedings of the 5th International Conference on Geotextiles, Geomembranes and Related Products, September 1994, Vol. 1, pp. 361-364.

Brand, S.R. and Duffy, D.M. (1987). "Strength of Pull-Out Testing of Geogrids." Proceedings of Geosynthetics 1987, Vol. 1, New Orleans, LA, pp. 226-236.

Bray, J.D. (1995). Personal Communications, Univ of California, Berkeley.

Broms, B.B., (1978). “Design of fabric reinforced retaining structures.” Proc. of the Symposium on Earth Reinforcement, ASCE, Pittsburgh, PA, April 27, 1978, 282-304.

Brugger, P.J., Gomes, R.D.O.M., and Conte, M. (2012). “Rebaixamento da Linha Férrea de Maringá Utilizando Muros em Solo Reforçado.” Proceedings of IGS Brasil CURSOS. (In Portuguese).

Budge, A.S., Dasenbrock, D.D., Mattison, D.J., Bryant, G.K., Grosser, A.T., Adams, M., and Nicks, J. (2014). “Instrumentation and Early Performance of a Large-Grade GRS-IBS Wall.” Geo-Congress 2014 Technical Papers Geo-characterization and Modeling for Sustainability, 4213-4227.

Buttry, K., McCullough, E., and Wetzel, R. (1996). “Temperatures and Related Behavior in Segmental Retaining Wall System.” Transportation Research Record: Journal of the Transportation Research Board, Vol. 1534, pp. 19-23.

Chai, J.C. (1992). Interaction between Grid Reinforcement and Cohesive-frictional Soil and Performance of Reinforced Wall/embankment on Soft Ground. Ph.D. Dissertation, Asian Institute of Technology, Bangkok, Thailand.

Chang, J.C., Hannon, J.B., and Forsyth, R.A. (1977). "Pullout Resistance and Interaction of Earthwork Reinforcement and Soil." Transportation Research Record 640, National Research Council, Washington, DC, pp. 1-7.

Chen, Y.M., Cao, W.P., & Chen, R.P. (2008). “An experimental investigation of soil arching within basal reinforced and unreinforced piled embankments.” J. G&G, 26(2):164–74.

Christopher, B.R. (1993). Deformation Response and Wall Stiffness in Relation to Reinforced Soil Wall Design. Ph.D. Dissertation, Department of Civil Engineering, Purdue University, West Lafayette, IN, 354 p.

Christopher, B.R., Gill, S.A., Giroud, J.P., Juran, I., Mitchell, J.K., Schlosser, F., and Dunnicliff, J. (1990a). Reinforced soil structures Volume I. Design and construction guidelines. Report No. FHWA-RD-89-043. Federal Highway Administration.

Christopher, B.R., Gill, S.A., Giroud, J.P., Juran, I., Mitchell, J.K., Schlosser, F., and Dunnicliff, J. (1990b). Reinforced soil structures Volume II. Summary of Research and Systems Information. Report No. FHWA-RD-89-044. Federal Highway Administration.

Christopher, B.R., Holtz, R.D. and Bell, W.D. (1986). "New Tests for Determining the In-Soil Stress-Strain Properties of Geotextiles." Proceedings of the Third International Conference on Geotextiles, Vol. 3, Vienna, Austria, April 1986, pp. 683-686.

Colletta, B., Letouzey, J., Pinedo, R., Ballard, J.F., and Bale, P. (1991). "Computerized X-ray Tomography Analysis of Sandbox Models: Examples of Thin-Skinned Thrust Systems." Geology, Vol. 19, pp. 1063–1067.

Costa, C.M.L. (2004). “Deformacoes Dependentes do Tempo em Muros de Solo Reforcado Com Geotexteis.” Ph.D. Dissertation, Escola de Engenharia de Sao Carlos, da Universidade de Sao Paulo, 330p. (In Portuguese).

Costa, C.M.L., Zornberg, J.G., de Souza Bueno, B., and Costa, Y.D.J. (2016). “Centrifuge Evaluation of the Time-Dependent Behavior of Geotextile-Reinforced Soil Walls.” Geotextiles and Geomembranes, Vol. 44, No. 2, pp. 188-200.

Costa, Y.D., Zornberg, J.G., Bueno, B.S., & Costa, C.L. (2009). “Failure Mechanisms in Sand over a Deep Active Trapdoor.” JGGE, ASCE, 135(11):1741-1753.

Cuelho, E.V. (1998). Determination of Geosynthetic Constitutive Parameters and Soil/Geosynthetic Interactions by In-Air and In-Soil Experiments. MS Thesis, Montana State University, MT.

Da Silva, A.E.F., Brugger, P.J., and Engenharia, B. (2012). “Análise do Comportamento de Muro de Contenção Portante em Solo Reforçado a partir de Monitoramento de Campo.” 12th Congresso Brasileiro de Mecanica dos Solos e Engenharia Geotechnica (COBRAMSEG). (In Portuguese).

Desrues, J., Chambon, R., Mokni, M., and Mazerolle, F. (1996). "Void Ratio Evolution Inside Shear Bands in Triaxial Sand Specimens Studied by Computed Tomography." Géotechnique, Vol. 46, No. 3, pp. 529–546.

Detert, O., and Thomson, G. (2013). “Geogrid-Reinforced Bridge Abutments: Report on a Full Scale Test and Executed Projects.” Advances in Geotechnical Infrastructure. Edited by C. F. Leung, S.H. Goh and R.F. Shen. 241-246.

Dove, J.E. and Frost, J.D. (1996). "A Method for Measuring Geomembrane Surface Roughness." Geosynthetics International, Vol. 3, No. 3, pp. 369–392.

Dove, J.E., and Frost, J.D. (1999). "Peak Friction Behavior of Smooth Geomembrane-Particle Interfaces." Journal of Geotechnical and Geoenvironmental Engineering, ASCE, Vol. 125, No. 7, pp. 544–555.

Drescher, A. (1976). "An Experimental Investigation of Flow Rules for Granular Materials using Optically Sensitive Glass Particles." Geotechnique, Vol. 26, No. 4, pp. 591–601.

Duncan, J.M. & Chang, C-Y. (1970). "Nonlinear analysis of stress and strain in soils." J. of the Soil Mechanics & Foundations Division, ASCE, 96(SM5):1629-1653.

Dyer, M.R. (1985). Observations of the Stress Distribution in Crushed Glass with Applications to Soil Reinforcement. Ph.D. Dissertation, University of Oxford, Oxford, UK.

Ehrlich, M., Mitchel, J. K. (1994) Working Stress Design Method For Reinforced Soil Walls, Journal of Geotechnical Engineering, ASCE, Vol. 120, No. 4, pp. 625-647.

Elias, V. (1979). "Friction in Reinforced Earth Utilizing Fine Grained Backfills." International Conference on Soil Reinforcement, Paris, France, pp. 435-8.

Elias, V.E., Christopher, B.R., and Berg, R.R. (2001). Mechanically Stabilized Earth Walls and Reinforced Soil Slopes Design and Construction Guidelines. Technical Report No. FHWA-NHI-00-043, National Highway Institute, Federal Highway Administration, Washington, D.C.

Elton, D.J., and Patawaran, M.A.B. (2004). "Mechanically stabilized earth reinforcement tensile strength from tests of geotextile-reinforced soil." Transportation Research Record: Journal of the Transportation Research Board, Vol. 1868, pp. 81-88.

Elton, D.J., and Patawaran, M.A.B. (2005). Mechanically stabilized earth (MSE) reinforcement tensile strength from tests of geotextile-reinforced soil. Alabama Highway Research Center, Auburn University, Aurburn, AL.

European Standards (2004). Geotextiles and Geotextile-related Products. Determination of Pullout Resistance in Soil. European Standards EN 13738:2004.

Ezzein, F.M., and Bathurst, R. (2011a). "A Transparent Sand for Geotechnical Laboratory Modeling." Geotechnical Testing Journal, Vol. 34, No. 6, pp. 1–12.

Ezzein, F.M., and Bathurst, R. (2011b). Development of a Geosynthetic Pullout Test Apparatus with Transparent Granular Soil. Proceedings 2011 Pan-American Canadian Geotechnical Society Geotechnical Conference, Toronto, Canada, 6p.

Fahel, A.R., Palmeira, E.M., and Ortigao, J.A.R. (2000). "Behaviour of Geogrid Reinforced Abutments on Soft Soil in the BR 101-SC Highway, Brazil." Geotechnical Special Publication, 257-270.

Fakharian, K. and Attar, I.H. (2007). “Static and seismic numerical modeling of geosynthetic-reinforced soil segmental bridge abutments.” Geosynthetics International, 14(4), 228-243.

Fannin, R.J. and Raju, D.M. (1993). "On the Pullout Resistance of Geosynthetics." Canadian Geotechnical Journal, Vol. 30, No. 3, pp. 409-417.

Farrag, K., Acar, Y.B., and Juran, I. (1993). "Pull-Out Resistance of Geogrid Reinforcements." Geotextiles and Geomembranes, Vol. 12, No. 2, pp. 133-159.

Franca, F.A.N., Bueno, B.S., and Zornberg, J.G. (2011). "Confined, Accelerated Creep Tests on Geosynthetics." Foundations and Geotechnical Projects. Vol. 2, No. 12, December, pp. 56–63.

Frost, J.D. and Kuo, C.-Y. (1996). "Automated Determination of the Distribution of Local Void Ratio from Digital Images." ASTM Geotechnical Testing Journal, Vol. 19, No. 2, pp. 107–117.

Geosynthetic Institute (1991). Geogrid Pullout. GRI Test Methods GRI GG5. Geosynthetic Institute (GRI).

Gill, D.R. and Lehane, B.M. (2001). "An Optical Technique for Investigating Soil Displacement Patterns." Geotechnical Testing Journal, Vol. 24, No. 3, pp. 324–329.

Gomes, R.C., Palmeira, E.M., and Lanz, D. (1994). “Failure and Deformation Mechanisms in Model Reinforced Walls Subjected to Different Loading Conditions.” Geosynthetics International, No. 1, No. 1, pp. 45-65.

Goodings, D.J. (1990). “Research on Geosynthetics in Reinforced Cohesive Soil Retaining Walls at the University of Maryland.” Geotechnical News, pp. 23-25.

Gotteland, Ph., Gourc, J.P., Villard, P., 1997. “Geosynthetics reinforced structures as bridge abutments: full scale experimentation and comparison with modelisations.” In: Wu, J.T.H. (Ed.), Mechanically Stabilized Backfill. A. A. Balkema Publisher, Rotterdam, pp. 25–34.

Gourc, J.P., Gotteland, P., Haza, E., Perrier, H., and Baraize, E. (1995). “Geotextile reinforced structures as bridge abutments: full-scale experimentation.” Proceedings of Geosynthetics 1995 Conference Proceedings, Nashville, TN, pp. 79-92.

Gray, D.H. and Ohashi, H. (1983). “Mechanics of Fiber Reinforcement in Sand,” Journal of Geotechnical Engineering, Vol. 109, pp. 335–353, American Society of Civil Engineers, Reston, VA.

Güler, E. and Goodings, D.J. (1992). “Centrifuge Models of Clay-Lime Reinforced Soil Walls.” Proceedings of Grouting, Soil Improvement and Geosynthetics, ASCE, pp. 1249-1260.

Gustafsson, L. and Knutsson, S. (1994). "An Image Analysis Method for Studying Movement in Granular and Solid Bodies." ASTM Geotechnical Testing Journal, Vol. 17, No. 1, pp. 95–100.

Hanumasagar, S.S., Roodi, G.H., and Zornberg, J.G. (2014). "Pullout Characterization of Geogrids Embedded in Blends of Dredged Material and Steel Slag Fines." Proceedings of the 10th ICG Conference, Berlin, Germany.

Hatami, K. and Bathurst, R.J. (2005). "Development and Verification of a Numerical Model for the Analysis of Geosynthetic-Reinforced Soil Segmental Walls Under Working Stress Conditions." Canadian Geotechnical Journal, Vol 42, No. 4, pp. 1066-1085.

Hatami, K. and Bathurst, R.J. (2006). "Numerical Model for Reinforced Soil Segmental Walls Under Surcharge Loading." Journal of Geotechnical and Geoenvironmental Engineering, Vol. 132, No. 6, pp. 673-684.

Hausmann, M.R. (1976). "Strength of Reinforced Earth," ARRB Proceedings, Vol. 8, ARRB Group, Melbourne, Australia.

Haza, E., Gotteland, P., and Gourc, J.P. (2000). "Design Method for Local Load on a Geosynthetic Reinforced Soil Structure." Geotechnical & Geological Engineering, Vol. 18, No. 4, pp. 243-267.

Helwany, S. M., Wu, J.T., and Froessl, B. (2003). "GRS Bridge Abutments—An Effective Means to Alleviate Bridge Approach Settlement." Geotextiles and Geomembranes, Vol. 21, No. 3, pp. 177-196.

Herold, A. (2002). "The first permanent road-bridge abutment in Germany built of geosynthetic-reinforced earth." Proceedings of the 7th ICG-Delmas, Gourc and Girard (eds).

Herold, A. (2005) "Brückenwiderlager aus KBE-Kunststoffbewehrte Erde, Einsatzgebiete Und Anwendungsgrenzen." Geotechnik-Kolloquium, Freiberg, Technische Institut für Geotechnik der Universität Bergakademie Freiberg, Heft 2005-2, pp. 195-217. (In German).

Herold, A. (2006) "Brückenwiderlager aus KBE-Kunststoffbewehrte Erde, Einsatzgebiete Und Anwendungsgrenzen." Sächsisches Textilforschungsinstitut Bautextilien-Symposium, Bautex 2006, Institut für Technische Textilien GmbH, Chemnitz, pp. 1-12. (In German).

Herold, A. (2007) "10 Jahre Verformungsbeobachtungen an KBE-Bauwerken – Ist die Dehnsteifigkeit der Geokunststoffe der Schlüssel zur korrekten Prognose des Verformungsverhaltens von KBE Stützbauwerken?" Geotechnik, Vol. 29, No. 2, pp. 79-86. (In German).

Herold, A. (2008) “Brückenwiderlager aus KBE-Hinweise fur Entwurf und Ausfuhrung.” Kolloquium "Bauen in Boden und Fels" in Ostfildern , Technische Akademie Esslingen e.V., Tagungshandbuch 2008, pp. 533-543. (In German).

Herold, A., Aydoğmuş, T., and Sander, H. (2008). “Large Constructions and Bridge Abutments: Solutions with Geosynthetic-reinforced Earth.” Proceedings of Structures Congress 2008 Crossing Borders, pp. 1-10.

Hird, C.C. and Stanier, S.A. (2010). Modelling Helical Screw Piles in Clay using a Transparent Soil. Proceedings of the 7th International Conference on Physical Modelling in Geotechnics, Zurich, International Society for Soil Mechanics and Geotechnical Engineering, Jun 28–July 1, Switzerland, p. 6.

Holtz, R.D. and Lee, W.F. (2002). Internal Stability Analyses of Geosynthetic Reinforced Retaining Walls. Washington State Department of Transportation, Report No. WA-RD 532.1, Olympia, Washington, USA.

Huesker Synthetic GmbH. The Lagoons – Dubai. Huesker Synthetic GmbH, Gescher.

Iacorossi, M. (2012). Earth Reinforced Retaining Structures. Report, Department of Civil Engineering, Columbia University, NY, USA.

Iacorossi, M., Ling, H.I., Gottardi, G., and Li, L. (2013). “Centrifuge Modeling of Earth-Reinforced Retaining Walls.” Proceedings of International Symposium on Design and Practice of Geosynthetic-Reinforced Soil Structures. Bologna, Italy.

Iglesias G.R., Einstein H.H., & Whitman R.V. (2013). “Investigation of soil arching with centrifuge tests.” JGGE, 140(2):248–56.

Ingold, T.S. (1979). “The Effects of Compaction on Retaining Walls.” Geotechnique, Vol. 29, No. 3, pp. 265-283.

Ingold, T.S. (1982). Reinforced Earth, Thomas Telford Ltd., London, United Kingdom.

Ingold, T.S. (1983). "A Laboratory Investigation of Grid Reinforcements in Clay." Geotechnical Testing Journal, Vol. 6, No. 3, pp. 112-119.

Ingold, T.S. (1983). "Laboratory Pull-Out Testing of Grid Reinforcements in Sand." Geotechnical Testing Journal. ASTM, Vol. 6, pp. 101–111.

Iskander, M. (1998). Transparent Soils to Image 3D Flow and Deformation. Proceedings of the 2nd International Conference on Imaging Technologies: Techniques and Applications in Civil Engineering, Davos, Switzerland, May 25–30, 1997, ASCE, New York, pp. 255–264.

Iskander, M. (2010). "Modeling with Transparent Soils, Visualizing Soil Structure Interaction and Multiphase Flow, Non-intrusively." Springer, New York, p. 331.

Iskander, M. and Liu, J. (2010). "Spatial Deformation Measurement Using Transparent Soil." Geotechnical Testing Journal, Vol. 33, No. 4, pp.1–8.

Iskander, M., Lai, J., Oswald, C., and Mannheimer, R. (1994). "Development of a Transparent Material to Model the Geotechnical Properties of Soils." Geotechnical Testing Journal, Vol. 17, No. 4, pp. 425–433.

Iskander, M., Liu, J., and Sadek, S. (2002a). "Transparent Amorphous Silica to Model Clay." Journal of Geotechnical and Geoenvironmental Engineering, Vol. 128, No. 3, pp. 262–273.

Iskander, M., Liu, J., and Sadek, S. (2003). Modeling 3D Flow and Soil Structure Interaction using Optical Tomography. Final Report, NSF Project No. CMS 9733064, p. 280.

Iskander, M., Sadek, S., and Liu, J. (2002b). "Optical Measurement of Deformation using Transparent Silica Gel to Model Sand." International Journal of Physical Modelling in Geotechnics, Vol. 2, No. 4, pp. 13–26.

Iwamoto, M.K., Ooi, P.S.K., Adams, M.T., and Nicks, J.E. (2013). "Composite Properties from Instrumented Load Tests on Soil Columns Reinforced with Geotextiles." Transportation Research Broad, TRB 2014 Annual Meeting.

Jaber, M.B. (1989). Behavior of Reinforced Soil Walls in Centrifuge Model Tests. Berkeley. Ph.D. Dissertation, University of California, Berkeley, 239p.

Jacobs, F., Ruiken, A., and Ziegler, M. (2012a). "Experimental Investigation of Geogrid Reinforced Soil under Plane Strain Conditions." Geosynthetics Asia 2012, 5th Asian Regional Conference on Geosynthetics, 10 to 14 December 2012, Bangkok, Thailand.

Jacobs, F., Ruiken, A., and Ziegler, M. (2012b). "Investigation of Geogrid Reinforced Soil with Large Scale “Element” Testing." GeoAmericas 2012, Lima, Perú, May 2012.

Jang, D.J., and Frost, D.J. (1998). "Sand Structure Differences Resulting from Specimen Preparation Procedures." ASCE Geotechnichal Special Publication no. 75, Geotechnical Earthquake Engineering and Soil Dynamics III, Dakuolas, Yegian, and Holtz (eds.), Seattle, Vol.1, pp. 234–245.

Jang, D.J., Frost, J.D., and Park, J.K. (1999). "Preparation of Epoxy Impregnated Sand Coupons for Image Analysis." ASTM Geotechnical Testing Journal, Vol. 22, No. 2, pp. 147–158.

Jayawickrama, P.W., Lawson, W.D., Wood, T.A., and Surles, J.G. (2014). "Pullout Behavior of Welded Grid Reinforcements Embedded in Coarse Granular Backfill." ASCE Geo-Congress, Atlanta, GA, February 2014.

Jewell, R.A. (1980). Some Effects of Reinforcement on the Mechanical Behavior of Soils. Ph.D. Dissertation, Cambridge University, Cambridge, UK.

Jewell, R.A. (1990a). "Reinforcement Bond Capacity." Géotechnique, Vol. 40, No. 3, pp. 513–518.

Jewell, R.A. (1990b). "Strength and Deformation in Reinforced Soil Design." Proceedings of the 4th International Conference on Geotextiles, Geomembranes and Related Products, The Hague, Netherlands, Vol. 3, pp. 913–946.

Jewell, R.A. (1991). "Application of Revised Design Charts for Steep Reinforced Slopes." Geotextiles and Geomembranes, Vol. 10, No. 3, pp. 203-233.

Jewell, R.A. (1996). Soil Reinforcement with Geotextiles. Ciria Special Publication 123, Thomas Telford Ltd., UK, 332 p.

Jewell, R.A., Milligan, G.W.E., Sarsby, R.W., and Dubois, D. (1984). Interaction between Soil and Geogrids. Proceeding of the Symposium on Polymer Grid Reinforcement in Civil Engineering, Science and Engineering Research Council and Netlon Limited, pp. 18–30.

Juran, I. and Christopher, B. (1989). "Laboratory Model Study on Geosynthetic Reinforced Soil Retaining Walls." Journal of Geotechnical Engineering, Vol. 115, No. 7, pp. 905-926.

Juran, I., Guermazi, A., Chen, C.L., and Ider, M.H. (1988). "Modelling and Simulation of Load Transfer in Reinforced Soil: Part 1." International Journal for Numerical and Analytical Methods in Geomechanics, Vol. 12, No. 2, pp. 141-155.

Kasugai, A., and Tateyama, M. (1992). "Application of geosynthetic-reinforced soil for bridge abutments." Earth Reinforcement Practice, Ochiai, Hayashi & Otani (eds), 1992, Balkema, Rotterdam, pp. 363-368.

Keller, G. and Devin, S. (2003). "Geosynthetic-reinforced soil bridge abutments." Transportation Research Record: Journal of the Transportation Research Board, Vol. 1819, pp. 362-368.

Kemeny, J.M., Devgan, A., Hagaman, R.M. and Wu, X. (1993). "Analysis of Rock Fragmentation Using Digital Image Processing." Journal of Geotechnical Engineering, Vol. 119, No. 7, pp. 1144–1160.

Ketchart, K. and Wu, J.T.H. (2002). "A Modified Soil-Geosynthetic Interactive Performance Test for Evaluating Deformation Behavior of GRS Structures." ASTM International, Vol. 25, No. 4, pp. 405-413.

Ketchart, K. and Wu, J.T.H. (1996). Long-Term Performance Tests of Soil-Geosynthetic Composites. Report No. CDOT-CTI-96-1, Colorado Department of Transportation, Denver, CO.

Ketchart, K. and Wu, J.T.H. (2001). Performance Test for Geosynthetic-reinforced Soil Including Effects of Preloading. Report No. FHWA-RD-01-018, Federal Highway Administration, Washington, DC.

Kharchafi, M. and Dysli, M. (1993). "Study of Soil-Geotextile Interaction by an X-Ray Method." Geotextiles and Geomembranes, Vol. 12, No. 4, pp. 307-325.

Kirschner, R., and Hermansen, E. (1994). “Abutments in Reinforced Soil for a Road Bridge.” Proceedings of the 5th International Conference on Geotextiles, Geomembranes, and Related Products. Singapore, September, 1994, pp. 259-260.

Kniss, K.T., Yang, K.-H., Wright, S.G., and Zornberg, J.G. (2007). “Earth Pressures and Design Consideration of Narrow MSE Walls.” Proceedings of the Conference of Texas Section-ASCE Meeting, Taylor, Texas, April, 2007.

Ko, H.Y. (1988a). “The Colorado Centrifuge Facility.” Proceedings of International Conference of Centrifuges in Soil Mechanics, James and Schofield (eds.), pp. 319-324.

Ko, H.Y. (1988b). “Summary of the State-of-the-art in Centrifuge Model Testing.” Proceedings of International Conference of Centrifuges in Soil Mechanics, James and Schofield (eds.), pp. 11-18.

Koerner, R.M. (1986). Direct Shear/Pull-Out Tests on Geogrids. Report No. 1, Department of Civil Engineering, Drexel University, Philadelphia, PA.

Koerner, R.M. (2005). Designing with Geosynthetics, Fifth Edition. Pearson Prentice Hall.

Koerner, R.M., Wayne, M.H., and Carroll, R.G., Jr. (1989). "Analytic Behavior of Geogrid Anchorage." Proceedings of the Geosynthetics’89 Conference, San Diego, CA, IFAI, pp. 525–536.

Kongkitkul, W., Hirakawa, D., Sugimoto, T., Kawahata, S., Yoshida, T., Ito, S., and Tatsuoka, F. (2008). “Post-construction Time History of Tensile Force in the Geogrid Arranged in a Full-Scale High Wall.” Proceedings of 4th GeoSynthetics Asia, Shanghai, pp. 64-69.

Kuo, C.-Y. and Frost, J.D. (1996). "Uniformity Evaluation of Cohesionless Specimens Using Digital Image Analysis." Journal of Geotechnical Engineering, Vol. 122, No. 5, pp. 390–396.

Lade, P.V. and Duncan, J.M. (1973). “Cubical triaxial tests on cohesionless soil.” Journal of Soil Mechanics and Foundations, Division of American Society of Civil Engineers, Vol. 99, No. 10, pp. 793-811.

Ladeira, M.A.S.A. (1995). Estudo dos Fenômenos de Interação Solo-Geossintetico Através de Ensaios de Arranque. (In Portuguese) MS Thesis, University of Porto, Portugal.

Lee, K.L., Adams, B.D., and Vagneron, J.M.J. (1973). “Reinforced Earth Retaining Walls.” Soil Mechanics and Foundation Engineering, ASCE, Vol. SM10, pp. 745–764.

Lee, K.Z., and Wu, J.T. (2004). “A Synthesis of Case Histories on GRS Bridge-supporting Structures with Flexible Facing.” Geotextiles and Geomembranes, Vol. 22, No. 4, pp. 181-204.

Lee, Y.-B. (2010). Deformation behavior of shored mechanically stabilized earth (SMSE) wall systems. PhD thesis, University of Colorado, Boulder, CO, USA.

Lee, Y.-B., Ko, H.-Y., and McCartney, J.S. (2010b). "Deformation Response of Shored MSE Walls under Surcharge Loading in the Centrifuge." Geosynthetics International, Vol. 17, No. 6, pp. 389-402.

Lee, Y.-B., McCartney, J.S., and Ko, H.-Y. (2010a). "Centrifuge Modeling of Shored Mechanically Stabilized Earth Walls." Proceedings of International Conference on Physical Modeling in Geotechnics, Zurich, Switzerland, pp. 481-486.

Lenart, S. (2014). Final report of development of reinforced soil bridge abutments. Report No. P 320/13-710-8, Oddelek za geotehniko in prometnice, Zavod za gradbeništvo Slovenije, 2014 (in Slovenian).

Lenart, S., Kralj, M., Medved, S.P., and Šuler, J. (2016). "Design and construction of the first GRS integrated bridge with FHR facings in Europe." Transportation Geotechnics, Vol. 8, pp. 26-34.

Leshchinsky, D. & Vulova, C. (2001). "Numerical investigation of the effects of geosynthetic spacing on failure mechanisms in MSE block walls." Geosynthetics Int., 8(4):343-365

Leshchinsky, D. and Boedeker, R.H. (1989). "Geosynthetic Reinforced Soil Structures." Journal of Geotechnical Engineering, Vol. 115, No. 10, pp. 1459-1478.

Leshchinsky, D., (1997). Design procedure for geosynthetic reinforced steep slopes. Technical Report REMR-GT-23, Jan. 1997, WES, Vicksburg, MS.

Leshchinsky, D., Kaliakin, V., Bose, P., & Collin, J. (1994). "Failure Mechanism in Geogrid-Reinforced Segmental walls: Experimental Implications." Soils & Foundations, Journal of the Japanese Society of Soil Mechanics & Foundation Engineering, 34(4):33-41.

Leung, S.K., Kry, P.R., and Wong, R.C.K. (1995). Visualization of deformation in unconsolidated Athabasca oil sand. Proceedings of the International Heavy Oil Symposium, Calgary, Alta., 18–21 June 1995. Society of Petroleum Engineers, Publication SPE 30315.

Li, C. (2002). Experimental studies on fiber-reinforced soil University of Colorado. Research Report, University of Colorado, Boulder, Colorado, USA.

Li, C. and Zornberg, J.G. (2013). "Mobilization of Reinforcement Forces in Fiber-Reinforced Soil." Journal of Geotechnical and Geoenvironmental Engineering, ASCE, Vol. 139, No. 1, January, pp. 107–115.

Liang, L., Saada, A., Figueroa, J.L., and Cope, C.T. (1997). "The Use of Digital Image Processing in Monitoring Shear Band Development." ASTM Geotechnical Testing Journal, GTJODJ, Vol. 20, No. 3, September, pp. 324–339.

Lin, H., Ling, H.I., Collin, J.G., Leshchinsky, D., and Rimoldi, P. (2013). “Centrifuge Modeling of Gabion Walls Reinforced with Geosynthetics.” Proceedings of International Symposium on Design and Practice of Geosynthetic-Reinforced Soil Structures. Bologna, Italy.

Ling, H.I. and Tatsuoka, F. (1994). “Performance of Anisotropic Geosynthetic-Reinforced Cohesive Soil Mass”, Journal of Geotechnical Engineering, ASCE, Vol. 120, No. 7, pp. 1166-1184.

Ling, H.I., Cardany, C.P., Sun, L-X., & Hashimoto, H. (2000). “Finite Element Study of a Geosynthetic-Reinforced Soil Retaining Wall with Concrete-Block Facing.” Geosynthetics Int., 7(2):137-162.

Ling, H.I., Tatsuoka, F., and Tateyama, M. (1995). “Simulating the Performance of GRS-RW by Finite Element Procedure.” Journal of Geotechnical Engineering, ASCE, Vol. 124, No. 4, pp. 330-340.

Ling, H.I., Wu, J.T., and Tatsuoka, F. (1992). “Short-Term Strength and Deformation Characteristics of Geotextiles Under Typical Operational Conditions.” Geotextiles and Geomembranes, Vol. 11, No. 2, pp. 185-219.

Liu, C., Zornberg, J.G., Chen, T-C., Ho, Y., and Lin, B. 2009. "Behavior of Geogrid-Sand Interfaces in Direct Shear Mode." Journal of Geotechnical and Geoenvironmental Engineering, ASCE, Vol. 135, No. 12, December, pp. 1863–1871.

Liu, J., Iskander, M. and Sadek, S. (2003). "Consolidation and Permeability of Transparent Amorphous Silica." Geotechnical Testing Journal, Vol. 26, No. 4, pp. 390–401.

Lo, S.R. (2004). Application of Numerical Modelling to the Design of Reinforced Soil Walls for Infrastructure Projects-Some Australian Experiences. In GeoAsia2004: 3rd Asian Regional Conference on Geosynthetics: Now and Future of Geosynthetics in Civil Engineering. June 2004.

Lopes, M.L. (1992). Walls Reinforced with Geosynthetics. (In Portuguese) Ph.D. Thesis, University of Porto, Portugal, 335 p.

Lopes, M.L. and Ladeira, M. (1996). "Influence of the Confinement, Soil Density and Displacement Ratio on Soil-Geogrid Interaction." Geotextiles and Geomembranes, Vol. 14, No. 10, pp. 543–554.

Lopes, M.L. and Ladeira, M. (1996). "Role of Specimen Geometry, Soil Height and Sleeve Length on the Pull-Out Behaviour of Geogrids." Geosynthetic International, Vol. 3, No. 6, pp. 701-719.

Marachi, N.D., Chan, C.K., Seed, H.B., and Duncan, J.M. (1969). Strength and Deformation Characteristics of Rockfill Materials. University of California Report TE-69-5, Berkeley, California, USA.

Mahajan, R.R. (2007). Centrifuge Model Studies on Geosynthetic Reinforced Soil Slopes. Ph.D. Dissertation. Indian Institute of Technology Bombay, India.

Maher, M.H. and Woods, R.D. (1990). "Dynamic Response of Sand Reinforced with Randomly Distributed Fibers," Journal of Geotechnical Engineering, Vol. 116, pp. 1116–1131, American Society of Civil Engineers, Reston, VA.

Malinowska, E.E. (2015). "Gabion Wall Testing during the Forced Overloading in the Geotechnical Centrifuge." Acta Scientiarum Polonorum. Architectura, Vol. 14, No. 3.

Mannheimer, R. and Oswald, C. (1993). "Development of Transparent Porous Media with Permeabilities and Porosities Comparable to Soils, Aquifers, and Petroleum Reservoirs." Ground Water, Vol. 31, No. 5, pp. 781–788.

Marques, J.M.M.C. (2005). "Finite Element Modelling of the Pull-Out Test of Geosynthetics." VIII International Conference on Computation Plasticity, E. Onate and D.R. Owen (eds.).

McGown, A., Andrawes, K.Z., and Kabir, M.H. (1982). "Load Extension Testing of Geotextiles Confined in Soil." In Proceedings of the 2nd International Conference on Geotextiles, Vol. 3, pp. 793-798. Roseville, Minnesota, August 1982.

McGown, A., Andrawes, K.Z., Pradhan, S., and Khan, A.J. (1998). "Limit State Design of Geosynthetic Reinforced Soil Structures." Proceedings of the 6th International Conference on Geosynthetics, pp. 144-179.

McKelvey, D., Sivakumar, V., Bell, A. and Graham, J. (2004). Modeling Vibrated Stone Columns in Soft Clay. Proceedings of the Institution of Civil Engineers: Geotechnical Engineering 157, Issue GE3, pp. 137–149.

Meyer, N., Nernheim, A., and Emersleben, A. (2003). "Influence of Normal pressure, Soil Density and Types of Geogrids on Soil-Geogrid Interaction Coefficient." E-Conference "Modern Trends in Foundation Engineering: Geotechnical Challenges and Solutions", IITM, India.

Milligan, G.W.E. and Palmeira, E.M. (1987). "Prediction of Bond between Soil and Reinforcement." Symposium on Prediction and Performance in Geotechnical Engineering, Calgary, pp. 147–153.

Min, Y., Leshchinsky, D., Ling, H.I., and Kaliakin, V.N. (1995). "Effects of Sustained and Repeated Tensile Loads on Geogrid Embedded in Sand." Geotechnical Testing Journal, Vol. 18, No. 2, pp. 204-225.

Minažek, K. and Mulabdić, M. (2013). "A Review of Soil and Reinforcement Interaction Testing in Reinforced Soil by Pullout Test." Građevinar 2013, Vol. 65, No. 3, pp. 235-250.

Mirlatifi, S., and Fatahi, B. (2012). “Numerical Analysis of Geosynthetic-reinforced Soil Wall as Bridge Abutment.” Proceedings of the 11th Australia - New Zealand (ANZ) Conference on Geomechanics Ground Engineering in a Changing World. Melbourne, Australia. July 2012, pp.1383-1388.

Mirlatifi, S.A.S. (2012). “Analysis, Design, and Construction Stages of Milad Geosynthetic-reinforced Soil Bridge Abutment in Tehran-Iran.” Australian Geomechanics, Vol. 47, No. 3, September 2012, pp. 125-132.

Mohamed, K., Abouzakhm, M., and Elias, M. (2011). “Applications and performance of geosynthetic-reinforced soil abutments on soft subsurface soil conditions.” Transportation Research Board.

Mora, C.F., Kwan, A.K.H. and Chan, H.C. (1998). "Particle Size Distribution Analysis of Coarse Aggregate Using Digital Image Processing." Cement and Concrete Research, Vol. 28, No. 6, pp. 921–932.

Moraci, N. and Gioffre, D. (2006). "A Simple Method to Evaluate the Pullout Resistance of Embedded in a Compacted Granular Soil Extruded Geogrids." Geotextiles and Geomembranes, Vol. 24, No. 2, pp. 116–128.

Moraci, N. and Recalcati, P. (2006). "Factors Affecting the Pullout Behaviour of Extruded Geogrids Embedded in a Compacted Granular Soil." Geotextiles and Geomembranes, Vol. 24, No. 4, pp. 220–242.

Morsy, A.M., Leshchinsky, D., and Zornberg, J.G. (2017a), “Effect of Reinforcement Spacing on the Behavior of Geosynthetic-Reinforced Soil,” In Proceedings of Geotechnical Frontiers 2017, American Society of Civil Engineers (ASCE), March 12-15, 2017 | Orlando, Florida, USA, pp. 112-125.

Morsy, A.M., Zornberg, J.G., Christopher, B.R., Leshchinsky, D., Tanyu, B.F., and Han, J. (2017b), “Experimental Approach to Characterize Soil-Reinforcement Composite Interaction,” In Proceedings of the 19th International Conference on Soil Mechanics and Geotechnical Engineering (19th ICSMGE), International Society for Soil Mechanics and Geotechnical Engineering (ISSMGE), September 17-22, 2017 | Seoul, Korea, pp. 451-454.

Morsy, A.M., and Zornberg, J.G. (2017), “A Tale of Two Bridges: Comparison between the Seismic Performance of Flexible and Rigid Abutments,” In Proceedings of the 3rd African Regional Conference on Geosynthetics (GeoAfrica 2017), International Geosynthetics Society (IGS), October 8-11, 2017 | Marrakech, Morocco, pp. 1000-1007.Myles, B. (1982) “Assessment of Soil Fabric Friction by Means of Shear.” Proceedings 2nd International Conference on Geotextiles, Las Vegas, p. 787-791.

Nancey, A., Rossi, D., and Boons, B. (2006). “Survey of a bridge abutment reinforced by geosynthetics, with optic sensors integrated in geotextile strips.” Proceedings of IGC 8th, September 18-22, Yokohama, Japan, pp. 1071-1074.

NAVFAC (1986). Foundations and Earth Structures. Design Manual DM-7.02. Naval Facilities Engineering Command.

NCMA (1997). Design Manual for Segmental Retaining Walls. Second Edition, National Concrete Masonry Association (NCMA), Publication Number TR 127A.

Nguyen, Q. (2012). GRS Abutments for Bridge Replacement National Wildlife Refuge. A New Era of Partnerships - Investing in America's Treasures, U.S. Department of Transportation, FHWA, EFLHD.

Nicks, J.E., Adams, M.T., and Stabile, T. (2013b). "Performance Testing for Geosynthetic Reinforced Soil Composites." Proceedings of the 5th International Young Geotechnical Engineers’ Conference.

Nicks, J.E., Adams, M.T., Ooi, P.S.K., and Stabile, T. (2013a). Geosynthetic Reinforced Soil Performance Testing—Axial Load Deformation Relationships. Report No. FHWA-HRT-13-066, Federal Highway Administration, McLean, VA.

Obaidat, M.T., Al-Masaeid, H.R., Gharaybeh, F., and Khedaywi, T.S. (1998). "An Innovative Digital Image Analysis Approach to Quantify the Percentage of Voids in Mineral Aggregates of Bituminous Mixtures." Canadian Journal of Civil Engineering, Vol. 25, pp. 1041-1049.

Ochiai, H, Otani, J., Hayashic, S., and Hirai, T. (1996). "The Pullout Resistance of Geogrids Reinforced Soil." Geotextiles and Geomembranes, Vol. 14, No. 1, pp. 19–42.

Ortigao, J.A.R., Fahel, A.R., Palmeira, E.M., and Simmonds, A.J. (2001). “Stability and deformation monitoring of geogrid reinforced embankments.” Proceedings of Transportation Research Board Meeting on Geo-Construction Processes, TRB Meeting, pp. 51-62.

Otani, J., Miyamoto, K., and Mukunoki, T. 2001. "Visualization of Interaction Behavior Between Soil and Reinforcement Using X-ray CT." Proceedings of Landmarks in Earth Reinforcement, Ochiai, H., Otani, J., Yasufuku, N., Omine, K (editors), A.A. Balkema, Tokyo, Japan, Vol. 1, pp. 117–120.

Ovesen, N. (1975). “Centrifuge testing applied to bearing capacity problems of footings on sand.” Geotechnique, Vol. 25, No. 2, pp. 394-401.

Palmeira, E.M. (1987). The Study of Soil-Reinforcement Interaction by Means of Large Scale Laboratory Tests. Ph.D. Thesis, University of Oxford, UK, 238 p.

Palmeira, E.M. (2004). "Bearing Force Mobilization in Pull-out Tests on Geogrids." Geotextiles and Geomembranes, Vol. 22, pp. 481–509.

Palmeira, E.M. (2009). "Soil-Geosynthetic Interaction: Modelling and Analysis." Geotextiles and Geomembranes, Vol. 27, No. 5, pp. 368–390.

Palmeira, E.M. and Milligan, G.W.E. (1989b). "Scale and Other Factors Affecting the Results of the Pullout Tests of Grids Buried in Sand." Géotechnique, Vol. 39, No. 3, pp. 551–584.

Palmeira, E.M. and Milligan, G.W.E., (1989a). "Large Scale Direct Shear Tests on Reinforced Soil." Soil and Foundations, Vol. 29, No. 1, pp. 18–30.

Pan, B., Qian, K., Xie, H. and Asundi, A. (2009). "Two-Dimensional Digital Image Correlation for In-plane Displacement and Strain Measurement: A Review." Measurement Science and Technology, Vol. 20, No. 6, 17 p.

Peterson, L. M. and Anderson, L.R. (1980). Pullout Resistance of Welded Wire Mats Embedded in Soil. Research Report Submitted to Hilfiker Co., Civil and Envir. Eng. Dept., Utah State Univ., Utah, USA.

Pham, T.Q. (2009). Investigating Composite Behavior of Geosynthetic-Reinforced Soil (GRS) Mass. Ph.D. thesis, University of Colorado Denver, Colorado, USA.

Porbaha, A. and Goodings, D.J. (1994). "Geotextile Reinforced Cohesive Slopes on Weak Foundations." Proceedings of Centrifuge, Vol. 94, pp. 623-628.

Porbaha, A. and Goodings, D.J. (1996). "Centrifuge Modeling of Geotextile-Reinforced Cohesive Soil Retaining Walls." Journal of Geotechnical Engineering, Vol. 122, No. 10, pp. 840-848.

Powell, W., Keller, G.R., and Brunette, B. (1999). "Applications for Geosynthetics on Forest Service Low-Volume Roads." Transportation Research Record, Vol. 1652, pp. 113-120.

Raffel M., Willert, C., and Kompenhans, J. 2007. "Particle Image Velocimetry: A Practical Guide." Springer, Berlin.

Railway Technical Research Institute (2012). Design Standards for Railway Structures and Commentary Earth Retaining Structure. Edited by Railway Technical Research Institute (RTRI), under supervision of Railway Bureau of Ministry of Land, Infrastructure, Transport and Tourism, (MLIT), Japan.

Raju, D.M. and Fannin R.J. 1998. "Load–Strain–Displacement Response of Geosynthetics in 614 Monotonic and Cyclic Pullout." Canadian Geotechnical Journal, Vol. 35, No. 2, pp. 183–193.

Rankine, W. (1857). "On the Stability of Loose Earth." Philosophical Transactions of the Royal Society of London, Vol. 147.

Raschke, S.A., Hryciw, R.D. and Donohoe, G.W. (1996). "Micro-Deformations in Sands by Digital Image Processing and Analysis." Transportation Research Record 1548, pp. 31–37.

Rimoldi, P. and Intra, E. (2009). "Design and Construction of Tall Reinforced Embankments in Static and Seismic Conditions." GIGSA GeoAfrica 2009 Conference, Cape Town, September 2009.

Roodi, G. H., & Zornberg, J. G. (2017). "Stiffness of soil-geosynthetic composite under small displacements. II: Experimental evaluation." Journal of Geotechnical and Geoenvironmental Engineering, ASCE, Vol. 143, No. 10.

Rui, R., van Tol, F., Xia, X. L., van Eekelen, S., Hu, G., & Xia, Y. Y. (2016). "Evolution of soil arching; 2D DEM simulations." Journal of Computers & Geotechnics, 73, 199-209.

Ruiken, A. and Ziegler, M. (2009). "Large Scale Laboratory Element Testing of Geogrid Reinforced Soil." Proceedings of GIGSA GeoAfrica 2009 Conference, Cape Town, September.

Sadek, S., Iskander, M. and Liu, J. (2002). "Geotechnical Properties of Transparent Silica." Canadian Geotechnical Journal, Vol. 39, No. 1, pp. 111–124.

Sadek, S., Iskander, M.G. and Liu, J. (2003). "Accuracy of Digital Image Correlation for Measuring Deformations in Transparent Media." Journal of Computing in Civil Engineering, Vol. 17, No. 2, pp. 88–96.

Santamarina, J.C. (1984). Effect of adjacent soils on reinforced soil structures-centrifuge model testing. Ph.D. Dissertation, Purdue University, West Lafayette, Indiana, USA.

Sarsby, R.W. (1985). "The Influence of Aperture Size/Particule Size on Efficiency of Grid Reinforcement." Proceedings of the 2nd Canadian Symposium on Geotextiles and Geomembranes, Edmonton, Alberta, pp. 7–12

Saxena, S.K. and Budiman, J.S. (1985). "Interface Response of Geotextiles." Proceedings of the 11th International Conference on Soil Mechanics and Foundation Engineering.

Schlosser, F. and Long, N.T. (1974). "Recent Results in French Research on Reinforced Earth." Journal of Construction Division, Vol. 100, pp. 223–237, American Society of Civil Engineers, Reston, VA.

Schofield, A. (1980). "Cambridge Geotechnical Centrifuge Operation." Geotechnique, Vol. 30, No. 3, pp. 227-268.

Schuettpelz, C., Fratta, D., and Edil, T. (2009). "Evaluation of the zone of influence and stiffness improvement from geogrid reinforcement in granular materials." Transportation Research Record: Journal of the Transportation Research Board, Vol. 2116, pp. 76-84.

Scott, R.F. (1963). “Principles of Soil Mechanics.” Addison Wesley, Reading, Mass, 550p.

Seed, R.B. & Duncan, J.M. (1984). A finite element analysis program for evaluating soil-structure interaction & compaction efforts. Report No. UCB/GT/84-02, Univ of California, Berkeley.

Shi, B., Murakami, Y., Wu, Z., Chen, J. and Inyang, H. (1999). "Monitoring of Internal Failure Evolution in Soils Using Computerization X-ray Tomography." Eng. Geol. (Amsterdam), Vol. 54, No. 3–4, pp. 321–328.

Snijders, B., and Brok, C. (2007). “N242 Bridge Abutments on geogrid reinforced soil near the city of Alkmaar in the Netherlands.” Proceedings of the 14th European Conference on Soils Mechanics and Geotechnical Engineering (Geotechniek ECSMGE). Madrid, Spain, September 2007, pp. 12-14.

Sommers, A.N. and Viswanadham, B.V.S. (2009). “Centrifuge Model Tests on the Behavior of Strip Footing on Geotextile-reinforced Slopes.” Geotextiles and Geomembranes, Vol. 27, No. 6, pp. 497-505.

Song, Z., Hu, Y., O’Loughlin, C., and Randolph, M.F. (2009). "Loss in Anchor Embedment During Plate Anchor Keying in Clay." Journal of Geotechnical and Geoenvironmental Engineering, Vol. 135, No. 10, pp. 1475–1485.

Soong, T-Y. and Koerner, R.M. (1997). "On the Required Connection Strength of Geosynthetically Reinforced Walls." Geotextiles and Geomembranes, Vol. 15, pp. 377-393.

Springman, S.M., Bolton, M.D., Sharma, J., and Balachandran, S. (1992). “Modelling and Instrumentation of a Geotextile in the Geotechnical Centrifuge.” Proceedings of the International Symposium on Earth Reinforcement Practice, Kyushu, September 1992, Vol. 167, p. 172.

Stadler, A.T. (2001). Geogrid Reinforcement of Piedmont Residual Soil. Report No. HWY-2001-02, North Carolina Department of Transportation, Raleigh, NC.

Sugimoto, M., Alagiyawanna, A. M. N. and Kadoguchi, K. (2001). "Influence of Rigid and Flexible Face on Geogrid Pullout Tests." Geotextiles and Geomembranes, Vol. 19, No. 5, pp. 257–328.

Suits, L.D., and Hsuan, Y.G. (2003). “Assessing the photo-degradation of geosynthetics by outdoor exposure and laboratory weatherometer.” Geotextiles and Geomembranes, Vol. 21, No. 2, pp. 111-122.

Tatsuoka, F. (1992). “Roles of facing rigidity in soil reinforcing.” Keynote Lecture, Proceedings of Earth Reinforcement Practice, IS-Kyushu ’92, Ochiai et al. eds., Vol. 2, pp. 831−870.

Tatsuoka, F. (1993). “Roles of Facing Rigidity in Soil Reinforcing.” Earth Reinforcement Practice, Keynote Lecture, Ochiai, H.,Hayashi, S. and Otani, J., Editors, Balkema, 1993, Proceedings of the International Symposium on Earth Reinforcement Practice, IS Kyushu 1992, Vol. 2, Kyushu, Fukuoka, Japan, November 1992, pp. 831-870.

Tatsuoka, F., and Yamauchi, H. (1987). “A Reinforcing Method for Steep Clay Slopes Using a Non-Woven Geotextile”, Geotextiles and Geomembranes, Vol. 4, pp. 241-268.

Tatsuoka, F., Tamura, Y., Nakamura, K., Iwasaki, K., and Yamauchi, H. (1987). “Behavior of Steep Slope Clay Embankments Reinforced With a Non-Woven Geotextile Having Various Face Structures.” Proceedings of the Post Vienna Conference on Geotextiles, Singapore, pp. 387-403.

Tatsuoka, F., Tateyama, M., Murata, O. & Tamura, Y. (1994). “Closure on ‘Geosynthetic-Reinforced Soil Retaining Walls with Short Reinforcement and a Rigid Facing.’” Recent Case Histories of Permanent GRS Retaining Walls, Balkema, Proc. of Seiken Sym. 11, Tokyo, Japan, 323-344.

Tatsuoka, F., Tateyama, M., Uchimura, T., and Koseki, J. (1997). Geosynthetic-Reinforced Soil Retaining Walls as Important Permanent Structures 1996-1997 Mercer Lecture. Geosynthetics International, Vol. 4, No. 2, pp. 81-136.

Tatsuoka, F.,Ando,H., Iwasaki, K. and Nakamura, K. (1986). “Performance of Clay Test Embankments Reinforced With a Non-Woven Geotextile”, Proceedings of the Third International Conference on Geotextiles, Vol. 3, Vienna, Austria, April 1986, pp. 355-360.

Tecnologia de Materiales. Muros de Solo Reforçado Como Estribos de Ponte S27 – Yanacocha. Tecnologia de Materiales (TDM), Peru. (In Portuguese).

Teixeira, S.H.C. (2003). Estudo da Interação Solo-Geogrelha em Testes de Arrancamento e a sua Aplicação na Análise e Dimensionamento de Maciços Reforçados. (In Poruguese) Ph.D. Thesis, School of Engineering, Univerity of São Paulo, São Carlos.

Teixeira, S.H.C., Bueno, B.S. and Zornberg, J.G. (2007). "Pullout Resistance of Individual Longitudinal and Transverse Geogrid Ribs." Journal of Geotechnical and Geoenvironmental Engineering, ASCE, January, Vol. 133, No. 1, pp. 37–50.

TenCate Geosynthetics (2015). Mirafi® HP570 Specifications. Nicolon Corporation.

Tensar North American Green (2001). The Mesa Systems Bridge Commerce in North Vancouver, B.C. Tensar North American Green.

Terzaghi K. (1936). “Stress distribution in dry and in saturated sand above a yielding trap-door.” Proc. of 1st int. conference on soil mechanics & foundation engineering. Cambridge, MA.

Terzaghi, K. & Peck, R.B. (1967). Soil mechanics in engineering practice. 2nd edition, John Wiley & Sons, Inc.

Thamm, B.R., Krieger, B., and Krieger, J. (1990). “Fullscale Test on Geotextile Reinforced Retaining Structure.” Proceedings of the 4th International Conference on Geotextiles, Geomembranes and Related Products, Hague, The Netherlands, Vol. 1, pp. 3-8.

The American Association of State Highway and Transportation Officials (2014). AASHTO LRFD Bridge Design Specifications. Seventh Edition, 2014.

Thomas, T.W., White, T.D., and Kuczek, T. (1994). "Siliceous content determination of sands using automatic image analysis." Transportation Research Record 1437, pp. 51–58.

Tzong, W.H. and Cheng-Kuang, S. (1987). "Soil-Geotextile Interaction Mechanism in Pullout Test." Proceedings of Geosynthetics 1987, Vol. 1, New Orleans, LA, pp. 250-259.

Vafaeian, M. and Abbaszadeh, R. (2006). “Laboratory Small Scale Tests to Study the Behaviour of Reinforced Soil Wall.” Proceedings of 8th International Conference on Geosynthetics, Kuwano, J., Kuseki, J. (eds.), Millpress Science, Rotterdam, Vol. 4, pp. 1409-1412.

Van Duijnen, P.G., Linthof, T., Brok, C.A.J.M., and Eekelen, S.J.M. (2012). “Measuring deformations of a 10 m high geosynthetic-reinforced earth retaining wall.” Proceedings of the 5th European Geosynthetics Congress. Valencia, 2012. Proceedings Vol 5. Topic: Soil Improvement and Reinforcement, pp. 157-161.

Vennapusa, P., White, D.J., Klaiber, F.W., Wang, S., and Gieselman, H. (2012). Geosynthetic-reinforced soil for low-volume bridge abutments. Report No. IHRB Project TR-621, Iowa Highway Research Board and Iowa Department of Transportation. 114p.

Vennapusa, P.K., White, D.J., and Keierleber, B. (2014). A Case Study of Geosynthetic-Reinforced Soil in a Low-Volume Bridge Abutment in Iowa. Geo-Congress 2014 Technical Papers Geo-characterization and Modeling for Sustainability. February 2014, pp. 4156-4166.

Viratjandre, C. (2000). “Shear strength of tire shred sand mixture.” Master of Philosophy Thesis, University of Colorado, Boulder, Colorado, USA.

Viswanadham, B.V.S. and König, D. (2004). “Studies on Scaling and Instrumentation of a Geogrid.” Geotextiles and Geomembranes, Vol. 22, No. 5, pp. 307-328.

Viswanadham, B.V.S. and Mahajan, R.R. (2007). “Centrifuge Model Tests on Geotextile-reinforced Slopes.” Geosynthetics International, Vol. 4, No. 6, pp. 365-379.

Wadey, L., and Idrees, M. (2014). Nadahini Creek Geosynthetic-reinforced Soil Integrated Bridge System. In Transportation 2014: Past, Present, Future-2014 Conference and Exhibition of the Transportation Association of Canada//Transport 2014: Du passé vers l'avenir-2014 Congrès et Exposition de'Association des transports du Canada.

Wakabayashi, T. (1950). "Photo-Elastic Method for Determination of Stress in Powdered Mass." Journal of the Physical Society of Japan, Vol. 5, No. 5, pp. 383–385.

Walters, D.A. (1995). Fracturing in Oil Sands. M.Sc. thesis, Department of Civil Engineering, The University of Calgary, Calgary, Alta.

Warren, K. A., Schlatter, W., Adams, M., Stabile, T., and LeGrand, D. (2010). “Preliminary Results for a GRS Integrated Bridge System Supporting a Large Single Span Bridge.” Proceedings of Earth Retention Conference 3, ASCE, Reston, VA, pp. 612-619.

Warren, K. A., Whelan, M. J., Hite, J., and Adams, M. (2014). “Three-Year Evaluation of Thermally Induced Strain and Corresponding Lateral End Pressures for a GRS IBS in Ohio.” In Geo-Congress 2014 Technical Papers Geo-characterization and Modeling for Sustainability. February 2014, pp. 4238-4251.

Warren, K.A., Whelan, M., Adams, M., and Nicks, J. (2013). “Preliminary Evaluation of Thermally Induced Strains and Pressured Developed in GRS Integrated Bridge System.” Geosynthetics Conference, Long Beach, CA.

Werner, G., and Resl, S. (1986). “Stability mechanisms in geotextile reinforced earth-structures.” In III International Conference on Geotextiles, Vienna, Austria, Vol. 4, pp. 1131-1135.

White, D.J., Take, W.A. and Bolton, M.D. 2003. "Soil Deformation Measurement Using Particle Image Velocimetry (PIV) and Photogrammetry." Geotechnique, Vol. 53, No. 7, pp. 619–631.

Wibowo, R. (1996). Bioremediation and Fracturing in Soil. M.Sc. thesis, Department of Civil Engineering, The University of Calgary, Calgary, Alta.

Wichter, L., Risseeuw, P., and Gay, G. (1986). “Large Scale Test on Bearing Behaviour of a Woven Reinforced Earth.” Proceedings of 3rd International Conference on Geotextiles, Vienna, Austria, pp. 1073-1078.

Williams, N.D. and Houlihan, M.F. (1987). "Evaluation of Interface Friction Properties between Geosynthetics and Soils." Proceedings of Geosynthetics 1987, Vol. 2, New Orleans, LA, pp. 616-627.

Won, G.W., Hull, T., De Ambrosis, L. (1996). “Performance of a geosynthetic segmental block wall structure to support bridge abutments.” In: Ochiai, H., Yasufuku, N., Omine, K. (Eds.), Earth Reinforcement, Vol. 1. A. A. Balkema Publisher, Rotterdam, pp. 543–548.

Wong, R. (1999). "Mobilized strength components of athabasca oil sand in triaxial compression." Canadian Geotechnical Journal, Vol. 36, No. 4, pp. 718–735.

Woodruff, R. (2003). Centrifuge modeling for MSE-shoring composite walls. MS Thesis, University of Colorado, Boulder, CO, USA.

Wright, S.G. and Duncan, J.M. (1991). “Limit Equilibrium Stability Analyses for Reinforced Slopes.” Transportation Research Record, No. 1330, pp. 40–46.

Wu, J., Pham, T.Q., and Adams, M. (2013). Composite Behavior of Geosynthetic-Reinforced Soil (GRS) Mass. Report No. FHWA-HRT-10-077, Federal Highway Administration, McLean, VA.

Wu, J.T.H. (2001). Revising the AASHTO Guidelines for Design and Construction of GRS Walls. Report No. CDOT-DTD-R-2001-16, Colorado Department of Transportation, 148 p.

Wu, J.T.H. (2006). Design and construction guidelines for geosynthetic-reinforced soil bridge abutments with a flexible facing (No. 556). Transportation Research Board.

Wu, J.T.H. and Helwany, S.M.B. (1996). "A Performance Test for Assessment of Long-Term Creep Behavior of Soil-Geosynthetic Composites." Geosynthetic International, Vol. 3, No. 1, pp. 107-124.

Wu, J.T.H., Ketchart, K., and Adams, M. (2001). GRS bridge piers and abutments. Report No. FHWA-RD-00- 038. Federal Highway Administration, US Department of Transportation, Washington, D.C. 136p.

Wu, J.T.H., Lee, K., Helwany, S., and Ketchart, K. (2006). Design and Construction Guidelines for Geosynthetic-Reinforced Soil Bridge Abutments with a Flexible Facing System. NCHRP Report 556, Project 12-59, National Cooperative Highway Research Program, Transportation Research Board, National Research Council, Washington, DC.

Wu, J.T.H., Lee, K.Z.Z., Helwany, S.B., and Ketchart, K. (2006). Design and Construction Guidelines for Geosynthetic-Reinforced Soil Bridge Abutments with a Flexible Facing. Report No. 556, National Cooperative Highway Research Program, Washington, DC.

Xiao, C., Han, J., and Zhang, Z. (2016). “Experimental Study on Performance of Geosynthetic-reinforced Soil Model Walls on Rigid Foundations Subjected to Static Footing Loading.” Geotextiles and Geomembranes, Vol. 44, No. 1, pp. 81-94.

Yamauchi, H. and Tatsuoka, F., Nakamura, K., Tamura, Y. and Iwasaki, K. (1987). "Stability of Steep Slope Clay Embankments ReinforcedWith a Non-WovenGeotextile," Proceedings of the Post Vienna Conference on Geotextiles, Singapore, pp. 370-386.

Yang, K.-H., Kniss, K.K., Zornberg, J.G., and Wright, S.G. (2008). "Finite-Element Analyses for Centrifuge Modeling of Narrow MSE Walls." Proceedings of the First Pan American Geosynthetics Conference, GEOAMERICAS-2008 (CD-ROM), International Fabrics Association Int., Rosevile, MN, USA, pp. 1246–1255.

Yang, K.H., Zornberg, J.G., Hung, W.Y., and Lawson, C.R. (2011). "Location of Failure Plane and Design Considerations for Narrow Geosynthetic Reinforced Soil Wall Systems." Journal of GeoEngineering, Vol. 6, No. 1, pp. 27-40.

Yang, Z. (1972). Strength and Deformation Characteristics of Reinforced Sand, PhD. Thesis, University of California at Los Angeles, Los Angeles, CA.

Yang, Z. and Singh, A. (1974). Strength and Deformation Characteristics of Reinforced Sand, International Meeting on Water Resources Engineering, Los Angeles, CA.

Yuan, Z. and Chua, K.M. (1991). "Numerical Evaluation of the Pullout Box Method for Studying Soil-Reinforcement Interaction." Transportation Research Record 1278, Transportation Research Board, Washington, D.C., pp. 116-124.

Zhang, W., Lai, Z., and Xu, G. (2002). "Centrifuge Model Tests of Geosynthetics Reinforced Retaining Walls." Proceedings of the International Conference on Physical Modelling in Geomechanics: ICPMG '02, Philips, Guo, and Popescu (eds.), pp. 999-1004.

Zhao, H. and Ge, L. (2010). Camera Calibration Using Neural Networks. Appendix in Moddeling with Transparent Soils by Magued Iskander, Springer, pp.299–312.

Zheng, Y., Fox, P.J., and Shing, P.B. (2015). "Verification of Numerical Model for Static Analysis of Geosynthetic Reinforced Soil Bridge Abutments." Proceedings Conference on Geosynthetics, pp. 152-160.

Zhou, J., Chen, Chen, J.-F., Xue, J.-F., and Wang, J.-Q. (2012). "Micro-Mechanism of the Interaction between Sand and Geogrid Transverse Ribs." Geosynthetics International, 2012, Vol. 19, No. 6, pp. 1072-6349.

Ziegler, M., Heerten, G., and Ruiken. G. (2008). "Progress in the Understanding of Geosynthetic/Soil Composite Material Behaviour in Geosynthetic-reinforced Earth Structures," Presented at The First Pan American Geosynthetics Conference and Exhibition, Cancun, Mexico.

Zornberg, J.G. (1994). Performance of Geotextile-reinforced Soil Structures. Ph.D. Dissertation, University of California, Berkeley, CA, USA.

Zornberg, J. G. (2002). “Peak versus Residual Shear Strength in Geosynthetic-reinforced Soil Design.” Geosynthetics International, Vol. 9, No. 4, pp. 301-318.

Zornberg, J.G. (2015). “Performance of a Geosynthetic-reinforced Bridge Abutment in the US.” Proceedings of the 2nd International GSI-Asia Geosynthetics Conference (GSI-Asia 2015), Seoul, Korea (Rep.), June 24-26, 2015.

Zornberg, J.G. and Arriaga, F. (2003). “Strain Distribution within Geosynthetic Reinforced Slopes.” Journal of Geotechnical and Geoenvironmental Engineering, Vol. 129, No. 1, pp. 32-45.

Zornberg, J.G. and Mitchell, J.K. (1994). "Reinforced Soil Structures with Poorly Draining Backfills. Part I: Reinforcement Interactions and Functions." Geosynthetics International, Vol. 1, No. 2, pp. 103-147.

Zornberg, J.G., Abu-Hejleh, N., and Wang, T. (2001). “Geosynthetic-reinforced Soil Bridge Abutments.” Geotechnical Fabrics Report, Vol. 19, No. 2, pp. 52-55.

Zornberg, J.G., Ferreira, J.A.Z. and Roodi, G.H. (2012). Experimental Results on Soil-Geosynthetic Interaction Stiffness. Center for Transportation Research (CTR), Report No. FHWA/TX-12/5-4829-01-3, Austin, Texas, September 2012, 232 p.

Zornberg, J.G., Ferreira, J.A.Z. and Roodi, G.H. (2013). Geosynthetic-reinforced Unbound Base Courses: Quantification of the Reinforcement Benefits. Center for Transportation Research (CTR), Report No. FHWA/TX-12/5-4829-01-2, Austin, Texas, August 2013, 757 p.

Zornberg, J.G., Ferreira, J.A.Z., Gupta, R.V., Joshi, R.V., and Roodi, G.H. (2009). Geosynthetic-Reinforced Unbound Base Courses: Quantification of the Reinforcement Benefits. Center for Transportation Research (CTR), Report No. FHWA/TX-10/5-4829-1, Austin, Texas, December 2009, Revised February 2012, 170 p.

Zornberg, J.G., Mitchell, J.K., and Sitar, N. (1997). “Testing of Reinforced Slopes in a Geotechnical Centrifuge.” Geotechnical Testing Journal, Vol. 20, No. 4, pp. 470-480.

Zornberg, J.G., Prozzi, J.A., Gupta, R., Luo, R., McCartney, J.S., Ferreira, J.Z. and Nogueira, C. (2008). Validating Mechanisms in Geosynthetic Reinforced Pavements. Center for Transportation Research (CTR), Report No. 0-4829-1, Austin, Texas, February 2008.

Zornberg, J.G., Roodi, G.H., Ferreira, J.Z., and Gupta, R. (2013). "Characterization of Soil-geosynthetic Interaction under Small Displacement Conditions." Proceedings of the 18th International Conference on Soil Mechanics and Geotechnical Engineering, 02-06 September, Paris, France, pp. 1385-1388.

Zornberg, J.G., Sitar, N., and Mitchell, J.K. (1998). "Limit Equilibrium as Basis for Design of Geosynthetic Reinforced Slopes." Journal of Geotechnical and Geoenvironmental Engineering, ASCE, Vol. 124, No. 8, pp. 684–698.

Zornberg, J.G., Sitar, N., and Mitchell, J.K. (1998a). “Performance of Geosynthetic Reinforced Slopes at Failure.” Journal of Geotechnical and Geoenvironmental Engineering, Vol. 124, No. 8, pp. 670-683.

Vita

Amr Mohamed Morsy was born in Cairo, Egypt on August 30, 1989, to his parents Mohamed Morsy and Hoda Thakeb. He has an elder brother Karim Morsy. Amr enrolled at Cairo University in September 2006 where he received his Bachelor of Science in Civil Engineering with first-class highest honors in July 2011. He started his graduate studies at Cairo University in September 2011 and earned his Master of Science in Civil Engineering with focus on Geotechnical Engineering in July 2013. In August 2013, Amr began his doctoral studies in Civil Engineering at the University of Texas at Austin.

Email address: amr.morsy@utexas.edu

This dissertation was typed by the author.